# THE EFFECT OF DEVONIAN METAMORPHISM AND METASOMATISM ON THE MINERALOGY AND GEOCHEMISTRY OF THE CAMBRIAN VMS DEPOSITS IN THE ROSEBERY-HERCULES DISTRICT, WESTERN TASMANIA

by

**Khin Zaw**

BSc (Rangoon University, Burma), MSc (Queen's University, Canada)

Submitted in fulfilment of the requirements
for the degree of Doctor of Philosophy

University of Tasmania
Hobart

1991

This thesis contains the results of research done in the Geology Department, University of Tasmania from June 1986 to June 1991. It contains no material which has been accepted for the award of any other degree or diploma in any university and, to the best of my knowledge and belief, contains no copy or paraphrase of material previously published or written by another person, except where due reference is made.

Khin Zaw

University of Tasmania
June 1991

# CONTENTS

page

## CHAPTER 9: STABLE ISOTOPE GEOCHEMISTRY



## CHAPTER 10: FLUID INCLUSION STUDIES

page

**CHAPTER 11: DISCUSSION OF CAMBRIAN VMS MINERALISATION, DEVONIAN OVERPRINT AND EXPLORATION IMPLICATIONS**

# List of Figures

## LIST OF TABLES

# ACKNOWLEDGEMENTS

I would like to thank my supervisor Dr R. R. Large, Director, Centre for Ore Deposit and Exploration Studies (CODES), for suggesting the initial research programme and for his inspiration and excellent advice on various aspects of the project, his patient guidance, support, enthusiasm, encouragement and constructive comments throughout all stages of this thesis.

I am deeply indebted to Marlene Large for helping my family to settle in Hobart during the cold and unfriendly Tasmanian winter of 1986.

The author thanks the University of Tasmania for financial support through a University of Tasmania Postgraduate Research Award. I am grateful to the Pasminco Mining Company (formerly Electrolytic Zinc Company of Australasia) for logistical support and for providing accommodation, transportation and much other assistance during my field work at the Rosebery mine.

The author wishes to thank the present staff and student members of CODES which includes Ron Berry, Garry Davidson, Bruce Gemmell, Dave Huston, Jocelyn McPhie, Joe Stolz, Kim Hein, Anthea Hill, Paul Kitto, Michael Roach, and also previous members (Sharon Adrichem, Ian Gordon, Steve Hunns, Greg Jenkins, Peter McGoldrick, Mark Rattenbury, Oliver Raymond, Peter Ruxton, and Richard Wedekind) for providing much critical and constructive advice and comment on the author's studies.

The author would like to thank geologists from Pasminco Company — Jim Farquhar, Fergus Fitzgerald, Geoff Iliff, Steve Hunns, Colin Lutherborrow, Russell Penney, Gerald Purvis, Mike Quayle and Paul Reid — for their discussion and interaction during the studies at the Rosebery mine. The author also benefited by discussions with Peter Legge,Terry Lees, John Howarth, Ian Matheson, Peter Rice, and Rod Sainty (formerly of Electrolytic Zinc Company). Sincere gratitude is extended to Dave Page of Pasminco for helping me to plot the diamond drill hole assay data on the cross-sections by "Prime" computer at Rosebery. I am indebted to Dr Ron Berry of CODES and Domingo Aerden of James Cook University for discussions of the structural relationships of the Rosebery–Hercules deposits.

The author greatly appreciates Dave Huston for reading the first version of each chapter and for his suggestions to improve the presentation. The author also wishes to thank various staff members of the Tasmanian Department of Mines and Energy; in particular to Dr Geoff

Green who read and helped to improve the stable isotope chapter and gave other advice and help on various aspects of the project.

Thanks are extended to many people who have assisted me during the research project.
— June Pongratz helped greatly by formating the thesis layout by the Pagemaker program and drafting many of the diagrams in the thesis;
— Mike Power Sr and Mike Power Jr for their introduction and help on the isotope lines;
— Wieslaw Jablonski for instruction on the operation of the electron microprobe and scanning electron microscope;
— Simon Stevens for his help in making thin-sections and polished thin-sections, and polishing probe mounts;
— Phillip Robinson and Nilar Hlaing for their assistance in the analytical work;
— Christine Higgins, Jeanette Hankin, Peter Cornish and Andrew Gillion for their general support;
— various staff members fo the Geology Department for their fruitful discussions and moral support, including Professor D. H. Green, Drs Rick Varne, Clive Burrett, Tony Crawford, Trevor Falloon, Russell Sweeny, Steve Eggins, Christian Ballhaus and the late Dr Ramsay Ford.

Special thanks are due to Jocelyn McPhie and June Pongratz for detailed proof reading and suggestions which substantially improved the final version of the thesis.

The author is indebted to the other graduate students of the Geology Department for their hospitality, companionship, support and encouragement; particularly to Yuenyong Panjasawatwong, Massimo Gasparon, Geoff Nichol, Michael Seitz, Ruth Lanyon, Baharuddin, Udi Hortono, Salman Palgunady, Thanis Wongwanich, Ai Yang, Pol Choadumrong, Sjafra Dwipa, Djojomihardjo Soetijos, Memet Rahmat Hermanto, Vanessa Guthrie, Greg Yaxley, Sampan Singharajwarpan, Ingvar Sigurdsson, and to all members of the Geology Department not already mentioned for their help and for providing a pleasant working environment.

The author also would like to thank Dr Terry Mernagh of Bureau of Mineral Resources, Canberra for helping with the Laser Raman spectroscopic analysis of fluid inclusions.

Finally, the author wishes to thank his wife Nilar Hlaing and two sons, Zin Aung Zaw (Pho Tha) and Aung Pye Zaw (Pho Khwa) for all their support and sacrifice to finish this thesis. The inordinate length of time spent in the Geology Department during this study will now be spent with them.

# ABSTRACT

The Rosebery, Hercules and South Hercules deposits in western Tasmania are composed of polymetallic massive to disseminated sulphide mineralisation hosted in felsic volcanics of the Cambrian Mt Read Volcanic belt. The deposits have been affected by regional metamorphism of upper greenschist facies and associated tectonic deformation related to the Devonian Tabberabberan Orogeny. The Devonian tectonic movement has resulted in folding, shearing and faulting (thrusting) of the ore lenses which caused significant changes in the overall configuration of the original stratiform ores and underlying stringer zones. In addition, the south-end of the Rosebery deposit has undergone metasomatic replacement related to a post-orogenic Devonian granite intrusion.

The VMS mineralisation at Rosebery consists of three primary sulphide–sulphate zones: lowermost pyrite–chalcopyrite zone (>4% Cu), overlain by a sphalerite–galena ± pyrite ± chalcopyrite zone, and followed by an uppermost massive barite zone. The south-end of the orebody has been overprinted by Devonian transgressive metasomatic mineral assemblages. Three major replacement zones can be distinguished: (1) magnetite–biotite ± chalcopyrite zone, (2) pyrrhotite–pyrite zone and, (3) tourmaline–quartz ± magnetite zone. Other metasomatic minerals such as fluorite, garnet and helvite are present.

The main Hercules deposit occurs 10 km south along strike from Rosebery and lies in a similar tuffaceous shale unit. The deposit consists of a number of disconnected stratabound Zn–Pb–Cu–Ag–Au ore lenses with similar metal distribution and alteration features to the Rosebery ores. The Hercules deposit shows a zonation from a massive to disseminated pyrite–chalcopyrite zone (>4% Cu) at the footwall through a massive sphalerite–galena ± pyrite zone and spotty sphalerite–galena ± pyrite zone to a carbonate ± barite zone at the top. The South Hercules deposit is located about one kilometer south of the main Hercules ore lenses at the same stratigraphic level. The deposit displays comparable mineralogical zonation with Rosebery and Hercules but contains low-grade lead and zinc, and has a low copper content (<1 wt % Cu) and relatively high (Au+Ag)/(Pb+Zn) ratio. The deposit consists of a disseminated to stringer sulphide zone with variably altered carbonate assemblages.

Metal zonation studies indicate that zinc occurs dominantly as blanket-like enrichment in the Rosebery district deposits and silver broadly follows zinc. Gold is largely concentrated at the top of the ore lenses. In the transgressive pyrrhotite–pyrite replacement zone of the Rosebery south-end, zinc is conspicuously depleted but gold values of more than 20 g/t Au are noted. In contrast, the other biotite-, magnetite-, and tourmaline-bearing replacement zones contain low gold grades (generally less than 5.0 g/t Au). Like zinc, silver is also depleted in the replacement zones but a significant amount of copper is present. Copper values as high as 2% are observed in the biotite–magnetite zone as well as the pyrrhotite–pyrite zone. This indicates that although zinc and silver were dissolved and removed during the Devonian replacement event, gold and copper appear to have been redistributed and recrystallised.

A detailed mineralogical study of gold in the F(J) lens indicates that the gold occurs as electrum inclusions in pyrite, as individual electrum grains in pyrrhotite, and in chalcopyrite veins cutting pyrrhotite. Similar mineragraphic investigations at Hercules and South Hercules show that gold occurs as individual electrum grains locked in the pyrite, and as patches or blebs in the remobilised and recrystallised sphalerite, galena and tetrahedrite. The Devonian metamorphic and metasomatic processes resulted in significant recrystallisation and remobilisation of these gold grains as indicated by their texture, grain size, and fineness variation.

The Devonian overprinting processes also resulted in the redistribution of FeS in sphalerites from the Rosebery district deposits. The sphalerite–hexagonal pyrrhotite–pyrite assemblages from the Rosebery south-end were used to apply the sphalerite geobarometer to estimate the pressure conditions during the Devonian replacement process. The estimated pressure is 3.0 ± 0.5 kb for the requilibration of sphalerite in the F(J) lens which would correspond to a depth of 8.0 ± 1.0 km. The correlation of the mole % FeS in sphalerite and the gold grades at the Rosebery, Hercules and South Hercules deposits displays complex patterns owing either to later Devonian metamorphic and metasomatic recrystallistion or to variation of the initial depositional conditions.

The VMS carbonates from both north- and south-ends of the Rosebery deposit display tightly constrained and similar isotopic patterns. The isotopic patterns imply that no later isotopic changes have taken place although the south-end of the Rosebery deposit was strongly overprinted by the high temperature (>300°C), pervasive Devonian replacement process. The $\delta^{18}O$ values of biotite and magnetite from the F(J) lens replacement zone were used to calculate the oxygen isotopic composition of the Devonian hydrothermal fluid. The calculated $\delta^{18}O(H_2O)$ values for the overprinting Devonian hydrothermal fluid vary from 8.0‰ to 12.0‰ and are consistent with a magmatic fluid.

Detailed sulphur isotopic investigations on the hand specimen scale indicate that there are no obvious $\delta^{34}S$ variations between the lead–zinc lenses of Cambrian volcanogenic origin and the pyrrhotite–pyrite assemblages of Devonian origin. The sulphur isotope values of the sulphide minerals from the South Hercules deposit range from $\delta^{34}S$ values of 8.2‰ to 14.1‰ and the calculated $\delta^{34}H_2S$ values in the ore fluids display a permissible correlation with gold grades. This correlation suggests the possibility of using the sulphur isotopic composition as a guide to assist in targeting the gold-rich sections of massive sulphide systems.

Fluid inclusion studies indicate that early formed low-temperature (ca. 200°C), low-salinity (<5 NaCl equiv. wt %) Type I inclusions with no appreciable $CO_2$ may be interpreted as primary, Cambrian exhalative fluids that have survived the Devonian recrystallisation. Fluid inclusion characteristics of necking down and healed microfractures together with trapped carbonate and barite daughter minerals identified by laser Raman spectroscopy suggest an extensive remobilisation and recrystallisation of carbonate minerals during the Devonian overprinting processes, which corroborates with the redistribution and recrystallisation of primary Cambrian sulphides (e.g. sphalerite) and gold, during Devonian metamorphic and metasomatic processes.

Although the VMS deposits in the Rosebery–Hercules area display no evidence for large-scale chemical remobilisation of ore constituents during metamorphism, the post-orogenic Devonian granite intrusion below the south-end of the Rosebery mine resulted in chemical remobilisation of the ore lenses. The early replacement assemblages in the F(J) lens formed from interaction of moderate to high temperature (≥ 330°C), saline (≥20 NaCl equiv. wt %) fluid with the original lead–zinc mineralisation. The later stage tourmaline veining and associated replacement assemblages resulted from lower temperature (≤ 300°C), less saline (≤20 NaCl equiv. wt %) fluid. During the Devonian metasomatic event gold may have been remobilised and recrystallised either as $Au(HS)_2^-$ or $AuCl_2^-$ complexes but the high temperature and salinity conditions favour the $AuCl_2^-$ complex. Copper also appears to have been recrystallised during the replacement process with minor remobilisation. In comparison to copper and gold, zinc, lead and silver have been dissolved and removed as the very soluble chloride complexes.

# CHAPTER 1: INTRODUCTION

## 1.1 INTRODUCTION ...

This research has involved investigation of the three separate areas of volcanic-hosted mineralisation in western Tasmania:

(1) F(J) lens of the Rosebery mine;

(2) J(K)-P and R lens of the Hercules mine; and

(3) the newly discovered South Hercules deposit.

The Rosebery, Hercules and South Hercules deposits are located about 125 km by road south of Burnie (Fig. 1.1). The Rosebery township nestles at the foot of Mt Black, and the Rosebery orebody dips eastwards under the mountain. The Hercules mine is situated some 7 km south of Rosebery, on the western side of Mt Hamilton and the South Hercules deposit lies 1 km along strike south of the main Hercules ore lenses.

## 1.2 AIMS OF THIS STUDY ...

The primary objective of this study was to determine the effect of Devonian metamorphism and metasomatism on the mineralogy and geochemistry of the Cambrian VMS deposits in the Rosebery–Hercules area. In order to achieve that objective, a research programme was developed with the following aims:

(1) to describe mineralogical zonation and base and precious metal distribution in F(J) lens, Rosebery mine, J(K)-P lens of Hercules mine and the South Hercules deposit;

(2) to study the detailed paragenesis, geochemistry and origin of the unusual magnetite and pyrrhotite bearing mineral assemblages in the F(J) lens of the Rosebery deposit;

(3) to undertake detailed mineralogical and geochemical studies of precious minerals in F(J) lens, Rosebery mine, J(K)-P and R lens of Hercules mine and the South Hercules deposit with particular emphasis on the remobilisation and recrystallisation of gold during the metasomatism and controls on the precious metal deposition and redistribution;

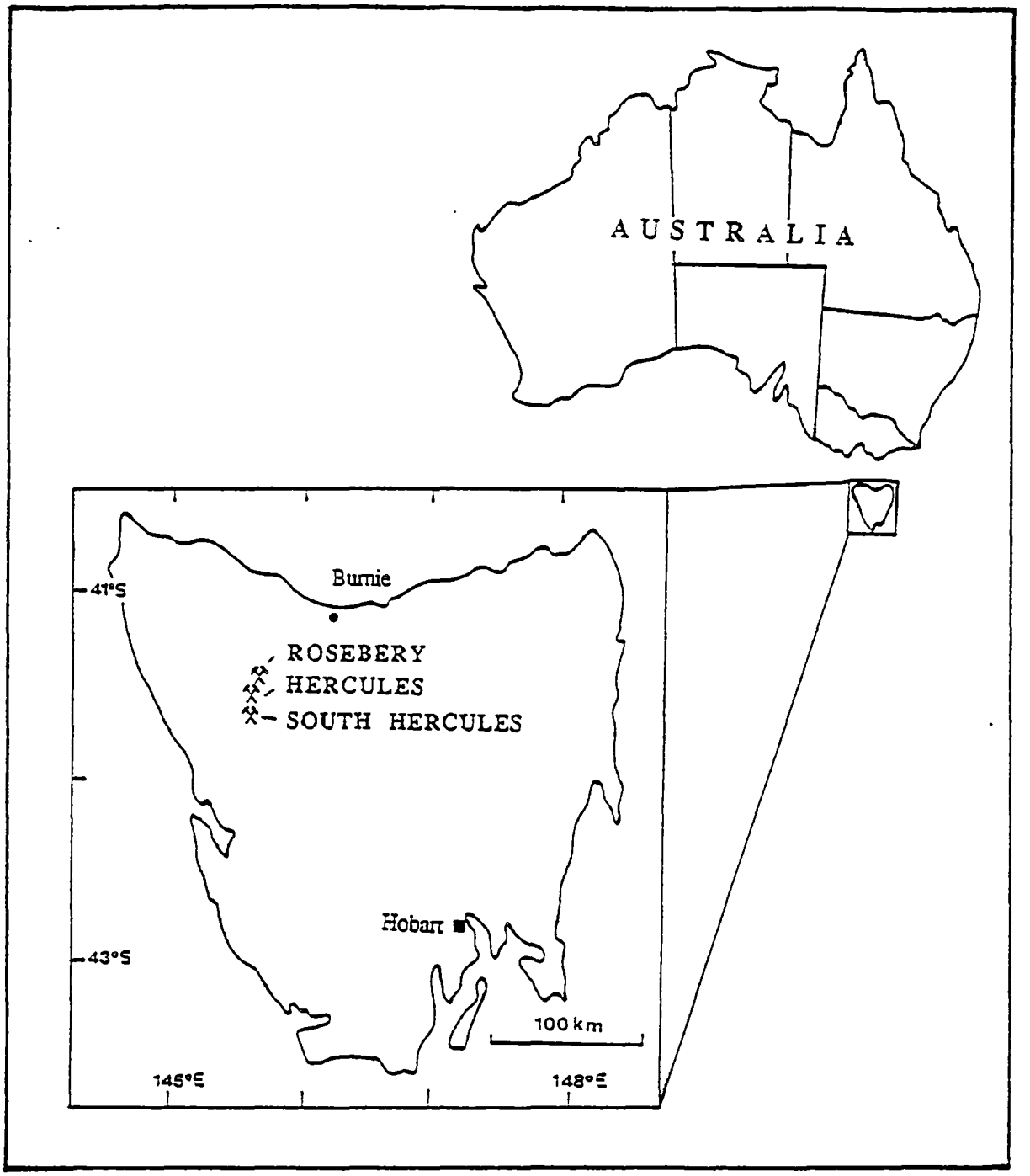


Fig. 1.1 Location map of the Rosebery, Hercules and South Hercules deposits, western Tasmania.

(4) to determine ore fluid sources for the three deposits and to evaluate fluid–rock interaction during ore formation and later recrystallisation and deformation in the Devonian using stable isotopes and fluid inclusion techniques; and

(5) to relate the results of this research to the development of improved mineral exploration and mineral beneficiation techniques, particularly as they relate to the gold resource in each deposit.

## 1.3 METHODS OF STUDY ...

The following methods of investigation have been used to achieve the aforementioned aims:

(1) detailed core logging of and sample collection from diamond drill holes (DDH) on selected E–W cross-sections;

(2) sample collection and geological examination in the accessible underground mine workings and exposures;

(3) construction of contoured assay cross-sections to understand the distribution of the base and precious metals and their inter-elemental variation and relationships;

(4) mineralogical and textural studies of the collected samples using thin sections, doubly polished thin sections and polished rock slabs;

(5) electron microprobe analysis to determine the compositional variation of replacement assemblages such as garnet, helvite, biotite and tourmaline in the F(J) lens at Rosebery mine and also gold and other ore minerals (e.g. sphalerite) from all three areas of mineralisation (Rosebery, Hercules and South Hercules);

(6) oxygen isotope analysis of the individual minerals (quartz, chlorite, biotite and tourmaline) and C and O isotope determination of the carbonate minerals in conjunction with fluid inclusion studies to evaluate the fluid-rock interaction and the source and/or sources of the ore fluids;

(7) atomic absorption spectrophotometric analysis of the carbonate samples to interpret the effect of minor elements on the C and O isotopic fractionation;

(8) sulphur isotope analysis of the sulphide minerals from the F(J) lens of the Rosebery mine and South Hercules deposit to apply in the interpretation of the source of the mineralising fluids; and

(9) fluid inclusion study of ore and gangue minerals by means of a USGS heating/freezing stage to determine the temperature and salinity of the ore forming fluids and physico-chemical conditions of ore deposition.

## 1.4 FIELD WORK ...

The author spent altogether twelve weeks at the Rosebery mine-site in 1986–87 and undertook detailed core logging and sample collection of DDH from the Rosebery deposit together with a detailed underground geological investigation and sampling along 15 Level, 16 Level, 17 Level and 18 Level including the sub-levels of the Rosebery mine. The author concentrated the field investigation on the Rosebery deposit and mostly sampled the drill cores from DDH collared in the F(J) lens of the Rosebery orebody.

The author also spent another eight weeks at the Rosebery mine-site in 1987–88 and undertook detailed core logging and sample collection of DDH from the Hercules and South Hercules deposits. Underground mine workings of the main Hercules mine can no longer be investigated as the mine has been closed-down since 1986. The South Hercules deposit is at the prospect stage and investigation of these deposits relied on diamond drill cores. More than 45 DDH with a total of about 3000 m of drill core were investigated in detail in this study.

# CHAPTER 2: GEOLOGY OF THE ROSEBERY MINE

## 2.1 INTRODUCTION ...

The stratigraphic and metallogenic relationships of the Rosebery–Hercules area as well as the Mt Read Volcanic sequence in western Tasmania have been extensively studied in recent years (e.g. Corbett, 1981; Corbett and Lees, 1987; Corbett et al., 1989) and hence in this chapter, only the important geological relationships of the Rosebery deposit that relate directly to this programme of research will be presented and discussed.

## 2.2 PREVIOUS STUDIES ...

The Rosebery, Hercules and South Hercules deposits are deformed stratiform polymetallic massive±disseminated sulphide ores of volcanogenic type and have been the subject of considerable research over the past twenty years. The Rosebery deposit has been most extensively studied by previous workers (e.g. Brathwaite, 1969, 1972, 1974; Eastoe, 1973; Smith, 1975; Dixon, 1980; Green et al., 1981; Green, 1983; Naschwitz, 1985; Huston and Large, 1988; Huston, 1989; Green and Iliff, 1989)

Several Pasminco Mining Company (formerly Electrolytic Zinc Company) geologists also variously contributed to the geology of the Rosebery–Hercules area in many unpublished reports. Sulphur isotopes on the Rosebery mine and other deposits in western Tasmania have also extensively been studied in the last few decades (e.g. Solomon et al., 1969; Green et al., 1981; Green, 1983; Eastoe et al., 1987; Solomon et al., 1988).

Other discussions on the general geological relationships of the Rosebery–Hercules area have been presented by many workers since the turn of this century (Hill, 1915a, b) and later (Finucane, 1932; Campana et al., 1958; Campana and King, 1963; Solomon, 1962, 1964, 1965, 1976, 1981; Hall et al., 1953, 1965; Loftus-Hills et al., 1967; Burton, 1975a, b; Adams et al., 1976), and more recently by Polya et al. (1986), Lees (1987), Corbett and Lees (1987), Corbett et al. (1989), Green (1990a) and Lees et al. (1990).

## 2.3 HISTORY AND PRODUCTION ...

The exploration history of the Rosebery–Hercules area dates back to 1891 when prospector A.E. Concliffe pegged ground over the Mt Read mine (subsequently part of the Hercules mine); three years later the main Hercules lenses were discovered by J. Will. Discovery of the Rosebery gossan is attributed to Tom McDonald, who in 1893 traced gold and sulphide boulders in Rosebery Creek to their source (Lees et al., 1990).

Limited production from the Rosebery and Hercules Mines, in the period 1900–1913, was railed for treatment to the Zeehan smelters but virtually ceased with their closure. The Electrolytic Zinc Company of Australasia Limited purchased the mines in the early 1920's, and completed a concentrating mill designed to selectively float and separate zinc from other economic minerals in 1929. Full production from both mines did not commence in earnest until after the depression years, in 1936.

Up to June 1991, the Rosebery deposit had yielded 15.5 million metric tonnes of ore grading 4.8 % Pb, 15.6 % Zn, 0.73 % Cu, 158 g/t Ag and 2.8 g/t Au and reserves are quoted as about 5.5 million metric tonnes of ore grading 3.6 % Pb, 11.3 % Zn, 0.5 % Cu, 124 g/t Ag and 2.4 g/t Au (Pers. comm., J. Faquhar, 1991).

## 2.4 REGIONAL GEOLOGY ...

The regional geological setting of western Tasmania is dominated by Cambrian volcano-sedimentary rocks of the Dundas Trough and Mt Read Volcanics (MRV) which occur between two Precambrian blocks (Corbett and Lees, 1987; Corbett et al., 1989). The Precambrian Tyennan Region occurs to the east and contains quartzites, schists and garnet amphibolites of medium- to high-grade metamorphic rocks, whereas the Precambrian Rocky Cape Region in the northwest consists of relatively unmetamorphosed, strongly folded sedimentary rocks (inset, Fig. 2.1; Corbett and Lees, 1987; Corbett et al., 1989).

The Rosebery, Hercules and South Hercules deposits are located within the Cambrian Mt Read Volcanic belt (Campana and King, 1963) which forms a longitudinal, arcuate belt at the eastern margin of Dundas Trough (Fig. 2.1). The Mt Read Volcanics also contain other massive sulphide orebodies at Hellyer, Que River and Mt Lyell.

The Mt Read Volcanics are predominantly rhyolites, dacites and andesites with minor basalts. Granitic bodies of probable subvolcanic type occur at Mt Murchison and Mt Darwin within the Mt Read Volcanic belt. Although these granitoid bodies are thought to be coeval with the Mt Read Volcanics, recent age determination by radiogenic isotopic investigation indicates that both granitoid plutons appear to be younger in absolute age than the associated volcanics (Adams et al., 1985). Corbett (1986) has attempted to subdivide the Mt Read Volcanics into three major groups; (1) the Western Volcano-sedimentary Sequence, (2) the

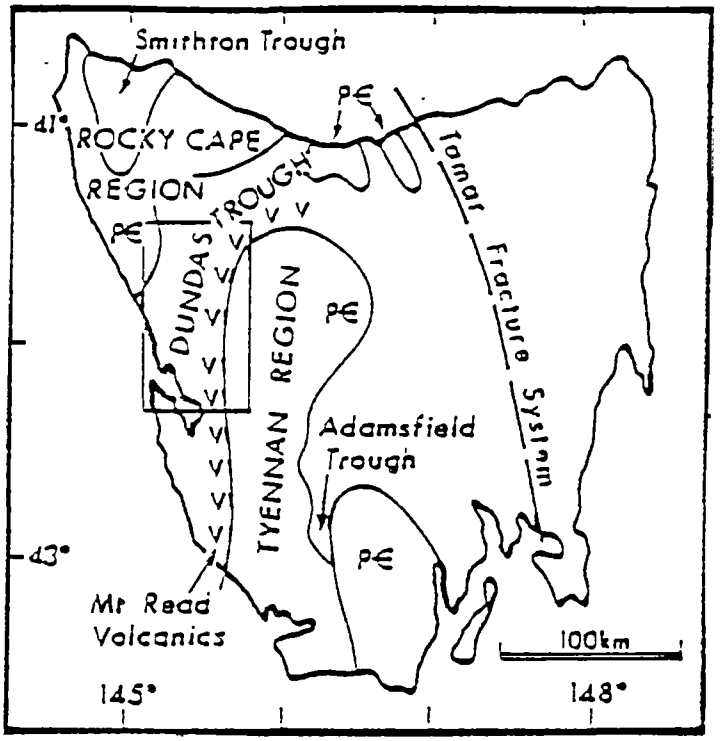


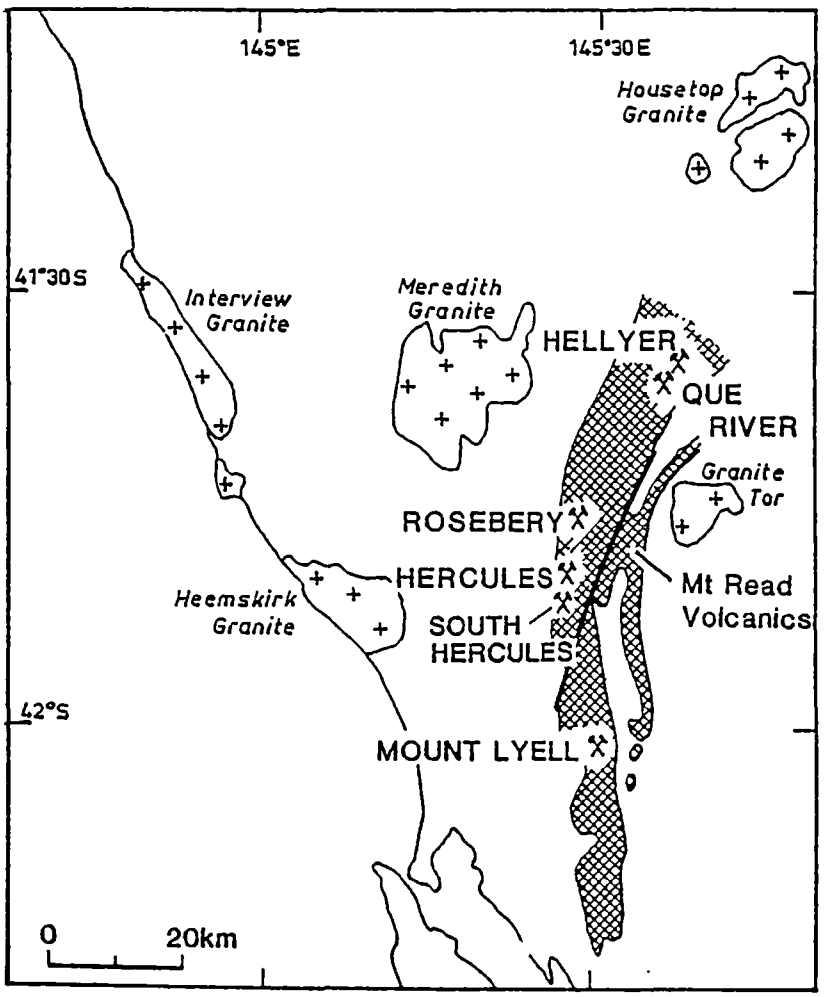


Fig. 2.1 Regional geological setting of the Rosebery, Hercules and South Hercules deposits, western Tasmania (after Corbett et al., 1989; Lees et al., 1990).

Central Volcanic Complex (CVC) and (3) the Tyndall Group. All significant base metal mineralisation in the Rosebery–Hercules area is located within the CVC.

The Henty Fault Zone (HFZ) is a NNE–SSW trending prominent structure in the Mt Read Volcanic Belt which bisects the CVC into two (northern and southern) segments. The HFZ was thought to be active during the Cambrian and reactivated in the Devonian and also shows dextral transcurrent movements (Berry, 1989). To the northwest of the HFZ, the CVC is overlain by a mixed volcanic and sedimentary sequence termed the Dundas Group (Corbett, 1986; Corbett and Lees, 1987) and to the east of the HFZ, the CVC is faulted against or overlain by the Tyndall Group (Corbett, 1986; Corbett and Lees, 1987).

The Mt Read Volcanics have undergone regional metamorphism and considerable deformation and have been intruded by granitoid plutons during the Devonian Tabberabberan Orogeny. The Devonian regional metamorphism had variable effects on the volcanogenic ores in the Mt Read Volcanics from prehnite–pumpellyite facies at the Hellyer and Que River deposits to middle to upper greenschist facies at the Rosebery, Hercules and South Hercules deposits (Corbett et al., 1989).

## 2.5 GEOLOGY OF ROSEBERY MINE ...

Comprehensive accounts of the geology of the Rosebery area have been given by many previous workers (e.g. Brathwaite, 1969, 1974; Burton, 1975a; Adams et al., 1976; Green et al., 1981; Green, 1983; Lees et al., 1990), and only the recent advances will be discussed here.

### 2.5.1 Stratigraphy ...

The major rock units in the Rosebery mine area are: (1) CVC, (2) Dundas Group and (3) Crimson Creek Formation (see Fig. 2.2). The CVC in the mine area is faulted against the sedimentary rock of Dundas Group and Crimson Creek Formation to the west by the Rosebery Fault which is a major east-dipping thrust fault. Recent drilling has shown the fault plane to extend some 400 m beneath the Rosebery orebody (Corbett and Lees, 1987).

The CVC can be subdivided into the following stratigraphic units at the Rosebery mine:

| | | |
|---|---|---|
| Top | Mt. Black volcanics (dacitic to andesitic lavas) | >1000 m |
| | Hangingwall epiclastics | 50–200 m |
| | Black slate | 0–30 m |
| | Host rock — tuffaceous shale | 35 m |
| Bottom | Footwall volcanics (feldspar-phyric ash flow tuffs) | >300 m |

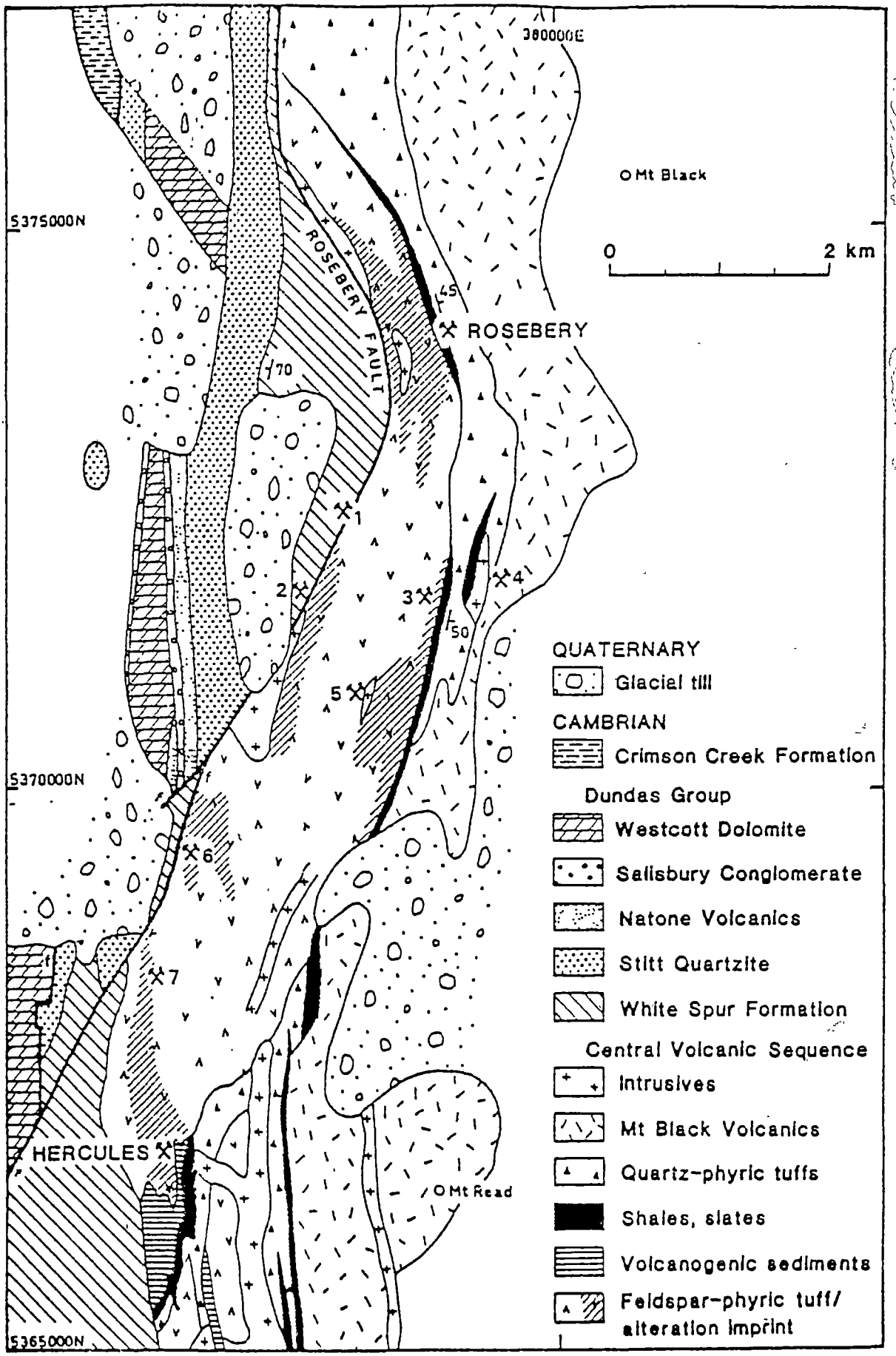


Fig. 2.2 Geology of the Rosebery area, western Tasmania. Prospects numbered are: 1 – Salisbury, 2 – Chamberlain, 3 – Rosebery lodes, 4 – Dalmeny, 5 – Koonya, 6 – Jupiter, 7 – Ring P.A. (after Lees et al., 1990).

The Rosebery deposit lies in a tuffaceous shale lens at the contact between the footwall volcanics and the hangingwall epiclastics. The footwall volcanics consist of feldspar-phyric, ashy, vitric to crystal-rich, tuffaceous rocks. The origin of these volcanics has been the subject of considerable controversy. Green et al. (1981) and Lees (1987) interpreted the footwall volcanics as subaerially erupted ignimbrites, whereas Allen and Cas (1990) consider them to be subaqueous mass flows. The footwall volcanics contain abundant altered "fiamme" and also exhibit a pumiceous texture. Immediately below the Rosebery ore horizon, this unit has been altered to quartz–sericite–chlorite schists. The contact between footwall volcanics and the host rock is often difficult to distinguish in the mine area due to the later hydrothermal alteration overprint.

The host rock is commonly siliceous and sericitic with disseminated pyrite, and in places it is strongly silicified. The host rock is locally chloritic and strongly sheared with recrystallised pyrite cubes up to 5 cm across, and is overlain by up to 30 m of pyritic black slate. The host rock and the overlying black slate are considered to represent a period of quiet sedimentation during ore deposition (Green et. al., 1981), but the black slate unit is absent in many places. Although the lack of the black slate unit above the host rock in the mine area particularly at the south-end of the mine can be accounted for by local sedimentary facies changes, the inclusion of black slate intraclasts in the hangingwall epiclastics unit (Brathwaite, 1974) suggests substantial erosion of the slate following ore deposition.

The hangingwall epiclastics consist of sericitised quartz-feldspar-phyric rocks. The presence of albite–chlorite–quartz–epidote mineral assemblages (Corbett and Lees, 1987) in the hangingwall epiclastics indicates lower greenschist metamorphic effects. The hangingwall epiclastic sequence markedly differs from the footwall volcanics in having both quartz and feldspar phenocrysts, more abundant diverse and often rounded lithic fragments, coarse lithic-rich basal zones, rare pumice, and a significant proportion of volcanogenic sedimentary rocks. The origin of these rocks is interpreted as subaqueously deposited mass flows (e.g. Brathwaite, 1969, Green et al., 1981, Allen and Cas, 1990). The hangingwall epiclastics are conformably overlain by the Mt Black volcanics which are composed of weakly sericitised and chloritised dacitic to rhyolitic lavas over 1000 m thick.

The Dundas Group unconformably overlies the CVC and consists of several sub-units in the Rosebery–Hercules mine area: (1) White Spur Formation — a quartz-phyric epiclastic sequence, (2) Stitt Quartzite, (3) Natone Volcanics, (4) Salisbury Conglomerate and (5) Westcott Dolomite. The Crimson Creek Formation is exposed in the western part of the Rosebery–Hercules area tectonically interfingering with the Dundas Group. The Crimson Creek Formation

consists of mafic greywacke interbedded with siltstones, mudstones and minor altered basalt.

Following the Devonian Tabberabberan Orogeny, intrusion of shallow-level, post-tectonic granitoid plutons in the mine area has resulted in recrystallisation and considerable modification of ore assemblages in the Rosebery orebody. The south-end orebody contains possible Devonian granite-related mineral assemblages which include pyrrhotite, pyrite, garnet, helvite, biotite and tourmaline (Solomon et al., 1987). The granite does not outcrop, but had been interpreted first by Large (1986), from limited gravity data, and later detailed gravity studies substantiated the existence of the granite about one kilometer below the Rosebery south-end orebody (Leaman and Richardson, 1989). Detailed mineralogy and geochemistry of the Devonian mineral assemblages are presented in Chapter 6.

### 2.5.2 Structure ...

The Rosebery Fault is a prominent Devonian structure in the Rosebery–Hercules area. Previous authors including Green et al. (1981) and Green (1983) provided evidence for a fault-bounded western margin to the CVC. The location and nature of this major structure is now known, from Bastyan Dam north of Rosebery, through the Salisbury, Chamberlain and Jupiter Mines, to Moore's Pimple (Corbett and Lees, 1987).

The fault dips east at 30°–40° and consists either of pyritic quartz–tourmaline vein–breccia in the Rosebery area, or a fault breccia elsewhere. It is interpreted to be a thrust fault with significant throw as it juxtaposes east-dipping and facing feldspar-phyric rocks of the CVC, with steeply dipping, west facing rocks near the top of the White Spur Formation (Corbett and Lees, 1987). Shearing has also been noted in the ore lenses and the host rocks and the shear planes dip at about 40°–45° to the east, parallel to the Rosebery Fault system (Berry, 1990).

### 2.5.3 Form and geometry of ore lenses ...

The Rosebery orebody is made up of a series of tabular sheets dipping 45° east. The ore lenses extend over a 1.5 km strike length to depths of at least 800 m at the south-end and 600 m at the north-end, but a gap with no economic mineralisation separates the small northern lenses from the main southern group of lenses (Fig. 2.3). A and B lenses are referred to as north-end and C, D, E, F, G, and H lenses are referred to as south-end. Under the recent mine terminology, the deeper part of the F lens is called "J" lens. Brathwaite (1969, 1972) first reported the folding of the Rosebery ore lenses due to the Devonian Tabberabberan Orogeny (Fig. 2.4) and a similar conclusion was reached by Green et al. (1981) and Green (1983). In comparison, Adams et al. (1976) interpreted that the folded structure resulted from synsedimentary slumping soon after ore deposition.

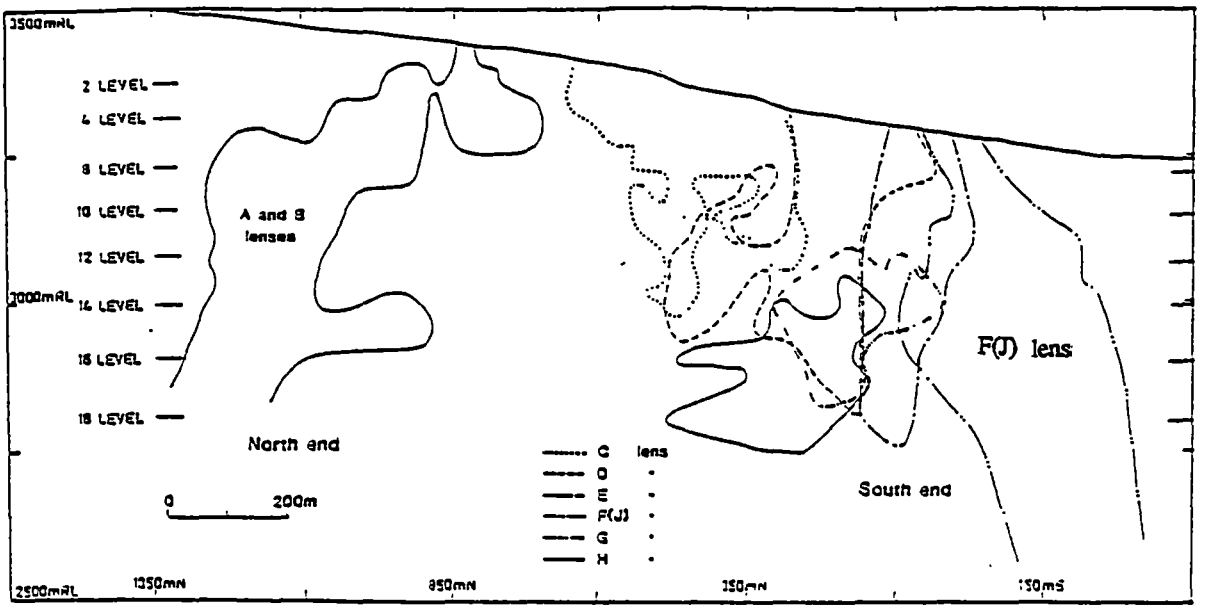


Fig. 2.3 Longitudinal projection of the Rosebery orebody showing relative position of ore lenses.

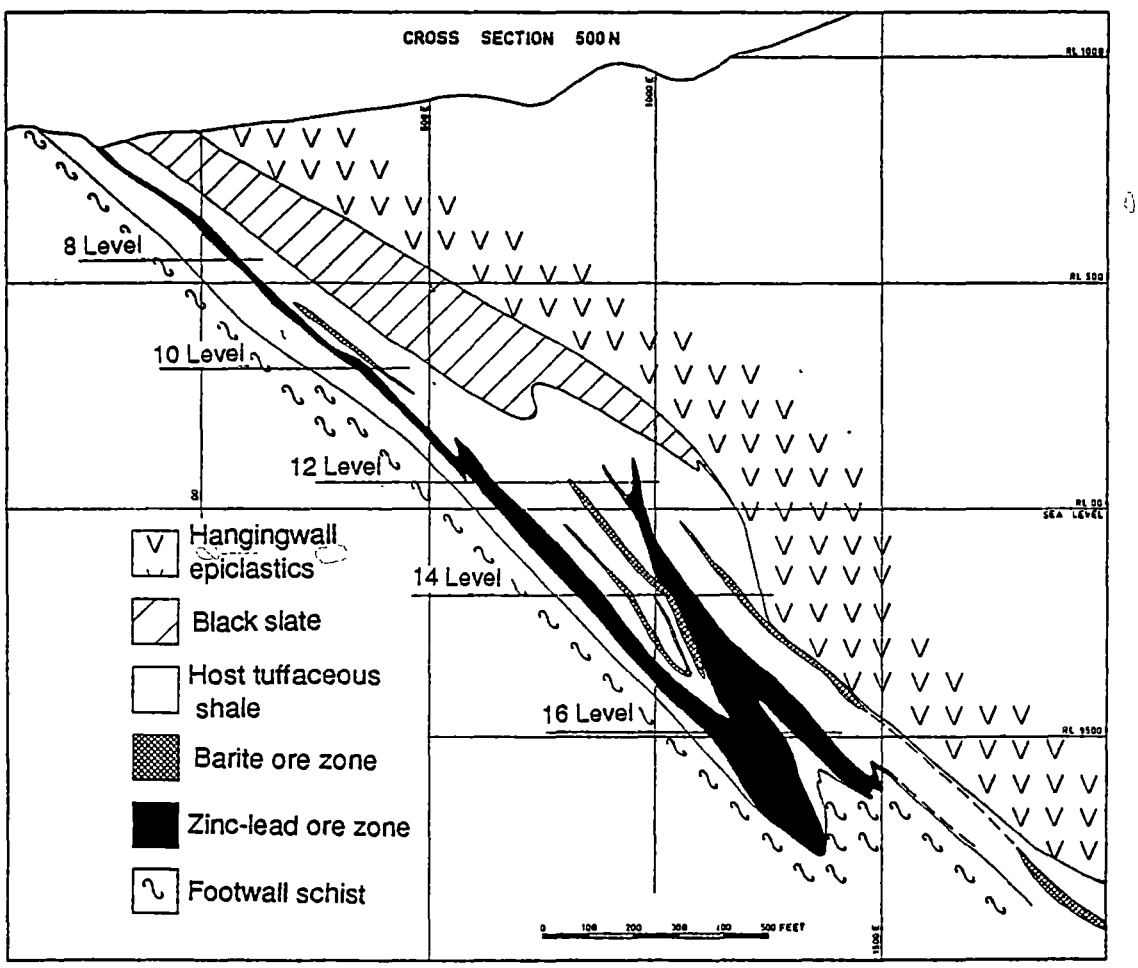


Fig. 2.4 Folded geometry of the Rosebery ore lenses. Modified after Brathwaite (1969, 1972).

### 2.5.4 Mineralisation ...

Brathwaite (1969) first recognised a distinct stratigraphic zonal sequence of the ore mineral assemblages at Rosebery. The following zonal mineral sequence (established by Brathwaite, 1969; Green et. al., 1981; Huston and Large, 1986; 1988; Huston, 1989) is present:

STRATIGRAPHIC TOP

---

Hematite-rich tuff

± Carbonate

———Barite———Carbonate

Massive sphalerite–galena ± pyrite

Massive pyrite–chalcopyrite

Disseminated pyrite–chlorite

---

STRATIGRAPHIC BOTTOM

Figures 2.5 and 2.6 show plan and cross-section of the zonation of the folded sulphide lenses. The complete zonal sequence is rarely present in any given lens; however the presence of parts of the sequence (e.g. pyrite–chlorite to massive sphalerite–galena or massive sphalerite–galena to barite) was taken as sufficient evidence to determine facing directions. The stratigraphic metal zonation is similar to that shown in many other volcanogenic massive sulphide deposits (e.g. Stanton, 1972; Large, 1977).

The mineralogy of the Rosebery ore lenses is relatively simple. The stratiform massive sulphide ore consists predominantly of pyrite, sphalerite, galena, chalcopyrite, and tetrahedrite–tennantite, with widespread minor arsenopyrite. The barite ore zone which occurs at the stratigraphic top of the orebody is commonly separated from the sphalerite–galena ± pyrite zone by intervening host rocks. The barite ore is generally lower grade than the zinc–lead ore, but contains essentially the same sulphide minerals in slightly different ratios. Compared to the sphalerite–galena ± pyrite zone, the massive barite zone is characterised by an enrichment in galena and tetrahedrite–tennantite (Brathwaite, 1969, 1974; Huston and Large, 1986). Disseminated to massive pyrite mineralisation with minor base metals may occur distally from or stratigraphically above, the zinc–lead mineralisation. The best gold mineralisation is concentrated close to the stratigraphic hangingwall of the deposit in the upper part of the zinc–lead or barite ore zones (Huston and Large, 1988).

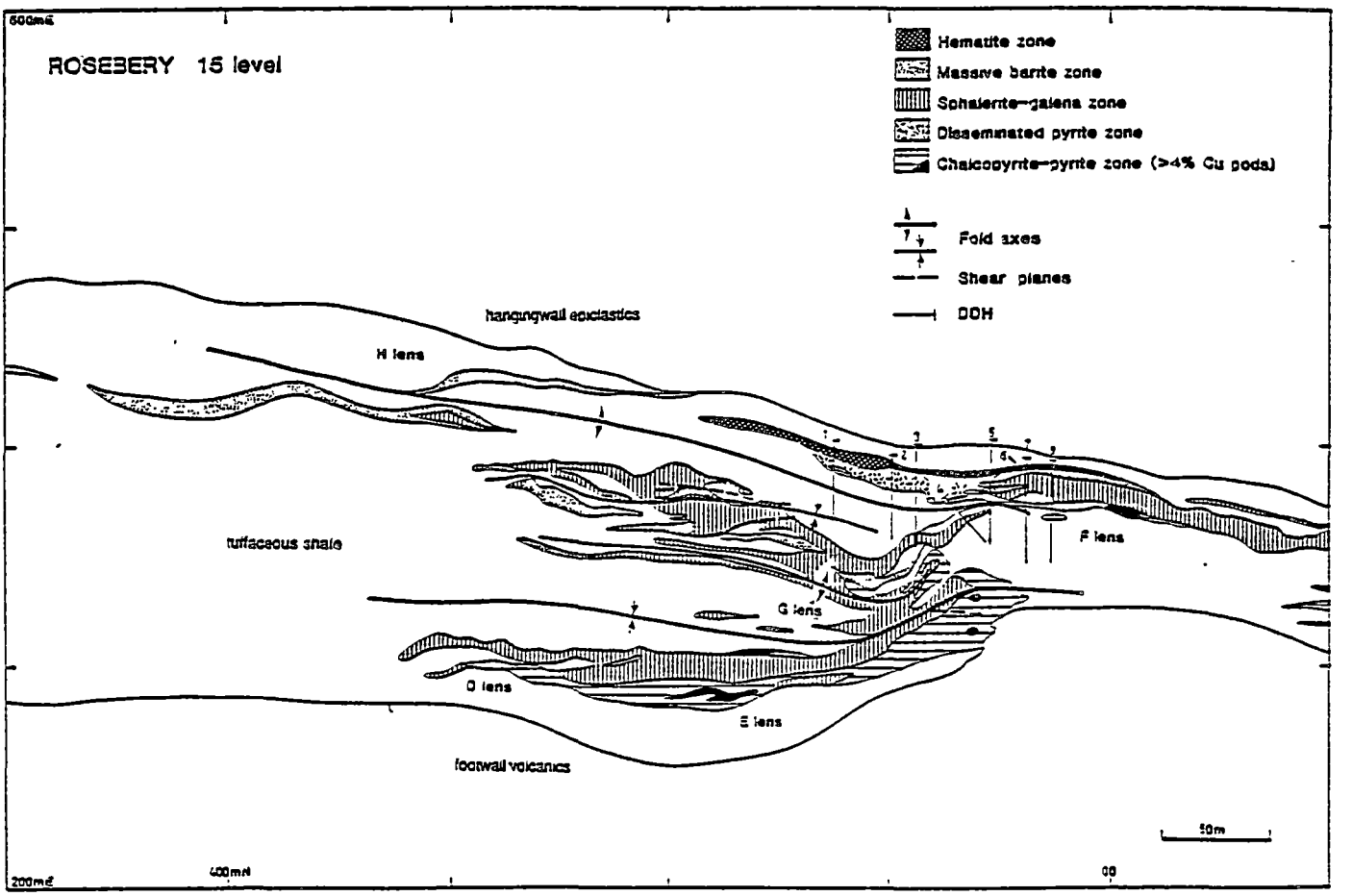


Fig. 2.5 Geological plan of 15 Level, Rosebery mine, drawn by relogging of diamond drill holes and re-interpretation of the existing geological information. Note the hematite and disseminated pyritic zones are continuous from "F" to "H" lens positions, indicating the same stratigraphic horizon. 1 = DDH R1804, 2 = DDH R1832, 3 = DDH R1829, 4 = DDH R1871, 5 = DDH R1859, 6 = DDH R 1828, 7 = DDH R1856 and 8 = DDH R1881 (Lees et al., 1990).

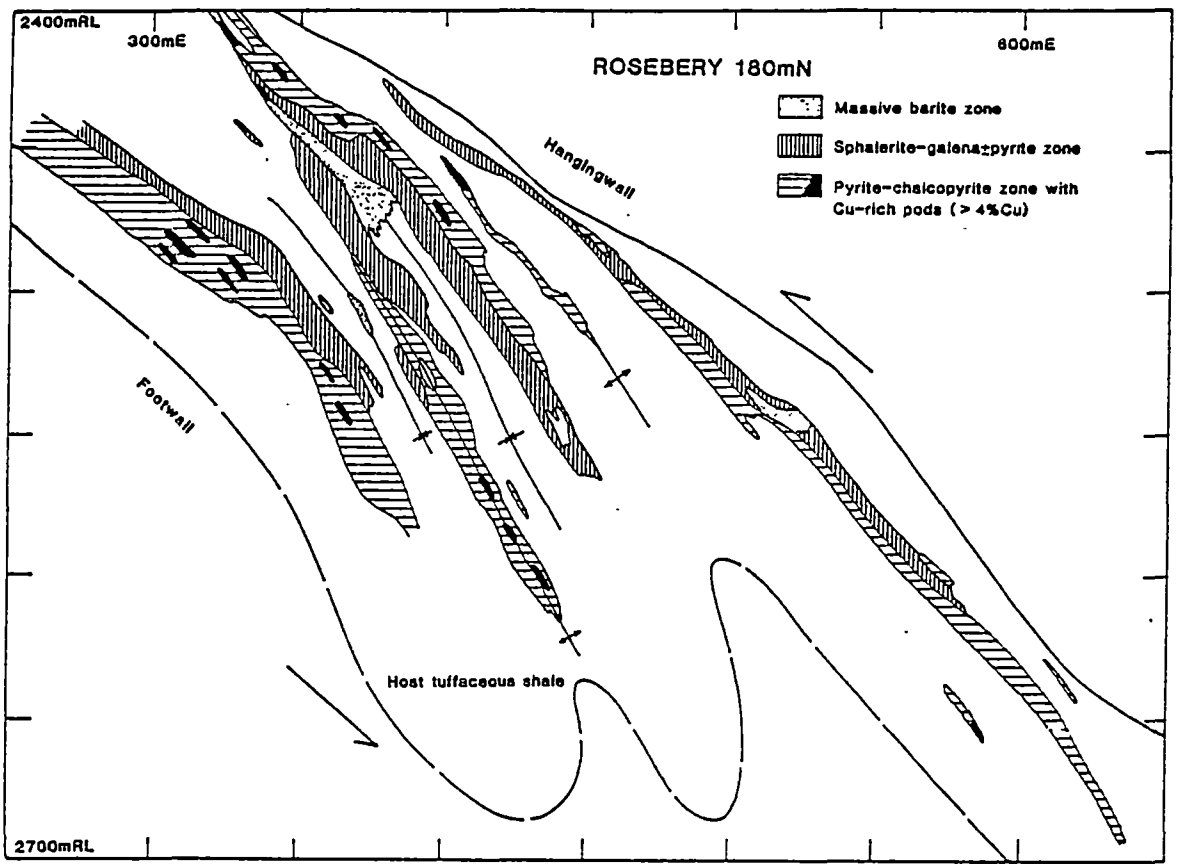


Fig. 2.6 Metal zonation of interpreted fold geometry of the 180mN E-W cross-section, Rosebery Mine, western Tasmania. (Lees et al., 1990).

Several small base- and precious-metal occurrences in the Rosebery–Hercules area (Nos 1 to 7 in Fig. 2.2) display diverse styles of mineralisation. Thin stratiform Pb–Zn–barite mineralisation with small footwall alteration zones, known from a horizon between the Ring P.A. and Jupiter prospects, occurs some 200–300 m stratigraphically below the Hercules mineralisation.The Rosebery Lodes prospect, some 3 km along strike south of the Rosebery deposit, contains thin bands of stratiform Pb–Zn–Ag–barite mineralisation in a host sequence similar to Rosebery.

At Dalmeny, stringer-type Pb–Zn mineralisation is hosted by sedimentary rocks within the quartz-phyric tuffaceous sequence, but is probably related to an adjacent altered felsic intrusive. At Koonya, sphalerite–galena veins, and a chlorite–pyrite–chalcopyrite stringer zone, occur adjacent to a quartz-porphyritic lava/intrusive contact within feldspar–phyric tuffaceous sedimentary rocks of the Rosebery–Rosebery Lodes footwall. Mineralisation along the Rosebery Fault at the Chamberlain and Salisbury prospects comprises quartz–tourmaline veins with disseminated sulphides containing minor Cu, Au, Sn, Bi, W, As; Pb and Ag may occur adjacent to the veins. These veins are thought to be related to post-tectonic Devonian granitoid intrusions (Lees et al., 1990).

### 2.5.5 Alteration ...

The dominant alteration feature at Rosebery is the presence of a blanket-like footwall sericitic and chloritic alteration zone. The host rocks, originally tuffaceous siltstones and shales, are also altered to quartz–sericite–pyrite ± chlorite ± carbonate schists. Mineralogical changes which characterise the footwall alteration are the destruction of feldspar, the sericitisation of pumice fragments, and silicification and pyritisation of the groundmass. Where alteration is intense, a well defined schistosity gives rise to an augen texture typical of "quartz schist" which commonly extends for several metres into the footwall below mineralisation.

The footwall volcanics/host rock contact cannot be easily recognised in the mine area due to this intense footwall alteration. Accompanying chemical changes in the footwall during alteration are enrichment in $SiO_2$, $K_2O$, MgO, MnO, Rb, S and $H_2O$ and depletion in $Na_2O$, CaO, $TiO_2$, $Al_2O_3$, Sr, Zr, Y and Nb (Green et al., 1981; Naschwitz, 1985). Sodium depletion due to breakdown of albite is the dominant process recorded. A loosely defined alteration halo of variously textured carbonate rocks surrounds the orebodies within the host rocks. Their intimate association with the ore indicates that they are genetically related to the ore-forming process, but the variety of morphology and composition present suggests different generations of carbonate formation.

Brathwaite (1969, 1974) considered that the Rosebery Mn-rich carbonates were deposited as chemical sediments and Dixon (1980) interpreted that Rosebery carbonates formed by mixing of exhalative fluid with seawater.

Lees et al. (1990) suggested possible origins for the various types of carbonates as follows: carbonate-altered feldspar; dolomite rhombs of sedimentary origin; spheroidal rhodochrosite pseudo-oolites which probably formed by precipitation of depleted ore forming fluids; massive recrystallised carbonates at the margins of ore lenses probably formed in pressure shadows during folding and disruption of ore lenses; and quartz–rhodochrosite–sulphide veins formed late in metamorphism. Similar carbonate alteration assemblages are noted at Hercules and South Hercules (Chapter 3). Isotopic and compositional variation of the carbonates will be described in Chapter 9.

# CHAPTER 3:
# GEOLOGY OF THE HERCULES–SOUTH HERCULES DEPOSITS

## 3.1 INTRODUCTION ...

The Hercules and South Hercules deposits are located within the CVC of the Cambrian Mt Read Volcanics and the regional geological setting of the Hercules–South Hercules area is similar to that of the Rosebery area to the north. The Hercules and South Hercules deposits occur in a similar tuffaceous shale unit at the same stratigraphic level (Fig. 3.1). The South Hercules deposit lies about 1 km along strike south of the main Hercules ore lenses (Fig. 3.2).

## 3.2 PREVIOUS STUDIES ...

The geological relationships and mineralisation of the Hercules–South Hercules area have previously been discussed by Hall et al. (1965), Hall (1967), Fitzgerald (1974), Burton (1975b), Lees (1987), Lees and Howard (1989) and Lees et al. (1990). The newly discovered South Hercules deposit is a zone of disseminated and stringer sulphides with significant gold, silver and base metal grades to the south of the Hercules mine. A brief account of the geology of the South Hercules deposit was made by Throop (1974), and recently more detailed reports are presented by Lees (1988) and Khin Zaw et al. (1990a).

## 3.3 HISTORY AND PRODUCTION ...

Although base and precious metal mineralisation was noted by early prospectors in the South Hercules area, no particular exploration efforts were attempted. The Electrolytic Zinc Company acquired the mining leases in the area in 1920, and drilled a series of holes near the Au-rich M lode, one of the southernmost Pb–Zn lenses of the old Hercules mine workings, but no further work was carried out. Diamond drilling was resumed in 1973–74 and several holes drilled in 1974 intersected the stringer Pb–Zn mineralisation with minor Au–Ag. The increase in precious metal prices led to renewed exploration activity in the South Hercules area in the early 1980's.

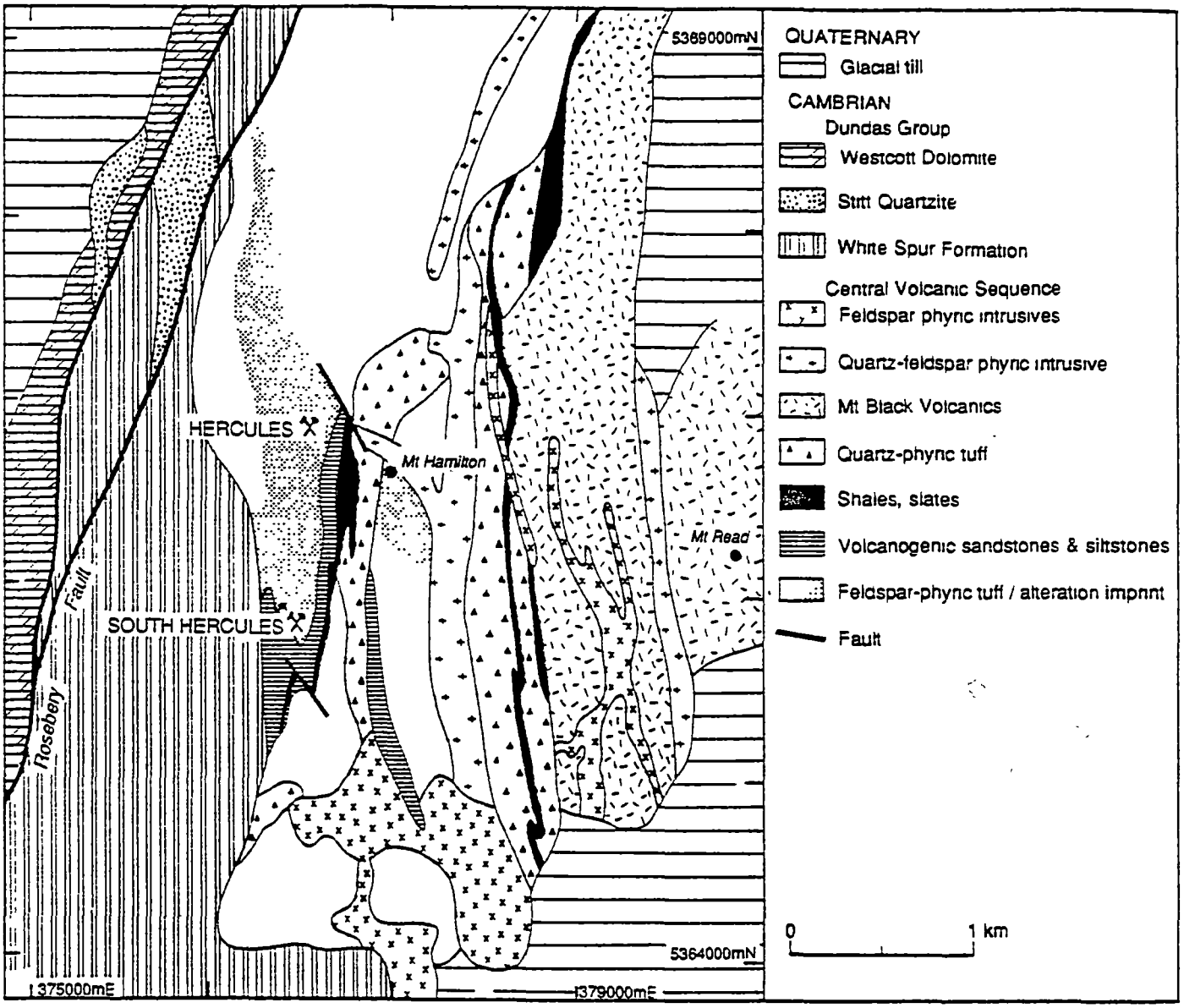


Fig. 3.1 Geology of the Hercules–South Hercules area, western Tasmania (after Lees, 1987; Lees et al., 1990).

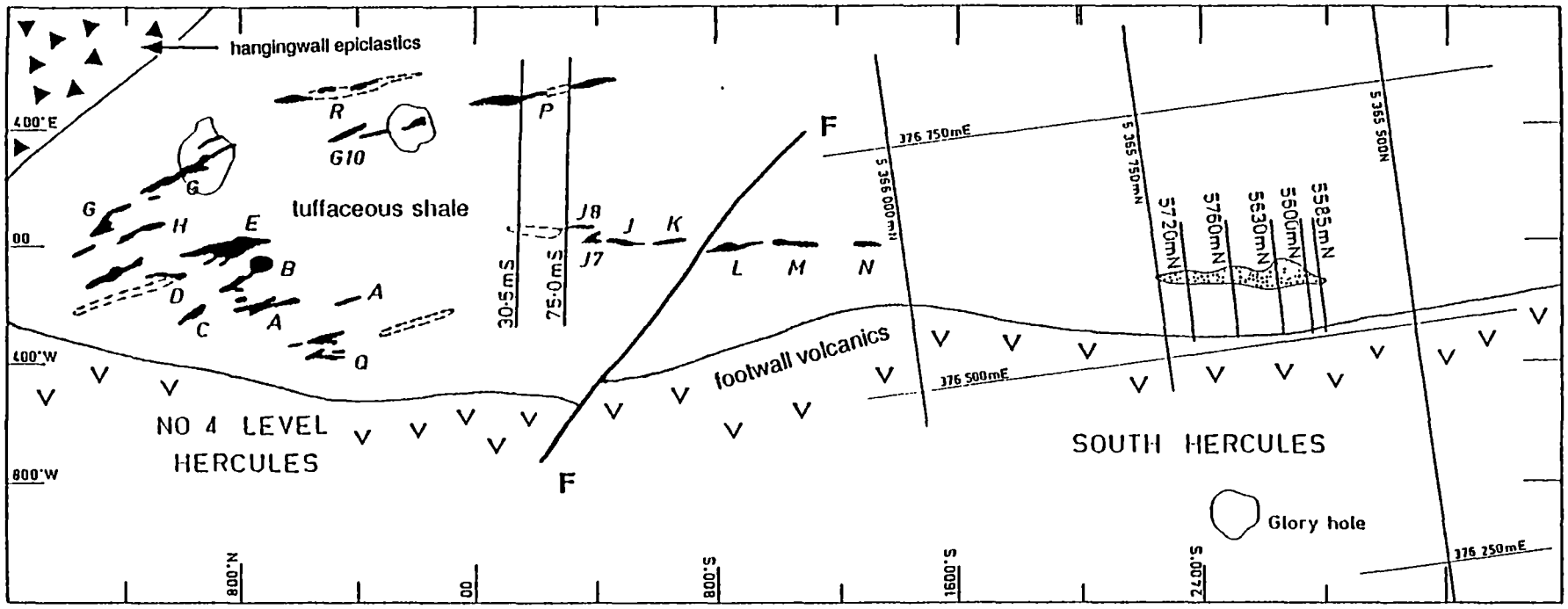


Fig. 3.2 Location of the Hercules ore lenses together with the South Hercules deposit. The dashed line outlines of the ore lenses indicate projection to the No.4 Level of the Hercules mine. (modified after data from Rosebery mine office).

From discovery in 1891 to June, 1985 at least 2.21 million metric tonnes of sulphide ore have been mined from the main Hercules deposit at an average grade of 5.6% Pb, 17.6% Zn, 0.42% Cu, 176 g/t Ag and 2.9 g/t Au (Lees et al., 1990). Drilling up to 1987 at the newly discovered South Hercules deposit gave a geological ore resource of 530, 910 metric tonnes grading 1.9% Pb, 3.1% Zn, 0.1% Cu, 170.2 g/t Ag and 2.5 g/t Au (pers. comm. S. Hunns, 1989).

## 3.4 STRATIGRAPHY ...

The stratigraphic sequence of the Hercules–South Hercules area is summarised below;

| | | |
|---|---|---|
| Top | Feldspar-phyric volcanics | >100 m |
| | Quartz-phyric volcanics | 0–50 m |
| | Black shales and slates | 0–50 m |
| | "Host Rocks" — pelitic to psammitic bedded tuffaceous sediments | 20–100 m |
| Bottom | Fiamme-bearing feldspar-phyric volcanics | >300 m |

The two most significant differences between this sequence and the Rosebery sequence are (a) the presence of the coarse, strongly silicified and chloritised volcanics with distinct fiamme-like texture immediately underlying most of the host rock horizon, and (b) the ashy, tuffaceous nature of the host rocks. The silicified footwall volcanics at Hercules and South Hercules contain abundant pyritic chloritic fiamme in a siliceous matrix; feldspars have been totally destroyed by the alteration.

The host rock at the main Hercules ore lenses is up to 100 m thick and consists of poorly bedded, psammitic to pelitic ash and tuffaceous sedimentary rocks. The main components are quartz and variably carbonated feldspar in a sericite–chlorite matrix. The host rock contains a number of lenses of massive sulphide ore.The host rock at South Hercules is similar to that of the area of the main Hercules ore lenses and consists of grey, fine-grained, siliceous, tuffaceous rocks and sericitic feldspar-phyric volcanics.

Various forms of carbonate are present in the host rock horizon (Lees, 1987; Lees and Howard, 1989; Lees et al., 1990). Diagenetic nodules of intergrown quartz and carbonate are common in the unmineralised host rocks. These nodules are 1–15 cm across and sometimes have cannon-ball shapes through which bedding can be traced, although cleavage often wraps around them. Carbonate "pisolites" are also common in a halo around the ore lenses.

These pisolites are spheroids from 1–10 mm across, usually composed of concentric layers and often tightly packed (Lees, 1987). Dolomite rhombs are known but are of limited extent and "fireworks textures" of radiating carbonate needles and colloform and botryoidal textures have also been noted (Lees, 1987). Massive recrystallised carbonate also occurs close to ores. Quartz–carbonate veins are also found at Hercules. The South Hercules deposit also displays similar variously textured carbonate assemblages; detailed descriptions of the South Hercules carbonates are presented in Chapter 4.

The hangingwall rocks at the Hercules–South Hercules area immediately overlying the host rock contains a significant sedimentary component of grey shales, poorly bedded siltstones and lithic wackes. The black shale unit which overlies the host rock consists of thinly bedded black slates with thin lithic wacke bands and minor other clastics. Pyrite, as disseminations, bands and nodules, is locally abundant. The shale-dominated sequence is followed by massive epiclastics of dacitic to andesitic composition. Like the Rosebery mine area, the hangingwall quartz- and feldspar-phyric epiclastics are sometimes lithic- and crystal-rich with black slate fragments and quartz crystals in a siliceous matrix. The base of the hangingwall sequence is commonly more lithic-rich (Lees, 1987; Lees and Howard, 1989; Lees et al., 1990).

## 3.5 STRUCTURE ...

Folding has long been recognised in the Hercules–South Hercules area (e.g. Hall et al., 1965; Hall, 1967). Folds are open to moderately tight, with strong axial plane cleavage at 60°–75°E that is subparallel to the strike of the host rocks. The ore is contained within strongly deformed zones, enclosed by either sericite–chlorite schists, disrupted pisolitic or massive carbonate, or strongly deformed host rocks. Although folded, the host rocks in the main Hercules area have an overall shallow dip of 20°–30°E and recent deep drilling (e.g. H704 and H710) suggests that the host rock continues to dip gently to the east (Lees, 1987).

Several faults are present in the Hercules–South Hercules area. A N–S trending, steeply dipping fault may occur locally as a fault breccia or shear zone near the contact of black slates and hangingwall lithic epiclastics, but the fault is not persistent and may have only a small displacement. A NW–SE trending set of faults has little or no displacement, and exhibits a thin fault gouge or breccia. The contact between the host rocks and the overlying massive epiclastics is seen in part to be a major reverse fault (Lees, 1987; Lees and Howard, 1989).

The bedding of the sedimentary rocks at *South Hercules* strikes 010° and dips 40°–45°E, but cleavage varies between strikes of 170° and 185° and invariably dips steeper than the bedding at 65°–70°E. A fault zone has been observed in the footwall of the northern part of the deposit (5700mN–5800mN) which comprises a shear zone often with pug zones and/or

quartz veins. Its strike is parallel to the strike of bedding. At the South Hercules deposit area, the host rocks and sedimentary rocks are offset about 100 m to the west by an apparent cross fault. An E–W shearing component was also recognised by recent structural mapping in the South Hercules area by Aerden (pers. comm., 1988).

## 3.6 FORM AND GEOMETRY OF ORE LENSES ...

E–W cross-sections of the Hercules and South Hercules deposits are shown in Figs. 3.3A and 3.3B).The Hercules–South Hercules area consists of numerous small ore lenses in the order of 100 m × 100 m × 5–10 m which are generally joined at some point to a neighbouring lens. The ore lenses vary in form from sheets to pods, strike close to north and consistently dip east at 60°–70°. In plan the ore lenses appear in the form of a disrupted fold (Fig. 3.2, and Lees, 1987; Lees and Howard, 1989; Lees et al., 1990) but due to the strong post-cleavage shearing, the exact nature of the fold cannot be demonstrated. Although some ore lenses (e.g. E lens and M lens) cut the bedding of the host rocks, most of the ore lenses lie parallel to the bedding. Crude layering of ore minerals is normally parallel to the cleavage.

These features led Hall (1967), and Lees (1987) to interpret that the ore lenses were probably originally stratiform, but have been realigned or transposed along the cleavage. However, Lees and Howard (1989) later suggested that the ore lenses are not stratiform but grossly stratabound within the host rock. The observed discordant nature of some of the ore lenses and the presence of abundant spotty, open-space filling textures with a zonal pattern, (Chapter 4) in the ore zone cast some doubt on the original stratiform origin for the entire Hercules ore lens system. The *South Hercules* deposit occurs as a lenticular body at the south of the main Hercules ore lenses (Fig. 3.3). As in the case of the main Hercules mine area the cleavage/bedding relationships at the South Hercules deposit give a distinct discontinuity, and the ore zone is parallel to the cleavage and it also contains abundant disseminated and stringer-style sulphide assemblages.

## 3.7 MINERALISATION ...

At Hercules, Lees (1987) and Lees et al. (1990) reported that the ore lenses, with the exception of "G" lens, are zoned both vertically and longitudinally. Massive to disseminated sphalerite–galena–pyrite ore forming the bulk of the mineable lenses give way below to massive pyrite with or without a siliceous pyrite–chalcopyrite-rich tail which pinches out at depth. The massive pyrite may become chalcopyrite-rich or vein-like near the host rock–footwall volcanics contact. "G" lens at the Hercules mine is the only barite-rich lens with banded or laminated

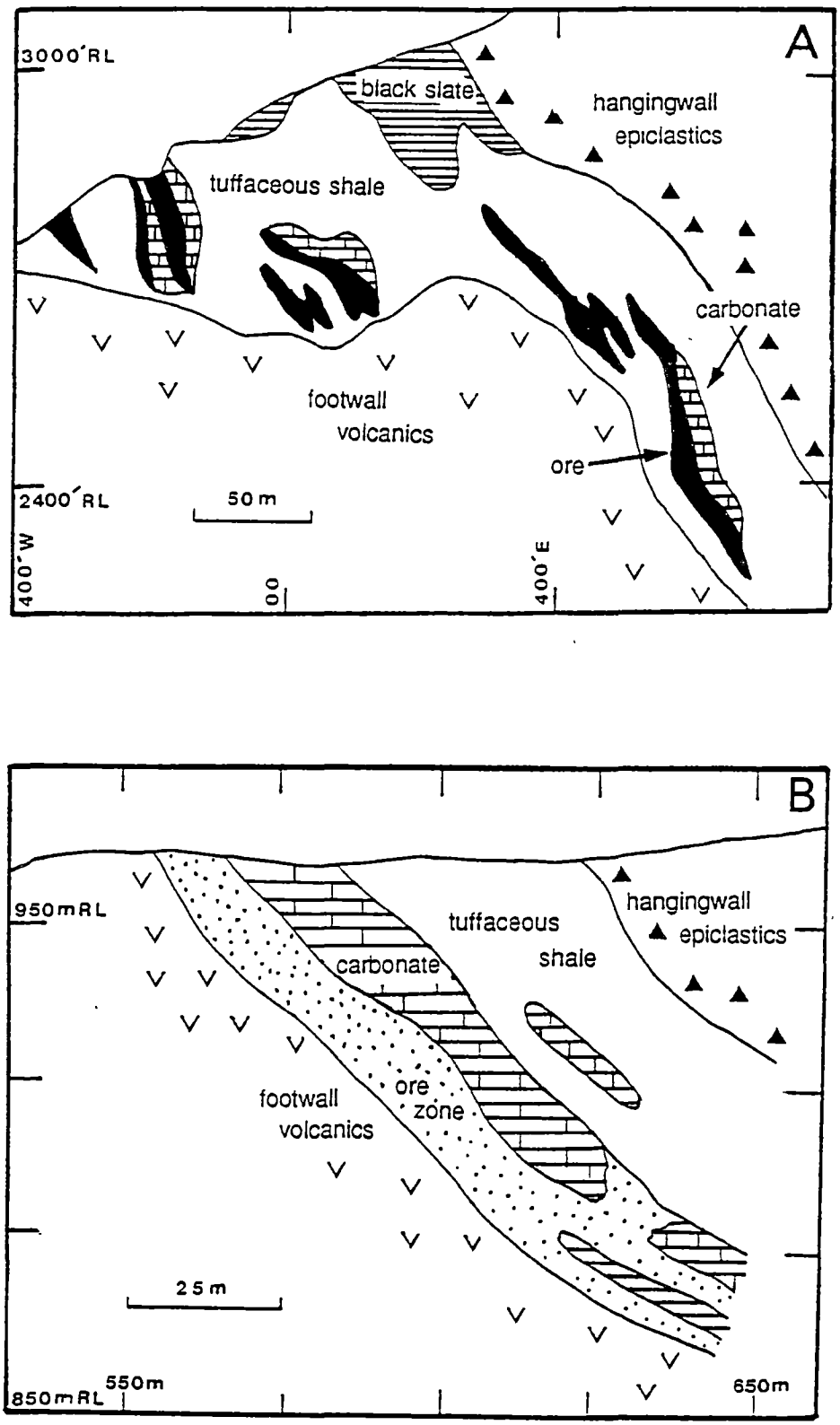


Fig. 3.3 A — East-west cross-section of the Hercules mine (after Lees and Howard, 1989; and B — east-west cross-section of the South Hercules deposit.

sulphide similar to those of Rosebery. Detailed metal zonation of the J(K)-P lens of the Hercules mine is presented in Chapter 4.

The Hercules ores appear to have been more deformed than those at Rosebery, and in places show foliated textures which were apparently produced by the strong deformation of original stratiform massive ores. The most obvious difference between the Rosebery and Hercules–South Hercules ore textures is the abundance of spotty textures in the latter. The spotty ore assemblages exhibit a zonal texture from the core to the rim of the spots. The coarse-grained sphalerite spots or blebs are rimmed by sericite or galena sometimes with chalcopyrite at the grain boundaries. In lower grade ores, sphalerite spots may be isolated or joined together in a matrix of silicified volcanics or pyritic chlorite–sericite schist. Lees (1987) reported an unusual ore texture at Hercules termed "porphyroblastic" ore which consists of very coarse-grained sphalerite with or without galena. Lees (1987) attributed these ore textures (e.g. spotty ore texture and sericitic ore texture) to metamorphic recrystallisation and annealing of the massive high grade ore.

The mineralisation at the *South Hercules* deposit is essentially composed of stringer to semi-massive base metal sulphides with subordinate Au–Ag grades. Spotty to blebby sulphide assemblages similar to the Hercules spotty ores are also common in this zone. The sulphide spots are commonly composed of sphalerite blebs with sericitic and pyritic rims with elevated Au enrichment. In one sample (Sample H1118-13 at 29.9 m, 5630mN), one sphalerite bleb was found to be studded with many discrete microscopic electrum grains.

The siliceous stringer-sulphide zone at South Hercules has variable Au–Ag distribution and forms a stratabound zone followed above by massive pyrite ± barite with significantly higher Au grades (up to 22.0 g/t Au). Irregular and patchy quartz–pink carbonate veins with coarse-grained, recrystallised, yellowish sphalerite and galena are observed in the ore zone and these veins may contain thin networks of sulphosalt veinlets with elevated Ag values (e.g. H1142-1 at 38.5 m, 5600mN). Sometimes Ag values may attain 2000 g/t. Detailed mineralogical zonation of the South Hercules deposit is presented in Chapter 4.

## 3.8 ALTERATION ...

At the Hercules mine, alteration of the footwall volcanics resulted in a zone of chloritised, pyritic pumice in a silicified groundmass extending for some 2 km north and at least 1 km south of the mine (Fig. 3.1). Intense alteration in the immediate footwall of the ore lenses has obliterated primary textures and resulted in augen-textured quartz–sericite schist. K-feldspar and Fe-, Mg- and Mn-rich chlorite occur in the footwall of Hercules (Eastoe et al., 1987). An Fe-chlorite–pyrite zone beneath the center of the Hercules deposit was also noted by Eastoe

et al. (1987) who considered it to represent a feeder zone. Carbonate alteration in the form of concretions and spheroids from 1–10 mm diameter are common in a halo around the ore lenses, tightly packed when close to ore and seldom more than 10m from ore (Lees, 1987; Lees and Howard, 1989).

The siliceous stringer to semi-massive sulphide mineralisation at the *South Hercules* deposit is associated with a spectacular pervasive carbonate alteration assemblage ranging from bladed, through spots, spheroids to recrystallised massive carbonates, and three carbonate zones can be distinguished: blebby, cherty and massive carbonate zones (Chapter 4). The carbonate altered zones lack precious metals and have low base metal grades. Intense quartz–sericite alteration with a schistose fabric is developed in the footwall volcanics below the ore at South Hercules.

# CHAPTER 4:
# MINERALOGICAL ZONATION IN THE F(J) LENS, ROSEBERY MINE, J(K)–P LENS, HERCULES MINE, AND THE SOUTH HERCULES DEPOSIT

## 4.1 INTRODUCTION ...

In this chapter, mineralogical zonation in the F(J) lens, Rosebery mine, J(K)-P lens, Hercules mine and the South Hercules deposit will be described together with their petrological and textural characteristics. Eleven E–W cross-sections from the F(J) lens of the south-end of the Rosebery mine (20mS, 100mS, 130mS, 145mS, 190mS, 200mS, 220mS, 250mS, 270mS, 280mS and 300mS), two from the J(K)-P lens of the Hercules mine (30.48mS and 70.00mS) and five from the South Hercules deposit (5585mN, 5600mN, 5630mN, 5670mN and 5720mN) were investigated.

## 4.2 F(J) LENS, ROSEBERY MINE ...

As was described before, the Rosebery deposit is a volcanogenic massive sulphide deposit that formed on the Cambrian seafloor by an exhalative process (e.g. Brathwaite, 1969, 1974; Green et al., 1981; Green, 1983; Huston and Large, 1986, 1988; Huston, 1989). Recent detailed mineralogical and zonation studies at the north-end (A and B lens) of the Rosebery deposit by Huston and Large (1988) and Huston (1989) essentially indicate three primary sulphide–sulphate zones:

(1) Massive barite zone

(2) Sphalerite–galena ± pyrite zone and

(3) Pyrite–chalcopyrite zone with Cu-rich pods (> 4% Cu).

The ore zones at the north-end (A and B lens) have distinct spatial occurrences: the pyrite–chalcopyrite zone occurs at the base of the sphalerite–galena ± pyrite zone which is in turn overlain by the massive barite zone. Narrow zones of stringer-like copper mineralisation were also observed as copper-rich pods within the massive pyrite–chalcopyrite zone or in highly chloritised footwall rocks. The mineralisation at the north-end is dominated by stratiform, massive sulphide minerals of sphalerite and galena with or without pyrite, minor chalcopyrite, tetrahedrite–tennantite and arsenopyrite. Gold occurs as electrum and is concentrated in the

upper part of the massive sphalerite–galena ± pyrite zone and in the massive barite zone at the top.

At the south-end of the Rosebery mine, the stratiform, massive sulphide lenses are associated with a transgressive zone comprising iron oxides and sulphides and other silicate minerals. Brathwaite (1969) first reported the pyrrhotite-bearing assemblages transgressing the sulphide lenses at the south-end and later deep drilling from surface has exposed an extensive zone of pyrrhotite- and magnetite-bearing sulphide lenses. In addition to pyrrhotite, a wide variety of other mineral assemblages is present from magnetite (hematite)–biotite, pyrrhotite–pyrite to tourmaline–quartz and other minerals such as fluorite, garnet and helvite.

Recent investigation along underground mine levels and logging of the diamond drill holes on the selected cross sections have revealed a spatial distribution and zonation of Fe–S–O assemblages transgressing the stratiform sulphide lenses. Figure 4.1 shows a geological plan for the sulphide lenses and the Fe–S–O zones on 17 Level and Figure 4.2 depicts the cross-section of the mineralogical zonation on an orebody scale. More detailed zonal patterns of the Fe–S–O assemblages and their relationship to the Pb–Zn lenses on 250mS, 270mS, 280mS and 300mS E–W cross-sections of the south-end orebody are shown in Figs 4.3–4.6. Detailed mineralogy and geochemistry of these mineral assemblages will be described in Chapter 6. The following three major zones can be essentially distinguished;

3. Tourmaline–quartz ± magnetite zone
2. Pyrrhotite–pyrite zone
1. Magnetite–biotite ± chalcopyrite zone

In this study, the above transgressive Fe–S–O zones in the F(J) lens of the Rosebery south-end orebody were investigated in detail and the following discussion will focus on their spatial and textural relationships.

### 4.2.1 Magnetite–biotite ± chalcopyrite zone ...

This zone is generally confined to the lower levels of the mine particularly below 17 Level. Magnetite is associated with pyrite to form massive bodies with or without biotite (Fig. 4.7A). Sometimes biotite occurs as a dominant constituent intermixing or intercalating with magnetite and pyrite (Fig. 4.7B). The pyrite–magnetite ± biotite assemblages may show a pseudo-banded texture (see Fig. 4.7A). Pyrite often occurs as cubes of various sizes in the magnetite ± biotite host. Hematite is also locally noted in association with magnetite, and in places only hematite is found together with pyrite (Fig. 4.7C). Hematite ± quartz zones up to half a metre across locally occur within the green biotite-rich alteration associated with magnetite assemblages (Fig. 4.7D). In places, hematite is found with barite-rich sulphide lenses (Fig. 4.7C).

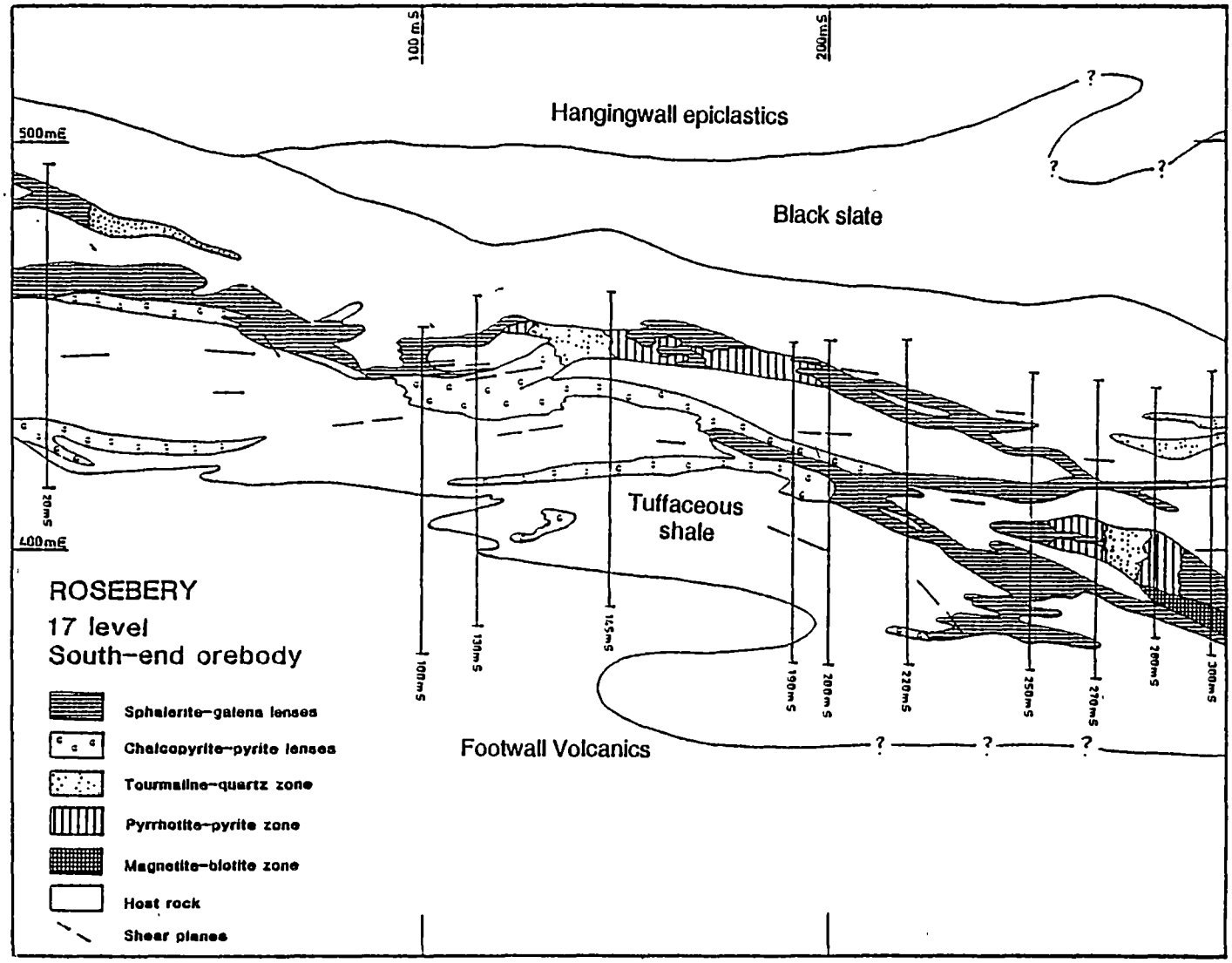


Fig. 4.1 Geological plan showing southern ore lenses, 17 Level, Rosebery mine, western Tasmania.

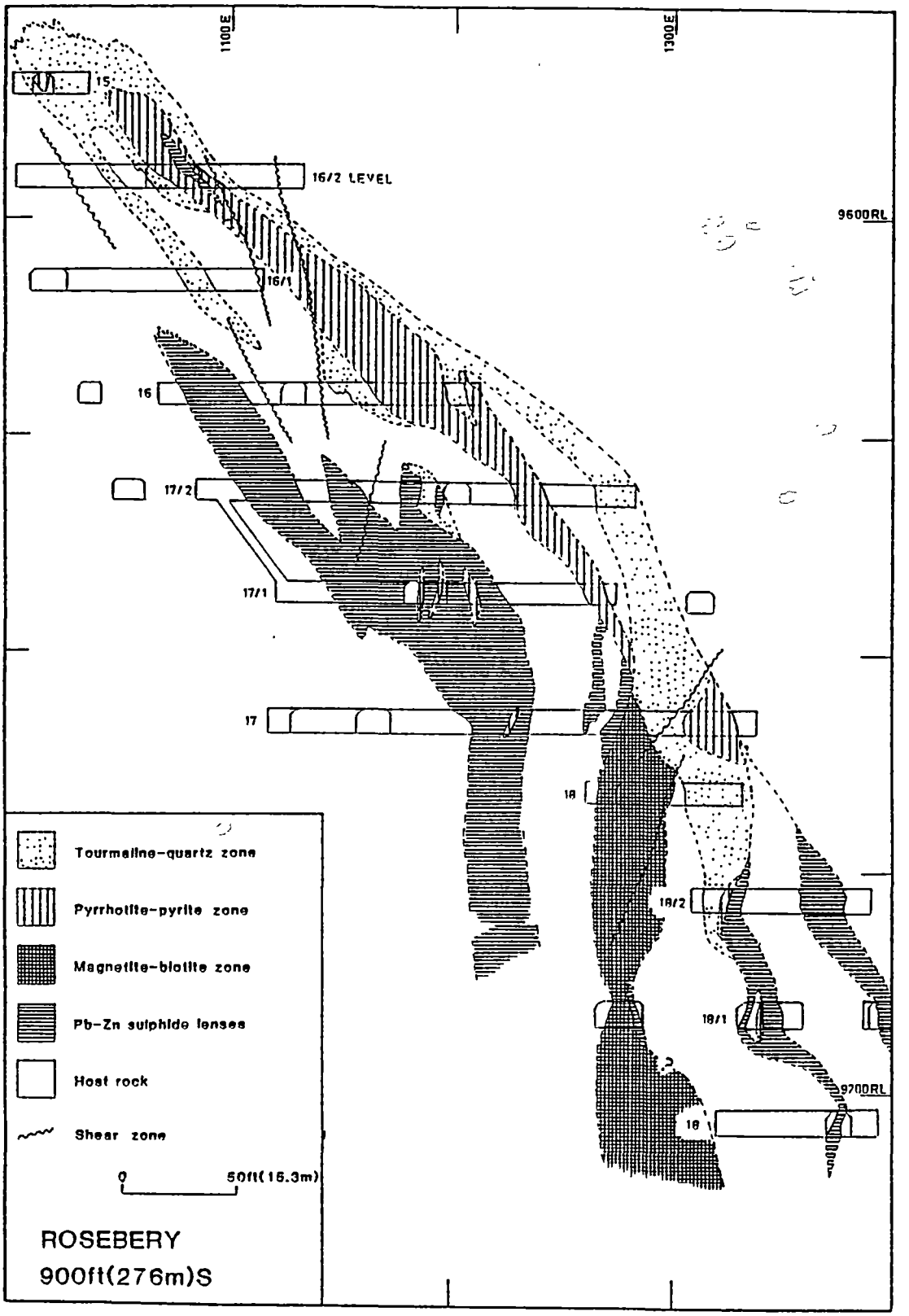


Fig. 4.2 Geological cross-section showing spatial distribution and zonation of Fe–S–O replacement assemblages transgressing the primary exhalative Pb–Zn sulphide lenses at F(J) lens, south-end orebody, Rosebery mine, western Tasmania.

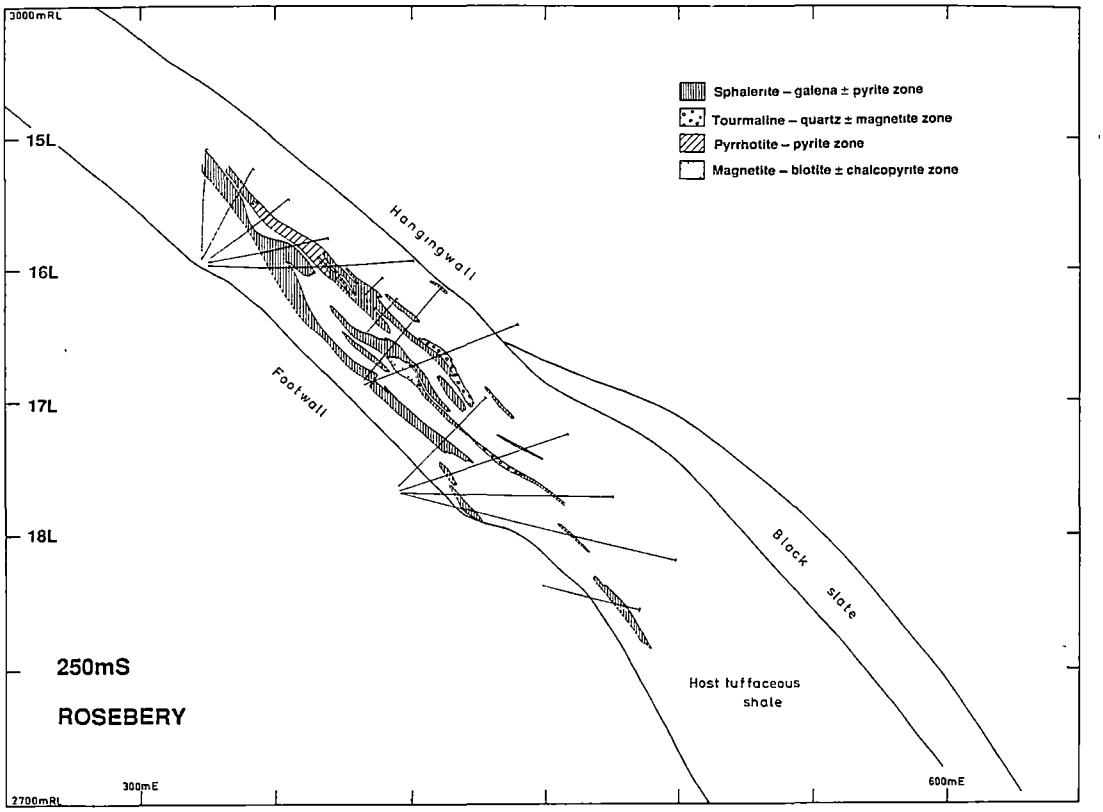


Fig. 4.3 Geology and mineral zonation of 250mS section, F(J) lens, south-end ore body, Rosebery mine, western Tasmania.

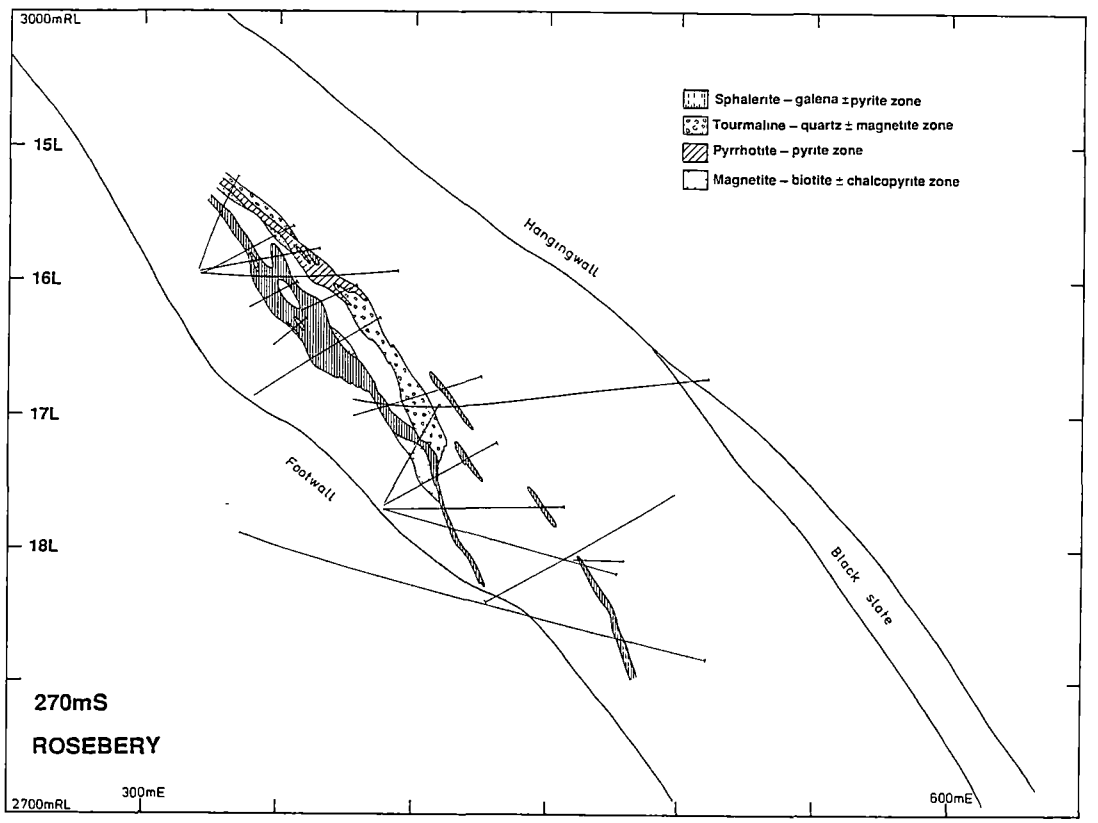


Fig. 4.4 Geology and mineral zonation of 270mS section, F(J) lens, south-end ore body, Rosebery mine, western Tasmania.

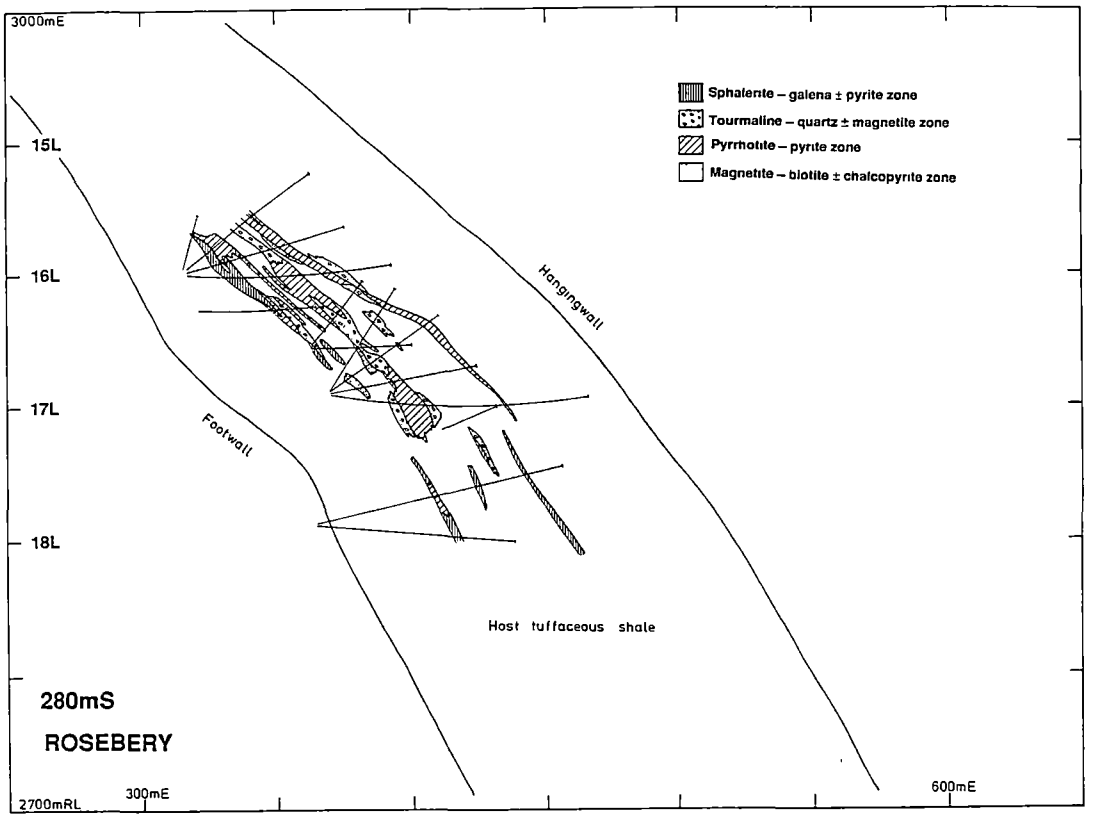


Fig. 4.5 Geology and mineral zonation of 280mS section, F(J) lens, south-end ore body, Rosebery mine, western Tasmania.

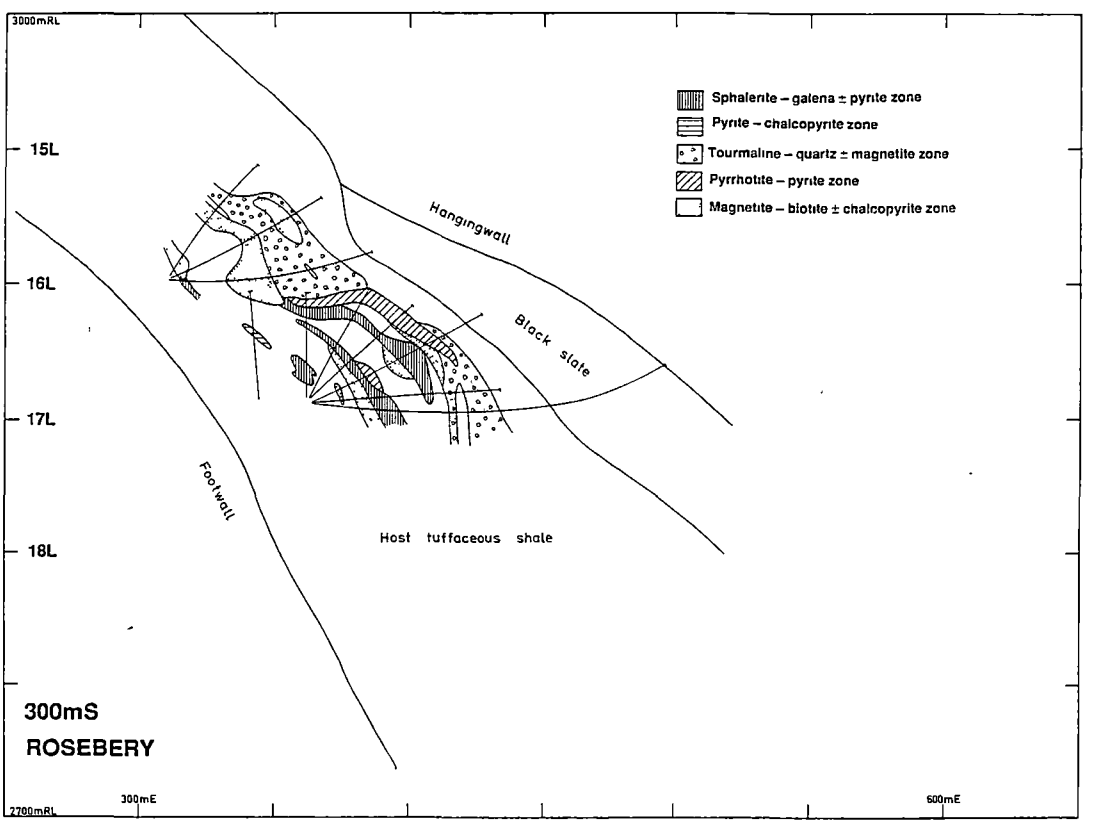


Fig. 4.6 Geology and mineral zonation of 300mS section, F(J) lens, south-end ore body, Rosebery mine, western Tasmania.

Fig. 4.7**A**. Pyrite-magnetite assemblages showing pseudo-banded texture. Sample No. KZ-1, Location 18 Level, 100mS, F(J) lens, south-end orebody, Rosebery Mine, western Tasmania. mag=magnetite, and py=pyrite.

Fig. 4.7**B**. Mixed dark magnetite and green biotite with minor pyrite cubes in magnetite-biotite ± chalcopyrite zone. Sample No. KZ-2, Location 18 Level, H lens, south-end orebody, Rosebery Mine, western Tasmania. Bio-mag=biotite-magnetite and py=pyrite.

Fig. 4.7**C**. Hematite-pyrite in contact with barite-pyrite assemblages in magnetite-biotite ± chalcopyrite zone. Sample No. R 4259 at 71.6m, F(J) lens, south-end orebody, Rosebery Mine, western Tasmania. Ba=barite, hem=hematite and py=pyrite.

Fig. 4.7**D**. Underground exposure of hematite±quartz assemblages enclosed in biotite (chlorite)-altered host rock. Location 16 Level between G and H lens, south-end orebody, Rosebery Mine, western Tasmania. hem=hematite and qtz=quartz.

Fig. 4.7**E**. Folded lead-zinc ore and pyrrhotite and pyrite assemblages. Note trace of the fold pattern by the sphalerite-rich dark bands from lead-zinc ore to pyrrhotite-pyrite assemblages and very thin dark brown sphalerite bands as remnants in pyrrhotite-pyrite assemblages. Sample No. 100892, University of Tasmania collection, collected by R. Brathwaite and rephotographed here. Pb-Zn =banded sphalerite-galena ± pyrite sulphide lenses and po-py=pyrrhotite-pyrite.

Fig. 4.7**F**. Underground exposure of pyrrhotite-pyrite assemblages and Pb-Zn sulphide lens. Location 16 No. 2 Sub-Level, 300mS, F(J) lens, south-end orebody, Rosebery Mine, western Tasmania. Pb-Zn =banded sphalerite–galena±pyrite sulphide lenses and po–py=pyrrhotite-pyrite.

Fig. 4.7**G**. Pyrrhotite-pyrite assemblages and Pb-Zn sulphide ores (sphalerite-galena± pyrite). Note 1) folded, thin baritic lens at the right, 2) increasing darkening of sphalerite colour towards replacement reaction front and 3) thin tourmaline-quartz vein cutting pyrrhotite-pyrite zone at the centre. Sample No. KZ-3, Location 16 Level, 300mS, F(J) lens, south-end orebody, Rosebery Mine, western Tasmania. Pb-Zn =banded sphalerite-galena ± pyrite sulphide lenses, po-py=pyrrhotite-pyrite ± sphalerite, Ba=barite and tour-qtz=tourmaline and quartz.

Fig. 4.7**H**. Tourmaline-quartz vein cutting pyrrhotite-pyrite assemblages. Sample No. KZ-4, Location 16 No. 1 sub-Level, 200mS, F(J) lens, south-end orebody, Rosebery Mine, western Tasmania. po-py=pyrrhotite-pyrite, po=pyrrhotite, tour-mag=tourmaline-magnetite and qtz=quartz.

Fig. 4.7**I**. Underground exposure of network of tourmaline±quartz veinlets cutting silicified, tuffaceous host rock. Location 15 Level, F(J) lens, south-end orebody, Rosebery Mine, western Tasmania. tour=tourmaline and tour-qtz=tourmaline and quartz.

Fig. 4.7**J**. Underground exposure of tourmaline-quartz vein cutting cleaved tuffaceous host rock. Note the vein is at an angle to the cleavage which suggests that tourmaline-quartz veining was post-cleavage. Location 15 Level, F(J) lens, south-end orebody, Rosebery Mine, western Tasmania. tour=tourmaline and tour-qtz=tourmaline and quartz.

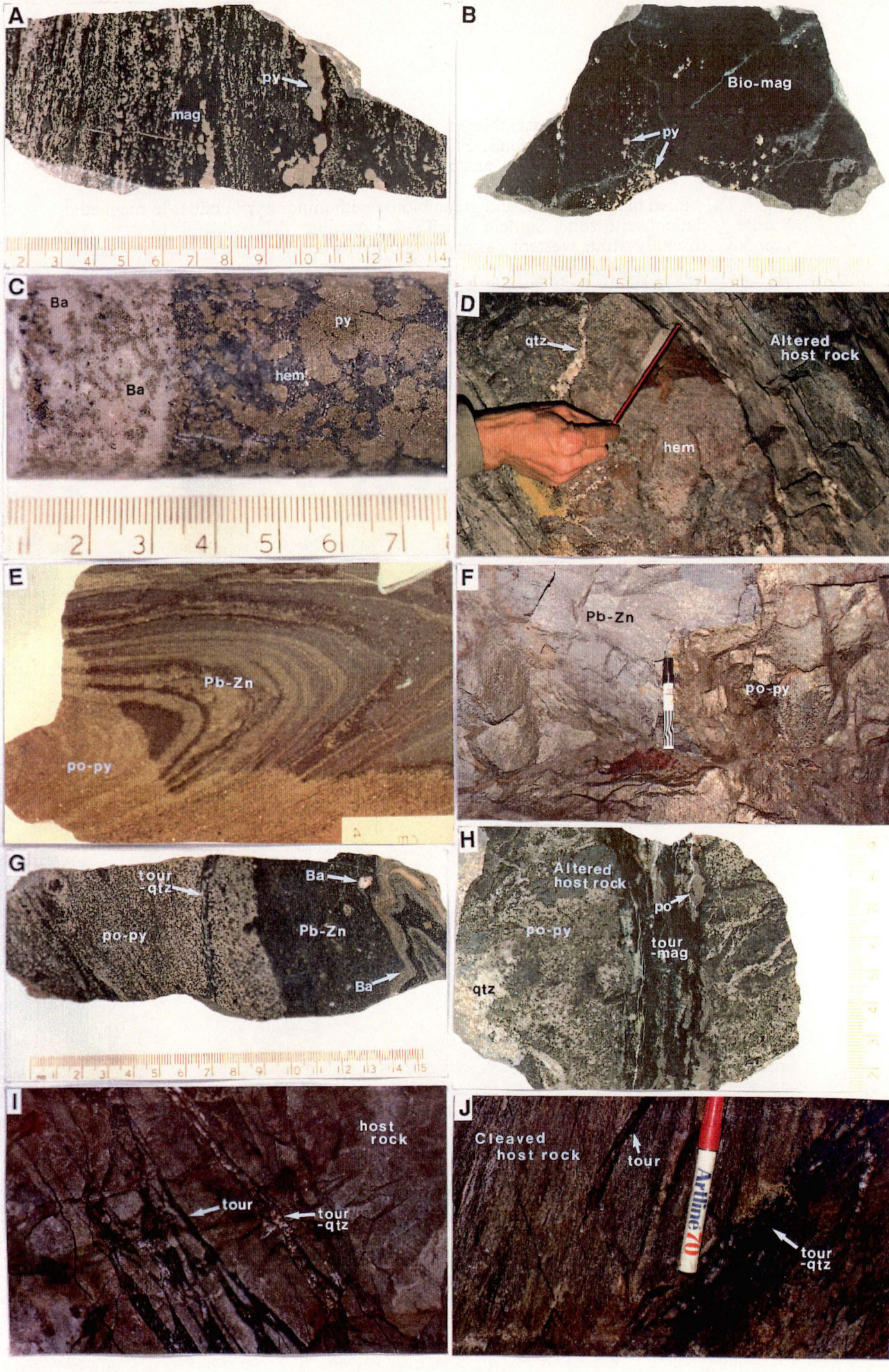
A
py
mag
B
Bio-mag
py
C
Ba
py
hem
Ba
D
qtz
Altered
host rock
hem
E
Pb-Zn
po-py
F
Pb-Zn
po-py
G
tour
-qtz
Ba
po-py
Pb-Zn
Ba
H
Altered
host rock
po
po-py
tour
-mag
qtz
I
host
rock
tour
tour
-qtz
J
Cleaved
host rock
tour
Artline
tour
-qtz

Biotite in this zone is green to dark green in colour, less flaky and mottled and can be visually mistaken for magnetite. The chlorite occurs in the sulphide lenses and the footwall and is associated with biotite. Sericite and K-feldspar are also found in this zone. The recrystallised chalcopyrite is present in a high concentration. Unusual assemblages such as garnet–biotite, garnet–helvite–tourmaline are noted in this zone. Garnet and helvite are usually found at deeper levels of the mine. Microprobe analyses of garnet, biotite, helvite and tourmaline are presented in Chapter 6.

### 4.2.2 Pyrrhotite–pyrite zone ...

Zones of pyrrhotite–pyrite extend from 14 Level down to 17 Level where they give way to magnetite-rich assemblages. Brathwaite (1974) first reported the pyrrhotite+pyrite assemblages transgressing the folded primary Pb–Zn sulphide lenses (Fig. 4.7E). Most of the sphalerite and galena in the banded sulphides appear to have been replaced by pyrrhotite and pyrite; only thin sphalerite-rich bands remain and retain the folded structure (Fig. 4.7E). Major zones of pyrrhotite–pyrite bodies cut across the Pb–Zn sulphide lenses in the F(J) lens along 16 No. 2 Sub-Level, 16 Level, 17 No. 2 Sub-level and 17 Level (Figs. 4.7F and 4.7G). In most cases, the pyrrhotite–pyrite zone is enclosed by the tourmaline–quartz ± magnetite zone which consists of quartz and tourmaline with a variable amount of magnetite and chlorite (Fig. 4.2).

The massive pyrrhotite–pyrite bodies range from 1 m to more than 20 m across. A zone of dark brown, coarse-grained sphalerite is commonly observed as a rim between the massive pyrrhotite–pyrite and the original sphalerite–galena lenses (Fig. 4.8). As described by Solomon et al. (1987) this pyrrhotite–pyrite zone varies from pyrrhotite-dominant to pyrite-dominant with or without tourmaline, magnetite and biotite. Below 17 Level no large bodies of pyrrhotite–pyrite were observed although thin lenses of pyrrhotite–pyrite with chalcopyrite may occur in the massive magnetite–biotite zone.

### 4.2.3 Tourmaline–quartz ± magnetite zone ...

The tourmaline–quartz zone envelops and overlies the massive pyrrhotite–pyrite zone. It is well exposed at the southernmost end of the F(J) lens. This zone consists of irregular and patchy quartz–tourmaline veins cross-cutting the host rock and other sulphide lenses (Fig. 4.7H). Tourmaline in this zone commonly forms networked, banded, thin veinlets (Fig. 4.7I). Underground examination indicates that the tourmaline–quartz veins demonstrably cut the cleavage of the tuffaceous host rocks (Fig. 4.7J). Though tourmaline and quartz are the dominant minerals in this zone, patches of pyrrhotite, pyrite and magnetite (± hematite) with chlorite, fluorite and carbonates were also noted.

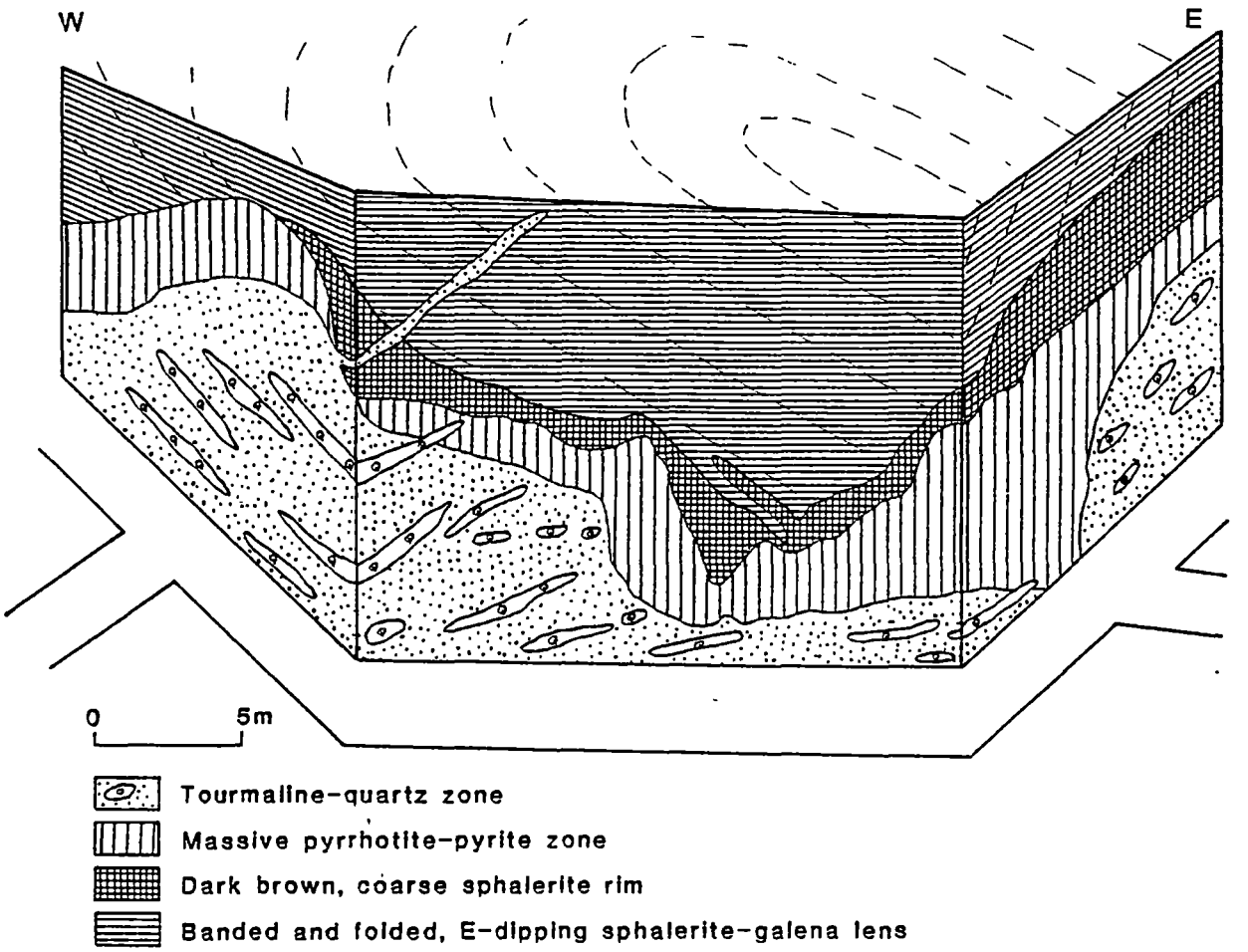


Fig. 4.8 A sketch showing pyrrhotite–pyrite and tourmaline–quartz assemblages replacing Pb–Zn lens. Note the banded Pb–Zn lens is dipping to the east and is apparently folded. Dark brown, coarse-grained sphalerite forms as a reaction rim between the Pb–Zn lens and the pyrrhotite–pyrite assemblage and is cross-cut by patchy tourmaline-quartz veins. The dashed line indicates the trace of fold pattern. Location 16, No.2 Sub-level, 900' (276mS), F(J) lens, south-end orebody, Rosebery mine, western Tasmania.

## 4.3 GENETIC SIGNIFICANCE OF TRANSGRESSIVE MINERAL ASSEMBLAGES ...

Brathwaite (1974) initially interpreted that the pyrrhotite–pyrite bearing assemblages transgressing the stratiform sulphide lenses in the south-end of the Rosebery mine were formed as a result of the Devonian metamorphism. Later drilling and geological investigation have indicated that the transgressive assemblages consist of a wide variety of other minerals from magnetite (hematite)–biotite to tourmaline–quartz, fluorite, garnet and helvite.

Many later workers attributed these Fe–S–O and silicate mineral assemblages to hydrothermal activity associated with post-kinematic Devonian granite plutons (Solomon et al., 1987; Lees, 1987; Green and Iliff, 1989; Lees et al., 1990). The granite does not outcrop but the existence of a shallow granite intrusion below the Rosebery south-end has been interpreted from gravity data (Large, 1986; Leaman and Richardson, 1989).

On this basis, the following geological criteria support the replacement origin of the transgressive mineral assemblages rather than the metamorphic origin:

(1) Minerals such as biotite, garnet and helvite found in the Rosebery south-end Fe-S-O zones are also reported from the other well-documented Devonian granite-related replacement deposits in western Tasmania (e.g. Mt Lindsay deposit, Kwak, 1983; Cleveland deposit, Collins, 1981; Barth, 1986).

(2) The occurrence of many replacement textures and alteration features between the transgressive mineral assemblages and the Cambrian exhalative mineral assemblages.

A zone of dark brown, coarse-grained sphalerite is commonly observed as a rim between the trangressive pyrrhotite–pyrite bodies and the primary sphalerite–galena lenses. This textural feature suggests that the rim was produced as a result of reaction between the stratiform Pb–Zn sulphide lenses and the hydrothermal fluids during the replacement process. Magnetite also appears extensively replacing massive pyrite lenses (Fig. 4.7A) and alteration of chlorite to biotite was also commonly found in the transgressive assemblages.

(3) The presence of the zonal arrangement of the transgressive mineral assemblages: magnetite–biotite ± chalcopyrite assemblages being confined to the lower levels of the mine, and the pyrrhotite–pyrite and other tourmaline–quartz ± magnetite toward the upper part of the orebody suggests replacement by fluids moving upwards from a high temperature source (see further discussion, Chapters 10 and 11).

(4) The regional gravity in the area provides strong evidence for the presence of a Devonian granite below the Rosebery south-end orebody (Fig. 4.9).

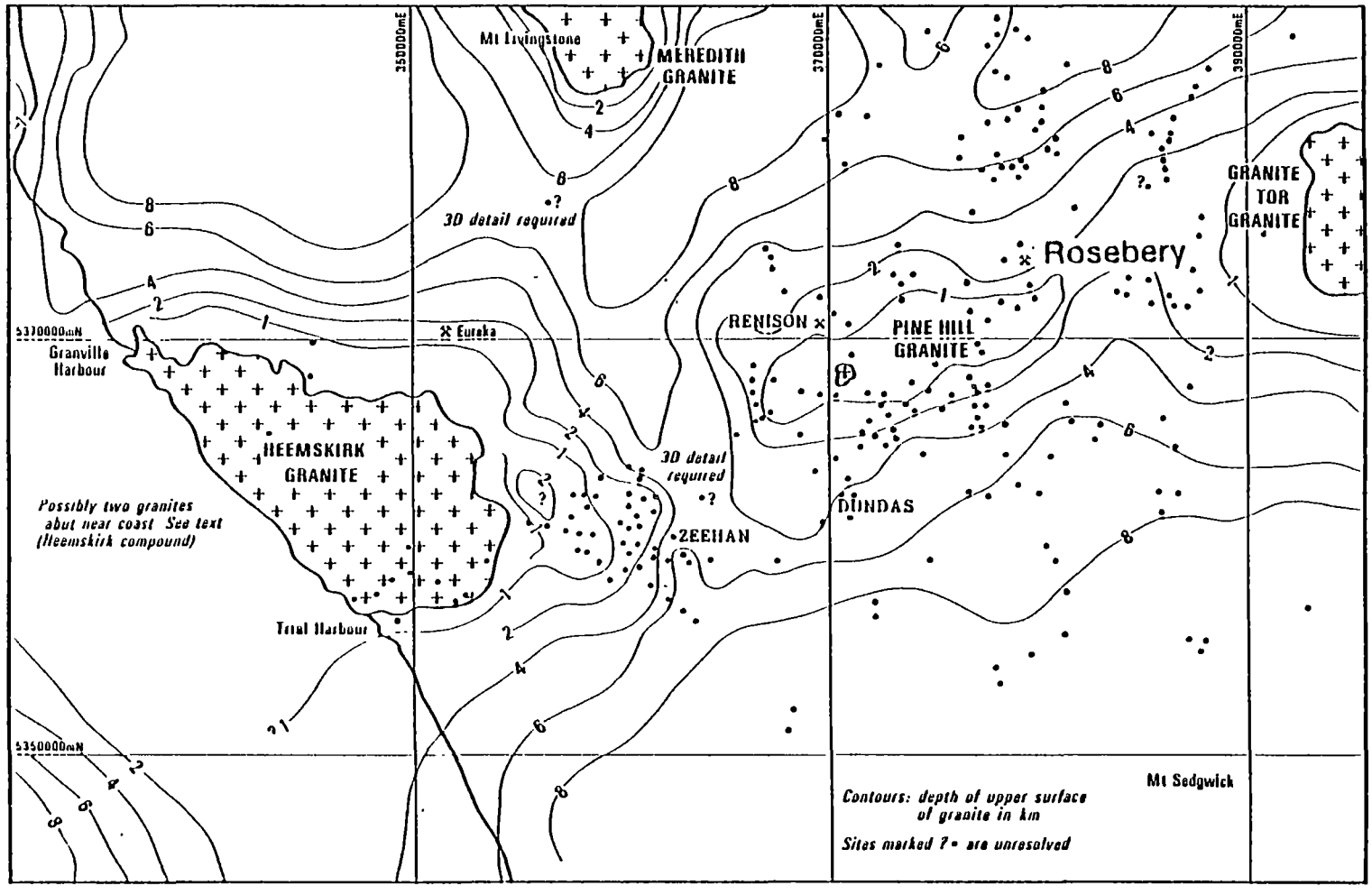


Fig. 4.9 Geophysical interpretation of Devonian granite in western Tasmania (after Leaman and Richardson, 1989). Mineralised sites are shown as dots and the contour intervals are in kilometers. Note the granite ridge passing from the Heemskirk granite through the Pine Hill granite and south-end of Rosebery to Granite Tor granite.

## 4.4 TIMING AND NATURE OF REPLACEMENT ASSEMBLAGES ...

The textural relationships suggest that the replacement of the primary, massive sulphide lenses by the Fe–S–O assemblages occurred after folding and deformation of the primary Pb–Zn sulphide lenses as the pyrrhotite–pyrite assemblages cut across the previous fold structures (Fig. 4.8). The relationship can also be seen on hand-specimen scale (Figs. 4.7E and 4.7G). This evidence, together with the network of post-cleavage tourmaline–quartz veining in the ore zone, indicates that the replacement process occurred after the folding event associated with the Devonian Tabberabberan Orogeny. It is therefore unlikely that these metasomatic assemblages are related to the pre-orogenic Cambrian granites.

Magnetite extensively replaces massive pyrite lenses to form massive bodies, with or without biotite, where replacement was complete. Pyrite may occur as cubes of various sizes in the magnetite ± biotite host and coalesced pyrite cubes are also variably altered by magnetite suggesting that the replacement of pyrite by magnetite has occurred after the recrystallisation of pyrite.

The pyrrhotite–pyrite zone provides the most convincing evidence for the Fe–S–O assemblages replacing the primary Pb–Zn sulphides as a reaction rim with Fe-rich sphalerite is present between them. The pyrrhotite–pyrite zone occurs mostly above the magnetite–biotite ± chalcopyrite zone and it may contain magnetite. A significant amount of gold is also present in the pyrrhotite–pyrite zone. No cross-cutting relation between the pyrrhotite zone and the magnetite zone was noted. These two Fe–S–O assemblages appear to belong to one and the same evolving metasomatic event.

In contrast, the tourmaline–quartz ± magnetite zone appears to have formed at a very late stage during the replacement process as evidenced by irregular and patchy quartz–tourmaline veins cross-cutting the host rock and other sulphide lenses (Fig. 4.7I) and mostly wrapped around the pyrrhotite–pyrite zone. Although tourmaline–quartz veins appear to be stratiform and parallel to the bedding in the drill core intersection, recent detailed underground examination indicated that the tourmaline–quartz veins demonstrably cut the cleavage of the tuffaceous host rocks (see Fig. 4.7J) suggesting that the tourmaline veins were formed after the Devonian cleavage development.

Hence, although the pseudo-banding of the tourmaline assemblages appears to resemble tourmalinites of stratabound origin (e.g. Taylor and Slack, 1984), the cross-cutting textural relationships and its association with other metasomatic minerals such as biotite, garnet, helvite and fluorite positively indicate that they are formed due to replacement (see also Chapter 6).

## 4.5 J(K)-P LENS, HERCULES MINE ...

As the Hercules mine was closed down during the commencement of this study, no underground workings were available for investigation. The mineralogical and metal distribution study was focussed on the J(K)-P lens and R lens based on diamond drill cores. The following zonation can be recognised at the Hercules mine:

4. Carbonate ± barite zone
3. Spotty sphalerite–galena ± pyrite zone
2. Massive sphalerite–galena ± pyrite zone
1. Massive to disseminated pyrite zone (with up to 4% Cu)

Figs 4.10–4.11 show the above mineralogical zonation on the 30.48mS and 75.00mS sections of the J(K)-P lens of the Hercules mine. A brief description of these zones is presented below:

### 4.5.1 Massive to disseminated pyrite zone (with up to 4% Cu) ...

A massive to disseminated pyrite zone with chalcopyrite forms the base of the ore lenses and is followed by a massive to spotty sphalerite–galena ± pyrite zone and then gives way stratigraphically upwards to a carbonate ± barite zone at the top of the lenses. Copper-rich pods (up to 4% Cu) within the disseminated to massive pyrite are also observed.

The mineralogy of the massive to disseminated pyrite zone consists dominantly of pyrite with lesser chalcopyrite and variable sphalerite and galena. Minor minerals include tetrahedrite–tennantite and bismuth sulphosalt minerals. The gangue mineralogy is dominated by chlorite and quartz with lesser sericite and carbonate.

### 4.5.2 Massive sphalerite–galena ± pyrite zone ...

The massive sphalerite–galena ± pyrite zone at the Hercules mine is similar to that of the north-end (A and B lens) of the Rosebery deposit as described by Huston and Large (1986, 1988) and Huston (1989). This zone occurs stratigraphically above the massive to disseminated pyrite zone and it merges either into low-grade ore at the edges or the spotty sphalerite–galena ± pyrite zone.

Mineralogically this ore zone consists of sphalerite, galena and pyrite with minor amounts of chalcopyrite, tetrahedrite–tennantite. Although arsenopyrite and magnetite were noted at

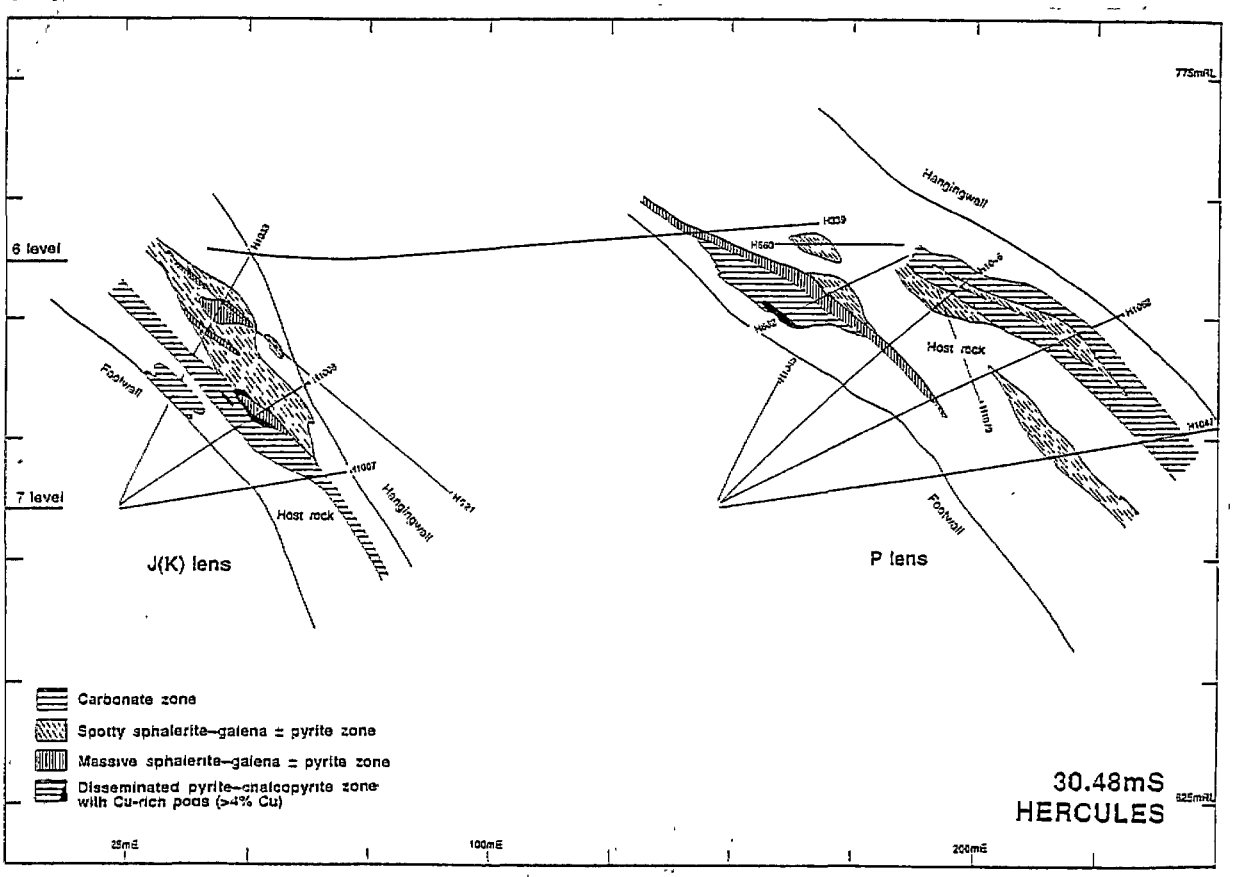


Fig. 4.10 Geology and mineral zonation of 30.48mS section, J(K)-P lens, Hercules mine, western Tasmania.

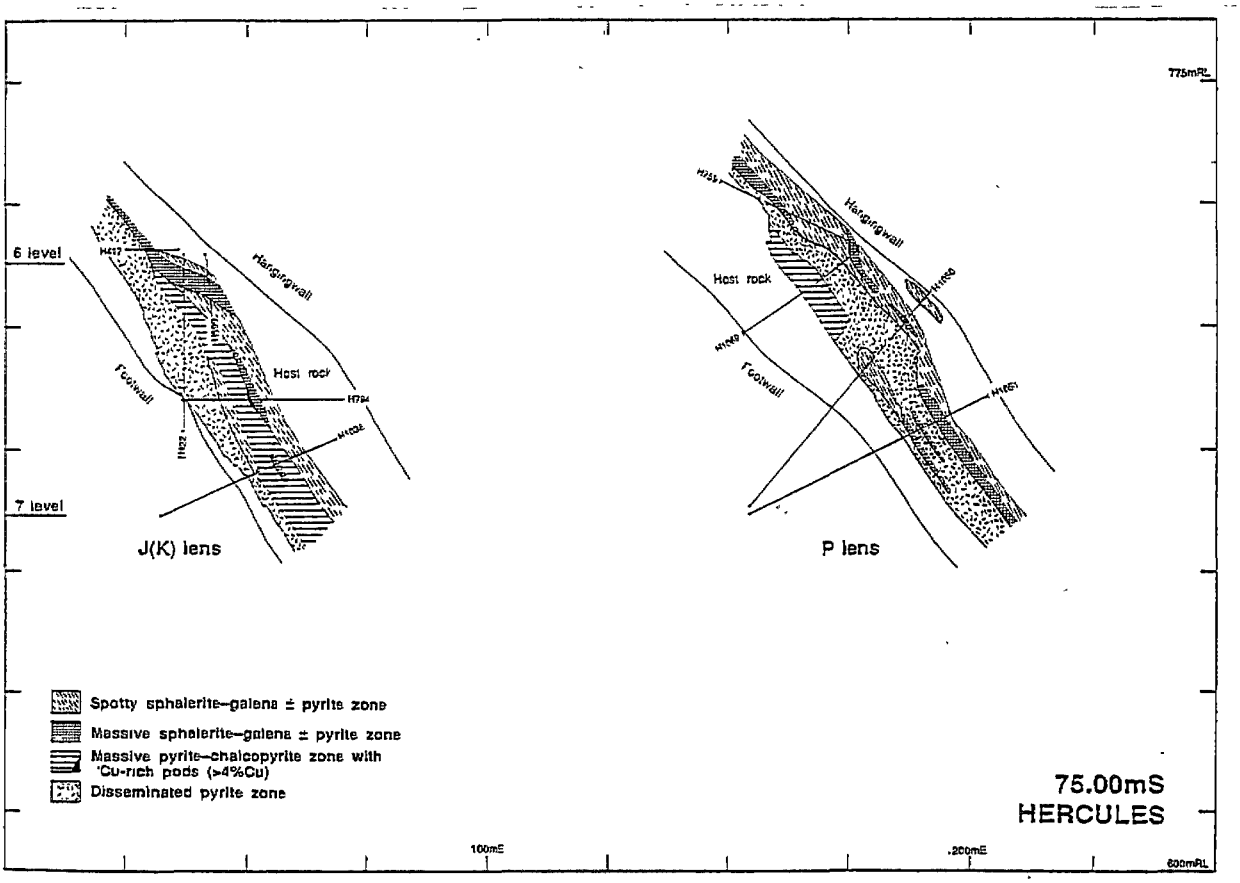


Fig. 4.11 Geology and mineral zonation of 75.00mS section, J(K)-P lens, Hercules mine, western Tasmania.

Rosebery (Brathwaite, 1969), neither arsenopyrite nor magnetite was found in the Hercules ore. Free electrum is also present in trace amounts. Gangue minerals include chlorite, quartz, carbonate and sericite. Fluorite is also rarely observed in this zone. A sample of recrystallised fluorite with gold flakes was collected at the Hercules mine (Chapter 7).

### 4.5.3 Spotty sphalerite–galena ± pyrite zone ...

Although both Rosebery and Hercules ores show massive sphalerite–galena ± pyrite zones, the spotty ores are not found at Rosebery. The spotty ores at Hercules consist of spots or blebs of sphalerite which are rimmed by sericite and often galena and chalcopyrite giving a macro-zonal texture.

The spotty ores are also rather common at South Hercules and the sphalerite blebs in these ores are 1–20 mm across and are commonly elongated and stretched. Mineralogically the spotty ore zone is similar to that of the massive sphalerite–galena ± pyrite zone and consists of sphalerite, galena and pyrite with minor amounts of chalcopyrite, tetrahedrite–tennantite. Free electrum is also present in trace amounts. Gangue minerals in this spotty ore zone include chlorite, quartz, carbonate and sericite.

### 4.5.4 Carbonate ± barite zone ...

The volcanogenic massive sulphide deposits in the Mt Read Volcanics Belt contain a higher content of carbonate minerals than previously described for similar deposits (e.g. Franklin et al., 1981). The carbonate ± barite zone occurs at the top of the sulphide lenses at Hercules. In comparison, although the upper part of the Rosebery deposit contains both carbonate and barite, barite is more abundant at the top of the Rosebery ore lenses. Various forms of carbonate are present at Hercules, from pisolitic, colloform and botryoidal aggregates to massive recrystallised, tightly packed aggregates. The South Hercules deposit also displays variously textured carbonate assemblages as presented below.

Quartz–carbonate veins are also found with minor Pb–Zn mineralisation. Most sphalerite grains in these veins are light yellow to yellowish brown in colour. Fluorite is found as a gangue mineral in the carbonate ± barite zone where it is purple to violet and may be intimately associated with pink carbonates. The fluorite displays variable textures, from rounded discrete grains to thin gash veins.

## 4.6 South Hercules deposit ...

Figures 4.12–4.15 show mineralogical zonation of the South Hercules deposit on E–W cross-sections (5600mN, 5630mN, 5670mN and 5720mN). Khin Zaw et al. (1990) initially classified the mineralogical zonation at the South Hercules deposit into two major types: carbonate

alteration and stringer to semi-massive mineralisation. Three different sub-zones for each major type can be defined:

II. Carbonate altered zone (no gold or silver)
    1. Blebby carbonate sub-zone
    2. Massive carbonate sub-zone
    3. Cherty carbonate sub-zone

I. Mineralised sulphide zone (variable gold and silver)
    1. Massive pyrite ± barite sub-zone
    2. Siliceous stringer sulphide sub-zone
    3. Sphalerite–galena ± pyrite sub-zone

### 4.6.1 Textural characteristics of mineralised sulphide zones ...

The mineralised sulphide zone was subdivided into three sub-zones. The *massive pyrite ± barite sub-zone* contains significant Au grades and mostly occurs at the top of the ore lens (H1142-2 at 43.0 m, 22 g/t Au, 5600mN). This sub-zone is characterised by compact massive pyrite (e.g. H1117-2 at 29.5 m and H1117-3 at 30.1 m, 5600mN) and colloform aggregates of pyrite (Fig. 4.16A), sometimes intermixed with chert (e. g. H1117-1 at 28.2 m, 5600mN) (Fig. 4.16B).

The barite in this sub-zone is remarkably bladed with prismatic grains up to 1 cm across, which may be pseudomorphs after anhydrite (e.g. H1145-2 at 62.35 m, 5670mN) (Fig. 4.16C). The colloform pyrite grains may coalesce or join together and give a prismatic, bladed texture like the barite crystals (Fig. 4.16C). The occurrence of arsenopyrite rhombs is noted above the barite occurrence in this sub-zone (e.g. H1123 at 12.25 m, 5720mN, H1100 at 36.00–46.20 m, 5720mN).

The massive pyrite ± barite sub-zone contains silica but very little other base metal sulphides. In places shearing has been noted; fine- to medium-grained, pyrite framboids in the silica-rich zone become stretched and deformed (e.g. H1114-7 at 39.8 m, 5630mN and H1164-1 at 94.2 m, 5630mN) (Fig. 4.16D). The massive pyrite ± barite sub-zone is comparable in texture, composition and Au enrichment with the distal pyrite zone of the Rosebery mine (Huston and Large, 1986) and the glassy silica–pyrite cap at Hellyer (McArthur, 1986, 1989, 1990) both of which contain appreciable gold values.

The *siliceous ± stringer sulphide sub-zone* is essentially a silicified and sericitic tuff with disseminated to stringer Pb–Zn mineralisation (Fig. 4.16E). This sub-zone varies in texture from a siliceous tuff with disseminated sulphides to sericitic tuff with elongated blotches or

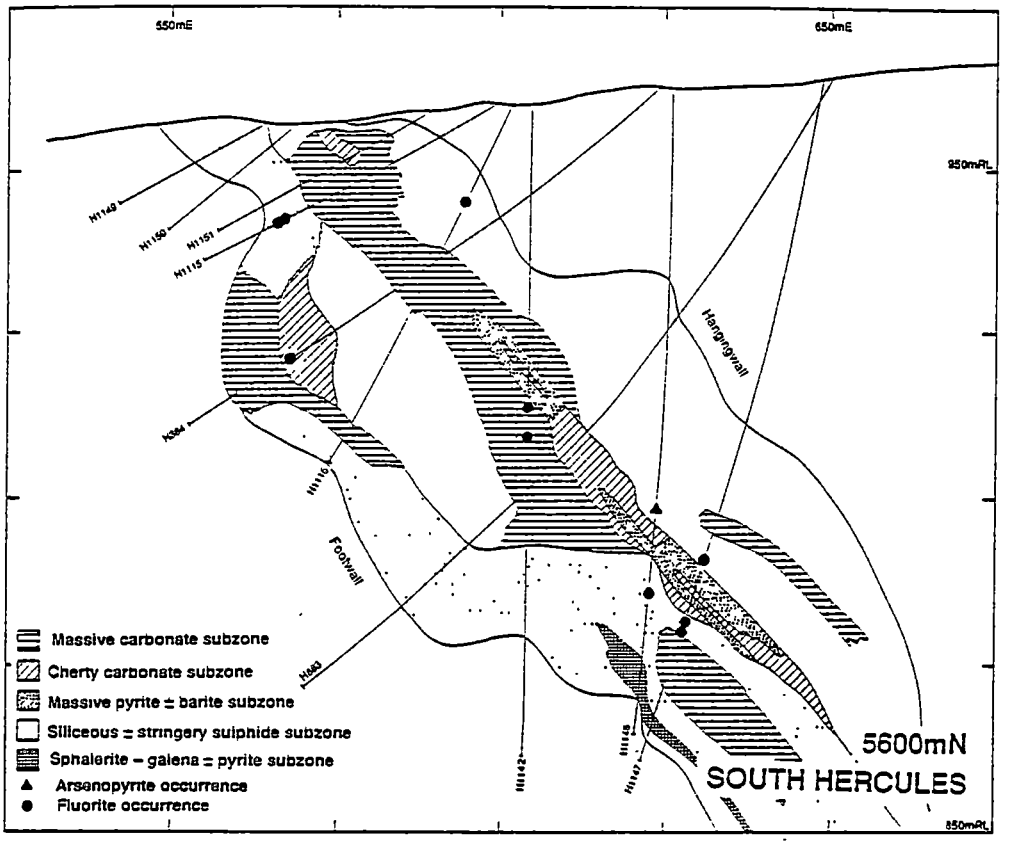


Fig. 4.12 Geology and mineral zonation of 5600mN section, South Hercules deposit, western Tasmania.

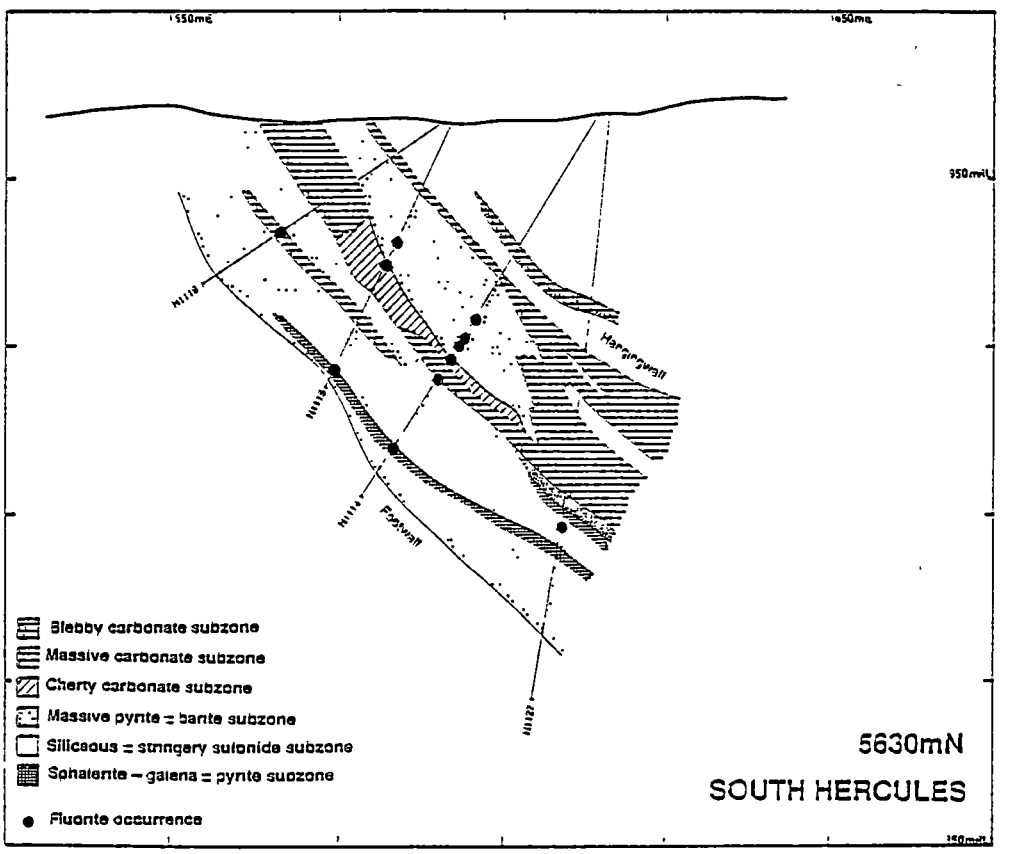


Fig. 4.13 Geology and mineral zonation of 5630mN section, South Hercules deposit, western Tasmania.

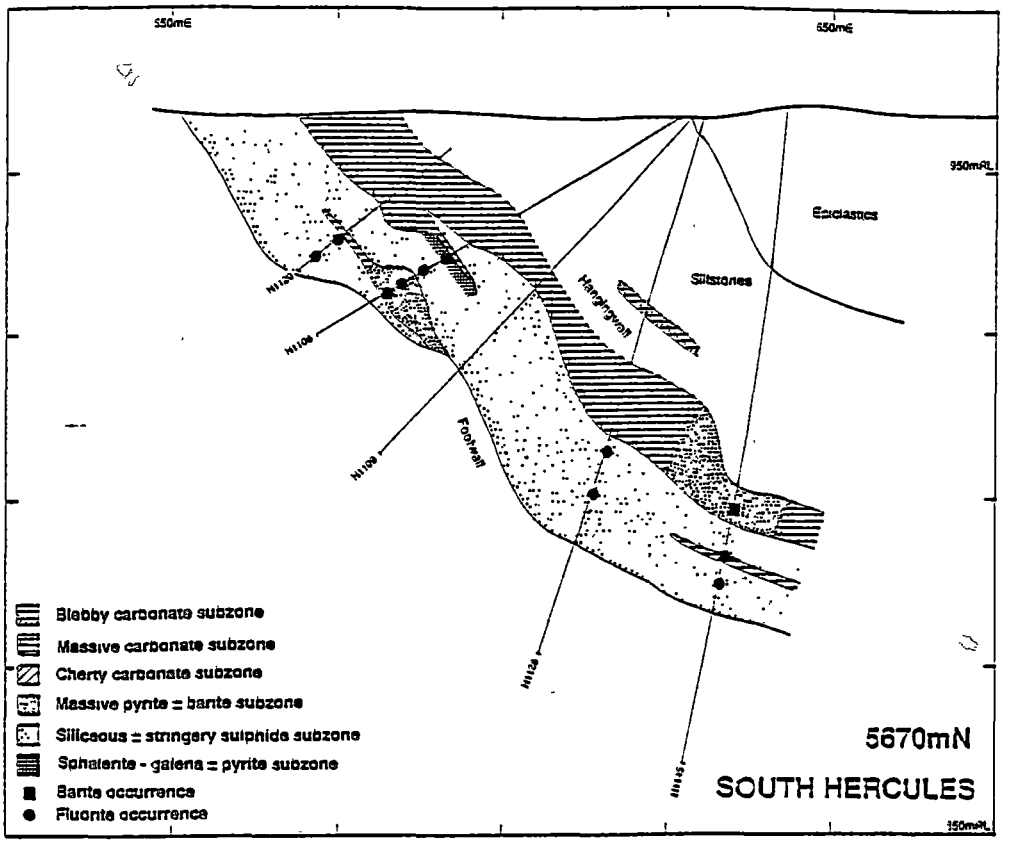


Fig. 4.14 Geology and mineral zonation of 5670mN section, South Hercules deposit, western Tasmania.

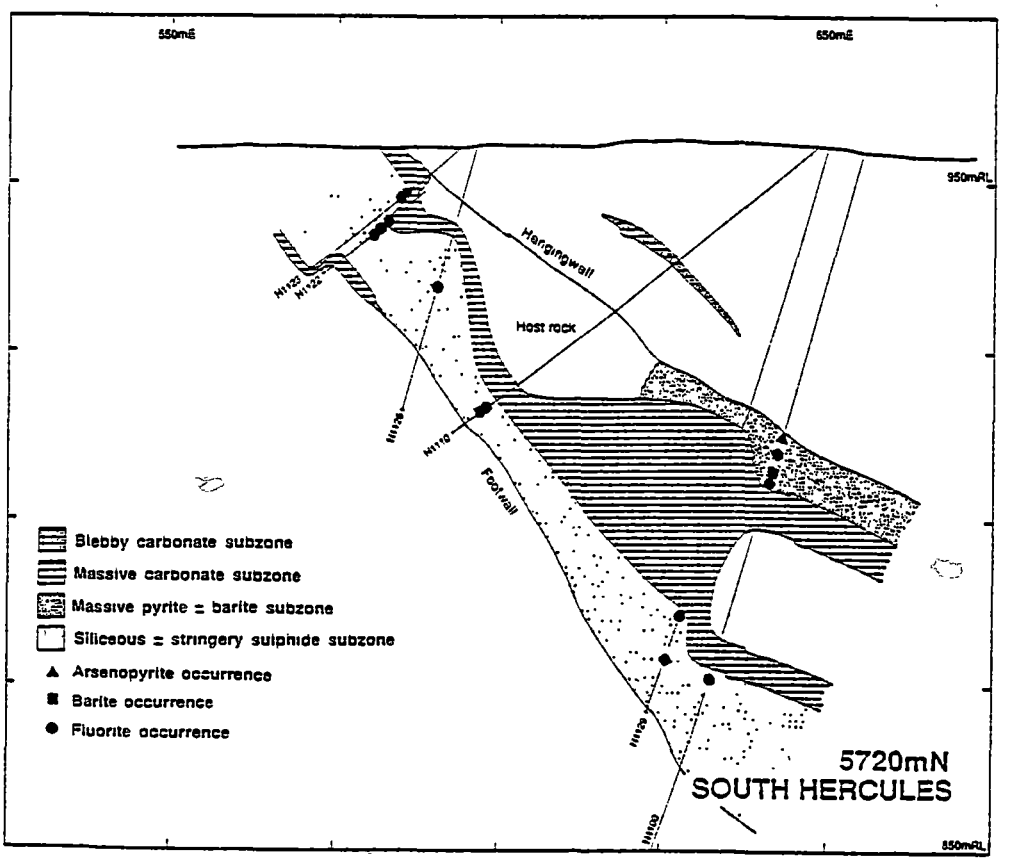


Fig. 4.15 Geology and mineral zonation of 5720mN section, South Hercules deposit, western Tasmania.

blebs of sphalerite rimmed by sericite (e.g. H1118 at 33.0 m, 5630mN). The size of the sericite-rimmed sphalerite spots or blebs ranges from 2 mm to more than 1 cm across (Fig. 4.16F). Under the microscope the nature of the sericitic rim can be clearly seen (Figs. 4.16G and 4.16H). In places the sphalerite spots are surrounded by galena or chalcopyrite.

The *massive sphalerite–galena ± pyrite sub-zone* has the form of thin stratiform lenses. The sphalerite in this sub-zone may accompany chalcopyrite, recrystallised galena and gold. This zone is sometimes spotty in texture and grades into the siliceous ± stringer sulphide sub-zone. It mostly occurs below the carbonate and massive pyrite ± barite sub-zones and it may contain a subordinate amount of gold.

### 4.6.2 Textural characteristics of carbonate altered zones ...

Carbonate alteration at the South Hercules deposit is the most spectacular alteration type and has significant textural variation. Lees (1988) reported different styles of carbonate textures from bladed, "fireworks", pods, cannonballs through spots, spheroids to recrystallised, tightly packed massive carbonate.

The carbonates at South Hercules essentially occur as fine-grained zoned spheroids with chloritic matrix in the core (Fig. 4.17A) or larger, botryoidal cannonball aggregates to coalesced, tightly packed spheroids or massive carbonates (Fig. 4.17B). The colour of the carbonate blebs may be pink or white (Fig. 4.17C) but a complete gradation of carbonate textures can be seen in many drill holes. In addition, 10 cm-thick, late fracture-filling quartz–carbonate ± fluorite veins (e. g. H1108-1 at 29.5 m, 5670mN) are not uncommon and cross-cut the recrystallised massive carbonates (Fig. 4.17E) and sometimes these late veins are composed entirely of massive pink carbonates ( Figs. 4.17D) and also cut the coalesced carbonate-bearing host rock (Fig. 4.17F).

In this investigation, the carbonate altered zone was subdivided into three carbonate sub-zones of blebby, massive and cherty assemblages. The *blebby carbonate sub-zone* occurs at the topmost part of the ore zone and is mostly confined to the hangingwall. This zone contains blebby to rounded carbonate, chlorite and quartz. Arsenopyrite is also noted in the blebby carbonate sub-zone well up in the hangingwall siltstone unit (e.g. H1128 at 31.50 m, 5670mN).

The *massive carbonate sub-zone* occurs below the blebby carbonate sub-zone and sometimes as a lateral equivalent of the massive pyrite ± barite sub-zone. The massive carbonate sub-zone may contain abundant coalesced carbonate spheroids. Irregular and thin pyrite bands are sometimes noted in the massive carbonate zones (Fig. 4.17G). The *cherty carbonate sub-zone* is similar to the massive carbonate sub-zone but more massive, and composed of finer grained carbonates, cherty in appearence, and contains cryptocrystalline silica (Fig. 4.17H). Both the main carbonate sub-zones wrap around the massive pyrite ± barite sub-zone.

Fig. 4.16A. Massive pyrite assemblage with colloform texture in massive pyrite±barite sub-zone, Sample No. H1117-2 at 29.5m, 5600mN (Fig. 4.18B) and Sample No. H1117-3 at 30.1m, 5600mN (below), South Hercules deposit, western Tasmania. Note patches of remobilised, yellowish to light brown sphalerites. py=pyrite and sp=sphalerite.

Fig. 4.16B. Cryptocrystalline chert intermixed with pyrite in the massive pyrite±barite sub-zone, Sample No. H1117-1 at 28.2m, 5600mN, South Hercules deposit, western Tasmania. py=pyrite.

Fig. 4.16C. Bladed barite crystals together with coalesced colloform pyrite grains in massive pyrite±barite sub-zone. Sample No. H1145-3 at 62.35m, 5670mN (above) and Sample No. H1145-5 at 70.3m, 5670mN (below), South Hercules deposit, western Tasmania. Note that the bladed barite appearing to be pseudomorphs of anhydrite ? and the bladed pyrite patches appear to be pseudomorphs after barite ? Ba=barite and py=pyrite.

Fig. 4.16D. Sheared massive pyrite from the massive pyrite±barite sub-zone, Sample No. H1164-1 at 94.2m, 5630mN, South Hercules deposit, western Tasmania. py=pyrite.

Fig. 4.16E. Disseminated and stringer Pb-Zn sulphide assemblages in siliceous host rock in siliceous±stringer sulphide sub-zone, Sample No. H1118-15 at 32.7m, 5630mN, South Hercules deposit, western Tasmania. sp-ga=sphalerite and galena.

Fig. 4.16F. Spotty sphalerite patches with pyritic and/or sericitic rims in siliceous± stringer sulphide sub-zone, Sample No. H1148-2A at 89.5m. 5600mN, South Hercules deposit, western Tasmania. sp=sphalerite.

Fig. 4.16G. Elongated, brown coloured sphalerite bleb with sericitic rim in spotty sulphide sub-zone, Sample No. 1118-3 at 67m, 5630mN, South Hercules deposit, western Tasmania. chl=chlorite, ser=sericite, and sp=sphalerite.

Fig. 4.16H. Same as above, under reflected light. Note minute blebs and patches of chalcopyrite in the sphalerite. sp=sphalerite, cp=chalcopyrite and py=pyrite.

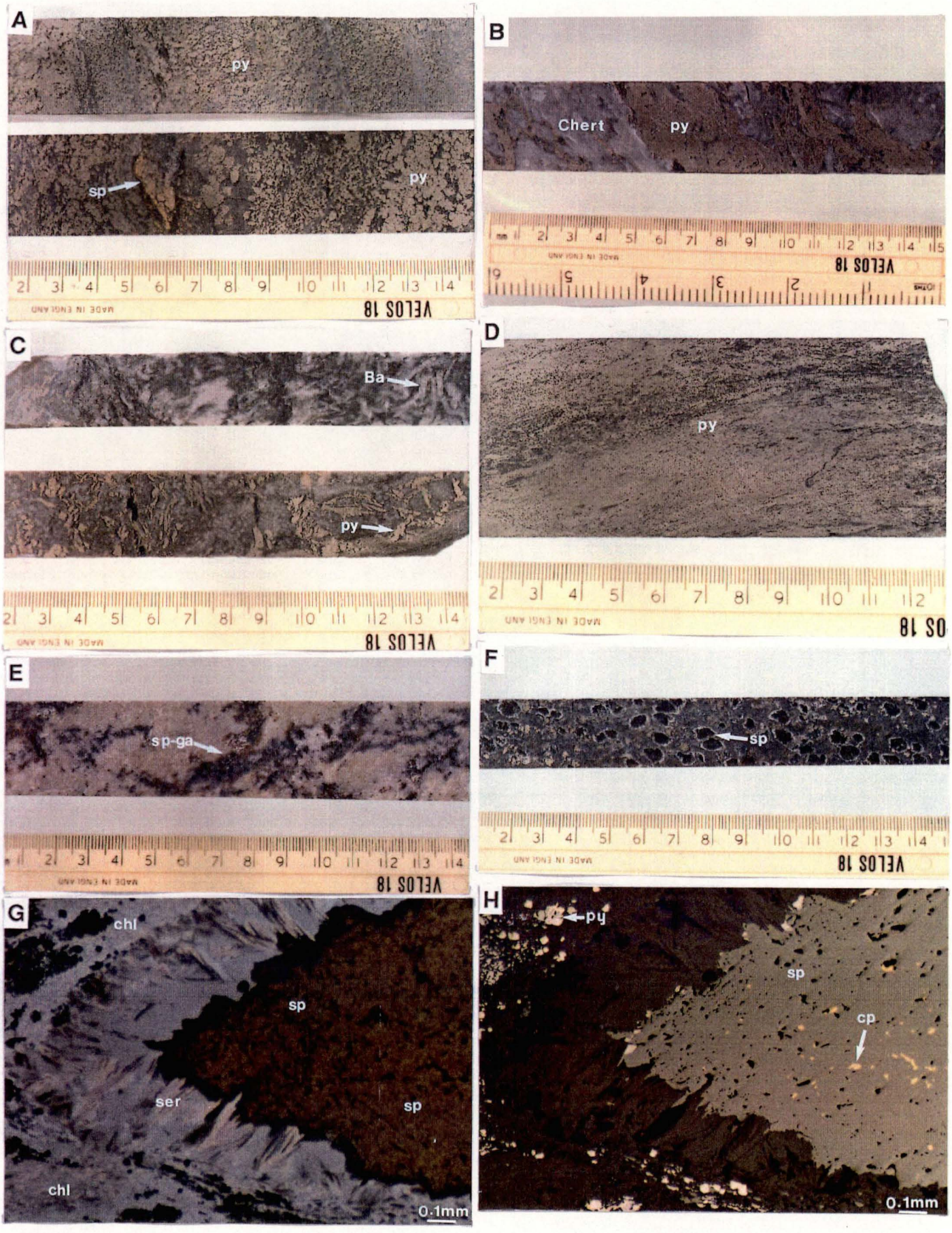
A
py
sp
py
B
Chert
py
C
Ba
py
D
py
E
sp-ga
F
sp
G
chl
sp
ser
sp
chl
0.1mm
H
py
sp
cp
0.1mm

Fig. 4.17A. Carbonate spheroids set in quartz-chlorite matrix of the massive carbonate sub-zone, Sample No. H1108-10A at 50.2m, 5670mN, South Hercules deposit, western Tasmania. Note that spheroids show chloritic cores and coalesce to form more massive carbonate which then merges with massive recrystallised carbonate. Also note the late pink carbonate vein at upper centre.

Fig. 4.17B. Recrystallised, cannonball carbonates set in chloritic matrix of the massive carbonate sub-zone, Sample No. H1132-5 at 74.0m, 5585mN, South Hercules deposit, western Tasmania. Note fluorite gash vein with carbonates at lower centre. Note also that the ball-shaped carbonates merge with recrystallised carbonate. Flo=fluorite.

Fig. 4.17C. Recrystallised, blebby to rounded white carbonates in chloritic matrix of the massive carbonate sub-zone, South Hercules deposit, western Tasmania, Sample No. H1142-6 at 49.6m, 5600mN.

Fig. 4.17D. Late quartz-carbonate vein cutting massive carbonate with bands of chlorite, Sample No. H1108-1 at 29.5m, 5670mN, South Hercules deposit, western Tasmania. chl=chlorite.

Fig. 4.17E. Late pink carbonate vein cutting massive carbonate in massive carbonate sub-zone, H1108-3A at 34.5m, 5670mN, South Hercules deposit, western Tasmania. Note chloritic patches in the massive carbonates.

Fig. 4.17F. Late pink carbonate±quartz vein cutting carbonate spheroids set in quartz-chlorite matrix in massive carbonate sub-zone, Sample No. H1108-10A at 50.2m, 5670mN, South Hercules deposit, western Tasmania. chl=chlorite.

Fig. 4.17G. Pyrite-rich bands in massive carbonate, Sample No. H1108-3B at 35.0m, 5670mN, South Hercules deposit, western Tasmania. py=pyrite.

Fig. 4.17H. Fine-grained, cherty carbonates with sulphide patches in cherty carbonate sub-zone, Sample No. H1117-A at 21.0m, 5600mN, South Hercules deposit, western Tasmania. ga=galena and sp=sphalerite.

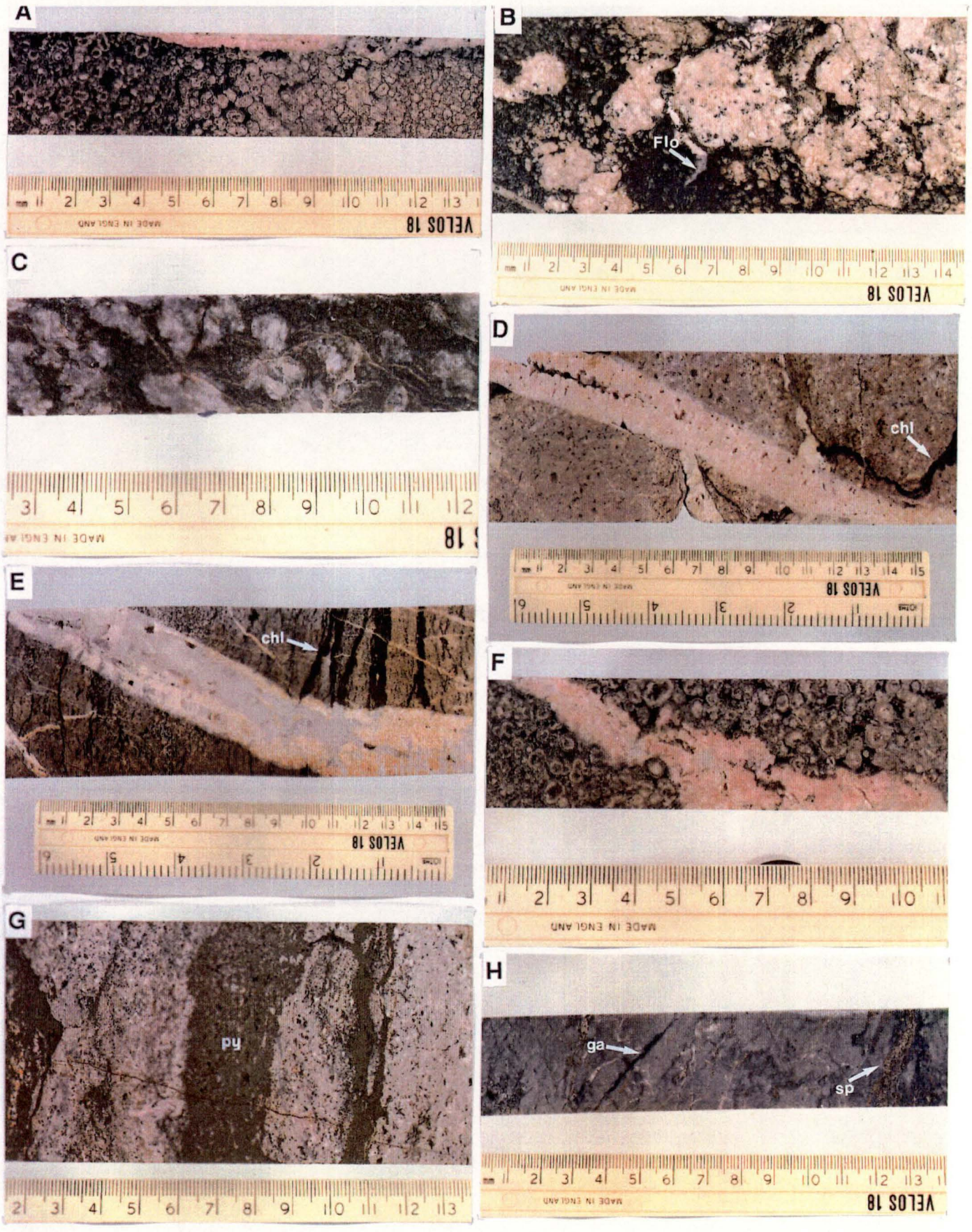
A
B
Flo
C
D
chl
E
chl
F
G
py
H
ga
sp

### 4.6.3 Distribution of fluorite and arsenopyrite in South Hercules ...

It is interesting to note that fluorite is found in almost all of the above mineralised and unmineralised sub-zones at South Hercules. The fluorite occurs as two different textural types: (1) rounded, discrete grains in a chlorite–carbonate matrix and (2) in the late quartz–carbonate ± fluorite veins or fluorite gash veins. It may be violet, green or purple.

The fluorite occurrences are sometimes associated with arsenopyrite. The position of fluorite occurrences were plotted on the E–W cross-sections of the South Hercules deposit to examine the relationships betweeen Au–Ag mineralisation and the fluorite. No systematic variation was recognised and no correlation between elevated Au–Ag grades and the occurrence of fluorite was observed.

Fluorite-rich zones may or may not accompany precious metals enrichment. Although fluorite occurs in different horizons of the deposit, arsenopyrite and barite are confined above the fluorite occurrences in the upper part of the ore zone (e.g. 5600mN and 5720mN) and are associated with elevated Au–Ag concentration (see 5720mN). Arsenopyrite occurs in zones which lack barite. Microprobe analyses of arsenopyrite grains give a restricted range of 29.8 to 30.0 As %. In one drill hole, assay values of up to 11% As were recorded in the massive pyrite ± barite zone at H1142 at 44.3 m, 5600mN where 22 g/t Au was also recorded. However, assay data for As were not sufficient to examine the Au–As relationships. Ore metal distribution of the South Hercules deposit will be presented in Chapter 5.

## 4.7 Genetic implications for the Hercules and South Hercules deposits ...

Although the Hercules and South Hercules ores appear to have undergone metamorphism and related deformation during the Devonian Tabberabberan Orogeny, granite-related metasomatic mineral assemblages such as biotite, garnet and helvite were not found in these deposits. The mineralogical zonation at the Hercules and South Hercules deposits is essentially similar to that of the Rosebery north-end ore lenses (Huston and Large, 1986, 1988; Huston, 1989) but differs from the Rosebery south-end where there is evidence of Devonian metasomatic overprints.

In the Kuroko and other volcanogenic massive sulphide deposits, massive pyrite occurs at the stratigraphic base of the deposits near the vent and chalcopyrite also tends to increase towards the vent (Large, 1977; Eldridge et al., 1983). Massive to disseminated pyrite lenses with Cu-rich pods (up to 4 wt% Cu) are recorded at the Hercules deposit and these pods may be the centres for the most intense, high temperature mineralising fluids during the Cambrian exhalative process.

Similar Cu-rich pods are noted at the Rosebery deposit (Green et al., 1981; Green, 1983; Huston and Large, 1986). In contrast to the main Hercules ore lenses, the South Hercules deposit displays no Cu-rich pods at the base or within the deposit and the overall grade is generally less than 1.0% Cu. The low copper content and relatively high (Au+Ag)/(Pb+Zn) ratios suggest a low temperature of ore formation (Chapter 5).

The spotty or blebby ores in the Hercules and South Hercules deposits appear to have particular genetic significance and they differ from the typical stratiform ores at Rosebery. The spotty ores consist of sphalerite blebs of 1 mm to 5 cm across with sericitic rims and often galena and chalcopyrite giving a zonal texture. These blebs are often foliated and stretched apparently due to strong deformation. In places the spotty or blebby ores may grade into massive sulphide ores. Lees (1987) termed the spotty ore textures as "porphyroblastic" ores and considered that they were formed as a result of Devonian metamorphism and deformation. According to Lees (1987) the spotty or blebby ores are metamorphic in origin.

Because the degree of metamorphism and deformation in the Hercules–South Hercules area is more or less similar to that at Rosebery, and the spotty ores are lacking at Rosebery, then it seems unlikely that metamorphism and deformation had produced the spotty textures. The zoning of the sulphide spots may simply reflect an original open-space filling and/or replacement process in porous volcanics below the seafloor which has been later deformed and the sulphide spots annealed. On this basis, the initial formation of the macro-zonal texture of the spotty ores are herein interpreted to be non-metamorphic in origin. Hence, the textures tend to suggest that they were primarily formed by sub-seafloor replacement of porous volcanics which were later annealed and recrystallised during Devonian deformation.

Other evidence which supports the sub-seafloor replacement origin for the Hercules and South Hercules deposits include:

(1) Most of the ore lenses are not strictly stratiform and show obvious cross cutting relationships with the host rock (e.g. E and M lenses at Hercules).

(2) Spotty sphalerite textures surround, and extend above, the massive lead–zinc lenses at Hercules, suggesting extensive replacement along strike from and stratigraphically above the massive sulphides.

(3) At South Hercules typical banded lead–zinc massive sulphide ore is commonly totally lacking. Disseminated, stringer and spotty sulphide textures are most common and occur in a stratabound zone overlain by irregular zones of carbonate.

(4) The irregular distribution and textural variety of the carbonate zones suggest that they may also form by sub-seafloor replacement of the tuffaceous host rocks.

## 4.8 DEVONIAN RECRYSTALLISATION ...

Lees (1987, 1988) first reported the various forms of carbonate textures from the Hercules and South Hercules deposits and considered that massive carbonates at the main Hercules ore lenses were formed due to Devonian metamorphic recrystallisation, and the quartz–carbonate veins were formed during deformation with remobilisation of quartz and carbonates. Present detailed investigation also indicate that the carbonates at Hercules and South Hercules display wide textural variation from bladed, disseminated, spheroids and recrystallised massive carbonates which are sometimes cut by late fracture-filling quartz–carbonate ± fluorite veins. Although Lees (1988) briefly described the carbonate texture of the South Hercules deposit, no relationship of carbonate textures to genesis was established.

The carbonates from the South Hercules deposit also appear to have suffered Devonian metamorphic recrystallisation. They essentially display two types: (1) spheroids with chloritic matrix and (2) massive recrystallised carbonates. Other textures vary between the two types. Although most of the carbonates at South Hercules appear to be recrystallised, the fine-grained zoned spheroids with chloritic matrix in the core are suggestive of a primary origin (e.g. Fig. 4.17A).

These zoned spotty carbonate spheroids are apparently recrystallised into larger, botryoidal cannonball aggregates, and may be coalesced into tightly packed spheroids or massive carbonates with or without fluorite gash veins (e.g. Fig. 4.17B) by later recrystallisation possibly during the Devonian Tabberabberan Orogeny. Although the colour of the carbonate blebs may be pink or white, a complete gradation of carbonate textures can be seen in many drill holes. This gradational texture may also suggest that the primary carbonate spheroids were gradually transformed into secondary, massive carbonates as the Devonian recrystallisation proceeded.

Similar to carbonates, the discrete fluorite grains in the South Hercules deposit appear to be of primary syn-hydrothermal origin and the fluorite gash veins are of possible Devonian origin. As in the case of carbonate minerals the primary discrete fluorite grains appear to have been recrystallised to form gash vein assemblages sometimes together with carbonates during the Devonian metamorphism. Similar textural variations of fluorite are also commonly noted in the carbonate ± barite zone in the main Hercules ore lenses.

# CHAPTER 5: ORE METAL AND ZINC RATIO DISTRIBUTION

## 5.1 INTRODUCTION ...

In this chapter, ore metal and zinc ratio distribution (100Zn/Zn+Pb) in the Rosebery district deposits will be discussed. Five E–W cross-sections from the F(J) lens of the south-end of the Rosebery mine, two from J(K)–P lens of the Hercules mine and five from the South Hercules deposit were investigated. Detailed geology and metal distribution diagrams are shown in Appendix I. The metal distribution study was undertaken (1) to define the nature of the ore metal zonation, (2) to deduce the conditions of ore formation, (3) to understand the variation of ore metal distribution caused by the Devonian overprinting event and (4) to use the ore metal and zinc ratio distribution as a guide for exploration in the Rosebery–Hercules area.

## 5.2 PREVIOUS WORK ...

Metal distribution at the Rosebery mine was initially investigated by Brathwaite (1969) to demonstrate the correlation among different elements in the orebody. Smith (1975) studied the distribution of the precious and volatile elements in the enclosing host rocks. Later Green et al. (1981) and Green (1983) studied ore metal distribution in the south-end orebody and Naschwitz (1985) in the north-end orebody. Recently Huston and Large (1986, 1988) and Huston (1989) made a detailed study of the distribution, mineralogy and geochemistry of ore metals in the north-end orebody along six cross sections (869mN, 960mN, 1036mN, 1113mN, 1189mN and 1265mN) and gave a comprehensive account of ore metal zonation.

The above metal zonation studies on the Rosebery deposit were undertaken to understand the metal distribution during the Cambrian exhalative environment but no detailed investigation has previously been carried out on the variation of ore metal distribution during the Devonian overprinting event. Hence, the F(J) lens of the Rosebery south-end which has been affected by the Devonian metasomatic process was chosen to investigate in detail in this study.

## 5.3 F(J) LENS, ROSEBERY MINE ...

In this study, the 220mS, 250mS, 270mS, 280mS and 300mS sections of the F(J) lens were investigated in detail. Figures 5.1 and 5.2 show the metal distribution on 270mS and 300mS sections of the F(J) lens. Assay data from Pasminco Company were used; analyses were undertaken at Rosebery mine-site laboratory by AAS method with precision of 0.1 wt %.

### 5.3.1 Zinc ...

As lead and zinc follow the same trends in the north-end (Huston and Large, 1986, 1988; Huston, 1989), only the distribution of zinc was investigated for the F(J) lens. Zinc occurs dominantly as a blanket shaped zone in the sphalerite–galena ± pyrite sulphide lenses. Although lead is not contoured, similar blanket-like enrichment of lead was observed at the north-end (Huston and Large, 1986, 1988; Huston, 1989). Zinc is conspicuously depleted in the trangressive pyrrhotite–pyrite replacement zone of the F(J) lens at the south-end of the Rosebery mine (Figs. 5.1A & B and 5.2A & B), but the enrichment of zinc is still noted in the unreplaced Pb–Zn sulphide parts of the F(J) lens.

### 5.3.2 Gold and silver ...

As noted by Huston and Large (1986, 1988) and Huston (1989) at the north-end, high gold values occur in the sphalerite–galena ± pyrite zones of the primary exhalative massive sulphide lenses. The other most significant distribution of high gold grades is in the pyrrhotite–pyrite replacement zones of the south-end orebody. The highest concentration of gold (29.9 g/t) was noted in DDH R3043 on the section 300mS, and 26.6 g/t Au was noted along DDH R3023 on the section 270mS. Zones containing more than 20 g/t Au are concentrated in the pyrrhotite–pyrite zone on the 270mS and 300mS (Figs. 5.1C & 5.2C).

In the other replacement zones, gold distribution was found to be erratic. The tourmaline–quartz ± magnetite replacement zone contains generally low gold grades (<3.0 g/t) but in places up to 9.0 g/t was observed, and similarly the biotite–magnetite replacement zone contains less than 5.0 g/t Au.

In contrast to gold, silver broadly follows zinc and is commonly concentrated in the sphalerite–galena massive sulphide lenses (Figs. 5.1D and 5.2D). Significant silver values may occur in the basal pyrite–chalcopyrite lenses, but in general this type of mineralisation contains less silver. The pyrrhotite-pyrite zones contain very little silver (<200 g/t Ag).

### 5.3.3 Copper and iron ...

Copper occurs dominantly in the pyrite–chalcopyrite zone of the primary exhalative sulphide lenses at Rosebery (Huston and Large, 1986, 1988; Huston, 1989). Cu-rich pods which

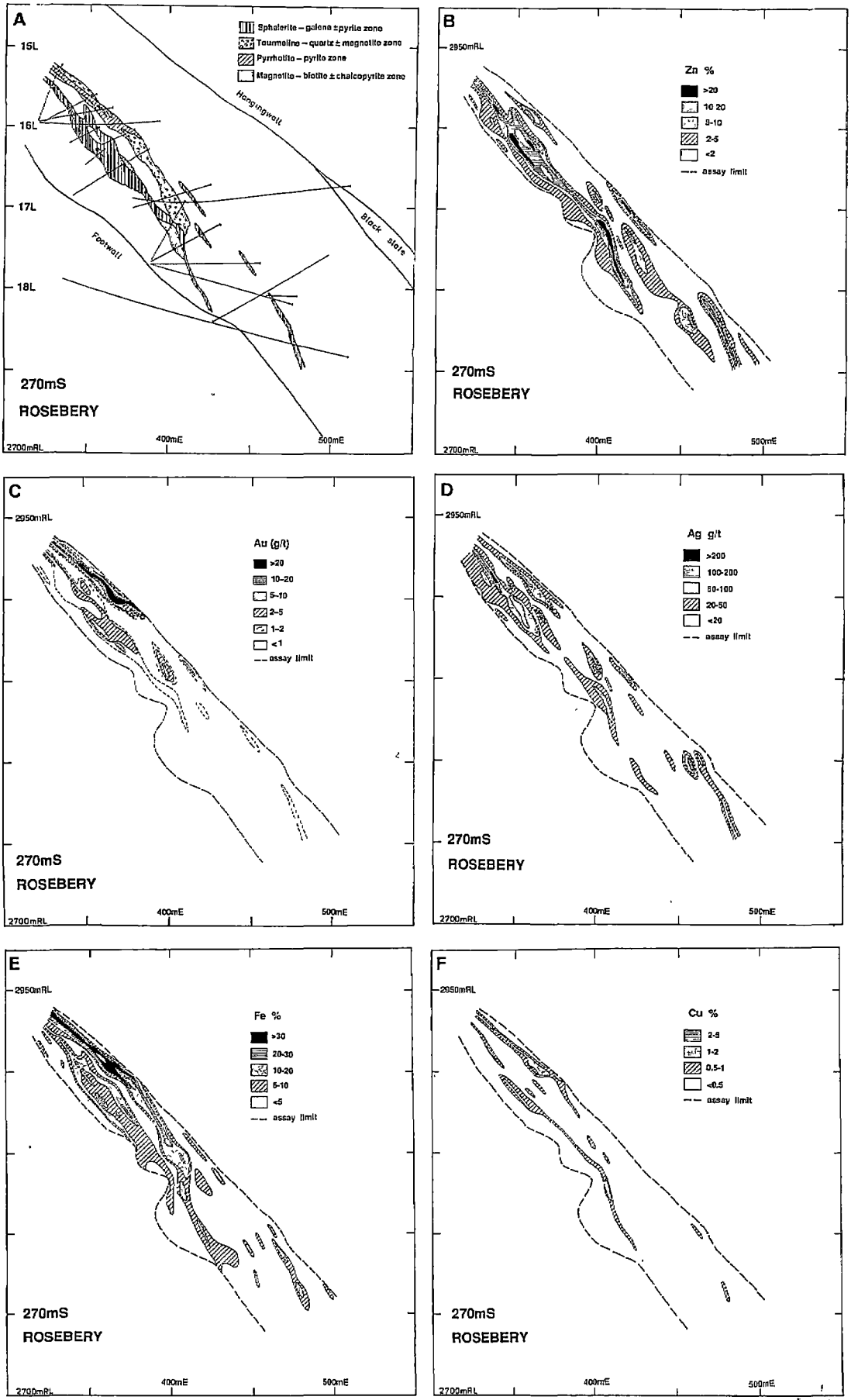


Fig. 5.1 Geology and mineral zonation of 270mS section, F(J) lens, south-end of Rosebery Mine, western Tasmania.

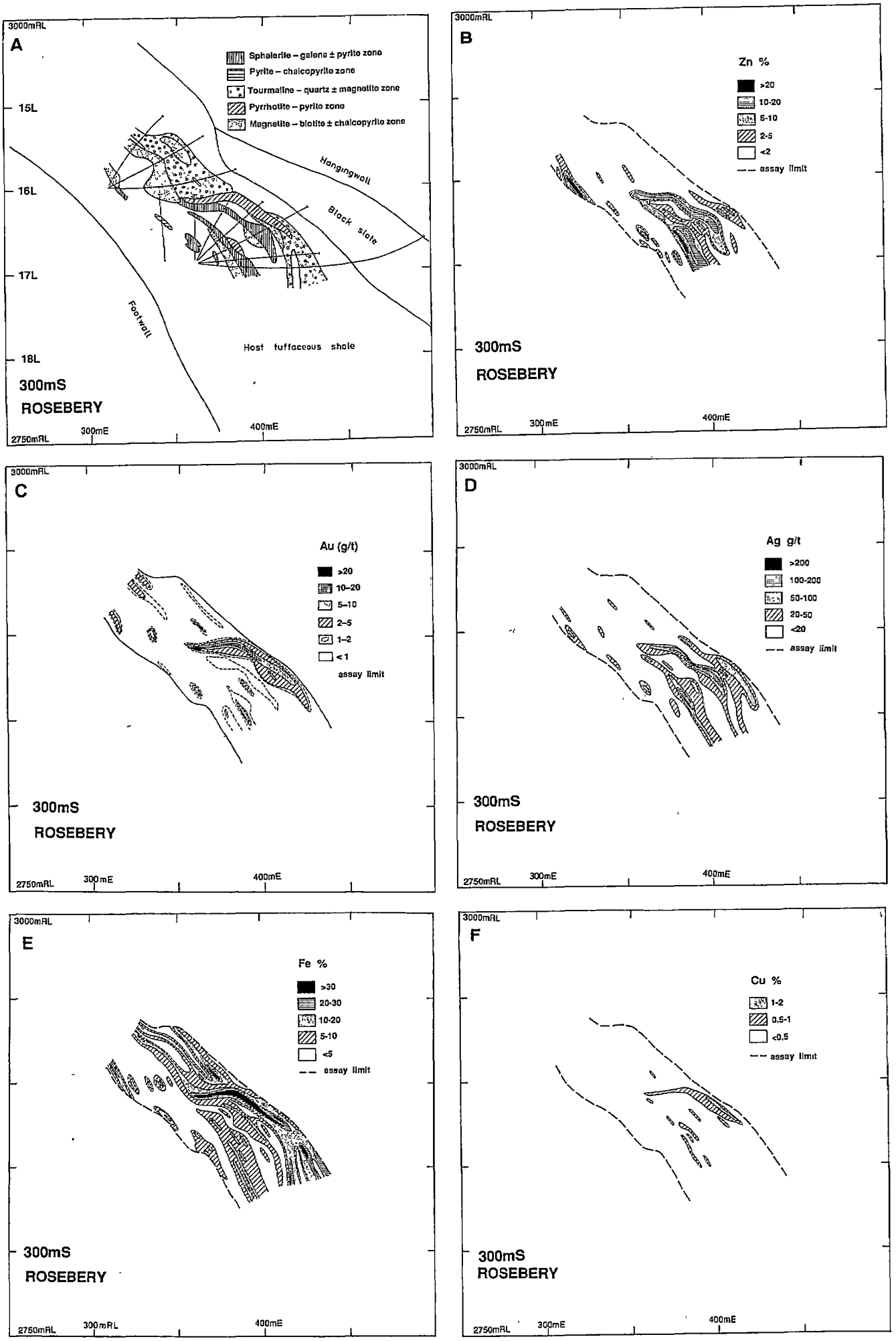


Fig. 5.2 Geology and mineral zonation of 300mS section, F(J) lens, south-end of Rosebery Mine, western Tasmania.

probably represent zones of high temperature fluid focus are represented by copper values greater than 4 %. Copper values as high as 2% are sometimes observed in the massive sphalerite–galena ± pyrite zones. In the massive barite zones, copper values rarely exceed more than 0.5%. In the Devonian replacement zones, enrichment of copper is noted in the magnetite ± biotite and pyrrhotite–pyrite assemblages (Figs 5.1F and 5.2F).

Iron shows two distinct distributions. The first high values occur with copper in the pyrite–chalcopyrite zones and the second high values of more than 30% Fe are concentrated in the pyrrhotite–pyrite replacement zones (Figs 5.1E and 5.2E).

## 5.4 HERCULES AND SOUTH HERCULES DEPOSITS ...

Although ore metal distribution at the Rosebery mine had been investigated by a number of previous workers, ore metal distribution in the Hercules–South Hercules area has only recently attracted attention. The distribution of lead, zinc, gold, silver, copper and iron in the J(K)–P lens, Hercules mine and gold, silver, copper and iron distribution in the South Hercules deposit were investigated in this study. In addition, zinc ratios [100 Zn/(Zn+Pb)] in the South Hercules deposit were also contoured and studied. Metal distribution discussion will be focussed on the 30.48mS section of the J(K)-P lens of the Hercules mine and 5600mN, 5630mN and 5670mN sections of the South Hercules deposit. No arsenic values were available for the Hercules mine and only limited arsenic assay values are available for assessment from the South Hercules deposit.

### 5.4.1 Lead and zinc ...

*(1) Hercules mine:* Lead and zinc occur dominantly in a lenticular zone in the sphalerite–galena–pyrite sulphide zones in the J(K)–P lens of the Hercules mine in a similar pattern to Rosebery north-end orebodies. The lead and zinc distribution on the 30.48mS section of the J(K)–P lens of the Hercules mine is shown together with geology in Figures. 5.3A, B & C.
*(2) South Hercules deposit:* Pb and Zn show a stratabound lenticular distribution in the South Hercules deposit (not shown in figures) but the spatial distribution of zinc ratios [100Zn/ Zn+Pb)] in the South Hercules deposit will be discussed (see below).

### 5.4.2 Gold and silver ...

*(1) Hercules mine:* Two major associations of gold mineralisation were noted in the J(K)–P lens of the Hercules mine. Significant gold mineralisation (>5 g/t) occurs in the massive sphalerite–galena ± pyrite zone enclosed within the spotty sulphide zone (Fig. 5.3D). This gold association is confined to the top of the ore zone.

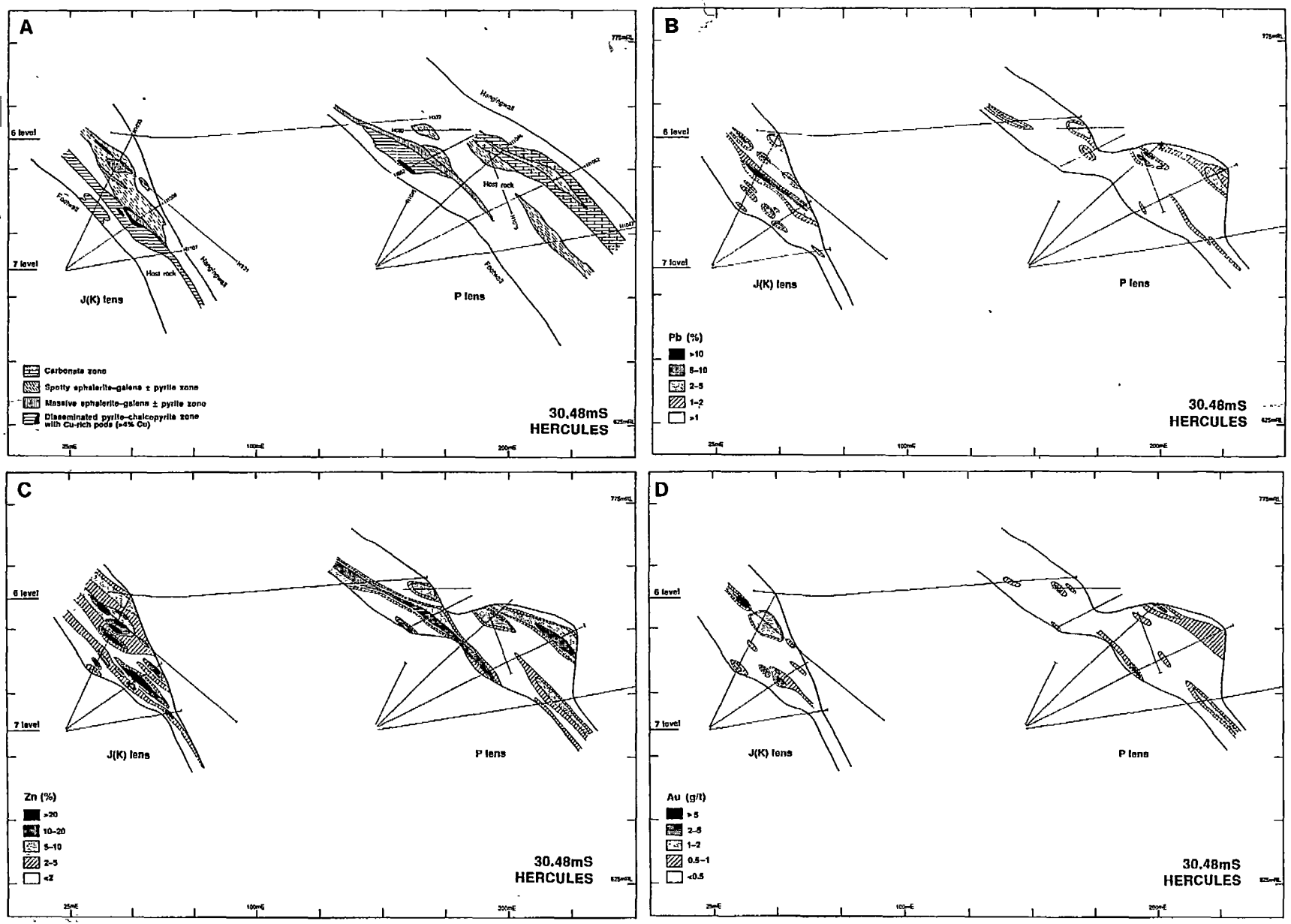


Fig. 5.3 Geology and mineral zonation of 30.48mS section, J(K)-P lens, Hercules Mine, western Tasmania.

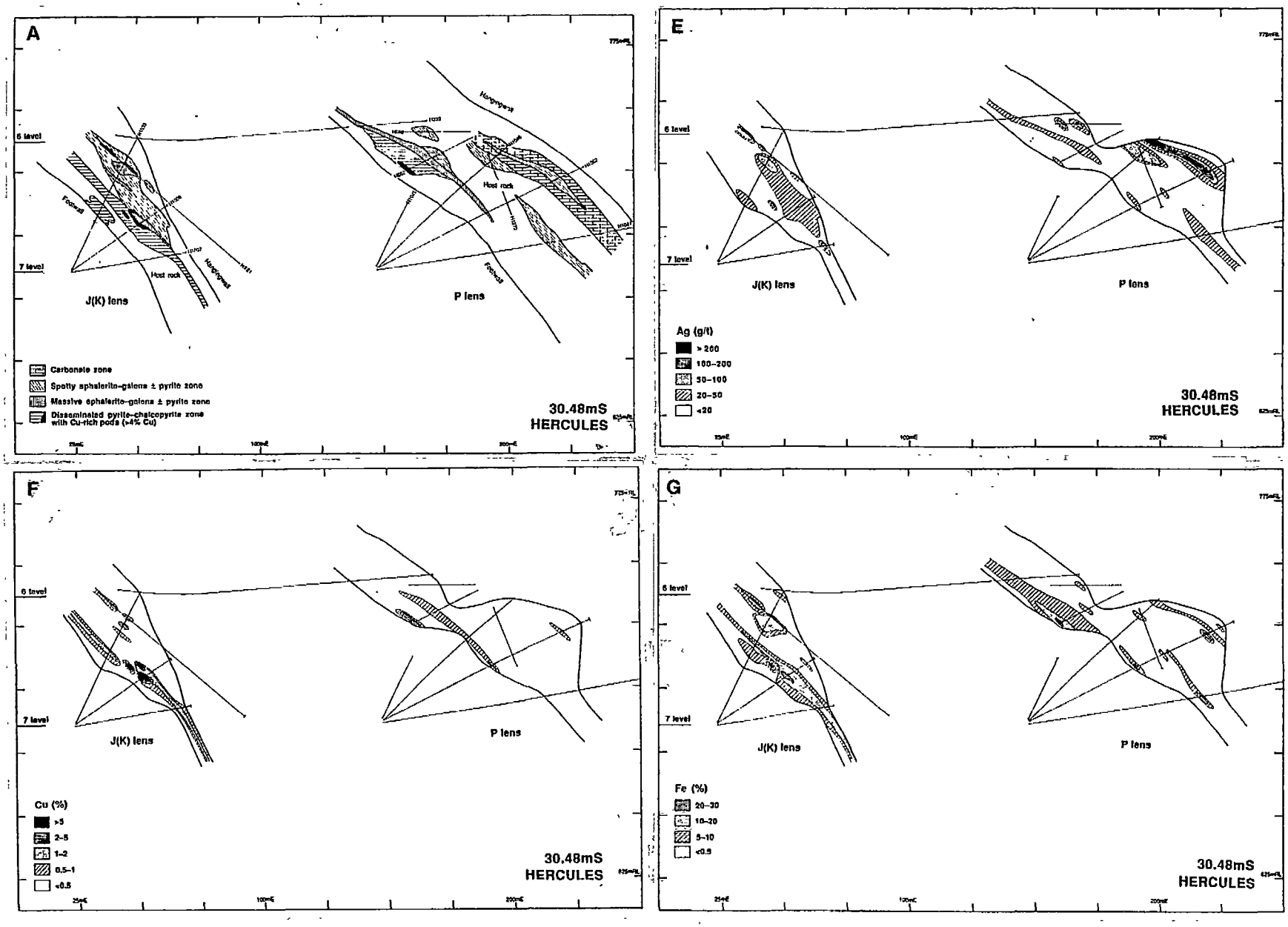


Fig. 5.3 Geology and mineral zonation of 30.48mS section, J(K)-P lens, Hercules Mine, western Tasmania.

A subordinate concentration of Au (up to 3.4 g/t) is also noted in the disseminated to massive pyrite–chalcopyrite zone (>4% Cu) at the base of the J(K)–P lens. The spotty sulphide zone and carbonate ± barite zone lack significant gold mineralisation but the carbonate ± barite zone at the top of the lens may contain minor gold (Fig. 5.3D). Silver broadly follows zinc and is commonly concentrated in the sphalerite–galena massive sulphide lenses. As with Rosebery significant silver values may occur in the basal pyrite–chalcopyrite lenses, but in general this type of mineralisation contains less silver (Fig. 5.3E).

*(2) South Hercules deposit:* Although the gold mineralisation at the South Hercules deposit has a patchy distribution, gold is notably enriched in the massive framboidal pyrite ± barite sub-zone at the top of the ore lens (e.g. 5600mN and 5670mN). The highest gold contour (>10 g/t) is largely confined to the massive pyrite ± barite sub-zone in the upper part of the South Hercules ore lens (Figs 5.4A & B, 5.5A & B and 5.6A & B). The massive sphalerite–galena ± pyrite and the siliceous, stringer sulphide sub-zones locally may attain more than 10 g/t Au (e.g. 5630mN), but the gold mineralisation in these sub-zones is generally patchy and erratic. In contrast, the carbonate zones are virtually lacking in gold mineralisation.

Silver shows a similar distribution pattern to gold but is more broadly distributed (Figs 5.4C, 5.5C and 5.6C). Silver grades greater than 500 g/t are always confined to the upper part of the orebody particularly in the pyrite ± barite sub-zone The siliceous, stringer sulphide sub-zone commonly contains silver values of 200–500 g/t and may attain over 500 g/t (e.g. 5630mN). The cherty carbonate sub-zone is generally devoid of silver but locally may contain up to 200 g/t Ag. Comparatively, arsenic appears to be enriched in the upper part of the ore zone with elevated gold and silver contents. Arsenic values of 8% are recorded together with 1300 g/t Ag and 18 g/t Au at DDH 1163.

### 5.4.3 Copper and iron ...

*(1) Hercules mine:* Copper occurs dominantly in the pyrite–chalcopyrite zone where it may exceed 4% Cu. Copper values as high as 2% are sometimes observed in the massive sphalerite–galena ± pyrite zones (Fig. 5.3F) but in the massive barite zones, copper values rarely exceed more than 0.5%. High values of iron occur with copper in the pyrite–chalcopyrite zones (Fig. 5.3G).

*(2) South Hercules deposit*: Copper values are conspicuously low in the South Hercules deposit, or less than 0.5% in all mineralogical zones (Figs 5.4D, 5.5D and 5.6D). Only the sphalerite–galena ± pyrite sub-zone contains elevated copper values of 0.5–1.0%. Iron is concentrated in the massive pyrite ± barite sub-zone at the upper part of the South Hercules deposit (Figs 5.4E, 5.5E and 5.6E). Iron contents of 5–10% are found in the massive pyrite

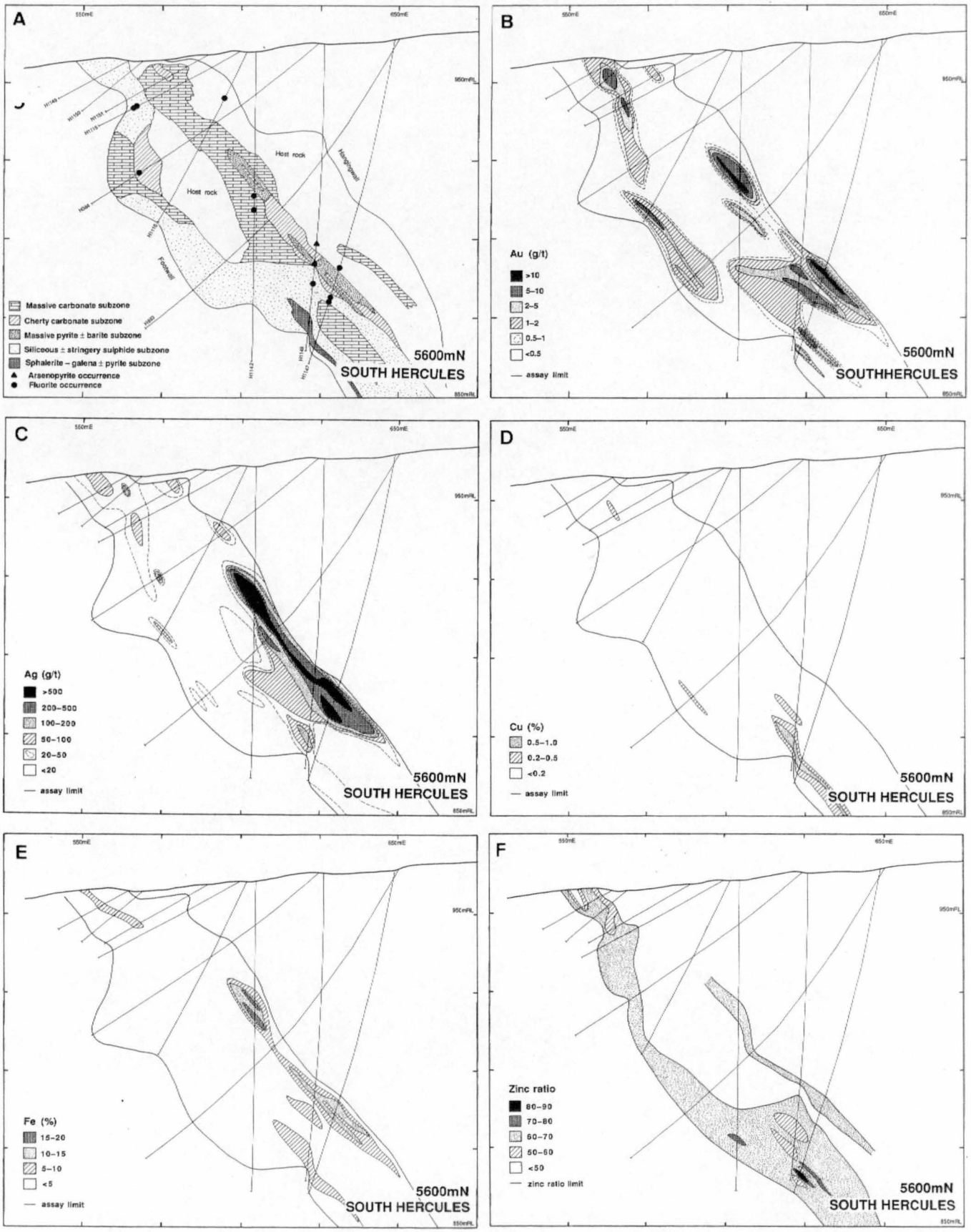


Fig. 5.4 Geology and mineral zonation of 5600mN section, South Hercules deposit, western Tasmania.

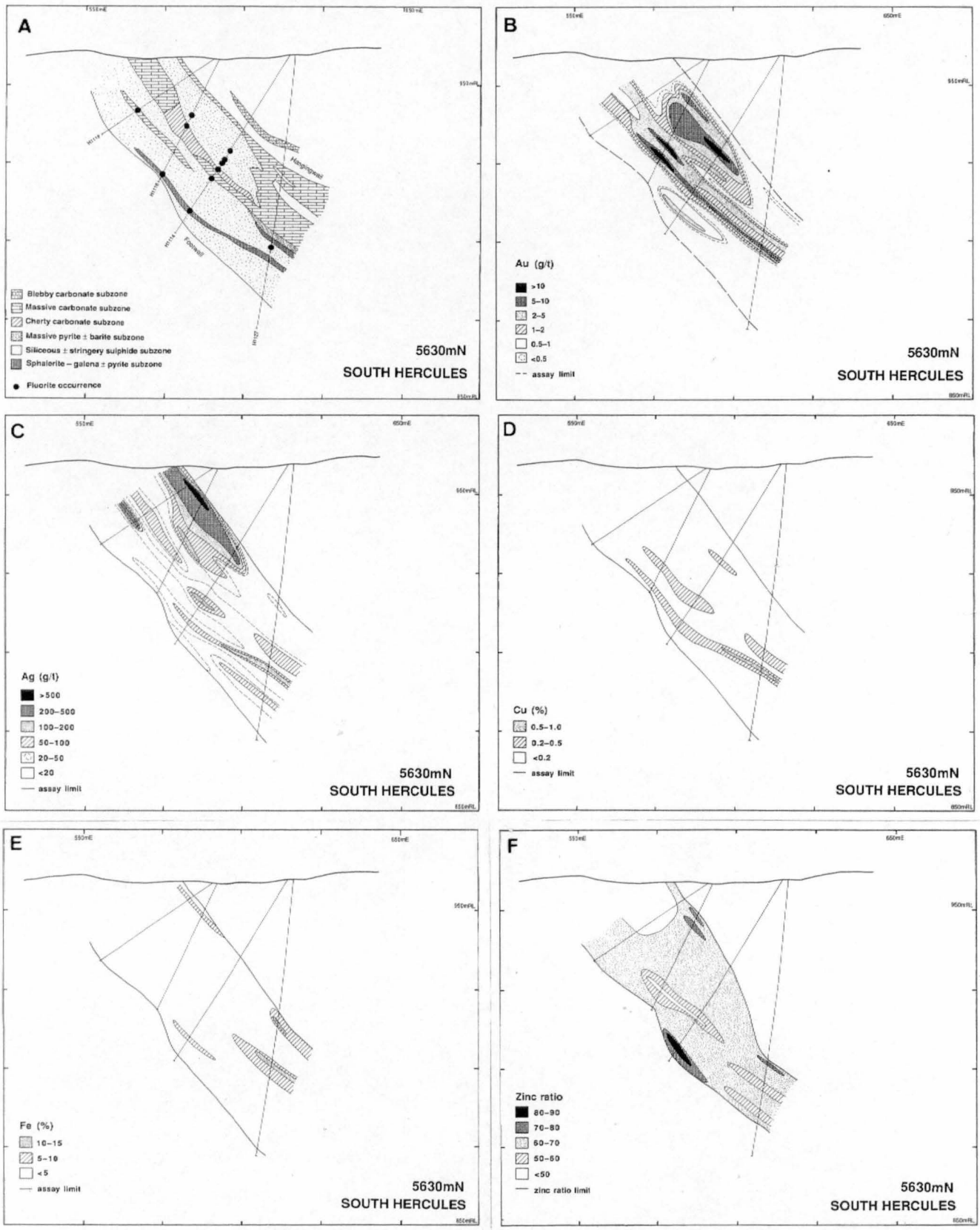


Fig. 5.5 Geology and mineral zonation of 5630mN section, South Hercules deposit, western Tasmania.

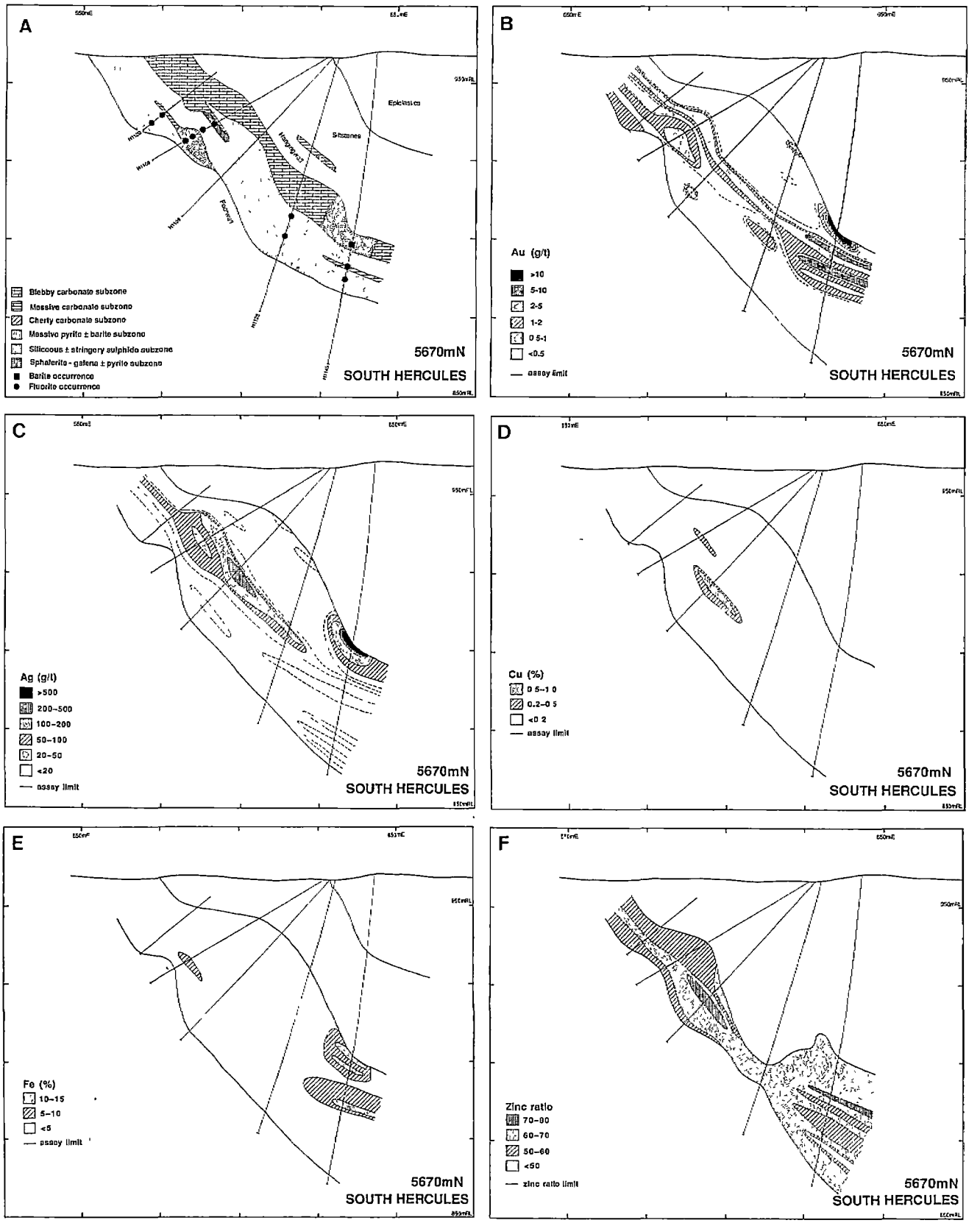


Fig. 5.6 Geology and mineral zonation of 5670mN section, South Hercules deposit, western Tasmania.

± barite sub-zone and sometimes iron values up to 20% have been noted (e.g. 5720mN). Between 5% and 10% Fe is concentrated in the sphalerite–galena ± pyrite sub-zone which occurs below the massive pyrite ± barite sub-zone. Other sub-zones are generally depleted in iron content.

## 5.5 ORE METAL ZONATION AND DEVONIAN REPLACEMENT PROCESS ...

A stratiform lenticular enrichment of lead and zinc was noted in the primary, Cambrian massive sulphide lenses of the north-end orebody of the Rosebery mine, Hercules mine and the South Hercules deposits. However, in the F(J) lens of the south-end of the Rosebery mine where primary Pb–Zn sulphide lenses have been replaced by Fe–S–O assemblages of Devonian origin, zinc is significantly depleted in the replacement zones.

The depletion of the zinc in the replacement zones suggests that zinc was dissolved and remobilised during the replacement process. Like zinc, silver is also depleted in the replacement zones and apparently silver together with zinc was remobilised under the same transporting medium. Although the distribution of lead in the F(J) lens is not known, as no particular study on lead was made, it appears that lead together with zinc and silver were enriched as blanket-like bodies in the primary sulphide lenses and dissolved and remobilised during the Devonian replacement process.

In contrast to zinc, lead, and silver, gold is distinctly enriched in the pyrrhotite–pyrite zone of Devonian origin and the primary, exhalative sulphide lenses also contain a high concentration of gold. This suggests that syngenetic gold appears to have been remobilised and redistributed in the pyrrhotite-pyrite assemblages during Devonian overprinting processes (Chapter 7).

A significant amount of copper is present in the magnetite ± biotite and pyrrhotite–pyrite replacement zones. This indicates that although zinc, lead and silver as well as gold were dissolved and remobilised during the Devonian replacement event, copper was only recrystallised. A second copper concentration zone was noted together with iron in the footwall pyrite–chalcopyrite zones of the primary sulphide lenses as copper-rich pods at the Rosebery and Hercules deposits.

As in the Kuroko and related volcanogenic massive sulphide deposits, this copper and iron enrichment at the base of the deposits probably reflects the hydrothermal venting position (Sato, 1972; Large, 1977). The Cu-rich pods (>4 wt% Cu) represent the central focus of the high temperature, exhaled hydrothermal fluids during Cambrian mineralisation. In contrast to Rosebery and Hercules, the South Hercules deposit displays low copper contents (<1 wt% Cu) and relatively high (Au+Ag)/(Pb+Zn) ratios suggesting a low temperature of ore formation (discussed further below).

The fact that iron is enriched in the pyrrhotite-pyrite bodies above the levels found in the Pb-Zn lenses or the Cu-pyrite zones in the F(J) lens of the Rosebery south-end suggests that the hydrothermal fluids expelled from the Devonian granite to replace the primary Cambrian sulphide lenses, were also Fe-rich. The source of iron may be magmatic or alternatively the iron could have been leached from the host rocks and the adjacent primary sulphide lenses.

## 5.6. Zinc ratio distribution

Huston and Large (1987) recently recognised that the zinc ratios [100 Zn/(Zn+Pb)] of Palaeozoic volcanogenic massive sulphide deposits, including the Rosebery–Hercules deposits in the MRV, have a restricted range of mean values (60–77) and low standard deviation (<15). Other styles of mineralisation in the MRV have a broader but lower range of mean values (39–60) and higher standard deviation (>26) particularly the Cambrian and Devonian vein style mineralisation.

The above restricted range of zinc ratio for the VMS deposits is best interpreted due to the saturation of lead-zinc in the ore solution which exhaled onto the sea-floor rather than due to the Pb–Zn content of the footwall source rocks (Huston and Large, 1987). On the basis of thermodynamic calculation, Huston and Large (1987) also explained that the zinc ratio for a saturated solution is dependent only on the temperature and activity of chloride (salinity), and is independent of pH, $a_{H_2S}$, and $fO_2$ as shown below:

$$\frac{m_{\Sigma Pb}}{m_{\Sigma Zn}} = \frac{\dfrac{a_{H^+}^2 a_{Cl^-}}{\gamma_{PbCl^+} K_5 a_{H_2S}} + \dfrac{a_{H^+}^2 a_{Cl^-}^2}{\gamma_{PbCl_2^0} K_6 a_{H_2S}} + \dfrac{a_{H^+}^2 a_{Cl^-}^3}{\gamma_{PbCl_3^-} K_7 a_{H_2S}} + \dfrac{a_{H^+}^2 a_{Cl^-}^4}{\gamma_{PbCl_4^{2-}} K_8 a_{H_2S}}}{\dfrac{a_{H^+}^2 a_{Cl^-}}{\gamma_{ZnCl^+} K_1 a_{H_2S}} + \dfrac{a_{H^+}^2 a_{Cl^-}^2}{\gamma_{ZnCl_2^0} K_2 a_{H_2S}} + \dfrac{a_{H^+}^2 a_{Cl^-}^3}{\gamma_{ZnCl_3^-} K_3 a_{H_2S}} + \dfrac{a_{H^+}^2 a_{Cl^-}^4}{\gamma_{ZnCl_4^{2-}} K_4 a_{H_2S}}}, \quad (1)$$

where $\gamma_i$ = activity coefficient of species $i$ and $K_n$ = equilibrium constant of reaction $n$ (see Table 4). When terms cancel, the equation reduces to:

$$\frac{m_{\Sigma Pb}}{m_{\Sigma Zn}} = \frac{\dfrac{1}{\gamma_{PbCl^+} K_5} + \dfrac{a_{Cl^-}}{K_6} + \dfrac{a_{Cl^-}^2}{\gamma_{PbCl_3^-} K_7} + \dfrac{a_{Cl^-}^3}{\gamma_{PbCl_4^{2-}} K_8}}{\dfrac{1}{\gamma_{ZnCl^+} K_1} + \dfrac{a_{Cl^-}}{K_2} + \dfrac{a_{Cl^-}^2}{\gamma_{ZnCl_3^-} K_3} + \dfrac{a_{Cl^-}^3}{\gamma_{ZnCl_4^{2-}} K_4}}. \quad (2)$$

The 100 Zn/(Zn + Pb) weight ratio (zinc ratio) may be calculated as follows:

Zinc ratio

$$= 100\ Zn/(Zn + Pb)$$

$$= 100/[1 + (m_{\Sigma Pb}/m_{\Sigma Zn})(\text{at. wt}_{Pb}/\text{at. wt}_{Zn})]. \quad (3)$$

Thus, a deposit precipitated from a saturated solution where the metals were transported dominantly as chloride complexes would be expected to have a constant zinc ratio at a particular temperature and salinity (Huston and Large, 1987).

Figures 5.7 and 5.8 show the relationships of zinc ratio, temperature and salinity. Lead–zinc ores deposited from saturated solutions above 270°C will have average zinc ratios of less than 50, while ores deposited below 270°C will have zinc ratios more than 50. Salinity does not have a significant effect on zinc ratio distribution. The zinc ratio varies with salinity in the 200°–250°C temperature interval (Figs. 5.7 and 5.8).

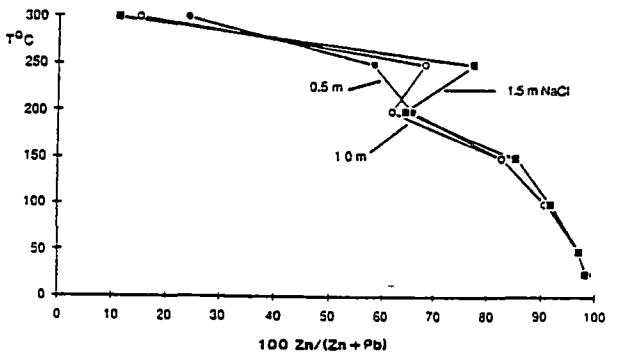


Fig. 5.7 Effect of temperature on the zinc ratio for salinities of 0.5, 1.0 and 1.5*m* NaCl (after Huston and Large, 1987).

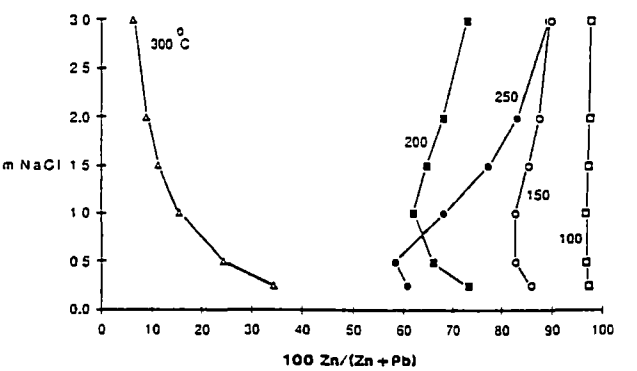


Fig. 5.8 Effect of salinity on the zinc ratio for temperatures from 100° to 300°C (after Huston and Large, 1987).

## 5.7 ZINC RATIO AT ROSEBERY, HERCULES, SOUTH HERCULES AND QUE RIVER ...

In this study, zinc ratio distributions in the F(J) lens of the Rosebery south-end orebody, the J(K)–P lens of the Hercules mine, the South Hercules and Que River deposits were investigated to shed light on the environment of ore deposition, and the style of mineralisation for the newly discovered South Hercules deposit. Spatial variation of the zinc ratio was also studied by contouring the values of the zinc ratio on E–W sections of the South Hercules deposit. The distribution of the zinc ratio in relation to other ore metals was also investigated. Only assay intervals with zinc values more than 1% and lead values more than 0.5% were used in order to obtain a reliable zinc ratio pattern for the deposits.

*(1) F(J) lens, Rosebery mine:* The zinc ratios from the available assay data of the drill holes on 220mS, 250mS, 270mS, 280mS and 300mS sections of the F(J) lens were calculated and the following means and standard deviations were recorded:

| | 220mS | 250mS | 270mS | 280mS | 300mS |
|---|---|---|---|---|---|
| Mean | 74.0 | 71.7 | 71.2 | 73.5 | 75.9 |
| S.D. | 8.8 | 10.2 | 8.9 | 10.6 | 10.6 |
| N | 103 | 204 | 135 | 92 | 95 |

The zinc ratio from the available assay data of the drill holes on the above five E–W sections of the F(J) lens is shown in Fig. 5.9. The zinc ratio gives a range of 45–95 with a mean value of 73.2 and standard deviation of 9.8 which compares favourably with that of the north-end of the Rosebery mine (Huston and Large, 1987) (Fig. 5.10).

*(2) Hercules mine:* The zinc ratios from the assay data of the drill holes on the 34.80mS and 75.00mS sections of the J(K)–P lens of the Hercules mine are shown in Fig. 5.11. The zinc ratio gives a range of 45–95 with a mean value of 72.4 and standard deviation of 11.9. A similar zinc ratio pattern with mean value of 75.7 and standard deviation of 14.3 was reported for the whole Hercules deposit by Huston and Large (1987).

*(3) South Hercules deposit:* The zinc ratios of the assay data from the drill holes on 5585mN, 5600mN, 5630mN, 5670mN and 5720mN E–W cross-sections of the South Hercules deposit were calculated in this study and a zinc ratio histogram for the South Hercules deposit is shown in Fig. 5.12. The distribution has one mode, with a mean value of 62.4 and a standard deviation of 7.6 and falls within the range of the Cambrian volcanogenic massive sulphide mineralisation in the Mt Read Volcanics.

(3) *Que River mine:* The Que River deposit is a tightly folded, Au-rich massive sulphide deposit (Large et al., 1988). In this study, the zinc ratio of the assay data from the drill holes

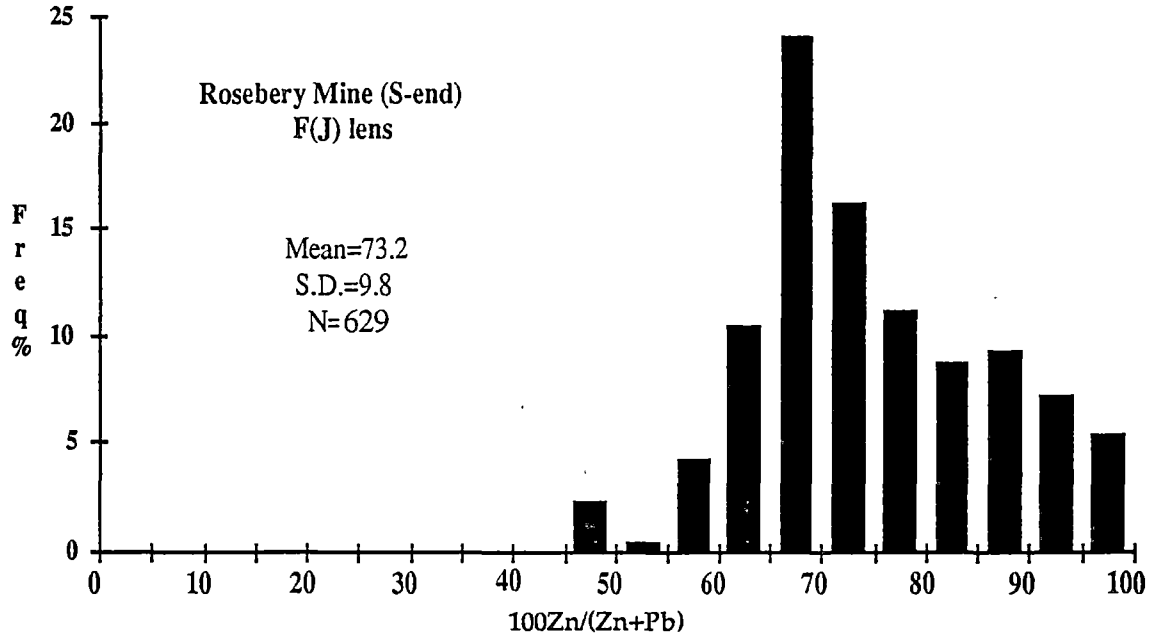


Fig. 5.9 Zinc ratio histogram for the F(J) lens of the south-end of the Rosebery mine, western Tasmania.

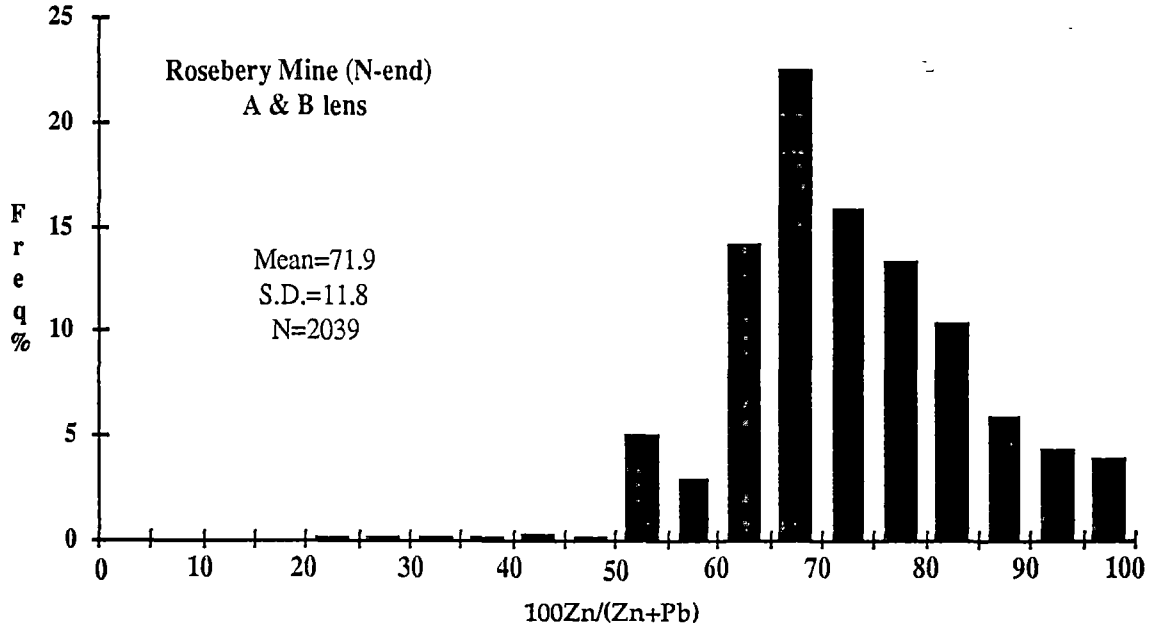


Fig. 5.10 Zinc ratio histogram for the A and B lens of the north-end of the Rosebery mine, western Tasmania (after Huston and Large, 1987).

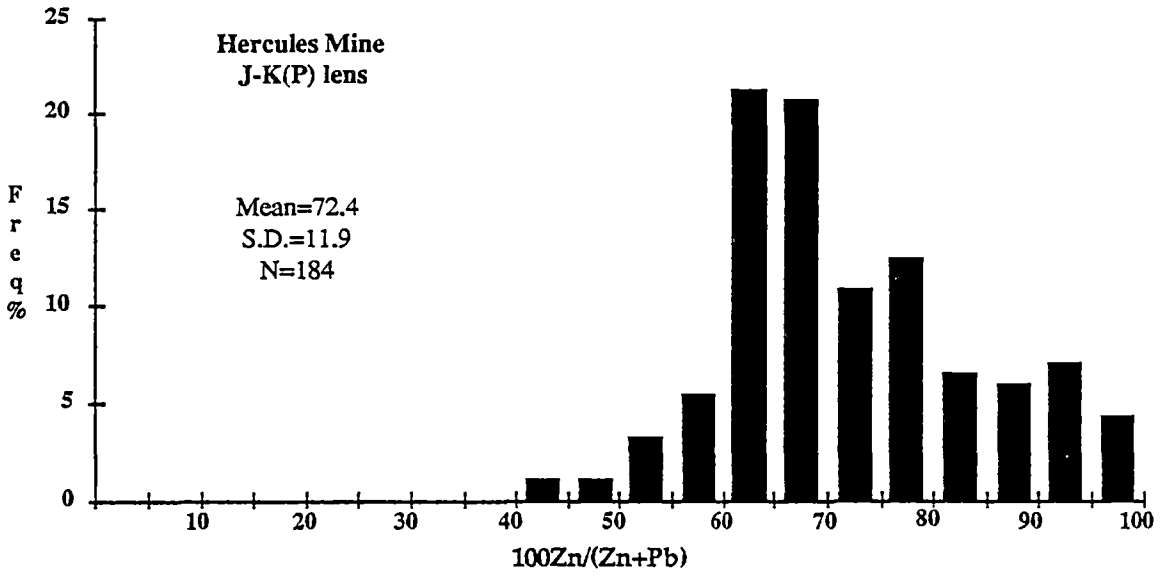


Fig. 5.11 Zinc ratio histogram for the J(K)-P lens of the Hercules mine, western Tasmania.

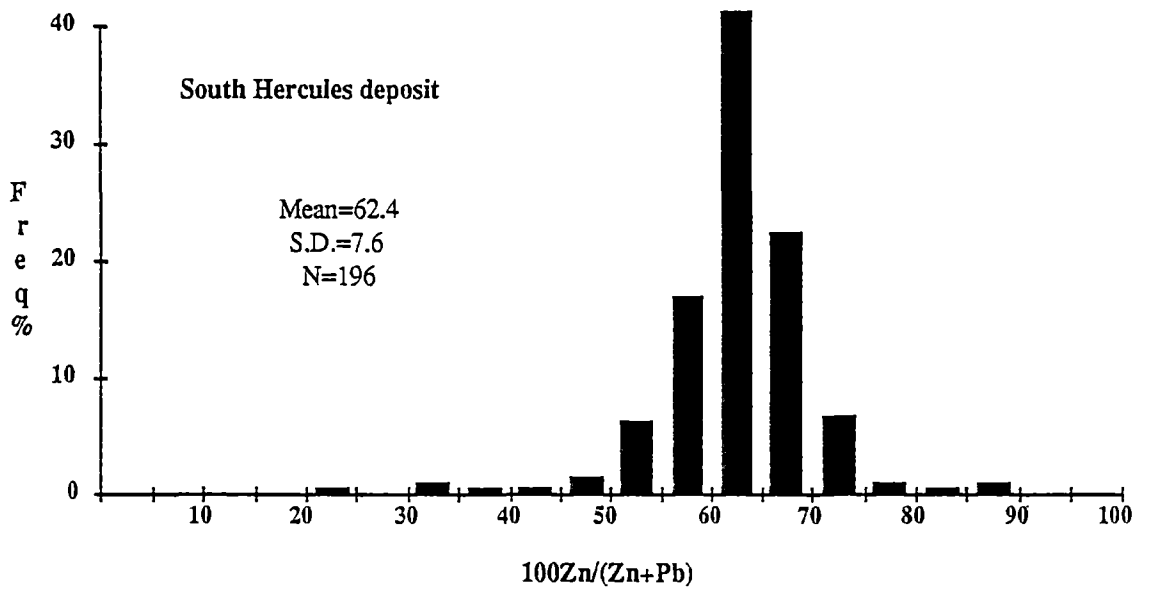


Fig. 5.12 Zinc ratio histogram for the South Hercules deposit, western Tasmania.

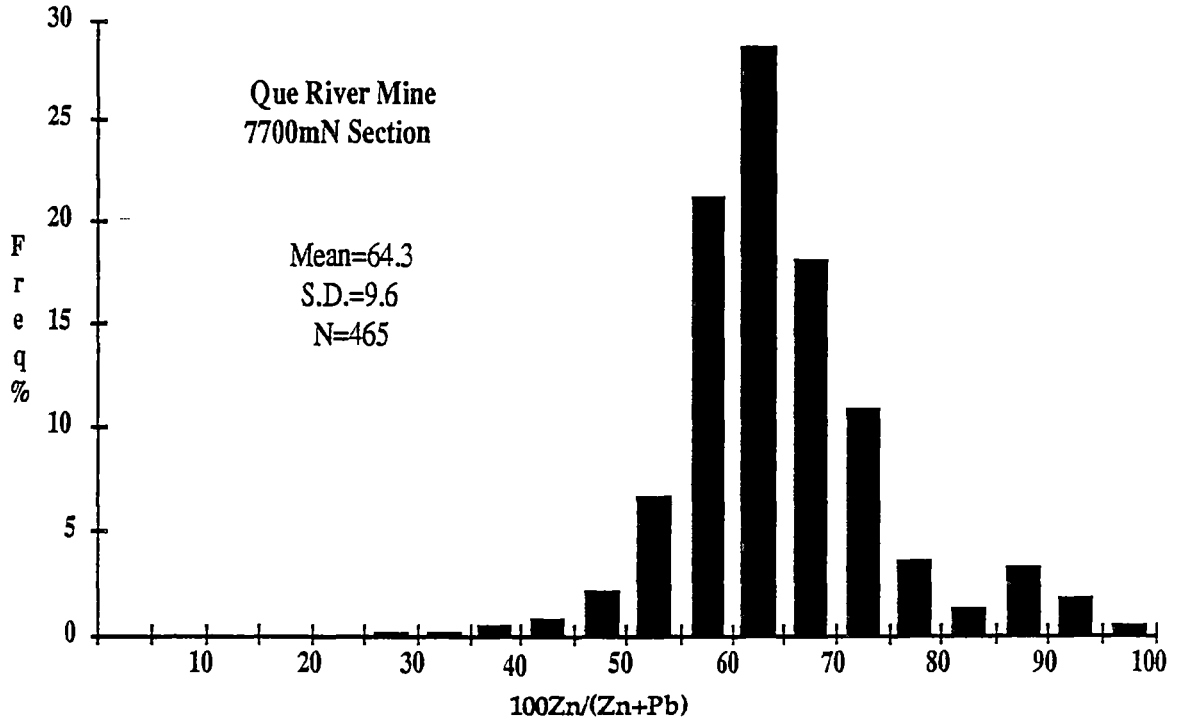


Fig. 5.13 Zinc ratio histogram for the 7700mN Section, Que River deposit, western Tasmania.

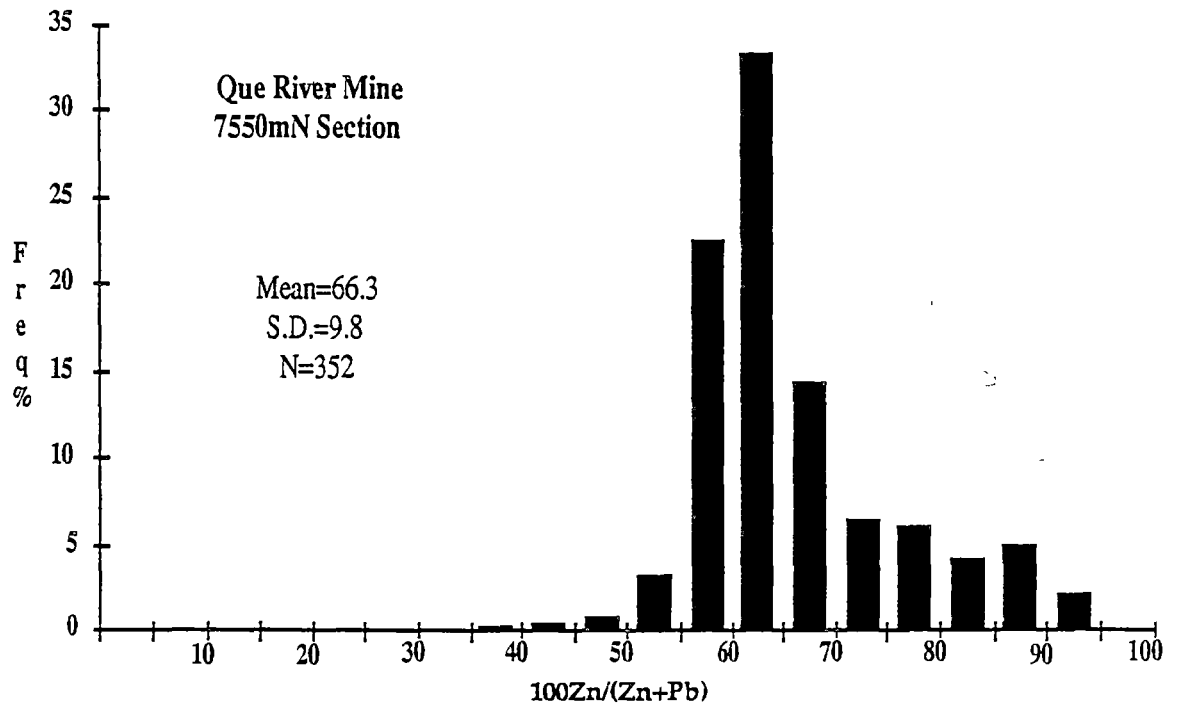


Fig. 5.14 Zinc ratio histogram for the 7550mN section, Que River deposit, western Tasmania.

on 7700mN and 7550mN sections of the Que River deposit were calculated and the zinc ratio histograms are shown in Figs. 5.13 and 5.14. The zinc ratio distribution for both sections shows one mode. The 7700mN section has a mean value of 64.3 and a standard deviation of 9.6, whereas the 7550mN section yielded a marginally higher mean value of 66.3 but similar standard deviation of 9.8. The zinc ratio distribution of both sections of the Que River deposit are very similar to that of the South Hercules deposit.

The zinc ratio distributions of the Rosebery, Hercules, South Hercules and Que River deposits are comparable with those of other Palaeozoic volcanogenic massive sulphide deposits including other VMS deposits in the Mt Read Volcanics (Huston and Large, 1987) but differ from the other styles of mineralisation particularly the Cambrian and Devonian vein style mineralisation which have a broader but lower range of mean values (39–60) and higher standard deviations (>26).

## 5.8 ZINC RATIO VS ORE METALS ...

The relationships between zinc ratio and Au, Ag, Cu and Fe in the South Hercules deposit were also studied to determine whether the chemical factors controlling zinc ratio (temperature and salinity) have affected metal concentration. Plots of the zinc ratio to the ore metals of the South Hercules deposit are depicted in Fig. 5.15A–E. It is interesting to note that the highest concentrations of Au (25 g/t), Ag (2200 g/t), As (8.0%) and Fe (23.0%) are restricted within the range of the zinc ratio (ca. 50–70) but in contrast there is a weak correlation between zinc ratio and Cu values. The zinc ratio vs As data are only for samples from DDH 1163 as assay data for arsenic are limited for the deposit.

The spatial distribution of high grade precious metals and the zinc ratio can also be observed by contouring the precious metals and the zinc ratio on the E–W cross-sections (Figs 5.4F, 5.5F and 5.6F). The zinc ratios were contoured with intervals of <50, 50–60, 60–70, 70–80 and 80–90. Au was contoured with intervals of <0.5, 0.5–1, 1–2, 2–5, 5–10 and >10 g/t and Ag with <20, 20–50, 50–100, 100–200, 200–500 and >500 g/t. The high grade precious metal zones (Au with >10 g/t and Ag with >500 g/t) are significantly confined within the 60–70 zinc ratio contour interval.

Hence, contouring of metals gives a more restricted range of zinc ratios (60–70) overlapping with high grade precious metals than the range (ca. 50–70) recorded by the metals versus zinc ratio plots (Fig. 5.15A & B). Fe also generally follows a similar trend of precious metals and zinc ratio. Fe was contoured for <5, 5–10, 10–20, 20–30 and >30 wt% and the Fe enrichment zones are restricted within the 60–70 zinc ratio range. Copper values at South Hercules are usually low (<0.5 wt%) and Cu shows no correlation with zinc ratio. Cu enrichment zones display variable zinc ratios (e.g. 5600mN and 5630mN E–W sections).

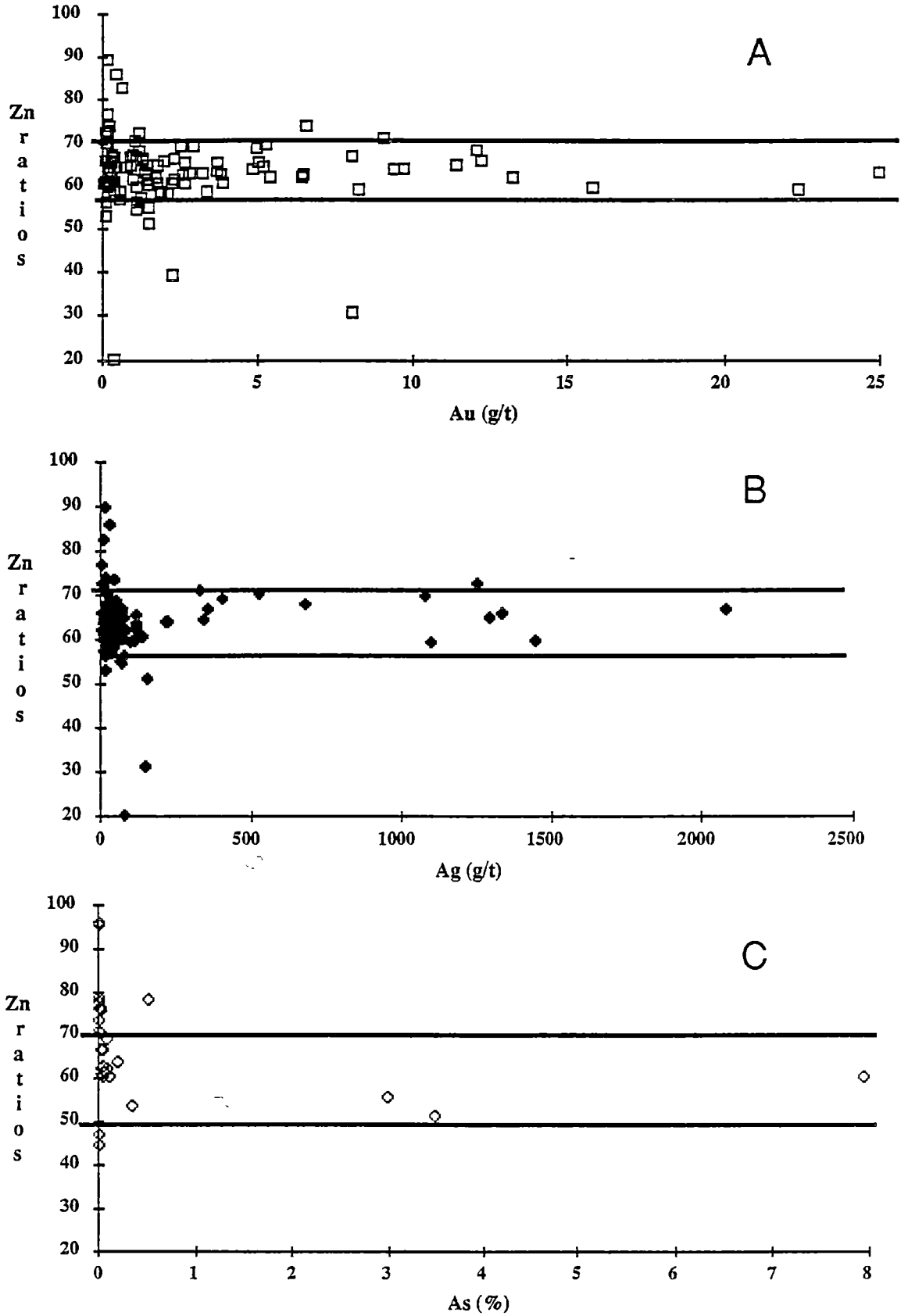


Fig. 5.15 A — Plot of zinc ratio vs Au (g/t) from the South Hercules deposit, western Tasmania. The horizontal bars represent zinc ratios 55 and 70. B — Plot of zinc ratio vs Ag (g/t). The horizontal bars represent zinc ratios 55 and 70. C — Plot of zinc ratio vs As (%). The horizontal bars represent zinc ratios 50 and 70.

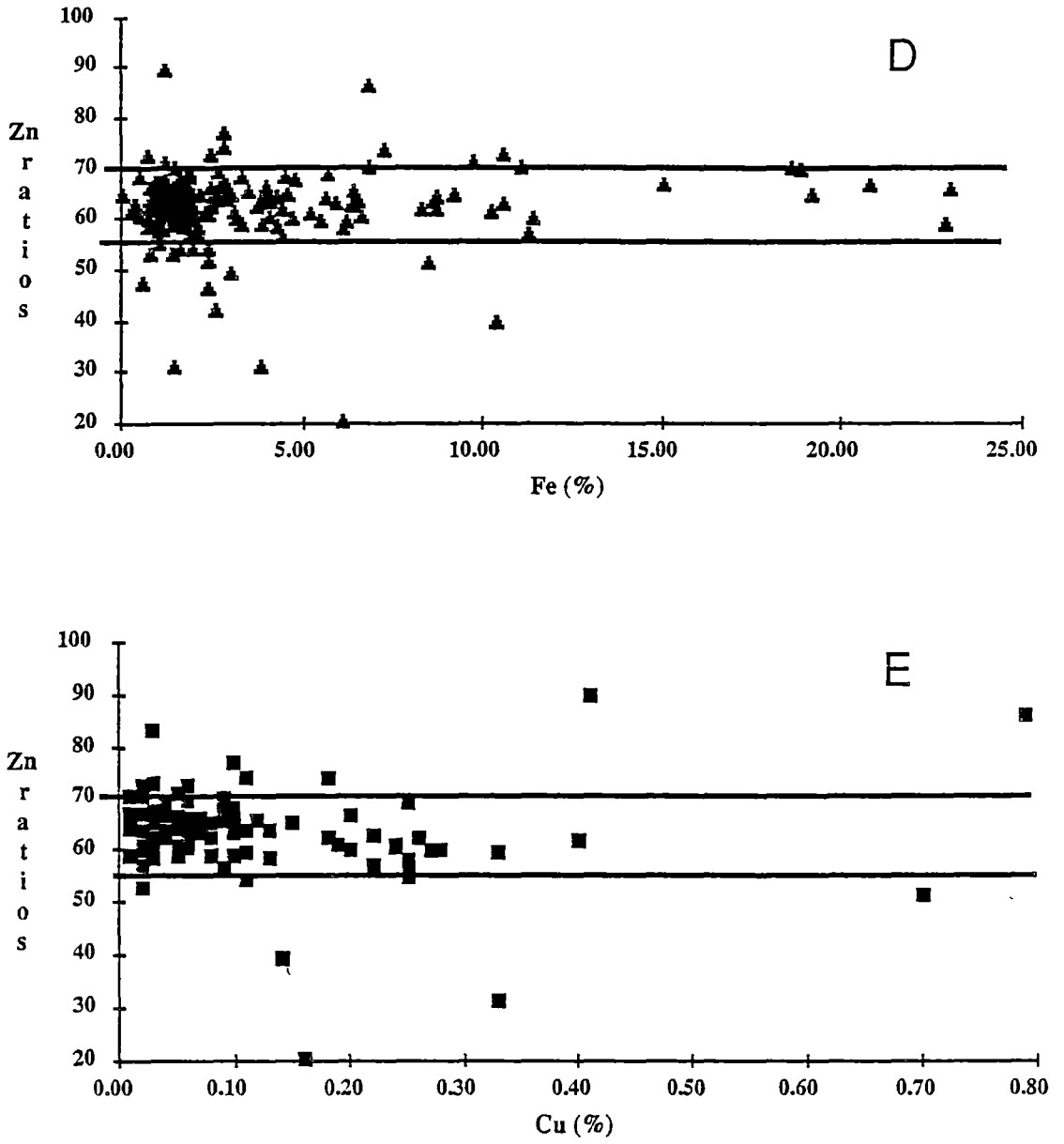


Fig. 5.15 D — Plot of zinc ratio vs Fe (%) from the South Hercules deposit, western Tasmania. The horizontal bars represent zinc ratios 55 and 70. E — Plot of zinc ratio vs Cu (%). The horizontal bars represent zinc ratios 55 and 70.

## 5.9 Zn vs Pb distribution ...

In this study, Zn (%) vs Pb (%) plots were also constructed to deduce the physico-chemical conditions of the ore fluids. The Zn vs Pb plot for the 270mS section, F(J) lens, Rosebery mine displays a roughly linear distribution (Zn/Pb = ~1.5, zinc ratio = 71.0) with few scattered points (Fig. 5.16). The plot for the J(K)–P lens of the Hercules deposit displays two trends; one trend with cut off values of about Zn/Pb = ~1.7, zinc ratio = 72.0) and the other with low lead and higher zinc values (Fig. 5.17).

The Zn vs Pb plot for the South Hercules deposit shows a linear trend (Zn = 1.6 Pb, zinc ratio = 61.5) with few scattered points (Fig. 5.18). The majority of the assay data display Zn values less than 10.0 wt% and Pb values less than 6 wt%. A similar distribution pattern was also recorded in the baritic mineralisation which occurs stratigraphically at the top of the Rosebery deposit (Huston and Large, 1987, 1988).

The Zn vs Pb plots for the 7700mN and 7550mN sections of the Que River deposit show that most of the data points fall along the line of (Zn = 1.5 Pb, zinc ratio = 60.0) (Figs 5.19 & 5.20). The Zn vs Pb distribution of the Que River deposit (Figs 5.19 and 5.20) display a comparable distribution pattern with that of the South Hercules deposit (Fig. 5.18) but the South Hercules deposit is lower in Zn and Pb values than that of the Que River deposit.

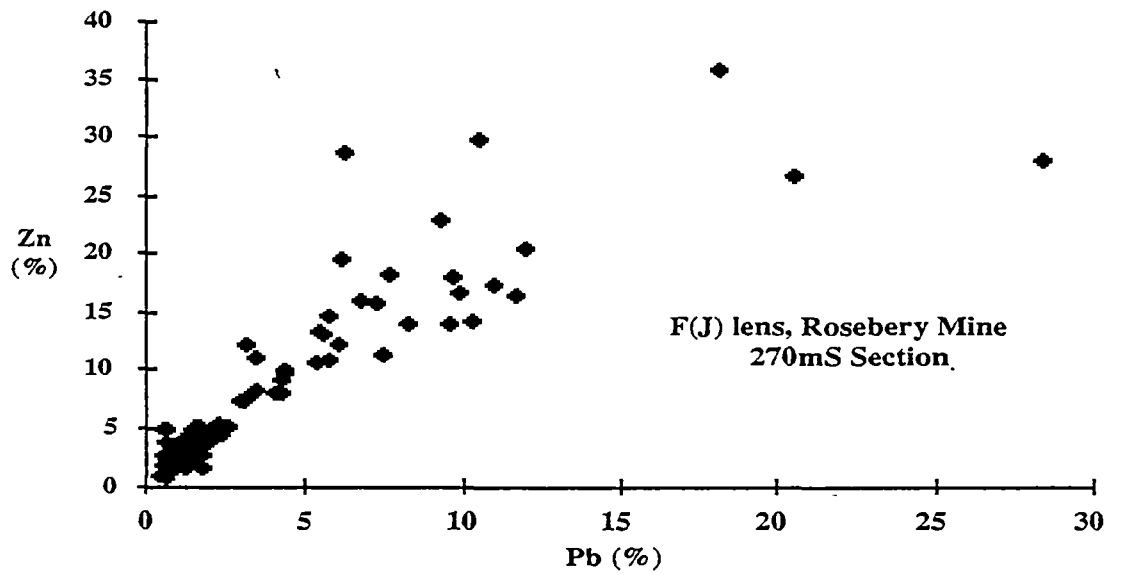


Fig. 5.16 Plot of Zn (%) vs Pb (%) from the 270mS section, F(J) lens of the Rosebery mine, western Tasmania.

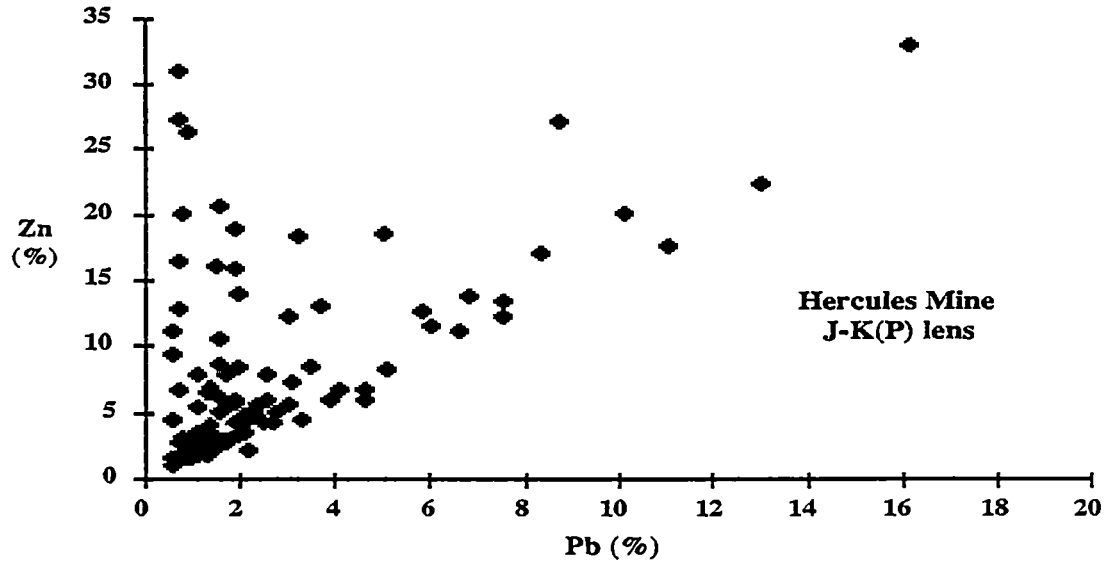


Fig. 5.17 Plot of Zn (%) vs Pb (%) from the J–K(P) lens of the Hercules mine, western Tasmania.

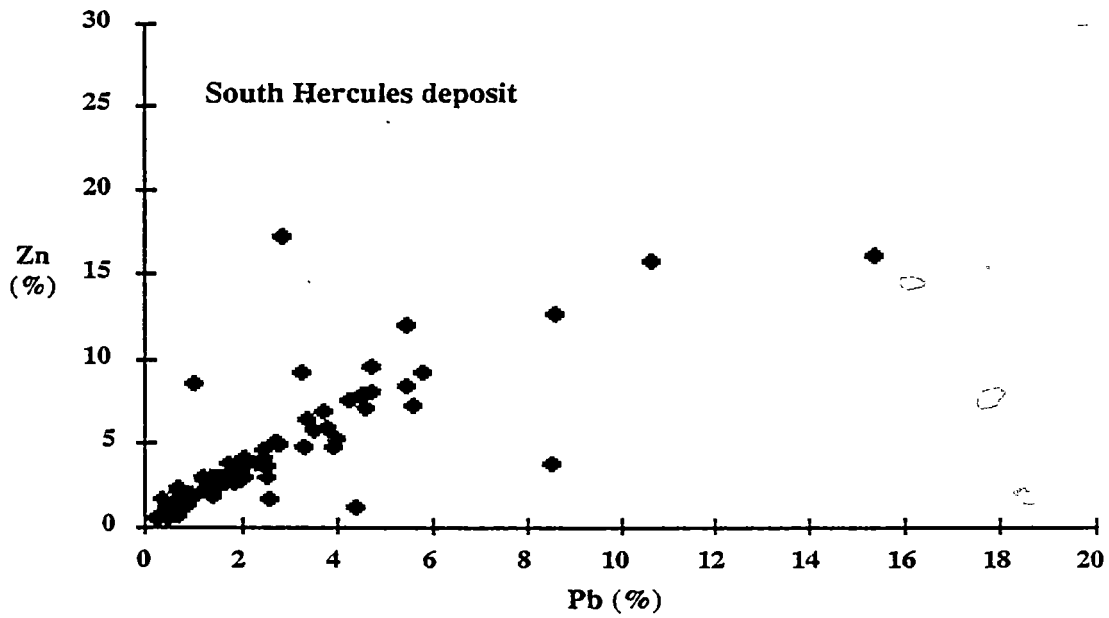


Fig. 5.18 Plot of Zn (%) vs Pb (%) from the South Hercules deposit, western Tasmania.

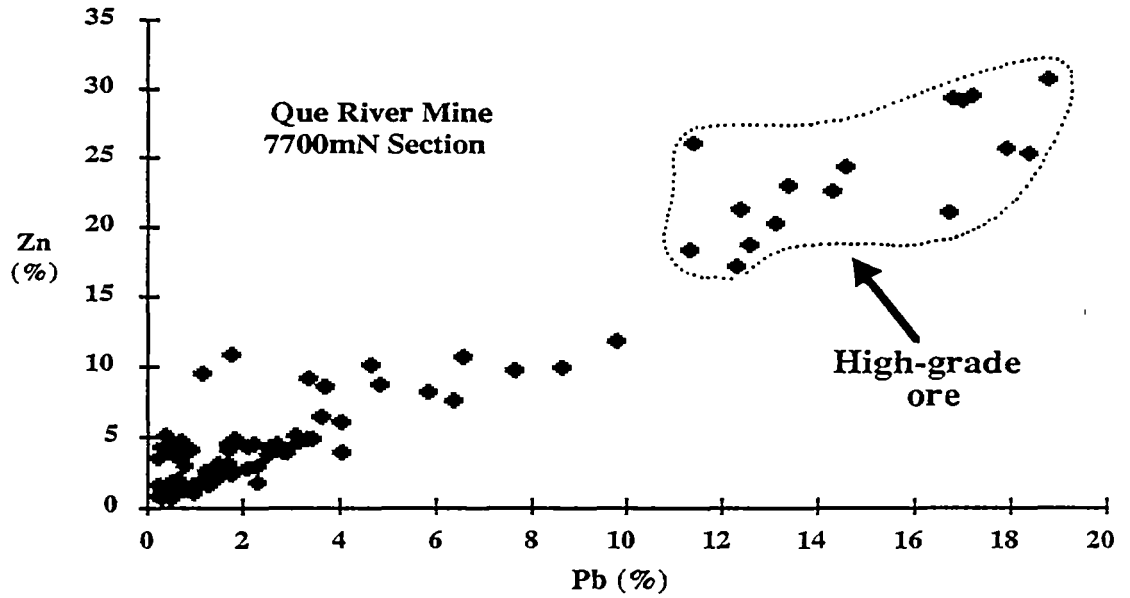


Fig. 5.19 Plot of Zn (%) vs Pb (%) from the 7700mN section, Que River mine, western Tasmania.

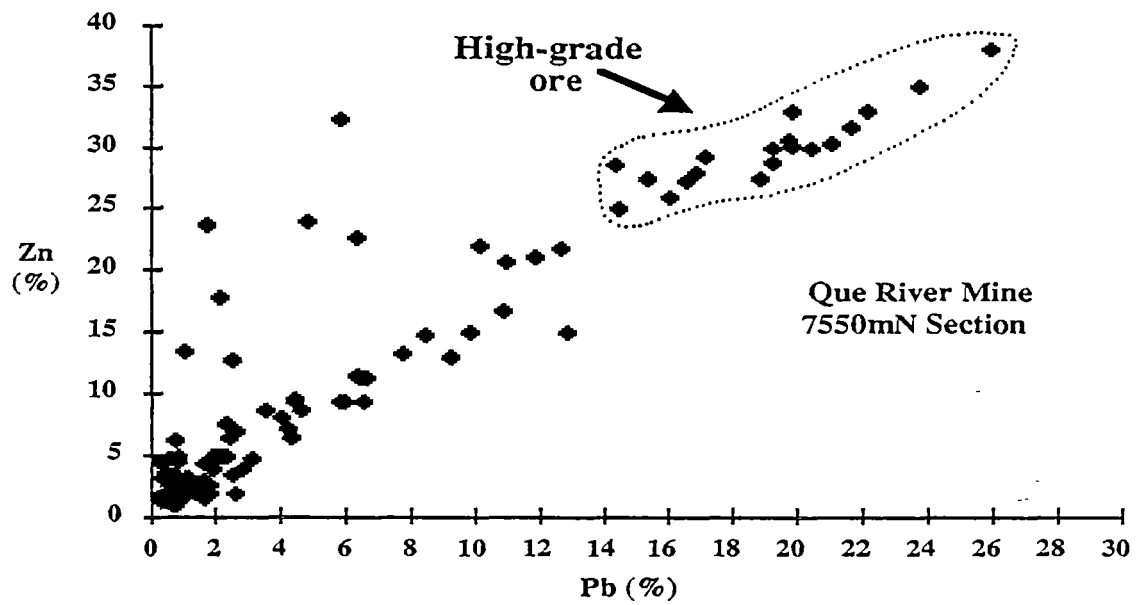


Fig. 5.20 Plot of Zn (%) vs Pb (%) from the 7550mN section, Que River mine, western Tasmania.

## 5.10 SIGNIFICANCE OF ZINC RATIO DISTRIBUTION ...

Although the ore lenses in the F(J) lens of the south-end of the Rosebery mine have been affected by granite-related metasomatic fluids of Devonian origin, the zinc ratio pattern of the original Cambrian stratiform sulphides have not changed appreciably. The $\delta^{34}S$ ratios in these sulphide deposits also did not alter during Devonian recrystallisation (Green et al., 1981; Green, 1983; Solomon et al., 1987; Chapter 9) and the $\delta^{13}C$ values of the carbonates in these sulphide deposits also appear to be resistant to the Devonian overprinting effects (Chapter 9).

The Zn vs Pb plots for the F(J) lens, Rosebery mine, J(K)–P lens, Hercules mine, the South Hercules deposits and 7700mN and 7550mN sections of the Que River deposit display linear relations. Such linearity is interpreted to be due to saturation of lead and zinc in the hydrothermal solutions, in that a solution saturated with respect to lead and zinc, with sufficient $H_2S$, would deposit these two metals giving a unique ratio for a specific temperature (Huston and Large, 1987). The linear lower limit in each case suggests saturation: the spread in values above the linear trend exhibited in the Hercules data indicates slight undersaturation of lead in the solutions or variation in the temperature or salinity of the hydrothermal fluids.

The Zn vs Pb plot for the South Hercules deposit shows a straight line (Zn = 1.6 Pb, zinc ratio = 61.5) with few scattered points above and below suggesting both Zn and Pb were consistently saturated in the ore fluids. A similar Zn vs Pb distribution pattern was also recorded in the baritic mineralisation which occurs stratigraphically at the top of the Rosebery deposit (Huston and Large, 1987). The baritic mineralisation was inferred to have formed under declining temperature of 200–250°C (Green et al., 1981) and this temperature estimate is comparable with the fluid inclusion homogenisation temperatures recorded for the South Hercules deposit (Chapter 10).

The other interesting point is that the highest concentrations of Au (25 g/t), Ag (2200 g/t), As (8.0%) and Fe (23.0%) at the South Hercules deposit are found restricted within the zinc ratio range of (ca. 50–70) and it suggests that saturation of lead and zinc in the ore solution was accompanied by deposition of high grade precious metals, arsenic and iron during the South Hercules ore formation.

The Zn vs Pb plots of the Que River and the South Hercules data show an analogous pattern with the only difference being the lack of high grade values for Zn vs Pb in the pattern for South Hercules. This points out the possibility of high grade base metal targets around the South Hercules area since the zinc ratio histograms for the South Hercules and Que River deposits have a similar mean value of ~60–65 and low standard deviation of <9.6.

The low standard deviation of the zinc ratio for the South Hercules deposit is also comparable to that of the Que River deposit and suggests a narrow range of temperature–salinity conditions for the formation of the deposit. On the basis of available thermochemical data, Huston and Large (1987) calculated the zinc ratio for ore fluids ranging in temperature from 25° to 300°C over a range of salinity from 0.25*m* to 3.0*m* (1.83–16.60 equiv. wt% NaCl). As was mentioned previously, the precious metals rich zones at the south Hercules deposit occur within the zinc ratio range of 60–70. Ore fluids with such a zinc ratio value can occur within the temperature and salinity ranges considered likely for volcanogenic massive sulphide deposits [150°–250°C and salinity of 0.5*m* (2.77 equiv. wt% NaCl) to 1.5*m* (16.60 equiv. wt % NaCl)] (see also Large, 1977; Pisutha-Arnond and Ohmoto, 1983).

More specifically, according to the zinc ratio calculations made by Huston and Large (1987), the zinc ratio of 60–70 at South Hercules corresponds to a maximum of 250°C if salinity is 0.5–1.0*m* (2.77–5.53 equiv. wt% NaCl) (see Table 5.1). This is consistent with the fluid inclusion study (see later). Type I fluid inclusions in sphalerite and barite at South Hercules which are thought to be associated with base and precious metal deposition give a maximum homogenisation temperature of 200°C and a salinity of <5.0 equiv. wt% NaCl.

The lower temperature of the ore formation at the South Hercules deposit is also consistent with lower Cu grades in the deposit, as copper can only be transported in higher temperature (>300°C) hydrothermal solutions (Barnes, 1979).

Table 5.1 Zinc ratios of saturated solutions at varying temperatures and salinities from thermodynamic data (after Huston and large, 1987).

| Temperature | Salinity | | | | | |
|---|---|---|---|---|---|---|
| | 0.25*m* | 0.5*m* | 1.0*m* | 1.5*m* | 2.0*m* | 3.0*m* |
| 200°C | 73 | 66 | 62 | 65 | 68 | 73 |
| 250°C | 61 | 58 | 68 | 77 | 83 | 89 |

## 5.11 SUMMARY ...

Metal distribution studies indicate that copper and iron are enriched at the base of the Rosebery and Hercules deposits, probably reflecting the hydrothermal venting position. The Cu-rich pods (>4 wt % Cu) represent the central foci of the high temperature, exhaled hydrothermal fluids during Cambrian mineralisation. In contrast to Rosebery and Hercules, the South Hercules deposit displays a low copper content (<1 wt% Cu) and relatively high (Au+Ag)/(Pb+Zn) ratios suggesting a low temperature of ore formation.

Zinc is conspicuously depleted in the trangressive pyrrhotite–pyrite replacement zone of the F(J) lens at Rosebery. Like zinc, silver is also depleted in the replacement zones and apparently silver together with zinc was remobilised under the same transporting medium. In contrast to zinc and silver, a significant amount of copper and gold is present in the pyrrhotite–pyrite replacement zones. This indicates that although zinc and silver were dissolved and remobilised during the Devonian replacement event, copper and gold were recrystallised and concentrated.

Iron enrichment was also noted in the Fe–S–O replacement zones of the F(J) lens suggesting that the hydrothermal fluids expelled from the Devonian granite were also Fe-rich. The source of iron may be magmatic or alternatively the iron could have been leached from the host rocks and the adjacent primary sulphide lenses.

The zinc ratio values of the F(J) lens, Rosebery mine, J(K)–P lens, Hercules mine, the South Hercules and Que River deposits fall within the zinc ratio values of the Phanerozoic Zn–Pb–Cu volcanogenic massive sulphides defined by Huston and Large (1987) and support the Cambrian volcanogenic origin for these deposits. Although the ore lenses in the F(J) lens of the south-end of the Rosebery mine have been affected by granite-related metasomatic fluids of Devonian origin, the zinc ratio pattern of the original Cambrian stratiform sulphides have not changed appreciably.

The highest concentrations of Au (25 g/t), Ag (2200 g/t), As (8.0%) and Fe (23.0%) at the South Hercules deposit are found restricted within the zinc ratio range of (ca. 50–70) and suggests that saturation of lead and zinc in the ore solution was accompanied by deposition of high grade precious metals, arsenic and iron during the South Hercules ore formation. The Zn vs Pb plots of the Que River and the South Hercules data show an analogous pattern with the only difference being the lack of high grade values for Zn vs Pb in the pattern for South Hercules. This points out the possibility of high grade base metal targets around the South Hercules area since the zinc ratio histograms for the South Hercules and Que River deposits have a similar mean value of ~60–65 and a low standard deviation of <9.6.

# CHAPTER 6: MINERALOGY AND GEOCHEMISTRY OF REPLACEMENT SILICATE MINERAL ASSEMBLAGES IN THE F(J) LENS, ROSEBERY MINE

## 6.1 INTRODUCTION ...

In this chapter, mineralogy, texture, paragenesis and geochemistry of the metasomatic silicate minerals will be described and presented.

## 6.2 MINERALOGY AND TEXTURE ...

The different mineral assemblages in the F(J) lens are listed in Appendix 6.1. The following mineralogical and textural characteristics of the metasomatic minerals were observed:

*Garnet:* Stillwell (1934) first reported spessartine garnet at the Rosebery mine which was later confirmed by Green et al. (1981) and Lees (1987) who attributed the garnet-bearing assemblage to post-depositional metamorphism. Garnet is usually found in the deeper levels of the F(J) lens and recorded in samples 88R-4A at 364.9 m, 200mS, 88R-6 at 366.1 m, 200mS and R1920-12 at 602 m, 100mS. Garnet occurs as creamy white, anhedral gains in hand specimen and is associated with pyrrhotite, pyrite, magnetite, biotite, tourmaline and fluorite.

Under the microscope, garnet crystals may exceed 5 mm in diameter and are light orange or pale brown, commonly anisotropic and very often zoned with or without penetration twinning (Figs. 6.1A, 6.1B and 6.1C). A few garnet crystals may show both anomalous anisotropism and pronounced zoning, but the coarsely crystalline subhedral aggregates show only weakly developed zoning, which is commonly parallel to crystal outlines. Some isotropic or nearly isotropic grains are also present. In sample 88R-6, garnet is altered to helvite, and both minerals are cross-cut by tourmaline–biotite veinlets or rimmed by prismatic tourmaline grains. In other samples, the garnet bearing assemblage was cut by quartz–carbonate–fluorite veins.

*Helvite:* Helvite crystals are also found at the deeper level of the mine. Helvite is recorded in Samples 88R-6 at 1201 m, 200mS and 17L-KZH-1. Under the microscope helvite from Rosebery is pink, rhombic in shape and locally appears to replace garnet (Fig. 6.1C). Some helvite grains are distinctly zoned (Figs. 6.1D). Other helvite crystals are found in association with pyrite.

*Biotite:* Biotite is commonly intergrown with magnetite. In hand specimen, biotite can be easily mistaken either for tourmaline or a dark green variety of chlorite. Pyrite euhedra are also first replaced by hematite or magnetite and then by biotite–magnetite (Chapter 4, Figs. 4.7A, B and C). Microscopically, the colour of biotite varies from green to brown (Figs. 6.1E, F). It forms thin veinlets or flakes and sometimes occurs as alteration products of garnets (Figs. 6.1A, C and D).

*Tourmaline:* Tourmaline was reported at the Rosebery mine by Finucane (1932) and Stillwell (1934) and later by Green (1983), Lees (1987), Plimer and Lees (1988) and Lees et al. (1990). Tourmaline is a most ubiquitous mineral and is found cross-cutting sulphide lenses and Host rock in the south-end orebody of the Rosebery mine. Tourmaline occurs as thin veinlets or lenses. Plimer and Lees (1988) described 3–5 cm thick tourmaline layers at Rosebery (15 Level) as "tourmalinite" or tourmaline exhalites but recent careful field and microscopic investigations of tourmaline assemblages do not support the tourmaline exhalite concept (discussed further below).

Tourmaline veinlets often cut the helvite and garnet and also sulphide assemblages (Chapter 4, Fig. 4.7H). Under the microscope, tourmaline occurs as euhedral, prismatic or stubby, trigonal grains. Zoned aggregates are observed with individual grains containing dark green cores with light green rims or vice versa (Fig. 6.1G). Prismatic, columnar tourmalines forming thin layers and tourmaline veins are also noted (Fig. 6.1H).

*Chlorite:* Chlorite is extensively associated with sericite in the footwall occurring as a blanket-like alteration zone of probable Cambrian hydrothermal origin which forms part of the footwall alteration zone to the ore deposit. Chlorite is also found together with biotite and tourmaline and in places flakes of chlorite and biotite are intermixed. Chlorite shows fine-grained felted appearance or coarse elongated "pressure shadow" grains next to sulphide minerals. Chlorite also occurs as an alteration product of biotite at the margin of the fluorite-bearing retrograde veins in biotite-magnetite assemblages.

Fig. 6.1A. Photomicrograph showing light orange to pale brown garnet grain cut by tourmaline-biotite veinlets. Plane polarised light. Sample No. 88R-6 at 366.1m, 200mS, F(J) lens, south-end of Rosebery Mine, western Tasmania. Gar=garnet, and Tm-Bi=tourmaline-biotite.

Fig. 6.1B. Same as above under X-nicols. Note anisotropism and penetrative twinning. Gar=garnet.

Fig. 6.1C. Photomicrograph showing light orange, subhedral garnet together with pink, wedge-shaped helvite crystal and green to dark green biotite and tourmaline. Dark coloured minerals are pyrite and pyrrhotite. Note garnet grains are cut by helvite veinlets and again both garnet and helvite crystals are altered by biotite-tourmaline veinlets. Plane polarised light. Sample No. 88R-6 at 366.1m, 200mS, F(J) lens, south-end of Rosebery Mine, western Tasmania. Tm-Bi-Mag=tourmaline-biotite-magnetite, HEL=helvite, Qtz=quartz and Gar=garnet.

Fig. 6.1D. Photomicrograph showing light brown to pink coloured helvite crystals together with altered anhedral to subhedral garnet grains. The green minerals are biotite and tourmaline and dark coloured minerals are pyrite and pyrrhotite. Note distinctly zoned, pink, wedge-shaped helvite crystal in the centre. Plane polarised light. Sample No.88R-6 at 366.1m, 200mS, F(J) lens, south-end of Rosebery Mine, western Tasmania. py–po=pyrite–pyrrhotite, Tm-Bi=tourmaline-biotite, HEL=helvite and Gar=garnet.

Fig. 6.1E. Photomicrograph showing flakes of green biotite with hematite. The biotite appears to have been altered from chlorite. Plane polarised light. Sample No. 3016-26 at 246' (75.5m), 300mS, F(J) lens, south-end of Rosebery Mine, western Tasmania. Bi=biotite, and Hem=hematite.

Fig. 6.1F. Photomicrograph showing brown biotite together with green biotite. Plane polarised light. Sample No. 88R-4 at 364.6m, 200mS, F(J) lens, south-end of Rosebery Mine, western Tasmania. py=pyrite and Bi=biotite.

Fig. 6.1G. Photomicrograph showing euhedral, zoned tourmaline crystals. The colour of the zones varies from one crystal to another. Sample No. R1920-1 at 549m, 200mS, F(J) lens, south-end of Rosebery Mine, western Tasmania. Qtz=quartz and Tm=tourmaline.

Fig. 6.1H. Photomicrograph showing prismatic, bladed tourmaline forming 3-5 cm thick tourmaline layers in 'tourmalinite' assemblages. Sample No. R3016-2B at 9.6m, 200mS, F(J) lens, south-end of Rosebery Mine, western Tasmania. Tm=tourmaline.

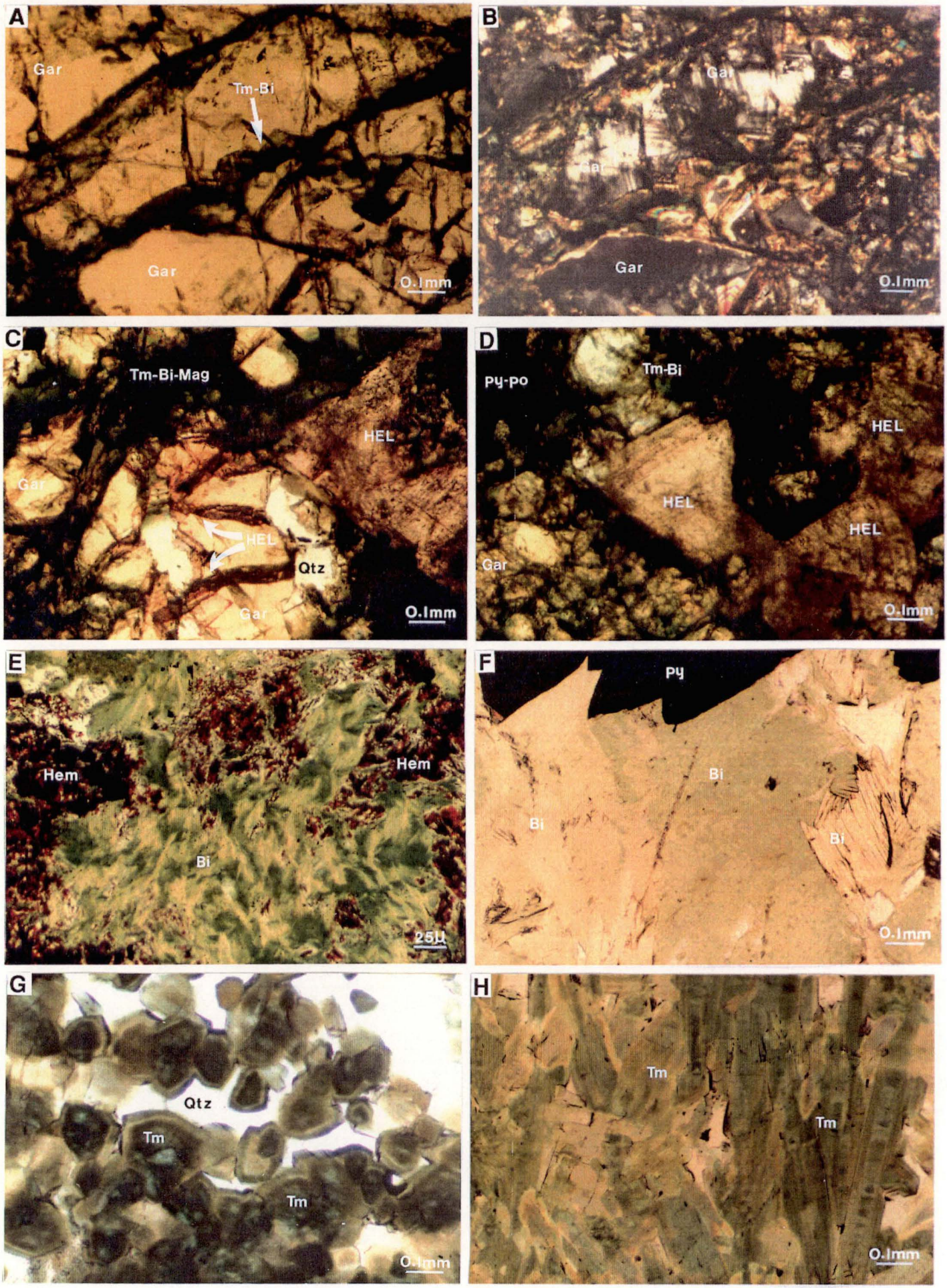
A
Gar
Tm-Bi
Gar
0.1mm
B
Gar
Gar
Gar
0.1mm
C
Tm-Bi-Mag
HEL
Gar
HEL
Qtz
Gar
0.1mm
D
Py-Po
Tm-Bi
HEL
HEL
HEL
Gar
0.1mm
E
Hem
Hem
Bi
25μ
F
Py
Bi
Bi
Bi
0.1mm
G
Qtz
Tm
Tm
0.1mm
H
Tm
Tm
0.1mm

*Sericite, K-feldspar and carbonate:* Sericite is commonly observed in the Rosebery deposit. Sericite may be found together with K-feldspar, biotite, tourmaline, and garnet. K-feldspar occurs as minor irregular, anhedral aggregates. Various forms of carbonates are noted in the F(J) lens (Chapter 4).

*Iron sulphides and oxides:* Iron sulphide and oxide minerals (pyrrhotite, pyrite, magnetite and hematite) are found as replacement minerals associated with the silicate minerals. Under the microscope, pyrrhotite occurs as creamy pink, anhedral grains replacing pyrite or as thin veinlets cutting pyrite cubes. Magnetite is commonly associated with bioitite. In places, red to brownish, bladed hematite replaces pyrite cubes. Further information on the opaque phases is provided in Chapter 4, section 4.2.

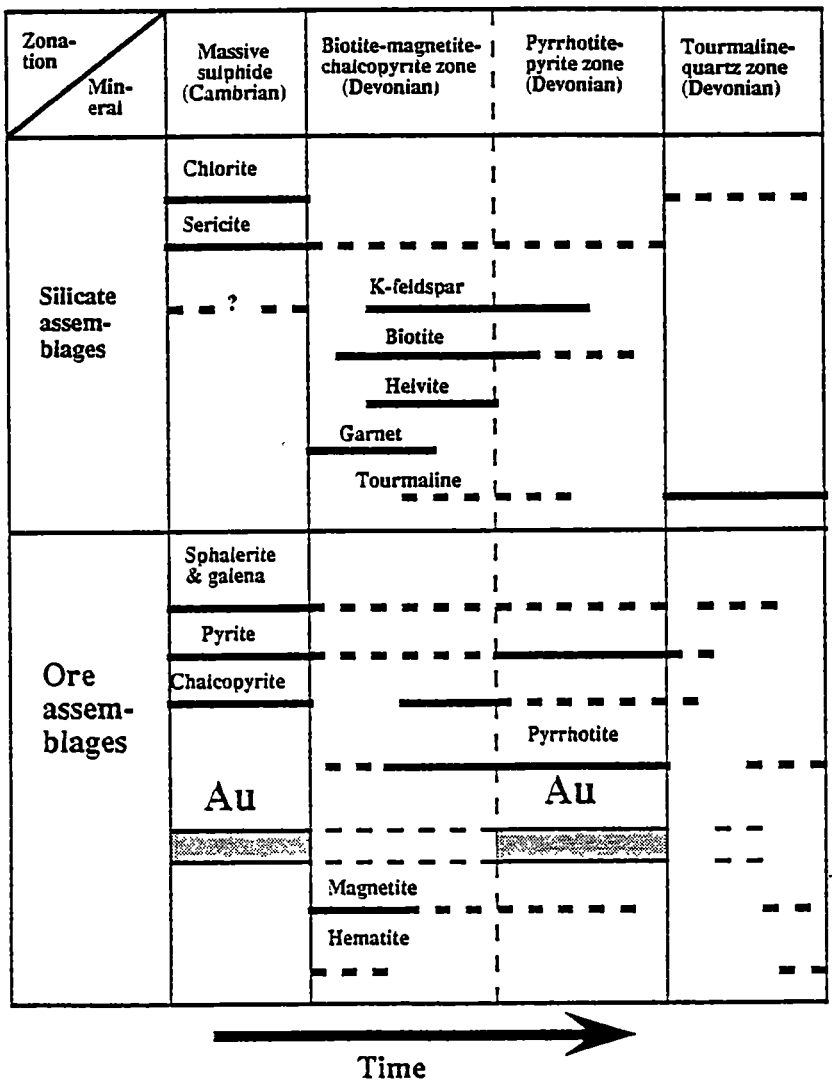


Fig. 6.2 Schematic diagram showing paragenetic relationships of replacement mineral assemblages in F(J) lens, Rosebery south-end, western Tasmania. The evidence used for the paragenetic relationships includes the microtextures discussed in section 6.2 and the macrotextural criteria presented in Chapter 4, section 4.2.

## 6.3 PARAGENESIS ...

Mineralogical and cross-cutting textural relations of the replacement minerals discussed in the previous section indicate a paragenetic sequence: garnet » helvite » biotite–tourmaline » tourmaline » tourmaline–fluorite. The general paragenetic relationships of the dominant silicate minerals and associated Fe–S–O assemblages in the F(J) lens are shown in Fig. 6.2. Garnet, helvite and biotite as well as magnetite are concentrated in the biotite–magnetite ± chalcopyrite zone.

Although tourmaline occurs throughout the zone, tourmaline is most abundant in the tourmaline–quartz zone. Microtextural relationships indicate that tourmaline formed after deformation and at very late stages of the metasomatism. Evidence in support of this comes from three observations: (1) most shear zones are filled with tourmaline–quartz veinlets, (2) tourmaline veinlets cut the sulphide assemblages and (3) the other silicate minerals (garnet, helvite and biotite) are also cut by tourmaline veinlets.

High grade gold (>20 g/t) is noted in the pyrrhotite–pyrite zone and the other zones contain erratic and variable gold grades (Chapter 5). The pre-exisitng Pb–Zn–Cu minerals and associated chlorite, sericite and carbonate are present in the F(J) lens. K-feldspar is also present. Chlorite appears to have been altered to biotite during the Devonian metasomatic process.

Beane (1982) proposed the following reations for the formation of biotite in the potassic zone of porphyry copper deposit; these processes produce pyrite, which remains intimately intergrown with altered biotite.

$$3Mg_5Al_2Si_3O_{10}(OH)_2 + 8KAlSi_3O_8 = 5KMg_3AlSi_3O_{10}(OH)_2$$
chlorite K-feldspar phologopite
$$+ 3KAl_3Si_3O_{10}(OH)_2 + 9SiO_2 + 4H_2O \qquad (1)$$
muscovite quartz

$$K(Mg_{0.6}Fe^{+2}_{0.4})_3AlSi_3O_{10}(OH)_2 + 1.2S_2 = 0.6KMg_3AlSi_3O_{10}(OH)_2$$
biotite phologipite
$$+ 1.2FeS_2 + 0.4KAlSi_3O_8 + 0.4H_2O + 0.6O_2 \qquad (2)$$
pyrite K-feldspar

The F(J) lens biotite-forming reaction was probably related with these reactions under moderate $fO_2$ conditions although the actual biotite-forming process may have been more complex. Presence of magnetite in the biotite-rich zone of the F(J) lens supports the moderate $fO_2$ conditions.

## 6.4 GEOCHEMISTRY OF REPLACEMENT MINERAL ASSEMBLAGES ...

Compositional variations of garnet, helvite, biotite, tourmaline, chlorite, sericite and K-feldspar were analysed in this study, and compared with data from other well documented Tasmanian Devonian replacement tin deposits (Cleveland and Mt Lindsay) and the Canadian CanTung high temperature skarn deposit.

### 6.4.1 Analytical techniques ...

The chemical analyses were carried out using a JEOL JXA–50A microprobe employing an accelerating voltage of 20kV, a beam current of $0.34 \times 10^{-7}$A, a beam diameter of 2–3 μm and a counting interval of 120 secs. At least 2–5 analyses were averaged to yield each analysis and analytical data are presented in Appendices 6.2–6.8.

## 6.5 COMPOSITION OF ROSEBERY GARNET ...

Microprobe analyses of the garnet samples are presented in Appendix 6.2 and plotted on the ternary diagram, spessartine ($Mn_3Al_2Si_3O_{12}$)/almandine ($Fe_3^{+2}Al_2Si_3O_{12}$)–grossularite ($Ca_3Al_2Si_3O_{12}$)–andradite ($Fe_3^{+3}Al_2Si_3O_{12}$) (Fig. 6.3). The iron content of the garnets is reported as FeO. In calculating the structural formulae, however, iron was partitioned so as to just fill the $R^{+3}$ sites.

Stoichiometric consideration indicates that the almandine molecule ranges from 1.3 mole % to 11.2 mole %, whereas the andradite component varies from 2.8–11.2 mole %. The garnets from the Rosebery mine consist predominantly of the spessartine composition from 74.2–84.9 mole % and contain minor grossularite (3.2–16.1 mole %). The MgO content is always negligible.

### 6.5.1 Comparison of Rosebery garnet with other garnets...

In Figure 6.4 the composition of garnets from the Rosebery mine is shown in comparison with compositions of garnets in the Mt Lindsay and Cleveland replacement deposits, western Tasmania (Kwak, 1983; Barth, 1986) and of typical, high-temperature skarn garnets from the CanTung mine, Northwest Territories (Khin Zaw, 1976). It is noted that the composition of the Rosebery garnets is comparable with that of the Cleveland deposit and displays overlapping compositional ranges.

The Rosebery garnet compositions are different from those of the high-temperature tungsten skarn deposit at the CanTung mine (pressure corrected temperature up to 520°C) in which the garnet contains more grossularite components (Khin Zaw, 1976). The similar

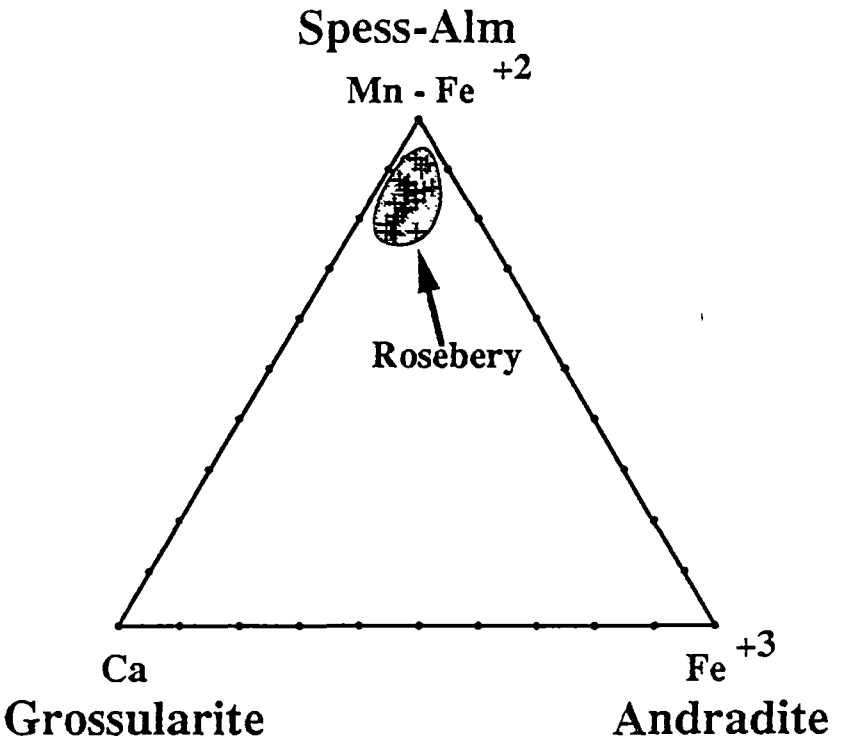


Fig. 6.3 Ternary plot of spessartine($Mn_3Al_2Si_3O_{12}$)/almandine($Fe_3^{+2}Al_2Si_3O_{12}$)–grossularite ($Ca_3Al_2Si_3O_{12}$)–andradite ($Fe_3^{+3}Al_2Si_3O_{12}$) showing the composition of garnets from the F(J) lens, south-end orebody, Rosebery mine, western Tasmania.

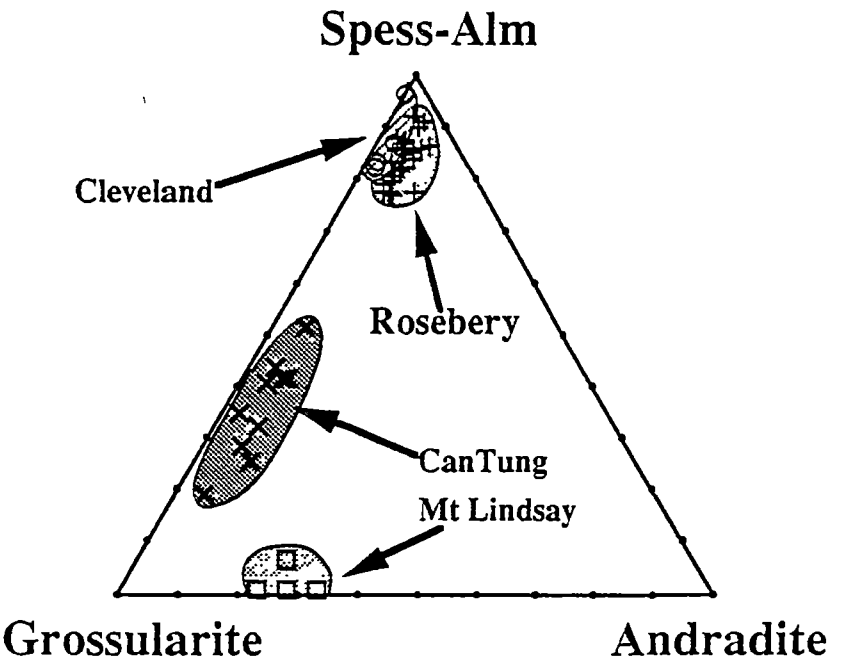


Fig. 6.4 Composition of garnets from the F(J) lens, south-end orebody, Rosebery mine together with compositional variation of garnets from Mt. Lindsay and Cleveland, western Tasmania (Kwak, 1983; Barth, 1986), and garnets from a typical, high-temperature skarn deposit, CanTung, NWT, Canada (Khin Zaw, 1976).

compositional ranges of garnets for the Rosebery and Cleveland deposits suggest similar metamorphic–metasomatic conditions, probably under a relatively low to moderate temperature range. Fluid inclusion data (Chapter 10) also suggest a moderate temperature (filling temperature of <330°C) for formation of the replacement assemblages.

In contrast, the garnets from Mt Lindsay contain very little spessartine–almandine composition but are more grossularite-rich with considerable andradite component. The inferred temperature of the Mt Lindsay W–Sn–F–Be skarns from mineral equilibria is >400°C (Kwak, 1983). Hence, the composition of garnets appears to have varied depending on temperature and other physico-chemical conditions such as $fO_2$.

Garnet is the most ubiquitous mineral in the majority of the skarn deposits. In a comphrehensive review on garnet compositions, Einaudi and Burt (1982) reported the compositional variation of skarn garnets, and Meinert (Fig. 2, 1983) related the compositional variation of garnets to different skarn types dominated by W, Sn, Zn (Pb), Mo, Cu and Fe.

According to Meinert (1983), the compositions of the garnets from the tin skarn deposits are generally restricted to more andraditic compositions and they may display grossularite-rich compositions as well, whereas the garnets in the tungsten skarns display a wide range of compositional variation and are commonly Fe- and/or Mn-rich and may approach the spessartine–almandine end-member. The composition of the garnets from the F(J) lens shows a combined spessartine and almandine composition (76.7–92.0 mole %) and is comparable and broadly similar to those of the tungsten skarn deposits.

In addition, Newberry (1983) used the compositional variation of garnets from tungsten (scheelite) skarn deposits as a criterion to classify the deposits into (1) strongly reduced skarns, (2) moderately reduced skarns and (3) oxidised skarns:

| | Strongly reduced skarn | Moderately reduced skarn | Oxidised skarn |
|---|---|---|---|
| Andradite mole % | 0–30 | 10–75 | 80–98 |
| Spessartine mole % | 3–35 | 5–40 | 0–3 |
| Almandine mole % | 3–40 | 2–35 | 0 |

According to Newberry's (1983) classification, the garnets from the F(J) lens of the Rosebery south-end fall in the reduced tungsten skarn class, and the F(J) lens garnet formation appears to have been under reducing conditions although hematite is locally noted in barite-rich massive sulphide lenses in the F(J) lens. Assay values up to 0.25 wt % $WO_3$ have been recently reported from the lower levels of the F(J) lens (Steve Hunns, per. comm., 1991).

## 6.6 COMPOSITION OF ROSEBERY HELVITE ...

Helvite group minerals are beryllium- and sulphur-bearing silicates with a general formula of $R_4Be_3(SiO_4)_3S$ (R = Mn, $Fe^{+2}$, Zn). The Mn-rich end-member is helvite, the $Fe^{+2}$ end-member is danalite, and the zinc end-member is genthelvite. Microprobe analyses of the helvite samples are presented in Appendix 6.3. Beryllium determination was not possible by means of the microprobe analysis. The Rosebery helvite contains up to 7.00 wt% Zn. A plot of Zn, Mn, and Fe for analyses of the helvite minerals from Rosebery is shown in Fig. 6.5. The Rosebery helvite displays up to 55.7 mole % danalite and up to 13.0 mole % genthelvite.

In Fig. 6.6, analyses from core to rim across a wedge-shaped helvite crystal are displayed. No appreciable change is apparent except for a slight enrichment in Mn and depletion in $Fe^{+2}$ at the rim.

### 6.6.1 Comparison of Rosebery helvite with other helvites ...

The occurrence of helvite and danalite is reported by many authors (e.g. Beus, 1962, 1966; Dunn, 1976; Burt, 1980) commonly in quartz-greisen veins (e.g. Cornwall, UK) and skarn deposits (e.g. Iron Mountain, New Mexico, USA). Danalite is also reported in western Tasmanian skarn deposits (e.g. Mt Lindsay, Kwak, 1983; Cleveland, Barth, 1986; Pine Hill and St Dizier, W. Barth, per. comm., 1987). The Mt Lindsay danalites are nearly end-member danalites ($danalite_{89.2}$: $helvite_{8.7}$:$genthelvite_{2.1}$) (Kwak, 1983).

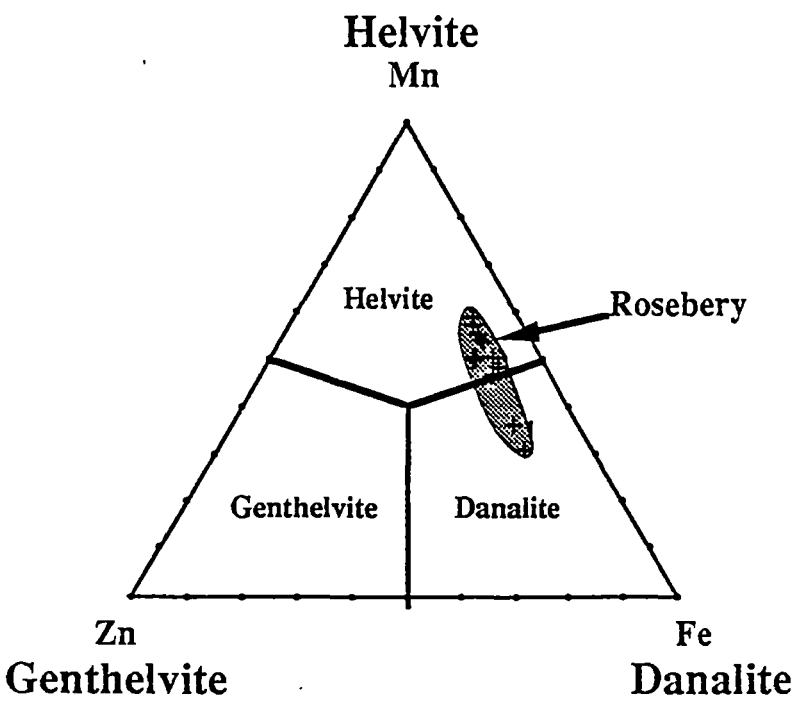


Fig. 6.5 Composition of helvites from the F(J) lens, south-end orebody, Rosebery mine, western Tasmania.

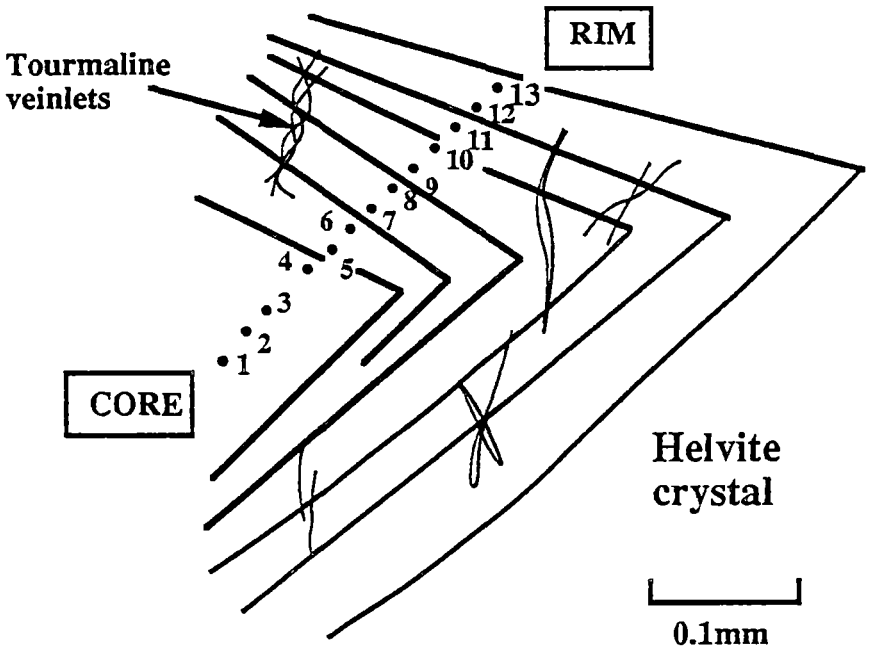


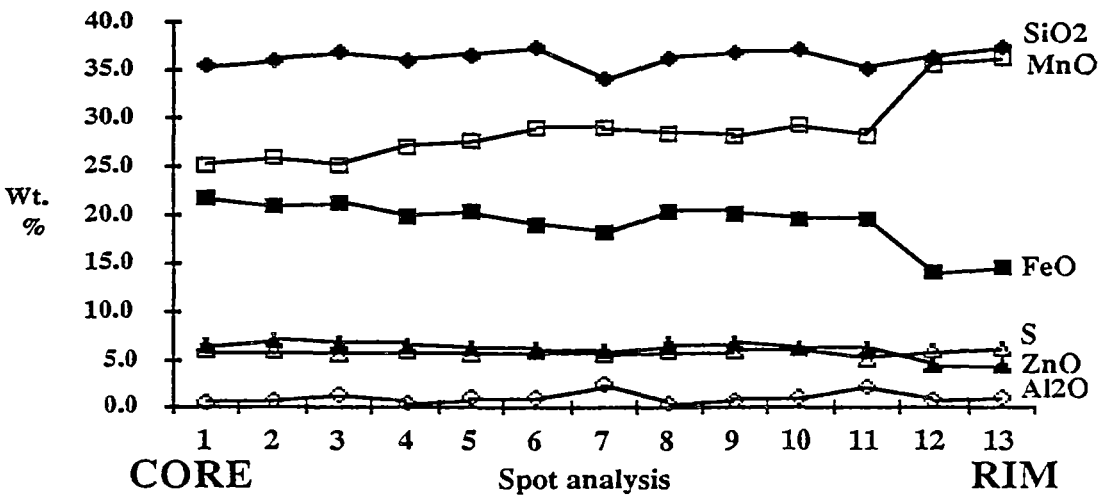


Fig. 6.6 A plot of compositional variation of a helvite grain from the core to the rim zones, F(J) lens, Rosebery mine. Note that Mn content increases from the core to the rim whereas $Fe^{+2}$ decreases towards the rim.

Helvite is also noted in syenite pegmatites in the Oslo region, Norway (Larsen, 1988). Clark and Feijer (1976) reported the occurrence of genthelvite (Zn-rich variety) at Cairngorm Mountains, Scotland. Dunn (1976) reviewed the occurrence of helvite group minerals from various localities, and Fig. 6.7 shows his compilation of the compositional data of natural helvite group minerals. It is interesting to note that pure end-member danalite is not recorded in the natural occurrences and there is a compositional gap between the Zn and Mn ends of the helvite series (see Fig. 6.7).

In Fig. 6.8, the compositional variation of the helvite minerals from Rosebery was plotted together with those from the other localities. The Rosebery helvite group minerals are found to be more Mn-rich than those from Cleveland, western Tasmania. The helvite group minerals from Mt Cairngorm, Scotland are genthelvite, whereas those from the Oslo region are Mn-rich with minor genthelvite components (Fig. 6.8).

Among natural helvite group minerals, the maximum danalite component is only 87 mole % (Dunn, 1976); danalite has not yet been synthesized (Burt, 1980), which may suggest that pure end-member danalite is probably unstable. Burt (1980) suggested the following two possible reactions for equilibrium of danalite with pyrite, pyrrhotite, hematite and magnetite.

6 hematite + 2 danalite = pyrite + 6 magnetite + 3 phenakite + quartz (1)

3 pyrite + 4 danalite = 10 pyrrhotite + 3 magnetite + 6 phenakite + 6 quartz (2)

The helvite group minerals from western Tasmania contain a significant component of danalite (Cleveland and Mt Lindsay) and the helvite from the F(J) lens contains up to 55.7 mole % danalite. Helvite is found in association with magnetite, pyrrhotite and pyrite and not with hematite: hence reaction (2) probably controlled helvite equilibrium as quartz is also abundant, although phenakite has not been identified in the F(J) lens.

Burt (1980) also demonstrated that danalite is stable under somewhat more sulphidising conditions than pyrrhotite and more oxidising conditions than fayalite. Danalite is sensitive to hypogene oxidation, whereas helvite and genthelvite are sensitive to S–O exchange (variation in $\log fO_2/fS_2$), as expressed in the following breakdown reactions:

$$6 \text{ danalite} + 7\ O_2 = 8 \text{ magnetite} + 9 \text{ phenakite} + 9 \text{ quartz} + 3\ S_2 \quad (3)$$

$$2 \text{ danalite} + 8\ S_2 = 8 \text{ pyrite} + 3 \text{ phenakite} + 6 \text{ quartz} + 4\ O_2 \quad (4)$$

$$2 \text{ danalite} + 4\ S_2 = 8 \text{ pyrrhotite} + 3 \text{ phenakite} + 8 \text{ quartz} + 4\ O_2 \quad (5)$$

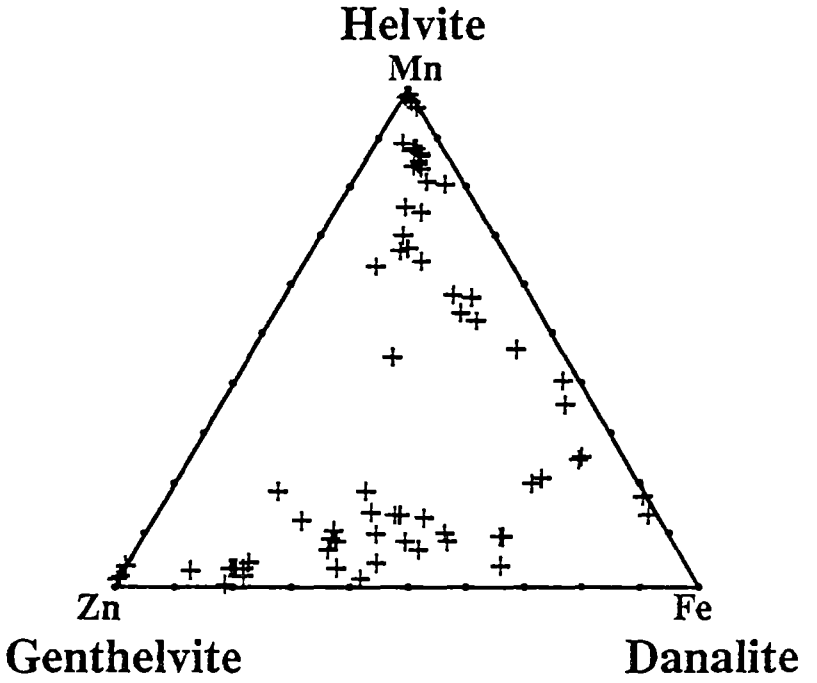


Fig. 6.7 Compositional variation of natural helvite group minerals from different localities compiled by Dunn (1976).

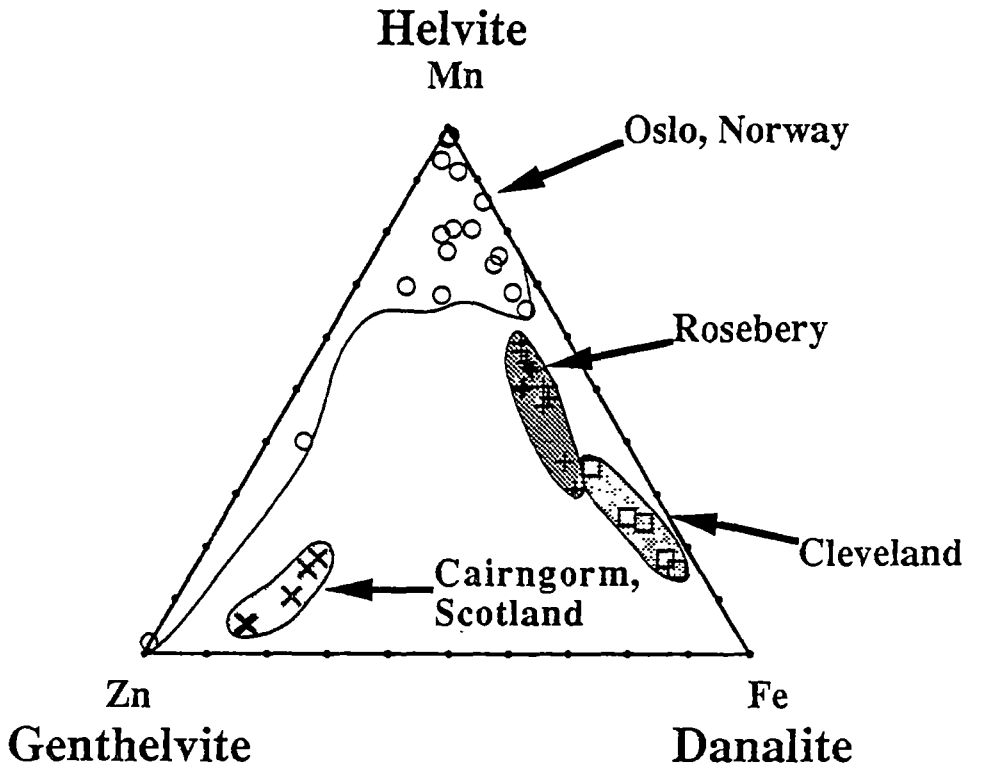


Fig. 6.8 Composition of helvites from the F(J) lens, south-end orebody, Rosebery mine together with compositional variation of helvite group minerals from Cleveland, western Tasmania (Barth, 1986), helvite group minerals in syenite pegmatite, Oslo region, Norway (Larsen, 1988) and genthelvite from Cairngorm Mountain, Scotland (Clark and Feijer, 1976).

Under increasing $CO_2$ conditions, danalite breaks down according to the following reaction:

$$2 \text{ danalite} + CO_2 = 6 \text{ siderite} + 3 \text{ phenakite} + 3 \text{ quartz} + 2 \text{ pyrrhotite} \quad (6)$$

The presence of $CO_2$ in the F(J) lens is indicated by fluid inclusion studies (Chapter 10). $H_2O$–$CO_2$ mixed fluid inclusions and $CO_2$-liquid bearing inclusions are abundant in the quartz, fluorite and helvite minerals from the F(J) lens. However, it must be borne in mind that the above reactions are theoretical considerations only, and as there is a lack of experimental data, absolute constraints on $fO_2$–$fS_2$–$fCO_2$ cannot be made.

The occurrence of helvite together with fluorite in the F(J) lens of the Rosebery mine indicates that most of the Be was introduced together with fluorine during the replacement process and accumulated in the form of helvite in the silicate-poor ore enriched in magnetite, pyrite and pyrrhotite.

## 6.7 Composition of Rosebery biotite ...

Microprobe data for the Rosebery biotites are shown in Appendix 6.4 and plotted in Fig. 6.9 (after Deer et. al., 1962) in terms of phlogopite $\{K_2Mg_6 [Si_6Al_2O_{20}] (OH)_4\}$, annite $\{K_2Fe_6 [Si_6Al_2O_{20}] (OH)_4$, eastonite $\{K_2Mg_5Al [Si_6Al_2O_{20}] (OH)_4\}$, and siderophyllite $\{K_2Fe_5Al [Si_6Al_2O_{20}] (OH)_4\}$ end-members. The representative microprobe data indicate $SiO_2$ (33.2–42.2 wt%), $TiO_2$ (0.0–1.2 wt%), $Al_2O_3$ (10.7–18.3 wt%), FeO (7.7–31.4 wt%), MnO (0.0–2.9 wt%), MgO (3.4–12.3 wt%), CaO (0.0–0.3 wt%), $K_2O$ (3.8–9.2 wt%) and $Cl^-$ (0.0–0.4 wt%). The biotites are generaly high in $K_2O$ (7.2–9.2 wt%) but altered biotite (Sample R3024-3C) has $K_2O$ as low as 3.8 wt%. Microprobe analyses across a single biotite grain in sample R3024-3C shows that $K_2O$ and FeO increased from the core to the rim. Both green and brown varieties in sample R3492-28 were analysed but no particular changes in $TiO_2$ and FeO between the two varieties were observed.

The biotite displays a significant variation in FeO with values up to 31.4 wt%. The biotite contains between 14.1 and 15.8 total cations. As the stoichiometric calculations assumed only $Fe^{+2}$, the higher $\Sigma$cations up to 15.8 suggest the presence of $Fe^{+3}$. The biotite displays a range of tetrahedral $Al^{IV}$ (1.81–2.73) and octahedral $Al^{VI}$ (0.02–2.75), and $100Mg/(Mg+Fe^{+2})$ values range from 22.2 to 54.1 which indicates they are compositionally biotites.

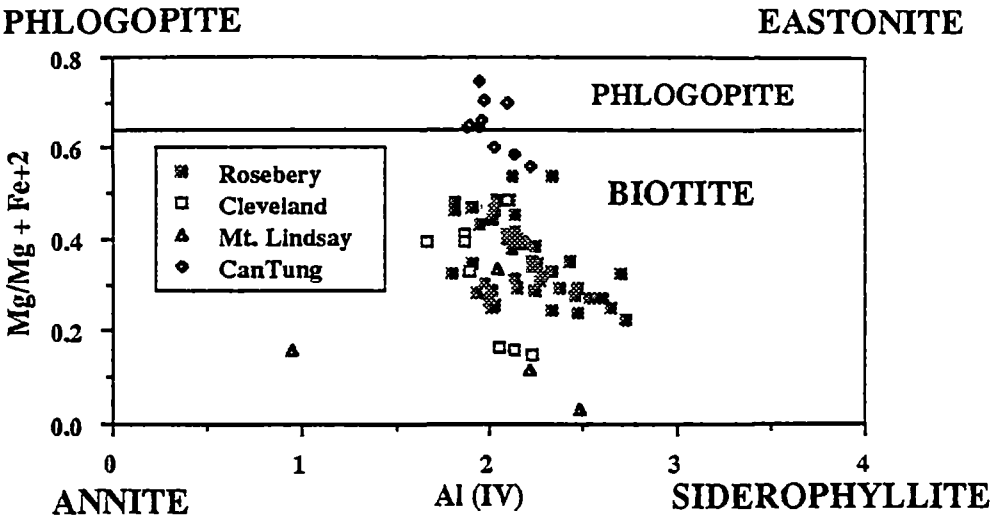


Fig. 6.9 A plot of $Mg/Mg+Fe^{+2}$ vs. $Al^{IV}$ for biotites from F(J) lens, south-end orebody, Rosebery mine together with compositional variation of biotites from Mt Lindsay and Cleveland, western Tasmania (Kwak, 1983; Barth, 1986), and biotite from CanTung mine, NWT, Canada (Khin Zaw, 1976).

### 6.7.1 Comparison of Rosebery biotite with other biotites ...

The compositional variation of biotites can be applied to distinguish different modes of its occurrence (e.g. magmatic vs metasomatic origins in the porphyry copper and skarn environments). The hydrothermal biotites in porphyry copper deposits are more magnesian than the magmatic biotites in the host intrusive stock (Bean, 1974; 1982; Jacobs and Parry, 1976). At the CanTung mine, the skarn biotites are more Mg-rich than the magmatic biotites in the nearby granitoid stock (Khin Zaw, 1976; Khin Zaw and Clark, 1978).

In Figure 6.9, the compositions of the Rosebery biotites are shown in comparison with those of Cleveland, and of typical, high-temperature W-bearing biotite skarns from the CanTung mine (Khin Zaw, 1976). Barth (1986) demonstrated that biotites from the Cleveland replacement deposit gave a range in $100Mg/(Mg+Fe^{+2})$ ratio of 15.8 to 48.3. The skarn biotites from Mt Lindsay display a range of $100Mg/(Mg+Fe^{+2})$ from 3.3 to 33.4 (Kwak, 1983). The Rosebery biotites are comparable with the biotites from the Mt Lindsay and Cleveland deposits, but their compositional difference from high temperature skarn deposits suggests a different mode of occurrence, probably indicating a low to moderate temperature of formation.

## 6.8 COMPOSITION OF ROSEBERY TOURMALINE ...

Tourmaline is a complex hydrous borosilicate mineral composed of Al, Ca, Fe, Mg and Na and occurs in a wide range of geological environments from sedimentary, metasomatic to granitic–magmatic. The general formula of the tourmaline group is $WX_3Y_6(BO_3)_3Si_6O_{18}(OH, F, Cl)_4$ where W = Na, Ca; X = $Fe^{+2}$, Mg, Mn, Al, $Fe^{+3}$, Li; and Y = Al, $Fe^{+3}$, Cr, V. The most common end-members after Henry and Guidotti (1985) are elbaite (W = Na; X = Li, Al; Y = Al), schorl (W = Na; X = $Fe^{+2}$, $Fe^{+3}$, Mn; Y = Al), dravite (W = Na; X = Mg; Y = Al) and uvite (W = Ca; X = Mg; Y = Al, Mg) (Fig. 6.10).

Recently Plimer and Lees (1988) undertook limited analyses of tourmalinites and other joint- and fracture-fill tourmalines in the south-end of Rosebery and also tourmalines in Devonian granites from western Tasmania. In this study, tourmaline in ten different samples from 100mS to 300mS of the F(J) lens, Rosebery were further analysed and the chemical data of the tourmalines are presented in Appendix 6.5.

Microprobe analyses of the Rosebery tourmalines show the compositional ranges: $SiO_2$ (31.1–36.63 wt%), $TiO_2$ (0.0 to 1.29 wt%), $Al_2O_3$ (22.1–33.4 wt%), FeO (9.9–24.5 wt%), MnO (0.0–0.8 wt%), CaO (0.0–1.3 wt%), $Na_2O$ (1.7–2.9 wt%), and $K_2O$ (0.0–1.9 wt%). $Cl^-$ was found to be less than the detection limit of 0.01 wt% and $B_2O_3$, $H_2O$, and $F^-$ cannot be determined by the microprobe.

The plots of Al–Fe–Mg and Mg–Fe–Ca indicate that the Rosebery tourmalines are predominantly of schorl $\{(NaFe_3^{+2}Al_6B_3Si_6O_{27}(OH,F)_4\}$ rather than dravite $\{NaMg_3Al_6B_3Si_6O_{27}(OH, F)_4\}$ and elbaite $\{(Na(Li, Al)_3Al_6B_3Si_6O_{27}(OH, F)_4\}$ (Figs. 6.11A and 6.11B). No systematic chemical changes across compositional zones in the tourmaline were recorded.

### 6.8.1 Comparison of Rosebery tourmaline with other tourmalines ...

Plimer and Lees (1988) analysed two tourmaline samples from the Meredith granite (Cleveland) and two from the Heemskirk granite and showed that they are exclusively of schorl composition and lie on the Al–Fe join of the Al–Fe–Mg plot or at the Fe-end of the Fe–Mg–Ca plot. In contrast, Barth (1986) analysed a large number of tourmalines from the Meredith granite and reported the presence of a considerable Mg content.

The compositional variation of the Rosebery tourmalines is shown in comparison to that of the tourmalines from the Meredith granite analysed by Barth (1986) (Figs. 6.12A and 6.12B). The compositional variation of tourmalines from the Appalachian–Caledonian massive sulphide deposits (Taylor and Slack, 1984) and from the Kidd Creek volcanogenic massive sulphide deposit, Timmins, Ontario (Slack and Coad, 1989), are also plotted together with

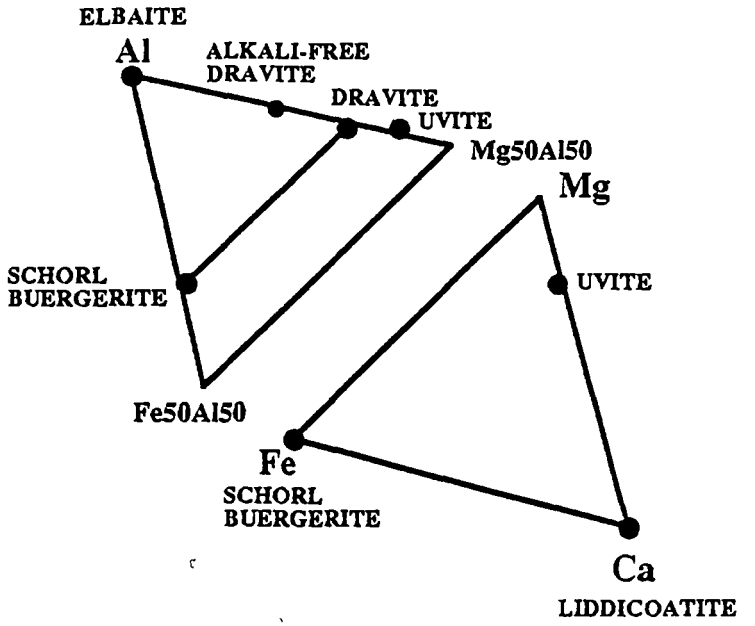


Fig. 6.10 Al-Fe-Mg and Mg-Fe-Ca diagrams for different end-members of the tourmaline group minerals after Henry and Guidotti (1985).

those of the Rosebery tourmalines in Figs 6.13A and 6.13B. This comparison shows that the tourmaline from Rosebery is similar in composition to the Meredith granite tourmaline and more Fe-rich than volcanogenic tourmaline reported from Kidd Creek and the Appalachian Caledonides.

## 6.9 COMPOSITION OF TOURMALINE AS A PETROLOGIC INDICATOR ...

In recent years, the compositional variation of tourmaline has attracted attention from many workers as a means of interpreting the mode of occurrence of the tourmaline and also of inferring the physico-chemical environment of the associated mineralisation. Tourmaline-rich rocks can originate by several different processes: (1) granitic–hydrothermal, (2) authigenic, (3) detrital, (4) regional metasomatic, (5) evaporitic-sabkha and (6) submarine-hydrothermal exhalative (Slack, 1982).

Processes (2) and (3) are not relevant for the F(J) lens tourmaline. Process (4), which involves the metamorphism of boron-rich illitic clays (Reynold, 1965) or the development of localised veins and segregations of tourmaline by metasomatism in regional metamorphic terrains, is also considered negligible for the formation of tourmaline-rich rock (Slack, 1982).

Certain stratabound deposits such as those in the Zambian Cu belt (Garlick and Fleischer, 1972) are considered to have been deposited under evaporitic or coastal sabkha type environments in which boron can accumulate to form a tourmaline-rich rock. However, such a process (5)

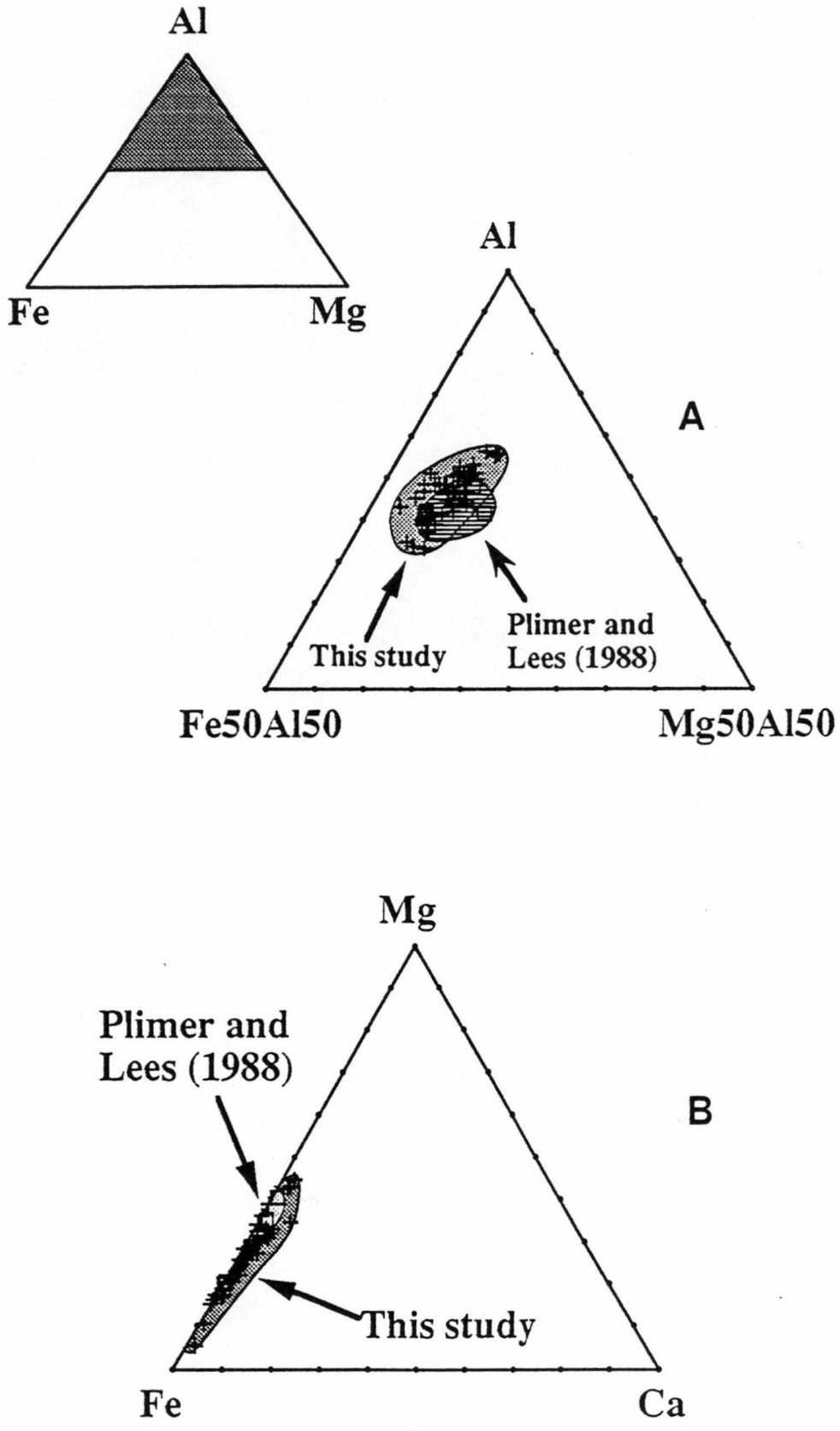


Fig. 6.11 A — Al-Fe-Mg plot for the compositional variation of tourmalines from the F(J) lens, Rosebery mine together with the analysis of the tourmalines from the tourmalinites of the Rosebery area by Plimer and Lees (1988). B — Fe-Mg-Ca plot for the compositional variation of tourmalines from the F(J) lens, Rosebery mine together with the analysis of the tourmalines from the tourmalinites of the Rosebery area by Plimer and Lees (1988).

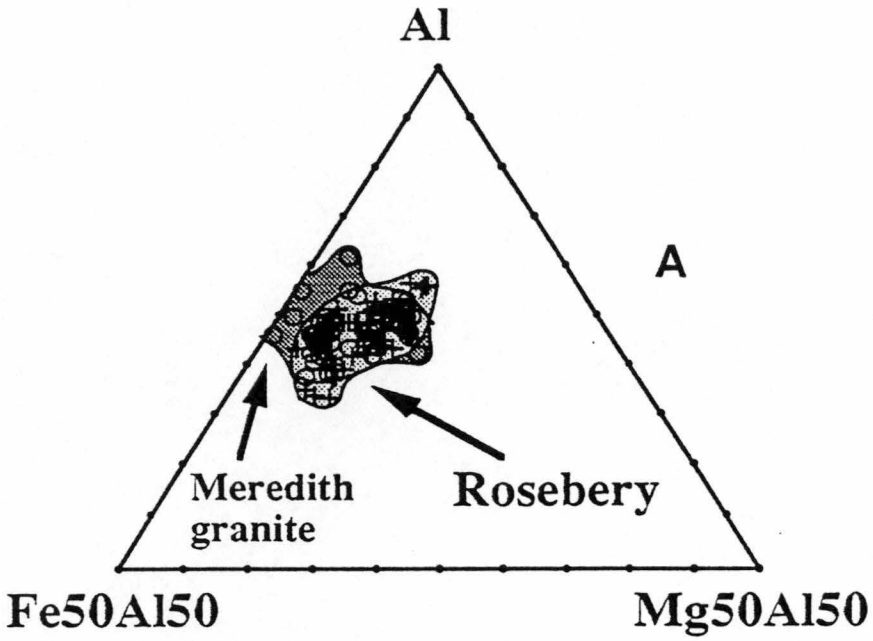


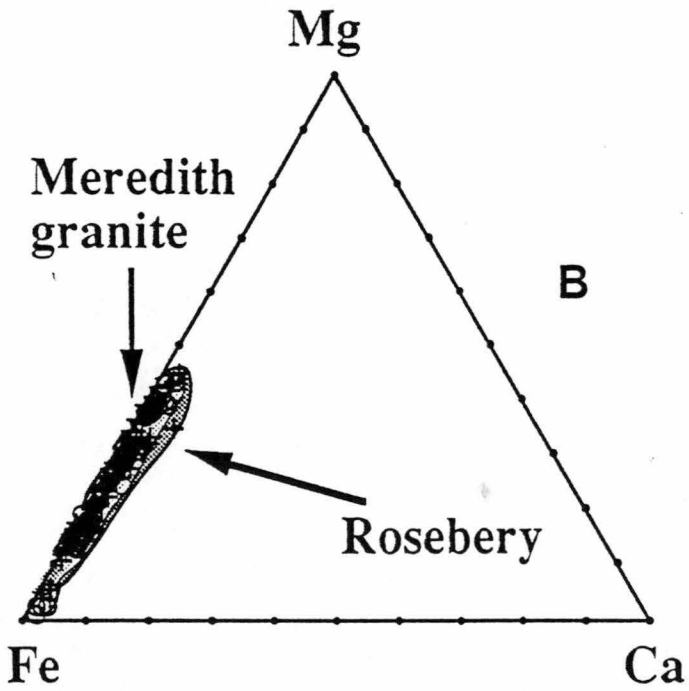


Fig. 6.12 A — Al-Fe-Mg plot for the composition of tourmalines from the F(J) lens, Rosebery mine together with compositional variation of tourmalines from the Meredith granite, Cleveland, western Tasmania (Barth, 1986). B — Fe-Mg-Ca plot for the composition of tourmalines from the F(J) lens, Rosebery mine together with compositional variation of tourmalines from the Meredith granite, Cleveland, western Tasmania (Barth, 1986).

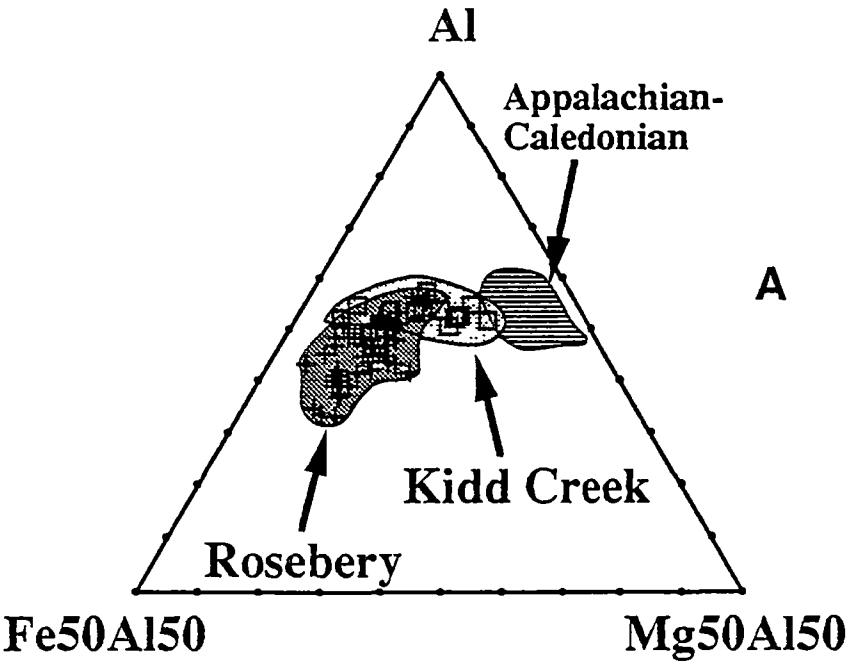


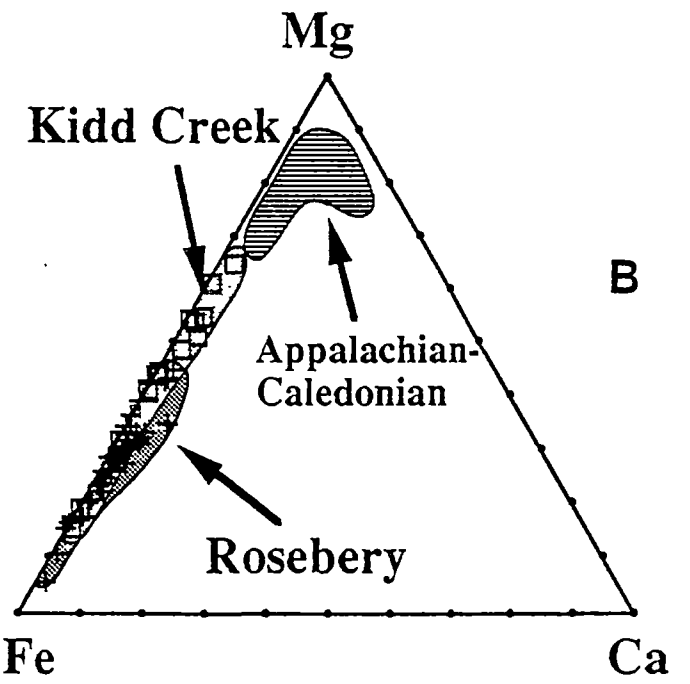


Fig. 6.13 A — Al-Fe-Mg plot for the composition of tourmalines from the F(J) lens, south-end orebody, Rosebery mine together with compositional variation of tourmalines from the Kidd Creek volcanogenic massive sulphide deposit,Timmins, Ontario, Canada (Slack and Coad, 1989) and Appalachian-Caledonian massive sulphide deposits (Taylor and Slack, 1984). B — Fe-Mg-Ca plot for the composition of tourmalines from the F(J) lens, south-end orebody, Rosebery mine together with compositional variation of tourmalines from the Kidd Creek deposit (Slack and Coad, 1989) and Appalachian–Caledonian massive sulphide deposits (Taylor and Slack, 1984).

could not form the Rosebery tourmaline-rich rocks as the Rosebery ore lenses formed under a relatively deep-water environment by exhalative processes. Hence, only processes (1) and (6) could have produced the Rosebery tourmalines and will be discussed in detail.

### 6.9.1 Granitic–hydrothermal tourmaline ...

Tourmaline in association with granite, pegmatites, aplites and hydrothermal veins has long been recognised and regarded as a product of late-stage magmatic processes. Tourmaline is commonly an important gangue mineral in hydrothermal veins (e.g. tungsten–tin veins at Panasqueira, Portugal, Kelly and Rye, 1979; Mawchi mine, Burma, Khin Zaw and Khin Myo Thet, 1983), and breccia pipes (e.g. Carlson and Sawkins, 1980) and porphyry tin deposits of Bolivia (Sillitoe et al., 1975).

This enrichment of tourmaline in the hydrothermal veins and breccias has even led some workers to consider boron as an agent for metal transport (e.g. Charoy, 1982) although no experimental data on speciation of boron complexes exists, and the solubility of boron is not known. Recently the composition (e.g. major and trace elements and REE) of tourmaline has been used as a petrologic indicator or recorder to understand the evolution and cooling history of granite and pegmatite bodies (Manning, 1982; London, 1986; Jolliff et al., 1986; Jolliff et al., 1987), and Archean lode gold deposits (King and Kerrick, 1986). Tourmaline is notably found in western Tasmania in association with granites (e.g. Heemskirk granite and Meredith granite) and related carbonate replacement tin and tungsten deposits (e.g. Renison Bell, Cleveland and Mt Bischoff).

### 6.9.2 Submarine–hydrothermal tourmaline ...

The presence of tourmaline in submarine hydrothermal ore deposits has been interpreted to indicate that this mineral is formed by the same hydrothermal exhalative processes that formed the massive sulphide deposits (e.g. Slack, 1982; Taylor and Slack, 1984; Slack et al., 1984; Plimer, 1988; Slack and Coad, 1989). Slack (1982) reviewed the occurrence of tourmaline in the Appalachian–Caledonian massive sulphide deposits. The tourmaline in these deposits are found as disseminations, clots and fracture fillings in massive sulphide bodies and adjacent wall rocks, and in some areas as stratiform layers composed of massive foliated tourmaline referred to as 'tourmalinites'.

Stratabound tourmaline is also reported from the Proterozoic sediment-hosted, Sullivan massive sulphide deposit, British Columbia (e.g. Ethier and Campbell, 1977; Beaty et al., 1988), the Broken Hill deposit, NSW and the Golden Dyke Dome deposit, Northern Territory

(Plimer, 1983, 1986). Stratabound tourmalinite was also recently reported as a distal strike equivalent of the Proterozoic Starra Au–Cu deposit, Queensland by Davidson (1990). Tourmalinite, as a product of exhalation, is also described in association with Pb–Zn–Ag mineralisation at Bottino, Apuane, Italy (Benuenuti et al., 1989).

Slack (1982) and Slack and Taylor (1984) considered that tourmalinites are facies equivalents of exhalative sulphide lenses and demonstrated that the tourmaline associated with massive sulphides are Mg-rich dravites in contrast to the Fe-rich schorls of felsic plutonic association. However, later studies of the tourmaline at the Kidd Creek volcanogenic sulphide deposits by Slack and Coad (1989) showed that the Kidd Creek tourmaline has a wide range of composition from Fe-rich dravites to end-member schorl with Fe/(Fe+Mg) ratios varying from 0.33 to 0.92. Plimer (1983) also showed that tourmaline in the Broken Hill deposits are Fe-rich.

## 6.10 Genetic significance of the Rosebery tourmaline ...

Plimer and Lees (1988) initially analysed tourmaline from the "tourmalinite" samples from Rosebery and reported Fe/(Fe+Mg) ratios of 0.6 to 0.8, whereas the joint-fill tourmaline had Fe/(Fe+Mg) ratios of 0.7 to 0.8. Present microprobe analyses give a range of Fe/(Fe+Mg) ratios from 0.5 to 0.9 for the tourmaline from the south-end of the Rosebery mine.

On the Al–Fe–Mg plot, the initial analyses of the four tourmalinite samples by Plimer and Lees (1988) display nearly identical composition to the other Rosebery tourmaline samples analysed in this study (Fig. 6.11A). The plot of Fe–Mg–Ca also indicates similar compositional ranges (Fig. 6.11B). Hence, the banded tourmalinites and the other fracture-fill tourmalines at Rosebery were the product of one and the same hydrothermal process and the previously reported difference in composition is probably due to random statistical differences related to the small sample set of Plimer and Lees (1988).

Plimer and Lees (1988) considered that the Rosebery tourmaline displays two distinct styles: (1) tourmalinite of submarine hydrothermal origin and (2) tourmaline of Devonian granite origin. In this study, the Rosebery tourmaline is found to be exclusively of granite origin. Plimer and Lees (1988) asserted that tourmalines forming 3–5 cm thick layers as "tourmalinite" in underground mine levels were formed by submarine chemical precipitation and were tourmaline exhalites.

Plimer and Lees (1988, p.100) stated that

*"It is suggested that late in the history of the formation of the Rosebery deposit, temperatures were low enough and the Eh and pH were high enough to allow tourmaline precipitation from a fluid with a high activity of boron. Debouchment of boron-bearing ore fluids earlier in the submarine hydrothermal history would have resulted in infinite dilution of boron in seawater. Replacement of earlier assemblages in the fluid conduit by late stage tourmaline is envisaged with maximum tourmaline precipitation as an exhalite shortly after deposition of the massive sulphides. Because tourmaline is the only possible precursor mineral to the tourmaline in the exhalites, it is suggested that the primary precipitate from the submarine hot fluid was a gel from which tourmaline, silica, iron oxides and iron sulphides precipitated*".

The following features are not consistent with the submarine exhalative origin of the tourmaline:

(1) Detailed examination of the undergound tourmalinite exposures (e.g. 15 Level) clearly indicates that the tourmaline assemblages cut across the Devonian cleavage (Chapter 4, Figs. 4.7I and 4.7J).

(2) Detailed microscopic investigation of the tourmalinite does not show any evidence for a pre-deformation texture. Tourmaline assemblages do not reveal any sedimentary textures such as graded bedding or cross lamination. Tourmaline clasts are also not reported in the Rosebery–Hercules area..

(3) The "bedded" tourmalinites are found to be localised occurrences with no stratigraphic continuity in comparison with the tourmalinite assemblages in other stratabound massive sulphide deposits (Taylor and Slack, 1984) which are traceable for more than one kilometer along strike.

(4) Tourmaline is not present in other volcanogenic massive sulphide deposits in the Mt Read Volcanic Belt and the tourmaline is only recorded at Rosebery where there is strong geophysical evidence for an inferred Devonian granite body at shallow depth below the southern end of the deposit.

(5) No sedimentary sequences of evaporitic origin were reported in the Mt Read Volcanic Arc which could have supplied boron during the convective circulation of hydrothermal ore fluids to form tourmalines.

Barth (1986) conducted extensive analyses of tourmaline from the Meredith granite south of Cleveland including vein tourmaline and tourmaline from the nearby host sandstones. The tourmalines from the Meredith granite are not strictly of schorl composition and contain a minor dravite component (Figs 6.12A, B). This is consistent with tourmaline in granitic rocks elsewhere (e.g. Neiva, 1974; Manning, 1982).

The Rosebery tourmaline and the tourmaline from the Meredith granite display comparable compositional fields (Figs. 6.12A and 6.12B). Hence, this similarity in compositional range suggests that the Rosebery tourmaline was also formed from a similar granite source. This conclusion is consistent with the inferred existence of a shallow granite intrusion below the Rosebery south-end orebody.

At Kidd Creek the tourmaline is zoned from an Fe-rich core to Mg-rich rim. Slack and Coad (1989) proposed that this chemical zoning is due to mixing between high-temperature Fe-rich hydrothermal fluids and cold, Mg-rich, entrained seawater causing systematic changes in the Fe/(Fe+Mg) ratio. No such chemical variation was observed in the Rosebery tourmaline.

## 6.11 Composition of Rosebery chlorite ...

The compositional variation of chlorites from the D, G and H lens of the Rosebery mine was investigated by Green et al. (1981) and Green (1983). In this study, chlorites from the F(J) lens were analysed by microprobe, and analytical data are listed in Appendix 6.6. The chlorites in the F(J) lens display variations in $SiO_2$ (23.6–25.5 wt %), $Al_2O_3$ (18.5–19.8 wt %), FeO (32.9–39.8 wt %), MnO (1.1–2.6 wt %), and MgO (4.6–9.1 wt %) but $K_20$ and CaO are uniformly lower than 1.0 wt %. The highest $K_2O$ content (0.74 wt %) is found in chlorite associated with biotite. Microprobe analyses across single chlorite grains indicate no significant variation. On a cation basis, the chlorites have Fe/(Fe+Mg) ratios of 0.39–0.83 and Si values of 5.08–5.66. In the chemical classification of Hey (1954) they are daphnite, ripidolite and brunsvigite (Fig. 6.14).

### 6.11.1 Comparison of Rosebery chlorite with other VMS chlorites ...

The compositional variation of the chlorite in volcanogenic massive sulphide deposits have been studied extensively (e.g. Mt Lyell, western Tasmania, Hendry, 1981; South Bay, Ontario, Urabe and Scott, 1983; Bruce deposit, Arizona, Larson, 1984 and Phelps Dodge deposit, Quebec, Kranidiotis and MacLean, 1987). Slack and Coad (1989) recently analysed chlorite from the Kidd Creek deposit and the composition of Kidd Creek chlorite is shown together with the chemical composition of the F(J) lens chlorite and D, G, and H lens chlorite (Green et al., 1981; Green, 1983) in Fig. 6.15.

The chlorite composition from the D, G, and H lens varies in Fe/(Fe+Mg) ratio from 0.67 to 0.86 with Si values 5.05–5.31 and falls in the fields of daphnite and ripidolite. The Kidd Creek chlorites display Fe/(Fe+Mg) ratios of 0.43–0.98 and Si values of 5.00–5.39 and are comparable with those of the D, G, and H lens. In comparison, the F(J) lens chlorites appear to be more siliceous with Si values up to 5.7.

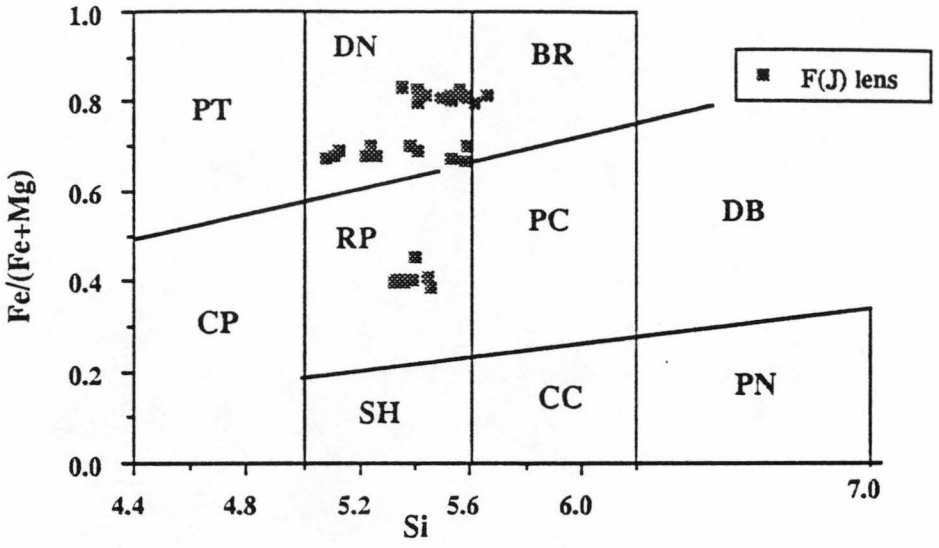


6.14 A plot showing the composition of the chlorites from the F(J) lens, Rosebery mine. Field boundaries after Hey (1954). Abbreviations; PT, pseudothuringite; CP, corundophilite; DN, daphnite; RP, ripidolite; SH, sheridanite; BR, brunsvigite; PC, pycnochlorite; CC, clinochlore; DB, diabantite; PN, pennite.

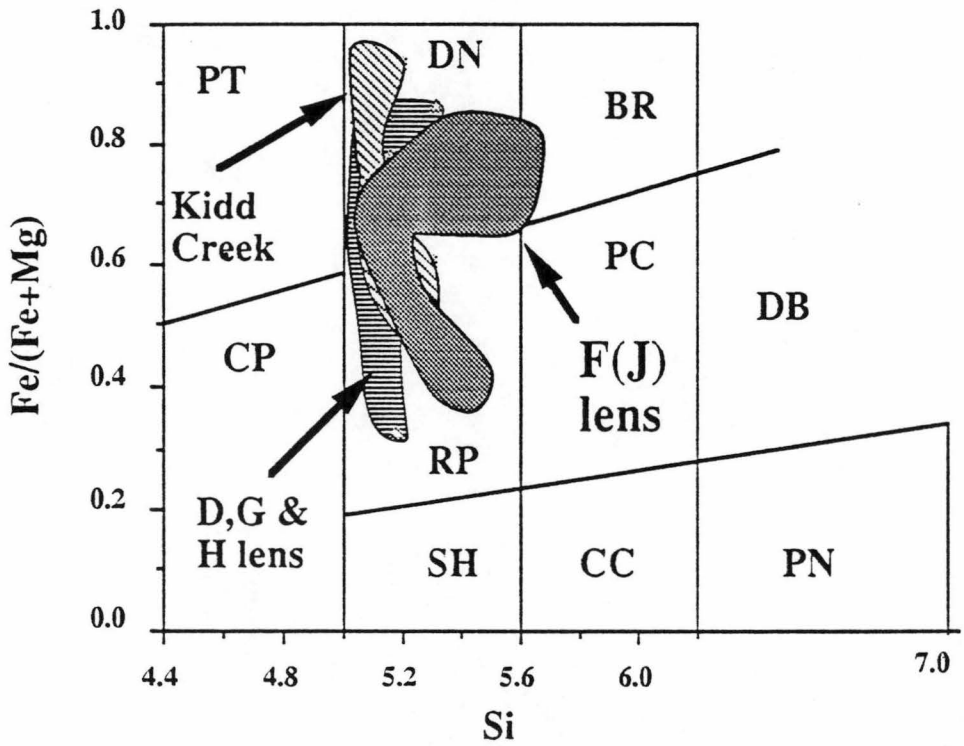


Fig. 6.15 A plot for the composition of chlorites from F(J) lens together with chlorite compositional data from D, G, and H lens of Rosebery (Green et al., 1981) and chlorite from Kidd Creek volcanogenic massive sulphide deposit, Timmins, Ontario (Slack and Coad, 1989). Field boundaries after Hey (1954). Abbreviations; PT, pseudothuringite; CP, corundophilite; DN, daphnite; RP, ripidolite; SH, sheridanite; BR, brunsvigite; PC, pycnochlorite; CC, clinochlore; DB, diabantite; PN, pennite.

### 6.11.2 Chlorite geothermometry ...

Walshe and Solomon (1981) and Walshe (1986) developed a thermodynamic model using the six-components solid-solution series of chlorite to provide estimates of physico-chemical conditions such as T, $fO_2$, $fS_2$, and $a_{H2S}$ in the hydrothermal environment. Several other authors (e.g. Reed, 1984; Cathelineau and Nieva, 1985; Shikazono and Kawahata, 1987) have also stressed that the composition of chlorite can be used as an indicator of hydrothermal conditions.

Cathelineau and Nieva (1985) have analysed the composition of chlorites and measured the temperatures from deep drill holes in a geothermal system. They found that $Al^{IV}$ of the chlorite increases with increasing temperature. Chlorites from the geothermal field used to calibrate their geothermometer come from a maximum depth of 2500 m. In this study, temperatures of formation of the F(J) lens chlorite were calculated using the method of Cathelineau and Nieva (1985). Use of their geothermometer for the F(J) lens chlorites yielded a temperature range of 267–328°C (mean = 297°C).

The thermodynamic model of Walshe (1986) was also applied to the compositional data of the F(J) lens chlorites to calculate the temperature of formation by means of a computer program held by the Tasmania Mines Department. The calculation for an assumed pressure of 1 kb produced only ten solutions for the 32 chlorite analyses. A temperature range of 270°–352°C (mean = 311°C) was revealed which compares favourably with the Cathelineau and Nieva (1985) chlorite geothermometer.

The accuracy of the above two geothermometers is unknown, as is the effect of pressure. Fluid inclusion studies (Chapter 10) indicate homogenisation temperatures up to 330°C and the fluid inclusion data are more compatible with the temperature data calculated using Walshe's (1986) chlorite model. The calculation made with the Walshe model also provided a range of $fO_2$ (–27.3 to –33.5) and a range of $a_{H2S}$ (–0.5 to –1.33) during the F(J) lens chlorite formation.

The F(J) lens chlorite shows a relationship between calculated log ($fO_2$) and temperature by the chlorite model. The temperature and the log ($fO_2$) data lie on a straight line suggesting a direct relationship. A similar trend was also noted for the chlorites from the Koonya prospect, 3 km along strike to the south of Rosebery (Hall, 1990). However, it is uncertain whether the temperatures recorded by the chlorite geothermometer represent the formation temperature in the Cambrian or the temperature of the later Devonian metasomatic overprint. Texturally, the F(J) lens chlorite is in equilibrium with the metasomatic minerals (biotite, magnetite, pyrrhotite, tourmaline etc.) and therefore it is likely that the calculated temperatures represent the metasomatic event during the Devonian.

## 6.12 COMPOSITION OF ROSEBERY SERICITE AND K-FELDSPAR ...

The chemical data for sericite and K-feldspar in the F(J) lens are presented in Appendices 6.7 and 6.8. The F(J) lens sericites contain $SiO_2$ (45.8–50.1 wt%), $TiO_2$ (0.3–1.4 wt%), $Al_2O_3$ (24.5–32.7 wt%), FeO (0.1–5.39 wt%), MnO (0.0–1.81), MgO (0.0–4.1 wt%), CaO (0.0–10.8 wt%), $Na_2O$ (0.0–1.5 wt%) and $K_2O$ (6.5–10.8 wt%) indicating a phengitic composition. Green et al. (1981) reported similar sericite compositions from G, H, F lens, except for the generally lower FeO content (1.6–3.9 wt% ). The higher FeO content of the F(J) lens phengites (up to 5.4 wt%), compared to the stratiform phengites in the G, H and F lens is probably due to enrichment during the Devonian metasomatic event.

Hendry (1981) also analysed phengites from the Mt Lyell volcanogenic Cu deposit and found FeO contents of 0.4–3.0 wt%. The Fe-rich phengites at Mt Lyell were considered by Hendry to be due to the reaction of silicates with Fe-bearing sulphides and oxides (pyrite and magnetite) during Devonian metamorphic recrystallisation. The presence of sericite and K-feldspar in the F(J) lens suggests that the Devonian replacement processes occurred under moderately acidic conditions (pH=5.5 to 6).

# CHAPTER 7: GOLD MINERALOGY AND GEOCHEMISTRY

## 7.1. INTRODUCTION ...

The volcanogenic massive sulphide deposits in western Tasmania are distinctly gold-rich (Large, 1990; Large et al., 1989; Large et al., 1990a). The Rosebery orebody alone contains 60 t of gold (approximately 40 t mined and 20 t in current reserves) and outranks such individual Australian gold deposits as Telfer (55 t), Hill 50 (55 t) and Warrego (50 t) (Purvis, 1985). Farquhar (1983) reported a total ore reserve of 1 million tonnes at 4.6 g/t Au in the F(J) lens of the Rosebery south-end orebody between 15 and 17 levels.

In this research programme, a mineragraphic study with special emphasis on the distribution, fineness and grain size of the gold minerals from the F(J) lens of the Rosebery south-end orebody, the J(K)–P and R lenses of the Hercules mine and the South Hercules deposit, was made to provide the basis for more efficient extraction and recovery of the gold ore resources. Au and Ag contents of the individual gold grains were determined as well as the Hg content of the gold grains.

## 7.2. ANALYTICAL TECHNIQUES ...

Both JEOL 50-A and CAMECA SX-50 microprobes were used to analyse Au, Ag and Hg contents of the selected gold grains. For the JEOL microprobe a 3 μm diameter beam of $2 \times 10^{-10}$ amps and an accelerating voltage of 20 kV was used, whereas for the CAMECA microprobe, a 1 μm diameter beam of $2 \times 10^{-10}$ amps and an accelerating voltage of 20 kV was applied. Prior to the microprobe analysis, the length and width of each gold grain were measured using the micrometer scale of the probe. From two to five spot analyses were later made on each gold grain by the probe and the results averaged. These data, as well as the average dimensions of the gold grains are presented in Appendices 7.1 through 7.4.

## 7.3. MINERALOGY OF GOLD IN THE F(J) LENS, ROSEBERY MINE ...

Although the F(J) lens of the Rosebery south-end orebody has the highest gold content of all the sulphide lenses at the Rosebery mine, little study has been done on the mineralogical,

textural and geochemical aspects of gold in the lens. Previous mineragraphic studies (Stillwell, 1934; Williams, 1960; Brathwaite, 1969, 1974; Green, 1983; Huston and Large, 1988; Huston, 1989) concentrated on the other lenses. A recent detailed mineralogical and geochemical study of gold distribution in the north-end Rosebery orebody by Huston and Large (1988) indicates six different styles of gold mineralisation (in order of significance):

(1) in massive sphalerite–galena–pyrite ore
(2) in massive barite mineralisation
(3) in the upper parts of pyrite–chalcopyrite pods
(4) in distal pyrite mineralisation (at the edges of sphalerite–galena–pyrite mineralisation and in the overlying Host rocks
(5) in footwall mineralisation (poorly understood) and
(6) in remobilised quartz–carbonate veins

In massive sphalerite–galena–pyrite ore of the north-end, gold occurs as electrum associated with galena and chalcopyrite in cracks within pyrite (Huston and Large, 1988), and a subordinate association with tetrahedrite was also noted by Brathwaite (1969). Gold also occurs in an unusual association of bismuthinite–bismuth–gold–maldonite at the north-end of 'E' lens (Huston and Large, 1988). In addition Green (1983) and Brathwaite (1974) noted visible gold in pyrite–chalcopyrite ore.

In the F(J) lens of the south-end, electrum is predominantly observed in the pyrrhotite and pyrite ore. Large et al. (1990a) reported that electrum in the southern ore lenses occurs as microscopic spherical inclusions (mean diameter 10–40 μm) in the marginal areas of pyrite grains and to lesser extent chalcopyrite, with some electrum (commonly in association with chalcopyrite) as thin films filling microfractures in pyrite and pyrrhotite. In this study, samples from the F(J) lens were studied and the following different modes of electrum occurrence were observed;

(1) in pyrite as inclusions (cf. Large et al., 1990a)
(2) in microfractures in euhedral pyrite grains (cf. Large et al., 1990a)
(3) in pyrrhotite as individual grains
(4) in chalcopyrite veins cutting pyrrhotite
(5) in association with chalcopyrite

Minute grains of electrum (<10 μm) commonly occur as inclusions in pyrite euhedra and are commonly associated with chalcopyrite (Figs 7.1A, 7.1B and 7.1C). A similar occurrence was noted by Huston and Large (1988) at the north-end, hence these grains are interpreted to be of relic Cambrian origin. Electrum may also be intimately associated with pyrrhotite veinlets cutting euhedral pyrite grains (Fig. 7.1D) which suggests that electrum was mobilised from the pyrite grains and recrystallised with pyrrhotite in the cross-cutting veinlets. Such

Fig. 7.1A. Electrum and chalcopyrite inclusion locked in pyrite euhedra. py=pyrite, Au=electrum, cp=chalcopyrite, po=pyrrhotite, sp=sphalerite, unlettered=gangue. Sample No. DDH R3492-17 at 118' (36.2m) on section 280mS.

Fig. 7.1B. Minute chalcopyrite and electrum inclusions in pyrite. py=pyrite, Au= electrum, cp= chalcopyrite, and unlettered=gangue. Sample No. DDH R3492-17 at 118' (36.2m) on section 280mS.

Fig. 7.1C. Chalcopyrite-electrum inclusion in euhedral pyrite grain. py=pyrite, po= pyrrhotite, cp=chalcopyrite, Au=electrum, unlettered=gangue; black striations in pyrrhotite are polishing marks. Sample No. DDH R3033-27 at 171' (52.5m) on section 300mS.

Fig. 7.1D. Electrum in pyrrhotite vein cutting pyrite grain. py=pyrite, po=pyrrhotite, Au= electrum, unlettered=gangue. Sample No. DDH R3492-17 at 118' (36.2m) on section 280mS.

Fig. 7.1E. Isolated electrum in pyrrhotite. Note lameller twinning of pyrrhotite at the rightside. cp=chalcopyrite, po=pyrrhotite, Au=electrum; unlettered black patches are polishing marks. Sample No. DDH R3034-7 at 100.5' (30.8m) on section 270mS.

Fig. 7.1F. Electrum in chalcopyrite vein cutting pyrrhotite. Note recrystallised pyrite grain enclosed in chalcopyrite at left-hand corner. py=pyrite, cp=chalcopyrite, sp=sphalerite, po=pyrrhotite, Au=electrum; black striations are polishing marks. Sample No. DDH R3024-3C at 137' (42m) on section 220mS.

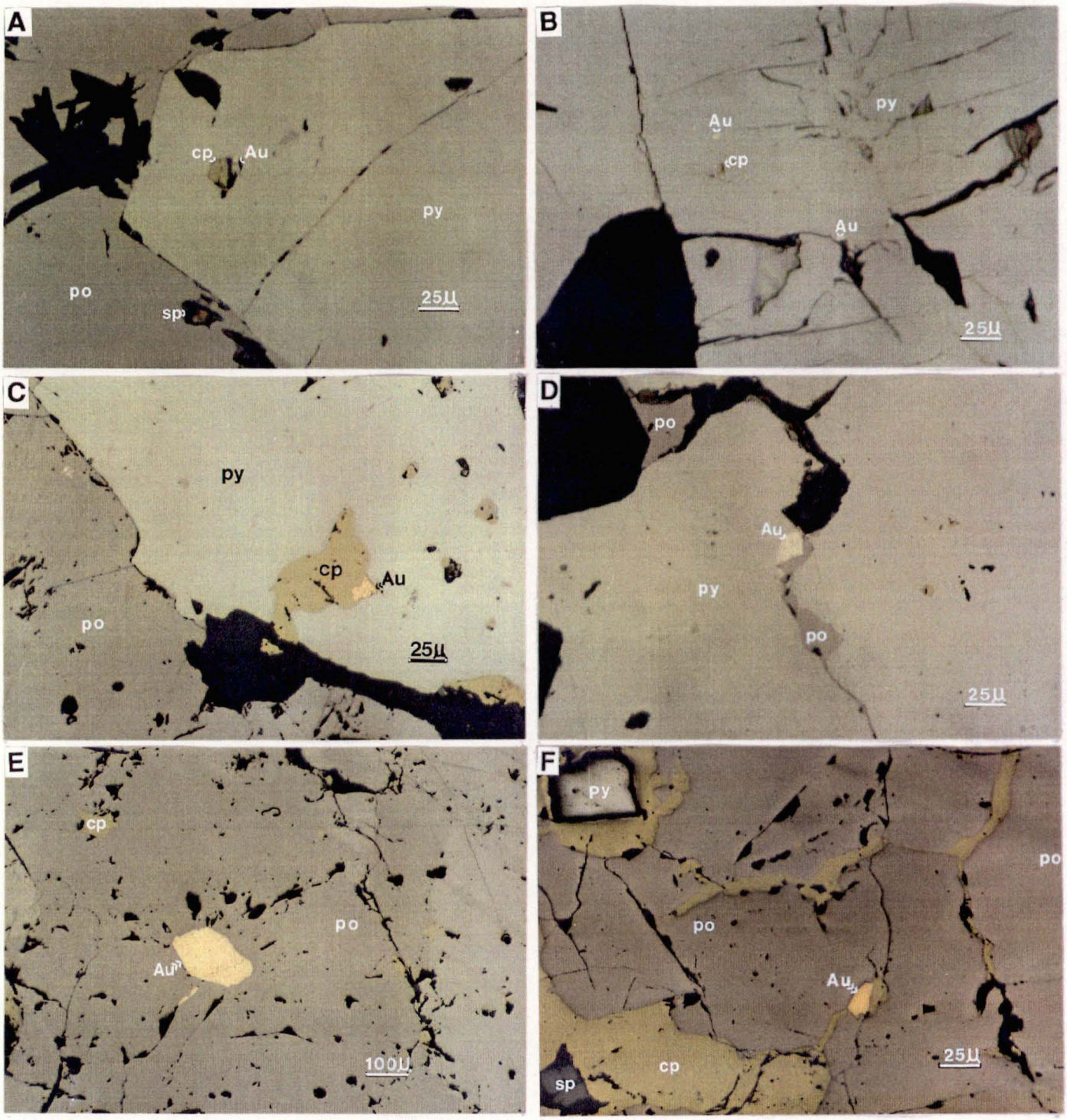
A
cp
Au
py
po
sp
25μ
B
Au
py
cp
Au
25μ
C
py
cp
Au
po
25μ
D
po
Au
py
po
25μ
E
cp
po
Au
100μ
F
py
po
po
Au
cp
sp
25μ

recrystallised electrum grains are sometimes up to 100 μm across (sample R3034-7 at 100.5' on section 270mS) (Fig. 7.1E).

Electrum is also noted in a distinct and spectacular association with copper in the F(J) lens. Electrum grains occur in chalcopyrite veins cutting massive pyrrhotite bodies (Fig. 7.1F). It also occurs in chalcopyrite 'pools' within pyrrhotite (Figs 7.2A, 7.2B and 7.2C). Some electrum grains with chalcopyrite (in sample R3024-3C @ 137' on section 220mS) attained an unusually large size of 150 μm x 100 μm across (Fig. 7.2C). Although no bismuthinite–gold–maldonite association was noted in the F(J) lens, native bismuth grains were commonly found as inclusions in the pyrrhotite (Fig. 7.2D), in the cracks in the pyrite (Fig. 7.2E) and in association with magnetite–pyrrhotite–pyrite–sphalerite and quartz (Fig. 7.2F). Bismuth can be easily mistaken for silver-rich electrum but was confirmed by microprobe. Bismuthinite was also noted in the F(J) lens (Figs 7.2B and 7.2E).

### 7.3.1 Grain size distribution of electrum at Rosebery ...

Figures 7.3 and 7.4 show histograms of electrum grain size from the north- and south-end of Rosebery. At the north-end, the electrum grains in the stratiform sphalerite–galena–pyrite zone display a size range from 1 μm to 160 μm with a broad mode at 6.3–25 μm (Fig. 7.3), whereas the electrum grains in the F(J) lens of the Rosebery south-end where Devonian metasomatic replacement occurred exhibit a similar size range but with a higher mode at 40–63 μm (Fig.7.4).

### 7.3.2 Fineness of electrum grains at Rosebery ...

The fineness {1000Au/(Au+Ag) by wt %} of gold grains from the north- and south-end of the Rosebery deposit is shown in Figs. 7.5 and 7.6. The fineness of electrum in the north-end ranges from 350 to 1000 (Fig. 7.5). The gold grains in the massive sphalerite–galena ± pyrite mineralisation yielded low fineness values from 300 to 650. In contrast, the gold grains in the bismuthinite vein and remobilised vein of possible Devonian origin gave higher fineness, greater than 900 (Huston and Large, 1988) (Fig. 7.5). The fineness values of the gold grains in the F(J) lens of the south-end of the Rosebery mine are presented in Appendices 7.1 and 7.2 and shown in Fig. 7.6. In the F(J) lens, the electrum grains locked in pyrite from the massive Pb–Zn sulphide lenses have lower fineness values between 450 and 500, whereas the other electrum grains have higher fineness values from 550 to 800 (Fig. 7.6).

### 7.3.3 Variation in fineness of electrum grains at Rosebery ...

It is noteworthy that fineness shows distinct zonation in some of the electrum grains from Rosebery (Fig. 7.7). Fineness is low at the rim and higher at the core.

Fig. 7.2A. Chalcopyrite-electrum intergrowth in pyrrhotite. Note euhedral pyrite grain at the upper left corner. cp=chalcopyrite, po=pyrrhotite, py=pyrite, unlettered=gangue or polishing marks. Sample No. DDH R3034-7 at 100.5' (30.8m) on section 270mS.

Fig. 7.2B. Chalcopyrite and electrum intergrowth in pyrrhotite. cp=chalcopyrite, po=pyrrhotite, Au=electrum, Bu=bismuthinite, sp=sphalerite, qtz=quartz; black striations =polishing marks. Sample No. DDH R3024-3C at 137' (42m) on section 220mS.

Fig. 7.2C. Close-up of Fig.7.2B showing large electrum grain in association with chalcopyrite. Au=electrum, cp=chalcopyrite, po=pyrrhotite, sp=sphalerite, qtz=quartz; unlettered black striations=polishing marks. Sample No. DDH R3024-3C at 137' (42m) on section 220mS.

Fig. 7.2D. Native bismuth in pyrrhotite. po=pyrrhotite, Bi=bismuth, unlettered=quartz at upper right-hand corner, other black striations are polishing marks. Sample No. DDH R3023-8 at 146'(44.8m) on section 270mS.

Fig. 7.2E. Native bismuth and chalcopyrite in cracks in pyrite grains. cp=chalcopyrite, po=pyrrhotite, py=pyrite, Bi=bismuth, Bu=bismuthinite, sp=sphalerite, unlettered= polishing marks. Sample No. DDH R3034-7 at 100.5' (30.8m) on section 270mS.

Fig. 7.2F. Native bismuth in association with magnetite–pyrrhotite–pyrite–sphalerite and quartz. Bi=bismuth, mag=magnetite, po=pyrrhotite, py=pyrite, sp=sphalerite, qtz= quartz, unlettered=polishing marks. Sample No. DDH R3034-7 at 100.5' (30.8m) on section 270mS.

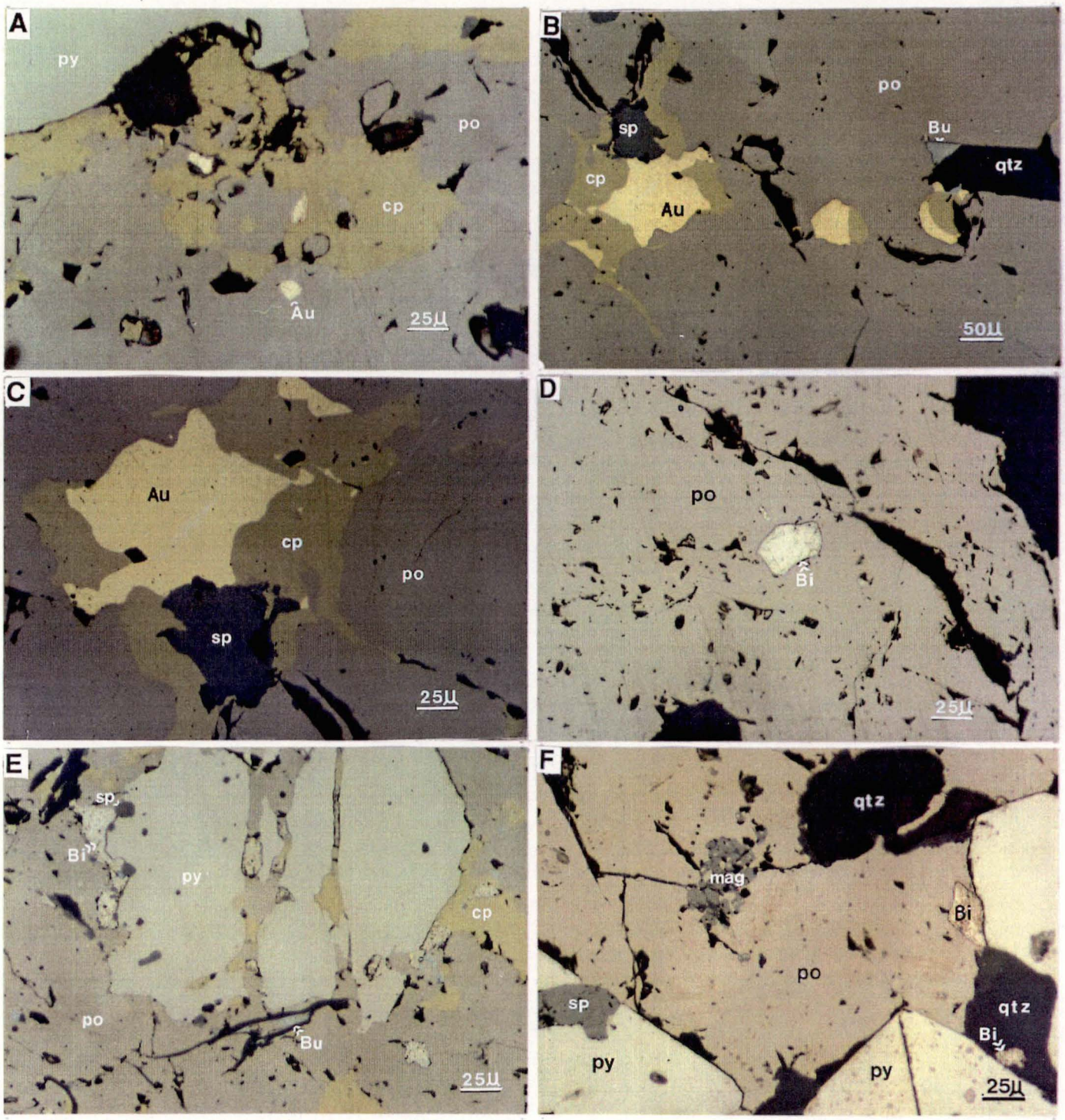
A
py
po
cp
Au
25μ
B
po
sp
Bu
qtz
cp
Au
50μ
C
Au
cp
po
sp
25μ
D
po
Bi
25μ
E
sp
Bi
py
cp
po
Bu
25μ
F
qtz
mag
Bi
po
sp
qtz
Bi
py
py
25μ

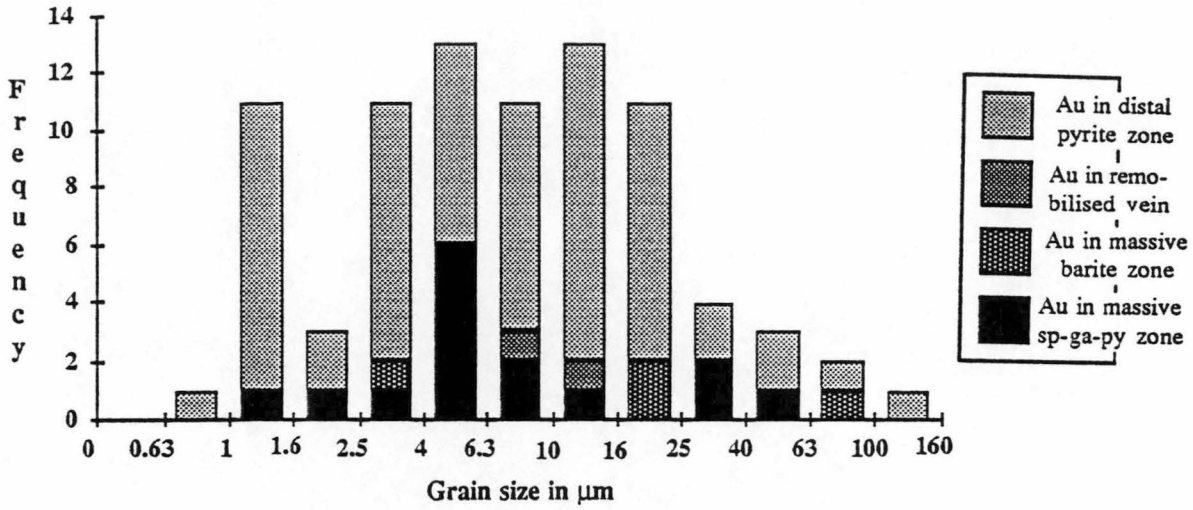


Fig. 7.3. Grain size distribution of electrum from the A and B lens, Rosebery north-end orebody, western Tasmania (after Huston and Large, 1988; Huston, 1989).

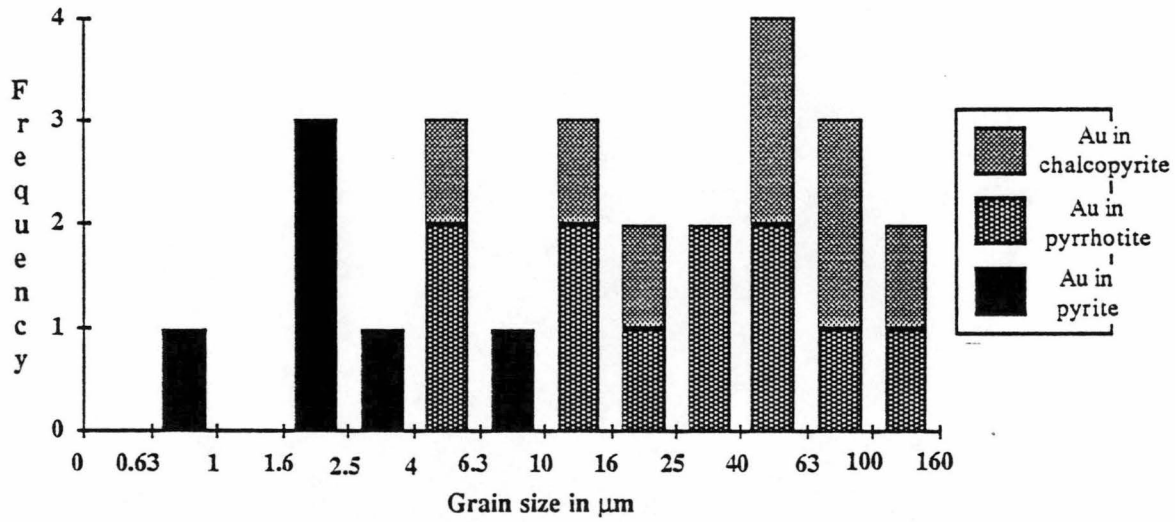


Fig. 7.4. Grain size distribution of electrum from the F(J) lens, Rosebery south-end orebody, western Tasmania.

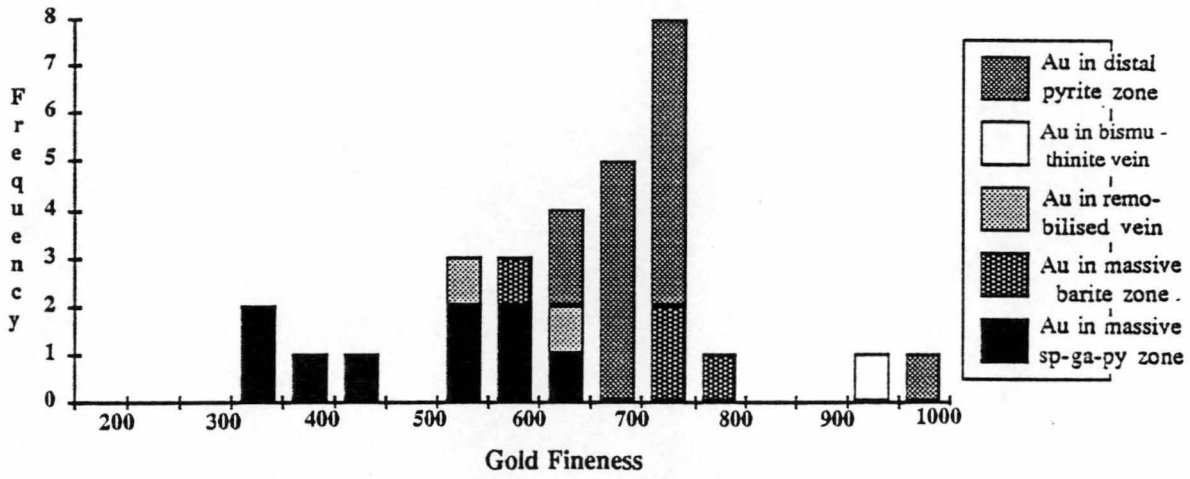


Fig. 7.5. Fineness of electrum from the Rosebery north-end orebody, western Tasmania (after Huston and Large, 1988; Huston, 1989).

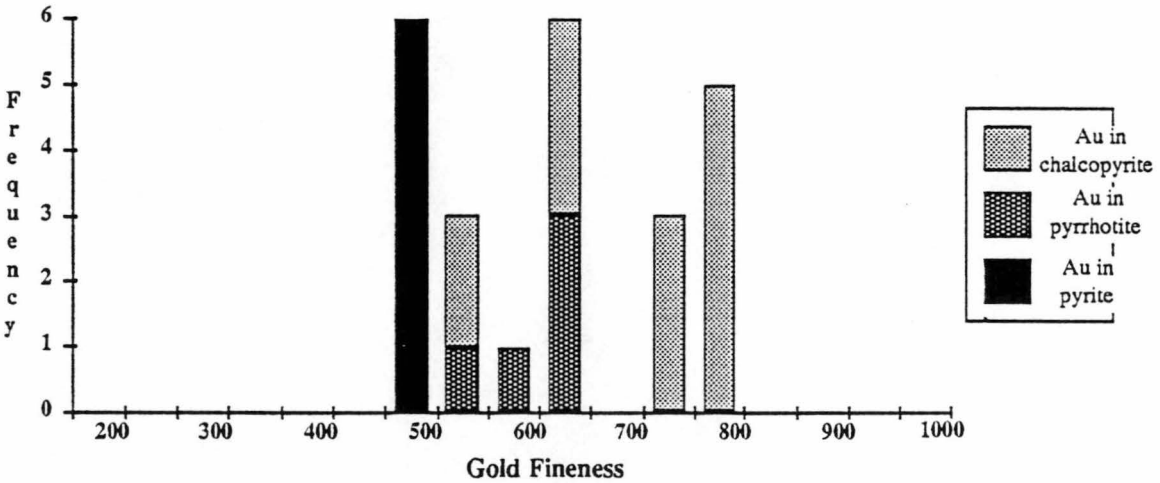


Fig. 7.6. Fineness of electrum from the F(J) lens, Rosebery south-end orebody, western Tasmania.

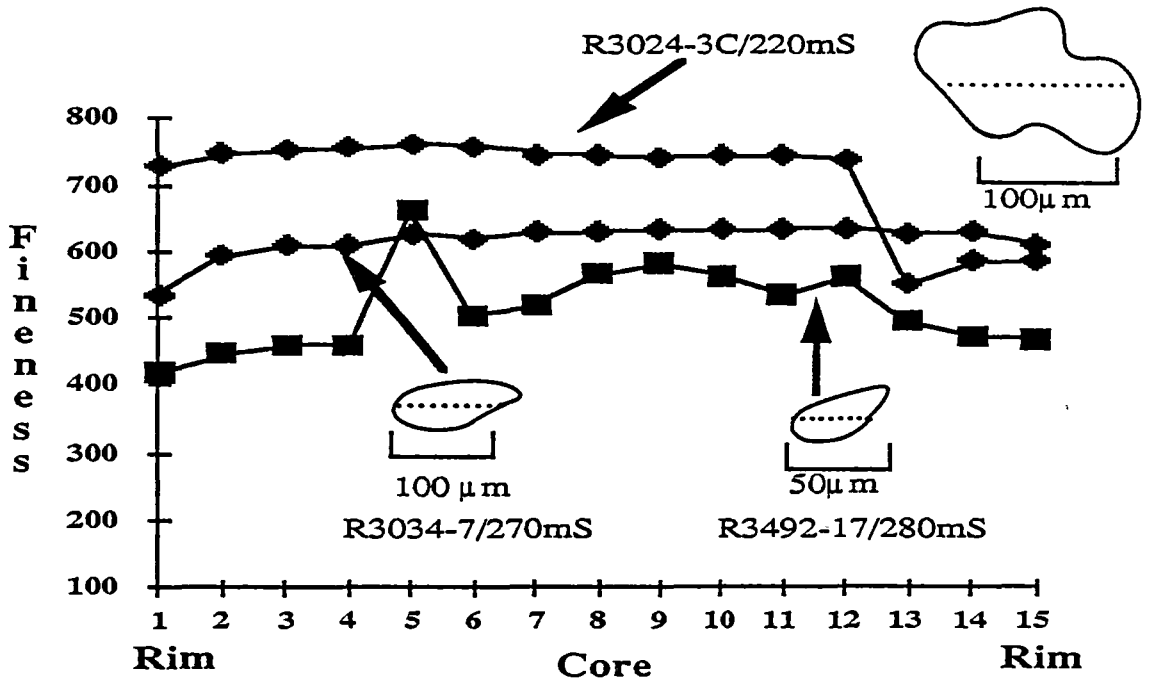


Fig. 7.7. Microprobe analyses across three gold grains in different samples collected from different E–W cross sections of the F(J) lens, Rosebery south-end orebody, western Tasmania. Note that fineness is high at the core and decrease towards the rim.

## 7.4. MINERALOGY OF GOLD AT SOUTH HERCULES–HERCULES ...

Mineragraphic investigations on the Au mineralogy of the South Hercules deposit indicate that gold occurs essentially as electrum in two major associations: (a) with pyrite and (b) with other sulphides such as sphalerite, galena and tetrahedrite. The following associations of electrum were recorded at the South Hercules deposit:

1. Individual electrum grains locked in pyrite (Figs. 7.8A, 7.8B and 7.8C)
2. Electrum with galena or chalcopyrite within recrystallised pyrite (Figs. 7.8D and 7.8E )
3. Electrum grains distributed in remobilised and recrystallised elongated sphalerite blebs;
   (a) as patches and minute blebs in the cracks of recrystallised sphalerite (Figs. 7.8F and 7.9A)
   (b) as individual coarse-grained electrum grains in recrystallised sphalerite (Figs. 7.9B and 7.9C) and
4. Electrum at the margin of or within tetrahedrite (Figs. 7.9D, 7.9E, 7.9F and 7.10A)

At South Hercules, the electrum grains locked in pyrite euhedra are fine-grained (Fig. 7.8A) and are sometimes associated with galena and sphalerite in the core of the pyrite euhedra (Fig. 7.8B). In places, electrum and galena appear to have been remobilised and recrystallised along the subgrain boundaries in the host pyrite crystal (Fig. 7.8C). Coarse, recrystallised electrum grains, are also noted in galena or chalcopyrite veins within massive pyrite (Figs. 7.8D and 7.8E).

Electrum in sphalerite also appears to have been remobilised and recrystallised with galena into cracks cutting the coarse sphalerite blebs (Figs. 7.8F and 7.9A). Coarse-grained, discrete, elongate to rounded electrum grains are also found in recrystallised sphalerite blebs and these electrum grains appear to have recrystallised along with the host sphalerite crystals (Figs. 7.9B and 7.9C). At the top of the South Hercules ore lens, electrum grains were observed in association with tetrahedrite. The electrum may occur within or at the margin of the host tetrahedrite (Figs. 7.9D, 7.9E, 7.9F and 7.10A). No gold grains were noted in association with barite, although barite is abundant at the upper part of the South Hercules ore zone.

The following gold associations are noted in the J(K)–P and R lenses of the Hercules mine;

1. Coarse electrum grains with galena in the core of the recrystallised pyrite
2. Coarse electrum grains associated with fluorite

At the Hercules mine where the massive sulphide lenses were affected by intense deformation, gold tends to occur as coarse grains up to 100 μm across (Sample No. H831-8 at 28.2m, 184.1mN) and commonly lies in the core of recrystallised pyrite grains with galena and sphalerite (Figs. 7.10B, 7.10C, 7.10D and 7.10E). It is also interesting to note that very coarse-grained, recrystallised gold flakes are found with fluorite at the Hercules mine (Fig. 7.10F).

Fig. 7.8A. Photomicrograph showing electrum locked in pyrite euhedra. Sample No. H1114-5 at 36.6m, 5630mN, South Hercules deposit, western Tasmania. Reflected light, Au=electrum, sp=sphalerite, py=pyrite, unlettered= gangue.

Fig. 7.8B. Photomicrograph showing electrum locked in pyrite euhedra together with galena and sphalerite. Sample No. H1129-2 at 79.8m, 5720mN, South Hercules deposit, western Tasmania. Reflected light, Au=electrum, ga=galena, sp=sphalerite, py=pyrite, unlettered=gangue.

Fig. 7.8C. Photomicrograph showing electrum together with galena along the subgrain boundaries of a pyrite grain. Sample No. H1114-5 at 36.6m, 5630mN, South Hercules deposit, western Tasmania. Reflected light, Au=electrum, ga=galena, py=pyrite, sp=sphalerite, unlettered=gangue.

Fig. 7.8D. Photomicrograph showing electrum in a network of remobilised galena veinlets in the cracks of recrystallised pyrite. Sample No. H1142-2 at 43.0m, 5600mN, South Hercules deposit, western Tasmania. Reflected light, Au=electrum, ga=galena, py-pyrite, unlettered=gangue.

Fig. 7.8E. Photomicrograph showing electrum with galena and chalcopyrite in a vein cutting recrystallised pyrite with galena and chalcopyrite. Sample No. H1148-2 at 89.4m, 5600mN, South Hercules deposit, western Tasmania. Reflected light, Au= electrum, ga=galena, cp=chalcopyrite, py=pyrite.

Fig. 7.8F. Photomicrograph showing patches and minute blebs of electrum grains with galena in light brown, recrystallised sphalerite. Sample No. H1118-13 at 29.9m, 5630mN, South Hercules deposit, western Tasmania. Reflected light, Au=electrum, ga=galena, sp=sphalerite.

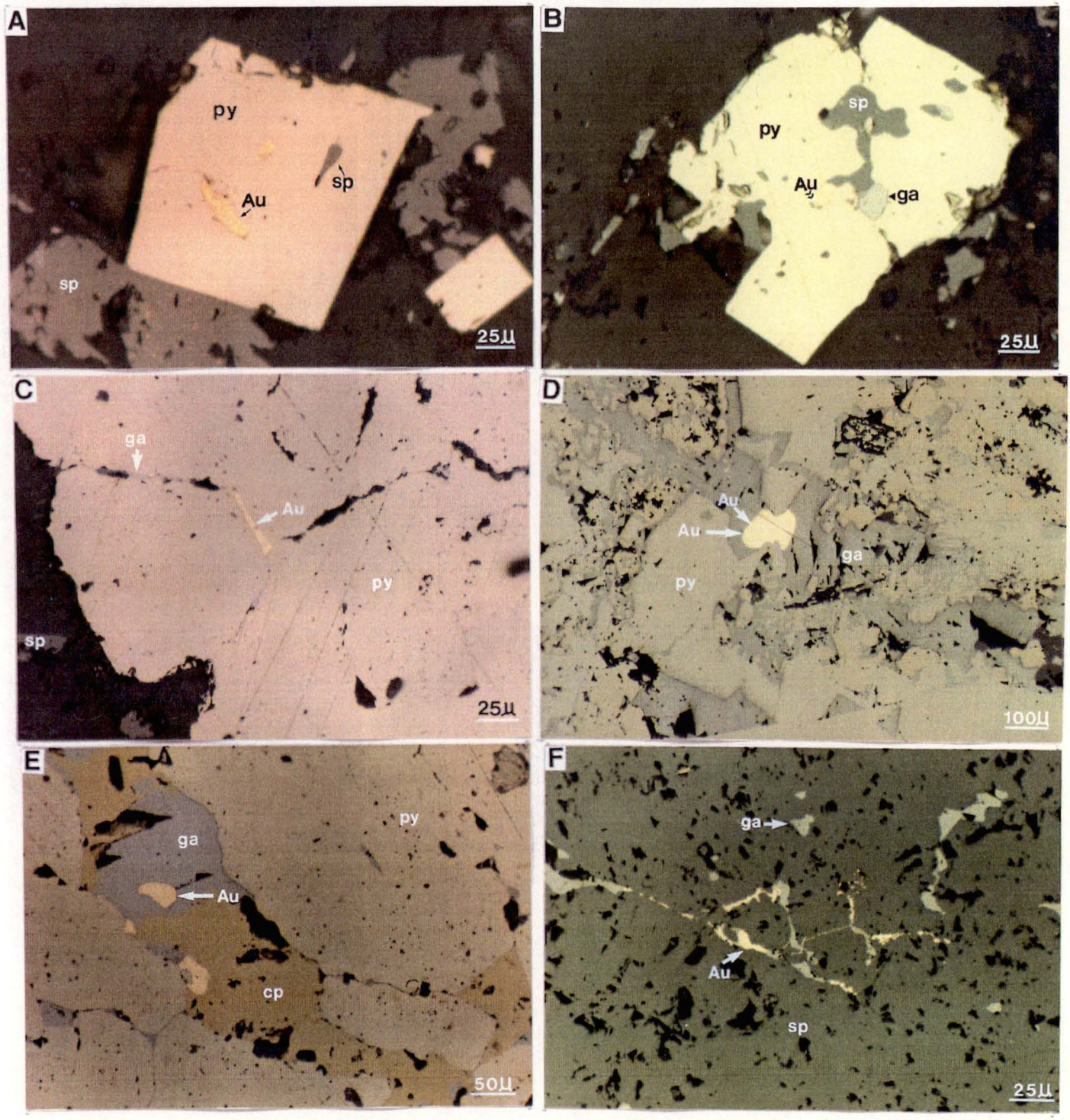
A
py
sp
Au
sp
25μ
B
sp
py
Au
ga
25μ
C
ga
Au
py
sp
25μ
D
Au
Au
ga
py
100μ
E
py
ga
Au
cp
50μ
F
ga
Au
sp
25μ

Fig. 7.9A. Photomicrograph showing patches and minute blebs of electrum grains in light brown, recrystallised sphalerite. Sample No. H1118-13 at 29.9m, 5630mN, South Hercules deposit, western Tasmania. Reflected light, Au = electrum, ga = galena, sp=sphalerite.

Fig. 7.9B. Photomicrograph showing an individual, discrete electrum grain in light brown, recrystallised sphalerite. Sample No. H1118-13 at 29.9m, 5630mN, South Hercules deposit, western Tasmania. Reflected light, Au=electrum, ga=galena, sp=sphalerite.

Fig. 7.9C. Photomicrograph showing the same view as in Fig. 7.9B but under plane polarised light (PPL); individual, discrete electrum grain in light brown, recrystallised sphalerite. Sample No. H1118-13 at 29.9m, 5630mN, South Hercules deposit, western Tasmania. Au=electrum, ga=galena, sp=sphalerite.

Fig. 7.9D. Photomicrograph showing patches and minute blebs of electrum grains in tetrahedrite. Sample No. H1142-4 at 45.5m, 5600mN, South Hercules deposit, western Tasmania. Reflected light, Au=electrum, tt=tetrahedrite, sp=sphalerite.

Fig. 7.9E. Photomicrograph showing discrete electrum grain in tetrahedrite. Sample No. H1142-4 at 45.5m, 5600mN, South Hercules deposit, western Tasmania. Reflected light, Au=electrum, tt=tetrahedrite, sp=sphalerite, unlettered=gangue.

Fig. 7.9F. Photomicrograph showing electrum grain along the grain boundaries of tetrahedrite and sphalerite. Sample No. H1142-4 at 45.5m, 5600mN, South Hercules deposit, western Tasmania. Reflected light, Au=electrum, tt=tetrahedrite, sp=sphalerite.

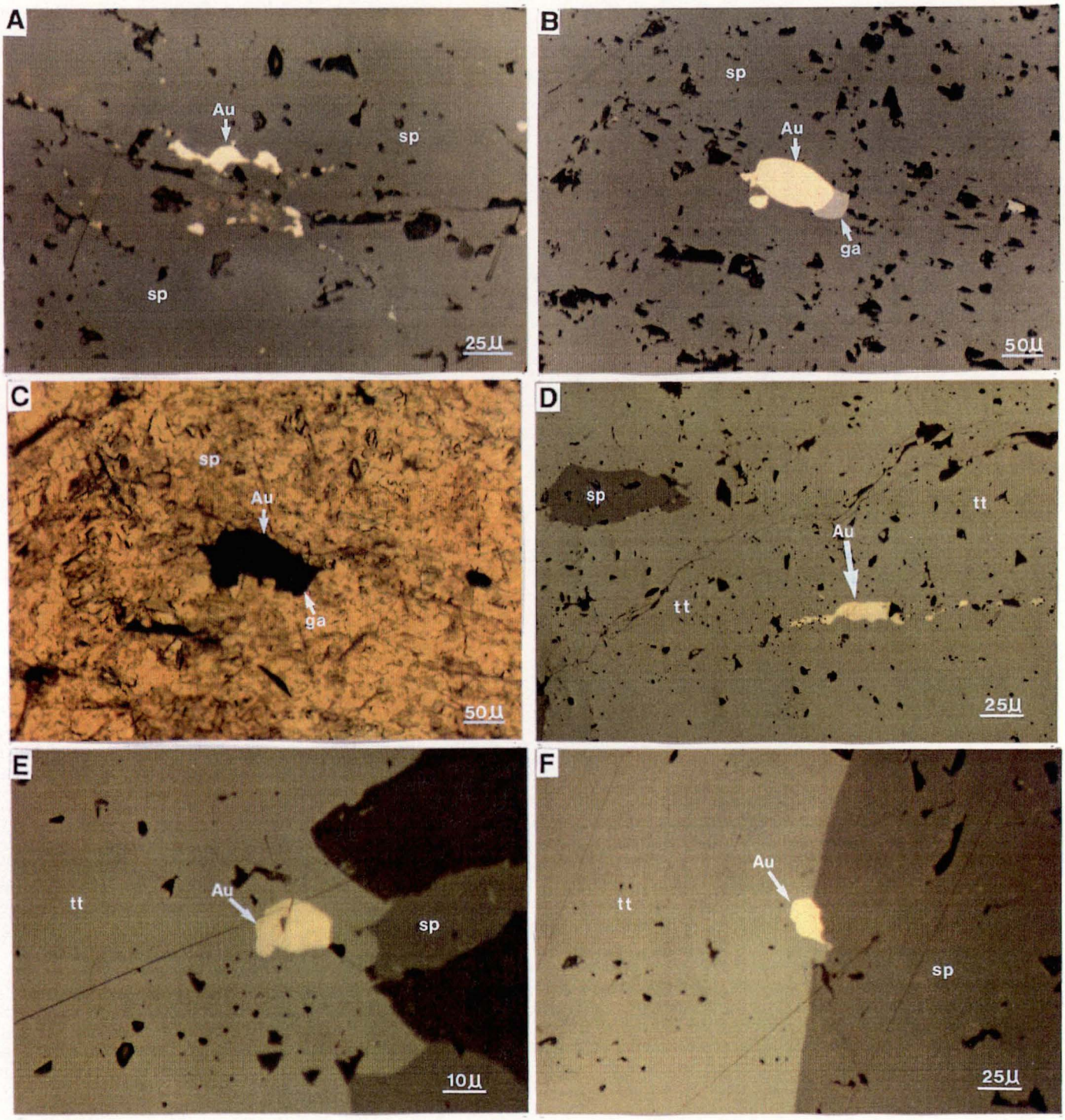
A
Au
sp
sp
25μ
B
sp
Au
ga
50μ
C
sp
Au
ga
50μ
D
sp
tt
Au
tt
25μ
E
tt
Au
sp
10μ
F
Au
tt
sp
25μ

Fig. 7.10A. Photomicrograph showing electrum with bournonite at the margin of tetrahedrite. Sample No. H1145-2B at 61.3m, 5670mN, South Hercules deposit, Tasmania. Reflected light, Au=electrum, bo=bournonite, tt=tetrahedrite, unlettered=gangue.

Fig. 7.10B. Photomicrograph showing electrum associated with galena enclosed in the core of recrystallised pyrite grains. Sample No. H145-2 at 287' (84.8m), 800' (243.8mN), R lens, Hercules mine, western Tasmania. Reflected light, Au= electrum, ga=galena, cp=chalcopyrite, py=pyrite.

Fig. 7.10C. Photomicrograph showing electrum with galena, sphalerite and chalcopyrite in a vein cutting recrystallised pyrite. Sample No. H831-8 at 92' (28.2m), 600' (184.1mN), Hercules mine, western Tasmania. Reflected light, Au=electrum, ga=galena, sp=sphalerite, cp=chalcopyrite.

Fig. 7.10D. Photomicrograph showing electrum with galena and sphalerite. Sample No. H831-8 at 92' (28.2m), 600' (184.05mN), Hercules mine, western Tasmania. Reflected light, Au=electrum, ga=galena, py=pyrite, sp=sphalerite.

Fig. 7.10E. Photomicrograph showing electrum associated with galena enclosed in the core of a recrystallised pyrite grain. Sample No. H145-1 at 227' (69.6m), 800' (243.84mN), R lens, Hercules mine, western Tasmania. Reflected light, Au=electrum, ga=galena, cp=chalcopyrite py=pyrite, unlettered=gangue.

Fig. 7.10F. Flakes of electrum (Au) associated with fluorite, Hercules mine, western Tasmania. Locality P lens. Sample provided by Mr. Geoff Iliff.

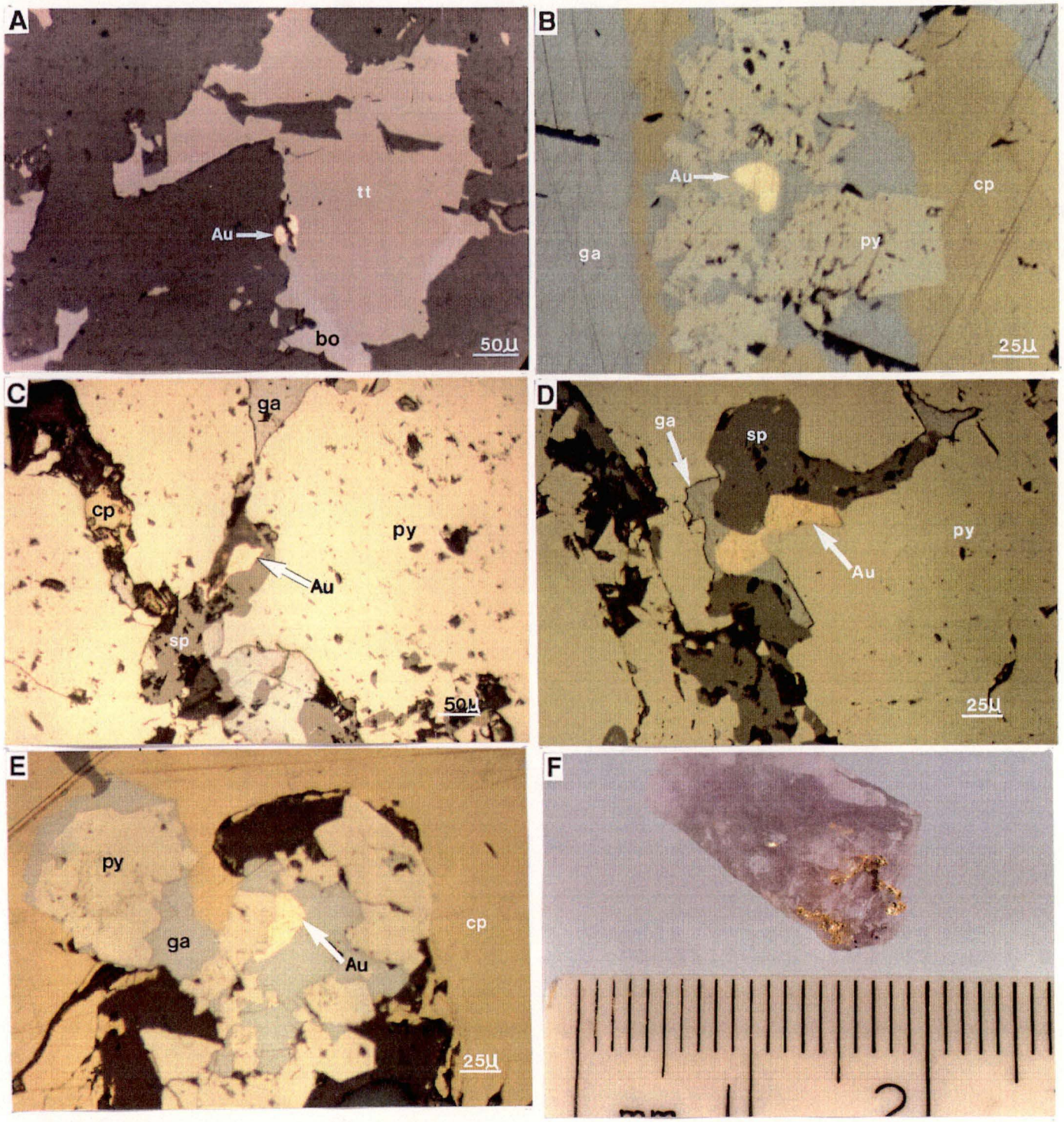
A
tt
Au
bo
50μ
B
Au
cp
ga
py
25μ
C
ga
cp
py
Au
sp
50μ
D
ga
sp
py
Au
25μ
E
py
ga
cp
Au
25μ
F
mm
1
2

### 7.4.1 Grain size distribution of electrum at South Hercules–Hercules ...

The size of the observed electrum grains from the South Hercules deposit are listed in Appendix 7.3. Figure 7.11 is a histogram that shows the grain size distribution of electrum according to mineralogical association. Overall the electrum grains from South Hercules range in size from 4 μm to 210 μm (Fig. 7.11). The electrum grains in the cracks of the light brown, recrystallised, blebby sphalerite patches gave a finer grain size range from 3.3 μm to 37.5 μm, whereas the individual, isolated electrum grains in these remobilised and recrystallised sphalerite patches are coarser in grain size, up to 210 μm across. The few electrum grains found in the R lens of the main Hercules Mine display uniformly coarse grain size (30 μm–75 μm) and the gold flakes associated with fluorite are as coarse as 5 mm across.

### 7.4.2 Fineness of electrum grains at South Hercules–Hercules ...

Microprobe data for the gold grains from the South Hercules and Hercules deposits are listed in Appendices 7.3 and 7.4. The fineness for all samples from the South Hercules deposit ranges from 428 to 966. The fineness of the electrum grains in the pyrite euhedra ranges from 600 to 950, whereas the fineness of electrum associated with the other sulphides (galena, sphalerite, tetrahedrite) ranges fromf 450 to 900 (Fig. 7.12).

The fineness distribution of the few electrum grains found in the R lens of the main Hercules mine displays a restricted range of 565–620, whereas the gold grains associated with recrystallised flourite have higher fineness of 875. Variation of fineness values across individual electrum grains from the South Hercules and Hercules deposits was also checked by the JEOL microprobe. No significant variation in fineness was recorded.

### 7.4.3 Variation of fineness vs. grain size at South Hercules ...

The plot of the fineness vs. grain size of all electrum grains measured from the South Hercules deposit is shown in Fig. 7.13. It shows two distinct groups, one for the electrum locked in the pyrite and the other for electrum in the other sulphides. A more detailed pattern for the electrum from South Hercules associated with sulphides other than pyrite is shown in Fig. 7.14.

Discrete Au grains in the blebby sphalerite patches show a wide range in grain size (7.5–180 μm) and fineness (400–800), whereas the other electrum in the cracks of the recrystallised sphalerite and galena or those electrum grains associated with tetrahedrite exhibit low fineness values (<650) and a finer, restricted, grain size range (5–80μm) (Fig. 7.14).

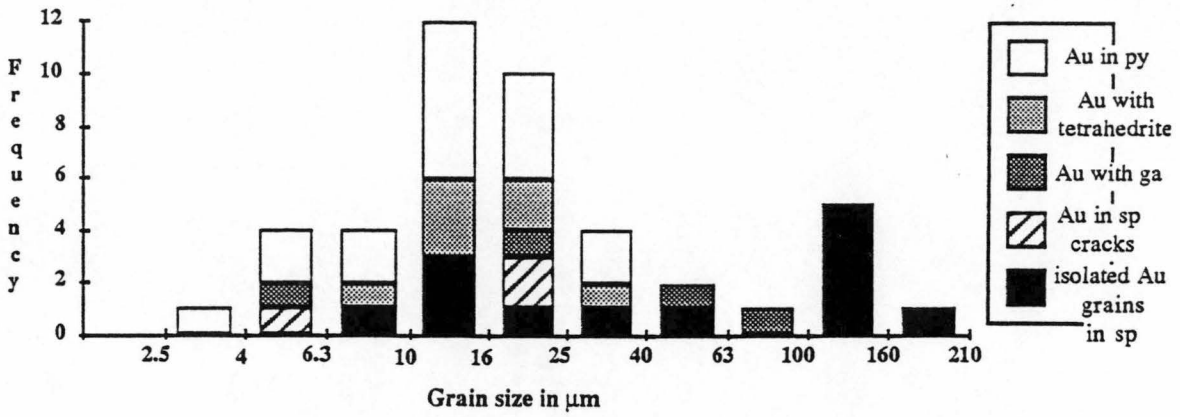


Fig. 7.11. Grain size distribution of electrum from the South Hercules deposit, western Tasmania. sp=sphalerite, ga=galena and py=pyrite.

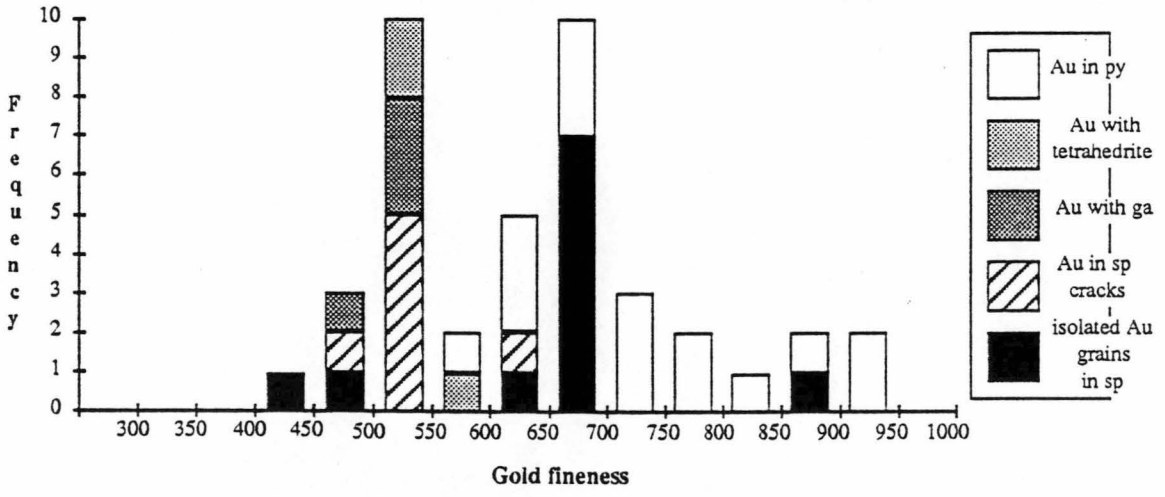


Fig. 7.12. Fineness of electrum grains from the South Hercules deposit, western Tasmania. sp=sphalerite, ga=galena and py=pyrite.

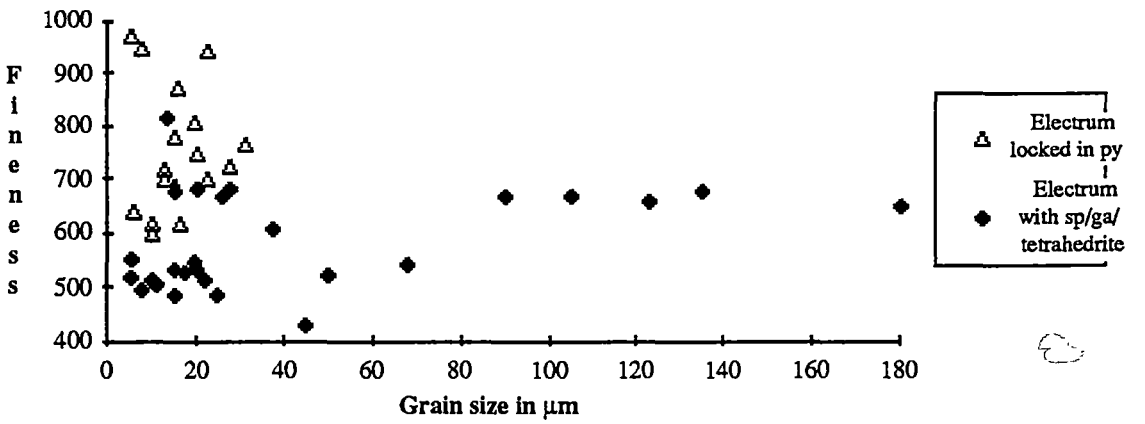


Fig. 7.13. Plot of fineness vs. grain size of electrum for all grains measured from the South Hercules deposit, western Tasmania. sp=sphalerite, ga=galena and py=pyrite.

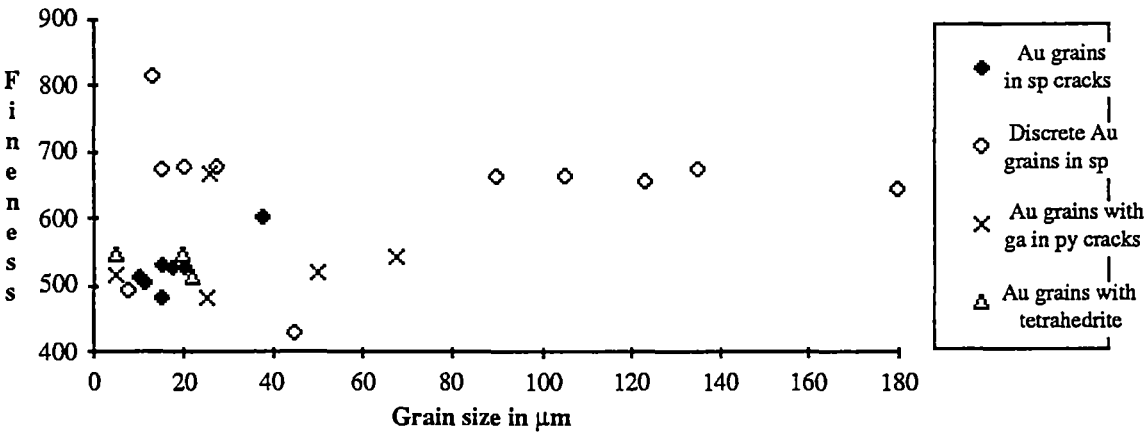


Fig. 7.14. Plot of fineness vs. grain size of electrum associated with different sulphides (galena, tetrahedrite and sphalerite) from the South Hercules deposit, western Tasmania. sp=sphalerite, ga=galena and py=pyrite.

## 7.5 REMOBILISATION AND RECRYSTALLISATION OF THE ELECTRUM ...

Conclusions concerning the origin, grain size and fineness of electrum in the three ore deposits are limited by the number of electrum grains discovered in over one hundred samples investigated. For this reason the conclusions discussed below are regarded as preliminary, and future observations of the electrum will be required before definitive conclusions can be drawn. The electrum grains in the Rosebery, Hercules and South Hercules deposits have been affected by the Devonian Tabberabberan Orogeny along with the associated sulphide minerals and the host rocks. The Devonian metamorphism and metasomatism has resulted in significant remobilisation and recrystallisation of the gold grains as indicated by (1) texture, (2) grain size, (3) fineness variation and (4) zoning.

(1) *Texture:* The fine-grained electrum (<10 μm) which occurs as inclusions in pyrite in the Rosebery north-end is interpreted to be of primary exhalative origin (Huston and Large, 1988; Huston, 1989). Similar minute electrum grains locked in pyrite are also noted in the F(J) lens of the Rosebery south-end orebody. In the F(J) lens, electrum is also associated with pyrrhotite veinlets cutting euhedral pyrite grains (Fig. 7.1D) and electrum grains commonly occur in chalcopyrite veins that cut massive pyrrhotite bodies (Fig. 7.1F). The presence of this gold in late veinlets suggests that gold was remobilised from the pyrite grains and re-precipitated in the pyrrhotite and chalcopyrite veinlets during Devonian metasomatic processes. Such remobilised gold grains attained a size up to 150 μm x 100 μm across during recrystallisation (Fig. 7.1E). The predominance of coarse electrum in the pyrrhotite zones also suggests the potential for high metallurgical recoveries of gold from this ore type.

Similarly electrum from South Hercules appears to have been remobilised to the subgrain boundaries in the host pyrite crystals (Fig. 7.8C). Where remobilisation and recrystallisation has proceeded, coarse, recrystallised electrum grains occur in galena or chalcopyrite veins within massive pyrite (Figs. 7.8D and 7.8E). Electrum in sphalerite at South Hercules also appears to have been remobilised and recrystallised, along with galena, into cracks within the coarse sphalerite blebs (Figs. 7.8F and 7.9A). Coarse-grained electrum grains are also found in recrystallised sphalerite blebs (Figs. 7.9B and 7.9C) or at the grain boundaries of the host tetrahedrite and sphalerite (Fig. 7.9F) and these electrum grains appear to have recrystallised along with the host sphalerite crystals.

(2) *Grain size:* The grain size distribution of gold at Rosebery indicates a mode of 4–25 μm for the north-end where the primary syngenetic gold association is dominant, whereas a bimodal distribution (one mode at around 4–6.3 μm and the other mode at around 16–63 μm) is observed in the F(J) lens of the south-end where remobilised and recrystallised electrum is

abundant (Fig. 7.15). The bimodal distribution suggests that the electrum in the F(J) lens has been remobilised and recrystallised to a coarser grain size during the Devonian replacement process.

Similarly at South Hercules, the fine-grained electrum of Cambrian, exhalative origin appears to have been remobilised and recrystallised as coarser electrum grains during Devonian recrystallisation. The grain size distribution of the electrum associated with sulphides other than pyrite displays a bimodal distribution with modes at 10–25 μm and 160 μm (Fig. 7.16).

Based on this initial data set it is concluded that the bimodal distribution at South Hercules also suggests that the electrum grains have suffered post-depositional changes possibly related to the Devonian deformation and recrystallisation. Electrum appears to have moved and migrated, together with easily deformed minerals such as galena, to the grain boundaries or fractures in the host pyrite grains, where the strain rate is low, and later electrum recrystallised as coarser grains. The coarser electrum grains at South Hercules–Hercules should be relatively easily recovered by standard metallurgical techniques although the electrum locked in the pyrite euhedra at South Hercules are finer in grain size (<5 μm to 40 μm) and metallurgical recovery will probably be low.

(3) *Fineness:* In view of the fineness of gold grains in terms of Cambrian versus Devonian processes, the north-end of the Rosebery deposit where the primary syngenetic gold association is dominant, displays fineness values of 300–1000, whereas the recrystallised association of Devonian origin in the south-end yields a fineness range of 500–800 (Fig.7.17). This fineness variation suggests that the electrum grains have possibly become homogenised during the Devonian metasomatic process. However the data set is too limited to be confident of the interpretation.

The electrum grains from South Hercules show a decrease in silver content possibly associated with the Devonian recrystallisation. The fineness of electrum locked in pyrite which has not been affected by the deformation have values between 600 and 950, whereas the gold associated with the other ductile sulphides (galena, sphalerite, and tetrahedrite) displays a lower fineness range from 450 to 900 (Fig. 7.18).

(4) *Zoning:* Huston (1989) noted gold grains with silver-rich rims in the Rosebery north-end. Gemmell (pers. comm., 1990) noted silver-rich rims at Hellyer, and Shimazaki (1974) also reported silver-rich rims from the Kuroko deposits of Japan. These Ag-rich rims are interpreted to be a primary feature and can be formed by a decrease in temperature or an increase in pH of the ore fluids during deposition of gold by the exhalative process (Huston et al., 1991 in prep.).

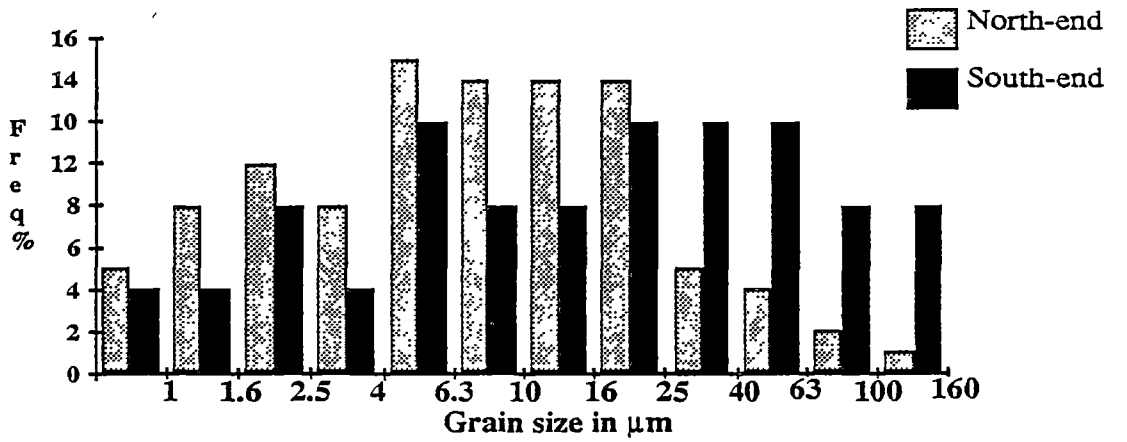


Fig. 7.15. Grain size distribution of electrum from the north- and south-end of the Rosebery deposit, western Tasmania (north-end data are from Huston and Large, 1988).

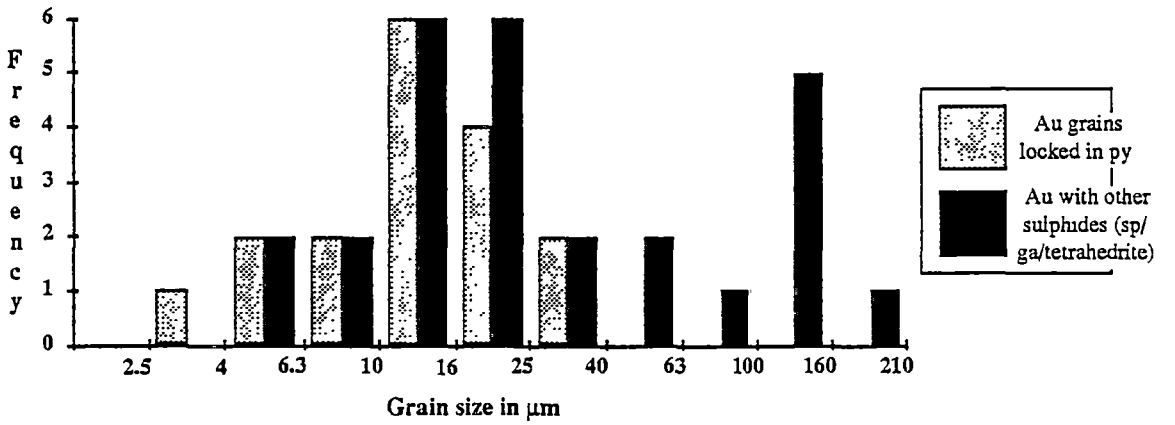


Fig. 7.16. Grain size distribution of electrum from the South Hercules deposit, western Tasmania. py=pyrite, sp=sphalerite and ga=galena.

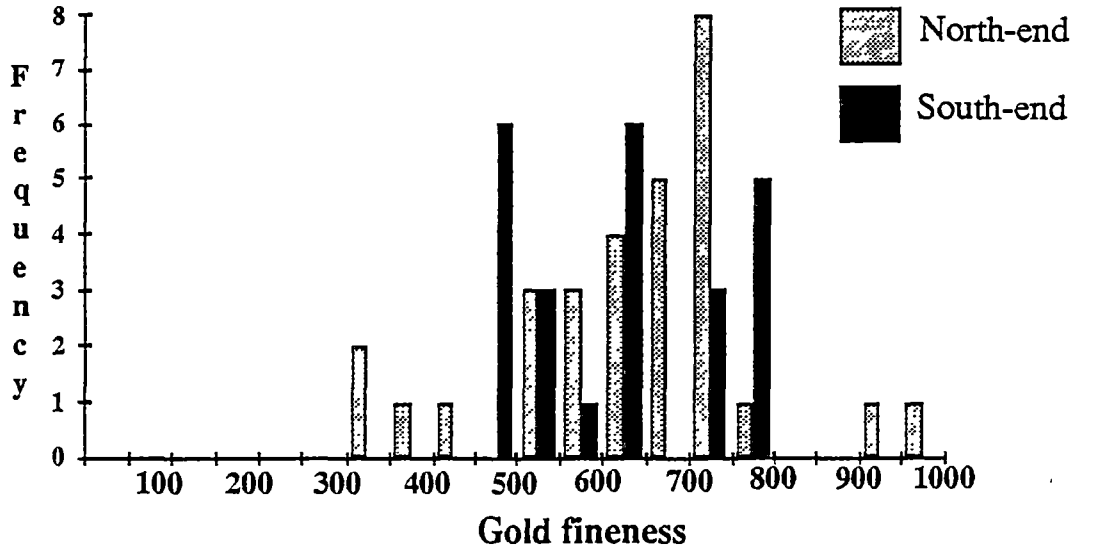


Fig. 7.17. Fineness variation of electrum from the Rosebery deposit, western Tasmania.

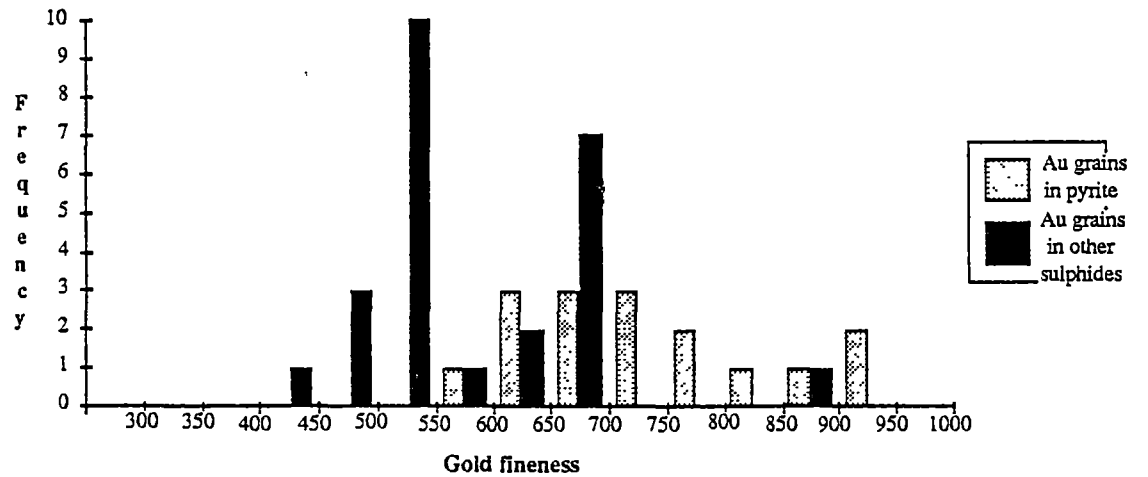


Fig. 7.18. Fineness of electrum from the South Hercules deposit, western Tasmania.

This study has shown that the electrum grains from the F(J) lens also have a distinct silver-rich rim. In contrast to the interpretation by Huston et al. (1991 in prep.), the zoning of electrum (Au) grains in the F(J) lens (Ag is enriched at the rim and Au is concentrated towards the core zones) is herein interpreted to be a secondary feature related to recrystallisation during the Devonian metasomatic process. The coarse-grained texture of these gold grains and associated tourmaline–garnet–helvite–biotite replacement assemblages in the F(J) lens support this interpretation. Particularly, Ag in the electrum grains appears to have diffused out to the rim during the high temperature (≥330°C) metasomatic event.

However, zoning of electrum grains is not observed at the South Hercules–Hercules deposits. Although these deposits have suffered Devonian metamorphic recrystallisation at low temperature (>250°C), the lack of zoning in the electrum grains is consistent with the absence of extensive, high temperature overprinting by Devonian granitoid-related fluids. During the low grade metamorphic process, the temperature was probably not high enough to cause the diffusion of Au and Ag to produce zoning patterns in the electrum grains although the overall grain size of the electrum grains in the South Hercules deposit has increased during the Devonian recrystallisation.

## 7.6 Hg CONTENT IN THE GOLD GRAINS ...

The mercury content of electrum from the South Hercules–Hercules deposits was determined by both JEOL and CAMECA microprobes and the results for South Hercules are shown in Fig. 7.19. The Hg content in the electrum locked in the pyrite euhedra ranges from less than the detection limit (~1.5 wt % Hg) to 18.2 wt %, whereas the electrum associated with other sulphides gave a range of 6.3–21.8 wt % Hg (Fig. 7.19).

The validity of the Hg analyses as determined by the JEOL microprobe with an energy-dispersive mode were also checked by the more accurate wavelength dispersive CAMECA microprobe. Detailed CAMECA probe analytical data are listed in Appendix 7.4. A comparison of the JEOL and CAMECA analyses for selected, individual electrum grains from the South Hercules deposit is shown in Table 7.1.

The comparison for individual electrum grains in each sample indicates that the JEOL microprobe analysis generally gave lower Au–Ag contents and higher Hg content than that of the CAMECA probe analysis. The difference is within 0.1–2.0 wt % for Au–Ag and 1.1–3.2 wt % for the Hg contents. The compositional variation for a group of electrum grains determined by the JEOL microprobe for different samples was also checked by the CAMECA probe to obtain the within-sample variation and the comparison is shown in Table 7.2. The comparisons show that within-sample variations of Au, Ag and Hg contents of electrum

(Table 7.2) are marginally higher than the variation in individual electrum grains (Table 7.1). This is due to differences in the number of grains and spots analysed for each sample by the different probe methods particularly for the within-sample variation analysis. As there is no substantial difference in Au, Ag and Hg contents determined by JEOL and CAMECA analyses, CAMECA probe analysis verified the presence of appreciable Hg in the electrum from the South Hercules deposit.

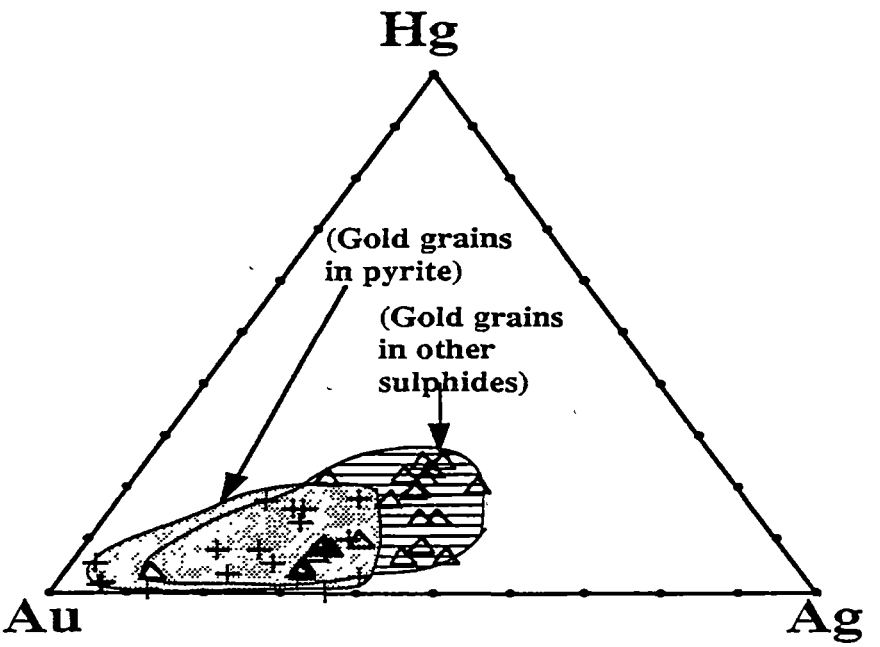


Fig. 7.19. Plot of Au–Ag–Hg composition (wt %) of electrum grains from the South Hercules deposit, western Tasmania. Crosses represent electrum locked in pyrites and triangles those electrum grains associated with other sulphides (galena, tetrahedrite and sphalerite).

Table 7.1 Comparison of JEOL and CAMECA microprobe analyses of individual electrum grains in different samples from the South Hercules deposit, western Tasmania.

| Sample No./ section | Type of microprobe | No. grains | No. spots | Au wt% | Ag wt% | Hg wt% | Total wt% | Gold occurrence |
|---|---|---|---|---|---|---|---|---|
| H1142-2 | JEOL | 1 | 12 | 44.4 | 40.8 | 13.8 | 99.0 | with galena |
| (5600mN) | CAMECA | 1 | 5 | 46.2 | 40.9 | 12.0 | 99.2 | with galena |
| H1148-2 | JEOL | 1 | 3 | 50.7 | 42.9 | 6.7 | 100.3 | with galena |
| (5600mN) | CAMECA | 1 | 4 | 51.2 | 43.3 | 5.6 | 100.2 | with galena |
| H1145-2B | JEOL | 1 | 2 | 38.6 | 36.3 | 24.6 | 99.5 | with tetrahedrite |
| (5670mN) | CAMECA | 1 | 3 | 40.6 | 38.0 | 21.4 | 99.9 | with tetrahedrite |
| H1129-2 | JEOL | 1 | 2 | 65.3 | 30.2 | 2.8 | 98.3 | in pyrite |
| (5720mN) | CAMECA | 1 | 5 | 65.6 | 32.0 | 1.0 | 98.6 | in pyrite |

Table 7.2 Comparison of JEOL and CAMECA microprobe analyses for groups of electrum grains in individual samples from the South Hercules deposit, western Tasmania.

| Sample No./ section | Type of microprobe | No. grains | No. spots | Au wt% | Ag wt% | Hg wt% | Total wt% | Gold occurrence |
|---|---|---|---|---|---|---|---|---|
| H1148-2 | JEOL | 3 | 13 | 47.4 | 44.9 | 7.2 | 99.5 | with galena |
| 5600mN | CAMECA | 3 | 8 | 49.3 | 44.2 | 5.7 | 99.2 | with galena |
| H1114-4 | JEOL | 5 | 21 | 69.9 | 19.3 | 9.9 | 99.2 | in pyrite |
| 5600mN | CAMECA | 3 | 10 | 70.2 | 18.8 | 10.3 | 99.4 | in pyrite |
| H1118-13 | JEOL | 18 | 50 | 52.2 | 33.5 | 13.4 | 99.2 | in sphalerite |
| 5630mN | CAMECA | 11 | 20 | 54.8 | 32.6 | 12.2 | 99.6 | in sphalerite |
| H1145-2B | JEOL | 3 | 9 | 42.8 | 35.9 | 21.8 | 100.5 | with tetrahedrite |
| 5670mN | CAMECA | 3 | 9 | 38.8 | 38.9 | 22.5 | 100.2 | with tetrahedrite |

### 7.6.1 Implication of the high Hg content in gold grains ...

Although mercury can be incorporated in sulphide minerals (e.g. pyrite, chalcopyrite and sphalerite) as well as in the sulphosalts, tellurides and electrum, very little attention has been given to Hg distribution in electrum from volcanogenic massive sulphide deposits. Ozerova et al. (1975) analysed the Hg content of sulphide ores and individual sphalerite, pyrite and chalcopyrite minerals from the massive sulphide deposits of the Urals, USSR and Kuroko-type deposits of Japan (e.g. Furutobe, Uchinotai and Hanaoka).

Ozerova et al. (1975) indicated that these deposits have varying Hg contents, and that metamorphosed massive sulphide deposits contain lower Hg concentrations than the unmetamorphosed ores, due to vapourisation and loss of Hg during metamorphism. However, some sulphide deposits in high grade metamorphic terrains contain high Hg contents (e.g. Sears, 1971; Jonasson and Sangster, 1975; Ryall, 1979a, 1981) which contradicts the interpretation of Ozerova et al. (1975).

Although the efficacy of the use of the Hg content in the ores, or in the individual sulphide minerals, as an indicator of the degree of metamorphism is not yet resolved, the Hg content in electrum was investigated in this study to apply the Hg distribution as a geochemical tool to deduce the post-depositional history of the sulphide ores. The higher concentration of Hg in the unmetamorphosed or less metamorphosed deposits can also provide the possibility of extraction of Hg from these deposits.

Ozerova et al. (1975) reported that Hg is selectively partitioned into sulphide minerals in the order of sphalerite>chalcopyrite>pyrite and that Zn and Hg contents in the sulphide ores have a positive correlation. A similar correlation was also observed for Canadian massive sulphide deposits (Sears, 1971). The abundance of Hg in massive sulphide deposits has led to the use of Hg as a pathfinder element in geochemical mineral exploration surveys (e.g. Gustavson, 1976; Strauss et al., 1977; Wu and Mahaffey, 1978; Ryall, 1979b; and Carr et al., 1986). On the basis of a Hg dispersion study on the Woodlawn massive sulphide deposit, NSW, Ryall (1979b) suggested the possible use of Hg as a pathfinder element for the exploration of massive sulphides deposits.

A high Hg content (10.0 wt %) in gold grains was noted from the volcanogenic mercury-rich sulphide deposit at Langsele, Skellefte district, northern Sweden (Nysten, 1986) and up to 8.5 wt % Hg in gold grains was also reported from the Tsugu gold–antimony vein deposit in Japan (Shikazono and Shimizu, 1988). Variation in Au, Ag, Hg and a range of other elements were studied in the gold grains from the Witwatersrand gold deposits by Hallbauer and Von Gehlen (1983), Hallbauer (1986), Oberthur and Saager (1986), Erasmus et al. (1987), and Reid et al. (1988). They reported 1.0–5.0 wt % Hg in gold grains. The presence of these

levels of Hg in the gold grains was attributed to the fact that the temperature during metamorphism of the Witwatersrand basin had not reached the level at which Hg is released from the gold grains.

Erasmus et al. (1982) heated gold particles from the Witwatersrand basin in a closed microscope heating stage, purged with argon gas, and monitored the release of Hg with a Hg detector. Mercury was found to liberate between 350°C and 420°C (Erasmus et al., 1982; Hallbauer, 1986). The results suggest that temperatures during the metamorphic stage of the Witwatersrand basin had been below this temperature range.

The presence of a significant Hg content in the electrum grains from the South Hercules deposit suggest that although the sulphide ores have been affected by Devonian metamorphic recrystallisation, the temperature of Devonian metamorphism did not reach the level at which Hg would have been released from the electrum grains (350–420°C). This interpretation is consistent with the fluid inclusion data (see later). Both primary and secondary inclusions in different minerals from the South Hercules deposit give an homogenisation temperature >250°C. The filling temperatures of the $CO_2$-bearing Type II inclusions which are related to the Devonian metamorphism never exceed 300°C.

Garrett (1989) recently used the proton induced X-ray emission (PIXE) microprobe to analyse Au, Ag, Hg and a variety of other trace elements contents in native gold grains from alluvial prospects throughout Elliott Bay, selected electrum grains from the Rosebery and Que River Mines, western Tasmania, and electrum grains from the Warrego Cu–Au deposit, Northern Territory. The Hg content in the gold grains from the Elliott Bay alluvial prospects ranges from 0.3 wt % to 0.5 wt %. This is comparable with recent studies on detrital gold grains from the Witwatersrand basin although a higher Hg content (1.0–5.0 wt %) was noted in the primary Witwatersrand gold grains. The gold grains from the Warrego Cu–Au deposit gave 0.2–0.4 wt %.

Hg in the three electrum grains from the Rosebery mine, one from the north-end (A and B lens) and two from the south-end (F-J lens), was analysed by Garrett (1989). The electrum in Sample R3397-1 from the north-end gave 0.5 wt % Hg while electrum in Samples R3024-3C and R3034-7 from the south-end yielded 0.3–0.5 wt % Hg. The electrum grain from the Que River mine had 0.9 wt % Hg. In contrast, the Hg content of the electrum grains from the South Hercules deposit gave a distinctly higher range of <1.5 to 21.8 wt % Hg although gold grains in the R lens of the main Hercules ore lenses contain 0.1–1.1 wt % Hg.

The difference in the Hg content in electrum between the South Hercules deposit and the Rosebery and Que River deposits can be attributed to (1) variation of Hg concentration in the original ore-bearing fluids and (2) the partitioning of Hg in different minerals and several other

physico-chemical factors such as temperature and pH etc. at the time of gold deposition and (3) the temperature reached during Devonian metamorphic and metasomatic recrystallisation.

The data in Table 7.3 show no relationship between the temperature of metamorphism and the Hg content of the orebody electrum. It therefore seems probable that the enrichment of Hg in the South Hercules electrum is related to the primary chemistry of the Cambrian ore fluid rather than later metamorphic or metasomatic effects. It is noteworthy that a Hg soil anomaly has been previously reported over the South Hercules deposit (Throop, 1974), and the possibility of using Hg contents in soil as a geochemical tool in the area should be further investigated.

Table 7.3 Hg content of electrum grains together with related metamorphic facies and fluid inclusion homogenisation temperature for some VMS deposits in western Tasmania.

| Deposit Name | Hg content of electrum | Metamorphic Facies | Fluid inclusion homogenisation temperature |
|---|---|---|---|
| Que River | 0.9 wt % | Prehnite-pumpellyite | 160°C-250°C* |
| Rosebery N-end | 0.5 wt % | Greenschist | – |
| Rosebery S-end | 0.3–0.5 wt % | Greenschist | 200°C-330°C** |
| South Hercules | <1.5–21.0 wt% | Greenschist | 140°C-300°C*** |

*metamorphic temperature data from Jenkins (1989)
**metasomatic temperature–Chapter 10
***metamorphic temperature–Chapter 10

## 7.7 ELECTRUM OCCURRENCE, VARIATION OF FINENESS AND GOLD TRANSPORT MECHANISM ...

Huston and Large (1989) and Large et al. (1989) argue that there are two major associations of gold in VMS deposits: (a) the Au–Zn–Pb–Ag±Ba association toward the top of the stratiform ore lenses, and (b) the Au–Cu association in the base of the massive sulphide and the footwall stringer zone. They suggest that these associations reflect the method of transport of gold either as a bisulphide complex (the Au–Zn association) or as a chlorocomplex (the Au–Cu association).

Huston and Khin Zaw (1988) and Huston et al. (1991 in prep.) have shown that electrum in the Zn–Pb–Ag–Au association has a relatively low but highly variable fineness, whereas electrum in the Cu–Au association tends to have higher and less variable fineness.

Thermodynamic modelling indicates that at low temperature (<300°C) and moderate to high pH (>4.5), gold is transported predominantly as a bisulphide complex and deposited upon mixing with oxidised seawater in the upper part of the massive sulphide system to produce the Zn–Pb–Ag–Au association, whereas at high temperature (>300°C) and low pH (<4.5), gold is transported predominantly as a chlorocomplex and precipitated by cooling and pH increase at the base of the massive sulphide lens to produce the Cu–Au association (Huston and Large, 1989; Large et al., 1989).

Huston and Khin Zaw (1988) and Huston et al. (1991 in prep.) considered that for gold bisulphide complex transport in deposits of the Zn–Pb–Ag–Au association, the fineness of electrum is controlled by the following reaction:

$$Au^0 + AgCl_2^- + 2H_2S = Ag^0 + Au(HS)_2^- + 2H^+ + 2Cl \quad \text{.....(1)}$$

The ratio $^{a}Au^0/^{a}Ag^0$ which can be related to fineness {1000Au/(Au+Ag) wt %} is controlled by the following equation;

$$\log (^{a}Ag^0/^{a}Au^0) = \log K_1 + \log (^{a}AgCl_2^-/^{a}Au(HS)_2^-) - 2pH + 2\log {}^{a}Cl^- + 2\log {}^{a}H_2S \quad \text{.....(2)}$$

The above reaction (2) indicates that $^{a}Ag^0/^{a}Au^0$ (and herein fineness) is controlled by $^{a}Au(HS)_2^-/^{a}AgCl_2^-$, $^{a}H_2S$, $^{a}Cl^-$, pH and temperature. Minor variation in any or all of the above parameters will lead to variations in the fineness of precipitated gold, which accounts for the wide variation of gold fineness in deposits of the Zn–Pb–Ag–Au association.

In contrast, for gold chlorocomplex transport in deposits of the Cu–Au association, the

fineness of electrum is controlled by the following reaction:

$$Au^0 + AgCl_2^- = Ag^0 + AuCl_2^- \quad \text{.....(3)}$$

The ratio ${}^aAu^0/{}^aAg^0$ is only related to ${}^aAuCl_2^-/{}^aAgCl_2^-$ and temperature as follows:

$$\log ({}^aAu^0/{}^aAg^0) = \log K_3 + \log ({}^aAuCl_2^-/{}^aAgCl_2^-) \quad \text{.....(4)}$$

Using available thermodynamic data, the fineness of electrum can be modelled. The activities of gold and silver can be related to their mole fractions in electrum using data from White et al. (1957). As these data were collected at 800°K (527°C), they are only an approximation of the true activity-composition relationships at the temperature of interest. Once the mole fraction of gold ($X_{Au}$) is established, the fineness may be determined as follows:

$$\text{Fineness} = 1000\, X_{Au}\, AW_{Au} / \{AW_{Ag} - X_{Au}\,(AW_{Ag} - AW_{Au})\} \quad \text{.....(5)}$$

where $AW_i$ is the atomic weight of the relevant metal.

As the dominant silver and gold species in the ore fluid have a –1 charge, the activity coefficients cancel and ${}^aAuCl_2^-/{}^aAgCl_2^-$ is approximately equal to the atomic Ag/Au ratio of the fluids (which is about twice the weight Ag/Au ratio). As the temperature of the Cu–Au association is restricted to (≥300°C), the fineness variation should also be restricted. Using the thermodynamic data (Table 7.4), Huston and Khin Zaw (1988) and Huston et al. (1991 in prep.) calculated the theoretical fineness of electrum assuming $\log {}^aH_2S = -2.5$ and $\log m_{NaCl}=10^{0.0}$ (Fig. 7.20).

As most volcanogenic massive sulphide deposits of the Zn–Pb–Ag–Au association have Ag/Au ratio of around 100 (Huston and Large, 1989; Large et al., 1989; Huston et al., 1991 in prep), the thermodynamic data which predict a fineness variation of between 100 and 900 for temperatures from 200°C to 275°C and pH values between 4.5 and 5.5 (Figs. 7.20A, 7.20B and 7.20C), matches with the observed variation of 320–820 (Fig. 7.21).

Thermodynamic modelling assuming gold chlorocomplexes (Fig. 7.20D) yields less satisfactory results and indicates that if the Ag/Au atomic ratio of the fluid is below 1000, gold fineness is always 1000, and modelling only matches observation when the Ag/Au atomic ratio of the fluids varies between 100,000 and 1,000,000 or (Ag/Au wt. ratio of between 50, 000 and 500, 000). This problem has to be resolved (Huston et al., 1991 in prep.). In this calculation, Helgeson's (1969) data have been theoretically extrapolated from low temperature data and at present no experimental data are available at higher temperature.

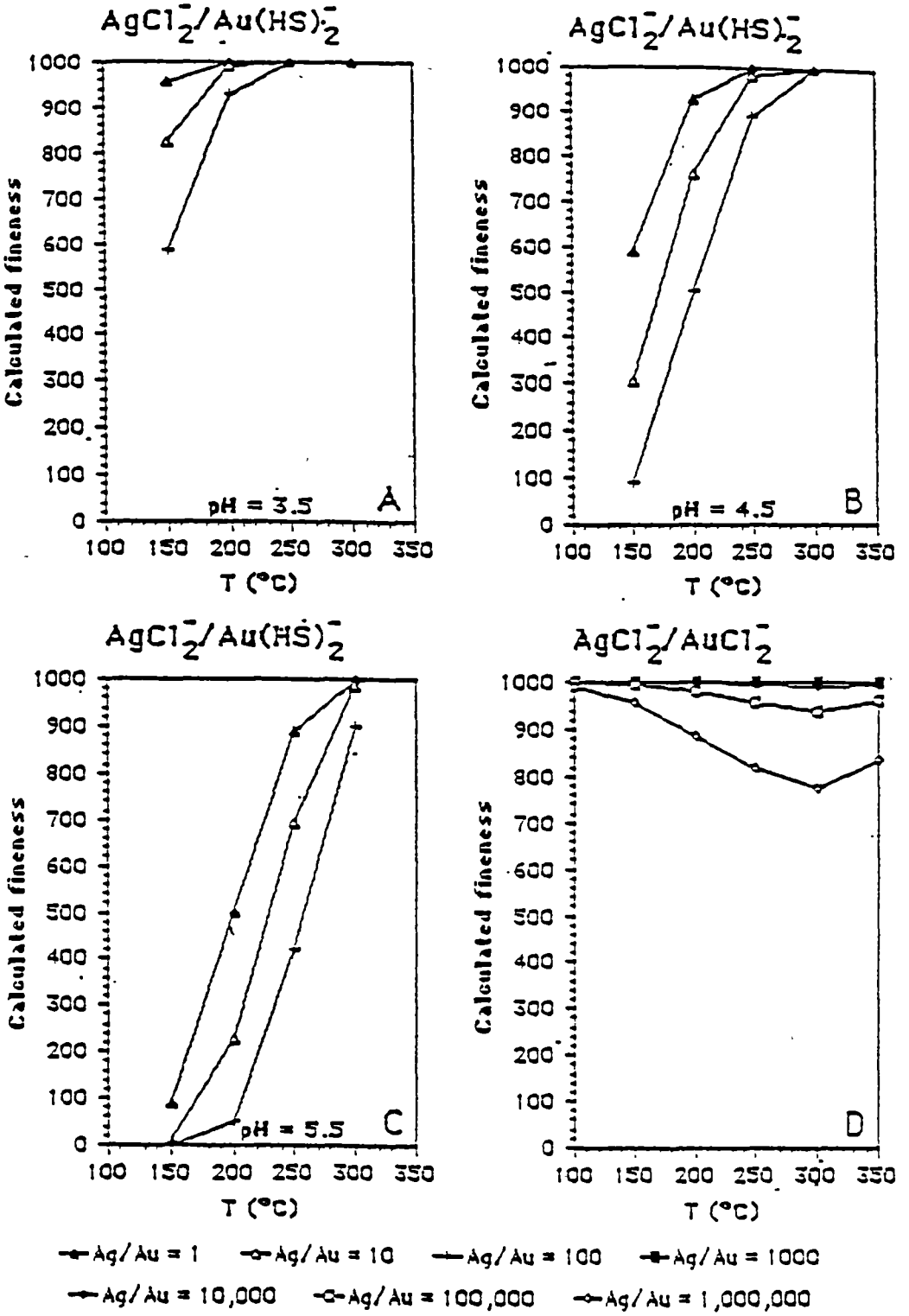


Fig. 7.20 Variation in the fineness of electrum with temperature assuming chlorocomplexing if silver throughout, bisulphide complexing of gold (A) through (C) and chlorocomplexing of gold in (D). Values of pH as stated; other fluid conditions are $^{a}$ $H_2S$ = -2.5 and log $m_{NaCl}$ = 10 $^{0.0}$ (after Huston and Khin Zaw, 1988; Huston et al., 1991 in prep.)

The fineness of gold grains in the F(J) lens, Rosebery Mine and the South Hercules deposit are shown together with those of the other Zn–Pb–Ag–Au and Cu–Au associations in Fig 7.21. The fineness values of the gold grains in the South Hercules deposit are comparable with those of the Zn–Pb–Ag–Au association (Fig 7.21). The gold at the South Hercules deposit is concentrated in the massive pyrite zone in the upper part of the lens and gold was most probably transported as the bisulphide complex at low temperature (<250°C) (fluid inclusion data) and neutral pH.

The gold locked in the pyrite from the F(J) lens yielded lower fineness values (450–470), whereas the fineness of gold associated with pyrrhotite varies from 500 to 660 and the gold associated with chalcopyrite displays restricted higher fineness values up to 800. The remobilised and recrystallised gold in the F(J) lens is of particular interest in that the fineness values are comparable with those of the gold from the Zn–Pb–Ag–Au association in the north-end of the Rosebery deposit (Huston and Large, 1988; Huston, 1989). However, the fineness values of electrum in the F(J) lens pyrite which considered to be of Cambrian origin do not correspond with neither fineness mode of the north-end (Fig 7.21). This discrepancy is probably due to sample distribution. More data from the north-end ores are necessary.

Table 7.4. Thermodynamic data used in calculations (after Huston et al., 1991 in prep.)

| Reaction | log $K_{eq}$ 150°C | 200°C | 250°C | 300°C | 350°C |
|---|---|---|---|---|---|
| $Au^0 + AgCl_2^- + 2H_2S = Ag^0 + Au(HS)^-_2 + 2H^+ + 2Cl^-$ | (-4.54) | -6.35 | (8.19) | (-10.5) | — |
| $Au^0 + AgCl_2^- = Ag^0 + AuCl_2^-$ | -7.8 | (-7.2) | (-6.8) | (-6.6) | (-6.9) |

Data from Seward (1973, 1976), Barton (1984), Bowers et al. (1984) and Helgeson (1969). Values in parentheses indicate extrapolations or interpolations.

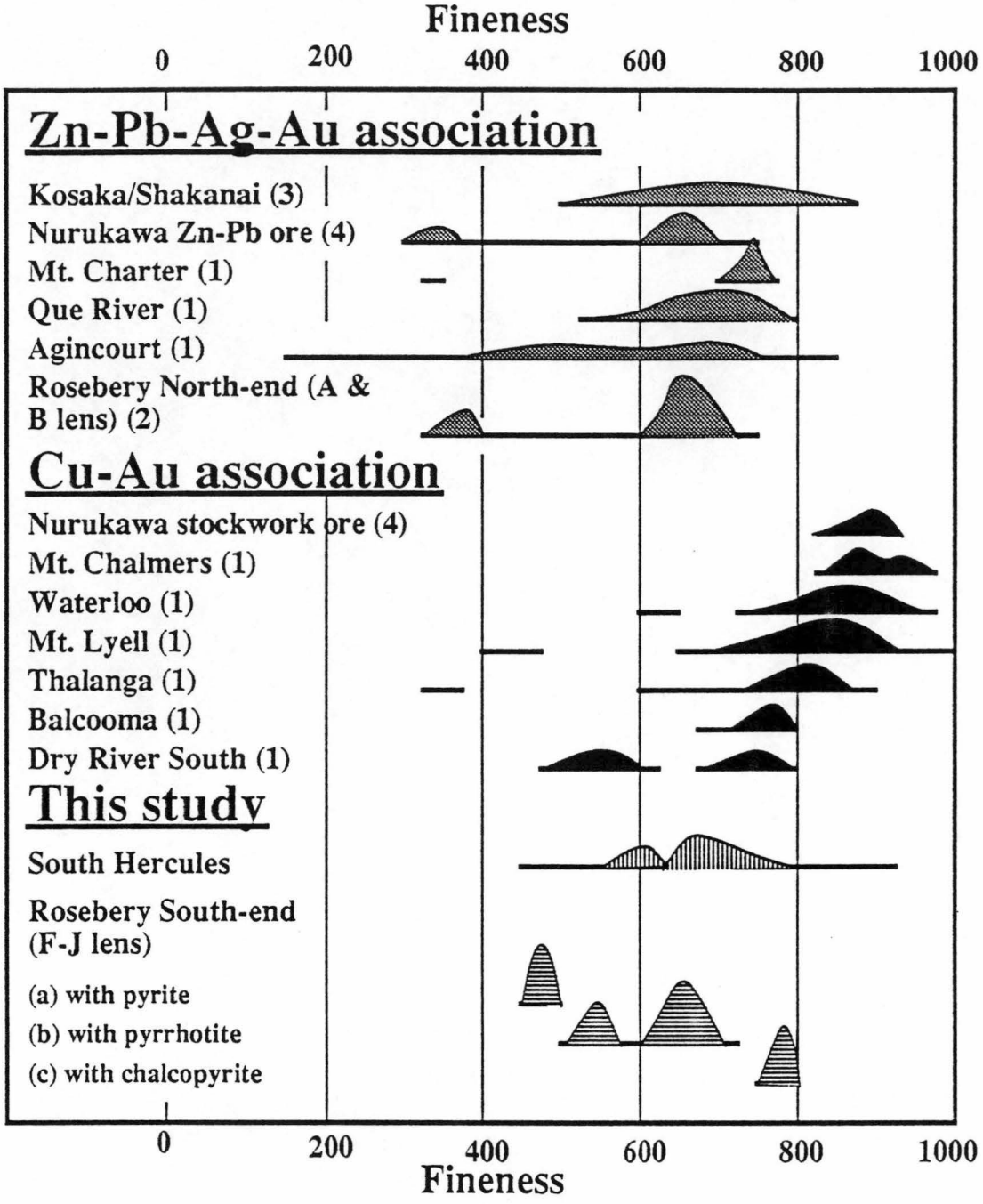


Fig. 7. 21 Variation of fineness of gold grains from the F(J) lens of the Rosebery south-end orebody and the South Hercules deposit, western Tasmania together with fineness values of gold from the other volcanogenic massive sulphide deposits. Data for (1) from Huston et al. (1991 in prep.), (2) from Huston and Large (1988) and Huston (1989), (3) from Shimazaki (1974) and (4) fromYamada et al. (1988).

Electrum is also noted in a distinct and spectacular association with copper in the F(J) lens. It commonly occurs in recrystallised chalcopyrite 'pools' within pyrrhotite. This distinct gold–copper association indicates a similar behaviour and complexing medium for both metals in the environment of Devonian replacement. The Cu enrichment in the F(J) lens suggests that copper was also mobilised and recrystallised as the chlorocomplex (Chapter 11). Gold tends to have been recrystallised with higher fineness values along with copper and this remobilised Cu–Au association is comparable in fineness values with those of the Cu–Au association observed in other volcanogenic massive sulphide deposits (e.g. Balcooma and Dry River South, Queensland) (Fig. 7.21).

Although the gold in the Pb–Zn–Ag lenses at the south-end of the Rosebery deposit was probably initially transported as the bisulphide complex with lower fineness (similar to the north-end), the gold appears to have been remobilised and recrystallised as the chlorocomplex with higher fineness at higher temperature (≥330°C) and moderate pH (as evidenced by the presence of carbonate, sericite, K-feldspar) during the Devonian metasomatic processes (Chapter 11).

# CHAPTER 8: COMPOSITIONAL VARIATION IN SPHALERITE

## 8.1 INTRODUCTION ...

In recent years there has been considerable interest in the use of the FeS content of sphalerite as a geobarometer and as a geochemical tool to decipher conditions of deposition in hydrothermal and metamorphic environments. In addition, the FeS content in sphalerite has been applied as a guide to the sulphidation reaction associated with gold mineralisation in volcanogenic massive sulphide deposits (e.g. Hannington and Scott, 1989). In this chapter, compositional variation of sphalerite from the Rosebery mine, J(K) and P lens of the Hercules mine and the South Hercules deposit were determined to (1) provide pressure (depth) estimates at the time of Fe–S–O replacement during the Devonian at the Rosebery mine, and (2) deduce the control of $a_{FeS}$ ($a_{S2}$) in relation to gold deposition and subsequent remobilisation.

## 8.2 TEXTURAL VARIATION OF SPHALERITE ...

Sphalerite grains from the Rosebery, Hercules and the South Hercules deposits display a wide variety in colour, grain size and texture. The sphalerite from barite zones at the upper part of the Rosebery north-end varies from light grey to light brown, whereas sphalerite from barite-poor massive sulphide lenses varies from light brown to orangy brown to dark brown. In both ore types, the sphalerite is commonly associated with pyrite, galena and chalcopyrite.

Sphalerite grains from the F(J) lens of the Rosebery south-end orebody, which have been overprinted by Devonian granitoid-related metasomatism, are more variable in texture. In the F(J) lens, sphalerite in the pyrrhotite–pyrite assemblage is massive, coarse-grained and dark brown in colour, whereas the sphalerite in the magnetite–biotite and quartz–tourmaline assemblages occurs as centimetre-scale semi-massive patches and blebs, and is yellowish brown. Although the "chalcopyrite disease" texture of Barton (1978) and Eldridge et al. (1983) is uncommon in the north-end, it is quite common in the south-end. Some sphalerite grains in the F(J) lens of the south-end are markedly zoned from iron-poor cores (2.2 mole % FeS) to iron-rich rims (14.8 mole % FeS). The Fe-rich layer is in contact with iron sulphides.

In contrast, sphalerite from the Hercules–South Hercules area appears to be more homogeneous, presumably because of annealing during metamorphism, and shows very little variation in Fe content across grains. Zoning of sphalerite is rarely seen. Chalcopyrite disease in the sphalerite is also much less common than in the F(J) lens. Homogeneous sphalerite blebs of about 5 cm or more across are found in the South Hercules deposit (Chapter 4). In addition, coarse-grained, light yellow sphalerite grains with recrystallised galena cubes and chalcopyrite grains are commonly noted in the irregular quartz–carbonate veins.

Although sphalerite grains from the Hercules–South Hercules area have suffered greenschist facies regional metamorphism along with the host rocks, no pyrrhotite–pyrite association was noted with the annealed sphalerite. Therefore it was not possible to use the FeS content of sphalerite as a meaningful pressure estimate during regional metamorphism. However, sphalerite associated with pyrrhotite–pyrite was noted in the Devonian granite replacement zone of the F(J) lens. The sphalerite–pyrrhotite–pyrite assemblages in the F(J) lens (Fig. 8.1) provide an opportunity to use the FeS content of sphalerite to estimate the pressure conditions during Devonian replacement processes.

## 8.3 ANALYTICAL TECHNIQUES ...

The FeS content of sphalerite was determined using both JEOL 50-A and CAMECA SX-50 microprobes. For the JEOL microprobe a 3 μm diameter beam of $2 \times 10^{-10}$ amps and an accelerating voltage of 20 kV was used, whereas for the CAMECA probe, a 1 μm diameter beam of $2 \times 10^{-10}$ amps and an accelerating voltage of 20 kV was applied. Each grain was analysed in at least 2–5 spots and the results averaged. Concentrations of other minor elements (manganese, cobalt, cadmium and copper) were also determined.

Although minor amounts of manganese, cadmium and copper were noted, no cobalt was detected. The detection limits of the microprobe analyses were: sulphur (0.09 wt %), manganese (0.10 wt %), iron (0.11 wt %), copper (0.16 wt %), zinc (0.21 wt %), cadmium (0.13 wt %) and cobalt (0.15 wt %). The sphalerite grains from Rosebery south-end, Hercules and South Hercules were determined by Khin Zaw and the sphalerite grains from Rosebery north-end were analysed by Khin Zaw and D. L. Huston. The results of the microprobe analyses of sphalerite are shown in Appendices 8.1, 8.2, 8.3 and 8.4.

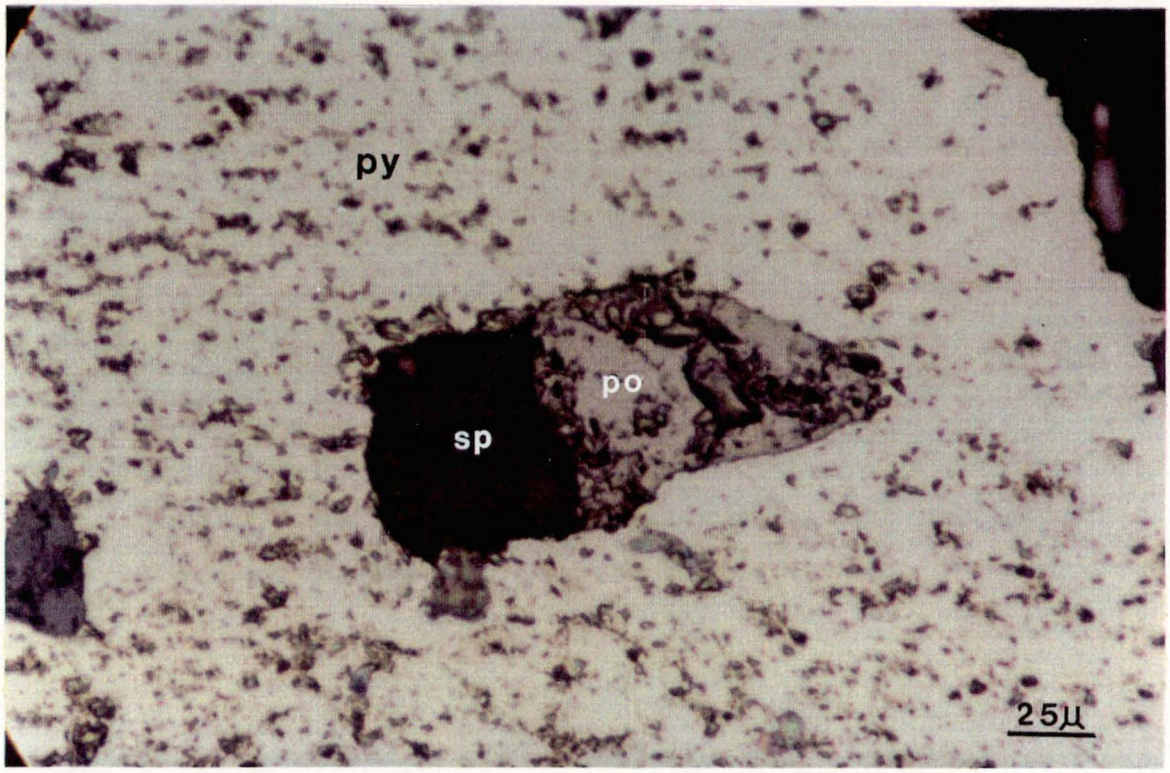


Fig. 8.1. Photomicrograph showing sphalerite and pyrrhotite inclusions in a pyrite grain. sp=sphalerite, po=hexagonal pyrrhotite, py=pyrite, unlettered patches are polishing marks. Sample No. DDH R3023-2 at 133' (40.8m), section 270mS, F(J) lens, Rosebery mine, western Tasmania.

## 8.4 FeS CONTENT OF SPHALERITE FROM ROSEBERY ...

Histograms of the mole % FeS in sphalerite from the A and B lens of the Rosebery north-end and the F(J) lens of the south-end orebodies are shown in Figs 8.2A, 8.2B and 8.2C. The mole% FeS in sphalerite for the entire Rosebery deposit displays a bimodal distribution (Fig. 8.2C). A mode of 16.0 mole % FeS was noted for the F(J) lens where Devonian metasomatism prevailed, whereas a mode of 2.0–4.0 mole % FeS was found for the other lenses.

## 8.5 FeS CONTENT OF SPHALERITE FROM HERCULES AND SOUTH HERCULES ...

A histogram of the mole % FeS in sphalerite from the Hercules–South Hercules deposit is shown in Fig. 8.3. The sphalerite from the J(K)–P lens of the Hercules mine has a narrow range of 2.0–8.0 mole % FeS, whereas the sphalerite from the South Hercules deposit gives a range of 4.0–10.0 mole % FeS.

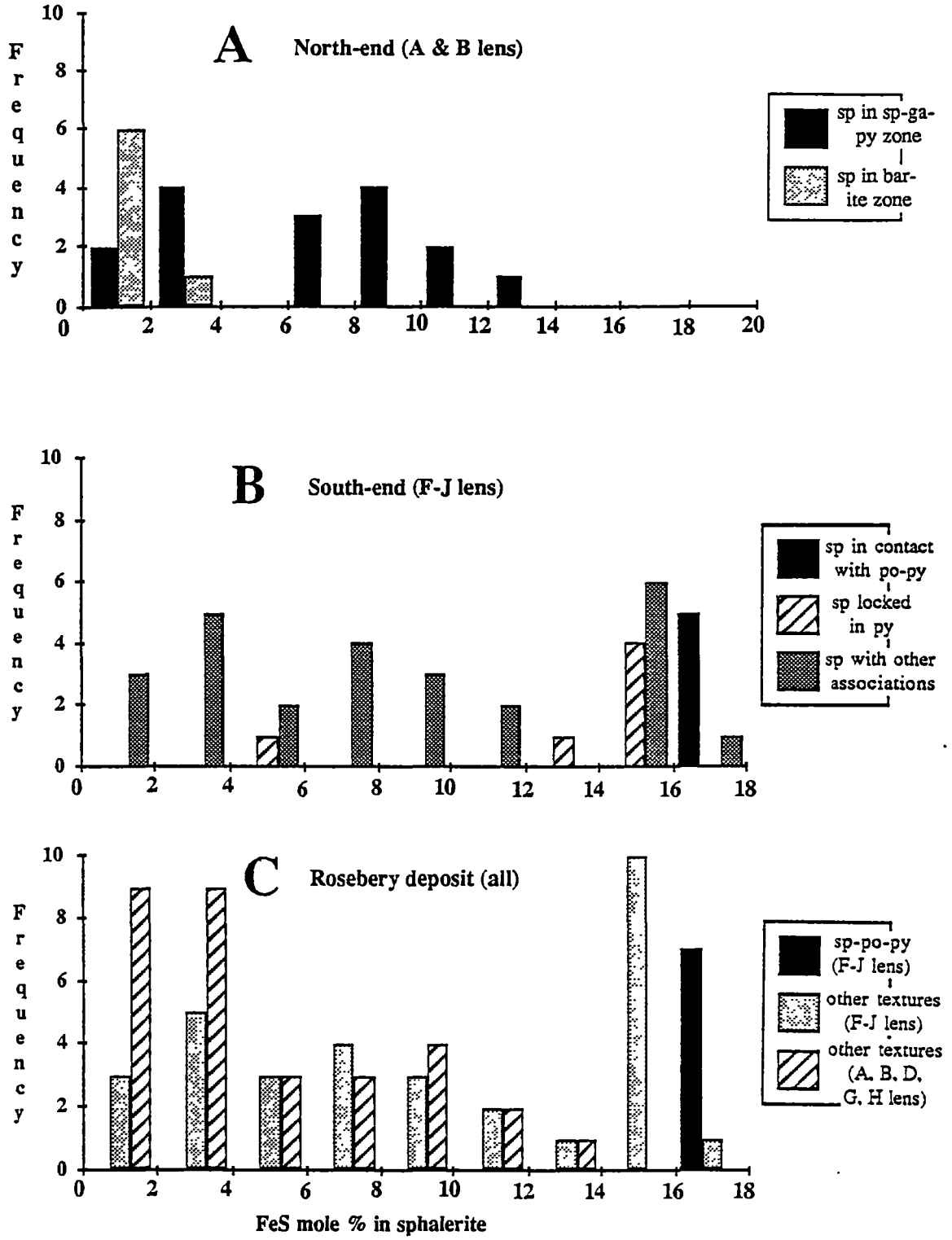


Fig. 8.2. Frequency distribution diagram for the mole % FeS in sphalerite (A) north- end, (B) south-end and (C) entire Rosebery deposit, western Tasmania. sp=sphalerite, po=pyrrhotite, ga=galena, py=pyrite. (Data for D, G and H lens are from Green et al., 1981).

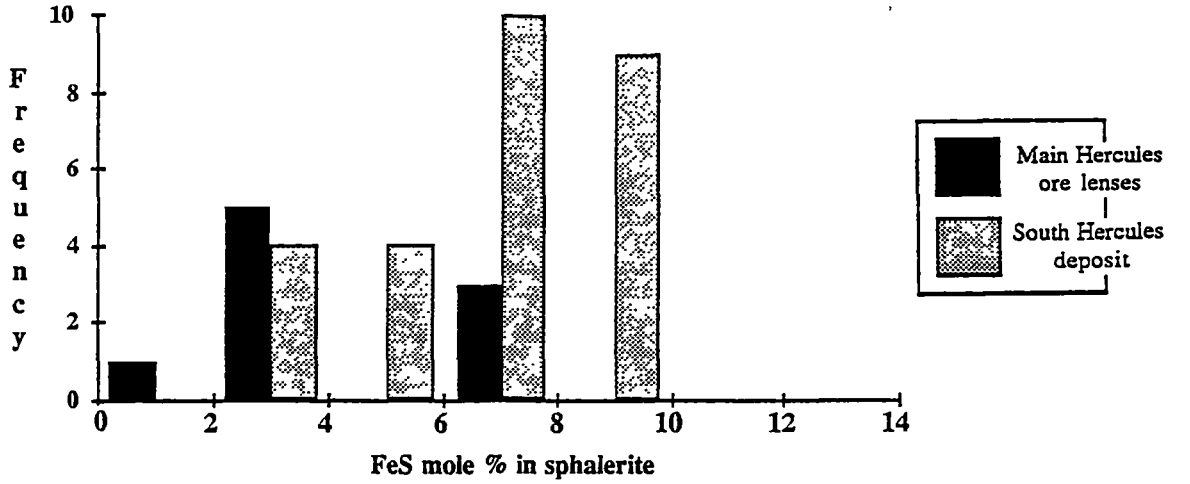


Fig. 8.3. Frequency distribution of mole % FeS in sphalerite from the main Hercules ore lenses and the South Hercules deposit, western Tasmania.

## 8.6 Effect of Devonian overprint on sphalerite composition ...

The effect of the Devonian overprint on the Cambrian mineralisation is evidenced by (1) zoning of sphalerite and (2) variation in FeS content of sphalerite.

*(1) Zoning of sphalerite:* the zoning appears to be due to the outward diffusion of FeS in sphalerite grains as suggested by Barton and Skinner (1979) and Mizuta (1988). The zoning of sphalerite in the F(J) lens can be related to recrystallisation during the Devonian replacement processes. Solomon et al. (1987) also noted the local zoning of FeS content in sphalerite at the south-end: the sphalerite from the lead–zinc ore has lower FeS content (4.6 wt %), whereas the sphalerite from the transition zone to pyrrhotite–pyrite ores of Devonian origin has a higher FeS content (6.6–8.8 wt %). Solomon et al. (1987) attributed this enrichment of FeS content due to remobilisation and recrystallisation during the Devonian metasomatism:

*(2) Variation of FeS content of sphalerite:* the mole % FeS in sphalerite from the Rosebery deposit displays a wide variability in composition. A bimodal distribution with modes of 4.0 and 16.0 mole % FeS was noted for the F(J) lens where Devonian metasomatism prevailed, whereas only one mode of 4.0 mole % FeS was found for the other lenses (Fig. 8.2C). This suggests that the primary exhalative mineralisation of the F(J) lens of Rosebery has suffered at least two periods of post-depositional re-equilibration, specifically viz. 1) possible annealing of the primary sulphides at the time of metamorphism (mean 4.0 mole % FeS) and 2) metasomatism related to shallow granitoid intrusion (mean 16.0 mole % FeS).

## 8.7 MINOR ELEMENT CONTENT OF SPHALERITE ...

The sphalerite from the Rosebery, Hercules and South Hercules deposits has minor copper, manganese and cadmium contents. Although microprobe analyses were performed to avoid the analysis of sphalerite grains with chalcopyrite disease, a few sphalerite grains have minor copper content. Two sphalerite grains from the Rosebery north-end have 0.8 mole % CuS and one grain from the Rosebery south-end contains 2.1 mole % CuS. One grain from Hercules has 2.7 mole % CuS and one grain from South Hercules contains 2.4 mole % CuS.

In this study, only analyses with detectable MnS and CdS were considered. Figure 8.4 shows a plot of mole % FeS versus mole % MnS in sphalerite from the Cambrian volcanogenic sulphide deposits (this study) compared with sphalerite from the lead–zinc deposits of Devonian origin from the Zeehan area, western Tasmania (Both, 1966). The manganese content in sphalerite from the north-end of the Rosebery mine ranges from the detection limit of the microprobe (<0.1 wt %) to 0.4 wt % (1.7 mole % MnS).

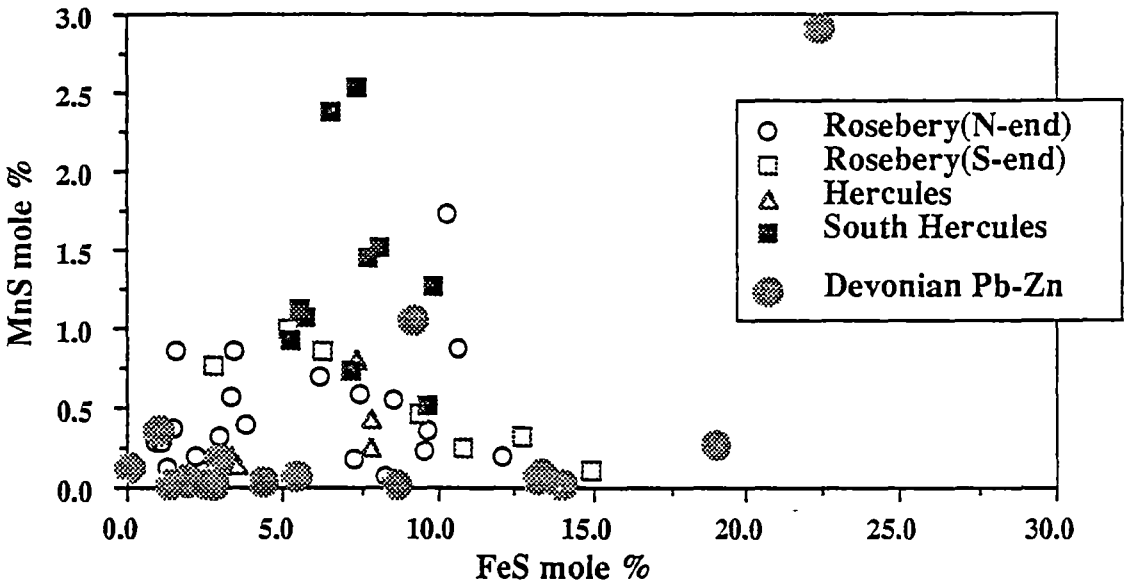


Fig. 8.4. Plot of mole % FeS vs. mole % MnS in sphalerite from the north- and south-ends of the Rosebery mine, Hercules mine and the South Hercules deposit, together with the composition of those sphalerites from the Devonian granite-related, lead–zinc deposits, western Tasmania. (Data for the Devonian Pb–Zn deposits are from Both, 1966).

The Mn content in sphalerite from the F(J) lens of the Rosebery south-end varies up to 1.0 mole % MnS, whereas the sphalerite from the Hercules mine has manganese contents up to 2.2 mole % MnS and the sphalerite from the South Hercules deposit has the highest manganese content, up to 1.5 wt % (2.6 mole % MnS) (Fig. 8.4). Green et al. (1981) reported up to 0.4 mole % MnS in sphalerite from the 'G' lens and 0.3 mole % MnS in sphalerite from the 'D' lens of the Rosebery mine. In comparison, the sphalerite from the Devonian granite-related, lead–zinc deposits always contains less than 1.1 mole % MnS except for the Silver Stream mine, Zeehan which has 2.9 mole % MnS in sphalerite (Both, 1966). Williams (1974, p. 665) also noted the unusual Mn content in sphalerite from the Silver Stream deposit and reported values up to 9.3 wt % Mn.

Sphalerite from Rosebery, Hercules and South Hercules generally has <0.2 mole % CdS (Fig. 8.5). Although Green et al. (1981) reported up to 0.38 mole % CdS in two sphalerite grains from 'G' lens, the other sphalerite grains from 'D' and 'H' lenses contain no CdS and one grain from 'D' lens has 0.2 mole % CdS. In comparison, sphalerite from the Devonian lead–zinc deposits contains significant Cd, generally more than 0.2 mole % CdS (Fig. 8.5).

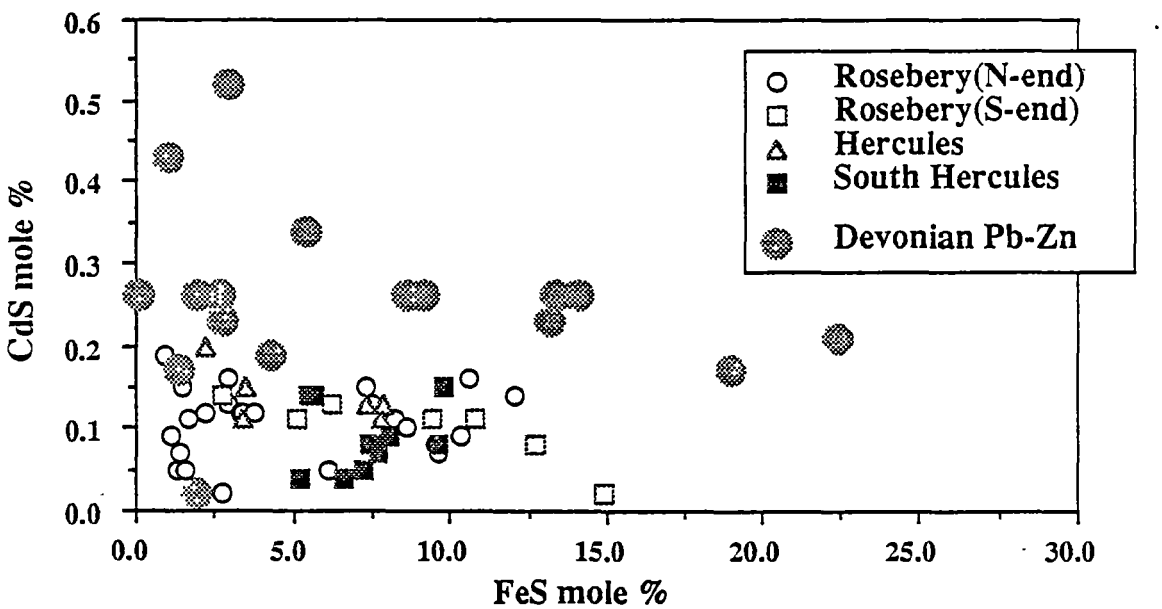


Fig. 8.5. Plot of mole % FeS vs. mole % CdS in sphalerite from the north- and south-ends of the Rosebery mine, Hercules mine and the South Hercules deposit, together with the composition of those sphalerites from the Devonian granite-related, lead–zinc deposits, western Tasmania. (Data for the Devonian lead–zinc deposits are from Both, 1966).

A ternary diagram relating FeS (mole %), MnS (mole % x 10) and CdS (mole % x 10) of Cambrian and Devonian sulphide deposits in Tasmania is shown in Fig. 8.6. Sphalerite grains from Cambrian and Devonian sulphide deposits display different compositional fields. The Cambrian sphalerites tend to have higher MnS, whereas the Devonian sphalerites contain more CdS.

In this study, the *average* weight percent ratios of Zn/Cd and Zn/Mn of the sphalerite grains from volcanogenic sulphide deposits (Rosebery north- and south-ends, Hercules and South Hercules deposits) and Devonian lead–zinc deposits in western Tasmania were calculated from the microprobe data, and the results are shown in Table 8.1. These data clearly demonstrate the high Zn/Mn ratio and lower Zn/Cd of sphalerite from the Devonian Pb–Zn deposits compared with the Cambrian VMS deposits.

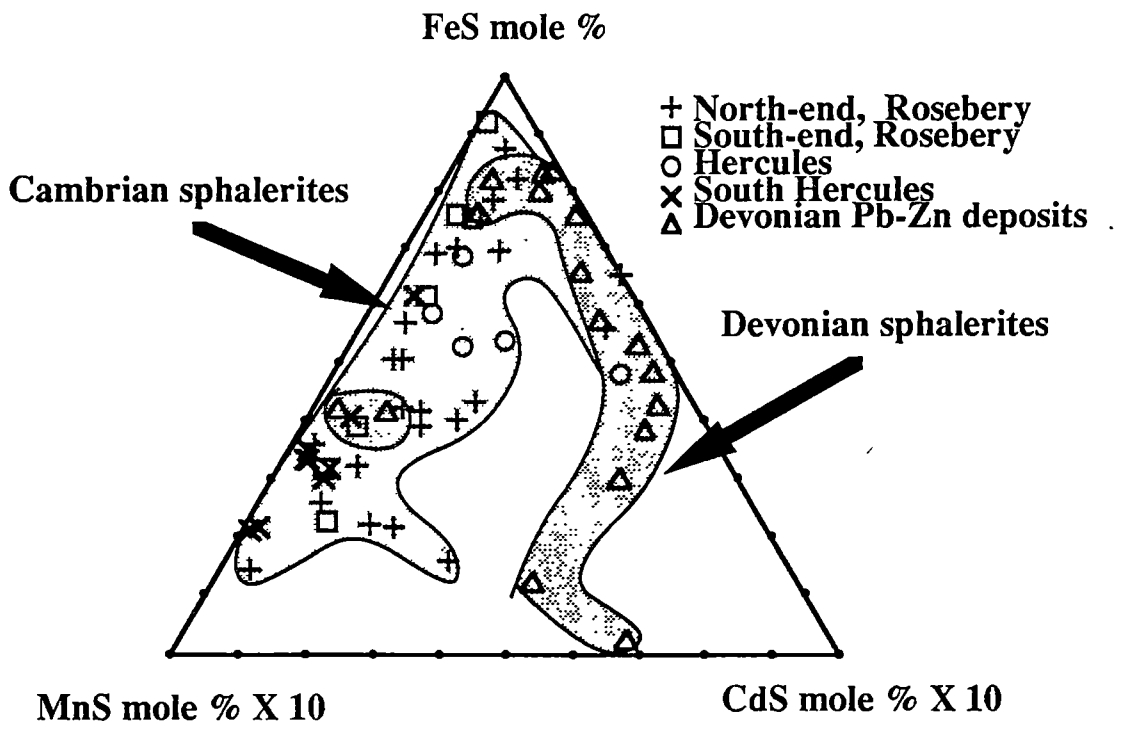


Fig. 8.6. A ternary plot of mole % FeS: mole % x 10 MnS: mole % x 10 CdS in sphalerites from the north- and south-ends of the Rosebery mine, Hercules mine and the South Hercules deposit, together with the composition of sphalerites from Devonian granite-related, lead–zinc deposits, western Tasmania. (Data for the Devonian Pb–Zn deposits are from Both, 1966).

Table 8.1 Average Zn/Mn and Zn/Cd wt % ratio of the sphalerites from Cambrian volcanogenic sulphide deposits and the Devonian lead–zinc deposits. (Data for the Devonian deposits from Both, 1966).

| | Rosebery N-end | Rosebery S-end | Hercules | South Hercules | Devonian lead–zinc deposit |
|---|---|---|---|---|---|
| **Zn/Mn** | 553 | 420 | 511 | 124 | 1696 |
| **Zn/Cd** | 290 | 321 | 417 | 304 | 214 |

## 8.8 SPHALERITE GEOBAROMETRY ...

Initial thermodynamic calculations by Barton and Toulmin (1966), which were later confirmed through experimental studies in the Fe–Zn–S system (Scott and Barnes 1971; Scott, 1973, 1976; Lusk and Ford, 1978; Hutchison and Scott, 1981; Bryndzia et al., 1988, 1990) demonstrated that the FeS content of sphalerite is a function of activity of FeS ($a_{FeS}$) in the system, which is itself controlled by the activity of sulphur ($a_{S2}$).

The above thermodynamic calculations and experimental studies have also indicated that the FeS content in sphalerite coexisting with hexagonal pyrrhotite and pyrite is pressure dependent. This variation of FeS content in sphalerite as a function of pressure also independent of temperature over the range 300°–550°C and has given rise to the concept of the sphalerite geobarometer.

### 8.8.1 FeS content of sphalerite and geobarometric implications ...

The sphalerite geobarometer has received wide application for sphalerite from hydrothermal environments such as skarn deposits (e.g. Khin Zaw, 1976), nickel deposits (Groves et al., 1975) and metamorphosed massive sulphide deposits which include deposits from the Snow Lake area, Manitoba (Bristol, 1974), Quemont Mine, Noranda, Quebec (Lusk et al., 1975), Sullivan, Canada (Ethier et al., 1976), Broken Hill, New South Wales (Scott et al., 1977), Ruttan Mine, Lynn Lake, Manitoba (Bristol, 1979), Calloway Mine, Ducktown, Tennessee (Ringler, 1979), Skellefte deposits, Sweden (Berglund and Ekstrom, 1980), Cobar deposits, Australia (Sangameshwar and Marshall, 1980; Brill, 1989), and several others (see Scott, 1976).

The sphalerite geobarometer was also applied to VMS deposits in the Swedish Caledonides and US Appalachians by Hutchison and Scott (1980) and later Sundblad et al. (1984) did more detailed work on the Swedish Caledonides deposits. A sphalerite geobarometric study was also made on the McPhun's Cairns stratiform sulphide deposit, Scotland (Willan and Hall,

1980) and recently Mole (1983) studied sphalerite composition in relation to deposition and metamorphism of the Foss stratiform Ba–Zn–Pb deposit, Aberfeldy, Scotland. Metamorphic petrologists have also used disseminated-sphalerite-bearing assemblages in metamorphic belts as an indicator of metamorphic pressure (Dewitt and Essene, 1974; Hutcheon, 1978; Brown et al., 1978).

Although the FeS content of sphalerite as a geobarometer has been extensively applied as mentioned above, results have varied widely and some workers have questioned the applicability of the barometer. The pressures derived from the results of sphalerite barometric studies are variable and often suggest pressures which are greater than those indicated by the silicate mineralogy of the adjacent rocks. The most controversial issue for the reliability of the sphalerite barometer is the post-depositional changes or retrograde changes in the composition of sphalerite even though sphalerite is one of the more refractory sulphide minerals.

Scott (1983) pointed out that the problem arises due to the cooling rate of the particular sulphide assemblages in the hydrothermal system or in the metamorphic environment. Scott (1983, p. 429) also mentioned that the sphalerite geobarometer was successfully applied for hydrothermal systems such as skarns (Shimizu and Shimazaki, 1981) and vein deposits (e.g. Hudson Bay Mountain area; Hutchison and Scott, 1981) in which cooling was reasonably fast, but that metamorphosed deposits which have cooled more slowly show evidence of retrograde changes in sphalerite composition particularly in Cu-rich environments. The resulting sphalerites are considerably depleted in FeS and give higher pressure estimates than expected from metamorphic conditions.

Scott (1983) suggested that to avoid this problem attending retrogression, sphalerite inclusions, and particularly those accompanying pyrrhotite that are totally encapsulated in pyrite (e.g. Fig. 8.1) should be sought and analysed. Presumably, such poikiloblastic inclusions were equilibrated during peak pressure (depth) regimes. They display the necessary buffer assemblages and would have been protected from later hydrothermal retrograde reactions by inert encapsulating pyrite.

The following criteria must be met in order to use the FeS content of sphalerite as a geobarometer (Scott and Barnes, 1971; Scott, 1973, 1976; Bryndzia et al., 1988).

(1) Sphalerites must have equilibrated with pyrite and hexagonal pyrrhotite. Both iron sulphides should be in mutual contact with the sphalerite.

(2) The temperature of sphalerite deposition also needs to be estimated and to exceed 274°C, which corresponds to the inversion temperature of hexagonal to monoclinic pyrrhotite.

(3) Precise microprobe analyses of sphalerite grains are required, as ±0.5 mole % uncertainty corresponds to ± 400–500 bars.

The pyrrhotite in the F(J) lens at Rosebery was found to contain both hexagonal and monoclinic pyrrhotite as evidenced by the microprobe analyses (confirmed by magnetic colloid methods and X-ray diffraction). Microprobe analyses of pyrrhotite gave a range of $X_{FeS}$ from 0.501 to 0.461. It is also assumed that hexagonal pyrrhotite in the early replacement zones within the F(J) lens has transformed to monoclinic pyrrhotite by cooling during the late quartz–tourmaline veining. Studies of fluid inclusions in helvite in the early Fe–S–O replacement assemblages give a minimum homogenisation temperature of about 330°C (Chapter 10).

### 8.8.2 Geobarometric implications of sphalerite FeS content in the F(J) lens ...

In this study, the FeS content of sphalerite grains strictly encapsulated in pyrite with hexagonal pyrrhotite (Fig. 8.2) or in mutual contact assemblages in the F(J) lens at Rosebery were used to estimate the pressure during the replacement event. To avoid interference by copper, the spalerite grains which contain >0.5 wt % copper were not considered in this study. Hutchison and Scott (1981) recommended against the use of sphalerite grains with chalcopyrite inclusions, since Cu appears to affect the equilibration of sphalerite grains. It was also noted that smaller sphalerite grains show less variation in FeS content and more depletion in Cu content.

The sphalerite grains from the F(J) lens have CdS contents less than 0.2 mole % and MnS contents less than 1.0 mole %. These minor elements do not affect the sphalerite geobarometer. On the basis of cell volume data, Scott and Barnes (1971) considered that these minor elements in concentrations up to several wt % beyond those normally found, should not affect the geobarometer. Experiments on the system Zn–Cd–Fe–S by Scott (1973, p. 470) also indicated no change in phase relations with several wt % CdS in the sphalerite.

The average mole % FeS ($16.4 \pm 0.5$, n=7) in sphalerite with pyrrhotite–pyrite assemblages was used to calculate the pressure by applying the following regression equation of Hutchison and Scott (1981):

$$P = 42.30 - 32.10 \log \text{mole \% FeS}$$

The average mole % FeS of sphalerite is equivalent to $3.0 \pm 0.5$ kb for the re-equilibration of sphalerite in the F(J) lens. Assuming an average rock density of 2.65 gm/cm$^3$, this pressure estimate would correspond to a depth of $8.0 \pm 1.0$ km.

Green et al. (1981) estimated a depth of 6 km to 8 km during Devonian metamorphism by stratigraphic reconstruction. Although many uncertainties can be encountered in such a reconstruction (e.g. facies changes, unconformities, a lack of knowledge concerning the

proportion of rock units removed by erosion prior to the Devonian granitoid intrusion, and the true thickness of folded Cambrian rocks in the mine area), it provides an optimum depth estimate. The depth estimate determined here by using the FeS mole % in the sphalerite in the F(J) lens is consistent with this.

## 8.9 FeS CONTENT OF SPHALERITE AND HYDROTHERMAL ORE DEPOSITION ...

The FeS content of sphalerite is dependent on temperature, pressure and the activity of FeS ($a_{FeS}$) in the system; the latter itself is controlled by activity of sulphur ($a_{S2}$). Thus variation in the FeS content in sphalerite reflects changes in these parameters in a hydrothermal system, and can provide a recorder for the physical and chemical characteristics of the environment of ore deposition and related post-depositional history.

The changing temperature and chemistry of mineralising solutions has left a delicate record in the growth-zoned sphalerites of vein and Mississippi Valley-type deposits (Mclimans et al., 1980). Sequential trends of sphalerite composition have been found from sedimentary exhalative deposits such as Sullivan, Canada (Campbell and Ethier, 1983). Mole (1983) considered that at the Foss stratiform Ba–Pb–Zn deposit, Aberfeldy, Scotland, Fe-rich sphalerite was deposited from the metalliferous brines in the vent and the Fe-poor sphalerite was formed from cooler, exhaled brines on the seafloor away from the vent.

Urabe (1974) ascribed the decrease in FeS content of sphalerite with stratigraphic height in the Kuroko deposits to declining temperature from the stockwork to the top of the stratiform ore. However, these changes may also be related to changes in total sulphur concentration and oxygen fugacity during mixing of the ore solutions with seawater. Green et al. (1981) noted at the Rosebery deposit that the FeS content of sphalerite decreased in parallel with the decrease in the Fe/(Fe+Mg+Mn) ratios of chlorites and the increase in $\delta^{34}S$ values from the stratigraphic bottom to the top.

Microprobe analyses in this study yielded 2–4 mole % FeS in sphalerite from the barite zone at the upper part of the Rosebery north-end ore body, whereas the sphalerite from the sulphide zone has a variable but higher mole % FeS (2–14 mole % FeS) (Fig. 8.2). This suggests a recognisable decrease in mole % FeS from the lead–zinc zone to the barite zone at the top as reported by Green et al. (1981).

Sphalerite compositional variations in sulphide ores of the Norwegian Caledonides were also studied by Craig et al. (1984) to provide data about changes in ($a_{S2}$) during ore formation and metamorphism . The variation of FeS content in sphalerite from the modern seafloor hydrothermal vents at 21°N on the East Pacific Rise is also attributed to periodic changes in ($a_{S2}$) during sphalerite deposition (Styrt et al., 1981; Hekinian et al., 1980; Scott, 1983).

### 8.9.1 $a_{FeS}$ and gold deposition ...

Hannington and Scott (1989) recently used the FeS content of sphalerite as a petrologic indicator for the sulphidation state of gold mineralisation in volcanogenic massive sulphide systems. Hannington and Scott (1989) showed that the *average* FeS content of sphalerite in some volcanogenic deposits (Noranda, Kuroko and modern seafloor deposits) has a correlation with Au grades of the deposits specifically the lower the FeS content of the sphalerite, the higher the Au grades. The trend was also true for a group of deposits within a single mining district (e.g. Archean deposits in Canada) (Fig. 8.7). Hannington and Scott (1989) attributed this correlation to changes in temperature and activity of sulphur ($a_{S2}$) or ($a_{FeS}$) which also control the deposition of gold (Fig. 8.8). Under similar pH conditions and $H_2S$ concentrations, contours of $Au(HS)_2^-$ concentration are parallel to those of the mole % FeS in sphalerite in $\log a_{S2}$–T space (Fig. 8.8). To the exploration geologists these simple indicators can be used as a guide for targeting the Au-rich parts of massive sulphide systems.

### 8.9.2 $a_{FeS}$ and gold relationships at Rosebery, Hercules and South Hercules ...

In this investigation, the compositional variation of sphalerite in the samples with known Au grades from the Rosebery, Hercules and South Hercules deposits have been plotted in Figs. 8.9 and 8.10. Mole % FeS of at least 2–5 sphalerite grains in each sample were *averaged* and plotted against Au grades. The recrystallised, light yellow sphalerites in the cross-cutting quartz–carbonate veins were not considered in this study.

There is no observable trend for the Rosebery orebody (Fig. 8.9) comparable with that for modern seafloor VMS deposits and for undeformed Kuroko deposits described by Hannington and Scott (1989). In particular, sphalerite from the barite zone has low FeS content (<5.0 mole %), but gold grades vary substantially from 1 g/t Au to nearly 40 g/t Au. In the underlying barite-poor polymetallic zone, no correlation at all was observed between gold grades and the FeS content of sphalerite.

Similarly, mole % FeS in sphalerite versus gold grades (g/t) in the Hercules and the South Hercules deposits give a variable and complex pattern. However, although no trend was found at the lower gold grades (<5.0 g/t), there is a vague correlation between the mole % FeS in sphalerite and the gold grades at higher gold grades (>5.0 g/t) at the South Hercules deposit (Fig. 8.10).

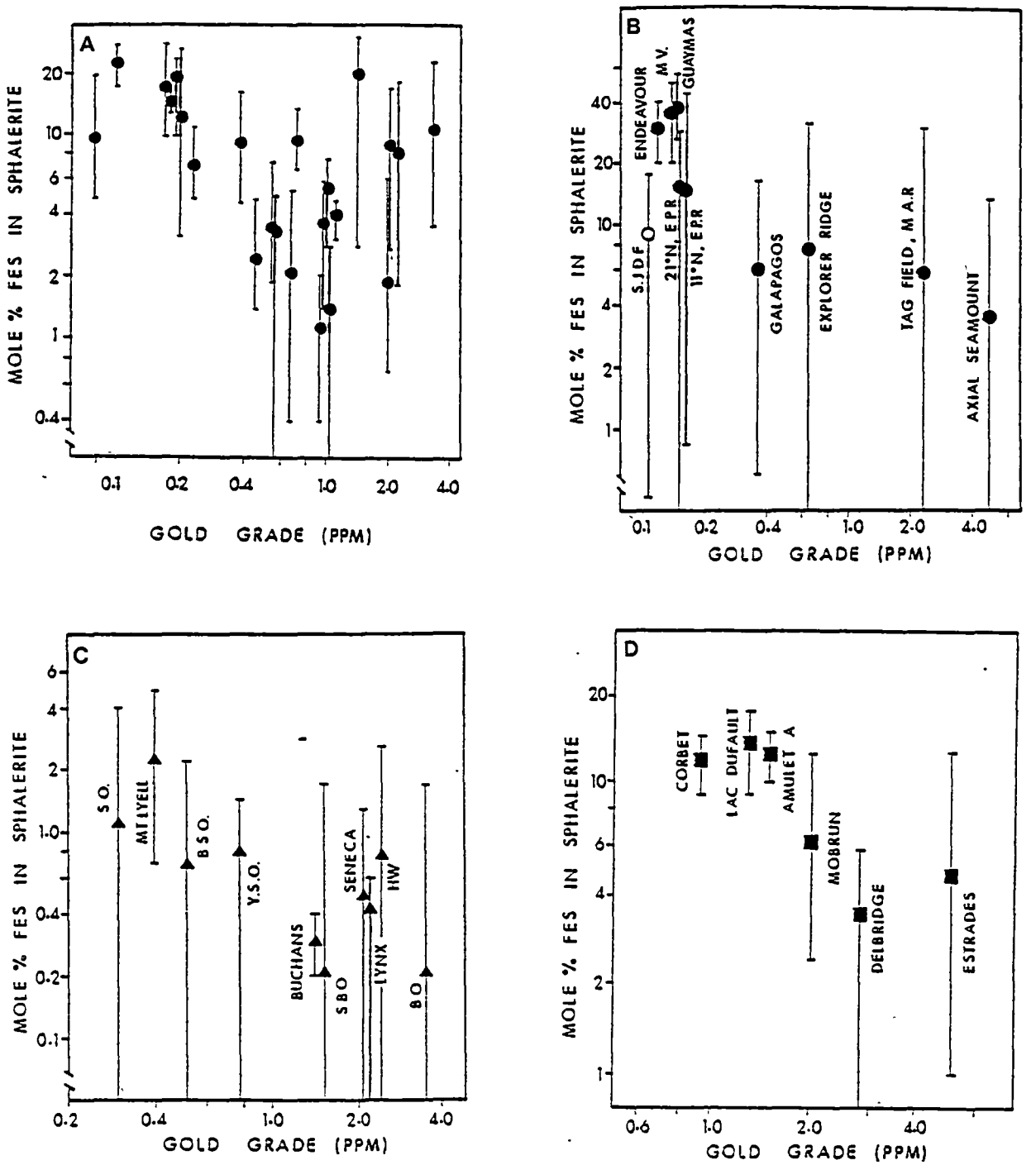


Fig. 8.7. A comparison of the *average* gold grade with FeS content in associated sphalerite. (A) Southern Explorer Ridge seafloor gold deposit, (B) group of individual modern seafloor gold deposits, (C) group of Phanerozoic Zn–Cu–Pb deposits in Japan (Kuroko deposits), Canada (Buchans, Seneca, Lynx and HW deposits) and Tasmania (Mt Lyell Cu–Au deposit). S.O.=siliceous ore, Y.S.O.=yellow siliceous ore, B.S.O.=black siliceous ore, S.B.O.=semi-black ore, and B.O.=black ore, and (D) Archean Cu–Zn deposits in northwest Quebec (after Hannington and Scott, 1989). Bars show range of sphalerite compositions.

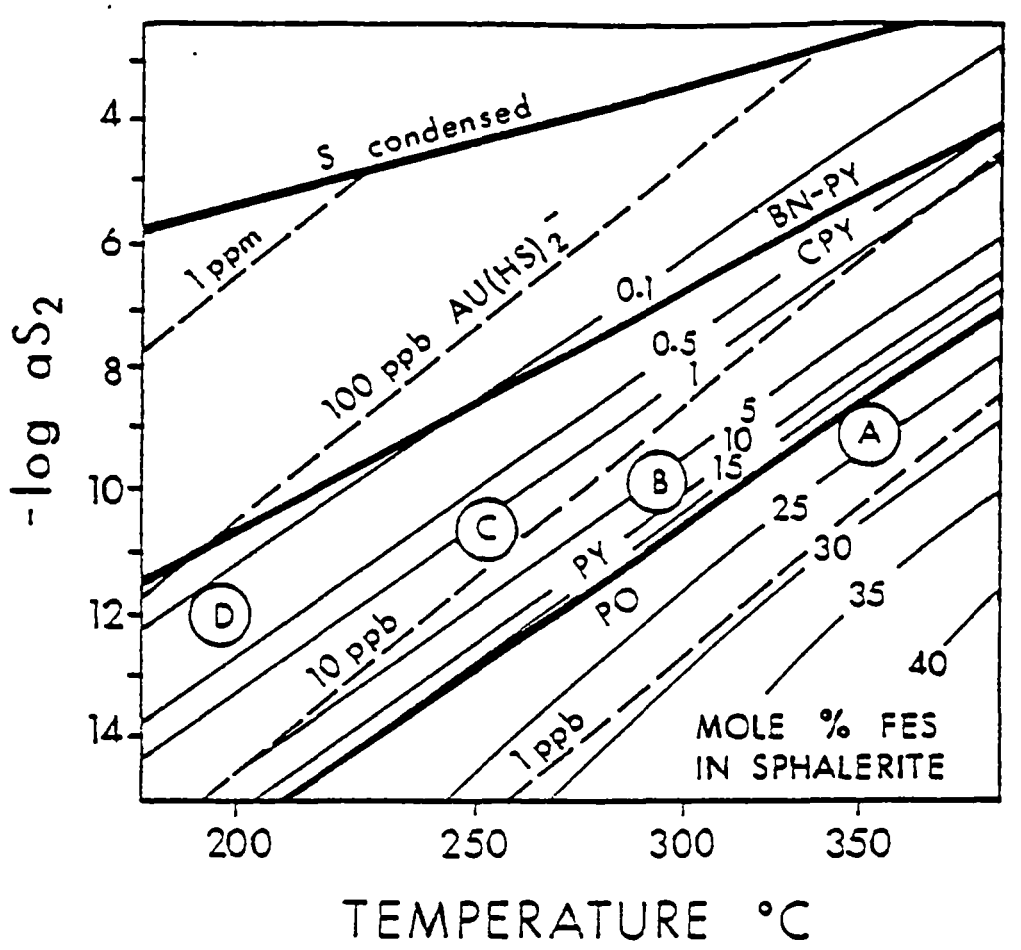


Fig. 8.8. Comparison of the composition of sphalerite with contours of $Au(HS)_2^-$ concentration (dashed lines). Contours of mole % FeS in sphalerite coexisting with the Fe sulphides (light solid lines) and the sulphidation boundaries for pyrite–pyrrhotite and bornite+pyrite–chalcopyrite (bold lines). Contours of $Au(HS)_2^-$ concentration are calculated at pH=5 and 250ppm $H_2S$. Higher $H_2S$ or pH will result in higher calculated concentrations of $Au(HS)_2^-$ for the same mole % FeS in sphalerite but will not affect the general correlation between gold solubility and sulphidation state (after Hannington and Scott, 1989). Note contours of mole % FeS in sphalerite are parallel to $Au(HS)_2^-$ concentration.

Average compositions of sphalerite and *average* gold grades from the Rosebery, Hercules and the South Hercules deposits are plotted in Fig. 8.11. Similar comparisons were made for Archean, Phanerozoic and modern seafloor massive sulphide deposits (Hannington and Scott, 1989). The comparison of the *average* mole % FeS in sphalerite with *average* gold grades of the massive sulphides at the Rosebery, Hercules and South Hercules deposits do not show any recognisable trends or relationships comparable with those recognised for Archean, Phanerozoic and modern seafloor massive sulphide deposits by Hannington and Scott (1989) (Fig. 8.7). The range of FeS content in sphalerite from the Rosebery–Hercules area is small and similar to those of the Archean and Phanerozoic deposits but different from the modern seafloor sulphide deposits.

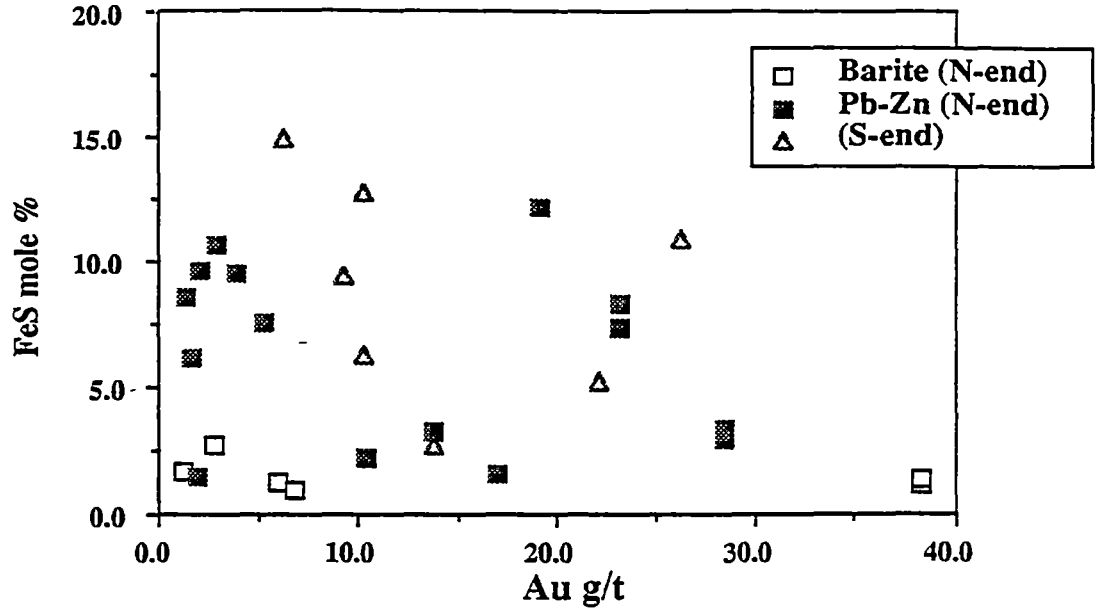


Fig. 8.9. Plot of *average* mole % FeS in sphalerite vs. gold grades (g/t) in the Rosebery barite zone and Pb–Zn zone, north-end and the F(J) lens, south-end, Rosebery mine, western Tasmania.

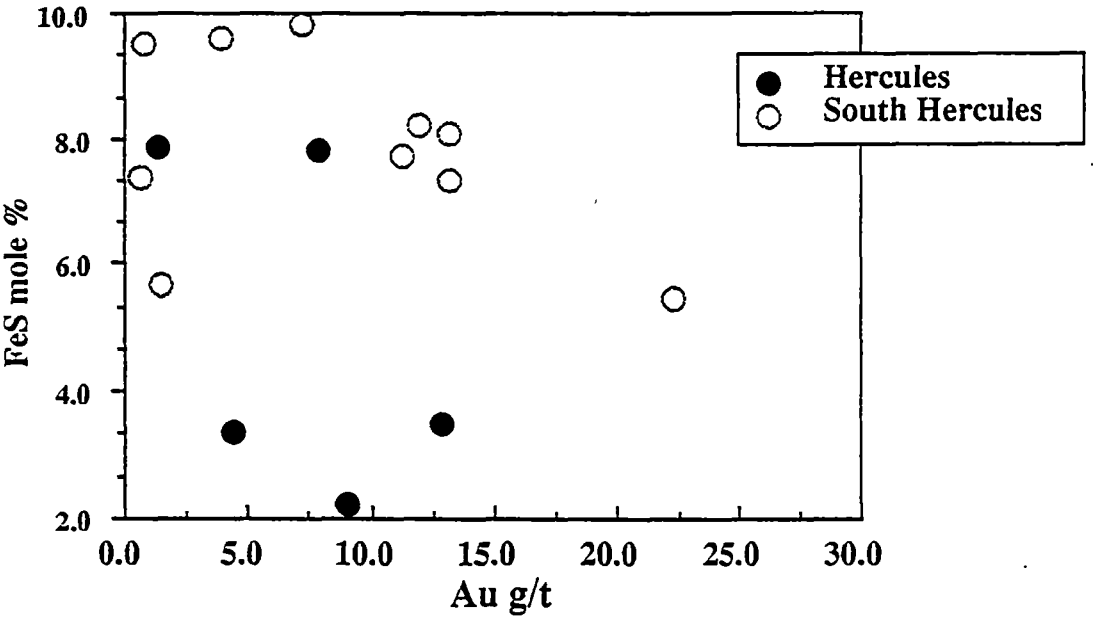


Fig. 8.10. Plot of *average* mole % FeS in sphalerite vs. Au grades (g/t) in the Hercules and South Hercules deposits, western Tasmania.

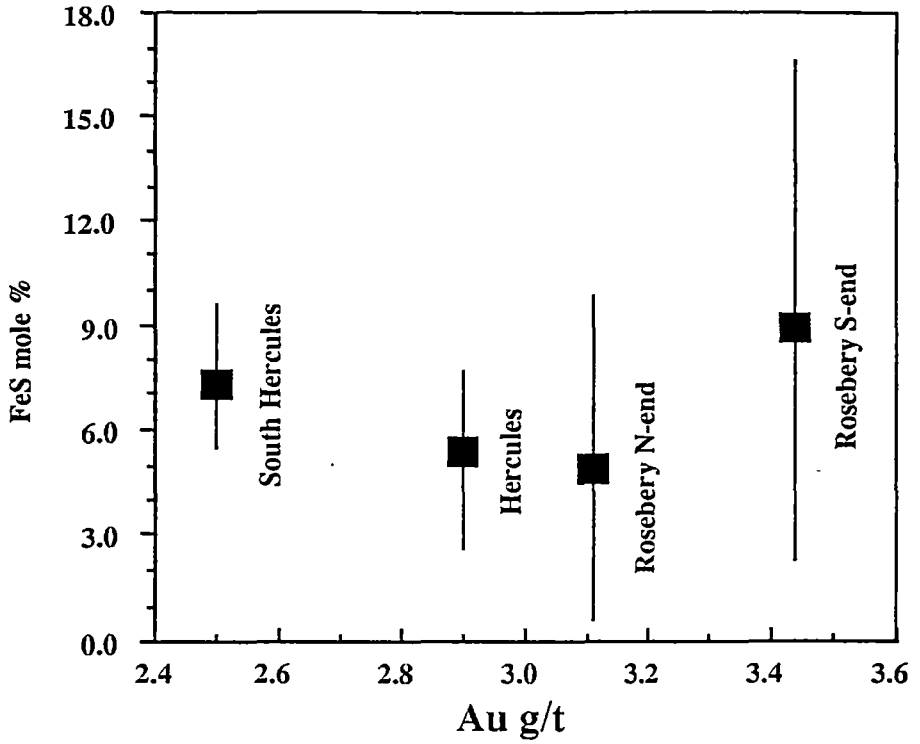


Fig. 8.11. Plot of the *average* production grade of gold versus the *average* FeS content in associated sphalerite, Rosebery, Hercules and South Hercules deposits, western Tasmania. Bars show the range of sphalerite compositions for each orebody.

### 8.9.3 Controls on gold deposition and remobilisation ...

The suggested correlation of the mole % FeS in sphalerite and the gold grades at South Hercules supports the premise that the transport and deposition of gold in these ores was controlled by bisulphide complexes (Huston and Large, 1989; Hannington and Scott, 1989). The solubility of $Au(HS)_2^-$ is partly dependent on the activity of sulphur ($a_{S2}$) which also controls the mole % FeS in sphalerite.

However, the overall trends for mole % FeS in sphalerite versus gold grades at the Rosebery, Hercules and South Hercules deposits appear to be much more complicated than those of the modern seafloor VMS deposits and the Phanerozoic and Archean deposits as described by Hannington and Scott (1989). These complex relationships can be accounted for by (1) the effect of later Devonian metamorphic and metasomatic recrystallistion on the FeS content of sphalerite (discussed further below) and (2) controls other than temperature and the activity of sulphur ($a_{S2}$) on the initial deposition of gold on the Cambrian seafloor.

The vague, general trend between the mole % FeS in the sphalerite and the gold grades above 5 g/t Au at the South Hercules deposit suggests that the initial, primary relationships of the mole % FeS in the sphalerite and the gold grades did not change, even though the deposit

was affected by later regional metamorphism related to the Devonian Tabberabberan Orogeny. However, Devonian granitoid-related metasomatism at the south-end of Rosebery possibly destroyed the mole % FeS in sphalerite versus gold relationships in the F(J) lens (Fig. 8.9). It is likely that the gold in the F(J) lens has been remobilised and recrystallised along with copper during the Devonian, probably as chloride complexes, resulting in no correlation between the mole % FeS in sphalerite and the gold mineralisation as the gold deposition was no longer controlled by the activity of sulphur ($a_{S2}$).

The other possible cause for the complex pattern of the mole % FeS in sphalerite and the gold mineralisation in the Rosebery–Hercules deposits is that factors other than temperature and ($a_{S2}$) controlled the transport and deposition of gold during Cambrian mineralisation. One such factor is pH which Huston and Large (1989) suggested was important. To illustrate the importance of pH in affecting gold solubility, at point A in Fig. 8.12, a fluid with ($a_{S2} = 10^{-9}$) can carry only ~300 ppb gold in solution at a pH of 6, whereas at point B in Fig. 8.12, a fluid with ($a_{S2} = 10^{-9}$) can carry ~30 ppb gold in solution at a pH of 5. As Hannington and Scott (1989) indicate that the pH in active, seafloor VMS deposits can vary from 3.5 to 5.5, pH must be an additional factor in controlling gold grades in VMS deposits. Although the correlation noted by Hannington and Scott (1989) may apply broadly, the complexities caused by changing pH and $f_{O2}$ of the fluids result in a breakdown of the correlation between gold grade and $a_{S2}$ (i.e. $X_{FeS}$) on a deposit or even district scale, as observed at Rosebery, Hercules and South Hercules.

## 8.10 Discussion of Cambrian versus Devonian mineralisation ...

This study has shown that the sphalerite from the Cambrian VMS deposits has lower Zn/Mn ratios (<600) and higher Zn/Cd ratios (>250) than the sphalerite from the Devonian granite-related Pb–Zn deposits in western Tasmania.

The Zn/Cd ratio of sphalerite has been proposed as genetic indicator for ore deposits by Jonasson and Sangster (1978), who observed an average ratio of 377 for sphalerite from Canadian Cu–Zn deposits of volcanosedimentary association, and an average Zn/Cd ratio of 117 for the Canadian vein-type deposits. Xuexin (1984) also calculated the Zn/Cd ratio of sphalerite compositional data available from the literature and reported that the highest Zn/Cd ratios (417–531) occur in sphalerite of volcanosedimentary type, while sphalerite from skarn deposits displays the lowest values (102–214). Hence the Zn/Cd ratio in sphalerite from veins and skarns of magmatic–hydrothermal deposits tends to be lower than that of volcanogenic ores. This is consistent with the Zn/Cd values of the sphalerite from the Cambrian volcanogenic

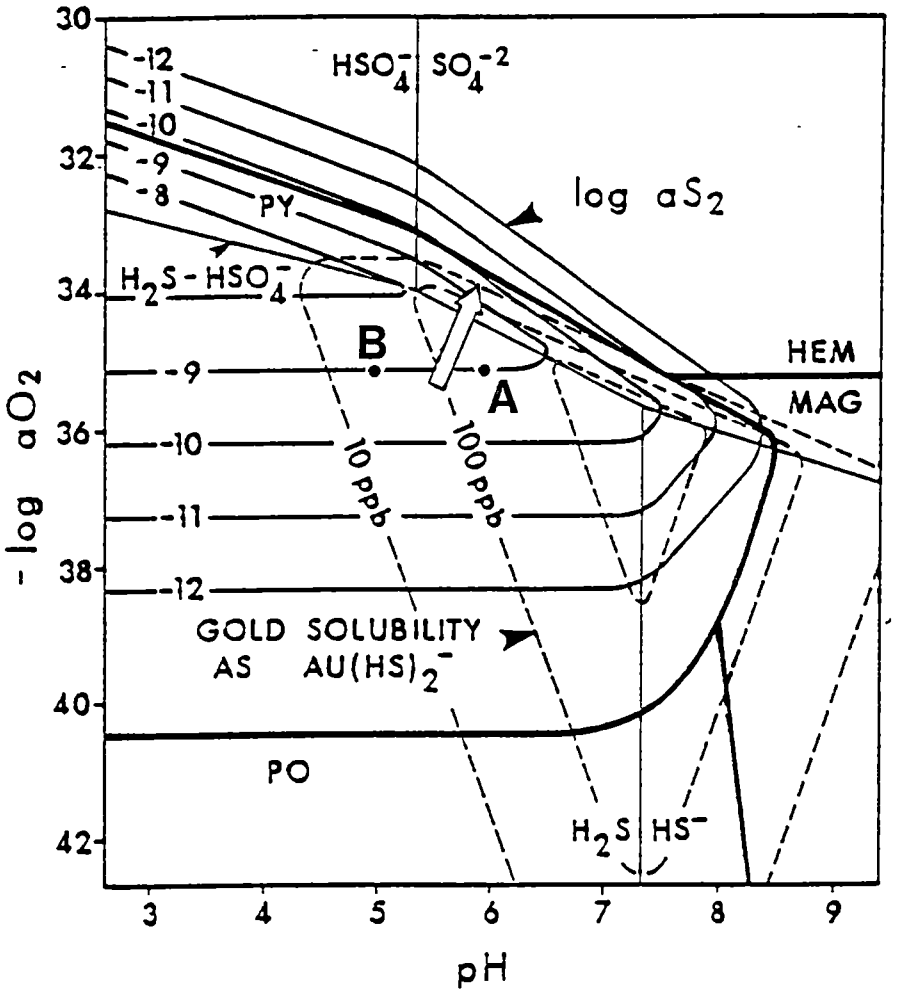


Fig. 8.12. $a_{O2}$-pH diagram showing the calculated solubility of gold as $Au(HS)^-_2$ in hydrothermal fluid at 250°C, $\Sigma H_2S=10^{-2.5}m$. Arrow denotes gold deposition by changes in $a_{S2}$ (after Hannington and Scott, 1989). Note changes in gold solubility control by changes in pH; fluid with ($a_{S22}=10^{-9}$) can carry ~300 ppb gold in solution at pH of 6 (at point A ), whereas fluid with ($a_{S2}=10^{-9}$) can carry ~30 ppb gold in solution at pH of 5 (at point B). PO=pyrrhotite, PY=pyrite, HEM=hematite, MAG=magnetite.

sulphides and the sphalerite from the granite-related, Devonian lead–zinc vein deposits in western Tasmania.

The apparent enrichment of manganese in the Cambrian VMS sphalerite and of cadmium in the Devonian sphalerite may depend on (1) post-depositional re-equilibration, (2) the initial conditions of sphalerite deposition such as T, P, and the activity of sulphur ($a_{S2}$), and (3) the source of the ore fluids and metals. Although the sphalerite of Cambrian origin has been affected by later Devonian recrystallisation, the manganese and cadmium content of the sphalerite may not have been changed significantly during the later recrystallisation. Scott and Barnes (1971) and Scott (1973) noted that minor elements up to several mole % in sphalerite do not affect the Zn–Fe–S system by changes in conditions such as temperature, pressure, and the activity of sulphur ($a_{S2}$).

The above argument can also be applied in relation to the differences in initial physico-chemical conditions during the deposition of the Cambrian and Devonian sphalerite. Although the temperature may have been higher for the Devonian sphalerite deposition, the overall abundance of minor elements in the sphalerite would not have been affected as the concentration of minor elements in sphalerite is independent of depositional conditions (Scott and Barnes, 1971; Scott, 1973). In addition, both Cambrian and Devonian sphalerite displays similar ranges of mole % FeS (up to 25.0 %) suggesting that the activity of sulphur ($a_{S2}$) during the deposition of both sphalerite types was broadly similar.

The most plausible cause of the differing manganese and cadmium contents in the Cambrian and Devonian sphalerites is the source region: the Devonian sphalerite is probably enriched in cadmium because the fluid came from a granitoid, whereas the Cambrian sphalerite has elevated manganese because the fluids were of seawater origin and reacted with manganese-bearing volcanic rocks. Manganese-rich rocks have also been reported in association with other stratiform base metal sulphide deposits (e.g. Gamsberg, South Africa, Stumpfl, 1979; Broken Hill, Australia, Spry, 1989; Spry and Wonder, 1989) and manganese anomalies have been used as guides to mineralisation (Wonder et al., 1988).

Spry and Wonder (1989) recently inferred, on the basis of thermodynamic calculations and geochemical studies, that the overall increase in Mn/Fe from the stratigraphic footwall to hangingwall in the Broken Hill deposit reflects an increase in $f_{O2}$ during mixing of the hydrothermal solution with seawater. In the Rosebery–Hercules area, Mn–carbonates (rhodocrosite, kutnahorite) are very common in the host rock and ore zone (Brathwaite, 1969, 1974; Dixon, 1980; also see Chapter 9), and may similarly result from mixing of the hydrothermal fluids with seawater under moderate to high oxidation conditions.

## 8.11 SUMMARY ...

Sphalerite grains from Cambrian and Devonian lead–zinc sulphide deposits in western Tasmania have different minor elements ratios that reflect different sources of the ore fluids. Cambrian sphalerite has an elevated manganese content owing to precipitation from fluids of seawater origin which have interacted with manganese-bearing volcanics, whereas Devonian sphalerite is enriched in cadmium because the source fluid was from Devonian granitoids. Sphalerite from the Cambrian volcanogenic massive sulphide deposits of Rosebery, Hercules and South Hercules were variably affected by the Devonian overprints resulting in a redistribution of FeS in the sphalerite.

The post-depositional variation of FeS in sphalerite in equilibrium with pyrrhotite and pyrite has enabled the use of the sphalerite geobarometer to estimate the depth conditions during the Devonian replacement processes at Rosebery. The calculated pressure is $3.0 \pm 1.0$ kbar for the re-equilibration of sphalerite in the F(J) lens which would correspond to $8.0 \pm 0.5$ km depth.

The complex relationship between mole % FeS in sphalerite and gold grades at Rosebery, Hercules and South Hercules is probably due to the redistribution of FeS in sphalerite during the Devonian metamorphic and metasomatic events, but it also indicates that initial deposition of gold on the seafloor was controlled by factors other than temperature and the activity of sulphur ($a_{S2}$)

# CHAPTER 9: STABLE ISOTOPE GEOCHEMISTRY

## 9.1 INTRODUCTION ...

A stable isotope study of the Rosebery, Hercules and South Hercules deposits was undertaken to investigate fluid–rock interaction and the source of the hydrothermal fluids involved in Cambrian mineralisation and the later Devonian replacement processes. Carbonate minerals from the three deposits were analysed for their oxygen and carbon isotopic composition, and oxygen isotopic compositions of selected minerals (quartz, chlorite, biotite, tourmaline and magnetite) were also measured. The sulphur isotopic compositions of the sulphide minerals from South Hercules and Rosebery south-end were also determined.

## 9.2 ANALYTICAL TECHNIQUES ...

Conventional procedures were employed to analyse the isotopic values of hydrothermal minerals from the deposits. The isotope ratio measurements were carried out on a VG Micromass 602D mass spectrometer in the Central Science Laboratory, University of Tasmania. Carbonate minerals were reacted with $H_3PO_4$ at 25°C to liberate $CO_2$ as described by McCrea (1950) and isotopic abundance ratios were measured and reported according to conventional notation as $\delta$ values in per mil (‰). The oxygen standard is Standard Mean Ocean Water (SMOW) and the carbon standard is the Cretaceous Peedee Belemnite (PDB). The analytical precision of $\delta^{13}C$ and $\delta^{18}O$ values in carbonates is estimated to be less than ±0.1‰.

Oxygen isotope analyses for silicate minerals employed standard procedures: initial reaction for 12 hours with $BrF_5$ at 520°C in evacuated nickel reaction vessels (Clayton and Mayeda, 1963), followed by conversion of the liberated oxygen to $CO_2$ by reaction with hot graphite as described by Taylor and Epstein (1962). Results are expressed in the standard $\delta$ values in per mil (‰) notation against SMOW. An internal standard, UT quartz, was run frequently and has been calibrated against the international isotope standard NBS-28. Duplicate samples have shown a precision of ±0.2‰.

For the sulphur isotope analysis, drilled sulphide mineral separates were combusted with excess $Cu_2O$ in vacuo to produce $SO_2$ (Robinson and Kusakabe, 1975) and the sulphur gas

was again separated to determine the $^{34}S/^{32}S$ ratios. The results are expressed in standard ($\delta$) notation in $\delta$ (‰) relative to Canyon Diablo Troilite (CDT). The analytical uncertainty is estimated to be ±0.2 per mil (‰). Sulphur isotope analyses for the sulphide minerals and oxygen and carbon isotopes for the carbonates were performed by the author, and Michael Power Jr. analysed all the other individual silicate and oxide minerals for their oxygen isotope ratios.

## 9.3 OXYGEN AND CARBON ISOTOPIC VALUE OF CARBONATES ...

In recent years, oxygen and carbon isotopic ratios of carbonates from hydrothermal ore deposits have been investigated to provide the physico-chemical constraints on the environment of ore deposition (e.g. for shale-hosted, Pb–Zn deposits in the MacArthur River region, Northern Territory, by Rye and Williams, 1981; Mississippi Valley-type deposits by Ravenhurst et al., 1987; Canadian Archean lode gold deposits by King and Kerrich, 1987; Australian Archean gold deposits by Golding et al., 1989; Proterozoic Au–Cu deposits at Starra, Queensland by Davidson, 1990). Application of carbon isotopic investigations for a variety of different types of ore deposits has also been reviewed by Rye and Ohmoto (1974), Ohmoto and Rye (1979) and Ohmoto (1986), but no detailed studies on the isotopic variation of carbonates associated with VMS deposits carbonates are recorded in the literature.

In this study, eleven carbonate samples from the Rosebery mine, eight samples from the Hercules mine, including one sample from M lens, and ten samples from the South Hercules deposit were analysed for $\delta^{18}O$ and $\delta^{13}C$ values. The results are listed in Appendix 9.1 together with additional data from the Rosebery Mine (Dixon, 1980) and from the Cleveland and Renison Bell tin–sulphide deposits, western Tasmania (Collins, 1981; Patterson et al., 1981).

An oxygen and carbon isotopic study of the carbonates in western Tasmania was initially undertaken by Dixon (1980) for the Rosebery orebody but his interpretation concentrated on the physico-chemical conditions ($f_{O2}$ and pH) of the venting hydrothermal fluids. In contrast, the aims of this study are to use the oxygen and carbon isotopic composition of the carbonates as an aid in defining the Cambrian and Devonian ore forming environments in the Rosebery–Hercules area, and also to apply the oxygen and carbon isotopic composition as a means of understanding the fluid–rock interaction during the evolution of hydrothermal processes of both Cambrian and Devonian origin. Initial results were presented at 7th International Isotope Geology Conference, Canberra (Khin Zaw and Large, 1990).

### 9.3.1 $\delta^{18}O$ value in carbonate minerals ...

Figure 9.1 shows a histogram of the $\delta^{18}O$ value of the carbonates from the Rosebery, Hercules and the South Hercules deposits. The $\delta^{18}O$ value of the carbonate minerals from the Rosebery

north-end range from +10.6‰ to +12.4‰, and the $\delta^{18}O$ values of the carbonate minerals from the Rosebery south-end vary from +10.6‰ to +13.5‰. In comparison, the $\delta^{18}O$ values of carbonate minerals from the main Hercules ore lenses range from +8.7‰ to +14.3‰, and the $\delta^{18}O$ values of carbonate minerals from the South Hercules deposit range from +9.8‰ to +16.7‰ (Fig. 9.1).

### 9.3.2 $\delta^{13}C$ value in carbonate minerals ...

Fig. 9.2 shows a histogram of $\delta^{13}C$ values in carbonate minerals from the Rosebery, Hercules and South Hercules deposits. The $\delta^{13}C$ values of carbonate minerals from the Rosebery north-end range from –8.8‰ to –0.6‰, and the $\delta^{13}C$ values of carbonate minerals from the Rosebery south-end vary from –6.8‰ to –1.5‰. In comparison, the $\delta^{13}C$ values of carbonate minerals from the main Hercules ore lenses range from –3.3‰ to –0.5‰ and the $\delta^{13}C$ values of carbonate minerals from the South Hercules deposit range from –3.5‰ to +0.6‰ (Fig. 9.2).

### 9.3.3 $\delta^{18}O$ and $\delta^{13}C$ variation in different textural types of carbonates ...

Figures 9.3 and 9.4 show the oxygen and carbon isotopic data of the different textural types of Cambrian hydrothermal carbonates from the Rosebery north- and south-ends. No consistent differences in isotopic compositions were noted between the textural types and no statistically significant correlation between $\delta^{13}C$ and $\delta^{18}O$ values was recorded in the samples analysed.

The carbon and oxygen isotopic data for the hydrothermal carbonates from the Hercules and South Hercules deposits, including data for the one carbonate sample from M lens are shown in Figs. 9.5–9.6. The carbon and oxygen isotopic values of the different carbonates from the Hercules deposit gave a statistically significant (90% confidence level) correlation coefficient of 0.52 (Fig. 9.5), and $\delta^{13}C$ and $\delta^{18}O$ values from the South Hercules deposit have a more significant correlation coefficient of 0.91 (Fig. 9.6). All textural types of carbonate occur along these trends.

### 9.3.4 Implication of $\delta^{18}O$ and $\delta^{13}C$ values of carbonates ...

The interpretation of the oxygen and carbon isotopic data of the carbonates from the Rosebery, Hercules and South Hercules deposits, as well as the oxygen and carbon isotope systematics of carbonates in western Tasmania, should be considered within the following geological constraints. Although various occurrences of carbonate minerals can be expected in western Tasmania, two broad generations are probable: (1) carbonates of Cambrian origin and (2) carbonates of Devonian origin.

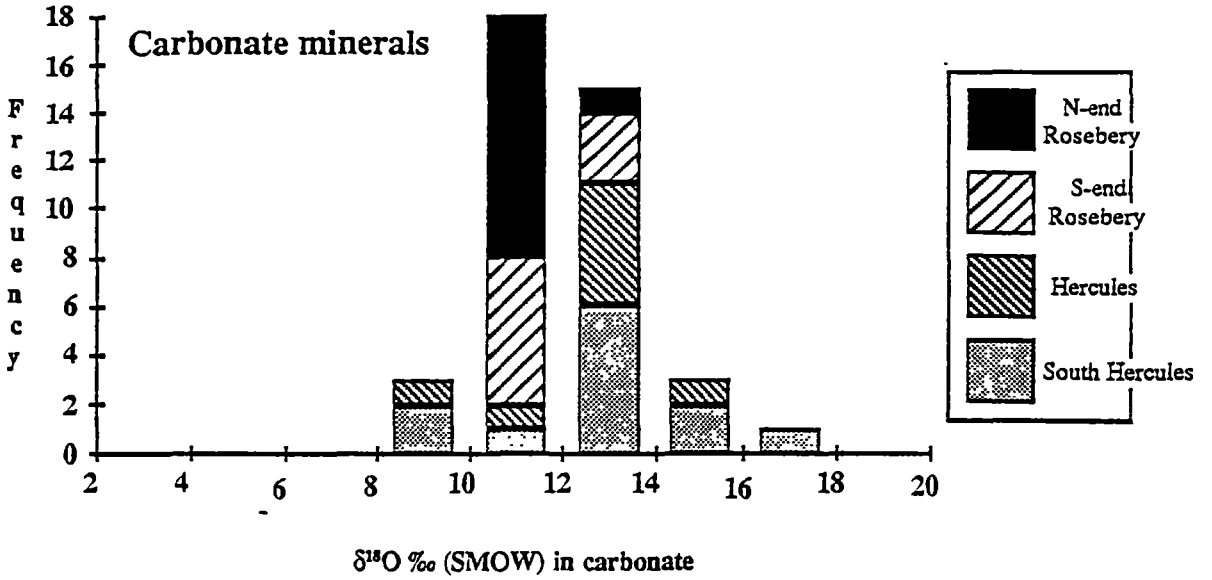


Fig. 9.1. Histogram showing $\delta^{18}O$ values of carbonate minerals from the Rosebery north- and south-ends, Hercules and South Hercules deposits, western Tasmania.

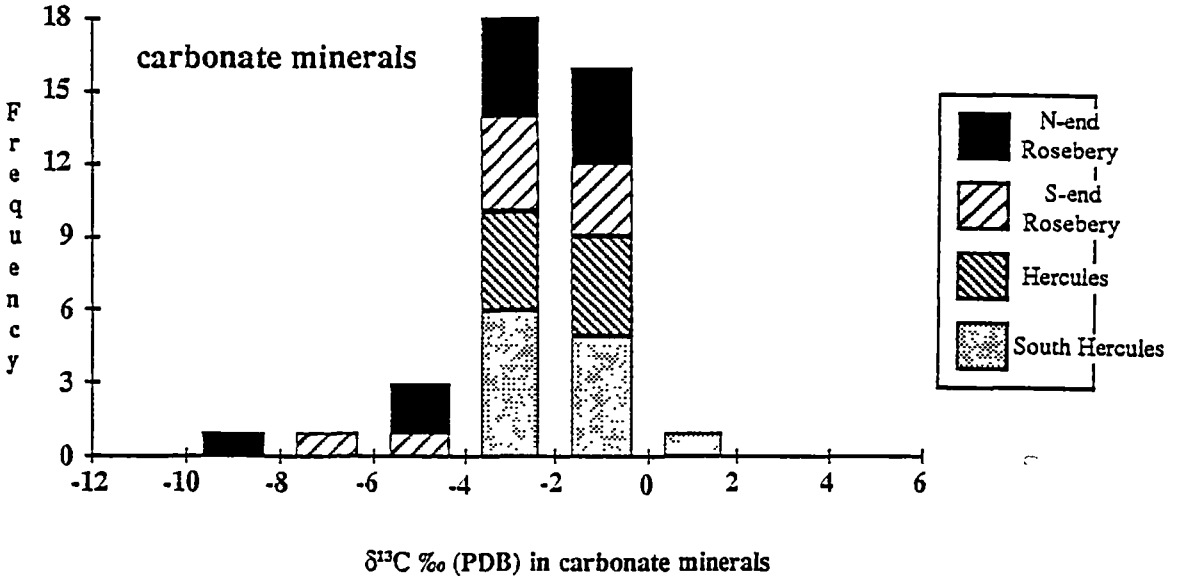


Fig. 9.2. Histogram showing $\delta^{13}C$ values of carbonate minerals from the Rosebery north- and south-ends, Hercules and South Hercules deposit, western Tasmania.

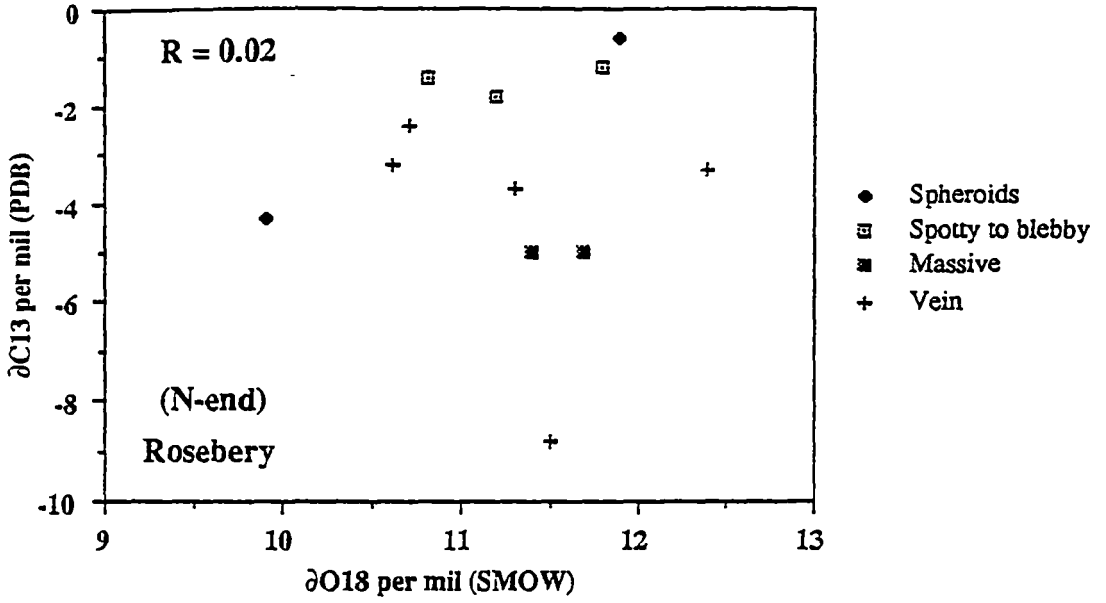


Fig. 9.3 Plot of $\delta^{18}O$ and $\delta^{13}C$ values of the Cambrian hydrothermal carbonates from the north-end of the Rosebery deposit, western Tasmania.

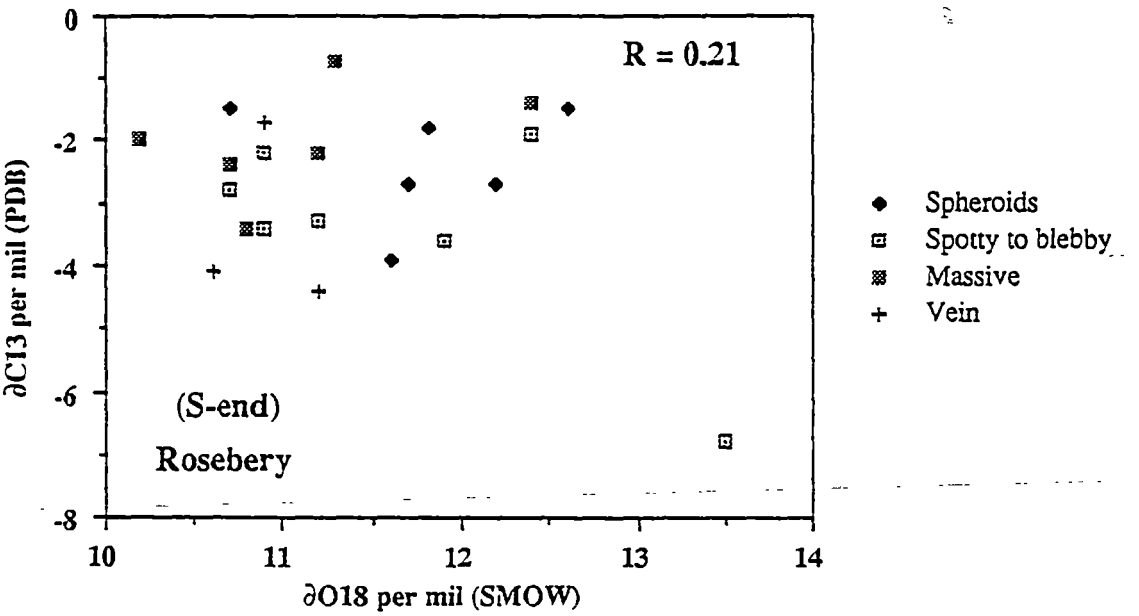


Fig. 9.4. Plot of $\delta^{18}O$ and $\delta^{13}C$ values of the Cambrian hydrothermal carbonates from the south-end of the Rosebery deposit, western Tasmania.

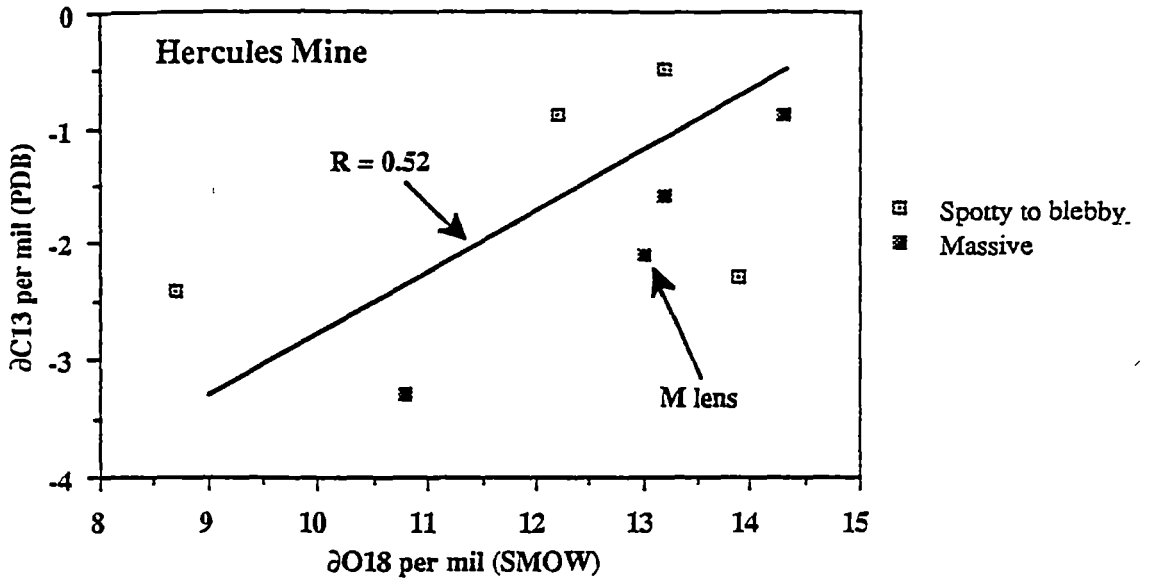


Fig. 9.5 Plot of $\delta^{18}O$ and $\delta^{13}C$ values of the Cambrian hydrothermal carbonates from the Hercules deposit, western Tasmania.

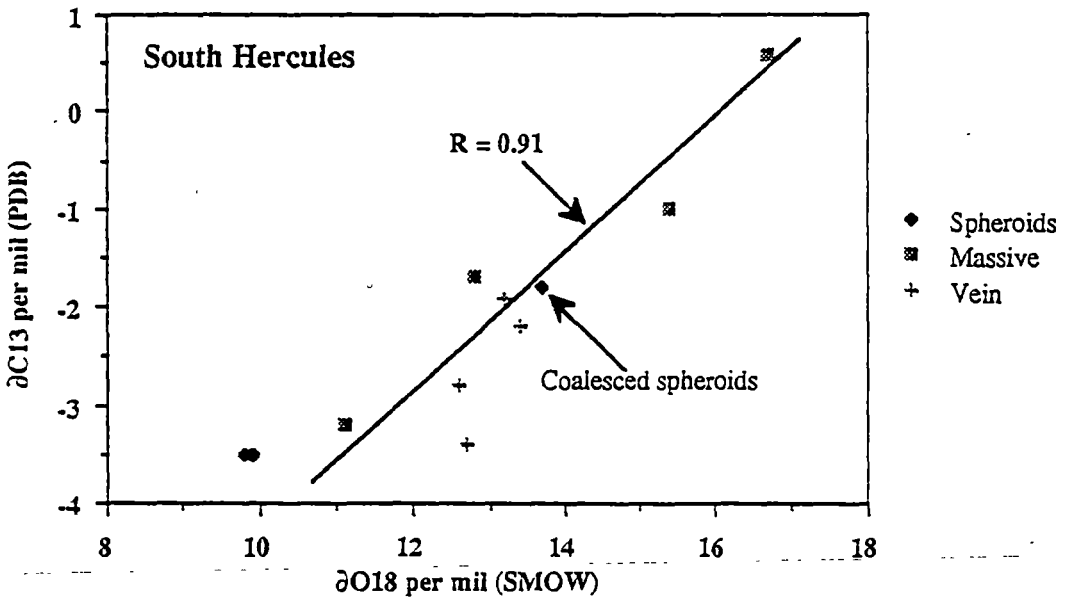


Fig. 9.6 Plot of $\delta^{18}O$ and $\delta^{13}C$ values of the Cambrian hydrothermal carbonates from the South Hercules deposit, western Tasmania.

(1) Carbonates of Cambrian origin are of two possible types;

(a) Primary (sedimentary ?) carbonate intercalated with volcanic and volcaniclastic rocks of Cambrian age in western Tasmania.

(b) Hydrothermal carbonate related to volcanogenic processes in association with massive sulphide deposits formed during submarine Cambrian volcanism. At the time of this ore-forming volcanic exhalation, primary (sedimentary ?) carbonate may re-equilibrate with the hydrothermal carbonate.

(2) Carbonates of Devonian origin:

During the Devonian granite intrusion, an additional new type of hydrothermal carbonate was generated within the aureole of the granites (e.g. vein carbonates at the Renison Bell deposit, Patterson et al., 1981).

The Cambrian carbonates may have also suffered isotopic exchange as follows:

(a) Isotopic exchange of Cambrian carbonates by interaction with magmatic fluids associated with the Cambrian granitoid intrusion. Presently available geological and isotopic evidence suggests that the age of Cambrian granitoid magmatism is post Rosebery ore formation (e.g. Adams et al., 1985) and thus there may have been later isotopic exchange of magmatic fluid and Cambrian carbonates.

(b) During the Devonian Tabberabberan Orogeny the recrystallisation of Cambrian carbonates may have equilibrated with Devonian fluids of metamorphic and/or metasomatic origin.

It is important to note that the isotopic ratios of the whole rock as well as individual minerals can vary according to conditions of the subsequent geological environment even if the rocks have equilibrated with a common fluid (Valley, 1986). The oxygen isotope composition of the whole rock samples from western Tasmania can be varied by (1) differences in mineral assemblages, (2) differences in the initial oxygen isotopic compositions and (3) difference in the extent of alteration overprints and post-cleavage veining. Green (1990b, 1990c) recently completed a detailed investigation on the rock alteration, mineral and oxygen isotope zonation in the Rosebery area and suggested that an integrated textural and mineralogical investigation is needed to apply oxygen isotopic systematics in order to infer the presence of Cambrian mineralisation and alteration and to deduce the extent of the Devonian overprinting event in western Tasmania.

The difference in oxygen and carbon isotope systematics of the individual carbonate minerals from the Rosebery, Hercules, and South Hercules deposits may provide insights into the isotopic exchange reflecting differences in the primary volcanogenic environment of ore

formation and/or the differing effect of the Devonian overprinting process. To infer such an isotopic exchange, the oxygen and carbon isotopic ratios of the carbonates from the north- and south-ends of the Rosebery deposit are plotted in Fig. 9.7 regardless of their textural variation.

As shown in Fig. 9.7, the isotopic compositions of the carbonates from the north- and south-ends of the Rosebery deposit are tightly constrained. Only one sample from the north-end and one sample from the F(J) lens of the south-end show unusual low $\delta^{13}C$ values. The nature of these anomalously depleted carbon isotopic ratios is not known, but may suggest the involvement of reduced organic carbon during the formation of the hydrothermal carbonates at the time of Cambrian volcanogenic mineralisation.

The $\delta^{13}C$ and $\delta^{18}O$ values of the carbonates from both the Hercules and South Hercules deposits are plotted together in Fig. 9.8. Regardless of the carbonate types these deposits show similar isotopic trends. The different isotopic distribution patterns of these VMS carbonates (tight cluster for Rosebery and linear trends for Hercules–South Hercules) are discussed below;

Similar isotopic patterns between the north-end and south-end of the Rosebery deposit suggests *either* (a) the pattern represents Cambrian volcanogenic processes and no later change has taken place *or* (b) $\delta^{18}O$ (and possibly $\delta^{13}C$ values) have been changed (or homogenised?) during the Devonian. Alternative (a) appears to be more likely as the tight cluster of the isotopic compositions at both the north- and south-ends of the Rosebery deposit implies that no later isotopic changes have taken place even though the south-end of the Rosebery deposit has been strongly overprinted by the high temperature (>300°C), pervasive Devonian replacement process.

The Hercules and South Hercules deposits lie further away from the Devonian granite intrusion and have not been strongly overprinted by the high temperature (>300°C), Devonian metasomatic process as evidenced by the lack of garnet–biotite–helvite assemblages in these deposits. However, these two orebodies have been affected by Devonian metamorphism. Fluid inclusion studies at the South Hercules deposit suggest that Devonian metamorphic recrystallisation occurred at temperatures below 300°C (Chapter 10) which appears to have been insufficient to appreciably change the isotopic composition of the carbonates. This is consistent with the proposition made by O'Neill (1987, p. 99) that '...well crystallised, large-grained, and mineralogically stable form of carbonate minerals are inert to exchange at low temperature'. These isotopic trends may reflect the primary volcanogenic isotopic characteristics and the spread represents the effect of a temperature gradient during Cambrian mineralisation. Rye and Ohmoto (1974) also indicated that hydrothermal carbonates are extremely resistant to isotopic exchange.

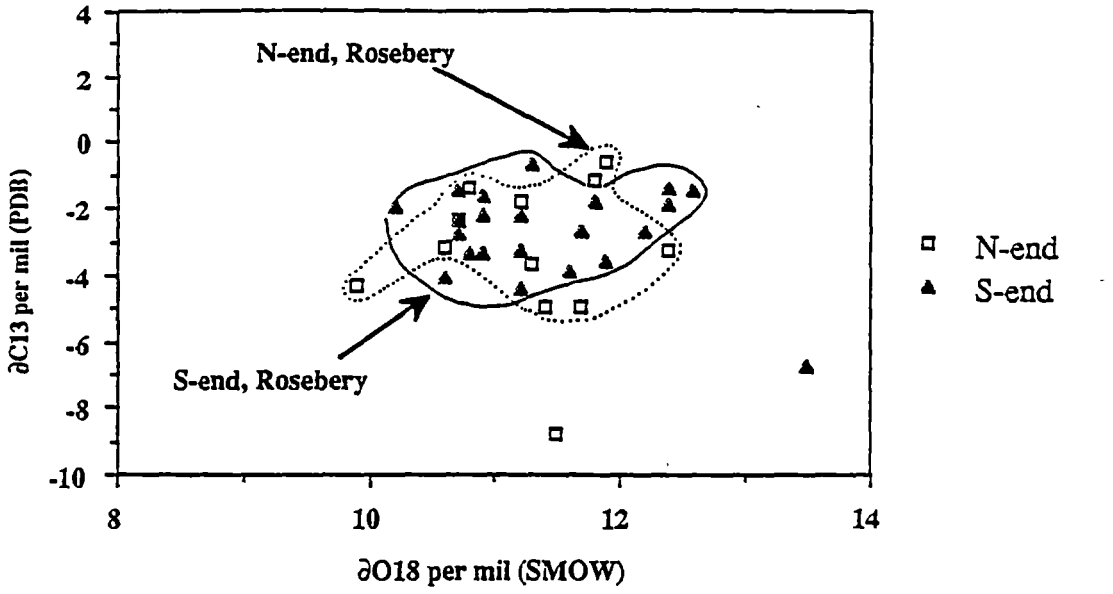


Fig. 9.7. Plot of $\delta^{18}O$ and $\delta^{13}C$ values of the Cambrian hydrothermal carbonates from the north- and south-ends of the Rosebery deposit, western Tasmania.

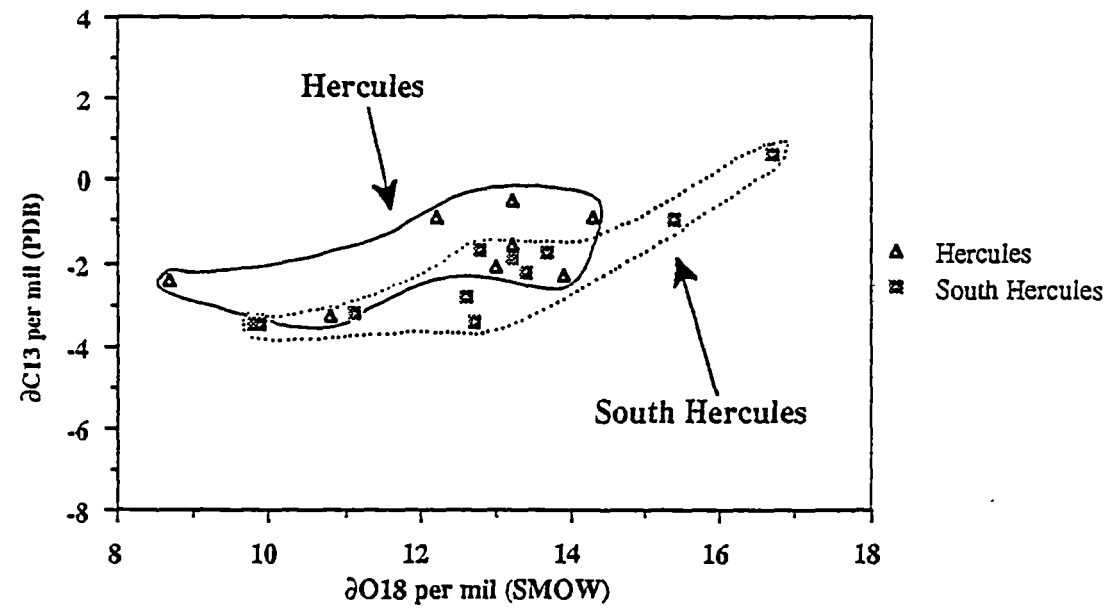


Fig. 9.8. Plot of $\delta^{18}O$ and $\delta^{13}C$ values of the Cambrian hydrothermal carbonates from the Hercules and South Hercules deposits, western Tasmania.

Ohmoto and Rye (1979) noted increasing $\delta^{13}C$ values in carbonate minerals formed in the later stages of the mineralisation for certain types of ore deposits (mostly of veins and skarns) and suggested that such a trend may be produced by (1) decreasing temperature (2) changes in $CO_2/CH_4$ ratios in the ore-forming fluids and/or 3) increasing contribution of $CO_2$ from other sources. Rye and Williams (1981) also recognised an increasing trend of $\delta^{13}C$ and $\delta^{18}O$ values from carbonates in the shale-hosted, Pb–Zn deposits in the MacArthur River region of the Northern Territory and considered that the isotopic trend was related to decreasing temperature.

The recognisable trends of $\delta^{13}C$ and $\delta^{18}O$ values of carbonates to heavier values in Fig. 9.8 may also be related to decreasing temperature during the later stages of Cambrian mineralisation and carbonate alteration. Other evidence cited in Chapters 5 and 10 suggests that the South Hercules deposit may have formed at lower temperatures compared to the Rosebery and Hercules deposits. With regard to Ohmoto and Rye's other suggestions (2) and (3) above, the presence of $CO_2$ was documented during the heating/freezing and the laser Raman spectroscopic investigation of the fluid inclusions (Chapter 10), but no $CH_4$ was recorded and no trends of increasing contribution of $CO_2$ nor changes in $CO_2/CH_4$ ratios were recognised.

Eastoe and Nelson (1988) considered that carbonates from Permian VMS deposits in Shasta County, California have (re)-equilibrated with magmatic fluid at 250-350°C or with seawater at 80-100°C. However, temperature variation (cooling) can be interpreted from the spread of $\delta^{13}C$ and $\delta^{18}O$ values of the carbonates from the Rosebery-Hercules area. Mixing of seawater and magmatic water is possible in the Rosebery-Hercules area, but the calculated isotopic values of volcanogenic fluids do not clearly show fractionation trend joining field boundaries of seawater and magmatic water (Figs. 9.13, 9.14 and 9.19).

## 9.4 EFFECT OF MAJOR AND TRACE ELEMENTS ON ISOTOPE SYSTEMATICS OF CARBONATES ...

In this study, major and trace elements (Ca, Mn, Mg, Fe, Na, and Sr) of the carbonate samples were analysed to investigate the effect of the compositional variation of carbonates on the $\delta^{13}C$ and $\delta^{18}O$ values of the carbonates.

### 9.4.1 Compositional variation of carbonates ...

The compositional variation of the VMS carbonates at the Rosebery deposit was first investigated by Brathwaite (1969, 1974) who reported that the different carbonate types at Rosebery are, in order of abundance: rhodochrosite, ferroan rhodochrosite, kutnahorite, dolomite and calcite. Brathwaite (1969, 1974) determined the composition of carbonates by a combination of X-ray diffraction and refractive index measurements following the method described by Prinz (1964).

In this study, the carbonates were analysed by atomic absorption spectrophotometric methods (AAS) after digestion with *6m* HCl using splits from samples used for isotope analyses. No microprobe analyses of the carbonates were undertaken as these analyses only provide compositional data on individual grains. Fe content can only be determined in pure carbonate separates by AAS and leaching of Fe from other minerals such as pyrite and chlorite was noted. The compositions of carbonates determined in this study are listed in Appendix 9.2 and shown in Figs. 9.9 and 9.10. The carbonate minerals dominantly fall on the calcite–rhodochrosite join.

The carbonates from Rosebery contain considerable magnesium. The carbonate minerals from Hercules have virtually no iron content, whereas the carbonates from Rosebery north- and south-ends and South Hercules have minor iron. The carbonates from Hercules and South Hercules are consistently more Mn-rich (up to 38.2 wt % Mn), than the carbonates from Rosebery.

### 9.4.2 Composition vs. isotopic variation of carbonates ...

The composition versus $\delta^{18}O$ and $\delta^{13}C$ values of the VMS carbonates are plotted in Figs. 9.11 and 9.12. The plots of oxygen and carbon isotope values against most of the major and trace element concentrations indicate no obvious correlations. However, a pattern of slightly increasing $\delta^{18}O$ values with increasing Mn content can be interpreted from the data (Fig. 9.11B). Mn-poor calcites show a narrow variation in $\delta^{18}O$ (10–12‰) while the Fe, Mg-poor calcite–rhodochrosite carbonates show a wide variation in $\delta^{18}O$ (8–17‰). Similarly the Fe, Mg-poor Ca–Mn carbonates show the widest variation in $\delta^{13}C$ (–9 to +1‰).

Figure 9.13 shows a plot of $\delta^{18}O$ and $\delta^{13}C$ values of the VMS carbonates with Mn content less than 25 wt %, whereas Fig. 9.14 depicts a similar plot for the VMS carbonates with Mn content more than 25 wt %. Oxygen and carbon isotopic ratios of the Mn-poor carbonates show a reasonably tight cluster (Fig. 9.13), whereas a fractionation in both oxygen and carbon isotopic values is most obvious in the Mn-rich carbonates (Fig. 9.14).

Devonian hydrothermal carbonates in western Tasmania are mostly Mg- and Fe-rich (e.g. Collins, 1981; Barth, 1986) and the Mn content of the VMS carbonates appears to reflect the Mn enrichment in the primary exhalative environment. If Mn content of the carbonates is considered to be un-related to the Devonian metamorphic and metasomatic overprints, it appears that the isotopic variation of VMS carbonates is also probably unrelated to the Devonian overprints and is a primary volcanogenic feature related to the composition and temperature of the Cambrian ore fluids. This conclusion further supports the previous interpretation that the isotopic composition of the VMS carbonates did not change appreciably during the later Devonian processes.

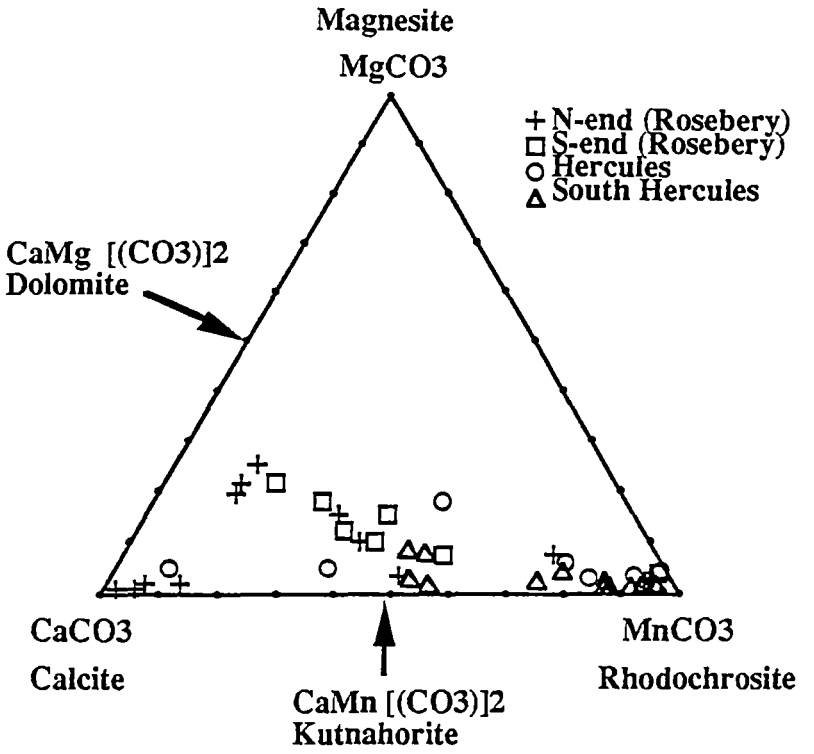


Fig. 9. 9. A ternary plot of $CaCO_3$–$MnCO_3$–$MgCO_3$ (mole %) for the compositional variation of carbonates from the Rosebery north- and south-ends, Hercules and South Hercules deposits, western Tasmania.

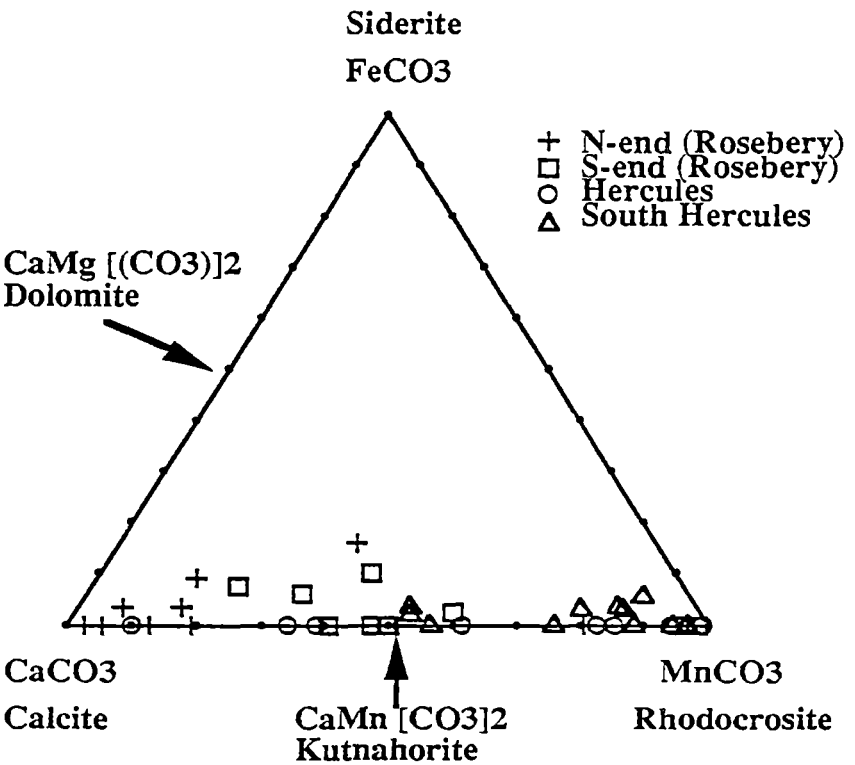


Fig. 9. 10. A ternary plot of $CaCO_3$–$MnCO_3$–$FeCO_3$ (mole %) for the compositional variation of carbonates from the Rosebery north- and south-ends, Hercules and South Hercules deposits, western Tasmania.

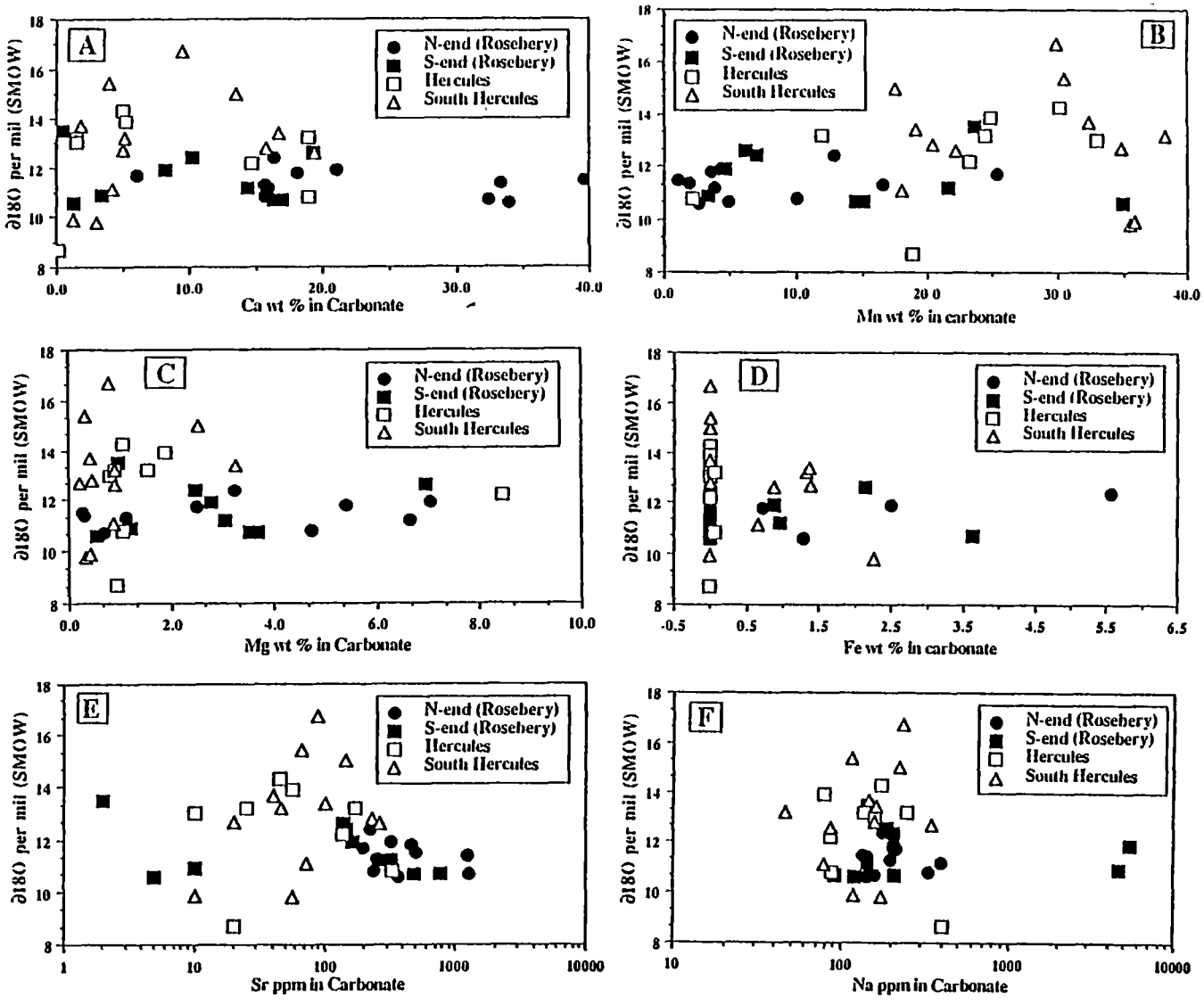


Fig. 9. 11. Plots showing compositional variation vs. $\delta^{18}O$values of carbonates from the Rosebery north- and south-ends, Hercules and South Hercules deposits, western Tasmania

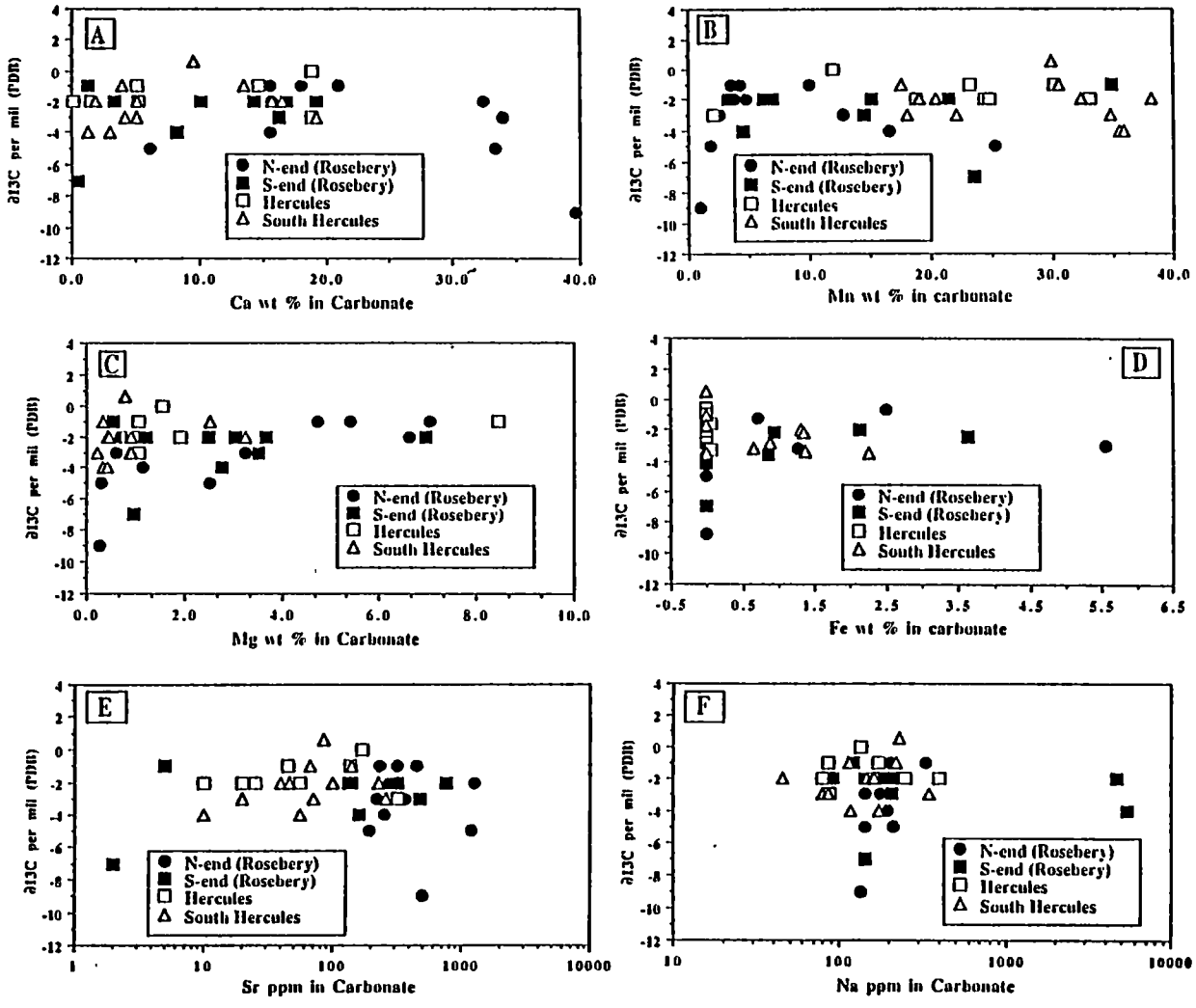


Fig. 9. 12. Plots showing compositional variation vs. $\delta^{13}C$ values of carbonates from the Rosebery north- and south-ends, Hercules and South Hercules deposits, western Tasmania

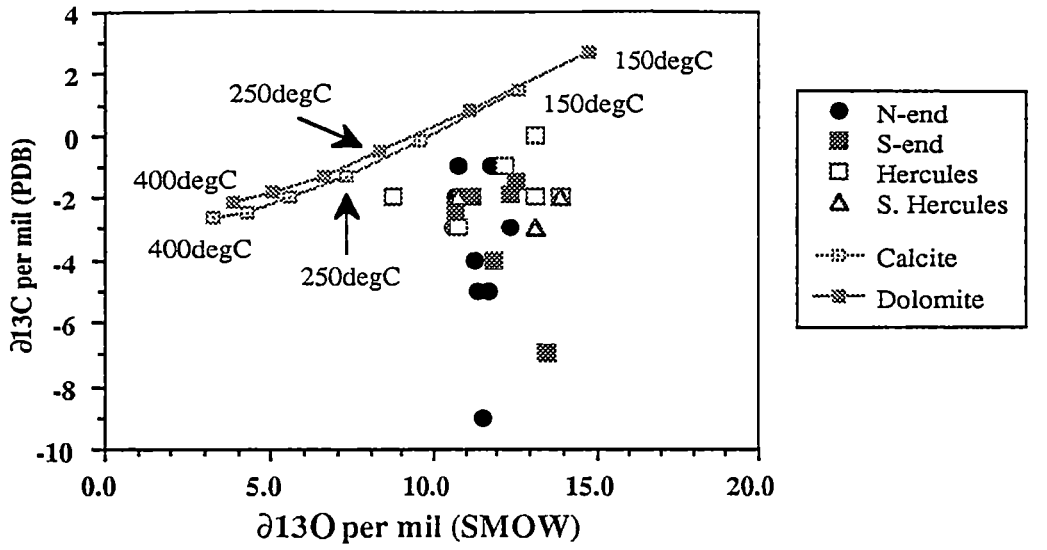


Fig. 9.13. Plot of $\delta^{18}O$ and $\delta^{13}C$ values of the VMS carbonates (with Mn content <25 wt %) from the Rosebery district deposits, western Tasmania. The equilibrium isotopic fractionation data for calcite and dolomite are calculated from calcite–$H_2O$ (O'Neil et al., 1969), dolomite–$H_2O$ (Golding and Wilson, 1983), calcite–$H_2CO_3$ (Ohmoto and Rye, 1979) and dolomite–$H_2CO_3$ (Ohmoto and Rye, 1979) assuming initial isotopic composition of fluid was $\delta^{18}O$=0 ‰ and $\delta^{13}C$=0 ‰.

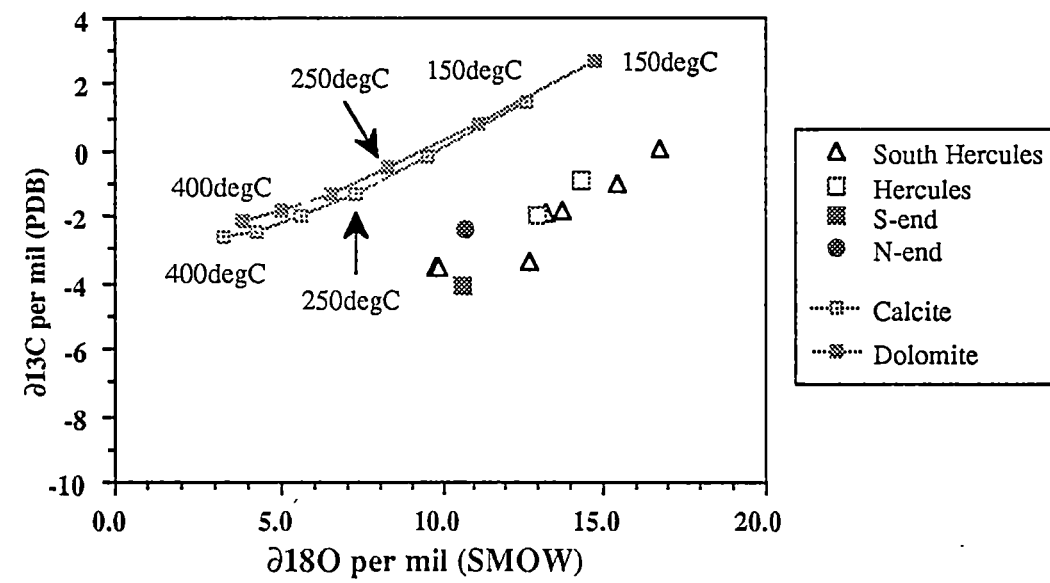


Fig. 9. 14. Plot of $\delta^{18}O$ and $\delta^{13}C$ values of the VMS carbonates (with Mn content >25 wt %) from the Rosebery district deposits, western Tasmania. The equilibrium isotopic fractionation data for calcite and dolomite are calculated as in Fig. 9.13.

In Figs. 9.13 and 9.14, $\delta^{18}O$ and $\delta^{13}C$ variation of calcite and dolomite calculated from the equilibrium isotopic fractionation data are also shown together with that of the VMS carbonates. Experimental fractionation data for Mn-rich carbonates (kutnahorite, rhodochrosite) are not available but the fractionation line may lie close to that of calcite and dolomite depending on the structure of the carbonate species (Osaki, 1973). The Mn-rich carbonates from the Rosebery district display a similar fractionation trend to that calculated for the calcite and dolomite, which also supports the previous interpretation of increasing $\delta^{13}C$ and $\delta^{18}O$ values of these VMS carbonates with decreasing temperature. The broad trend suggests that the South Hercules VMS carbonates appear to have formed over a lower temperature range than those of the Rosebery and Hercules VMS carbonates.

It is also interesting to note that a shift of $\delta^{13}C$ values of about 3–4‰ to heavier values is needed if we assume the temperature range of VMS carbonates in the Rosebery district is 150°–250°C. In other words, carbon lighter than the seawater carbon was involved in the system, possibly magmatic or organic carbon. Organic carbon was likely at the temperature range of the VMS carbonate deposition. In modern areas where significant quantities of sedimentary cover overly the heat source (e.g. Guayamas Basin, Einsele, 1986), organic carbon is added to the fluid. $\delta^{13}C$ values of calcite from sulphide chimneys from the southern Trough of the Guaymas Basin vary from –14.0‰ to –9.6‰ (Peter et al., 1987).

## 9.5 COMPARISON WITH DEVONIAN CARBONATES ...

The carbon and oxygen isotopic compositions of the Devonian hydrothermal carbonates from the Cleveland and Renison Bell tin deposits are plotted in Fig. 9.15 together with carbon and oxygen isotopic ratios of the Cambrian hydrothermal carbonates from the Rosebery, Hercules and South Hercules deposits. No isotopic ratios of igneous carbonates from Devonian granites in western Tasmania are available and only limited studies on isotopic composition of Cambrian sedimentary carbonates from western Tasmania have been undertaken (Collins, 1981; Patterson et al., 1981). Hence, the isotopic composition of Cambrian marine carbonates (Veizer and Hoefs, 1976; Veizer et al., 1980) and of igneous calcites (Bowman et al., 1985a) were used.

It is interesting to note that the Cambrian VMS carbonates and the Devonian carbonates display different isotopic characteristics. The Devonian hydrothermal carbonates have fairly restricted heavy oxygen isotopic ratios and generally lighter carbon isotopic values, whereas the VMS carbonates display a wide spread of both oxygen and carbon isotopic values. In comparison, the Cambrian sedimentary carbonate displays distinctly heavier oxygen isotopic values, and the igneous calcite has a considerably lighter carbon and oxygen isotopic composition (Fig. 9.15).

Although the isotopic values of the Devonian granite-related carbonate and the VMS carbonate in western Tasmania display some overlap with those of the Cambrian sedimentary carbonates, the VMS carbonate has considerably heavier carbon than typical igneous carbonate. In contrast, the Devonian hydrothermal carbonate tends to have lighter carbon, similar to typical igneous carbonate or carbonatite.

The VMS carbonates do not show any overlapping or family of coupled C–O isotopic depletion trends approaching the igneous or mantle values as was reported for metamorphosed carbonates from many contact aureoles (Fig. 6, Valley, 1986). The lack of such a relationship in the VMS carbonates from the Rosebery–Hercules area also supports the previous interpretation that the VMS carbonates were not well equilibrated or exchanged with later Devonian metamorphic and/or metasomatic fluids.

The difference in isotopic signature of the VMS and Devonian carbonates has the potential to be used as an additional geochemical tool with which to differentiate between carbonate alteration associated with Cambrian versus Devonian styles of mineralisation.

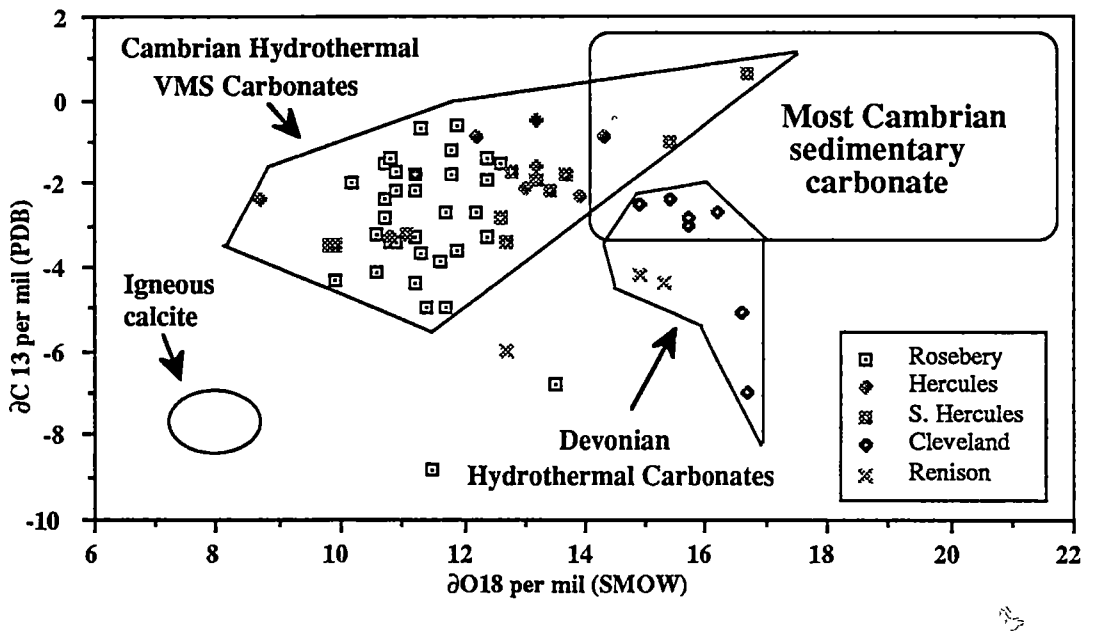


Fig. 9.15. Plot of $\delta^{18}O$ and $\delta^{13}C$ values of the Cambrian hydrothermal carbonates from Rosebery (north- and south-ends), Hercules and the South Hercules deposits together with those of the Devonian hydrothermal carbonates from the Cleveland and Renison Bell tin deposits, western Tasmania. The field of igneous calcite is from Bowman et al., (1985a) and of most Cambrian sedimentary carbonates is after Veizer and Hoefs (1976) and Veizer et al. (1980).

## 9.6 $\delta^{18}O$ VALUES IN QUARTZ, CHLORITE, BIOTITE, MAGNETITE AND TOURMALINE ...

Oxygen isotopic compositions of individual minerals, quartz, chlorite, biotite, tourmaline and magnetite from the Rosebery district deposits are presented in Appendix 9.3, and the range of oxygen isotopic values is listed in Table 9.1 and plotted in Figs. 9.16–9.18. Oxygen isotopic ratios of these individual minerals were analysed to apply oxygen isotope geothermometry and to estimate the isotopic composition of the mineralising fluids.

Table 9.1 $\delta^{18}O$ values of different minerals from the Rosebery district deposits.

| Mineral | Rosebery N-end | Rosebery S-end | Hercules | South Hercules |
|---|---|---|---|---|
| Quartz | +10.7 to +14.2‰(13)* | +11.9 to +15.1‰(5) | +13.0 to +15.6‰(5) | +14.0 to +15.9‰(8) |
| Chlorite | +6.9 to +11.6‰(4) | +7.4 to +11.0‰(6) | +6.7 to +9.8‰(2) | |
| Biotite** | | +4.9 to +10.7‰(16) | | |
| Magnetite | | +1.5 to +2.1‰(3) | | |
| Tourmaline | | +10.6 to +11.9‰(5) | | |

*No. of analyses
**includes some chlorite

### 9.6.1 Oxygen isotope geothermometry ...

Oxygen isotope fractionation between co-existing minerals is temperature dependent and therefore allows the use of the difference in $\delta^{18}O$ ratios in silicate and/or oxide mineral pairs as a geothermometer (e.g. Taylor, 1979; Faure, 1986). However, the temperature given by the oxygen isotope thermometry only reflects the temperature at which the minerals had equilibrated their oxygen with a common reservoir source. The oxygen isotope thermometer is based on three assumptions: (1) the exchange reactions must have reached equilibrium; (2) the isotopic compositions were not altered subsequent to the establishment of equilibrium; and (3) the temperature dependence of the fractionation factors is known from experimental determinations or theorectical calculations (e.g. Taylor, 1979; Faure, 1986).

The sensitivity of the thermometers depends on the difference in the slopes of the fractionation lines for each mineral and the temperature. At increasing temperatures, the difference in fractionation factors for any given pairs of minerals (hereafter referred to as $\Delta$ value) decreases until it approaches the analytical uncertainty. The most sensitive thermometers are therefore based on mineral pairs whose fractionation lines (relative to water) have strongly

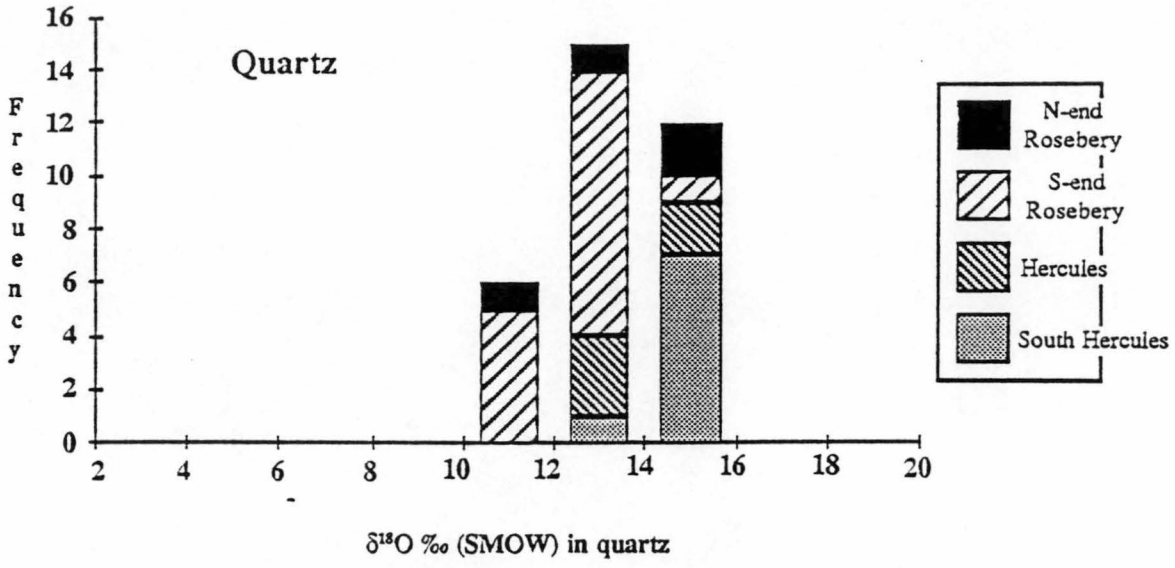


Fig. 9.16. Histogram showing $\delta^{18}O$ values of quartz from the Rosebery north- and south-ends, Hercules and South Hercules deposits, western Tasmania.

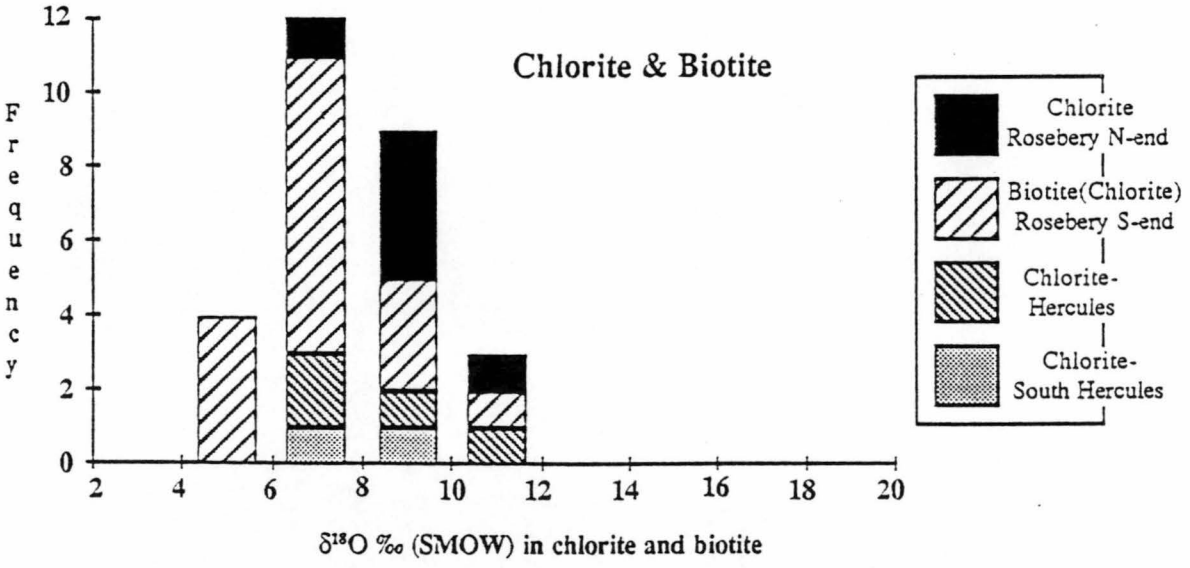


Fig. 9.17. Histogram showing $\delta^{18}O$ values of chlorite from the Rosebery north-end, Hercules and South Hercules deposits and biotite and mixture of biotite–chlorite from the Rosebery south-end, western Tasmania.

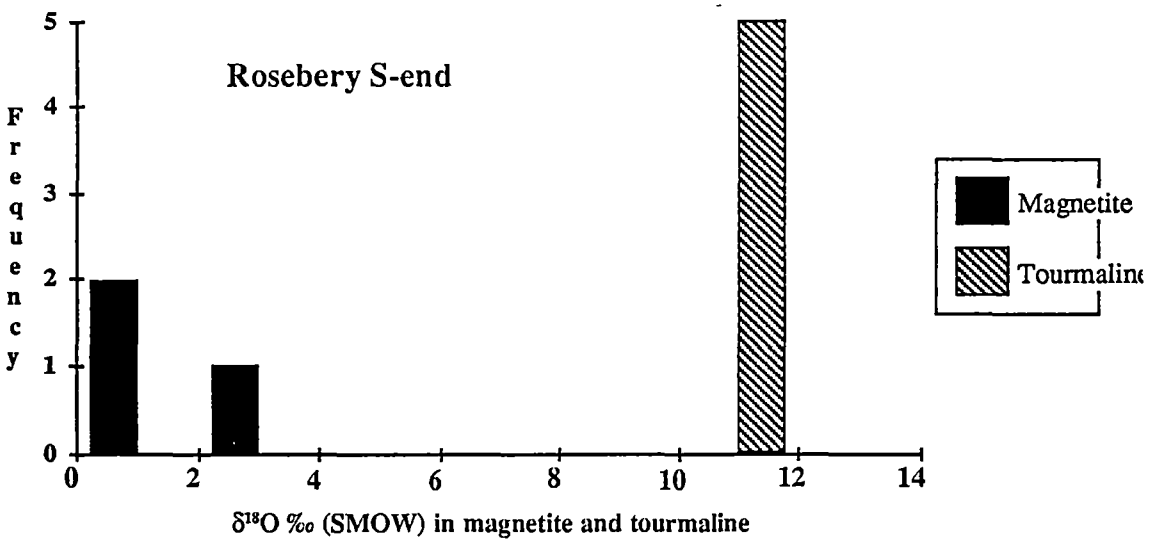


Fig. 9.18. Histogram showing $\delta^{18}O$ values of magnetite and tourmaline from the Rosebery south-end, western Tasmania.

diverging slopes, such as quartz–magnetite. When three or more oxygen-bearing minerals equilibrate isotopically at the same temperature, any pair of these minerals must yield that temperature. Such concordance of the isotopic temperatures is a necessity and can be used to a test whether isotopic equilibrium was achieved in a system.

Using the available fractionation factors for quartz, carbonate, chlorite, biotite, and magnetite it was possible in this study to determine temperatures of deposition and test for isotopic equilibrium between groups of minerals. Quartz–carbonate, quartz–chlorite, chlorite–carbonate, quartz–biotite and quartz–magnetite pairs were investigated and the temperature data are shown in Table 9.2. The experimental or empirical fractionation data reported by O'Neil et al. (1969), Bottinga and Javoy (1973, 1975), Matsuhisa et al. (1979), Wenner and Taylor (1971), Lafferty and Golding (1985) and Faure (1986) were used for the following geothermometers:

$$\Delta_{\text{quartz–calcite}} \quad T°C = 0.60\ (10^6 \times T_{(K)}^{-2})$$

$$\Delta_{\text{quartz–chlorite}} \quad T°C = 2.01\ (10^6 \times T_{(K)}^{-2}) + 1.99$$

$$\Delta_{\text{calcite–chlorite}} \quad T°C = 1.20\ (10^6 \times T_{(K)}^{-2}) + 1.30$$

$$\Delta_{\text{quartz–biotite}} \quad T°C = 2.54\ (10^6 \times T_{(K)}^{-2}) + 0.85$$

$$\Delta_{\text{quartz–magnetite}} \quad T°C = 5.2\ (10^6 \times T_{(K)}^{-2})$$

Table 9.2 Oxygen isotope temperature for mineral pairs from the Rosebery north- and south-ends, Hercules and south Hercules deposits, western Tasmania.

| Sample No. | Mineral pairs (T°C) | | | | |
|---|---|---|---|---|---|
| | qtz–carbonate | qtz–chlorite | carbonate–chlorite | qtz–biotite | qtz–magnetite |
| Rosebery N–end | | | | | |
| R3456 | 727 | | | | |
| R4297 | 232 | 383 | 259 | | |
| R4482 | 361 | 1712 | 826 | | |
| 5L–880mN | | 694 | | | |
| Rosebery S-end | | | | | |
| R3023-11/270mS | | | | 424 | |
| R3334–6B/280mS | | | | 375 | |
| R3164-8/280mS | | | | 518 | |
| R3492-21/280mS | | | | 540 | |
| R3016-6/300mS | | | | 1428 | |
| R3016-27/300mS | | | | 949 | |
| R3033-31/300mS | | | | 602 | |
| R3033-33/300mS | | | | 664 | |
| R3033-22A/300mS | | | | | 402 |
| Hercules | | | | | |
| H1032-4B | 146 | 722 | 1141 | | |
| H831-14A | | 381 | | | |
| H1008-22 | | 431 | | | |
| H1033-2 | | 480 | | | |
| South Hercules | | | | | |
| H1108-1 | 530 | | | | |
| H1108-10A | | | 176 | | |
| H1142-4B | | | 2197 | | |

The five quartz–carbonate pairs from the Rosebery north-end, Hercules and South Hercules yielded a wide range of 146°–727°C, and similarly, the quartz–chlorite pairs from Rosebery north-end and Hercules gave 381–1712°C. The carbonate–chlorite pairs yielded the widest temperature range of 176°–2197°C. These temperature ranges cannot be interpreted as related to either the Cambrian or later Devonian events. Eight quartz–biotite pairs and one quartz–magnetite pair from the F(J) lens of the Rosebery south-end were also investigated in this study. The quartz–biotite pairs gave 375°–664°C with one extremely high temperature of 1428°C. Two out of eight pairs gave temperatures of 375°C and 424°C, and fall within the expected range of biotite stability (Beane, 1974, 1980).

In comparison, consistent quartz–biotite temperature estimates of 410–460°C were reported for the tungsten skarn formation at Pine Creek, California (Brown et al., 1985). Bowman et al. (1985b) also reported 485°–525°C by the quartz–biotite oxygen isotope geothermometer for the tungsten skarn formation at CanTung Mine, Canada which is consistent

with the inferred fluid inclusion trapping temperature reported by Khin Zaw (1976).

The quartz–magnetite pair from the Rosebery south-end F(J) lens has a more reasonable oxygen isotope temperature estimate of 402°C. The highest uncorrected homogenisation temperature recorded in the helvite in the F(J) lens is ~330°C (Chapter 10). A pressure correction of +50°C needs to be applied to the fluid inclusion homogenisation temperature when comparing it to the isotopic temperature.

The wide temperature ranges for the F(J) lens minerals recorded by the oxygen isotope geothermometer could be due to one or both of the following problems:

(a) The quartz–chlorite and quartz–biotite oxygen isotopic fractionation factors used in this study are based on empirical data and the effect of cations such as iron, magnesium and manganese on the geothermometer is not known. The oxygen isotopic fractionation factor used for the carbonates is pure calcite but most carbonates in this study are Mn-rich with minor iron and magnesium (Figs. 9.9 and 9.10).

(b) The other problem can be impurity of the samples. Although the purity of the samples were checked by microscopy, submicroscopic contamination by other co-existing minerals cannot be avoided. For instance, the quartz–biotite mineral pairs which yielded temperatures above 450°C may be due to the incorporation of minor chlorite in the biotite samples. Mineralogical and textural studies indicate abundant evidence of alteration of chlorite to biotite during the Devonian replacement process (Chapter 6). This problem can be tested in the future by the recently developed microanalytical techniques for isotopic analysis such as laser ablation.

If the above problems are considered to be minimal, the wide temperature ranges recorded by the oxygen isotope geothermometers in the F(J) lens imply that isotopic equilibrium has not been attained for most of the mineral pairs studied. This is also supported by the lack of concordance of the isotopic temperatures for the three co-existing minerals pairs. In comparison, consistent temperatures obtained by the quartz–biotite geothermometer for the Pine Creek skarn (Brown et al., 1985) and CanTung skarn deposits (Bowman et al., 1985b) suggest that these systems were isotopically well equilibrated.

### 9.6.2 Isotopic composition of hydrothermal fluids ...

The oxygen and carbon isotopic composition of the hydrothermal fluids associated with the Cambrian mineralisation and later Devonian replacement processes can be calculated if the temperature of formation of the different minerals and the experimental data for the mineral–water system are known.

*Cambrian VMS fluid:* In the preceding sections, it was indicated that the carbon and oxygen isotopic compositions of the VMS carbonates in the Rosebery district deposits did not change appreciably during Devonian recrystallisation. Experimental data on the kinetics of oxygen isotope exchange and studies of geothermal systems also suggest that minerals such as quartz, feldspar, muscovite, and chlorite re-equilibrate readily under hydrothermal conditions (e.g. Cole and Ohmoto, 1986; O'Neill, 1987) but carbonate does not. If this is the case, the isotopic ratios of the VMS carbonates will reflect the original isotopic composition of the volcanogenic fluid, and can be calculated if the temperature of the carbonate deposition is known.

Although no workable fluid inclusions are found in the carbonate minerals from the Rosebery district (Chapter 10), a temperature range of ~150–250°C for the deposition of these carbonates can be reasonably inferred from the fluid inclusion homogenisation temperatures of other minerals (e.g. quartz, barite and sphalerite) associated with them. Green et al. (1981) and Green (1983) also interpreted a formation temperature of about 250°C during the development of barite ore at the top of the massive sulphide lens where abundant carbonates are present.

Figures 9.19A and B show the estimated oxygen and carbon isotopic composition of the Cambrian volcanogenic fluid during carbonate deposition. The isotopic composition of the volcanogenic fluid was calculated from the $\delta^{18}O$ and $\delta^{13}C$ values of the VMS carbonates from the Rosebery district deposits assuming temperatures of carbonate deposition at 250°C and 150°C. At the lower temperature, the oxygen isotopic composition of the volcanogenic fluid is close to that of seawater, whereas the carbon isotopic value is lighter than that of seawater (Fig. 9.19B). These light carbon isotopic compositions are in agreement with the previous interpretation of possible incorporation of organic carbon in the system. The overall calculated isotopic composition of the volcanogenic fluid is consistent with the fluid being derived from evolved seawater. Hydrothermal carbonates from the Buchans deposit (Lucky Strike Mine), Canada, also have $\delta^{13}C$ values of –1.6‰ to 0.5‰ indicative of a seawater source (Kowalik et al., 1981).

*Devonian hydrothermal fluid:* As was estimated for the Cambrian volcanogenic fluid, the oxygen isotopic composition of the Devonian fluid which formed the metasomatic mineral assemblages can be estimated if the temperature of mineral formation and equilibrium isotopic fractionation data for the mineral–water systems are known. The $\delta^{18}O$ values of biotite and magnetite samples from the F(J) lens were used to calculate the oxygen isotopic composition of the Devonian hydrothermal fluid as these minerals were formed during the Devonian metasomatic processes. Fluid inclusion homogenisation temperatures (Chapter 10) recorded

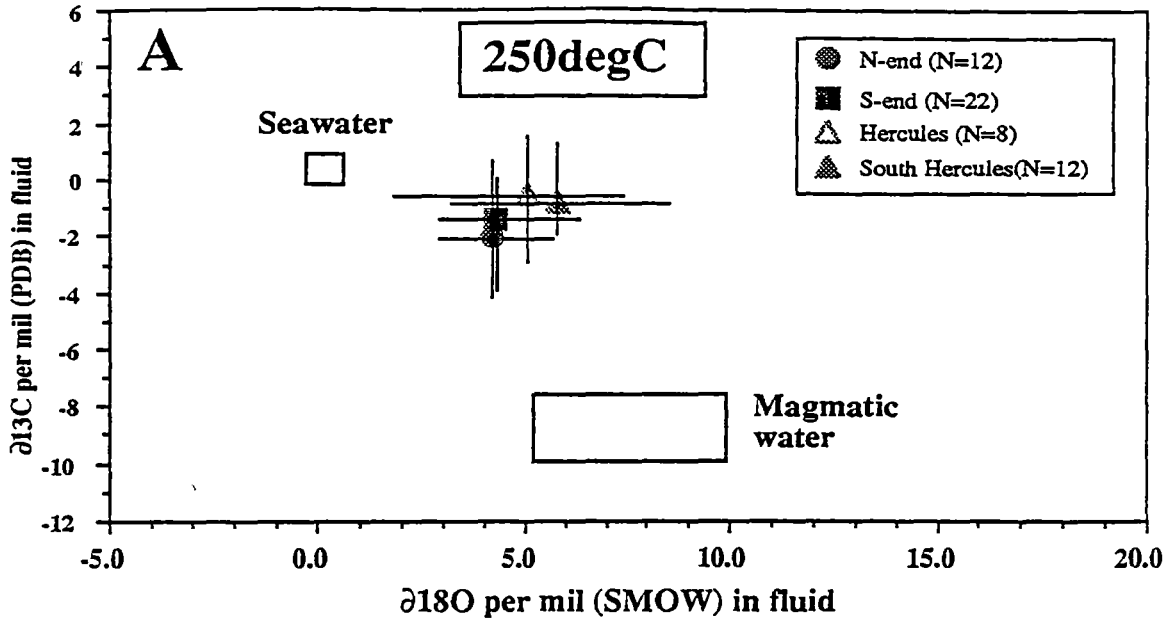


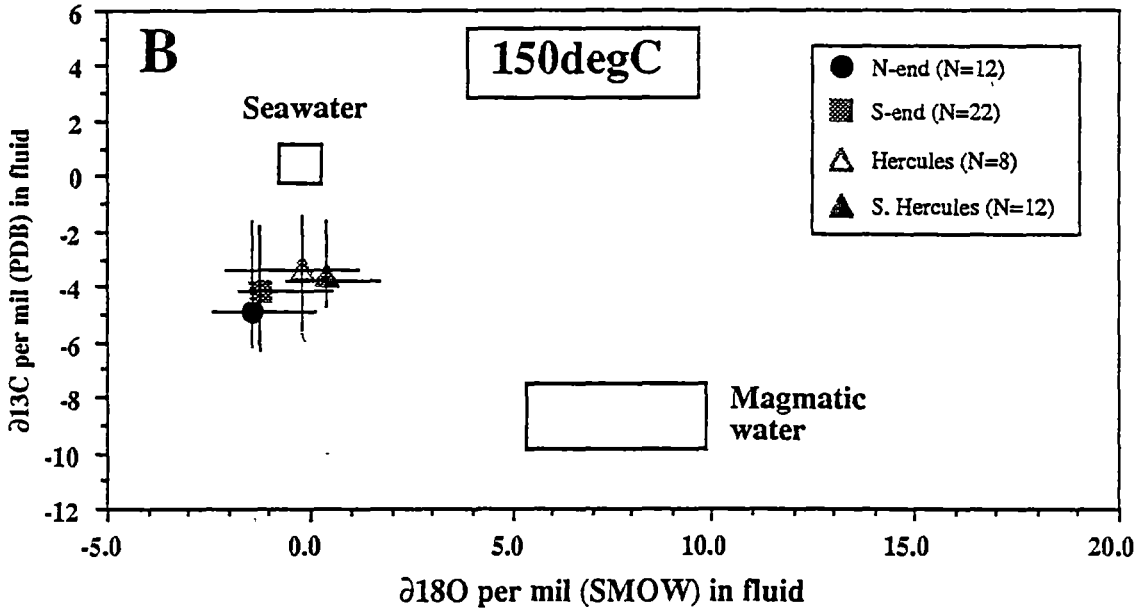


Fig. 9.19. Isotopic composition of volcanogenic fluids calculated from oxygen and carbon isotopic values of VMS carbonates of the Rosebery district, assuming 250°C (A) and 150°C (B) for the temperatures of carbonate deposition and using calcite–$H_2O$ and calcite–$H_2CO_3$ equilibrium isotopic fractionation data of O'Neil et al. (1969) and Ohmoto and Rye (1979). The data points represent the *mean* isotopic composition for each deposit and the range of the isotopic values is shown as bars. The $\delta^{18}O$ and $\delta^{13}C$ ratios of the seawater and magmatic fluid are those reported by Rye and Ohmoto (1974), H.Taylor (1979), B. Taylor (1987) and Ohmoto and Rye (1979).

for the biotite–magnetite zone were also used in the calculation. As shown in Table 9.3 and Fig. 9.20, the calculated $\delta^{18}O$ values of the Devonian fluid are in the range of 8.5‰ to 12.6‰ with a mode of 10.0‰ and are consistent with a magmatic origin as metamorphic fluid tends to have higher $\delta^{18}O$ values up to 25‰ (Taylor, 1989). The $\delta^{18}O(H_2O)$ values can be varied depending on experimental data for different mineral–water fractionation but, whichever calibration is used, there is only about 1–2‰ variation in the calculated $\delta^{18}O(H_2O)$.

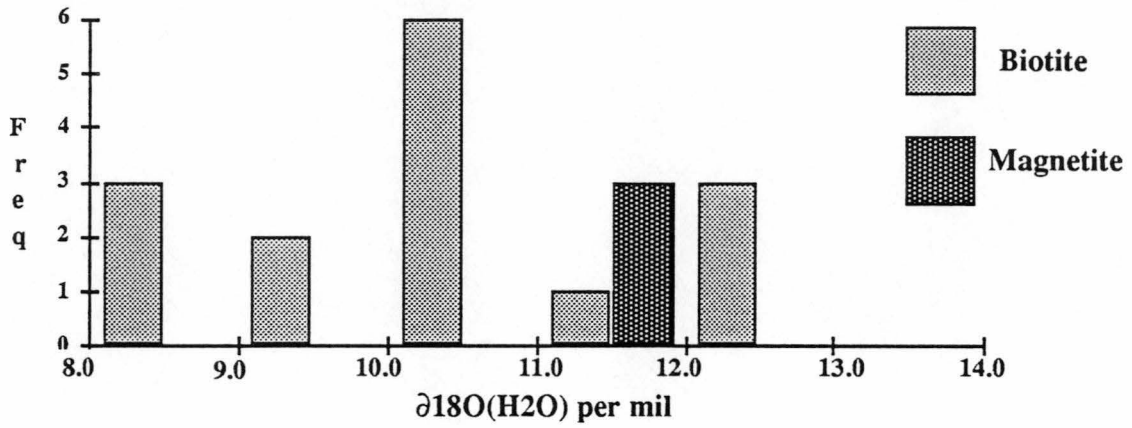


Fig. 20. Histogram showing oxygen isotopic variation of the Devonian fluid which formed the metasomatic mineral assemblages in F(J) lens, Rosebery south-end, western Tasmania. The $\delta^{18}O(H_2O)$ values were calculated at 330°C using biotite–water and magnetite–water fractionation data listed in Lafferty and Golding (1985) after Hoernes (1980).

Table 9.3 Calculated oxygen isotopic composition of the Devonian hydrothermal fluids.

| Mineral | $\delta^{18}O(H_2O)$ at 300°C* | $\delta^{18}O(H_2O)$ at 330°C* |
|---|---|---|
| Biotite | 8.8-12.8 ‰ (N=16)** | 8.5-12.6 ‰ (N=16)** |
| Magnetite | 11.2-11.8‰ (N=3)*** | 11.1-11.6 ‰ (N=3)*** |

* from fluid inclusion homogenisation temperatures in quartz associated with biotite–magnetite assemblages (Chapter 10)
** from biotite–water fractionation data listed in Lafferty and Golding (1985) after Hoernes (1980)
*** from magnetite–water fractionation data listed in Lafferty and Golding (1985) after Hoernes (1980)

### 9.6.3 Water–rock ratio ...

Oxygen isotope data can be used as a geochemical tool to investigate the water–rock interaction (e.g. Taylor, 1979). The effect of water–rock interaction for felsic volcanic rocks in the Kuroko district has been closely modelled by oxygen isotopic variation (e.g. Green et al., 1983). Green (1986) also reported that the altered footwall felsic volcanics at the Hercules mine have higher whole rock $\delta^{18}O$ values than those of the unaltered footwall rocks and recently Green (1990b, 1990c) reported a detailed investigation of the rock alteration, and mineral and oxygen isotope zonation in the Rosebery area and modelled the seawater–rock interaction during ore formation by the use of whole rock $\delta^{18}O$ values.

The water–rock interaction during ore deposition can also be studied by the oxygen isotopic variations of the individual hydrothermal minerals such as carbonate and magnetite (e.g. Taylor, 1979; Sverjensky, 1981; Shelton, 1983). Variation in isotopic compositions for the minerals, in open and closed systems, as a function of varying water–rock ratios can be modelled as follows;

$$\text{Closed system} \quad W/R = \frac{\delta^{18}O_f\,(\text{min}) - \delta^{18}O_i\,(\text{min})}{\Delta\,(\text{min-H2O}) + \delta^{18}O_i\,(H_2O) - \delta^{18}O_f\,(\text{min})} \qquad \text{.....(1)}$$

$$\text{Open system} \quad W/R = \{\ln\,(W/R)_{\text{closed}} + 1\} \qquad \text{.....(2)}$$

where W/R = mole ratio of water to individual mineral, $\delta^{18}O_i$ (min) and $\delta^{18}O_f$ (min) = initial and final oxygen isotopic compositions of the mineral, $\delta^{18}O_i$ ($H_2O$) = oxygen isotopic composition of the water, and $\Delta_{(\text{min-H2O})}$ =oxygen isotopic fractionation between the mineral and water.

Due to very high W/R ratios at the time of carbonate alteration at the seawater–rock interface during the Cambrian, realistic W/R ratios cannot be estimated from the isotopic data of VMS carbonates. According to calculations made by Green (1990b, 1990c) on $\delta^{18}O$ values of whole rock, W/R ratios during Cambrian mineralisation can vary from 1 to infinity.

W/R ratios during the Devonian metasomatic processes can be estimated using $\delta^{18}O$ values of the Rosebery F(J) lens magnetite and magnetite–water fractionation data of Hoernes (1980). The system is considered closed and the initial oxygen isotopic ratio of the minerals in the system is assumed to be 7.5–15.0‰ (av. 11.5‰) which is similar to the isotopic composition of the Cambrian felsic volcanic rocks suggested by Green (1990b, 1990c). The average $\delta^{18}O$ values of magnetite is about 1.8‰ for the three magnetite samples from the F(J) lens and this value is used as the final oxygen isotopic composition. The $\delta^{18}O(H_2O)$ values of the Devonian

hydrothermal fluid can be calculated to be 10.6–11.0‰ (av. 10.8‰) at 350°C. The magnetite–$H_2O$ fractionation factor at 350°C is –9.3. Hence, the simplified calculation using equation 1 indicates a W/R ratio of 3.0 to 3.5 during the initial stage of the Devonian replacement processes. In comparison, Brown et al. (1985) estimated a W/R ratio of 11.0 during the tungsten skarn formation at Pine Creek, California.

## 9.7 SULPHUR ISOTOPES ...

Sulphur isotope geochemistry has become an important part of the investigation of the genesis of sulphide deposits. Sulphur isotopic variation in ores may provide data on: (a) the source of sulphur, (b) the temperature of mineral deposition, (c) the physico-chemical environment, (d) the mechanism of mineral deposition and (e) exploration guides (Taylor, 1987). Detailed sulphur isotopic investigations have been carried out by many workers in the Rosebery–Hercules area (e.g. Solomon et al., 1969; Green et al., 1981; Green, 1983; Lees, 1987; Eastoe et al., 1987; Solomon et al., 1988). Previous sulphur isotopic studies of the Rosebery–Hercules area emphasised the source of sulphur in the ore fluids. No sulphur isotopic investigation has previously been undertaken at the newly discovered South Hercules deposit.

In this study, a sulphur isotopic study was undertaken to deduce the source of sulphur at the South Hercules deposit and to investigate the sulphur isotope variation during the Devonian replacement processes in the F(J) lens of the Rosebery south-end orebody. In addition, the variation of sulphur isotopic values with gold grade was investigated at the South Hercules deposits. The sulphur isotopic data collected in this study are presented in Appendix 9.4 and shown in Fig. 9.21.

### 9.7.1 $\delta^{34}S$ values for sulphides from South Hercules ...

At Rosebery, Green et al. (1981) and Green (1983) recorded that $\delta^{34}S$ values for sulphides in the spalerite–galena-rich ore gave a higher $\delta^{34}S$ range (10.8–17.2‰) than the massive pyrite–chalcopyrite ore (7.8–10.8‰), whereas $\delta^{34}S$ values for sulphides in the stratigraphically higher barite zone gave even higher values (13.9–19.8‰) and barite yielded tightly clustered $\delta^{34}S$ values of 34.6–41.2‰ (Figs. 9.21A, B, and C). Sulphur isotope data from the F(J) lens yielded comparable $\delta^{34}S$ values (12.9–18.6‰) with that of spalerite–galena-rich ore (Fig. 9.21D). Green et al. (1981), Green (1983) and Solomon et al. (1988) concluded that most of the sulphur in the Rosebery sulphides was derived from reduction of seawater sulphate, although some contribution from a magmatic source was possible, and that $H_2S$ was the dominant sulphur species present in the ore fluid.

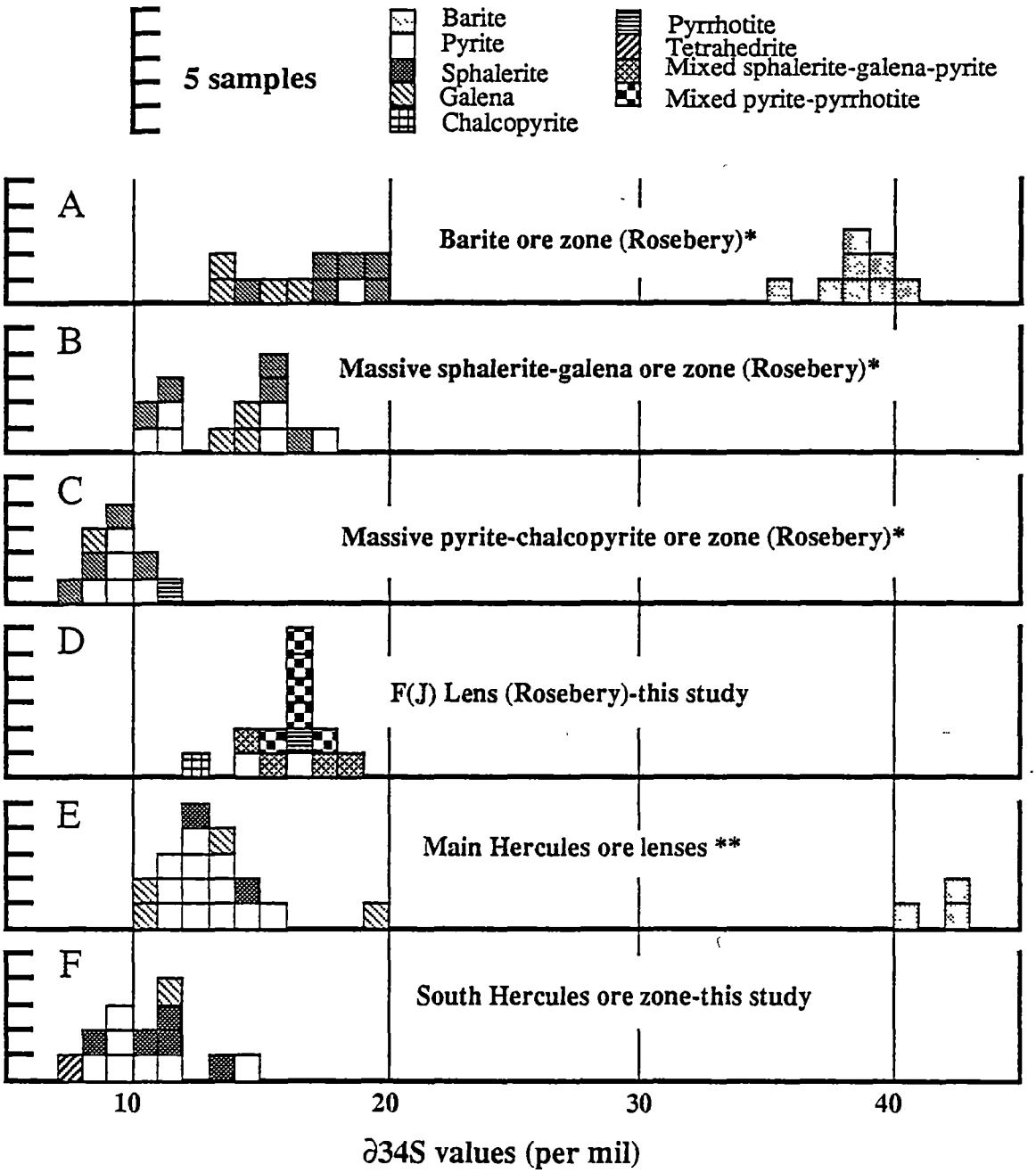


Fig. 9.22. Sulphur isotope data from the Rosebery, Hercules and South Hercules deposits, western Tasmania.
* data after Green et al. (1981) and Green (1983).
** data after Solomon et al. (1969), Lees (1987) and Solomon et al. (1988).

Green et al. (1981), Green (1983) and Solomon et al. (1988) suggested that $\delta^{34}S_{\Sigma S}$ of the ore fluid increased with time due to an increase in the proportion of seawater sulphur to leached magmatic sulphur from the volcanics. The significantly higher $\delta^{34}S$ values from the sulphides in the barite orebody compared to those of the zinc–lead orebody was considered to be due to lower temperature (about 250°C) during the barite ore deposition, compared to sulphide lens formation (about 300°C) (Green et al., 1981; Green, 1983; Solomon et al., 1988).

Sulphur isotope values from the main Hercules mine were determined by Solomon et al. (1969, 1988) and Lees (1987). $\delta^{34}S$ values of sulphides range from 10.7‰ to 19.2‰, whereas three barite samples have a narrow range of 40.7–42.7‰ (Fig. 9.21E). In comparison, the sulphur isotope analyses in this study for the South Hercules deposit gave $\delta^{34}S$ values of 8.2–14.1‰ for pyrite, 8.2–13.4‰ for sphalerite, 7.8‰ for one tetrahedrite and 11.9‰ for one galena sample (Fig. 9.21F). The sulphur isotope values at Hercules and South Hercules are in the same range as those of Rosebery, and consistent with sulphur derived from seawater (Ohmoto and Rye, 1979). Hence, similar conclusions to those of Green et al. (1981) can be drawn regarding the origin of sulphur in the South Hercules orebody.

The textural groups of the sulphide minerals (e.g. disseminated to massive sphalerite and colloform to massive pyrite) from the South Hercules deposit do not show any obvious difference in isotopic variation, suggesting that later Devonian metamorphic recrystallisation did not significantly affect the isotopic composition of the sulphide minerals.

### 9.7.2 $\delta^{34}S$ values versus gold grades at South Hercules ...

Ohmoto (1972) indicated that the sulphur isotope variation in a particular hydrothermal system is controlled by pH, temperature, $fO_2$ and concentration of sulphur species such as $H_2S$ and $SO^{=}_4$. Huston and Large (1989) and Large et al. (1989) suggested that the transport and deposition of gold in the Zn–Pb–Ag–Au association of volcanogenic massive sulphide deposits was controlled by the pH, temperature, and $fO_2$.

Hannington and Scott (1989) also indicated that the transport and deposition of gold in active hydrothermal vents on the modern seafloor as well as in ancient VMS deposits are dependent on the pH, temperature and $a_{s2}$ of the hydrothermal system. Although comparable physico-chemical controls for $\delta^{34}S$ variation and the gold mineralisation are present, no comprehensive studies on the relationships between $\delta^{34}S$ and gold grade exists in the literature. Hence the sulphur isotopic investigation at South Hercules was focussed on the relationships of the $\delta^{34}S$ values of sulphides and the gold grades in selected samples. As has been described, abundant carbonate in the South Hercules system would have buffered the pH to near neutral conditions during ore deposition.

Figure 9.22 shows a plot of the $\delta^{34}S$ ($H_2S$) values of the ore fluids and gold grades (g/t Au). The $\delta^{34}S$ ($H_2S$) values of the ore fluids were calculated from the sulphur isotopic composition of pyrite, sphalerite and galena assuming deposition at 250°C. The gold grades were taken from the Electrolytic Zinc Company assay results of 1–2 metre samples. The relation between sulphur isotopic values and gold grades has a correlation coefficient of 0.50 (n = 13), which is significant at the 95% confidence level. The gold grades increase with increasing $\delta^{34}S$ ($H_2S$) values in the ore fluids although one pyrite value falls off the trend. These results are consistent with the independent observations by Green et al. (1981) and Huston and Large (1988) that both $\delta^{34}S$ values and gold grades increase toward the stratigraphic top of the Rosebery orebody. In contrast, there was a poor relationship between mole % FeS in sphalerite versus gold grades (Chapter 8).

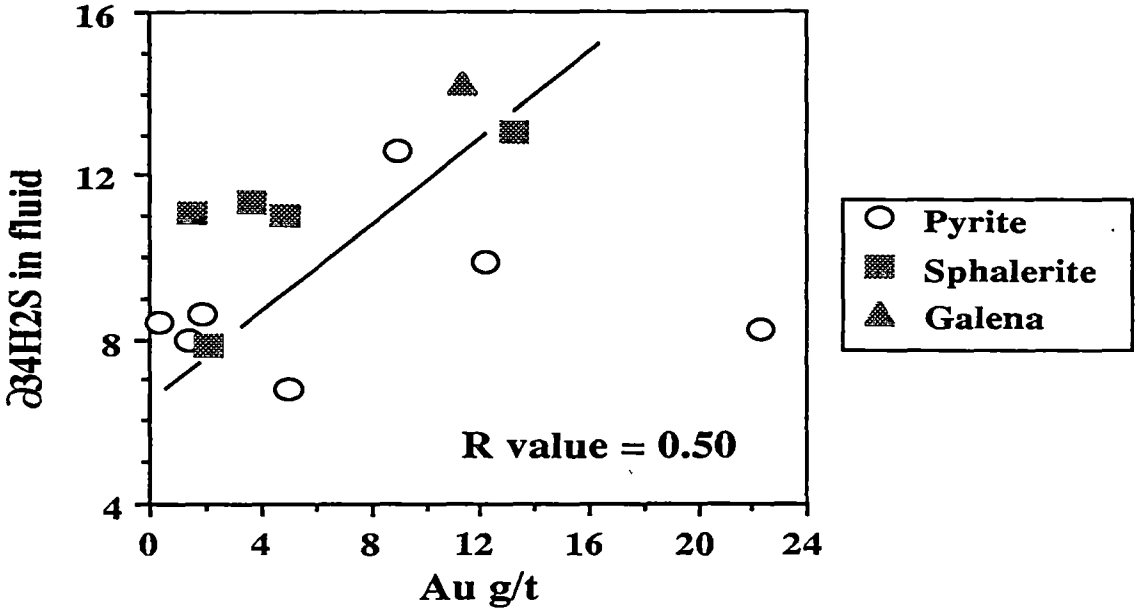


Fig. 9.22. Plot of $\delta^{34}S$ ($H_2S$) in ore fluid vs. gold grades (g/t) in the South Hercules deposit, western Tasmania. The $\delta^{34}S$ ($H_2S$) values in the ore fluids were calculated at 250°C using equilibrium isotopic fractionation data of pyrite–$H_2S$, sphalerite–$H_2S$, and galena–$H_2S$ after Ohmoto and Rye (1979).

If we assume that the recognisable trend of $\delta^{34}S$ ($H_2S$) values in the ore fluids versus gold grade is statistically valid, this would suggest that the chemical factors controlling gold deposition also controlled the variation in $\delta^{34}S$ values of the accompanying sulphide minerals. This relationship also provides constraints on possible mechanisms for the gold deposition at South Hercules. The following gold deposition mechanisms can be envisaged:

(1) Gold deposition at South Hercules took place by decreasing temperature.

(2) Gold deposition at South Hercules took place due to mixing between seawater and hot reduced ore fluid as the hydrothermal fluid moved up toward the seafloor. The reduction of seawater $SO^{=}_4$ to $H_2S$ is a significant source of sulphur under a highly reduced condition.

(3) Gold deposition at South Hercules occurred at an evolved late stage of the massive sulphide forming system under increasing $\delta^{34}S_{\Sigma S}$ of ore fluid with time due to an increase in the proportion of seawater sulphur to leached magmatic sulphur from the volcanics (G. R. Green, per. comm. 1991).

Figures 9.23A and 9.23B show that contours of gold solubility as the $Au(HS)_2^-$ complex and of $\delta^{34}S$ ($H_2S$) values of accompanying sulphides (e.g. pyrite) are parallel within T–$f_{O2}$ space. For the gold deposition mechanism (1), if the ore fluids cooled from 250°C to 200°C under equilibrium condition at constant $fO_2$, gold grades will increase (Fluid path A–A', Figs. 9. 23A and B) while $\delta^{34}S$ ($H_2S$) values of accompanying sulphides will decrease from 20.0‰ to 1.0‰ (Fluid path B–B', Figs. 9.23A and B). This condition will show a negative correlation between $\delta^{34}S$ ($H_2S$) values and gold grades but the South Hercules deposit displays a reverse, positive correlation (Fig. 9.22) and hence the mechanism (1) is unlikely.

For the gold deposition mechanism (2), a linear correlation of gold and $\delta^{34}S$ ($H_2S$) values can be expected if the gold deposition occurred as the hot reduced ore fluid mixed with seawater (Fluid path C–C', Figs. 9.23A and B) at the top of volcanic pile and the sulphur is derived from the reduction of seawater $SO^{=}_4$ to $H_2S$ under highly reduced conditions. Ohmoto (1986) also indicated that at temperatures below 350°C, sulphide and sulphate precipitation is not caused by simple cooling, but rather by mixing of a sulphate-bearing fluid (e.g. seawater) with the ore fluids. Although this gold deposition process is a possible mechanism, isotopic equilibrium was unlikely to be attained at these low temperatures of mixing at the seawater–rock interface (Ohmoto and Lasaga, 1982).

The gold deposition mechanism (3) is the most likely mechanism. The $\delta^{34}S_{\Sigma S}$ of the ore fluids increased with time due to an increase in the proportion of seawater sulphur to leached magmatic sulphur from the volcanics. Gold was precipitated at an evolved late stage in the Cambrian hydrothermal event from relatively oxidised, low temperature ore fluids. Both processes will lead to an increase in gold grades and $\delta^{34}S$ ($H_2S$) values of the accompanying

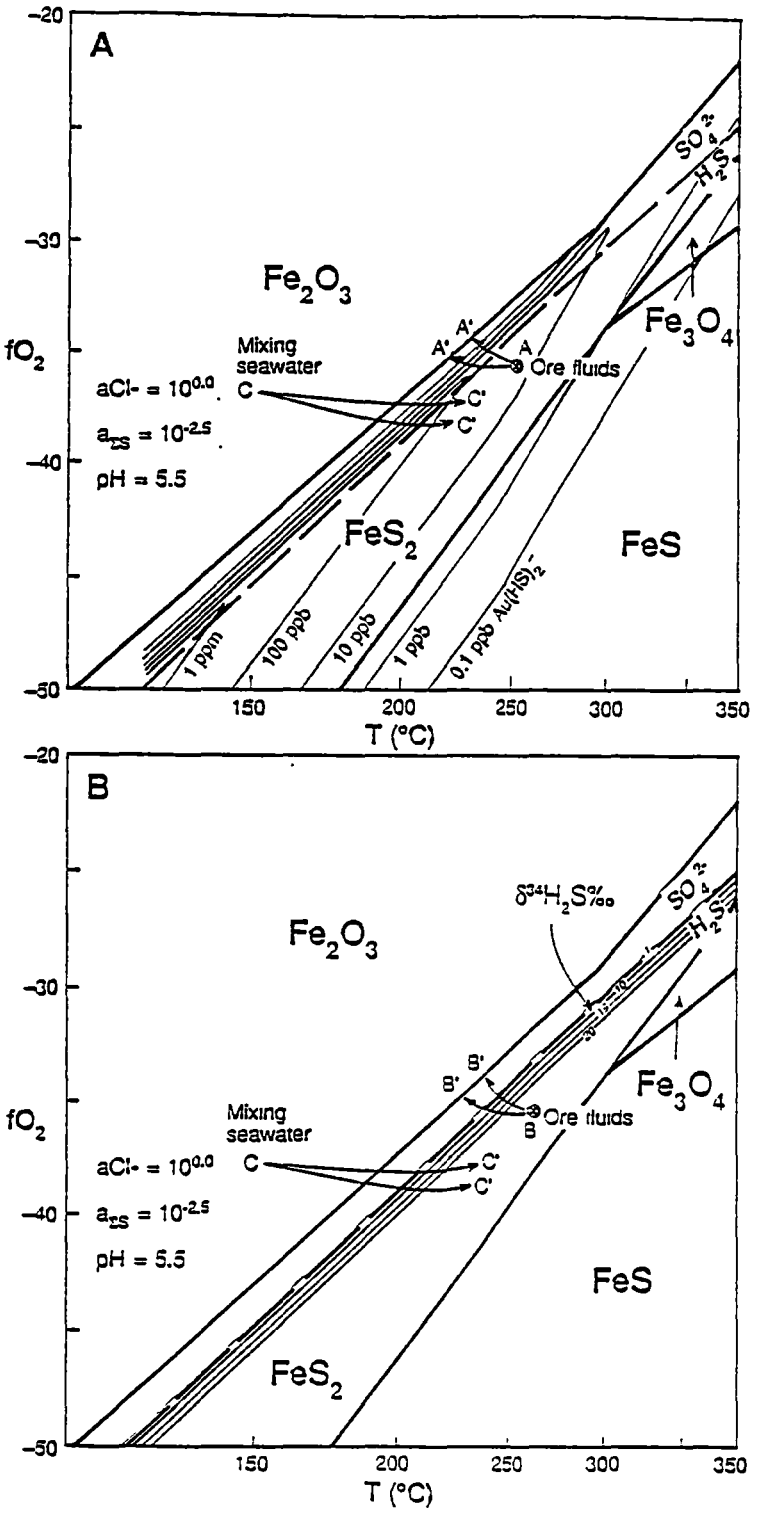


Fig. 9.23. fO2-T diagrams showing the solubility of gold as $Au(HS)_2^-$ (after Huston and Large, 1989) (**A**) and variation of $\delta^{34}S$ ($H_2S$) in the ore fluid ( after Large, 1975, unpub. data) (**B**). Note the family of lines of ore fluid moved across the gold solubility cliff under a gradient of decreasing temperatures (A-A') and decreasing $\delta^{34}S$ ($H_2S$) values in fluids (B-B') and mixing with seawater (C-C').

sulphides. However, more sulphur isotopic analyses are needed to further test the positive correlation of the gold grades and sulphur isotopic variation. Sulphur isotopic fractionation between sulphide and sulphate minerals from the South Hercules deposit also should be studied to test whether these minerals have been deposited in isotopic equilibrium.

The permissible correlation of the $\delta^{34}S$ values versus gold grades also suggest that detailed sulphur isotopic investigations may be used as an additional guide to assist in targeting gold-rich sections of massive sulphide systems.

### 9.7.3 Variation of $\delta^{34}S$ ratios in F(J) lens of Rosebery south-end ...

In Chapters 4 and 6, it was concluded that the Cambrian sulphide lenses of volcanogenic origin have been replaced by Fe–S–O assemblages derived from the granite-related fluids of Devonian age. Green et al. (1981) and Green (1983) initially investigated the sulphur isotopic composition in the F lens and reported $\delta^{34}S$ values from the pyrite–pyrrhotite assemblages (16.1‰ for pyrite and 15.2‰ for pyrrhotite) similar to those of the stratiform sphalerite–galena lenses.

Green et al. (1981) and Green (1983) indicated that sulphur isotopic compositions of the Cambrian sulphides did not change during Devonian metamorphism. In a later study, Solomon et al. (1987) reported that sphalerite and mixed sphalerite and pyrite from the Pb–Zn sulphide lens in the F(J) lens vary in $\delta^{34}S$ values from 12.7‰ to 18.2‰ and the pyrrhotite–pyrite from the Devonian granite-related mineralised zone display $\delta^{34}S$ values from 10.8‰ to 18.2‰. They also concluded that there was no significant change in the sulphur isotope composition during the replacement process.

In this study, sulphur isotopic variations across an individual sample in which lead–zinc sulphide lenses have been replaced by pyrrhotite–pyrite assemblages was undertaken to determine whether $\delta^{34}S$ variations could be detected on the hand specimen scale. Figure 9.24 shows sulphur isotopic variation of the mixed sulphide assemblages from the lead–zinc sulphide lenses to the pyrrhotite–pyrite zone. In the galena–sphalerite–pyrite zone, $\delta^{34}S$ values show considerably more variation (15.2 to 18.6‰) than within the pyrite–pyrrhotite zone (16.0 to 17.1‰). These data suggest that, on the hand specimen scale, there has been homogenisation of the sulphur isotope ratios during the Devonian metasomatic process.

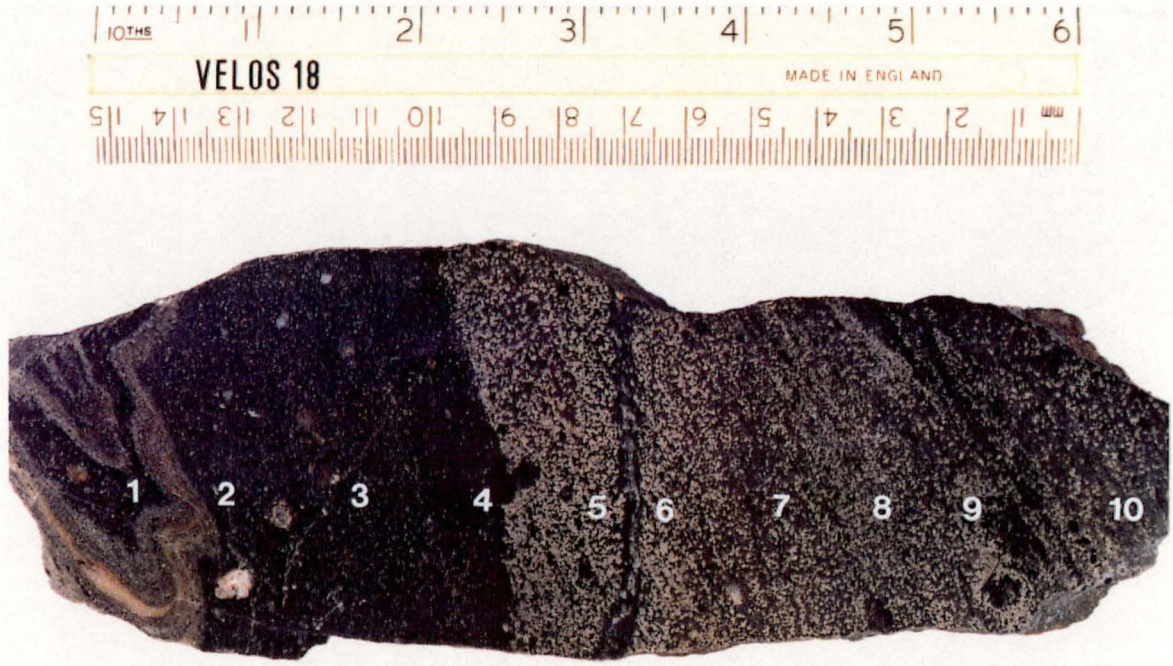


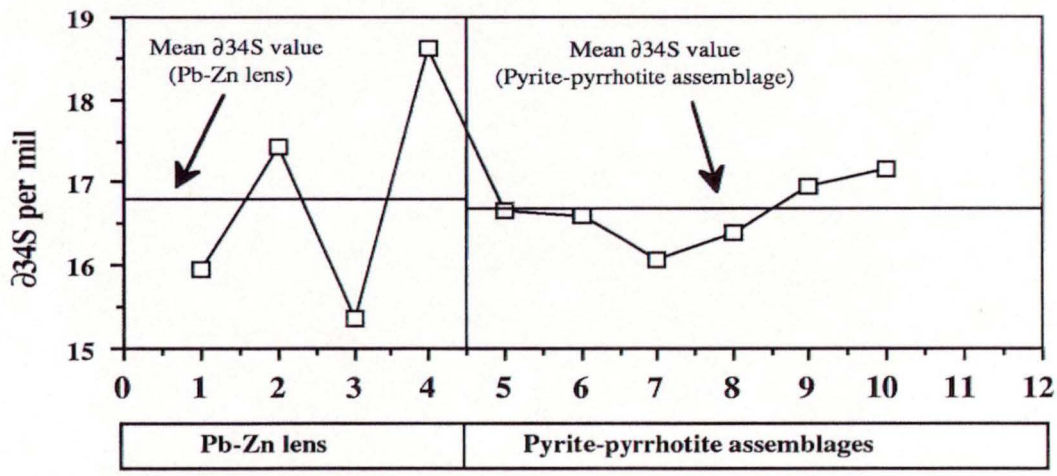


Fig.9.24. Variation of sulphur isotopic composition of mixed sulphide samples (pyrite–sphalerite–galena ± chalcopyrite) across from the primary folded lead–zinc lenses to the pyrrhotite–pyrite assemblages of Devonian metasomatic origin. Note the similar mean $\delta^{34}S$ values in both the lead–zinc zone and the pyrrhotite–pyrite zone, but sulphur isotopic variation appears to have been homogenised during the Devonian metasomatic process.

## 9.8 SUMMARY ...

- The carbonates from the Cambrian VMS sulphide deposits are predominantly of calcite–kutnahorite–rhodochrosite composition with minor iron and magnesium substitution. The VMS carbonates vary in texture from bladed carbonate, disseminated carbonate, spheroidal carbonate, recrystallised massive carbonate to vein carbonate but they do not display any enrichment or depletion in oxygen and carbon isotopic ratios with any particular textural carbonate types.

- The tightly constrained isotopic composition of the VMS carbonates from both the north- and south-ends of the Rosebery deposit implies that no later isotopic changes have taken place even though the south-end of the Rosebery deposit has been strongly overprinted by the high temperature (>300°C), pervasive Devonian replacement process. The isotopic compositions of the VMS carbonates in the Hercules and South Hercules deposits also retain their primary features although these two orebodies have been affected by Devonian metamorphic recrystallisation which occurred at temperatures below 300°C (Chapter 10). Hence, the isotopic values of the VMS carbonates from the Rosebery district deposits reflect the primary, volcanogenic signature of the Cambrian mineralisation.

- The oxygen and carbon isotopic values versus major and trace element compositions in the VMS carbonates indicate no obvious correlations. However, the oxygen and carbon isotopic composition of the VMS carbonates with >25 wt % Mn display a fractionation trend which may be relate to decreasing temperature of deposition. Overall the data suggest that the South Hercules VMS carbonates formed at lower temperatures and from more Mn-rich ore fluids compared to the Rosebery and Hercules VMS carbonates.

- The VMS carbonates also display different oxygen and carbon isotopic distribution patterns from those of the Devonian carbonates. The VMS carbonates have wider range of oxygen and heavier carbon isotopic values, whereas the majority of the Devonian carbonates show fairly constrained oxygen and lighter carbon isotopic ratios. On this basis, the combined carbon–oxygen isotopic ratios of the carbonates can be used as an additional guide to distinguish Cambrian and Devonian mineralisation in western Tasmania.

- As the carbon and oxygen isotopic compositions of the VMS carbonates in the Rosebery district deposits did not change appreciably during Devonian recrystallisation, the original

isotopic composition of the volcanogenic fluid which formed these VMS carbonates can be estimated. The calculated isotopic composition of the volcanogenic fluid is consistent with fluid derived from evolved seawater with possible incorporation of organic carbon in the system.

- The $\delta^{18}O$ values of biotite and magnetite from the F(J) lens replacement zone were also used to calculate the oxygen isotopic composition of the Devonian hydrothermal fluid. The calculated $\delta^{18}O(H_2O)$ values for the overprinting Devonian hydrothermal fluid vary from 8.0‰ to 12.0‰ with a mode of 10.0‰ and are consistent with a magmatic fluid. The W/R ratio during Cambrian mineralisation was >1 to infinite, whereas the W/R ratio during the Devonian replacement process was estimated to be about 3.5 at 350°C.

- The oxygen isotope geothermometric studies for the quartz–carbonate, quartz–chlorite, chlorite–carbonate, quartz–biotite pairs yielded variable results which are complicated due to impurities in the samples or disequilibrium conditions during ore formation.

- The sulphur isotope values of the sulphide minerals from the South Hercules deposit range from 8.2‰ to 14.1‰ and the sulphur is considered to have been derived from seawater sulphate. The permissible correlation of calculated $\delta^{34}S$ ($H_2S$) values in the ore fluids with gold grades in the South Hercules deposit suggests that gold deposition took place at an evolved stage of the massive sulphide forming system under the increasing $\delta^{34}S_{\Sigma S}$ values of ore fluids with time due to an increase in the proportion of seawater sulphur to leached magmatic sulphur from the volcanics. The permissible correlation of the $\delta^{34}S$ values with gold grades also suggests that the sulphur isotopic composition of the base metal sulphides can be used as a guide to targeting gold-rich massive sulphide systems.

# CHAPTER 10: FLUID INCLUSION STUDIES

## 10.1 INTRODUCTION ...

In this chapter, fluid inclusion data for the Rosebery, Hercules and the South Hercules deposits are presented. No previous fluid inclusion study has been undertaken in the Rosebery–Hercules area. This study was carried out with the following aims: (1) to understand the thermal aspects of the ore deposition, (2) to determine the effect of Devonian overprinting on the fluid inclusions, and (3) to infer the condition of gold and base metal mineralisation and mobilisation. In this investigation, quartz, barite, fluorite, sphalerite, carbonate and helvite were studied.

Fluid inclusions in quartz from the host rock and ore zone of the Rosebery north-end were initially investigated from the sample set collected by D. L. Huston but no workable inclusions were found. Hence, the fluid inclusion study of the Rosebery deposit focusses on the Rosebery south-end orebody (twenty-three samples) and two samples from the pyritic footwall of the north-end. In addition, seven samples from the J–K(P) and R lenses of the Hercules deposit and thirteen samples from the South Hercules deposit were investigated.

## 10.2 METHOD OF STUDY ...

The Fluid Inc. modified USGS heating/freezing stage was used in this study. The general methods and procedure for heating/freezing experiments are reported elsewhere (e.g. Khin Zaw and Khin Myo Thet, 1983; Khin Zaw, 1984) and the methodology of studying $CO_2$-bearing inclusions are applied as reported by Collins (1979) and Khin Zaw (1987). The precision of the temperature measurements is better than ±1°C for heating and ±0.3°C for freezing. Accuracy of the measurements was insured by calibration against the triple point of $CO_2$ (–56.6°C), the freezing point of water (0.0°C), the critical point of water (374.1°C) and synthetic fluid inclusions.

Doubly polished plates were examined in detail under the petrographic microscope prior to the heating and freezing experiments. The fluid inclusions were first located under low magnification to record their distribution, origin, size and types, and to determine their spatial,

temporal and textural relationships. Phase relations were studied under high power objectives (× 100). Descriptions and occurrence of the fluid inclusion samples are presented in Appendices 10.1 and 10.2.

Inclusions which contained daughter NaCl minerals were heated to dissolve the NaCl crystals and determine the salinity as an equivalent NaCl weight percent from the equation of Potter et al. (1977). Those inclusions which did not contain daughter NaCl crystals were frozen, then heated to melt the ice crystals to calculate the salinity as equivalent NaCl weight percent from the equation of Potter et al. (1978).

Some fluid inclusions in this study show evidence of $CO_2$. Hence, the apparent salinity obtained by the freezing of aqueous solutions for these inclusions with no daughter minerals will be higher than the actual salinity. In $CO_2$-bearing inclusions, $CO_2$ hydrates formed upon cooling which extracts $CO_2$ and $H_2O$ from the solution, and results in an increase in the apparent salinity (Collins, 1979). Thus, for the two-phase, liquid and vapour inclusions which show $CO_2$ clathration (formation of $CO_2$ hydrates), the decomposition temperature of the hydrates was determined and the salinity was estimated using the equation of Bozzo et al. (1973).

Laser Raman spectroscopic analyses of the fluid inclusions were also undertaken using the DILOR MICRODIL-28® at the Bureau of Mineral Resources (BMR), Canberra to quantitatively determine the composition of the gaseous components ($H_2S$, CO, $CO_2$, $CH_4$, $SO_2$, $H_2$, $NH_3$, $N_2$), and to identify the daughter minerals.

## 10.3 CLASSIFICATION OF INCLUSION TYPES ...

Characteristics of fluid inclusions in different minerals from the Rosebery–Hercules area are shown in Fig.10. 1. The inclusions can be classified into four major types based on the phases observable in the inclusions at room temperature and their paragenesis. The following inclusion types are observed:

**Type I:** Two-phase, solitary, liquid and vapour inclusions with no $CO_2$. Type I inclusions appear to be the earliest inclusion type as they are isolated, occasionally negative in shape, located away from healed microfractures and cross-cut by other inclusion types (see Figs 10.1A, 10.1D and 10.1F).

**Type II:** Two-phase, liquid–vapour inclusions which may contain daughter minerals (Figs. 10.1B, E, G and H). Type II inclusions are the most abundant inclusion type, and occur as trails as well as clusters and are commonly necked down. Microthermometric and Laser Raman studies indicate that presence of $CO_2$ is an uniform phenomenon for Type II inclusions. Type II inclusions are grouped as 'single' type from Type I inclusions by their textural and petrographic characteristics. Type II inclusions are found in all minerals studied for fluid

inclusions. Daughter minerals in Type II inclusions include cubes of halite and other anisotropic minerals that are rounded to subhedral and sometimes rhomb-shaped. Laser Raman spectroscopy confirmed that the latter are carbonate minerals (see below). Most carbonate daughter minerals did not dissolve at temperatures above 375.0°C.

**Type III:** $CO_2$–liquid bearing inclusions which contain $CO_2$–liquid, $H_2O$–liquid and vapour with or without carbonate daughter minerals. Type III inclusions are found in fluorite associated with tourmaline in the late quartz–tourmaline veins at the Rosebery south-end (Fig. 10.1C). Type III inclusions are also found in quartz from the replacement zones of the F(J) lens. Type III inclusions are rarely seen in minerals from the Hercules and South Hercules deposits. $CO_2$–liquid in Type III inclusions homogenised into the vapour phase.

**Type IV:** Two-phase, liquid-rich inclusions with variable liquid and vapour ratios. Type IV inclusions are found in all minerals studied. Their irregular shape, and variable liquid to vapour ratios indicate a secondary origin. They cross-cut all other inclusion types. The randomly distributed array of these secondary Type IV inclusions and their textural features possibly suggest post- or syn-deformational shearing during their formation. These inclusions are probably recrystallised from other earlier inclusion types during deformation.

Fluid inclusions were also classified in a temporal sense as primary, secondary and pseudosecondary relative to the time of trapping as defined by Roedder (1984). The minerals studied in this investigation do not show any growth zoned pattern and hence the relationship of fluid inclusions and the growth zoning of minerals cannot be used as evidence for a primary origin of the fluid inclusions. Negative shape or isolated, solitary nature are not applied in this study as evidence for primary origin. No positive evidence of a primary origin was observed during microscopic study. Hence all inclusions studied are considered to be of secondary origin. Despite this, some of the early inclusions may relate to Cambrian and Devonian mineralising fluids.

## 10.4 FLUID INCLUSION PETROGRAPHY ...

Textural relationships, distribution and characteristics of the different types of fluid inclusions in different host minerals are described below.

### 10.4.1 Fluid inclusions in sphalerite ...

Sphalerite occurs as banded or disseminated assemblages at the Rosebery, Hercules and South Hercules deposits. Although sphalerite is a major ore mineral, it does not provide a good record for the evolution of fluids with time. It is easily recrystallised and becomes brown or dark brown during Devonian metamorphic and metasomatic processes. This results in poor optical clarity for fluid inclusion study.

*Rosebery:* Banded sphalerite samples from the Rosebery south-end contain many trails of Type II inclusions (sample R4174 at 33m, F lens and 16L-2, 35N, E lens). The recrystallised, Fe-rich, nearly black sphalerite (samples R1526 at 1046' and R4172 at 91.5 m, F lens) and Fe-poor, yellowish sphalerite (sample R4495 at 52.2 m, F lens) in the late quartz ± carbonate veins also contain trails of Type II inclusions along healed fractures, which suggests a secondary origin.

*Hercules–South Hercules:* Most of the sphalerite samples from the Hercules and South Hercules deposits are dark brown due to strong metamorphic recrystallisation, and the fluid inclusions in these sphalerite samples are also strongly annealed and optically unsuitable for fluid inclusion study. However, two sphalerite samples from the South Hercules deposit (H1145-5 at 45.7 m, 5600mN and H1114-13 at 50.0 m, 5630mN) appear to have been less affected by metamorphic annealing and their light brown colour also provides sufficient optical clarity for textural investigation of the fluid inclusion types. In one sample (H1142-5 at 45.7 m, 5600mN), light brown sphalerite contains both types I and II inclusions. Type I inclusions are observed in the core of the crystal, and they are surrounded by trains of Type II inclusions (Fig. 10.1F).

### 10.4.2 Fluid inclusions in barite ...

Barite occurs mostly with sphalerite and carbonate minerals. Although barite has better optical quality than sphalerite, no growth patterns of the mineral relative to fluid inclusions were observed.

*Rosebery:* Three barite samples from the Rosebery deposit were studied. The first two are from E lens in association with massive sphalerite (sample 16L-2, 35N, E lens and R4174 at 33 m, F lens). The third is a barite sample collected from the barite-rich H lens (sample R3808 at 153 m). Barite from Rosebery contains both Types I and II inclusions and very rarely Type III.

*Hercules–South Hercules:* One barite sample from the Hercules Mine (1450'N/ 200'S) and three barite samples from the South Hercules deposit (H1145-2B at 61.3 m, 5670mN, H1100-1 at 29.5 m, 5720mN and H1100-2 at 63.5 m, 5720mN) were investigated in this study. Type I and II inclusions were observed (Figs. 10.1D and 10.1E). Trails of Type II inclusions are commonly found in the barite crystals (Fig. 10.1E) and sometimes these trails of Type II inclusions cross-cut the groups of Type I inclusions.

Fig. 10.1A. Low salinity, two-phase, liquid and vapour, Type I inclusion in quartz, Sample No. 3033-22 at 149', F(J) lens, Rosebery south-end, western Tasmania.

Fig. 10.1B. Negative-shaped, Type II, $CO_2$-bearing inclusion in helvite with two carbonate daughter minerals (d). Sample No. 88R-6 at 1200m, F(J) lens, Rosebery south-end, western Tasmania.

Fig. 10.1C. $CO_2$-liquid bearing Type III inclusion with two carbonate daughter minerals (d), Sample No. R1477 at 1096', F(J) lens, Rosebery south-end, western Tasmania. $CO_2(L) = CO_2$ liquid.

Fig. 10.1D. Types I (ty 1) and II (ty 2) inclusions in barite. Note alignment of Type I inclusions cross-cut by trails of Type II inclusions with variable salinity. Sample No. R3808 at 153m, H lens, Rosebery south-end, western Tasmania.

Fig. 10.1E. Trails of Type II inclusions in barite. Sample No. H1145-2B at 61.3m, 5670mN, South Hercules deposit, western Tasmania.

Fig. 10.1F. Solitary Type I (ty 1) inclusion surrounded and cross-cut by trails and arrays of many $CO_2$-bearing Type II (ty 2) inclusions in sphalerite. Note that many Type II inclusions are dark or opaque due to the dark brown colour of the host sphalerite but the Type I inclusion location is very light brown. Sample No. H1142-5 at 45.7m, 5600mN, South Hercules deposit, western Tasmania.

Fig. 10.1G. Type II inclusions in sphalerite. Sample No. H1142-5 at 45.7m, 5600mN, South Hercules deposit, western Tasmania.

Fig. 10.1H. Stubby Type II inclusions in quartz, d=carbonate daughter mineral. Sample No. H1142-5 at 45.7m, 5600mN, South Hercules deposit, western Tasmania.

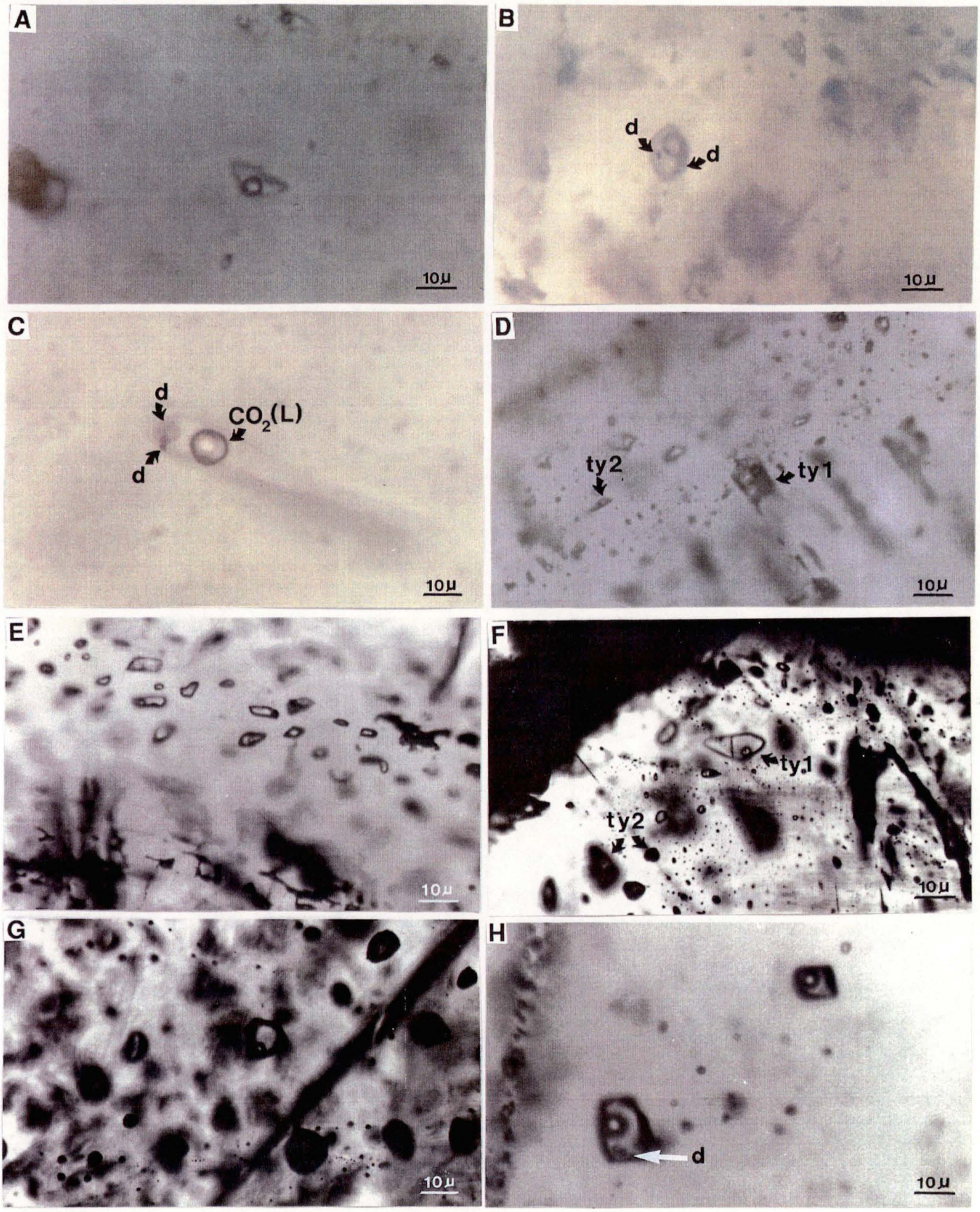
A
10μ
B
d
d
10μ
C
d
$CO_2$(L)
d
10μ
D
ty2
ty1
10μ
E
10μ
F
ty1
ty2
10μ
G
10μ
H
d
10μ

### 10.4.3 Fluid inclusions in quartz ...

All types of inclusions were found in quartz, as quartz occurs in different generations and provides the best mineral recorder of the evolution of fluids with geologic time.

*Rosebery:* Type I, solitary, two phase, liquid and vapour inclusions are commonly found in quartz (Fig. 10.1A). Type II, $CO_2$-bearing inclusions are also seen in a quartz sample collected from the footwall of G lens, 17 Level. The quartz is associated with sulphides (sphalerite, galena and chalcopyrite) and carbonates. Solitary Type I inclusions may be found surrounded by trails of Type II inclusions.

Type I inclusions are also found in the quartz from the thin quartz–chalcopyrite veins in the footwall massive pyrite (sample 15L-1, 600mN) of D lens. The quartz from the remobilised, patchy, irregular quartz–carbonate ± sphalerite veins contains abundant Type II inclusions. The quartz from all the replacement zones of the F(J) lens also contains Type II as well as Type III inclusions. Halite daughter crystals are rarely identified by microscopy in fluid inclusions in the quartz from the biotite–magnetite zone of the F(J) lens but birefringent carbonate daughter minerals are commonly observed.

*Hercules–South Hercules:* Quartz occurs both in the matrix and in veins. Matrix quartz grains generally contain only secondary Type IV inclusions. The Type I and II inclusions in the matrix quartz grains were destroyed or were too small (<5 μm) to be useful for microthermometry.

Vein quartz associated with sphalerite, galena, chalcopyrite and sulphosalts shows abundant, multiple arrays of fluid inclusions. Due to these arrays, Type I and Type II inclusions in quartz cannot be easily distinguished. Hence, the inclusions in quartz are considered to be Type II, $CO_2$-bearing inclusions. Type II inclusions in quartz are subhedral to stubby and may contain carbonate daughter minerals (Fig. 10.1H).

### 10.4.4 Fluid inclusions in fluorite ...

Fluorite occurs mostly as gash veins or rounded to subhedral grains in the altered host rock. It may also occur as an accessory mineral in quartz–tourmaline–magnetite veins of Devonian origin. Heating of $CO_2$-bearing inclusions in fluorite often led to decrepitation due to the rapid increase of internal pressure. Stretching of inclusions as described by Bodnar and Bethke (1984) and Wilkins (1986) was also a common problem for large fluid inclusions in fluorite, but smaller inclusions (<5 μm) provide meaningful homogenisation temperatures.

*Rosebery:* Fluorite commonly occurs in the south-end in association with biotite, tourmaline and helvite, whereas fluorite is rarely reported at the Rosebery north-end. Fluorite also occurs in the late quartz–tourmaline–magnetite veins in the hangingwall of the Rosebery south-end

orebody. Fluorite commonly contains Type III, $CO_2$–liquid bearing inclusions (Fig. 10.1C). These inclusions may contain carbonate daughter minerals (Fig. 10.1C).

*Hercules–South Hercules:* As was mentioned previously, two textural types of fluorite were recognised at the Hercules and South Hercules deposits: (1) discrete, rounded fluorite grains of possible primary Cambrian hydrothermal origin, and (2) recrystallised grains in gash veins of possible Devonian origin (Chapter 4). It is interesting to note that most of the discrete fluorite grains contain no workable inclusions. It appears that fluid inclusions of primary exhalative origin in fluorite were destroyed during Devonian metamorphic recrystallisation. Gash vein fluorite contains abundant fluid inclusions, but only Type II and IV inclusions can be recognised and the inclusions are mostly recrystallised and necked down. Type II inclusions mostly occur as multiple arrays.

### 10.4.5 Fluid inclusions in carbonate ...

The carbonate minerals in the Rosebery–Hercules area occur as major zones of massive and disseminated carbonates either lateral to, above or below the lead–zinc lenses. These carbonates display wide textural variation including bladed carbonate, disseminated carbonate, carbonate spheroids, recrystallised massive carbonate, and vein carbonate (Chapters 2, 3 and 4).

*Rosebery:* Fluid inclusions in the carbonate spheroids in the G lens from the host rock horizon on 17 Level and in the carbonate from a quartz–carbonate vein between G and H lens on the 16 Level were investigated but most inclusions were <5 μm and not suitable for fluid inclusion study.

*Hercules–South Hercules:* Although carbonate minerals from the Hercules and South Hercules deposits (sample H1062-1 at 185' and H1108-9A at 46m) contain inclusion Types I and II, no workable inclusions were recognised. Most carbonate samples are cloudy due to recrystallisation and are not suitable for fluid inclusion study.

### 10.4.6 Fluid inclusions in helvite ...

Helvite and garnet are only found in the Devonian replacement zone of the F(J) lens, Rosebery south-end. Helvite from the biotite–magnetite ± chalcopyrite zone contains Type II inclusions with carbonate daughter minerals (Fig. 10.1B). The garnet was also studied but no workable fluid inclusions were found.

## 10.5 FLUID INCLUSION MICROTHERMOMETRY ...

Heating and freezing of fluid inclusions from selected samples from the Rosebery south-end and the South Hercules deposit were undertaken, and the data are listed in Appendices 10.3 and 10.4. Only quartz, fluorite and helvite from the Rosebery south-end were studied.

Although samples from the Hercules mine were optically examined for their fluid inclusion characteristics, no heating/freezing experiments were carried out for these samples. Freezing point depression was expressed as NaCl equiv. wt %. First melting temperatures of –31.0°C to –41.0°C also suggest that other salts such as calcium, magnesium, potassium, iron and manganese may be present in both Type I and II inclusions in quartz from Rosebery. Similarly, first melting temperatures at South Hercules yielded –23.0°C to –50.0°C.

### 10.5.1 Homogenisation temperatures for F(J) lens, Rosebery ...

Figure 10.2 shows a histogram of homogenisation temperature data for the different inclusion types in the minerals from the F(J) lens, Rosebery south-end. Type I inclusions in quartz give a homogenisation temperature range of 194°C –296°C. Type II inclusions mostly decrepitated as the internal pressure of $CO_2$ increases very rapidly during heating experiments.

Homogenisation temperatures of Type II inclusions in quartz vary from 185°C to 336°C and decrepitation temperatures range from 259°C to 345°C, whereas Type II inclusions in helvite give a filling temperature range of 300°–330°C. Type I inclusions give a mode of 240°C whereas a mode of 340°C was recorded for the Type II inclusions (Fig. 10.2). Homogenisation temperatures of Type III inclusions in fluorite from a late quartz–tourmaline–magnetite vein yielded 237°–265°C (not plotted in Fig. 10.2). The $ThCO_2$(L–V)–V of the Type III inclusions in quartz and fluorite give a homogenisation temperature range of 14.0°C–27.0°C with a mode of 22.0°C (Fig. 10.3).

The $ThCO_2$(L–V)–V data provide density of $CO_2$ inclusions from 0.15 to 0.25 g $cm^{-3}$ according to the phase relation given by Shepherd et al. (Fig. 6.17, 1985). Some workers (e.g. Parry, 1986; Ramboz and Charef, 1988) estimate $CO_2$ content in fluid inclusions by microthermometry. A large amount of error can be involved in such estimation as it requires measurements such as the size of the inclusion and bubble to obtain the exact degree of filling, and the dissolved salt content. Fluid inclusions are three dimensional objects and measurement can only be made in two dimensions. Despite these problems, bulk composition of the Devonian metasomatic fluids was roughly calculated as $X_{H2O}$=0.7, $X_{NaCl}$=0.2, $X_{CO2}$=0.1.

### 10.5.2 Homogenisation temperatures for South Hercules ...

Homogenisation data for Type I inclusions from the South Hercules deposit are shown in Fig. 10.4. Type I inclusions in fluorite give a homogenisation temperature range of 145°–176°C whereas homogenisation temperatures of Type I inclusions in barite range from 150°C to 210°C and Type I inclusions in the light brown sphalerite yield a homogenisation temperature range of 129°–185°C (Fig. 10.4).

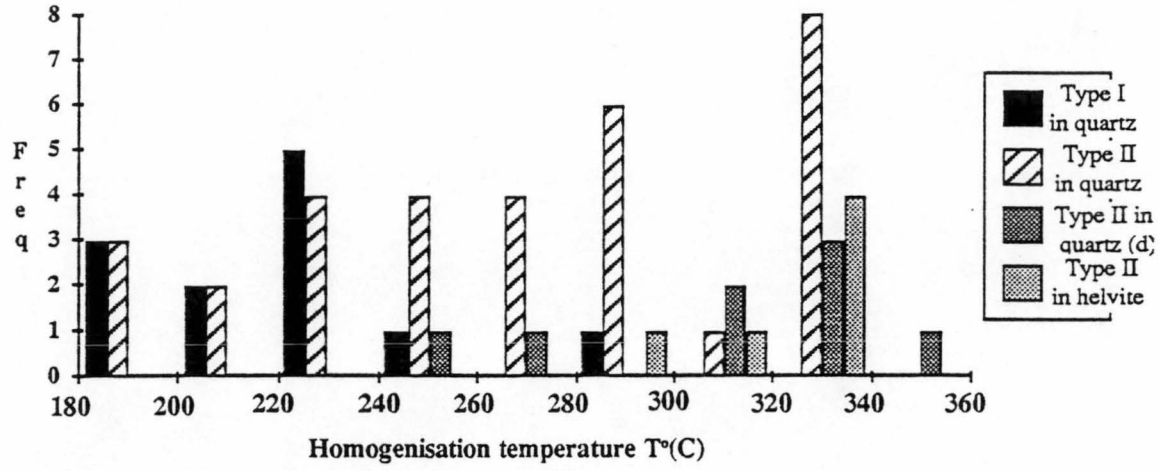


Fig.10.2. Histogram showing the homogenisation temperature of Type I and Type II inclusions, F(J) lens, Rosebery mine, western Tasmania. (d) = decrepitation temperature.

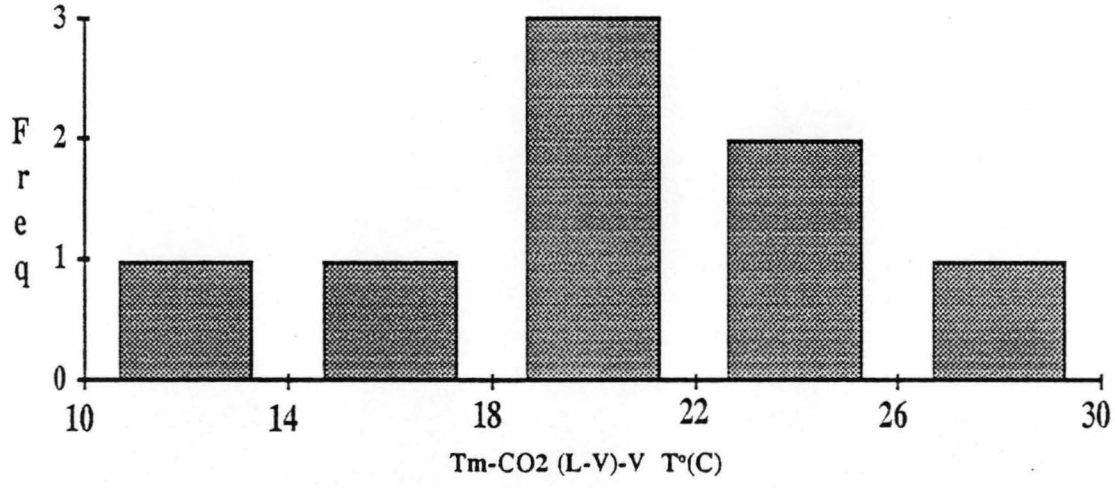


Fig. 10.3. Histogram showing the homogenisation temperature of $CO_2$-liquid bearing Type III inclusions in quartz, F(J) lens, Rosebery mine, western Tasmania.

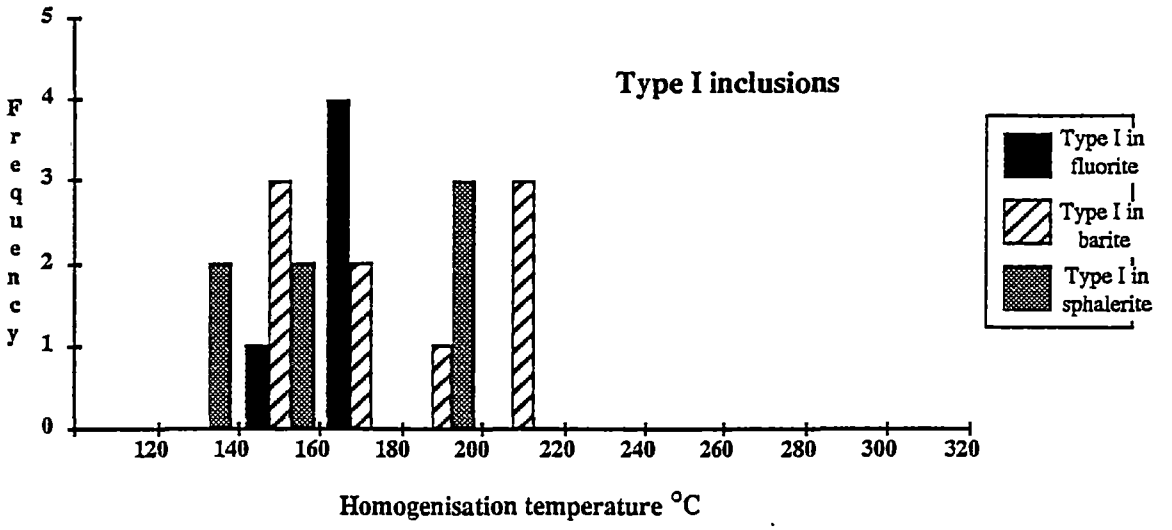


Fig. 10.4. Histogram showing the distribution of homogenisation temperatures of Type I inclusions from the South Hercules deposit, western Tasmania.

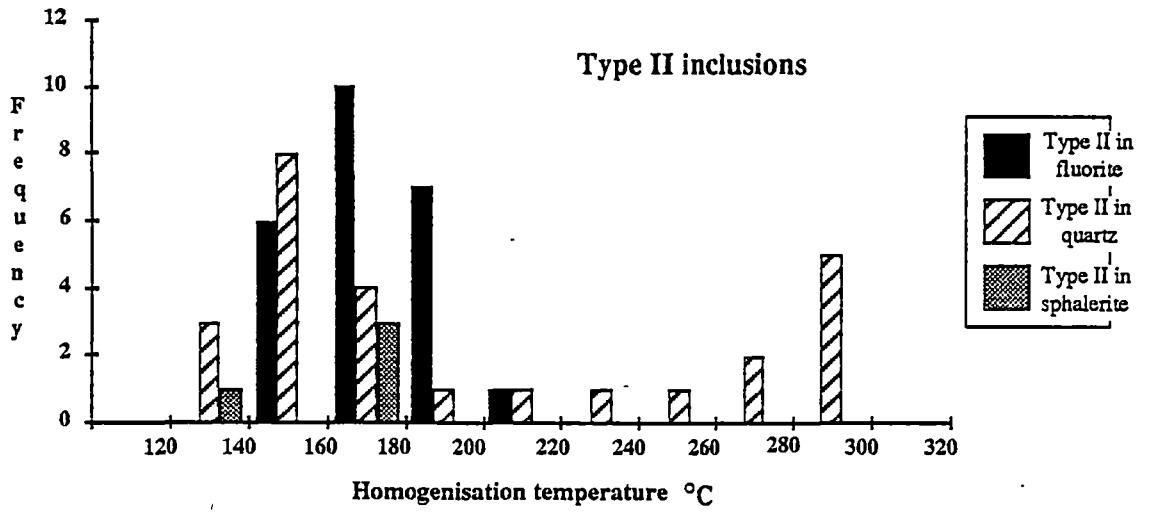


Fig. 10. 5. Histogram showing the distribution of homogenisation temperatures of Type II inclusions from the South Hercules deposit, western Tasmania.

A histogram showing the distribution of homogenisation temperatures for Type II inclusions from the South Hercules deposit is shown in Fig. 10.5. Homogenisation temperatures of Type II inclusions in fluorite vary from 142°C to 202°C with a mode of 180°C. Type II inclusions in quartz vary from 132°C to 299°C and show a bimodal distribution at 160°C and 300°C. This bimodal distribution suggests that the fluid inclusions have been recrystallised, possibly during the Devonian.

Only four heating runs for Type II inclusions in sphalerite were made, which yielded homogenisation temperatures between 124.0°C and 174.0°C. As Type II inclusions mostly lie in the dark brown, annealed parts of the sample, they are difficult to observe clearly. In addition, Type II inclusions in sphalerite decrepitated due to increases in internal pressure of $CO_2$. Hence, although these inclusions are large enough (>10μm) for fluid inclusion study, difficulties arise during heating experiments.

### 10.5.3 Salinity data for F(J) lens, Rosebery ...

Results of salinity determinations are shown in Fig. 10.6. The salinities of Type I inclusions in quartz varied from 2.4–8.7 NaCl equiv. wt %. As Type II, $CO_2$-bearing inclusions show evidence of clathration, the decomposition temperature of the clathrate (Te) was used for the salinity data when clathration temperatures were recorded. Type II inclusions gave a range of

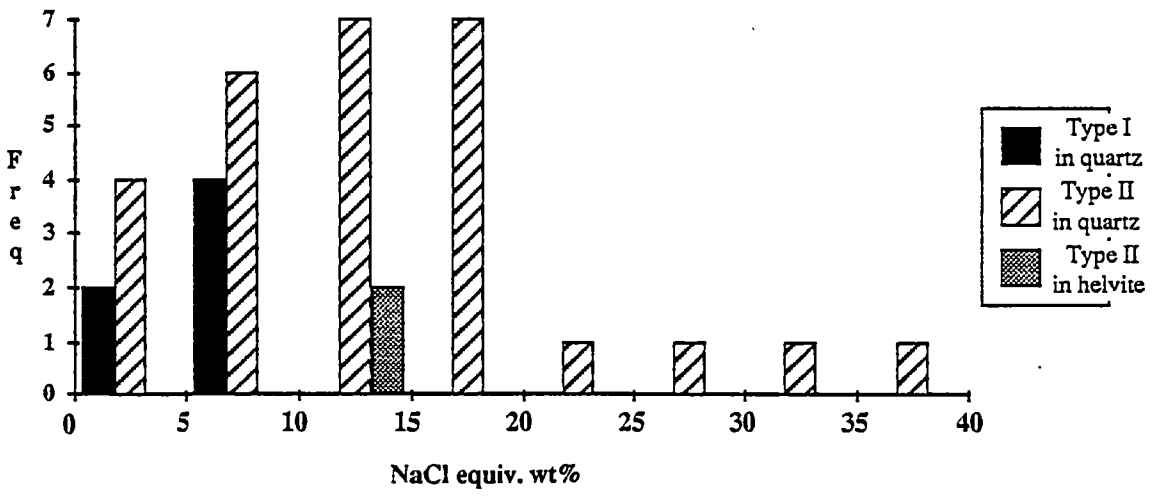


Fig.10.6. Frequency–salinity histogram for the Type I and II inclusions, F(J) lens, Rosebery mine, western Tasmania.

salinity from 0.5 to to 37.3 NaCl equiv. wt %. Type III, $CO_2$-liquid bearing inclusions in fluorite from late veins yielded 2.0–6.0 NaCl equiv. wt % (not plotted in Fig. 10.6).

### 10.5.4 Salinity data for South Hercules ...

Salinity data for the South Hercules deposit are shown in Figs 10.7 and 10.8. The salinity of Type I inclusions in fluorite from the South Hercules deposit gave 0.9–1.6 NaCl equiv. wt %, whereas Type I inclusions in barite range of 0.5–4.2 NaCl equiv. wt % and two Type I inclusions in sphalerite gave 0.4–0.7 NaCl equiv. wt % (Fig. 10.7). Type I inclusions are notably low-salinity inclusions.

Type II, $CO_2$ bearing inclusions in fluorite give variable salinities from 1.4 to 19.8 NaCl equiv. wt %. Similarly, Type II inclusions in quartz yielded a range of 0.5–13.6 NaCl equiv. wt %. Only two Type II inclusions in sphalerite were frozen and gave 4.2– 7.0 NaCl equiv. wt % (Fig. 10.8).

## 10.6 Laser Raman Spectroscopy ...

In recent years, two molecular vibrational spectroscopy techniques have been used for non-destructive analysis of individual fluid inclusions: (1) Laser Raman Spectroscopy (LRS) and (2) Fourier Transform Infra-red Spectroscopy (FTIR). At present, the application of the FTIR method to the study of fluid inclusions is severely limited by mineral opacity under the infra-red beam and lower magnification (310×) relative to the Laser Raman spectroscopic analysis (1000×). Hence, inclusions less than 20 μm are not suitable for the FTIR method. Also FTIR can be used only as a qualitative technique.

In comparison, the laser Raman spectroscopic method can be used as a quantitative technique to determine the composition of fluid inclusions, particularly the gaseous components (e.g. $H_2S$, CO, $CO_2$, $CH_4$, $SO_2$, $H_2$, $NH_3$, $N_2$), of the inclusion fluids with a detection limit as low as 0.1 mole %. The disadvantage of LRS is that simple ionic species such as $Ca^+$, $Na^+$, $K^+$, $Cl^-$ and their salts NaCl, KCl and $CaCl_2$ are not Raman-active either in pure crystalline form or aqueous solutions and cannot be easily determined by the laser Raman method (Pasteris et al., 1986). However, hydrated solid phases that precipitate by controlled freezing can be identified by laser Raman spectroscopy (Dubessy et al., 1982; Mernagh and Wilde, 1989).

Laser Raman analysis also can be used in identifying daughter minerals and in the partial chemical analysis of polynuclear components in aqueous solutions (e.g. $CO_3^{2-}$ and sulphur species such as $H_2S$, $HS^-$, $HSO_4^{2-}$, $SO_4^{2-}$) (e.g. Rosasco and Roedder, 1979; Dhamelincourt

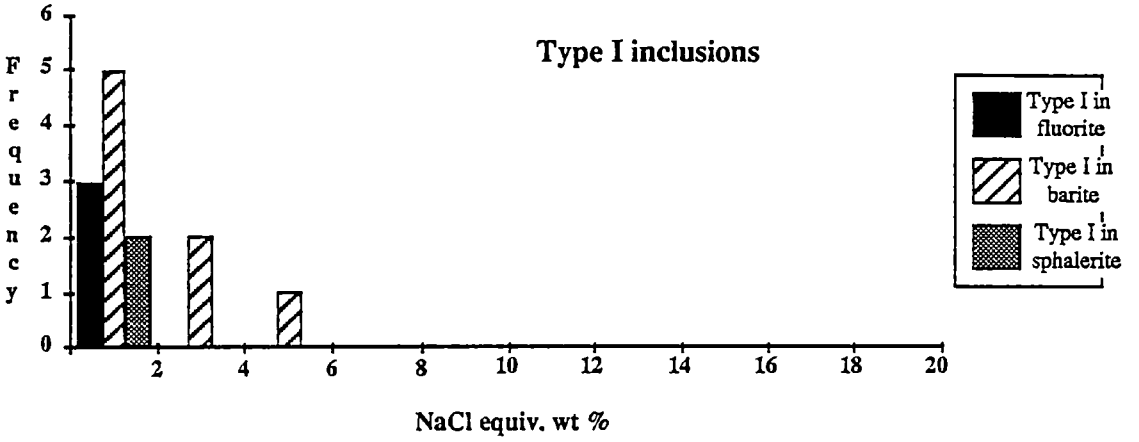


Fig. 10.7. Frequency-salinity histogram for the Type I inclusions from the South Hercules deposits, western Tasmania.

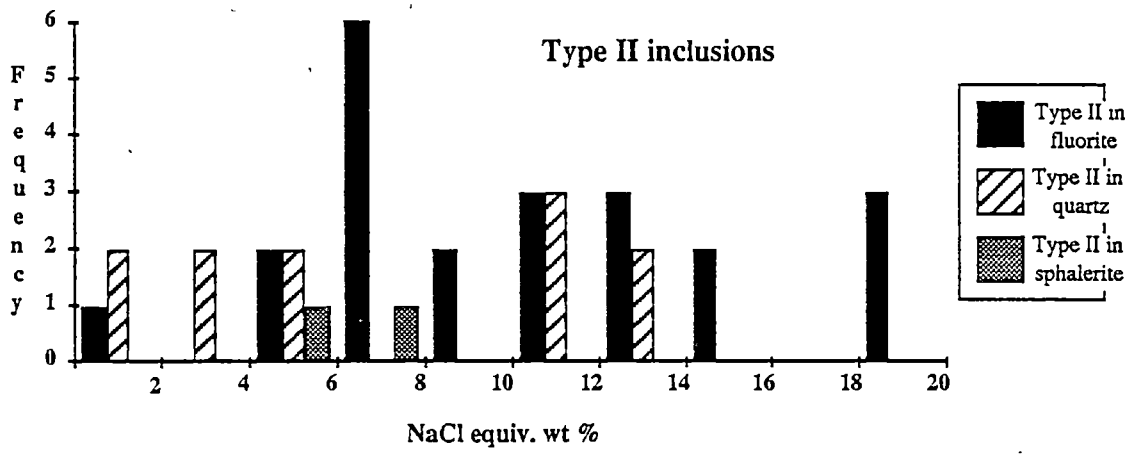


Fig. 10.8. Frequency-salinity histogram for the Type II inclusions from the South Hercules deposit, western Tasmania.

et al., 1979; Dubessy et al., 1982; Guilhaumou et al., 1984; Touray et al., 1985). Two different types of microlaser Raman probes are presently used: (1) RAMANOR U-1000 which is the later model of the MOLE (Pasteris et al. 1986) (2) DILOR MICRODIL-28® (Barbillat et al., 1985; Burke and Lustenhouwer, 1987; Liu and Mernagh, 1990). In this study, the DILOR MICRODIL-28® at BMR is used. The instrument is manufactured by Dilor Co., Lille, France. A brief outline of the DILOR MICRODIL-28® is presented below. Pasteris et al. (1986) describe the RAMANOR U-1000.

### 10.6.1 DILOR MICRODIL–28® ...

Figure 10.9 shows a diagrammatic sketch of the illumination and collection paths in the DILOR MICRODIL-28®. Samples in a diamond-anvil cell are irradiated with a laser beam ~2 μm in diameter using an Olympus BH-2 microscope. The 514.5 nm green line of a Spectra 2020 3W argon ion laser was used as the excitation source at a power of ~600 mW at the source (~60 mW on the sample) (Liu and Mernagh, 1990).

The incident laser excitation is linearly polarised in the X direction (Fig.10.10) and travels along a path which includes a half-wave plate for rotating the plane of polarisation, a microscope beam splitter and an objective. The scattered light is collected at an angle of ~$180^0$ by the same objective, before passing through the beam splitter and a diaphragm which acts like a spatial filter and controls the effective numerical aperture of the objective without modifying the excitation volume within the sample.

The scattered radiation then passes into a F/5 double monochromator with two 1800 groove/mm plane holographic gratings. This is followed by a conventional stigmatic spectrograph with plane grating and large aperture objectives. Two gratings of 600g/mm and 1800g/mm mounted back to back on a rotating disc provide dispersions of ~1500–2300 $cm^{-1}$ and ~300–400 $cm^{-1}$ respectively, depending on the absolute wavelength position. In these experiments, Raman spectra were recorded from 75 $cm^{-1}$ to 1600 $cm^{-1}$ using a spectral resolution of around 3 $cm^{-1}$ and are accurate to ± 1 $cm^{-1}$ (Liu and Mernagh, 1990).

The DILOR MICRODIL-28® has two detectors and can be operated as a scanning spectrometer by using the monochannel photomultiplier tube located directly after the double monochromator. However, all spectra recorded in this study were obtained by using the multichannel detector situated after the spectrograph. This consists of a multichannel plate intensifier coupled to a 512 photodiode array and both are cooled to $-20^0$C by a Peltier semiconductor element. Raman spectra recorded at room temperature were typically acquired after 20 accumulations with 5 seconds integration time. The detectors are linked via an IB10 interface to a Cleveland 286 SP personal computer and the data are recorded and interpreted using software supplied by Dilor. The resulting Raman spectra are then plotted on a Houston Instrument HIPLOT DMP- 40 plotter (Liu and Mernagh, 1990).

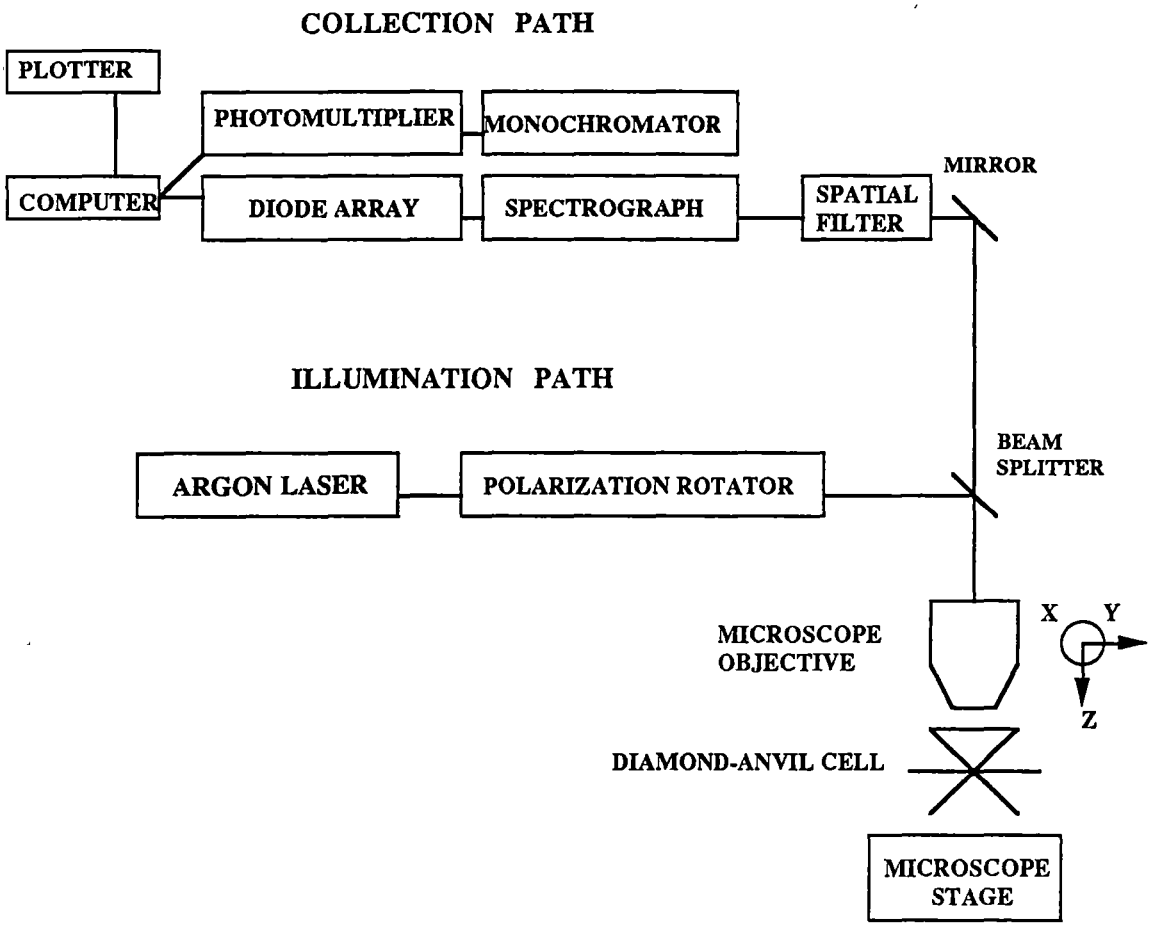


Fig. 10.9. Diagrammatic sketch of the components of the laser Raman microprobe. See text for further description (after Liu and Mernagh, 1990).

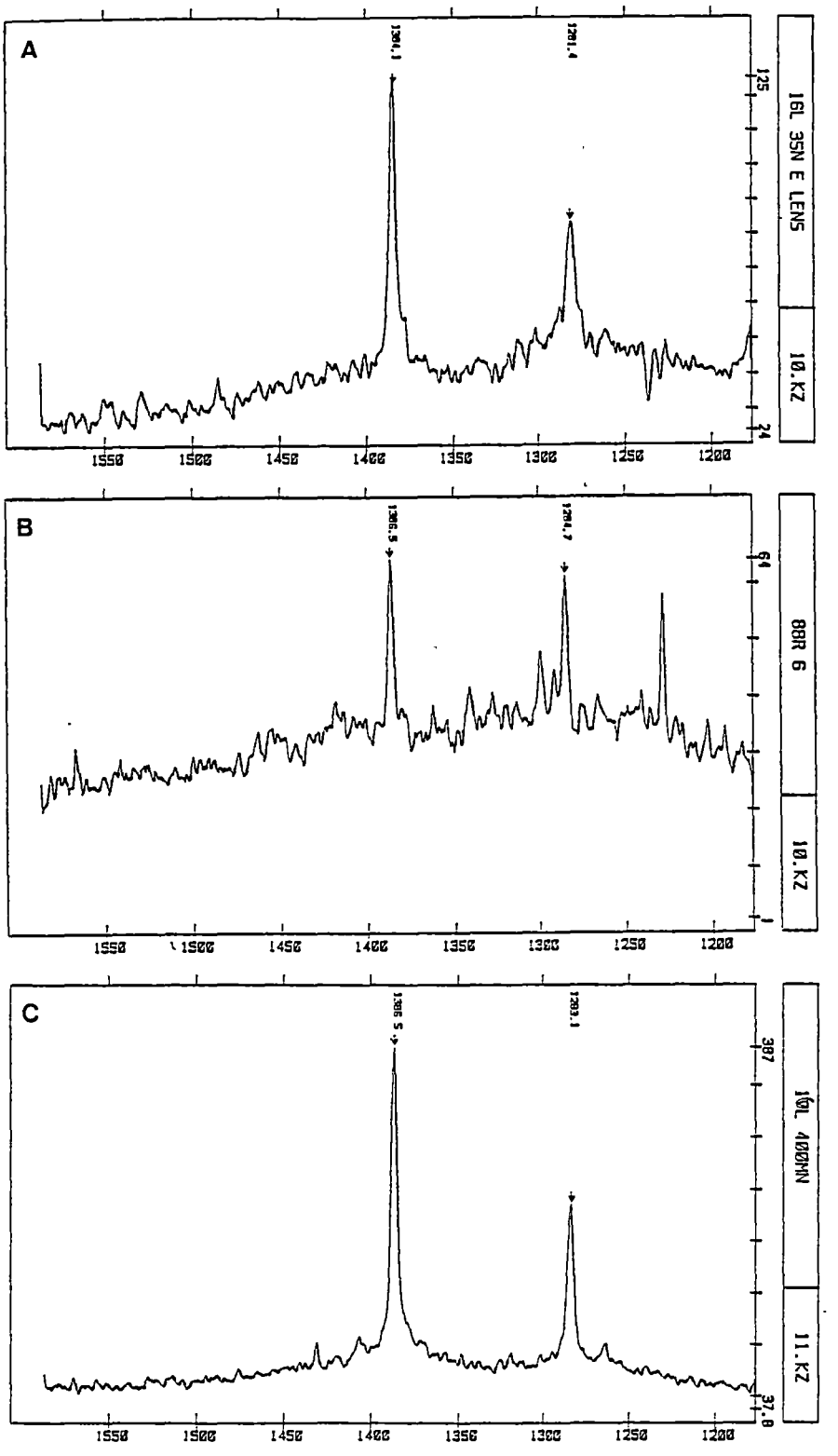


Fig. 10.10 Laser Raman spectra of $CO_2$ in the vapour phase in fluid inclusions from different minerals from the Rosebery south-end, western Tasmania. A. Barite from the lead–zinc sulphide ore zone, Sample No. 16L-2, 35mN, E lens. B. Helvite from the magnetite–biotite zone, Sample No. 88R-6. C. Quartz from remobilised quartz–carbonate vein in the barite zone, 16L-4, 400mN, H lens. Laser power 40mW (at sample) with 3 $cm^{-1}$ band pass. Spectra were averaged from 10 accumulations at 10 seconds counting time.

### 10.6.2 Microanalysis of unopened inclusions ...

The laser Raman spectroscopic method is the most important development in the field of non-destructive analysis as it is a powerful technique for *in situ* pin-point analysis of individual, unopened fluid inclusions. The Raman spectra emerges at a longer or shorter wavelength that is characteristic of the substance irradiated, but the wavelength is shifted from that of the exciting radiation by a specific amount (expressed in frequency, i.e. wave numbers in units of $cm^{-1}$) (Roedder, 1984).

The most important features are that the magnitude of the shift does not change with a change in the exciting radiation, and the Raman scattered light may be almost monochromatic. Hence, the shift for each Raman line is a result of transfer of energy between the incident radiation and molecular vibration in a sample. The laser provides an exceedingly intense, monochromatic light source and its radiation can be focussed down to submicrometer scale. This permits such high levels of irradiation that quantitative analysis can be obtained from particles of μm scale and enables the microanalysis of unopened fluid inclusions as small as 5 μm (Roedder, 1984).

The other development of the non-destructive methods for unopened fluid inclusions at present are Proton-Induced X-ray Emission analysis (PIXE) or Proton-Induced Gamma-ray Emission analysis (PIGE) (e.g. Horn and Traxel, 1987; Anderson et al., 1989; Ryan et al., 1991 in press). In parallel development, Frantz et al. (1987) have recently provided a preliminary record of synchrotron-induced X-ray fluorescence microbeam techniques (SXFM) in the detection of certain ionic species in synthetic fluid inclusions lying at depths as much as 80 μm below the surfaces of quartz crystals.

### 10.6.3 Volatile content of fluid inclusions ...

The composition of the volatile phases in fluid inclusions is very important in understanding the physical and chemical nature of the ore-forming fluids. Pasteris et al. (1986) reported the presence of high-density $CH_4$-dominated fluid inclusions at the Carlin gold deposit by laser Raman analysis. A significant amount of $N_2$ was also observed by laser Raman spectroscopy in the gases of fluid inclusions in quartz from the gold-rich zone of the Juno and TC8 deposits, Tennant Creek, Australia (Khin Zaw et al., 1990b).

In this study, laser Raman spectroscopy was used to scan for $H_2S$, CO, $CO_2$, $CH_4$, $SO_2$, $H_2$, $NH_3$, $N_2$ in the gaseous phases of inclusions from the Rosebery, Hercules and South Hercules deposits. Laser Raman analysis confirmed the presence of $CO_2$ which was earlier reported by microthermometry. Other gas species such as $H_2S$, CO, $CH_4$, $SO_2$, $N_2$, and $NH_3$

were not detected by laser Raman analysis. The samples studied are shown in Appendix 10.5. It is interesting to note that $CO_2$ is commonly found in Type II and Type III inclusions.

Although the presence of $CO_2$ in fluid inclusions in most of the samples from Rosebery, Hercules and South Hercules was confirmed by laser Raman analysis, only four $CO_2$ spectra from the Rosebery south-end were acquired (Table 10.1 and Fig. 10.10). The laser Raman shift of up to 1386.5 $cm^{-1}$ suggests a high $CO_2$ pressure as it is close to that for liquid $CO_2$ (pers. comm. Terry Mernagh, 1990).

Table 10.1 Laser Raman spectra ($cm^{-1}$) of $CO_2$ in fluid inclusions from different host minerals of the Rosebery south-end, western Tasmania.

| Sample No. | Host Mineral | Major ($cm^{-1}$) | Minor ($cm^{-1}$) | Associated minerals |
|---|---|---|---|---|
| 88R-6, F lens, II* | helvite | 1386.5 | 1284.7 | magnetite, biotite |
| 16L-2, E lens, III | barite | 1384.1 | 1281.4 | massive sphalerite |
| 16L-4, H lens, II | quartz | 1386.5 | 1283.1 | recrystallised galena |
| R3492-20, F lens, II | quartz | 1386.5 | 1281.4 | pyrrhotite, pyrite |

*inclusion types

### 10.6.4 Daughter mineral identification ...

Laser Raman spectroscopic study is particularly useful in identifying daughter minerals which have polynuclear components such as $SO_4^{2-}$ or $CO_3^{2-}$ in their structures as these compounds produce strong sharp Raman spectra. Rosasco and Roedder (1979) measured $SO_4^{2-}$ contents of inclusion fluids from a porphyry copper deposit, although the precision is low with a reported value of 12,000 ± 4000 ppm. The presence of anhydrite daughter minerals in fluid inclusions can also be confirmed by the laser Raman method (Roedder; 1984). Recently Wilde et al. (1989) recorded anhydrite, dolomite, hematite and chlorite daughter minerals in fluid inclusions from the Nabarlek, Koongarra, and Jabiluka deposits of the Northern Territory, Australia.

Herman et al. (1987) reported that laser Raman spectroscopy can be used to identify carbonate minerals and even to distinguish calcite, dolomite, and aragonite structural groups. The minerals considered are carbonate minerals such as calcite ($CaCO_3$), magnesite ($MgCO_3$), siderite ($FeCO_3$), rhodochrosite ($MnCO_3$), smithsonite ($ZnCO_3$), dolomite [$(CaMg(CO_3)_2$], ankerite [$(CaFe(CO_3)_2$], kutnahorite [$(CaMn(CO_3)_2$].

The Raman spectra of the calcite group minerals show the strongest peak at approximately 1090 $cm^{-1}$. The shifts in spectral position of this line for the different carbonates from this

group are small but systematic. The pronounced shifts were also noted for the lines observed in the region of 300 $cm^{-1}$, and other weak lines are located at 714–739 $cm^{-1}$ and 1450–1760 $cm^{-1}$ (Fig. 1, Herman et al., 1987). The minerals having the dolomite structure have a mixed cation composition, and their Raman spectra resemble those of the calcite group carbonates. Although the set of line positions is unique for each mineral within the dolomite group (Fig.2, Herman et al., 1987), the spectrum of kutnahorite is analogous to that produced by calcite and by rhodochrosite at the strongest line of approximately 1090 $cm^{-1}$.

During the course of the fluid inclusion microthermometry, unidentified, rounded to subhedral, birefringent daughter minerals were a constant puzzle. These birefringent minerals were commonly found in quartz, barite, sphalerite, fluorite and helvite from the Rosebery, Hercules and South Hercules deposits. They mostly occur in the Type II and III inclusions. Hence, different mineral samples were selected for identification of the daughter minerals by laser Raman spectroscopic analysis (Appendices 10.3 and 10.4) . Table 10.2 lists the major and minor laser Raman spectra bands or Raman shifts ($cm_{-1}$) recorded for the daughter minerals and Fig. 10.11 shows laser Raman spectra of daughter minerals in the inclusions from the Rosebery–Hercules area.

Most of the birefrigent daughter minerals obtained Raman shifts with major lines at 1085.5–1086.7$cm^{-1}$ (Table 10.2). These lines suggest that the carbonates are not dolomites which have 1099$cm^{-1}$ as a major line. The results are more consistent with calcite, rhodochrosite and kutnahorite (cf. Herman et al., 1987), but these three cannot be accurately distinguished. Two of the daughter minerals were checked for minor lines which yielded 720.8–1424.5–1726.1$cm^{-1}$ and 1419.7–1745.4$cm^{-1}$ (Table 10.2). The carbonate daughter mineral in sample 16L-3 which has the major Raman line of 1086.7$cm^{-1}$ and minor lines of 720.8–1424.5–1726.1$cm^{-1}$ is probably kutnahorite (Fig. 10.12).

It is also interesting to note that the daughter mineral in a fluid inclusion in quartz from the barite-rich H lens yielded a Raman shift at 987.4–1141.4$cm^{-1}$ which is the characteristic Raman spectra of barite given by Griffith (1970).

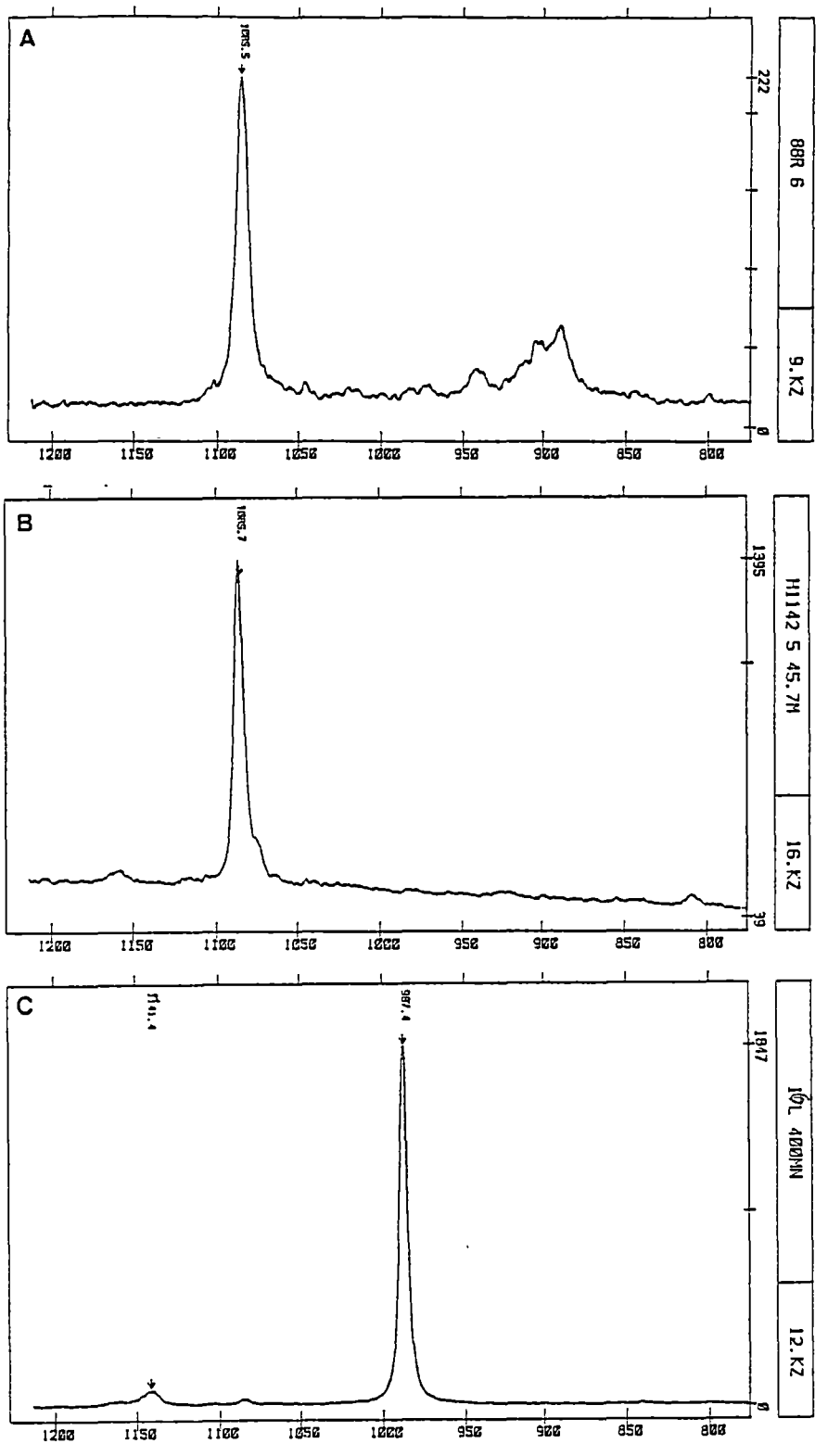


Fig. 10.11. Laser Raman spectra of daughter minerals in fluid inclusions from different minerals from the Rosebery and South Hercules deposits, western Tasmania. **A.** Carbonate daughter mineral in a fluid inclusion in helvite from the magnetite–biotite zone, Sample No. 88R-6 at 1200m, F(J) lens, Rosebery south-end. **B.** Carbonate daughter mineral in a fluid inclusion in quartz from the South Hercules deposit, Sample No. H1142-5 at 45.7m. C. Barite daughter mineral in a fluid inclusion in quartz from a remobilised quartz–carbonate vein in the barite zone, Sample No. 16L-4, 400mN, H lens, Rosebery south-end. Laser power 40mW (at sample) with 3 $cm^{-1}$ band pass. Spectra were averaged from 10 accumulations at 10 seconds counting time.

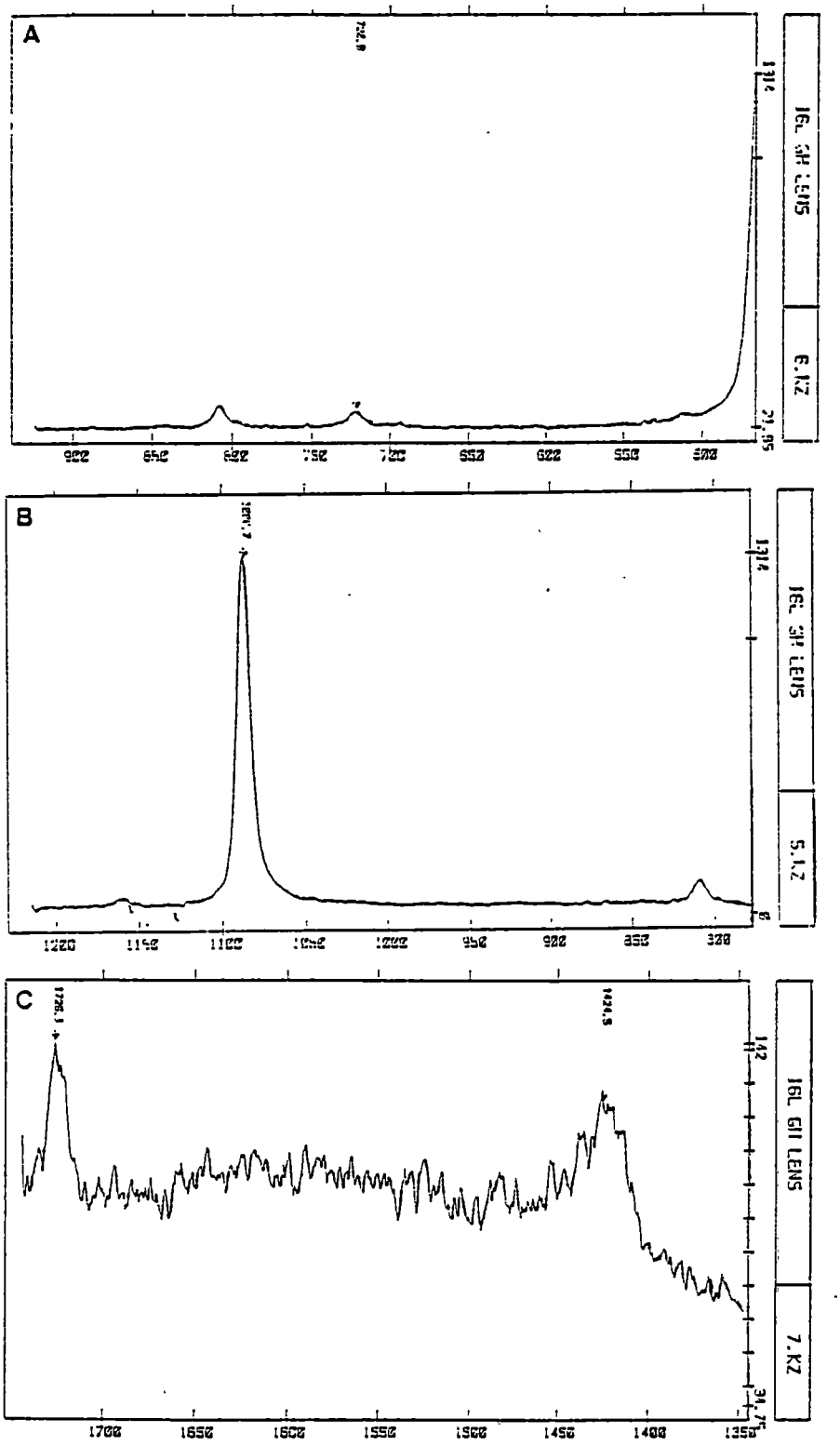


Fig. 10.12. Laser Raman spectra of kutnahorite? daughter minerals in fluid inclusions in quartz from the tourmaline–quartz zone showing major and minor lines. A. Minor line at 720 $cm^{-1}$. B. Major line at 1086.7 $cm^{-1}$. C. Minor lines at 1726.1 $cm^{-1}$ and 1424.5 $cm^{-1}$. Sample No. 16L-3, between G and H lens, Rosebery south-end, western Tasmania. Laser power 40mW (at sample) with 3 $cm^{-1}$ band pass. Spectra were averaged from 10 accumulations at 10 seconds counting time.

Table 10.2 Laser Raman spectra band ($cm^{-1}$) of daughter phases in Type II fluid inclusions from the different host minerals of Rosebery south-end and South Hercules deposit, western Tasmania.

| Sample No. | Host Mineral | Major ($cm^{-1}$) | Minor ($cm^{-1}$) | Daughter phase |
|---|---|---|---|---|
| Rosebery south-end | | | | |
| 15L-1, FW, D lens | quartz | 1085.5 | – | carbonate |
| 15L-1, FW, D lens | quartz | 1086.7 | – | carbonate |
| 16L-3, bet G & H lens | quartz | 1086.7 | 720.8–1424.5–1726.1 | carbonate* |
| 88R-6, F lens | helvite | 1085.5 | – | carbonate |
| R4495 at 52m, F lens | sphalerite | 1085.5 | – | carbonate |
| 16L-4, 400mN, H lens | quartz | 987.4–1141.4 | – | barite |
| 16L-4, 400mN, H lens | quartz | 1089 | – | carbonate |
| 16L-4, 400mN, H lens | quartz | 1086.5 | – | carbonate |
| 16L-4, 400mN, H lens | quartz | 1084 | – | carbonate |
| 106780, F lens | quartz | 1085.5 | – | carbonate |
| R4407, FW, F lens | quartz | 1085.5 | 1419.7–1745.4 | carbonate |
| R3492-20, F lens | quartz | 1085.7 | – | carbonate |
| South Hercules | | | | |
| H1142-5 | quartz | 1085.7 | – | carbonate |

*possibly kutnahorite

## 10.7 PROBLEMS OF FLUID INCLUSION STUDIES ON METAMORPHOSED ORE DEPOSITS ...

Although detailed fluid inclusion studies have been undertaken on the relatively unmetamorphosed Kuroko massive sulphide deposits (e.g. Pisutha-Arnond and Ohmoto, 1983), Roedder (1984) indicated that very few studies have been made of metamorphosed massive sulphide ore deposits, in large part because they frequently are not amenable to study. If an ore deposit has been either formed by, or subjected to, high-grade metamorphic events, a genetic link is difficult to prove (Roedder, 1984). During later metamorphism of an ore deposit, the original inclusions will be lost if the host is recrystallised. Most commonly, complete recrystallisation and even transport and redeposition of the ores takes place, and new inclusions are trapped that registered the metamorphic environment.

If the host mineral is not recrystallised, and if the inclusions were trapped at a sufficiently high temperature and low density that internal pressure during metamorphism does not cause decrepitation, they may survive the metamorphism. Ripley and Ohmoto (1977) demonstrated that primary exhalative fluids were recognisable in fluid inclusions from the strongly

metamorphosed stratabound copper deposit at Raul Mine, Peru. A few very small inclusions were found in quartz from this deposit. These yielded a filling temperature of 350°C ± 10°C interpreted as representative of the original depositional conditions (Ripley and Ohmoto, 1977). The host rocks have only been metamorphosed to the upper greenschist-lower amphibolite facies at temperatures of 400°–500°C (Ripley and Ohmoto, 1977). Since the inclusions were all <5 μm, they were presumed to be capable of withstanding a metamorphic cycle including ~100°C of overheating without decrepitating or stretching.

Broman (1987) recently undertook a fluid inclusion study of a massive sulphide deposit in the Skellefete district, Sweden which have been metamorphosed to greenschist facies and encountered problems in finding suitable fluid inclusions due to metamorphic recrystallisation of the ore and gangue minerals. Broman (1987) reported two groups of primary fluid inclusions, one with homogenisation temperatures of 130°–220°C and the other with 220°–340°C. Both groups had salinities less than 10.0 NaCl equiv. wt %. Secondary inclusions with homogenisation temperatures of 150°–240°C and salinities of 12.0–21.0 NaCl equiv. wt % were also observed, but no daughter minerals and $CO_2$-bearing inclusions were recorded in the Skellefete massive sulphide deposits.

Broman (1987) interpreted that the sulphide ores were formed under non-boiling conditions during two major stages of hydrothermal, exhalative activity at temperatures of 210°C and 295°C respectively. The ore-forming fluids were Ca–Na–Cl-bearing hydrothermal solutions with a salt content of 4.0 ± 2.0 NaCl equiv. wt %. Later recrystallisation of the ores occurred at lower temperatures involving solutions with higher salinities. However, his interpretation of primary inclusions relating to exhalative fluids may be questioned since no single textural criterion for primary origin of the fluid inclusions in relationship with growth of the host minerals was given.

In a similar investigation, Wilkins (1977) found at the strongly metamorphosed Broken Hill deposits, New South Wales, that inclusions from the period of ore deposition had been eliminated by repeated deformation and recrystallisation. He considered that the inclusions provided only a record of the sequence of metamorphic fluids since the period of high-grade metamorphism and indicated that there is no easy way to prove whether or not the early formed inclusions have developed their present compositions by diffusive loss of water or other components during the long period of retrograde metamorphism. Both (1978) has also shown that some of the Broken Hill deposits have been remobilised during retrograde metamorphism.

Rutherford (1963) recorded dense $CO_2$ inclusions in a Canadian massive sulphide deposit. Carignan et al. (1979) reported homogenisation temperatures of 100°–480°C in quartz from

the Millenbach massive sulphide deposit in Canada. Walshe and Solomon (1981) found homogenisation temperature of 130°–150°C (calculated trapping temperature of 200°–225°C at 1 kb) for fluorite veins in the Mt Lyell copper-gold deposit, western Tasmania that have been metamorphosed to the lower greenschist facies.

## 10.8 IMPLICATIONS OF FLUID INCLUSION MICROTHERMOMETRY ...

The interpretation of the present fluid inclusion microthermometric data for the VMS mineralisation in the Rosebery–Hercules area has to deal with the problems described above for other metamorphosed ore deposits. Evidence that recrystallisation and redistribution of precious metals (e.g. gold) and ore minerals (e.g. sphalerite) took place during the later Devonian metamorphic and metasomatic processes has been described in chapters 5–8.

The studied minerals do not show any growth zoning which can be used to demonstrate that the fluid inclusions are definitely primary in origin. No other fluid inclusion textures and characteristics of primary origin were observed except that the low temperature, low salinity Type I inclusions appear to be early as they are isolated and solitary, and are cross-cut by other inclusion types.

Two major fluid systems were assumed to have been associated with the VMS mineralisation in the Rosebery district: (1) fluids of Cambrian exhalative origin and (2) fluids of Devonian origin (metamorphic fluids and/or granite related fluids). Evidence of fluid inclusions which can be unequivocally ascribed to the Cambrian exhalative origin cannot be established in the Rosebery north-end or south-end orebodies.

However, it is tempting to interpret the early Type I fluid inclusions with filling temperatures of ~190°–240°C and salinities <10 NaCl equiv. wt % with no appreciable $CO_2$ as primary exhalative fluids that have survived the Devonian recrystallisation (Fluid 'A', Fig. 10.13). The age of these fluid inclusions cannot be established, so it is equally possible that the Type I inclusions may be related to the $H_2O$-rich, exsolved fluids of Devonian origin. Type II, $CO_2$-bearing inclusions with high salinity strongly suggest a Devonian granite connection (Fluid 'B', Fig. 10.13).

Because helvite from the Rosebery south-end has been clearly shown to be a Devonian metasomatic mineral, Type II fluid inclusions found in helvite from the Rosebery south-end (not plotted in Fig. 10.13) provides the best constraints on the hydrothermal fluids associated with the Devonian replacement processes. Type II inclusions in helvite yielded a homogenisation temperature range of 300°–330°C with considerable dissolved salts up to 15.0 NaCl equiv. wt %. Hence, the present fluid inclusion data indicate that the hydrothermal fluids associated with

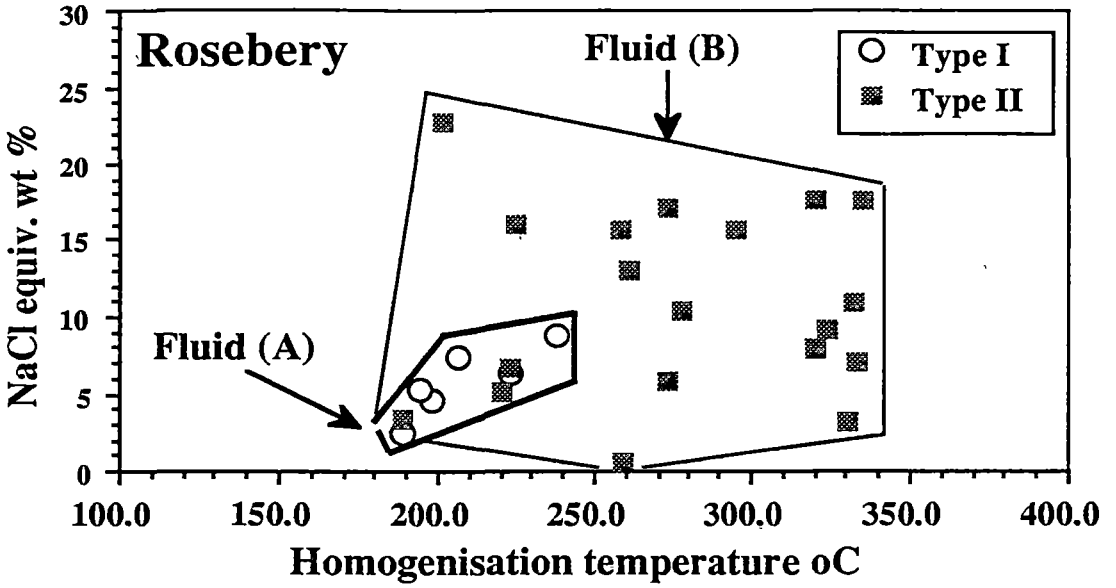


Fig. 10.13. Temperature–salinity (NaCl equiv. wt %) plot of Types I and II inclusions in quartz from the Rosebery deposit, western Tasmania. Note two different fluids (A & B). Fluid (A) is a low temperature, low salinity fluid probably representing the fluid of exhalative origin associated with the Rosebery mineralisation in the Cambrian. Fluid (B) is of variable temperature, higher salinity, and $CO_2$-bearing and was derived from the Devonian granite.

the Devonian replacement process were moderate to high temperature, saline, $CO_2$-bearing complex brines. The fluids with this temperature and composition are likely to have been derived from the inferred Devonian granitoid intrusions below the Rosebery orebody.

No pressure correction was attempted in this study as detailed studies on composition of fluid inclusions have not been undertaken in this research. Even if these compositional data were obtained, experimental data for isochoric relations in the complex NaCl-$CaCl_2$-KCl-$CO_2$-$H_2O$ system are not yet readily available in the literature to make meaningful pressure corrections. Variation in salinity and presence of $CO_2$ in fluid inclusions also suggest that $CO_2$ may have effervesced during the Devonian metasomatic process. If this was the case, the inclusions were trapped at the liquid-vapour boundary, and no pressure (depth) correction is needed and the homogenisation temperatures are justified as trapping temperatures.

Combined with fluid inclusion data for the Types II and III inclusions in quartz and fluorite, trends or changes in the temperature and fluid composition in different replacement zones can be determined (Table 10.3). These data suggest that there was no significant variation in temperature across the various replacement zones although salinity appears to have decreased from 37.0 NaCl equiv. wt % in the early biotite–magnetite zone to 3.0 NaCl equiv. wt % in later pyrrhotite–pyrite and tourmaline–quartz zones. The late fluorite-bearing retrograde veining stage appears to have occurred at cooler temperatures (237°–265°C) and declining salinity (2–6 NaCl equiv. wt %).

Table 10.3 Homogenisation temperature and NaCl equiv. wt % variation in different replacement zones of the F(J) lens, Rosebery, western Tasmania.

| | Homogenisation T°C | NaCl equiv. wt % |
|---|---|---|
| Biotite–magnetite zone* | 300.0–330.0 | 12.0–37.0 |
| Pyrrhotite–pyrite zone** | 273.0–331.0 | 3.0–16.0 |
| Tourmaline–quartz zone** | 185.0–334.0 | 3.0–11.0 |
| Fluorite±tourmaline± magnetite±quartz vein*** | 237.0–265.0 | 2.0–6.0 |

* data from Type II inclusions in quartz and helvite
**data from Type II inclusions in quartz
***data from Type II and III inclusions in fluorite

Fluid inclusion studies at South Hercules also indicate that two groups of fluids were involved during the formation of the deposit. Figure 10.14 shows a plot of the homogenisation temperature versus salinity for the two groups: one with low temperature (125°–210°C) and low salinity (<4.2 NaCl equiv. wt %), and the other with variable temperature (125°–300°C), higher salinity (up to 15.0 NaCl equiv. wt %) and $CO_2$-bearing. The low-temperature, low-salinity fluids are texturally associated with Type I inclusions and it is likely that these fluids represent the Cambrian fluids of exhalative origin (Fluid 'A' in Fig. 10.14). Similar low-temperature (~250°C) and low-salinity inclusions were reported in the Japanese Kuroko deposits (Pisutha-Arnond and Ohmoto, 1983).

The second, high-salinity and $CO_2$-bearing fluids are associated with Type II inclusions which cross-cut the Type I inclusions. Hence, the fluids related to Type II inclusions were generated later, probably during the Devonian metamorphic recrystallisation (Fluid 'B' in Fig. 10.14). In contrast to Rosebery, South Hercules lies further away from the Devonian granite intrusion and would not have been strongly overprinted by the high-temperature, magmatic fluids. However, it has been extensively affected by the Devonian metamorphism. The Type II inclusion fluids are most probably related to this Devonian metamorphic event. They also display two sub-groups clustering at 125°–200°C and 250°–300°C. The reason for these two clusters is not understood but may be due to recrystallisation of Type I inclusions or exsolution of $CO_2$–$H_2O$ fluids during the Devonian metamorphic process.

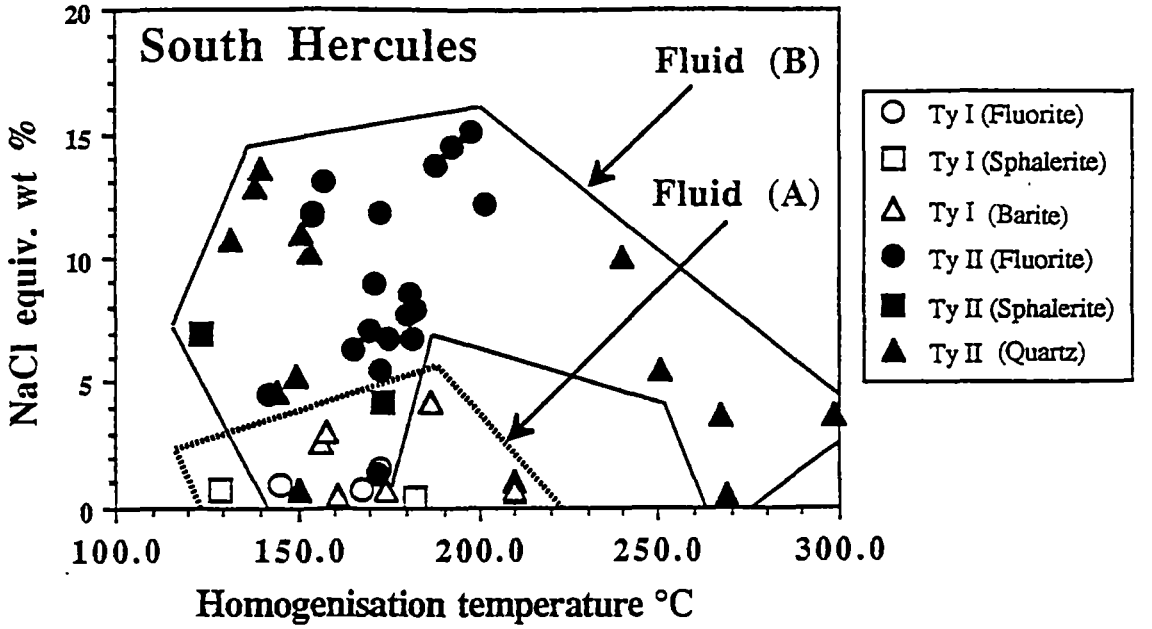


Fig. 10.14. Temperature–salinity (NaCl equiv. wt %) plot of Types I and II inclusions in different minerals from the South Hercules deposit, western Tasmania. Note two different fluids (A & B). Fluid (A) is a low temperature, low salinity fluid probably representing the fluid of exhalative origin associated with the South Hercules mineralisation in the Cambrian. Fluid (B) is of variable temperature, higher salinity, and $CO_2$-bearing and was probably associated with the Devonian overprinting event.

## 10.9 Implications of laser Raman spectroscopy for Cambrian mineralisation and Devonian recrystallisation ...

Fluid inclusions from the Rosebery, Hercules and South Hercules deposits contain abundant carbonate daughter minerals. At Rosebery, the carbonate daughter minerals are very widespread and found in all minerals studied; including remobilised quartz–carbonate veins in the hangingwall as well as in the ore zone and footwall, and in all major replacement zones. The fluid inclusions from Hercules and South Hercules also contain carbonate daughter minerals.

Although the present Laser Raman analysis cannot positively identify the species of carbonate daughter minerals, it constrains the possibility to calcite, kutnahorite and rhodochrosite. The compositional range of the carbonate minerals from the Rosebery–Hercules area is also dominantly calcite–kutnahorite–rhodocrosite with minor iron and magnesium contents (Figs 9.9 and 9.10). In one case, a barite daughter mineral was recorded in quartz from a remobilised quartz–galena vein in H lens.

Hence, the above comparable compositional range of daughter minerals and pre-existing minerals in the enclosing host rocks suggests that the Cambrian VMS carbonates of mostly

calcite–kutnahorite–rhodocrosite composition were dissolved, remobilised and later trapped in the Types II and III inclusions during the Devonian metamorphic and metasomatic processes. The textural, compositional and isotopic characteristics of massive as well as vein carbonates (Chapters 2, 3 and 9) also support this conclusion as evidence of remobilisation and recrystallisation of these carbonates was observed.

In unusual or perhaps extreme conditions, even primary barite in the barite orebody has been dissolved, remobilised and trapped in later secondary fluid inclusions as daughter minerals. The remobilisation and recrystallisation of carbonates and barite is consistent with the compositional variations of sphalerite from the VMS deposits of the Rosebery–Hercules area which also show evidence of recrystallisation during Devonian events (Chapter 8). Similarly gold was extensively remobilised and recrystallised during Devonian processes (Chapter 7).

## 10.10 SUMMARY ...

Fluid inclusions were found in many different minerals including sphalerite, barite, quartz, fluorite, carbonate, and helvite from the Rosebery, Hercules and South Hercules deposits. Four types of fluid inclusions can be distinguished, but the studied minerals do not show any growth zoning which can be used to establish primary origins. Early formed low-temperature, low-salinity Type I inclusions with no appreciable $CO_2$ may represent primary, Cambrian exhalative fluids that have survived the Devonian recrystallisation; however, there is no independent conclusive fluid inclusion evidence to confirm this interpretation.

However, abundant fluid inclusion characteristics of necking down and healed microfractures together with trapped carbonate and barite daughter minerals identified by laser Raman spectroscopy suggest extensive remobilisation and recrystallisation of carbonate minerals, which corroborates other indication of the redistribution and recrystallisation of primary Cambrian sulphides (e.g. sphalerite) and gold during Devonian metamorphic and metasomatic processes.

# CHAPTER 11: DISCUSSION OF CAMBRIAN VMS MINERALISATION, DEVONIAN OVERPRINT AND EXPLORATION IMPLICATIONS

## 11.1 INTRODUCTION ...

In this final chapter, geological, mineralogical, geochemical and fluid inclusion data from previous chapters will be used to infer the physico-chemical conditions of the Cambrian VMS ore forming environment and of the post-depositional Devonian overprinting processes for gold-rich massive sulphide deposits in the Rosebery–Hercules area. Exploration implications will also be considered.

## 11.2 CAMBRIAN VMS MINERALISATION ...

Large et al. (1990b) recently discussed four distinct styles of submarine volcanic-related mineralisation in the Mt Read volcanics:

1. Seafloor Zn–Au (–Pb–Ag–Cu–Ba) polymetallic massive sulphides (e.g. Hellyer, Rosebery).
2. Footwall Au–Ag–base metal–sericite–silica ± adularia veins and disseminated stockwork systems (e.g. Que River precious metal zone).
3. Deep level Cu–Au–pyrite–chlorite disseminated and stockwork zones(e.g. Mt Lyell).
4. Magnetite–hematite–pyrite ± Cu ± Au vein and replacement systems associated with granitic intrusives (e.g. Jukes Pty, Lake Selina).

Seafloor Zn–Au (–Pb–Ag–Cu–Ba) polymetallic massive sulphide deposits have concentrations of gold in the upper part of the zinc–barite-rich massive sulphide (e.g. Rosebery, Huston and Large, 1988), whereas the seafloor Cu–Au massive sulphides have concentrations of gold (with copper) in the stockwork zone and lower massive sulphide ore (e.g. Mt Chalmers, Queensland, Large and Both, 1980). Gold–base metal–silica–sericite ± adularia mineralisation is defined by the precious metal zone (PMZ) in the lateral footwall stringer system of the Que River deposit (McGoldrick et al., 1990). Deep level Cu–Au–pyrite–chlorite disseminated and stockwork zones have concentrations of gold (with copper) in the footwall stringer zone and lower massive sulphide ore (Mt Lyell). In this discussion, the magnetite vein and replacement systems (style 4) will not be considered because they are not recognised or else are not an important style of mineralisation in the Rosebery–Hercules area.

Large (1991, in press) also considered the geological setting of VMS deposits from a morphological point of view and indicated that the morphology of VMS deposits within submarine volcanic settings can vary from mound-shaped lenses to asymmetric mounds, pipes, sheets, layered lenses, stacked lenses and stockwork zones. Figure 11.1 shows the possible morphological variations of VMS deposits in western Tasmania.

It is well documented that the Rosebery ore lenses formed on the Cambrian seafloor by an exhalative process (e.g. Brathwaite, 1969, 1974; Green et al., 1981; Green, 1983; Huston and Large, 1988; Green and Iliff, 1989; Lees et al., 1990; Chapters 2 and 3) and are therefore consistent with the seafloor Zn–Au (–Pb–Ag–Cu–Ba) polymetallic massive sulphide mineralisation style of Large et al. (1990b) and Large (1991, in press). Similar mineralisation styles are found at the Hellyer and Que River deposits in western Tasmania.

The Rosebery deposit is composed of sheet-like stratiform sulphide lenses without a defined alteration pipe (Fig. 11.1A). The deposit is zoned from a pyrite–chalcopyrite zone at the base through a sphalerite–galena ± pyrite zone and to a massive barite ± carbonate zone at the top. The Hellyer and Que River deposits in western Tasmania show similar mineralogical zonation but in terms of morphology, the Hellyer deposit is mound-shaped with an underlying well defined alteration pipe (Fig. 11.1B), and the Que River deposit is a variant with stacked lenses (Fig. 11.1C).

The Hercules deposit occurs as smaller ore lenses varying in form from upright lenses to pods. The ore lenses are also generally zoned from a siliceous pyrite–chalcopyrite-rich zone or massive pyrite zone at the base to massive or disseminated sphalerite–galena–pyrite and barite ± carbonate zones at the top (the barite ± carbonate zone may be absent in some lenses). Recent geological investigations on the Hercules deposit drew similar conclusions as to the volcanogenic origin of the ore (e.g. Lees, 1987; Lees and Howard, 1989; Lees et al., 1990).

### 11.2.1 Morphology and style of mineralisation at the Hercules deposit ...

Although the main Hercules deposit is comparable in mineral zonation and ore metal distribution with that of the Rosebery deposit, the Hercules ore lenses are not typical seafloor polymetallic massive sulphides. The ore lenses at Hercules are not stratiform but grossly stratabound within the Host rock. Lees (1987) considered that primary stratiform ore lenses at Hercules were transposed along the cleavage to give their present cross-cutting attitude. However, it is unlikely that transposition alone can adequately explain the physical and chemical remobilisation of originally stratiform massive sulphide ore into the current cross-cutting configuration.

It has been argued in Chapter 4 that the spotty sphalerite ore textures at Hercules tend to suggest a sub-seafloor emplacement largely due to replacement with minor open-space filling

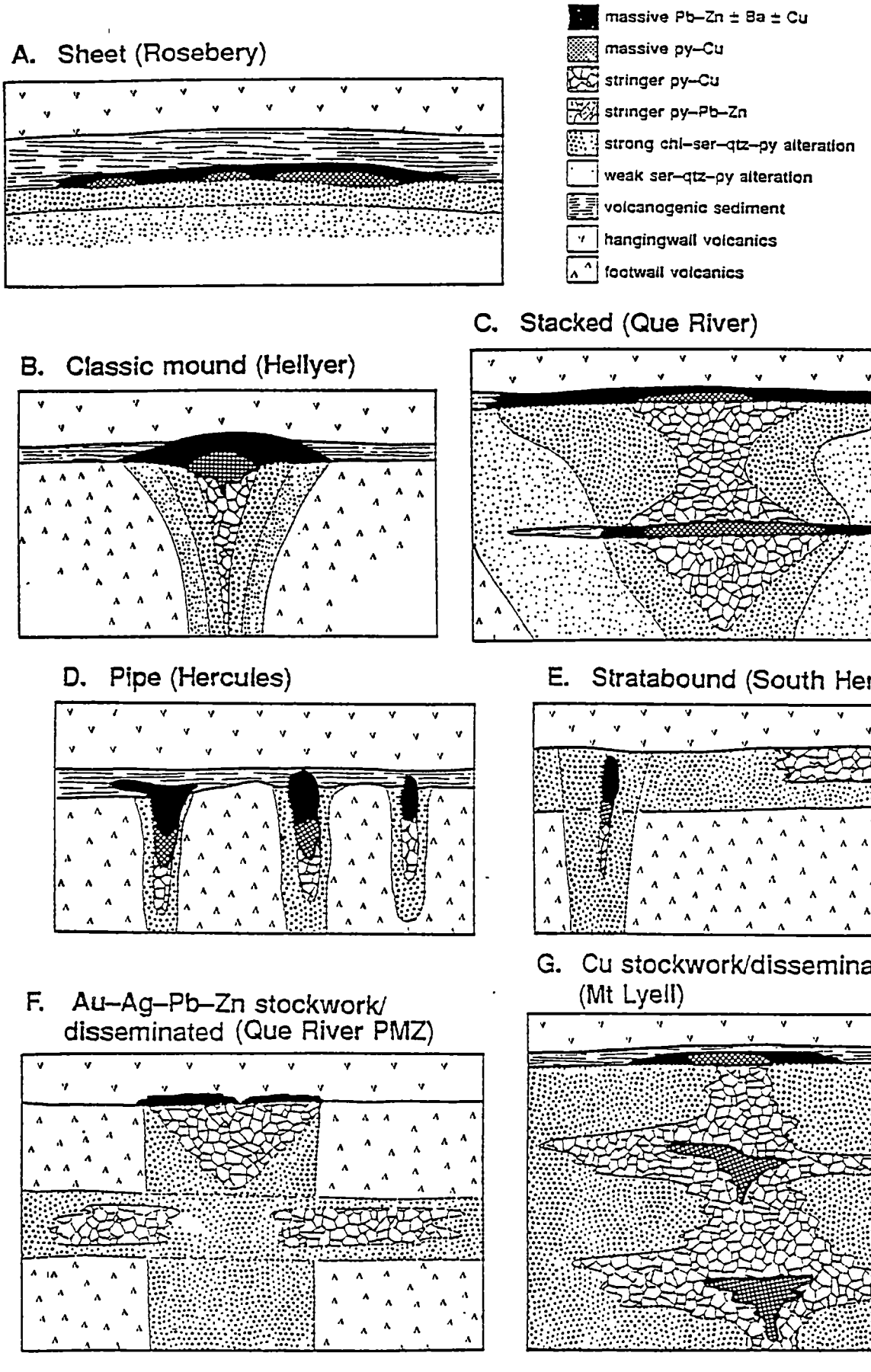


Fig. 11.1. Morphological variation of massive ± disseminated volcanic-hosted deposits in western Tasmania (adapted from Large 1991, in press).

in porous volcanics. The cross-cutting nature of the ore lenses to bedding (e.g. E lens and M lens) also supports the sub-seafloor replacement origin. Allen and Hunns (1990) also reported various cross-cutting relationships of the ore lenses in the Hercules–South Hercules area. Hence, the main Hercules ore lenses appear as cross-cutting pipes of polymetallic massive sulphides with associated stratabound lenses which formed largely by replacement of the volcanics below the seafloor (Fig. 11.1D).

Franklin (1990) recently reported massive sulphide deposits currently forming within poorly consolidated sediments immediately sub-seafloor in the Middle Valley on the Juan de Fuca Ridge and the Escanaba Trough. Porous volcanic sandstone or unconsolidated volcanic debris flows, below finer impermeable siltstones, may form favourable hosts for sub-seafloor replacement mineralisation. Similar to the Middle Valley and Escanaba Trough mineralisation, sub-seafloor replacement processes may have occurred in the Hercules area within the porous psammitic bedded volcanic Host rock which lies below the impervious dark grey shales and slates. Boiling of ore fluids has been invoked for such an environment (e.g. Finlow-Bates and Large, 1978).

Eastoe et al. (1987) noted K-feldspar and Mg-rich chlorite in the footwall of Hercules and also suggested that boiling of the ore fluids may have occurred. However, no fluid inclusion evidence for boiling was observed in this study (Chapter 10). Alternatively, sub-seafloor replacement may have resulted from cooling and/or oxidation of the ore fluids with or without mixing with convecting seawater.

### 11.2.2 Morphology and style of mineralisation at the South Hercules deposit ...

The following geological, mineralogical, geochemical and isotopic evidence strongly suggests that the South Hercules deposit is also a Cambrian, volcanogenic style of mineralisation.

1. Volcanic stratigraphy — the South Hercules deposit lies along strike from the Hercules deposit and occurs in a similar tuffaceous volcanic host rock.
2. Metal association — the metal association of South Hercules is the same as other Cambrian VMS deposits.
3. Zinc ratio — the zinc ratio of the South Hercules deposit falls within the zinc ratio values of the Phanerozoic Zn–Pb–Cu volcanogenic massive sulphide deposits and Cambrian massive sulphides in the Mt Read Volcanics given by Huston and Large (1987).
4. $\delta^{34}S$ values — the $\delta^{34}S$ values of sulphides in South Hercules ranges from 8.2‰ to 14.1‰ and are comparable with $\delta^{34}S$ values of the other VMS deposits in the Mt Read Volcanics.

However, on the basis of the present drilling limit, the South Hercules deposit contains low-grade lead, zinc, and copper values (<1 wt % Cu) but relatively high (Au+Ag)/(Pb+Zn) ratios. The South Hercules deposit consists of a mineralised sulphide zone associated with

carbonate assemblages generally at the upper part of the ore zone. The mineralised sulphide zone consists of the massive pyrite ± barite sub-zone, the siliceous ± stringer sulphide sub-zone and the sphalerite–galena ± pyrite sub-zone. The sulphide assemblages at the South Hercules deposit consist dominantly of stringer and siliceous disseminated types with only thin massive sulphide lenses in comparison with the Rosebery and main Hercules ore lenses.

The absence of Cu-rich pods at the base in the deposit and the presence of massive pyrite ± barite assemblages with elevated gold, silver and arsenic in the upperpart of the sulphide lens suggest that the South Hercules mineralisation may be the upperpart of a larger mineralised system. The gold–arsenic–pyrite ± barite association in the South Hercules deposit shows comparable characteristics with the colloform pyrite–silica–gold–arsenic association at the top of the Hellyer massive sulphide deposit (McArthur, 1986, 1989, 1990) and is also comparable to the distal pyrite–gold mineralisation at Rosebery (Huston and Large, 1988). The stratabound nature, presence of inferred open-space filling and replacement textures and high (Au+Ag)/(Pb+Zn) ratios suggest that the South Hercules mineralisation formed from the interaction of low temperature (<250°C) hydrothermal fluids with seawater within the porous volcanics just below the seawater–rock interface (Fig. 11.1E).

Figure 11.2 shows a schematic presentation of the formation of the South Hercules deposit. Most of the sulphur in the South Hercules sulphides was derived from reduction of seawater sulphate, although some contribution from a magmatic source was possible. $\delta^{34}S_{\Sigma S}$ of the ore fluids increased from $\delta^{34}S$ values of 8‰ to 14‰ with time due to an increase in the proportion of seawater sulphur ($\delta^{34}S$ = ~30‰) to leached magmatic sulphur in volcanics ($\delta^{34}S$ = 0–5‰) in an analogous mechanism to that suggested by Green et al. (1981) and Green (1983) for Rosebery. This process is related to the primary, large-scale convection of seawater (Fig. 11.2). Gold deposition in the South Hercules deposit occurred at an evolved late stage of the ore forming process from low temperature, relatively oxidised ore fluids at the top of the volcanic pile. Mixing of seawater with ore fluids occurred at the seawater–rock interface to cause gold deposition by dilution and/or further oxidation.

Precious metal zone (PMZ) or gold–base metal–silica–sericite ± adularia mineralisation in the footwall stringer system of the Que River deposit (McGoldrick et al., 1990) is similar in mineralisation style to that of the South Hercules deposit but occurred at a deeper level below the seafloor (Fig. 11.1F). This style of mineralisation may represent a submarine version of an epithermal stockwork feeding a seafloor massive sulphide deposit and may represent a transition towards epithermal Au–Ag mineralisation (McGoldrick et al., 1990).

Another style of stockwork/disseminated, but copper–gold sub-seafloor mineralisation is present in the Mt Lyell deposit in western Tasmania (Fig. 11.1G). In the copper–gold

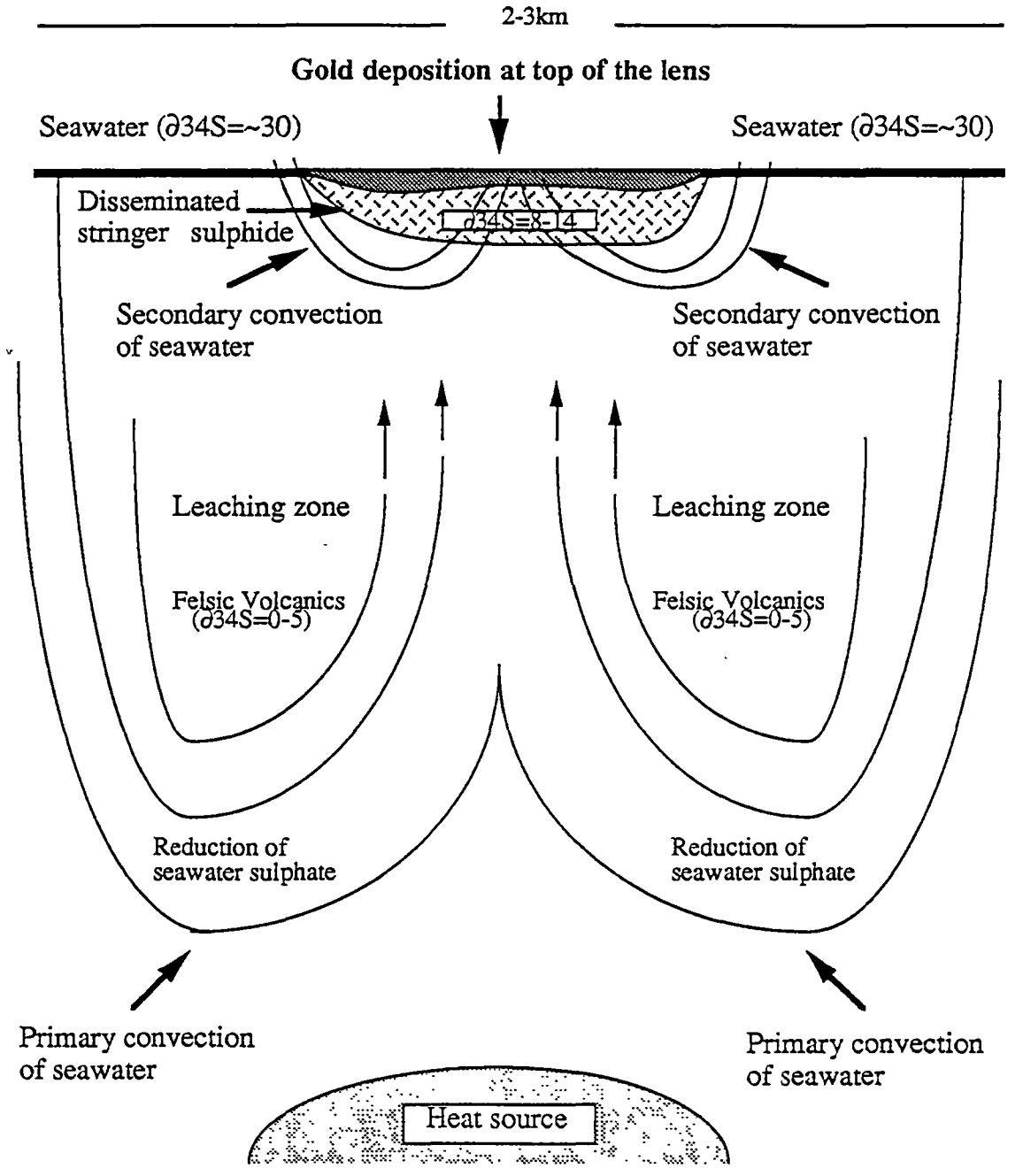


Fig.11.2. Idealised diagram showing the formation of the South Hercules deposit encompassing the interpretative models of Green et al. (1981), Green (1983), Eastoe et al. (1987), Huston and Large (1989), Huston (1989) and Solomon et al. (1988). Note that gold deposition at the top of the South Hercules sulphide lens occurred due to the decreasing temperature and increasing $SO^{=}_{4}/H_2S$ ratio by mixing between oxidised seawater and hot reduced ore fluids as the hydrothermal fluids moved up toward the seafloor. The mixing process formed under secondary convection of seawater at the seawater-rock interface.

stockwork, minor lead–zinc sulphide lenses may be present at the stratigraphic top of the system. This style develops from hot and dense hydrothermal fluids which move laterally through permeable volcanic horizons (or along favourable contacts) below the seafloor (Large et al., 1990b).

### 11.3. Effect of Devonian Tabberabberan Orogeny

The Cambrian VMS deposits in western Tasmania have been affected by tectonic deformation and related regional metamorphism during the Devonian Tabberabberan Orogeny. The orogenic movement has resulted in folding, shearing and thrust faulting of the ore lenses, which caused significant changes in the overall configuration of the original stratiform ores and underlying stringer zones in the Mt Read Volcanics.

*Structural deformation:* The effect of deformation and related changes in shape of the orebody depends on the competency of the ore lenses and the enclosing host rocks and also the extent, style and nature of the Devonian orogenic movements. The structural deformation in the Devonian produced sheath folding (Brathwaite, 1969; Lees et al., 1990b) and/or thrust stacking (Berry, 1990) at Rosebery (Figs. 11.3A and B).

The ore lenses at Hercules were folded during the Devonian and are enclosed by either sericite–chlorite schists, disrupted pisolitic or massive carbonate, or strongly deformed host rocks (Figs. 11.3C and D). The ore is aligned parallel to the cleavage and mostly cross-cuts the bedding. In comparison, the deformation style in other western Tasmanian massive sulphide ores varies from broad open folding (Hellyer) (Drown and Downs, 1990) (Figs. 11.3E and F) to up-right isoclinal folding (Que River) (Large et al., 1988) (Figs. 11.3G and H).

*Regional metamorphism:* The regional metamorphism related to the Devonian Tabberabberan Orogeny in the Mt Read Volcanics varies from prehnite–pumpellyite facies at the Hellyer and Que River deposits to middle and upper greenschist facies at the Rosebery, Hercules and South Hercules deposits. The regional metamorphic conditions at the Rosebery deposit was defined by Green et al. (1981) and Green (1983) using silicate assemblages, arsenopyrite, chlorite and sulphur isotope geothermometry, and sphalerite geobarometry. Green et al. (1981) and Green (1983) reported the following conditions; temperature ≥300°C and pressure = 3.1–5.2 kb by sphalerite geobarometry, and inferred a similar temperature range for the Devonian metasomatism (see below).

The pressure estimates of 3.1–5.2 kb by sphalerite geobarometer are high compared with geological estimates (1.6–2.1 kb) and the sphalerite composition was considered to have been re-equilibrated below 248°C, the upper stability limit of monoclinic pyrrhotite (Green et al., 1981; Green, 1983). Although re-equilibration of the sphalerite composition was manifest in

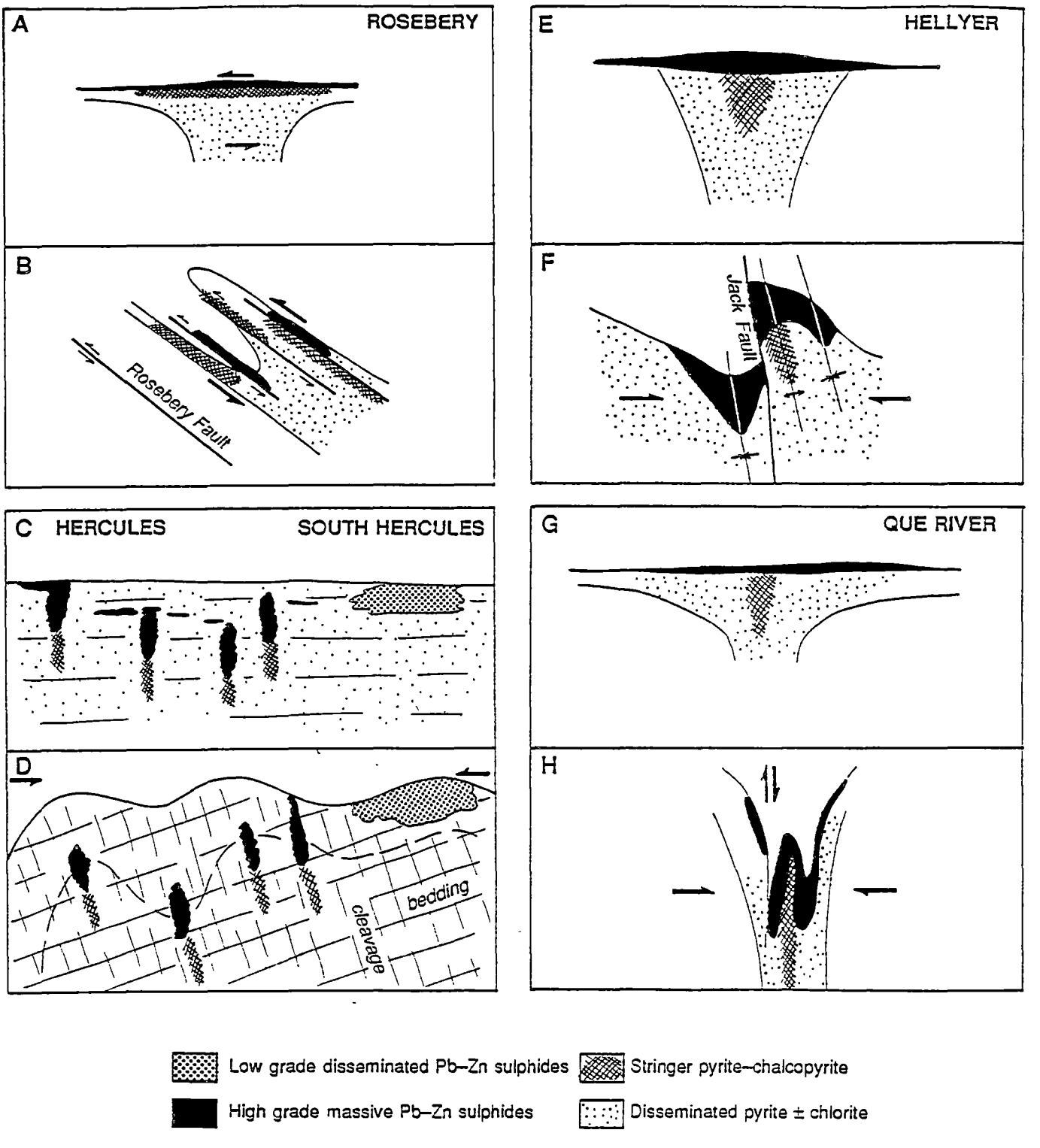


Fig. 11.3. Diagrammatic presentation of Devonian deformation styles in Cambrian massive ± disseminated volcanic-hosted deposits in western Tasmania. (A-B) Folding and/or thrusting of sheet-like stratiform ore lens at Rosebery. (C-D) Folding and localisation of stratabound ore lenses along cleavage at Hercules–South Hercules. (E-F) Faulting and broad open folding of mushroom-shaped ore lens at Hellyer. (G-H) Tight isoclinal folding of stratiform ore lens at Que River.

this study, the sphalerite encapsulated in pyrite together with hexagonal pyrrhotite from the metasomatic zone of the F(J) lens does not appear to have been re-equilibrated and gave meaningful pressure estimates of 3.0 ± 0.5 kb (Chapter 8).

Textural variety of carbonate-bearing assemblages in the Rosebery–Hercules area indicate the effect of Devonian metamorphic recrystallisation. The zoned, spotty carbonate spheroids grade into larger, cannonball aggregates or coalesce into tightly packed spheroids or massive carbonate due to later metamorphic recrystallisation. These textures are also cross-cut by post-cleavage carbonate ± quartz veins. The VMS carbonates appear to have been not only recrystallised but also frequently show evidence of dissolution, remobilisation and precipitation in late stage Devonian dilational vein sets.

The gold grains in the Rosebery, Hercules and South Hercules deposits have been affected by deformation and metamorphism during the Devonian Tabberabberan Orogeny along with the associated sulphide minerals and the host rocks. In the case of the Rosebery south-end, the ore lenses have been further affected by Devonian metasomatic processes (see below). The Devonian effects have resulted in significant recrystallisation and remobilisation of the gold grains, indicated by their texture, grain size, and fineness variation. The gold mineralisation in the Rosebery deposit also displays a bimodal distribution in grain size and fineness. The bimodal distribution suggests that the grain size and fineness values of the gold grains have increased during the Devonian overprinting processes.

The effect of Devonian regional metamorphism on the volcanogenic deposits in the Rosebery–Hercules area is exemplified by the fluid inclusion data from the South Hercules deposit. The fluid inclusion data from South Hercules have been interpreted to indicate two types of fluids: early low-temperature (200°C) and low-salinity (<4.2 NaCl equiv. wt %) fluid and later with $CO_2$-bearing, high-temperature (up to 300°C), and higher salinity (20 NaCl equiv. wt %) fluid.

The low-temperature, low-salinity fluids associated with the earlier Type I inclusions are likely to be fluids of exhalative origin generated at the time of Cambrian mineralisation. The high-temperature, high-salinity and $CO_2$-bearing fluids in the later Type II fluid inclusions were most likely related to the Devonian metamorphic recrystallisation.

The $a_{S2}$ during the formation of the South Hercules deposit can be estimated using microprobe analyses of the FeS content of sphalerite, the arsenic content in arsenopyrite, and the experimental data given by Scott (1983). The condition of $a_{S2}$ during the ore formation and later Devonian recrystallisation can also be bracketed by fluid inclusion data (Fig. 11.4). Arsenopyrite from the South Hercules deposit has a very consistent arsenic content. All four samples analysed give 30.0 atomic wt % As (Chapter 4). This consistent composition of the

arsenopyrite suggests that the original arsenopyrite composition has been homogenised during Devonian metamorphism. The FeS content of sphalerites from the South Hercules deposit ranges from 2.4 mole % FeS to 10.3 mole % FeS. The upper limit of 10.3 mole % FeS in the sphalerite suggests possible re-equilibration of the sphalerite during Devonian recrystallisation.

The lower limit of the 2.0 mole % FeS isopleth for sphalerite is above the arsenopyrite stability field and the higher limit of the 10.0 mole % FeS isopleth is within the arsenopyrite field. The sphalerite was probably formed under higher $a_{S2}$ but later re-equilibrated at higher temperature and possibly lower $a_{S2}$. The 10.0 mole % FeS and 30.0 atomic wt % As isopleths cross-cut each other at a temperature of about 340°C and $a_{S2}$ ($< 10^{-8.8}$) giving the maximum $a_{S2}$–T conditions for possible Devonian re-equilibration of the South Hercules deposit. This temperature estimate is in good agreement with the fluid inclusion data as the uncorrected filling temperatures for the Type II inclusions are <300°C. However, the sphalerite and arsenopyrite grains analysed are from different samples and hence, the chemical equilibria between the sphalerites and arsenopyrites cannot be fully established.

In Fig. 11.4, the temperatures of formation are defined by fluid inclusion filling temperature data of 250°C for Cambrian fluids and 300°C for Devonian fluids. Hence, it is likely that the South Hercules deposit was formed under low temperature (200°–250°C) and possibly low $a_{S2}$ ($10^{-17.0}$ to $10^{-11.0}$), whereas the later Devonian recrystallisation processes occurred under higher temperatures (200°–300°C) and under higher $a_{S2}$ ($10^{-13.5}$ to $10^{-9.0}$).

*Mobilisation and remobilisation of ore constituents:* Marshall and Gilligan (1987a and 1987b) recently defined mobilisation and remobilisation: "*mobilisation is a process which involves the translocation and concentration of originally dispersed metallic constituents, and remobilisation is the translocation resulting in modified concentration and distribution of pre-existing metalliferous concentration*". Both mobilisation and remobilisation are produced by means of "chemical" (liquid-state), "mechanical" (solid-state), and mixed processes. Mobilisation and/or remobilisation processes can occur in time–space relations from micro- to regional scale (Wolf, 1987; Marshall and Gilligan, 1987b).

The importance of large volumes of water or high water–rock ratios and focussing of fluid flow during mobilisation and/or remobilisation, have been emphasised by many authors (e.g. Fyfe, 1987; Hobbs, 1987; Marshall and Gilligan, 1987b; and Cox et al., 1987), as well as other aspects such as grade of metamorphism (e.g. Skinner and Johnson, 1987; Barnes, 1987; Plimer, 1987; Gilligan and Marshall, 1987), brittle–ductile strength (Cox, 1987; Gilligan and Marshall, 1987), and source region (e.g. Keays, 1987) during mobilisation and/or remobilisation. However, the majority of the above investigators focussed their attention on the mechanical aspects of mobilisation and/or remobilisation during regional metamorphism, and few workers

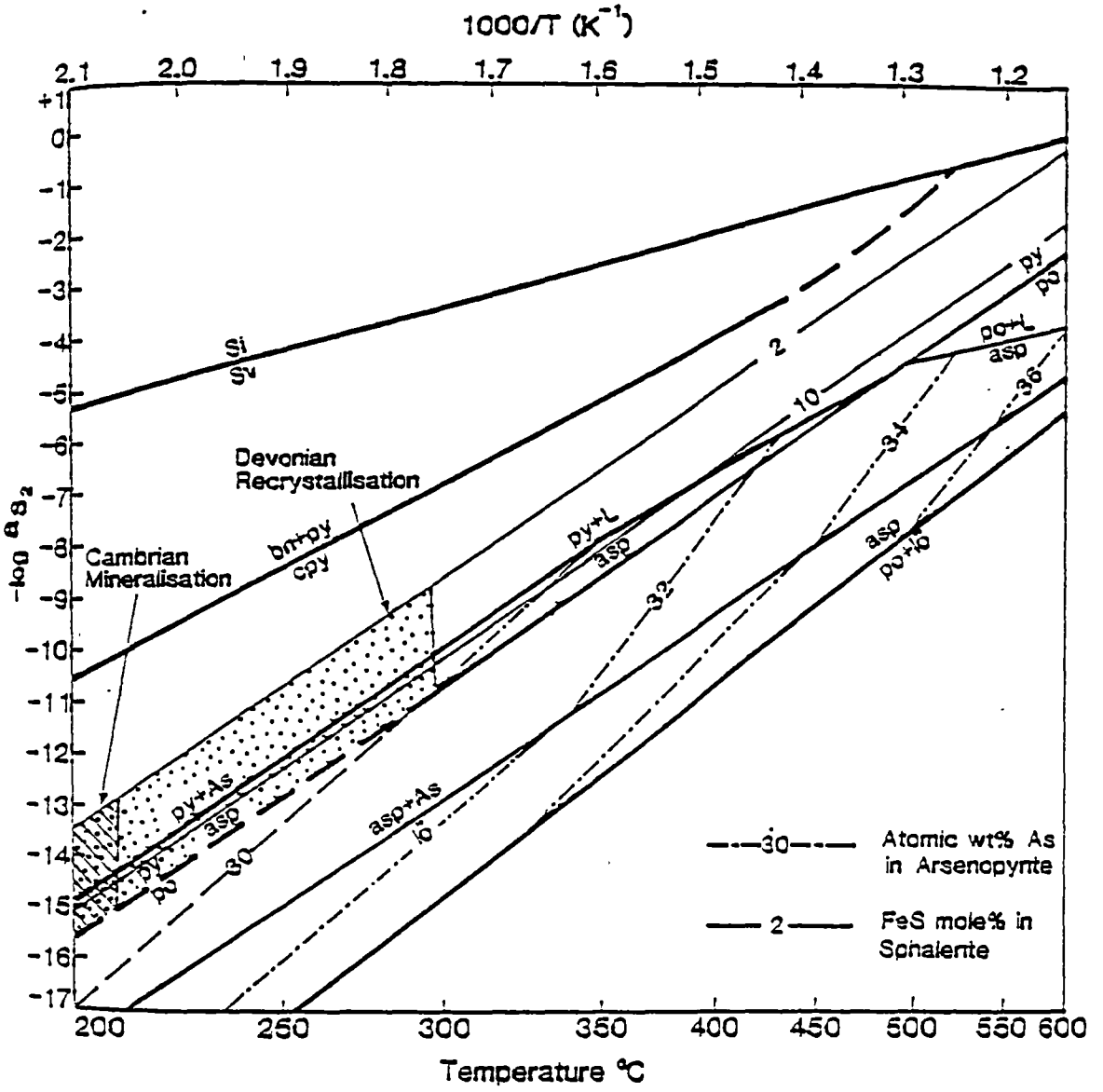


Fig. 11.4. Activity of sulphur–temperature plot at low pressure outlining the isopleths of mole % FeS in sphalerite and atomic wt (%) As in arsenopyrite from the South Hercules deposit, western Tasmania. The location of isopleths and of the reported sulphidation equilibria are taken from Scott (1983). The FeS content in the sphalerite from the South Hercules deposit ranges from 2.0 mole % FeS to 10.0 mole % FeS whereas the the atomic wt (%) As in the arsenopyrite gives a consistent average of 30.0 atomic wt %. The isopleths of the mole % FeS in the sphalerites and the atomic wt (%) As in arsenopyrite are delimited by the maximum fluid inclusion filling temperature data (210°C) of the earlier, low-salinity, Type I inclusions for the formation of the South Hercules mineralisaton and the maximum filling temperature (300°C) of the later, higher salinity, $CO_2$-bearing, Type II inclusions which are associated with the Devonian overprint. Note that the South Hercules deposit was formed under low temperature (150°C-210°C) and possibly low $a_{S2}$ ($_{10}^{-15.7}$ to $_{10}^{-13.0}$) and the Devonian recrystallisation occurred under higher temperature (200°C-300°C) and under higher $a_{S2}$ ($_{10}^{-15.7}$ to $_{10}^{-9.0}$)

considered the chemical aspects of the mobilisation and/or remobilisation (e.g. Solomon et al. 1987; Marshall and Gilligan, 1987b).

Using the above definition by Marshall and Gilligan (1987a, 1987b), the Devonian metamorphism and metasomatism of the pre-existing Cambrian sulphide ores in the Rosebery–Hercules area is regarded as a remobilisation process. Gilligan and Marshall (1987) reviewed the behaviour of different pre-existing sulphide ores during mechanical remobilisation in terms of internal textures such as submicroscopic dislocation, grain flattening and annealing, and in terms of external structures such as boundin, piercement, elongation, folding and transposition.

The VMS deposits in the Rosebery–Hercules area display mechanical remobilisation (e.g. elongation of sphalerite blebs and carbonate spheroids), and recrystallistion of ores as well as carbonate minerals during the Devonian regional metamorphism. However, the Rosebery–Hercules ore lenses do not show any of the remobilisation features found in high grade metamorphic terranes such as "droppers" (tongues of high grade ore in the footwall) at the Broken Hill orebody which are considered to have formed during mixed solid/fluid remobilisation processes (e.g. Gilligan and Marshall, 1987; Barnes, 1987). There is no evidence of large-scale chemical remobilisation of ore constituents during the metamorphism based on the metal zonation and distribution studies (Chapter 5).

In contrast, the post-orogenic granite intrusion below the south-end of the Rosebery mine resulted in widespread chemical remobilisation of the ore lenses. The mineralogical and geochemical features of the Devonian metasomatic overprinting process in the F(J) lens of the Rosebery south-end will be discussed first, followed by the chemical and thermodynamic aspects of the remobilisation of ore constituents in the F(J) lens on the basis of metal zonation and distribution, and fluid inclusion and ore metal solubility data.

## 11.4 Effect of post-orogenic Devonian granite intrusion ...

The Devonian Tabberabberan Orogeny was followed by the intrusion of shallow-level granitoid plutons. The granite does not outcrop at Rosebery but the existence of a shallow granite intrusion below the south-end of the orebody has been interpreted from gravity data (Leaman and Richardson, 1989). Owing to the shallow-level granitoid intrusion, the primary massive sulphide ore lenses at the Rosebery south-end have been replaced by mineral assemblages comprising iron oxides and sulphides, plus silicates such as biotite, garnet, tourmaline and helvite, and fluorite. The significant and important features of the replacement process in the F(J) lens of the Rosebery south-end discussed in the previous chapters are herein summarised below in point form:

1. The replacement occurred after the ores were affected by the Devonian deformation and metamorphism. Such replacement mineral assemblages have not been recorded in any other volcanogenic ores in western Tasmania.
2. Three major replacement zones can be distinguished: (1) the magnetite–biotite ± chalcopyrite zone, (2) the pyrrhotite–pyrite zone and (3) the tourmaline–quartz ± magnetite zone. The magnetite–biotite ± chalcopyrite zone is generally confined to the lower levels of the mine particularly below 17 Level. The pyrrhotite–pyrite zone occurs mostly above the magnetite–biotite ± chalcopyrite zone. A significant enrichment of gold is present in the pyrrhotite–pyrite zone. Hematite is also locally found in the magnetite–biotite assemblages which are replacing barite-rich, primary sulphide lenses.
3. The tourmaline–quartz zone formed at a later stage during the replacement process as indicated by irregular and patchy quartz–tourmaline veins cross-cutting the host rock and other sulphide lenses. Although the tourmaline–quartz veins appear to be stratiform and parallel to the bedding in the drill core intersection, detailed underground examination indicates that the tourmaline–quartz veins cut the cleavage of the tuffaceous host rocks suggesting that the tourmaline veins were formed after the Devonian cleavage development.
4. Although biotite is present in the replacement zone, the biotite formation reaction remains unclear. Biotite is intimately intermixed with chlorite. The occurrence of biotite tends to increase in the deeper levels of the mine. The chlorite in the primary sulphide lenses and the footwall appears to alter to biotite. The biotite has altered back to chlorite during the retrograde fluorite–quartz veining event as evidenced by abundant chloritised biotite at the vein margins.
5. The garnet from the Rosebery mine consists predominantly of spessartine (74.0–85.0 mole % ) and minor grossularite (3.0–16.0 mole %). The Rosebery helvite contains up to 7.0 wt. % Zn. The Rosebery biotite displays a range of tetrahedral $Al^{iv}$ (1.81–2.73) and octahedral $Al^{vi}$ (0.02–2.75), with $100Mg/(Mg+Fe^{+2})$ values from 22.0 to 54.0. The Rosebery garnet, helvite and biotite are comparable with those from Devonian granite-related replacement W–Sn–F deposits in western Tasmania. Rosebery tourmaline has a schorl composition which is comparable in composition to tourmaline from the Devonian Meredith Granite but more Fe-rich than the volcanogenic tourmaline reported from Kidd Creek and the Appalachian Caledonides.
6. Mn-rich carbonates, sericite, and K feldspar are also present in the F(J) lens of the south-end of the Rosebery deposit.
7. The homogenisation temperatures for the biotite–magnetite zone range between 300°C and 330°C and those for the pyrrhotite–pyrite zone have a comparable range of 275°C to 330°C.

The homogenisation temperatures for the later tourmaline–quartz zone vary from 200°C to 300°C. The later fluorite vein stage also occurred at lower homogenisation temperatures (240°–265°C). Salinity ranged from 10 to 35 NaCl equiv. wt % in the early biotite–magnetite zone, from 5 to 15 NaCl equiv. wt % in the pyrrhotite–pyrite zone, and from 5 to 10 NaCl equiv. wt % in the tourmaline–quartz zone. The presence of $CO_2$ in the replacement zones was noted by microthermometry and confirmed by LRS investigation of the fluid inclusions.

The mineralogical and geochemical and features, and fluid inclusion data described above for the Devonian metasomatic overprinting processes in the F(J) lens of the Rosebery south-end has been shown diagrammatically in Fig. 11.5.

## 11.5 Initial composition of Devonian fluid and metasomatic process ...

The initial metasomatic fluid expelled from the granite pluton below Rosebery (Fig. 11.5A) was relatively hot (≥330°C), $CO_2$-bearing, and saline. This hydrothermal fluid is consistent with a magmatic origin. At the Renison cassiterite–pyrrhotite deposit, the ore fluid had a temperature of about 350°C and salinity of about 1–2*m* NaCl (Patterson et al., 1981).

The pH and oxidation conditions of the Devonian fluid cannot be easily inferred. Patterson et al. (1981) estimated the $fO_2$ values of $10^{-31}$ to $10^{-38}$ at Renison from the $CO_2/CH_4$ molar ratio in fluid inclusions but the extent of re-equilibration of gases after trapping was not known and contamination can be a serious problem during the sample extraction. LRS determination of the gases in the individual fluid inclusions from the F(J) lens replacement zone indicated only oxidised carbon ($CO_2$) and no reduced carbon ($CH_4$).

Recent assay data of drill core samples for tungsten and tin in the F(J) lens show that about 0.25% $WO_3$ but relatively low tin (<0.01% Sn) (per. comm., Steve Hunns, 1991). In western Tasmania, tungsten and magnetite are associated with oxidised skarns (e.g. Kara, St. Dizier), whereas tin and pyrrhotite are found with reduced skarns (e.g. Renison). The tungsten enrichment in the F(J) lens suggests that the Devonian fluid was relatively oxidising. Detailed investigation of the gases in the fluid inclusions (e.g. $H_2$ and $O_2$) is needed in order to understand the oxidation state of the Devonian fluid. The presence of magnetite, carbonate, sericite and K-feldspar in the F(J) lens, however, suggests that the *environment* of the initial replacement process was moderately oxidising and had a moderately acid to near neutral pH. The higher salinity and the presence of $CO_2$ in the Devonian fluid also imply a moderate pH (Ellis, 1970).

The biotite–magnetite zone formed from ascending Devonian granite-related fluid of high temperature (≥330°C) and high salinity (average 15 NaCl equiv. wt %) (Fig. 11.5B) and the

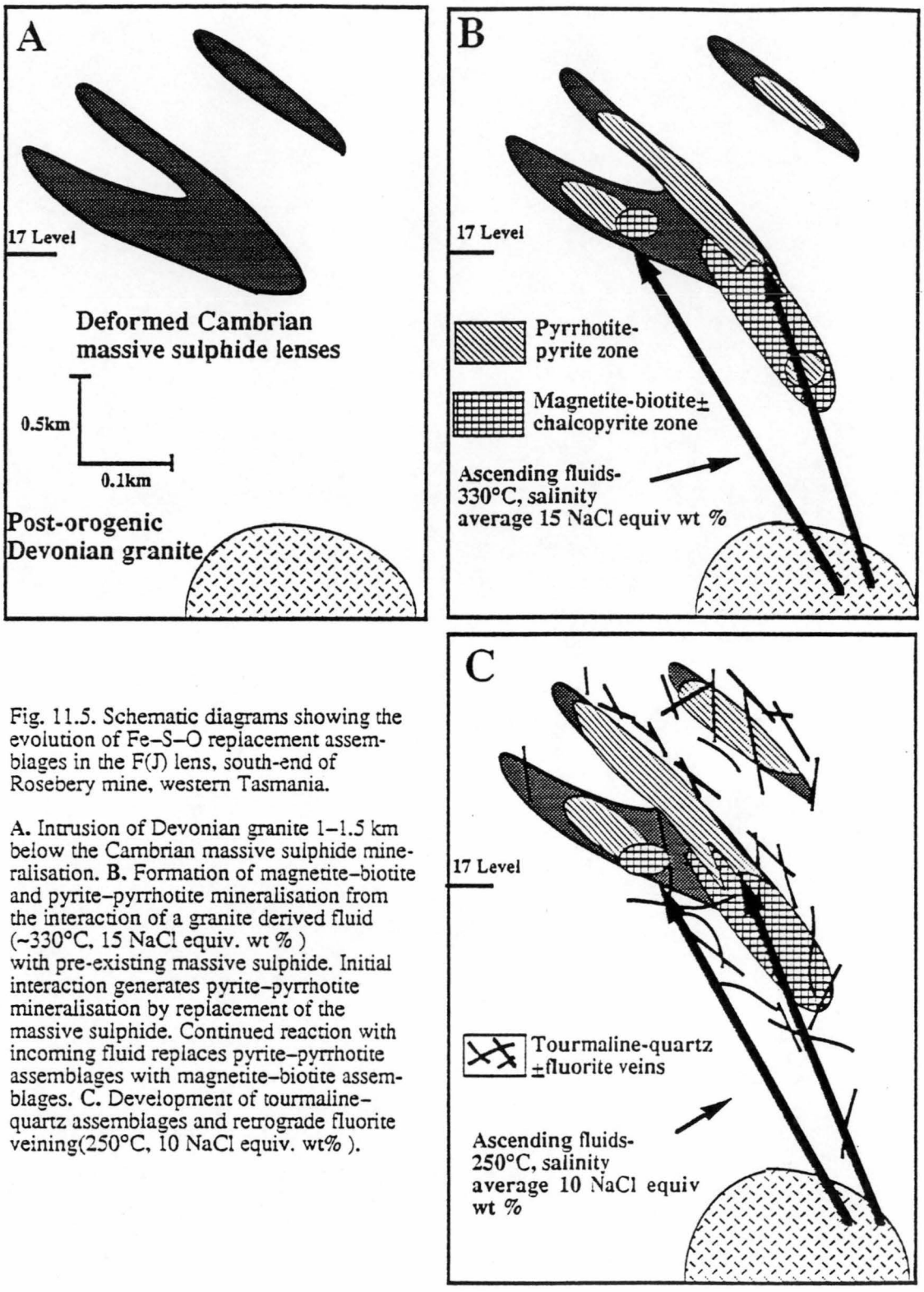


Fig. 11.5. Schematic diagrams showing the evolution of Fe–S–O replacement assemblages in the F(J) lens, south-end of Rosebery mine, western Tasmania.

A. Intrusion of Devonian granite 1–1.5 km below the Cambrian massive sulphide mineralisation. B. Formation of magnetite–biotite and pyrite–pyrrhotite mineralisation from the interaction of a granite derived fluid (~330°C, 15 NaCl equiv. wt % ) with pre-existing massive sulphide. Initial interaction generates pyrite–pyrrhotite mineralisation by replacement of the massive sulphide. Continued reaction with incoming fluid replaces pyrite–pyrrhotite assemblages with magnetite–biotite assemblages. C. Development of tourmaline–quartz assemblages and retrograde fluorite veining(250°C, 10 NaCl equiv. wt% ).

fluid evolved to form the pyrrhotite–pyrite zone under similar temperature and salinity (Fig. 11.5B). The temperature and salinity appears to have declined during the development of the later tourmaline–quartz zone and fluorite-bearing retrograde veining stage (~250°C, average 10 NaCl equiv. wt %) (Fig. 11.5C).

## 11.6. Chemical model for theredistribution of gold and base metals in the F(J) lens

Huston and Large (1989) thermodynamically modelled the concentration of gold in volcanogenic massive sulphide deposits and reported that gold in the upper part of the zinc-rich massive sulphide lenses (e.g. Rosebery, Hercules, Hellyer, Que River) was transported as $Au(HS)_2^-$ whereas gold in the stringer and base of copper-rich massive sulphide deposits (e.g. Mt Chalmer and Mt Morgan, Queensland; Millenbach, Quebec; Nurukawa, Japan) was transported as $AuCl^-_2$. They concluded that the temperature, pH and $fO_2$ of the ore forming fluid have an important controls on gold deposition and therefore gold grades.

High gold grades in zinc-rich massive sulphide are promoted by near neutral, oxidised and low temperature (150°–275°C) fluids as indicated by the presence of barite–carbonate ± (feldspar) gangue. High gold grades in the copper-rich stringers and base of the massive sulphide are promoted by higher temperatures (275°–350°C), relatively oxidised fluids as indicated by barite or hematite gangue, and relatively acid fluids as indicated by kaolinite gangue (Huston and Large, 1989).

In $fO_2$–T space significant gold transport by $Au(HS)_2^-$ occurs only in the pyrite stability field at relatively low temperatures (<300°C). On the other hand, gold transport by $AuCl_2^-$ is not restricted by iron mineral equilibria, but is greatest in the hematite, magnetite and pyrite fields at high temperatures (>300°C) and high $fO_2$ ($>10^{-30}$) (Huston and Large, 1989). As the Rosebery VMS mineralisation formed largely under relatively low temperatures (<300°C) on the Cambrian seafloor (Green et al., 1981; Green, 1983), it can be concluded that the primary, exhalative gold mineralisation at Rosebery was deposited in equilibria with pyrite.

The Devonian replacement process has resulted in recrystallisation, remobilisation and redistribution of gold as well as base metals from the Cambrian exhalative massive sulphide lenses (Chapters 5 and 7). A significant amount of recrystallised chalcopyrite is also present in the magnetite–biotite ± chalcopyrite and pyrrhotite–pyrite zones. The Devonian metasomatic process has also caused the redistribution of iron in sphalerite within the ore lenses, as evidenced by the zoning of sphalerite and the bimodal distribution of the FeS content of sphalerite in the F(J) lens.

Geochemical, mineralogical, and textural evidence suggests that the pre-existing gold (or electrum) in the Cambrian volcanogenic massive sulphide lenses was remobilised, and

redistributed (Chapters 5 and 7). The primary, exhalative sphalerite–galena±pyrite sulphide lenses in the unmodified F(J) lens and the Rosebery north-end orebody contain high gold values (10–25 g/t Au). The pyrrhotite–pyrite zone of Devonian origin contains ≥ 20 g/t Au (e.g. 270mS and 300mS sections). In contrast, the other biotite-, magnetite-, and tourmaline-bearing replacement zones contain generally low gold grades, below 5.0 g/t Au. The relatively high concentration of gold in the primary, exhalative sulphide lenses and the later pyrrhotite replacement zones implies that no additional gold has been introduced during the Devonian metasomatic event, but remobilisation and redistribution has occurred.

In any hydrothermal system, five parameters can be considered to be important in controlling fluid evolution: (1) temperature, (2) salinity, (3) pH, (4) $fO_2$ (or other measure of redox potential), and (5) total sulphur content. Evidence presented previously suggests that, with the exception of late stage tourmaline veining, the system was nearly isothermal (~350°C), and salinity remained more or less constant at below 20 NaCl equiv. wt %. Consequently three factors may have played important roles in this mineralising system: (1) pH, (2) $fO_2$, and (3) total sulphur content. Figures 11.6 and 11.7 are designed to illustrate the thermodynamic changes in the system through replacement processes. Figure 11.6 illustrates changes in $a_{H2S}$ and $fO_2$ of the system.

The assemblage of pyrite–pyrrhotite–magnetite suggests that significant changes took place in either $a_{H2S}$ or $fO_2$. $a_{H2S}$ was used as the abcissa as fluid conditions were reduced and relatively acid, conditions under which $H_2S$ is the dominant sulphur species in solution. As a consequence, the higher $fO_2$ range (i.e. above the magnetite–hematite buffer) in the diagram is not applicable as oxidised sulphur species would be more important. In the region of interest, however, Fe–S–O mineral stabilities are independent of pH. Figure 11.7 was designed to show how changes in pH would affect the fluid path and metal solubilites. It was constructed at total sulphur conditions in which pyrite, pyrrhotite and magnetite co-exist along the pyrite–pyrrhotite join (i.e. the pyrite–pyrrhotite–magnetite triple point on Fig. 11.6).

The Devonian fluid was in equilibrium with pyrite, magnetite and pyrrhotite during various stages of replacement. Pyrite–hematite assemblages although present (cf. Fig. 4.7C), are inferred to occur locally only in zones containing significant quantities of barite. Figures 11.6 and 11.7 show a hypothetical fluid path (A–D) for the Devonian replacement fluid based on the mineral assemblages observed in the F(J) lens. Overall the replacement process moved from an early $H_2S$-poor environment to a later $H_2S$-rich environment [magnetite–pyrite ± pyrrhotite to pyrite–pyrrhotite ± magnetite] at relatively constant $fO_2$ (about $10^{-30 \pm 2}$) as the metasomatic process proceeded.

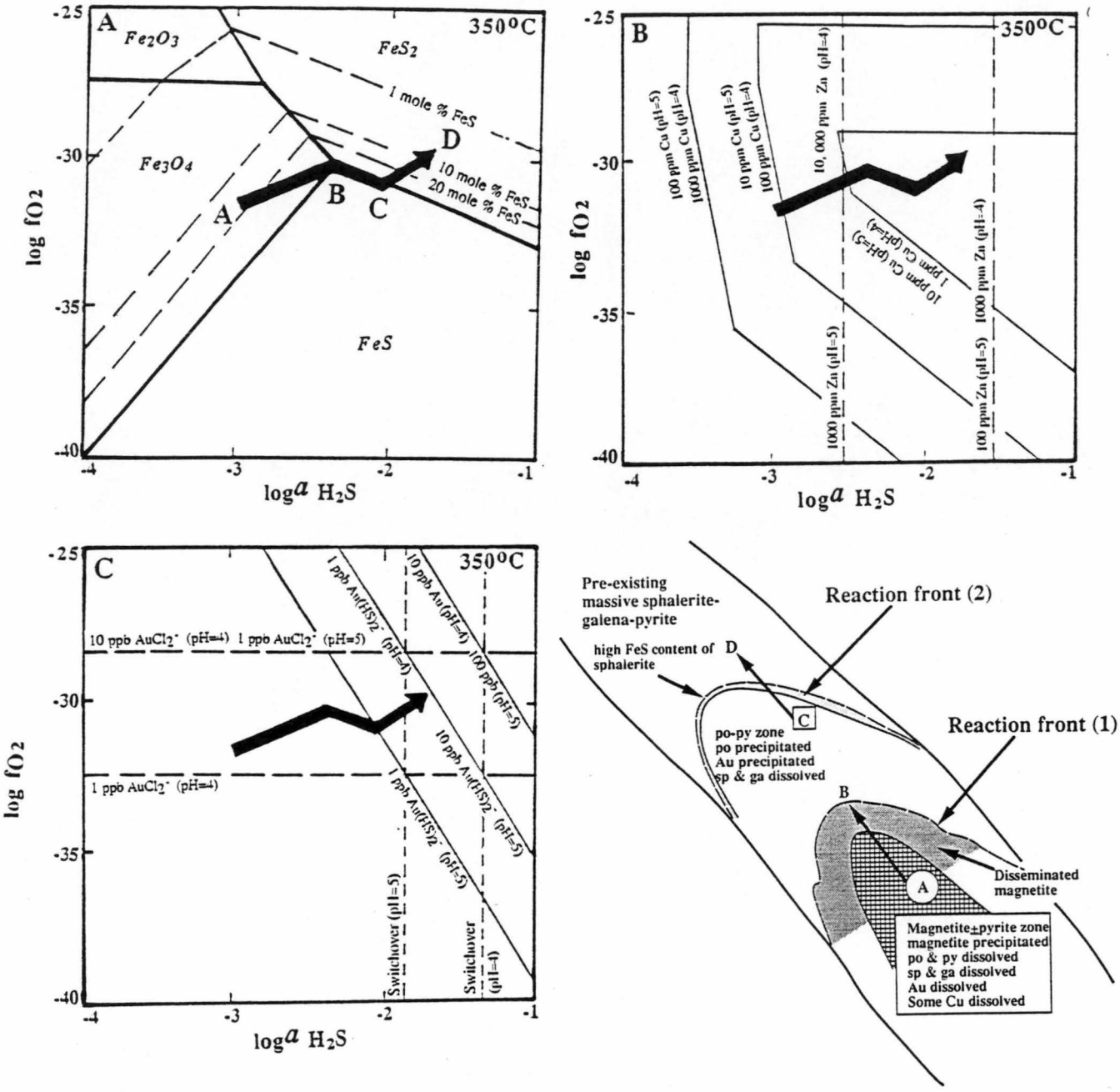


Fig. 11.6. $fO_2$–$a_{H2S}$ diagrams showing a hypothetical fluid path (A-D) of the Devonian metasomatic fluid at 350°C. The contours of the FeS content of sphalerite are shown as mole % FeS. Thermodynamic data are from Walshe and Solomon (1981), Huston and Large (1989), and Shenberger and Barnes (1989).

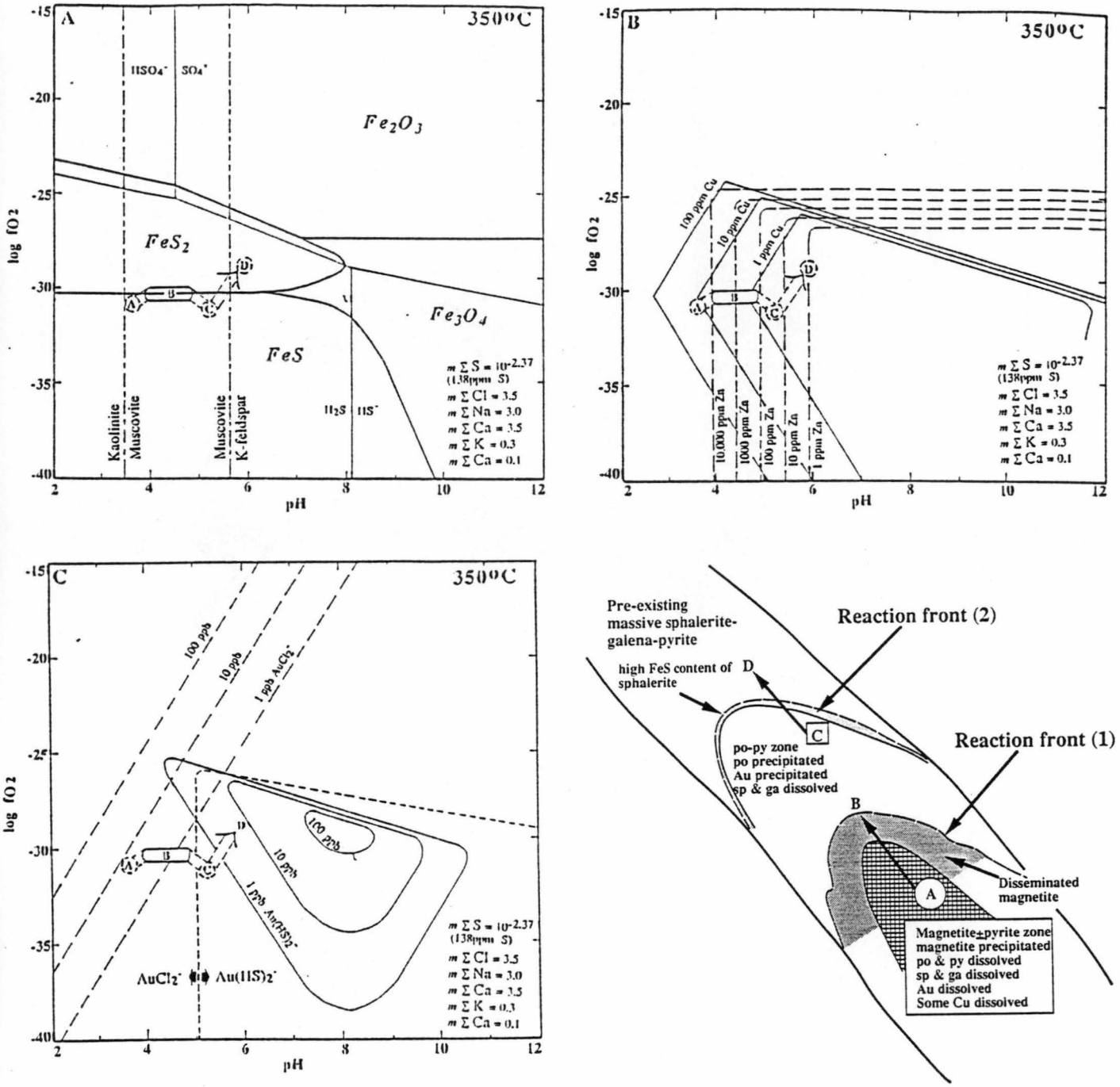


Fig. 11.7. $fO_2$–pH diagrams showing a hypothetical fluid path (A-D) of the Devonian metasomatic fluid at 350°C. Point B is the only part of the fluid path that plots on this diagram. Path A to B is projected from lower $m_{\Sigma S}$, whereas path B-C-D is projected from higher $m_{\Sigma S}$. Thermodynamic data are from Walshe and Solomon (1981), Huston and Large (1989), and Shenberger and Barnes (1989).

The Devonian replacement process occurred along two separate fronts: (1) front one, at which magnetite–pyrite replaced pyrrhotite–pyrite, and (2) front two, at which pyrrhotite–pyrite replaced massive spalerite–galena–pyrite. In the following discussion, the evolution of a fluid passing through the Devonian replacement zone will be considered in terms of changes in mineralogy and chemistry. For the purpose of the discussion, changes in fluid chemistry will be considered after an incipient mineral zonation developed. Incipient development of the pyrrhotite–pyrite zone probably involved reactions important at reaction front two. The entering fluids were initially in equilibrium with magnetite; then they evolved into equilibrium with pyrrhotite–pyrite along reaction front one; and finally they came into equilibrium with sphalerite–galena–pyrite along reaction front two.

*Reaction front one:* Injection of high temperture, moderately acid, sulphur deficient fluids resulted in the replacement of pyrrhotite–pyrite by magnetite according to the reactions:

$$3FeS_2 + 6H_2O = Fe_3O_4 + 6H_2S + O_2 \quad (1a)$$

$$6FeS + 6H_2O + O_2 = 2Fe_3O_4 + 6H_2S \quad (1b)$$

These reactions caused significant increases in $a_{H2S}$. However, changes in $fO_2$ were minimal compared to changes in $a_{H2S}$. The direction of the average change in $fO_2$ (i.e. to more reduced or oxidised conditions) depended on the pyrrhotite–pyrite ratio of the pyrrhotite–pyrite assemblages being replaced. A molar pyrrhotite–pyrite ratio of 2:1 would result in no average change in $fO_2$. The replacement of pyrrhotite–pyrite by magnetite–biotite ± pyrite assemblages caused the fluid to evolve from point A to point B (Figs 11.6A and 11.7A). The exact path of evolution was probably most complex, and tended toward the pyrite–magnetite and pyrrhotite–magnetite joins locally (broken lines on Fig. 11.6A). Overall the reaction tended toward the pyrite–pyrrhotite–magnetite join (point B) where pyrite and pyrrhotite saturated. As significant base metal sulphides are not present in the lower portion of the pyrrhotite–pyrite zone, sphalerite and galena dissolution reactions were not important at reaction front one, and no significant changes in pH occurred.

*Reaction front two:* The fluid remained in equilibrium with magnetite, pyrite and pyrrhotite only instantaneously, and proceeded toward equilibrium with sphalerite–galena–pyrite along reaction front two (path B–C–D). Reaction front two involved the replacement of pre-existing massive sphalerite–galena–pyrite with pyrrhotite–pyrite. This resulted in sphalerite, galena and tetrahedrite dissolution, but pyrrhotite and minor chalcopyrite precipitation. It also resulted in an increase in the FeS content of sphalerite. The following reactions were probably important at the reaction front:

$$4ZnS + 4CuCl^0 + 4FeS + 4Cl^- + 4H^+ + O_2 = 4CuFeS_2 + 4ZnCl^0_2 + 2H_2O \quad (2a)$$

$$ZnS + FeCl^0_2 = FeS + ZnCl^0_2 \quad (2b)$$

$$ZnS + 2Cl^- + 2H^+ = ZnCl^0_2 + H_2S \quad (2c)$$

$$PbS + 2Cl^- + 2H^+ = PbCl^0_2 + H_2S \quad (2d)$$

$$2ZnS + 2FeS_2 + 4Cl^- + 4H^+ + 2H_2O = 2FeS_{ss} + 2ZnCl^0_2 + 4H_2S + O_2 \quad (2e)$$

Reactions 2a, 2b and 2c resulted in the dissolution of sphalerite and galena, the precipitation of pyrrhotite and the development of chalcopyrite disease. In total, the reactions produced $H_2S$ and consumed $O_2$ to move the fluid along the pyrite–pyrrhotite join from point B to point C. Reactions 2a and 2c consumed $H^+$, which increased fluid pH.

At point C, pyrrhotite became destabilised, and the fluid moved into the pyrite stability field. From point C to point D, the fluid continued to dissolve base metal sulphide minerals until saturation of the fluid was reached at point D and reaction ceased. The decrease in base metal content associated with pyrrhotite–pyrite was caused by direct dissolution of sphalerite and galena (reactions 2c and 2d), and by the increase in FeS content of sphalerite according to reactions 2b and 2e. Reactions 2c, 2d, and 2e produced $H_2S$ and consumed $H^+$, hence increasing the fluid pH. Reaction 2e also produced oxygen, increasing the $fO_2$ of the system. The production of $H_2S$ and $fO_2$ pushed the fluid into the pyrite stability field from point C to point D. Reaction 2b introduced iron into the system and accounts for the increased iron content of the pyrrhotite–pyrite zone relative to massive sphalerite–galena–pyrite zone.

### 11.6.1 Redistribution of metals during metasomatic process ...

The interaction of Devonian granite–derived fluid with pre-existing Cambrian sulphide has significantly changed the metal distribution in the resulting replacement assemblages (Chapter 5). Lead, zinc and silver have been leached from the replacement zones and lost from the system. On the other hand, gold has been leached from the magnetite–biotite zone and reprecipitated in the pyrite–pyrrhotite zone; no new gold was added from the granite fluid (p. 11.17). Copper has a broadly similar distribution to gold in that, on average, it is enriched in the pyrite–pyrrhotite zone. However, the magnetite–biotite zone also contains sporadic areas of copper enrichment. From these broad trends, the change in fluid conditions deduced from Fe–S–O assemblages and activity–activity diagrams in Figs 11.6 and 11.7, metal solubilities can be modelled.

*Zinc, lead, and silver:* In moderately reduced fluids ($H_2S$ dominant), zinc, lead and silver sulphides share broadly parallel solubility controls, as follows:

$$Me_mS + mnCl^- + 2H^+ = mMeCl_n^{2-n/m} + H_2S$$
(for sphalerite and galena, m = 1; for acanthite, m = 2) (3)

The above form of reaction directly controls the solubility of sphalerite and galena, but for silver-bearing sulphosalts the concentrations of arsenic and antimony in solution are also important. In all cases, however, the solubility is highest in acid, $H_2S$-poor fluids and lowest in near neutral, $H_2S$-rich fluids. In the case of zinc, the granitic fluid was capable of carrying over 10,000 ppm before it began to interact with the massive sulphide (point A, Figs. 11.6A and B). As interaction with the massive sulphide proceeded, $a_{H2S}$ and pH increased, causing a substantial decrease in the solubility of lead and zinc. At point D (Figs. 11.6A and B), where reaction ceased, zinc solubility had decreased to less than 100 ppm, and the solution became saturated. Hence, sphalerite, galena and silver-bearing minerals were dissolved from the replacement zones, where the fluids were highly undersaturated, and remobilised out of the system entirely.

*Gold and copper:* In high temperature hydrothermal systems, gold can be transported as either $Au(HS)_2^-$ or $AuCl_2^-$. The mechanisms of solution and precipitation for these complexes are substantially different, as illustrated by the following reactions:

$$4Au + 8H_2S + O_2 = 4Au(HS)_2^- + 2H_2O + 4H^+ \quad (4)$$
$$4Au + 8Cl^- + 4H^+ + O_2 = 4AuCl_2^- + 2H_2O \quad (5)$$

A decrease in $fO_2$ will decrease the solubility of gold as either complex, whereas an increase in pH will cause an increase in gold solubility as $Au(HS)_2^-$ but a decrease in gold solubility as $AuCl_2^-$. An increase in $a_{H2S}$ will increase the solubility of $Au(HS)_2^-$, but it will not affect the stability of $AuCl_2^-$.

As gold was leached from the magnetite–biotite ± pyrite assemblage, gold solubility must have initially been quite high. Gold solubility must have dropped dramatically in the pyrite–pyrrhotite zone as gold was concentrated in this zone. Based on Fe–S–O mineral stabilities, the fluid pH and $a_{H2S}$ increased substantially during replacement (Figs 11.6 and 11.7), but both of these changes dramatically increase the stability of $Au(HS)_2^-$, which is inconsistent with the dissolution of gold from the magnetite–biotite zone and reprecipitation in the pyrite–pyrrhotite zone.

Conversely, high gold solubility as $AuCl_2^-$ is favoured at low pH. Therefore the initial fluid in equilibrium with the low pH magnetite–biotite±pyrite assemblage would dissolve

significant gold. As the replacement and dissolution of sphalerite or galena along path B–C–D (Figs. 11.6A and C) involves a significant increase in pH, gold would be rapidly precipitated as the fluids reacted in the pyrite–pyrrhotite zone. Hence, $AuCl_2^-$ was probably the dominant gold complex during Devonian replacement of the Cambrian massive sulphide in the south-end of the Rosebery deposit. This interpretation is supported by the fluid conditions inferred from the Fe–S–O and K-silicate mineral assemblages, which imply that $AuCl_2^-$ is the dominant gold complex in solution (cf. Fig. 11.7C).

As the dissolution of chalcopyrite in the presence of pyrite (reaction 6) is similar to the dissolution of gold as a chlorocomplex, the distribution of copper should be similar to that of gold.

$$4CuFeS_2 + 4Cl^- + 4H^+ + O_2 = 4FeS_2 + 4CuCl^o + 2H_2O \qquad (6)$$

Again the increase in pH associated with Devonian replacement resulted in fluids, which were initially undersaturated in chalcopyrite in the magnetite–biotite zone where copper solubility was 10 ppm, to saturate and precipitate chalcopyrite in the pyrite–pyrrhotite zone where copper solubilities were less than 1 ppm (Fig. 11.7B). The relatively low solubility of copper in the magnetite–biotite zone resulted in imperfect dissolution and relic patches of copper mineralisation in the magnetite–biotite zone.

## 11.7 EXPLORATION IMPLICATIONS ...

As was stressed by Large et al. (1990b) and Large (1991, in press) and discussed above, the Cambrian volcanogenic sulphide mineralisation in Mt Read Volcanics of western Tasmania displays an array of mineralisation styles (Fig. 11.1). The seafloor massive sulphides represent the best exploration target for high-grade base-metal and gold mineralisation. Zinc–barite-rich massive sulphide deposits (e.g. Rosebery, Que River, Hellyer) have mean grades of 21% Pb+Zn and 2–4 g/t Au with the best grades concentrated close to the stratigraphic hangingwall of the deposit.

Although the Hercules and South Hercules deposits are of the volcanogenic Cambrian style, they differ from the typical exhalative zinc–gold or copper–gold deposits. The Hercules ore lenses are of sub-seafloor replacement origin and were later metamorphosed and strongly deformed. The South Hercules mineralisation appears to occur at the higher level of the volcanogenic massive sulphide system, probably at the seawater–rock interface. The sub-seafloor replacement to sea water–rock interface environment, and later deformation and metamorphism in the Hercules–South Hercules area provide new constraints and targets for future exploration in the area.

Large (1990) and Lees et al. (1990b) also maintained that folding and shearing in the Devonian has produced an array of deformation styles in the western Tasmanian massive sulphide ores varying from broad open folding (Hellyer), through upright isoclinal folding (Que River) to sheath folding and thrust stacking (Rosebery) (Fig. 11.2). Hence, understanding the style of deformation and its effect on the ores is a critical part of future exploration and selection of target areas.

For instance, because the lead–zinc ore lenses have been folded and thrust over the chalcopyrite–pyrite ore and alteration system during the Devonian deformation at Rosebery, the potential for lead–zinc ore down dip at depth is poor. However, the possiblilty that chalcopyrite–pyrite ore may extend down dip is good. The presence of a separate ore lens system with its own alteration pipe down dip in a similar fashion to the present Rosebery ore lenses is also possible (Fig. 11.8).

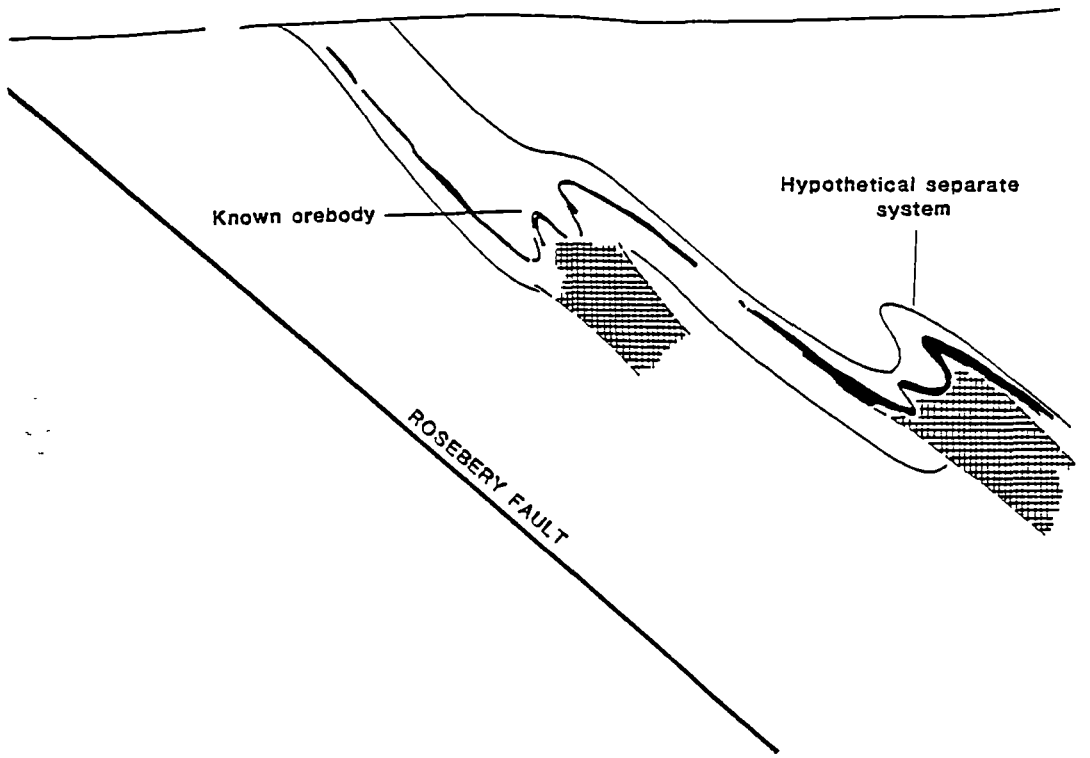


Fig. 11.8. Schematic diagram showing hypothetical separate vent system.

The zinc ratio distribution appears to be applicable for mineral exploration in the Rosebery–Hercules area and the zinc ratio distribution the South Hercules area can be used as a guide for base metal targets. The massive pyrite ± barite zone with elevated gold, silver and arsenic metals at the top of the sulphide lens in the South Hercules deposit shows characteristics of the upper part of a volcanogenic massive sulphide system and suggests a potential for the discovery of high–grade base metal mineralisation at depth in the South Hercules area.

Microprobe analyses indicate the presence of significant mercury in the gold grains from the South Hercules deposit. The gold grains locked in the pyrite euhedra contain up to 18.2 wt % Hg whereas the Hg content in the gold grains associated with other sulphides ranges from 6.3 to 21.8 wt %. The enrichment of the Hg in the gold grains from the South Hercules deposit suggests the possibility of the application of Hg abundance as a tool for future geochemical exploration in the Hercules–South Hercules area. Future investigation for the Hg distribution in other sulphides (e.g. sphalerite) should be undertaken.

The VMS carbonates display oxygen and carbon isotopic distribution patterns different from the Devonian carbonates. The VMS carbonates have more variable oxygen and heavier carbon isotopic values compared to the Devonian carbonates. On this basis, the combined carbon/oxygen isotopic ratios of hydrothermal carbonates can be used as an additional guide to distinguish Cambrian versus Devonian mineralisation for regional mineral exploration programmes in western Tasmania.

The possible correlation between $\delta^{34}S$ values of sulphides and gold grades in the South Hercules deposit implies that the gold was deposited due to decreasing temperature and increasing $fO_2$, which are also the controls on the sulphur isotope variation in a particular hydrothermal system, and suggests that sulphur isotopes are potentially useful guides to targeting the gold-rich part of massive sulphide systems.

# REFERENCES


Adams, C. J., Black, L. P., Corbett, K. D., and Green, G. R., 1985, Reconnaissance isotopic studies bearing on the tectonothermal history of early Palaeozoic and late Proterozoic sequences in western Tasmania: Aust. Jour. Earth Sci., v. 32, p.7–36.

Adams, R. L., Burton, C. C. J., Druett, J. G., Hanson, N. H., and McNaught I. S., 1976, The Rosebery and Hercules zinc–lead deposits: *in* Ore Deposits of Western Tasmania, Intern. Geol. Cong., 25th, Sydney 1976, Excursion Guide 31AC: 31–36.

Allen, R. L., and Cas, R. A. F., 1990, The Rosebery controversy: Distinguishing prospective submarine ignimbrite-like units from true subaerial ignimbrites in the Rosebery–Hercules Zn–Cu–Pb massive sulphide district, Tasmania: *in* Gondwana: Terranes and Resources, 10th Australian Geological Convention, Hobart, Geol. Soc. Aust. Abstr., No. 25, p. 31–32.

Allen, R. L., and Hunns, S. R., 1990, Geology of the Hercules and South Hercules ore bodies: *in* The Mt Read Volcanics and related ore deposits, eds., Corbett, K., and Large, R. R., Excursion Guide E1, p. 15–27.

Anderson, A. J., Clark, A. H., Xin–Pei Ma, Palmer, G. R., MacArthur, J. D., and Roedder, E., 1989, Proton-induced X-ray and gamma-ray emission analysis of unopened fluid inclusions: Econ. Geol., v. 84, p. 1277–1292.

Barbillat, J., Dhamelincourt, P., and Delhaye, M., 1985, Non-destructive microprobing by means of instruments for Raman and fluorescence spectroscopy: *in* Microbeam Analysis, ed., Armstrong J. T., San Francisco Press, pp. 15–18.

Barnes, H. L., 1979, Solubilities of ore minerals: *in* Geochemistry of Hydrothermal Ore Deposits, ed., Barnes, H. L., 2nd edition, New York, John Wiley and Sons, p. 404–460.

Barnes, R. G., 1987, Multi-stage mobilisation and remobilisation of mineralisation in the Broken Hill Block, Australia: *in* Mechanisms and Chemical (Re)mobilisation of Metalliferous Mineralisation, eds, Marshall, B., and Gilligan, L. B., Ore Geology Reviews, v. 2, p. 247–267.

Barth, W. H., 1986, Geology of the Cleveland tin mine, Tasmania, Australia with special reference to mineral chemistry and rare earth distribution: Unpub. Ph.D. thesis, Univ. Heidelberg, 309 p.

Barton, P. B. Jr, 1978, Some ore textures involving sphalerite from the Furutobe Mine, Akita Prefecture, Japan: Mining Geology (Japan), v. 28, p. 293–300.

Barton, P. B. Jr., 1984, Redox reactions in hydrothermal fluids: *in* Fluid-mineral equilibria in hydrothermal systems, eds., Henley, R. W., and Truesdell, A. H., and Barton, P. B., Rev. Econ. Geol., v. 1, pp. 99–114.

Barton, P. B. Jr., and Skinner, B. J., 1979, Sulphide mineral stabilities: *in* Geochemistry of Hydrothermal Ore Deposits , ed., Barnes, H. L., 2nd ed., New York, John Wiley & Sons. p. 278–403.

Barton, P.B., Jr., and Toulmin, P. III, 1966, Phase relations involving sphalerite in the Fe–Zn–S system: Econ. Geol., v. 61, p.815–849.

Bean, R. E., 1974, Biotite stability in the porphyry copper environment: Econ. Geol., v. 69, p. 241–256.

Bean, R. E., 1982, Hydrothermal alteration in silicate rocks, southwestern North America: *in* Advances in geology of the porphyry copper deposits of southwestern North America, ed., Titley, S. R., Tucson, Univ. Arizona Press, p. 117–137.

Beaty, D. W., Taylor, H. P., Jr., and Coad, P. R., 1988, An oxygen isotope study of the Kidd Creek, Ontario, volcanogenic massive sulphide deposit: evidence for a high $\delta^{18}O$ ore fluid: Econ. Geol., v. 83, p. 1–17.

Benvenuti, M., and Lattanzi, P., 1989, Tourmaline-associated Pb–Zn–Ag mineralisation at Bottino, Apuane Alps, Italy: Geologic setting, mineral textures, and sulphide chemistry: Econ. Geol., v. 84, p. 924–939.

Berglund, S., and Ekstrom, T. K., 1980, Arsenopyrite and sphalerite as T–P indicators in sulphide ores from northern Sweden: Mineral. Deposita, v. 15, p. 175–187.

Berry, R. F., 1989, The history of movement on the Henty Fault Zone, western Tasmania: An analysis of fault striations: Aust. Jour. Earth Sci., v. 36, p.189–205.

Berry, R. F., 1990, The structure of the Rosebery Mine sequence, western Tasmania: *in* Gondwana: Terranes and Resources, 10th Australian Geological Convention, Hobart, Geol. Soc. Aust. Abstr., No. 25, p. 278–279.

Beus, A. A., 1962, Beryllium (translation from Russian): Freeman, San Francisco, 161p.

Beus, A. A., 1966, Geochemistry of beryllium and genetic types of beryllium deposits (translation from Russian): Freeman, San Francisco, 401 p.

Bodnar, R. J., and Bethke, P. M., 1984, Systematics of stretching of fluid inclusions I: Fluorite and sphalerite at 1 atmosphere confining pressure: Econ. Geol., v.79, p. 141–161.

Both, R. A., 1966, The zoned ore deposits of the Zeehan mineral field: unpub. M.Sc. thesis, Univ. Tasmania, Hobart, 343 p.

Both, R. A., 1978, Remobilisation of mineralisation during retrograde metamorphism, Broken Hill, New South Wales, Australia: *in* Mineralisation in Metamorphic Terranes, ed., Verwoerd, W. J., J. L. van Schaik Ltd., Pretoria, South Africa, pp. 481–489.

Bottinga, Y., and Javoy, M., 1973, Comments on oxygen isotope geothermometry: Earth Planet. Sci. Letters, v. 20, p. 250–263.

Bottinga, Y., and Javoy, M., 1975, Oxygen isotope partitioning among the minerals in igneous and metamorphic rocks: Rev. Geophysics Space Physics, v. 13, p. 401–418.

Bowers, T. S., Jackson, K. J., and Helgeson, H. C., 1984, Equilibrium activity diagrams for coexisting minerals and aqueous species at pressures and temperatures to 5 kb and 600°C: Springer–Verlag, Berlin, 397 p.

Bowman, J. R., O'Neil, J. R., and Essene, E. J., 1985a, Contact skarn formation at Elkhorn, Montana–II: origin and evolution of C–O–H skarn fluids: Am. Jour. Sci., v. 80, p. 240–244.

Bowman, J. R., Covert, J. J., Clark, A. H., and Mathieson, G. A., 1985b, The CanTung E-zone scheelite skarn orebody, Tungsten, Northwest Territories: Oxygen, hydrogen, and carbon isotope studies: Econ. Geol., v. 80, p. 1872–1895.

Bozzo, A. T., R. Chen and A. J. Barduhn, 1973, The properties of hydrates of chlorine and carbon dioxid: *in* Fourth International Symposium on Fresh Water from the Sea, eds., Delyannis, A., and Delyannis, E., v. 3, p. 437–451.

Brathwaite, R. L., 1969, The geology of the Rosebery ore deposits: Unpub. Ph.D. thesis, Univ. Tasmania, Hobart, 218 p.

Brathwaite, R. L., 1972. The structure of the Rosebery ore deposit, Tasmania: Proc. Aust. Inst. Min. Metall., v. 241, p. 1–14.

Brathwaite, R. L., 1974, The geology and origin of the Rosebery ore deposit, Tasmania: Econ. Geol., v. 69, p. 1086–1101.

Brill, B. A., 1989, Trace element contents and partitioning of elements in ore minerals from the CSA Cu–Pb–Zn deposit, Australia: Can. Mineralogist, v. 27, p. 263–274.

Bristol, C. C., 1974, Sphalerite geobarometry of some metamorphosed orebodies in the Flin Flon and Snow Lake districts, Manitoba: Can. Mineralogist, v. 12, p. 308–315.

Bristol, C. C., 1979, Application of sphalerite geobarometry to ores from the Ruttan Mine: Econ. Geol., v. 74, p. 1496–1503.

Broman, C., 1987, Fluid inclusions of the massive sulphide deposits in the Skellefte district, Sweden: Chem. Geol., v. 61, p. 161–168.

Brown, P. E., Essene, E. J., and Kelly, W. C., 1978, Sphalerite geobarometry in the Balmat-Edwards district, NewYork: Am. Mineralogist, v. 63, p.250–257.

Brown, P. E., Bowman, J. R., and Kelly, W. C., 1985, Petrologic and stable isotope constraints on the source and evolution of skarn-forming fluids at Pine Creek, California: Econ. Geol., v. 80, p. 72–95.

Bryndzia, L. T., Scott, S. D., and Spry, P. G., 1988, Sphalerite and hexagonal pyrrhotite geobarometer: Experimental calibration and application to the metamorphosed sulphide ores at Broken Hill, Australia: Econ. Geol., v. 83, p. 1193–1204.

Bryndzia, L. T., Scott, S. D., and Spry, P. G., 1990, The sphalerite and hexagonal pyrrhotite geothermometer: Correction and application: Econ. Geol., v. 85, p. 408–411.

Burke, E. A., and Lustenhouwer, W. J., 1987, The application of a multichannel laser Raman microprobe (Microdil–28) to the analysis of fluid inclusions: Chem. Geol., v. 61, p. 11–17.

Burt, D. M., 1980, The stability of danalite, $Fe_4Be_3(SiO_4)_3S$: Am. Mineralogist, v. 65, p. 355–360.

Burton, C. C. J., 1975a, Rosebery zinc–lead–copper orebody, *in* Economic Geology of Australia and Papua New Guinea, Vol. 1 Metals, ed., C.L. Knight, pp 619–626, The Australian Inst. Min. Metall., Melbourne.

Burton, C. C. J., 1975b, Hercules and Farrell orebodies, Rosebery District, *in* Economic Geology of Australia and Papua New Guinea, Vol. 1 Metals, ed., C.L. Knight, pp 626–628, The Australian Inst. Min. Metall.: Melbourne.

Campana, B., and King, D., 1963, Palaeozoic tectonism, sedimentation and mineralisation in West Tasmania: Geol. Soc. Aust. Jour., v. 10, p. 1–54.

Campana, B., Dickinson, S. B., King, D., and Matheson, R. S., 1958, The mineralised rift valleys of Tasmania: *in* F. L. Stillwell Anniversary Volume, Aust. Inst. Min. Metall., Melbourne, pp. 41–60.

Campbell, F. A., and Ethier, V. G., 1983, Environment of deposition of the Sullivan orebody: Mineral. Deposita, v. 18, p. 39–55.

Carignan, J. L., Brown, K. A., and Gelinas, L., 1979, Etude microthermetrique preliminaire des inclusions fluides asscices au gisment volcanogene de Millenbach [abs.]: Geol. Soc. Assoc. Canada Abstract with Programs, v. 4, p. 42.

Carlson, S. R., and Sawkins, F. J., 1980, Mineralogic and fluid inclusion studies of the tourmaline Cu–Mo-bearing breccia pipe, northern Peru: Econ. Geol., v. 75, p. 1233–1238.

Carr, G. R., Wilmshurst, J. R., and Ryall, W. R., 1986, Evaluation of mercury pathfinder techniques: Base metal and uranium deposits: Jour. Geochem. Explor., v. 26, p. 1–117.

Cathelineau, M., and Nieva, D., 1985, A chlorite solid solution geothermometer: the Los Azufres (Mexico) geothermal system: Contr. Mineral. Petrol., v. 91, p. 235–244.

Charoy, B., 1982, Tourmalinisation in Cornwall, England: *in* Metallisation Associated with Acid Magmatism, ed., Evans, A. M., John Wiley and Sons, pp. 63–70.

Clark, A. M., and Fejer, E. E., 1976, Zoned genthelvite from the Cairngorm Mountains, Scotland: Mineral. Mag., v. 40, 637–639.

Clayton, R. N., and Mayeda, T. K., 1963, The use of bromine pentafluoride in the extraction of oxygen from oxides and silicates for isotopic analysis: Geochim. et Cosmochim. Acta, v. 27, p. 43–52.

Cole, D. R., and Ohmoto, H., 1986, Kinetics of isotopic exchange at elevated temperatures and pressures: *in* Stable isotopes in high temperature geological processes, eds., Valley, J. W., Taylor, Jr., H. P., and O'Neil, J. R., Mineral. Soc. Amer. Reviews in Mineralogy 16, p. 41–90.

Collins, P. L. F., 1979, Gas hydrates in fluid inclusions and the use of freezing for estimation salinity: Econ. Geol., v. 74, p. 1435–1444.

Collins, P. L. F., 1981, The geology and genesis of the Cleveland tin deposit, western Tasmania: Fluid inclusion and stable isotope studies: Econ. Geol., v. 76, p. 365–392.

Corbett, K. D., 1986, The geological setting of mineralisation in the Mt. Read Volcanics, *in* The Mount Read Volcanics and Associated Ore Deposits, ed., Large, R.R., p. 1–10, A symposium, Geol. Soc. Australia, Tas. Div., Burnie, November, 1986, Programme with abstract.

Corbett, K. D., and Lees, T., 1987, Stratigraphic and structural relationships and evidence for Cambrian deformation at the western margin of the Mt Read Volcanics, Tasmania: Aust. Jour. Earth Sci., v. 34, p. 45–67.

Corbett, K. D., Solomon, M., McClenaghan, M. P., Carswell, J. T., Green, G. R., Iliff, G., Lees, T. C., Howarth, J. W., McArthur, G. J., and Wallace, D. B., 1989, Cambrian Mt Read volcanics and associated mineral deposits: *in* Geology and Mineral Resources of Tasmania, eds., Burrett, C. F., and Martin, E. L., Geol. Soc. Australia, Spec. Pub. 15, p. 84–153.

Corbett, K.D., 1981, Stratigraphy and mineralisation in the Mt. Read Volcanics, western Tasmania: Econ. Geol., v. 76, p. 209–230.

Cox, S. F., 1987, Flow mechanisms in sulphide minerals: *in* Mechanisms and Chemical (Re)mobilisation of Metalliferous Mineralisation, eds, Marshall, B., and Gilligan, L. B., Ore Geology Reviews, v. 2, p. 65–86.

Cox, S. F., 1987, Etheridge, M. A., and Wall, V. J., 1987, The role of fluids in syntectonic mass transport, and the localisation of metamorphic vein-type ore deposits: *in* Mechanisms and Chemical (Re)mobilisation of Metalliferous Mineralisation,eds, Marshall, B., and Gilligan, L. B., Ore Geology Review, v. 2, p. 133–171.

Craig, J. R., Ljokjell, P., and Vokes, F. M., 1984, Sphalerite compositional variations in sulphide ores of the Norwegian Caledonides: Econ. Geol., v. 79, p. 1727–1735.

Davidson, G., 1990, Starra and Trough Tank: Iron–formation-hosted gold–copper deposits of north-west Queensland: Unpub. Ph.D. thesis, Univ. Tasmania, Hobart, 380 p.

Deer, W. A., Howie, R. A., and Zussman, J., 1962, Rock-Forming Minerals, vol 3: Longman, London, 270 p.

DeWitt, D. B., and Essene, E. J., 1974, Sphalerite geobarometry applied to Grenville marbles (abstr.)., Geol. Soc. America Abstr. with Programs 6, p. 709–971.

Dhamelincourt, P., Wallart, F., Lechercq, M., N'Guyen, A. T., and Landon, D. O., 1979, Laser Raman molecular microprobe (MOLE): Anal. Chemistry, v. 51, p. 414A–421A.

Dixon, G. H., 1980, Geological, geochemical and stable isotope studies of the carbonates at Rosebery: Unpub. B.Sc. (Hons) thesis, Univ. Tasmania, Hobart, 150 p.

Drown, C. G., and Down, R. C., 1990, Deformational style and strain partitioning at the Hellyer volcanogenic massive sulphide deposit: *in* Gondwana: Terranes and Resources, 10th Australian Geological Convention, Hobart, Geol. Soc. Aust. Abstr., No. 25, p. 176–177.

Dubessy, J., Audeoud, D., Wilkins, R., and Kosztolanyi, C., 1982, The use of the Raman microprobe MOLE in the determination of the electrolytes dissolved in the aqueous phase of fluid inclusions: *in* Current Research in Fluid Inclusions, eds., Kreulen, R., and Touret, J., Chem. Geology, v. 37, p. 137–150.

Dunn, P. J., 1976, Genthelvite and helvite group: Miner. Mag., v. 40, p. 627–636.

Eastoe, C. J., 1973, The Rosebery host rock horizon: Unpub. B.Sc. (Hons) thesis, Univ. Tasmania, Hobart, 148p.

Eastoe, C. J., and Nelson, S.E., 1988, A Permian Kuroko-type hydrothermal system, Afterthought-Ingot area, Shasta County, California: Lateral and vertical sections, and geochemical evolution: Econ. Geol., v. 83, p. 588–605.

Eastoe, C. J., Solomon, M., and Walshe, J. L., 1987, District scale alteration associated with massive sulphide deposits in the Mt Read Volcanics, western Tasmania: Econ. Geol., v. 82, p. 1239–1258.

Einaudi, M. T., and Burt, D. M., 1982, Introduction – Terminology, classification, and composition of skarn deposits: Econ. Geol., v. 77, p. 745–754.

Einsele, G., 1986, Interaction between sediments and basalt injection in young Gulf of California-type spreading centers: Geologische Rundschau, v. 75, p. 197–208.

Eldridge, C. S., Barton, P. B. Jr., and Ohmoto, H., 1983, Mineral texture and their bearing on formation of the Kuroko orebodies: *in* The Kuroko and related volcanogenic massive sulphide deposits, eds., Ohmoto, H., and Skinner, B. J., Econ. Geol., Mon. 5, p. 241–281.

Ellis, A. J., 1970, Quantitative interpretation of chemical characteristics of hydrothermal systems: Geothermics Spec. Issue, v. 2, p. 516–528.

Erasmus, C. S., Sellschop, J. P. F., and Hallbauer, D. K., 1982, Report to Council for Mineral Technology: Randburg, Report No. M54, 18p.

Erasmus, C. S., Sellschop, J. P. F., and Watterson, J. I. W., 1987, New evidence on the composition of mineral grains of native gold: Nucl. Geophys., v. 1, no. 1, p. 1–23.

Ethier, V. G., and Campbell, F. A., 1977, Tourmaline concentrations in Proterozoic sediments of the southern Cordillera of Canada and their economic significance: Can. Jour. Earth Sci., v. 14, No. 3, p. 2348–2363.

Ethier, V. G., Campbell, F. A., Both, R. A., and Krouse, H. R., 1976, Geological setting of the Sullivan orebody and estimates of temperature and pressure of metamorphism: Econ. Geol., v. 71, p. 1570–1588.

Farquhar, J., 1983, 'F' lens pyrrhotite gold reserves: Electrolytic Zinc Company of Australasia , Internal memo, 5p.

Faure, 1986, Principles of Isotope Geology: 2nd edition, John Wiley and Sons., Berlin, 456p.

Finlow-Bates, T., and Large, D. E., 1978, Water depth as major control on the formation of submarine exhalative ore deposits: Geol. Jahrb, v. D30, p. 27–39.

Finucane, K. J., 1932, The geology and ore deposits of the Rosebery district: Chem. Eng. Min. Rev., v. 25, p. 5–7, p. 43–46.

Fitzgerald, F. G., 1974, The Primrose Pyroclastics in the Hercules–White Spur area, western Tasmania: Unpub. B.Sc. (Hons) thesis, Univ. Tasmania, Hobart, 188p.

Franklin, J. M., 1990, Volcanogenic massive sulphide deposits, ancient and modern: *in* Gondwana: Terranes and Resources, 10th Australian Geological Convention, Hobart, Geol. Soc. Aust. Abstr., No. 25, p. 11–13.

Franklin, J. M., Lydon, J. W., and Sangster, D. F., 1981, Volcanic-associated massive sulphide deposits: Econ. Geol. 75th Anniv. Vol., p. 485–627.

Frantz, J. D., Mao, H. K., Zhang, Y. G., Wu, Y., Thompson, A. C., Underwood, J. H., and Giauque, R. D., 1987, Analysis of fluid inclusions by X-ray fluorescence using synchrotron radiation [abs.]: Geol. Soc. America Abstract with Programs, v. 19, p. 667.

Fyfe, W. S., 1987, Tectonics, fluids and ore deposits: Mobilisation and remobilisation: *in* Mechanisms and Chemical (Re)mobilisation of Metalliferous Mineralisation, eds, Marshall, B., and Gilligan, L. B., Ore Geology Reviews, v. 2, p. 21–36.

Garlick, W. G., and Fleischer, V. D., 1972, Sedimentary environment of Zambian copper deposition: Geologie en Mijnbouw, v. 51, p. 277–298.

Garrett, S. J. M., 1989, The geology and gold drainage geochemistry of the Lewis River Volcanics, Elliott Bay, southwest Tasmania: Unpub. B.Sc. (Hons) thesis, Univ. Tasmania, Hobart, 163 p.

Gilligan, L. B., and Marshall, B., 1987, Textural evidence for remobilisation in metamorphic environments: *in* Mechanisms and Chemical (Re)mobilisation of Metalliferous Mineralisation, eds, Marshall, B., and Gilligan, L. B., Ore Geology Reviews, v. 2, p. 205–229.

Golding, S. D., and Wilson, A. F., 1983, Geochemical and stable isotope studies of the No. 4 lode, Kalgoorlie, western Australia: Econ. Geol., v. 78, p. 438–450.

Golding, S. D., Mcnaughton, N. J., Barley, M. E., Groves, D. I., Ho, S. E., Rock, N. M. S., and Turner, J. V., 1989, Archean carbon and oxygen reservoirs: Their significance for fluid sources and circulation paths for Archean mesothermal gold deposits of the Norseman–Wiluna belt, western Australia: *in* The Geology of Gold deposits: Perspective in 1988, eds., Keays, R. R., Ramsay, W. R. H., and Groves, D. I., Econ. Geol. Mon. 6, p. 520–536.

Green, G. R., 1983, The geological setting and formation of the Rosebery volcanic-hosted massive sulphide orebody, Tasmania: Unpub. Ph.D. thesis, Univ. Tasmania, Hobart, 288 p.

Green, G. R., 1986, Stable isotope and alteration investigations of the Mt Read Volcanics: I. The Hercules and Boco areas, *in* The Mt Read Volcanics and Associated Ore Deposits , ed., Large, R. R., A symposium, Geol. Soc. Australia, Tas. Div., Burnie, November, 1986, Programme with abstract, p. 39–41.

Green, G. R., 1990a, Paleozoic geology and mineral deposits of Tasmania, *in* Geology of the Mineral deposits of Australia and Papua New Guinea, ed., Hughes, F. E., pp. 1207–1223, The Australasian Institute of Mining and Metallurgy, Melbourne.

Green, G. R., 1990b, Rock alteration, mineral and oxygen isotope zonation in the Rosebery district, Tasmania: 10th Australian Geological Convention, Hobart, Geol. Soc. Aust. Abstr., No. 25, p. 15–16.

Green, G. R., 1990c, Alteration mineralogy, whole rock geochemistry and oxygen isotope zonation in the area north of the Grand Centre Prospect, Rosebery mine leases: Unpub. Report to Electrolytic Zinc Company of Australasia, 118p.

Green, G. R., and Iliff, G., 1989, Rosebery: *in* Geology and Mineral Resources of Tasmania, eds., Burrett, C. F., and Martin, E. L., Geol. Soc. Australia, Spec. Pub. 15, p. 132–137.

Green, G. R., Solomon, M., and Walshe, J. L., 1981, The formation of the volcanic-hosted massive sulphide ore deposit at Rosebery, Tasmania: Econ. Geol., v. 76, p. 304–338.

Green, G. R., Ohmoto, H., Date, J., and Takahashi, T., 1983, Whole-rock oxygen isotope distribution in the Fukazawa–Kosaka area, Hukuroko district, Japan, and its potential application to mineral exploration: *in* The Kuroko and related volcanogenic massive sulphide deposits, eds., Ohmoto, H., and Skinner, B. J., Econ. Geol., Mon. 5, p. 395-411.

Griffith, W. P., 1970, Raman studies on rock-forming minerals. Part II: Minerals containing MO3, MO4, and MO6 groups: Jour. Chem. Soc., (A) 1970, p. 286–291.

Groves, D. I., Binns, R. A., Barrett, F. M., and McQueen, K. G., 1975, Sphalerite compositions from western Australian nickel deposits, a guide to equilibria below 300°C: Econ. Geol., v. 70, p. 391–396.

Guilhaumou N., Velde, B., and Beny, C., 1984, Raman microprobe analysis of gaseous inclusions in diagenetically recrystallised calcites: Bull. Mineralogie., v. 107, p. 193–202.

Gustavson, J. B., 1976, The use of mercury in geochemical exploration for Mississippi Valley type of deposits in Tennessee: Jour. Geochem. Explor., v. 6, p.251–277.

Hall, G., Cottle, V. M., Rosenhain, P. B., and McGhie, R. R., 1953, Lead–zinc ore deposits of Read–Rosebery and Mt Farrell: Empire Mining Metallurgy Cong. 5th, Melbourne, p.1145–1159.

Hall, G., Cottle, V. M., Rosenhain, P. B., McGhie, R. R., and Druett, J. G., 1965, Lead–zinc ore deposits of Read–Rosebery: *in* Geology of Australian ore deposits, eds., J. McAndrew and Madigan, R. T., p. 485–489, 8th Commonwealth Mining and Metallurgical Congress, Melbourne and the Australian Institute of Mining and Metallurgy, Melbourne.

Hall, R. J., 1967, The geology of the Hercules Mine area, Williamsford: Unpub. B.Sc. (Hons) thesis, Univ. Tasmania, Hobart, 227 p.

Hall, S., 1990, The Koonya prospect, Rosebery, Tasmania: Unpub. B.Sc. (Hons) thesis, Univ. Tasmania, Hobart, 115 p.

Hallbauer, D. K., 1986, The mineralogy and geochemistry of Witwatersrand pyrite, gold, uranium, and carbonaceous matter: *in* Mineral Deposits of South Africa , eds., Anhaeusser, C. R., and Maske, S., Geol. Soc. S. Afr., Johannesburg, v. I & II, p. 731–752.

Hallbauer, D. K., and Von Gehlen, K., 1983, The Witwatersrand pyrites and metamorphism: Mineral. Mag., v. 47, p. 473–479.

Hannington, M. D., and Scott, S. D., 1989, Sulfidation equilibria as guides to gold mineralisation in volcanogenic massive sulphides: Evidence from sulphide mineralogy and the composition of sphalerite: Econ. Geol., v. 84, p. 1978–11995.

Hekinian, R., Fevrier, M., Bischoff, J. L., Picot, P., and Shanks W. C., 1980, Sulphide deposits from East Pacific Rise near 21° N: Science, v.207, p. 1433–1444.

Helgeson, H. C., 1969, Thermodynamics of hydrothermal systems at elevated temperatures and pressures: Am. Jour. Sci., v. 267, p. 729–804.

Hendry, D. A. F., 1981, Chlorites, phengites, and siderites from the Prince Lyell ore deposit, Tasmania, and the origin of the deposit: Econ. Geol., v. 76, p. 285–303.

Henry, D. J., and Guidotti, C. V., 1985, Tourmaline as a petrogenetic indicator mineral: an example from the staurolite-grade metapelites of NW Maine: Am. Mineralogist, v. 70, p. 1–15.

Herman, R. G., Bogdan, C. E., Sommer, A. J., and Simpson, D. R., 1987, Discrimination among carbonate minerals by Raman spectroscopy using the laser microprobe: Applied Spectroscopy, v. 41, No. 3, p. 437–440.

Hey, M. H., 1954, A new review of the chloites: Mineral. Mag., v.30, p. 277–292.

Hills, C. L., 1915a, The zinc–lead deposits of the Read–Rosebery district, Part I (Mt Read Group): Bull. Geol. Surv. Tasm., No. 19.

Hills, C. L., 1915b, The zinc–lead deposits of the Read–Rosebery district, Part II (Rosebery Group): Bull. Geol. Surv. Tasm., No. 23.

Hobbs, B. E., 1987, Principles involved in mobilisation and remobilisation: *in* Mechanisms and Chemical (Re)mobilisation of Metalliferous Mineralisation, eds, Marshall, B., and Gilligan, L. B., Ore Geology Reviews, v. 2, p. 37–45.

Hoefs, J., 1980, Stable Isotope Geochemistry: Springer–Verlag, New York, Heidelberg, Berlin, 2nd edition, 208 p.

Horn, E. E., and Traxel, K., 1987, Investigations of individual fluid inclusions with the Heidelberg proton microprobe – a non-destructive analytical method: Chem. Geology, v. 61, p. 29–35.

Hoernes, S., 1980, A BASIC-programme for the calculation of O-isotope temperatures: Contr. Mineral. Petrol., v. 74, p. 107–108.

Huston, D. L., 1989, Aspects of the geology of massive sulphide deposits from the Balcooma district, northern Queensland and Rosebery, Tasmania: Implications for ore genesis: Unpub. Ph.D. thesis, Univ. Tasmania, Hobart, 380p.

Huston, D. L., and Large, R. R., 1986, The distribution, mineralogy and geochemistry of precious metals in the north-end orebody, Rosebery Mine, Tasmania: Unpub. Report to Electrolytic Zinc Company of Australasia, 132 p.

Huston, D. L., and Large, R. R., 1987, Genetic and exploration significance of the zinc ratio {100Zn/(Zn+Pb)} in massive sulphide systems: Econ. Geol., v. 82, p. 1521–1539.

Huston, D. L., and Khin Zaw, 1988, Controls on the fineness and grain size of electrum in volcanogenic massive sulphide depossits: *in* AMIRA Report (84/P210), p. 61–70.

Huston, D. L., and Large, R. R., 1988, The distribution, mineralogy and geochemistry of gold and silver in the north-end orebody, Rosebery, Tasmania: Econ. Geol., v. 83, p. 1181–1192.

Huston, D. L., and Large, R. R., 1989, A chemical model for the concentration of gold in volcanogenic massive sulphide deposits: Ore Geology Reviews, v. 4, p. 171–200.

Huston, D. L., Bottrill, R. S., Creelman, R. A., Khin Zaw, Ramsden, T. R., Rand, S. and Large, R. R., 1991 in prep., Geological and geochemical controls on the mineralogy and grain size of gold bearing phases, eastern Australia volcanogenic massive sulphide deposits: Econ. Geol.

Hutcheon, I., 1978, Calculation of metamorphic pressure using the sphalerite–pyrrhotite–pyrite equilibrium: Am. Minerlogist, v. 63, p. 87–95.

Hutchison, M. N., and Scott, S.D., 1980, Sphalerite geobarometry applied to metamorphosed sulfide ores of the Swedish Caledonides and U.S. Appalachians: Norges Geol. Unders sokelse, No. 360 , p. 59–71.

Hutchison, M. N., and Scott, S.D., 1981, Sphalerite geobarometry in the Cu–Fe–Zn–S system: Econ. Geol., v. 76, p. 143–153.

Jacobs, D. C., and Parry, W. T., 1976, A comparison of the geochemistry of biotite from some Basin and Range stocks: Econ. Geol., v. 71, p. 1029–1035.

Jenkins, G. W., 1989, Thermal and chemical conditions of formation of the Que River massive sulphides and precious metal zone: *in* AMIRA Report (84/P210), p. 43–46.

Joliff, B. L., Papike, J. J., and Shearer, C. K., 1986, Tourmaline as a recorder of pegmatite evolution: Bob Ingersoll pegmatite, Black Hills, South Dakota: Am. Minerlogist, v. 71, p. 472–500.

Joliff, B. L., Papike, J. J., and Laul, J. C., 1987, Mineral recorders of pegmatite internal evolution: REE contents of tourmaline from the Bob Ingersoll pegmatite, South Dakota: Geochim. et Cosmochim. Acta, v. 51, p. 2225–2232.

Jonasson, I. R., and Sangster, D. F., 1975, Variations in the mercury content of sphalerite from some Canadian sulphide deposits: *in* Geochemical Exploration 1974: eds., Elliot, J. L., and Fletcher, W. K., Assoc. Expl. Geochem. Spec. Pub. No. 2, Elsevier, Amsterdam, p. 313–332.

Jonasson, I. R., and Sangster, D. F., 1978, Zn/Cd ratios for sphalerites from some Canadian sulphide ore samples: Geol. Surv. Can. Pap., No. 78–1B, p. 195–201.

Keays, R. R., 1987, Principles of mobilisation (dissolution) of metals in mafic and ultramafic rocks – The role of immiscible magmatic sulphides in the generation of hydrothermal gold and generation of volcanogenic massive sulphide deposits: *in* Mechanisms and Chemical (Re)mobilisation of Metalliferous Mineralisation, eds, Marshall, B., and Gilligan, L. B., Ore Geology Reviews, v. 2, p. 47–63.

Kelly, W. C., and Rye, R. O., 1979, Geologic, fluid inclusion, and stable isotope studies of the tin–tungsten deposits of Panasqueira, Portugal: Econ. Geol., v. 74, p. 1721–1822.

Khin Zaw, 1976, The Cantung E-zone orebody, Tungsten, Northwest Territories: A major scheelite skarn deposit, Unpub. M.Sc. thesis, Queen's University, Kingston, Ontario, 409p.

Khin Zaw, 1984, Geology and geothermometry of vein-type W–Sn deposits at Pennaichaung and Yetkanzintaung propects, Tavoy township, Tenasserim Division, Southern Burma: Mineral. Deposita, v. 19, p. 138–144.

Khin Zaw, 1987, A preliminary fluid inclusion study on Tennant Creek deposit: *in* Geology and Geochemistry of Gold–Copper Iron Oxide Systems , Vol. 2, Tennant Creek Workshop, July 1987, University of Tasmania, p. 1–8.

Khin Zaw and Clark, A. H., 1978, Fluoride–hydroxyl ratios of skarn silicates, Cantung E–zone scheelite orebody, Tungsten, Northwest Territories: Canadian Mineralogist, v. 16, p. 207–221.

Khin Zaw and Khin Myo Thet, 1983, A note on a fluid inclusion study of tin–tungsten mineralisation at Mawchi Mine, Kayah State, Burma: Econ. Geol., v. 78, p. 530–534.

Khin Zaw and Large, R. R., 1990, $\delta^{18}O$ and $\delta^{13}C$ isotopic variation of hydrothermal carbonates from the Rosebery, Hercules and South Hercules deposits, western Tasmania: interplay of Cambrian vs. Devonian systems: *in* 7th International Conference on Geochronology, Cosmochronology and Isotope Geology, Canberra, Australia, Geol. Soc. Aust. Abstr., No. 27, p. 114.

Khin Zaw, Large, R. R., and Hunns, S., 1990a, Geology and geochemistry of the precious metal-rich South Hercules volcanogenic sulphide deposit, western Tasmania: *in* Gondwana: Terranes and Resources, 10th Australian Geological Convention, Hobart, Geol. Soc. Aust. Abstr., No. 25, p. 10–11.

Khin Zaw, Huston, D. L., Mernagh, T., and Hoffman, C., 1990b, A fluid inclusion study of Tennant Creek ironstones: Implications for ore genesis and exploration: *in* Gondwana: Terranes and Resources, 10th Australian Geological Convention, Hobart, Geol. Soc. Aust. Abstr., No. 25, p. 290.

King, R. W., and Kerrich, R., 1986, Tourmaline in Archean lode gold deposit (abstr.): Geol. Soc. Amer. Abstracts with Programs, v. 18, p. 657.

King, R. W., and Kerrich, R., 1987, Fluorapatite fenitization and gold enrichment in sheeted trondhjemites within the Destor–Porcupine fault zone, Taylor Township, Ontario: Can. Jour. Earth Sci., v. 24, No. 3, p. 479–502.

Kowalik, J., Rye, R. O., and Sawkins, F. J., 1981, Stable isotope studies of the Buchans, Newfoundland polymetallic sulphide deposits: *in* The Buchans Orebodies: Fifty years of Geology and Mining, eds., Swanson, E. A., Strong, D. F., and Thurlow, J. G., Geol. Assoc. Can. Spec. Paper 22, p. 229–254.

Kranidiotis, P., and MacLean, W. H., 1987, Systematic of chlorite alteration at the Phelps Dodge massive sulphide deposit, Matagami, Quebec: Econ. Geol., v. 82, p. 1898–1911.

Kwak, T. A. P., 1983, The geology and geochemistry of the zoned, Sn–W–F–Be skarns at Mt Lindsay, Tasmania, Australia: Econ. Geol., v. 78, p. 1440–1465.

Lafferty, S., and Golding, S. D., 1985, Isotope geology laboratory report: Report No.3, Department of Geology and Mineralogy, University of Queensland, 147p.

Large, R.R., 1977, Chemical evolution and zonation of massive sulphide deposits in volcanic terraines: Econ. Geol., v. 72, p. 549–572.

Large, R.R., 1986, Integration of geology and geophysics in the development of exploration models for massive sulphide tin deposits in western Tasmania: *in* Genesis of Tin–Tungsten Deposits & their Associated Granitoids, IGCP Project 220, Bur. Miner. Resour. Geol. Geophys. Aust. Rec. 1986/10, p. 40.

Large, R. R., 1990, The gold-rich seafloor massive sulphide deposits of Tasmania: Geologische Rundschau, v. 79, p. 265–278.

Large, R. R., 1991 in press, Australian volcanic-hosted massive sulphide deposits: features, styles and genetic models: Econ. Geol.,

Large, R. R., and Both, R. A., 1980, The volcanogenic sulphide ores at Mt Chalmers, eastern Queensland: Econ. Geol., v. 75, p. 992–1009.

Large, R. R., Herrmann, W., and Corbett, K.D., 1987, Base metal exploration of the Mount Read Volcanics, western Tasmania: Pt I. Geology and exploration, Elliott Bay: Econ. Geol., v. 82, p. 267–290.

Large, R. R., McGoldrick, P. J., Berry, R. F., and Young, C. H., 1988, A tightly folded, gold-rich, massive sulphide deposit: Que River mine, Tasmania: Econ. Geol., v. 83, p. 681–693.

Large, R. R., Huston, D. L., McGoldrick, P., Ruxton, P. A., and McArthur, G., 1989, Gold distribution and genesis in Australian volcanogenic massive suphide deposits and their significance for gold transport models: *in* The Geology of Gold deposits: Perspective in 1988, eds., Keays, R. R., Ramsay, W. R. H., and Groves, D. I., Econ. Geol. Mon. 6, p. 520–536.

Large, R. R., Huston, D. L., McGoldrick, P., McArthur, G., Wallace, D., Carswell, J., Purvis, G., Creelman, B., and Ramsden, T., 1990a, Gold in western Tasmania: *in* Geological aspects of the discovery of important minerals in Australia, eds., Glasson, K. R., Rattigan, J. H., Blaikie, A. H., and Woodcock, J. T., The Australian Institute of Mining and Metallurgy, Melbourne.

Large, R. R., Berry, R., Huston, D. L., Gemmell, B., and Khin Zaw, 1990b, Integration of genetic theories with exploration criteria to develop viable exploration models for VMS deposits: *in* Gondwana: Terranes and Resources, 10th Australian Geological Convention, Hobart, Geol. Soc. Aust. Abstr., No. 25, p. 106.

Larsen, A., 1988, Helvite group from syenite pegmatites in the Oslo region, Norway: Norsk Geologisk Tidsskrift, v. 68, p. 119–124.

Larson, P. B., 1984, Geochemistry of the alteration pipe at the Bruce Cu–Zn volcanogenic massive sulphide deposit, Arizona: Econ. Geol., v. 79, p. 1880–1896.

Leaman, D. E., and Richardson, R. G., 1989, The granites of west and northwest Tasmania – a geophysical inurpretation: Dep. Mines Tasmania Geol. Surv. Bull. 66.

Lees, T., 1987, Geology and mineralisation of Rosebery–Hercules area, Tasmania, Unpub. M.Sc. thesis, Univ. of Tasmania, Hobart, p. 184.

Lees, T., 1988, The South Hercules ore deposit: Unpub. Report to Electrolytic Zinc Company of Australasia, 13p.

Lees, T., and Howard, J. W., 1989, Hercules: *in* Geology and Mineral Resources of Tasmania, eds., Burrett, C. F., and Martin, E. L., Geol. Soc. Australia, Spec. Pub. 15, p. 137–139.

Lees, T., Khin Zaw, Large, R. R., and Huston, D. L., 1990, Rosebery and Hercules copper–lead–zinc deposits: *in* Geology of the Mineral deposits of Australia and Papua New Guinea, ed., Hughes, F. E., pp. 1241–1247, The Australasian Institute of Mining and Metallurgy, Melbourne.

Liu, L., and Mernagh, T. P., 1990, Phase transitions and Raman spectra of calcite at high pressure and room temperature: Am. Mineralogist, v. 75, p. 801–806.

Loftus-Hills, G. D., Solomon, M., and Hall, R. J., 1967, The structure of the bedded rocks west of Rosebery, Tasmania: Geol. Soc. Australia Jour., v. 14, p. 333–337.

London, D., 1986, Formation of tourmaline-rich gem pockets in miarolitic pegmatites: American Mineralogist, v. 71, p. 396–405.

Lusk, J., and Ford, C. E., 1978, Experimental extension of the sphalerite geothermometer to 10 kbar: Am. Mineralogist, v. 63, p. 516–519.

Lusk, J., Campbell, F. A., and Krouse, H. R., 1975, Application of sphalerite geobarometry and sulfur isotope geothermometry to ores of the Quemont mine, Noranda, Quebec: Econ. Geol., v.70, p. 1070–1083.

Macrea, J. M., 1950, The isotope chemistry of carbonates and a paleotemperature scale: Jour. Chem. Physics, v. 18, p. 849–857.

Manning, D. A. C., 1982, Chemical and morphological variation in tourmalines from the Hub Kapong batholith of peninsular Thailand: Mineral. Mag., v. 45, p. 139–147.

Marshall, B., and Gilligan, L. B., 1987a, Introduction and summary: *in* Mechanisms and Chemical (Re)mobilisation of Metalliferous Mineralisation, eds, Marshall, B., and Gilligan, L. B., Ore Geology Reviews, v. 2, p. 1–9.

Marshall, B., and Gilligan, L. B., 1987b, An introduction to remobilisation: Information from orebody geometry and experimental considerations: *in* Mechanisms and Chemical (Re)mobilisation of Metalliferous Mineralisation, eds, Marshall, B., and Gilligan, L. B., Ore Geology Reviews, v. 2, p. 87–131.

Matsuhisa, Y., Goldsmith, J. R., and Clayton, R. N., 1979, Oxygen isotope fractionation in the system quartz–albite–anorthite–water: Geochim. et Cosmochim. Acta, v. 43, p. 1131–1140.

McArthur. G. J., 1986, The Hellyer massive sulphide deposit: *in* The Mount Read Volcanics and Associated Ore Deposits, ed., Large, R. R., A symposium, Geol. Soc. Australia, Tas. Div., Burnie, November, 1986, Programme with abstract, p. 11–20.

McArthur. G. J., 1989, Heyller: *in* Geology and Mineral Resources of Tasmania, eds., Burrett, C. F., and Martin, E. L., Geol. Soc. Australia, Spec. Pub. 15, p. 144–148.

McArthur. G. J., 1990, Metal and textural zonation in the Hellyer massive sulphide deposit: *in* Gondwana: Terranes and Resources, 10th Australian Geological Convention, Hobart, Geol. Soc. Aust. Abstr., No. 25, p. 108.

McLimans, R. K., Barnes, H. L., and Ohmoto, H., 1980, Sphalerite stratigraphy of the Upper Mississippi Valley zinc–lead District, Southwest Wisconsin: Econ. Geol., v. 75, p. 351–361.

McGoldrick, P. J., Large, R. R., and Jenkins, G. W., 1990, The footwall precious metal zone at Que River: Transition from a VMS to an epithermal mineral assemblage: *in* Gondwana: Terranes and Resources, 10th Australian Geological Convention, Hobart, Geol. Soc. Aust. Abstr., No. 25, p. 293.

Meinert, L. D., 1983, Variability of skarn deposits: Guides to exploration: *in* Revolution in the Earth Sciences – Advances in the past half-century, ed., Boardman, S. J., Kendall/Hunt Publishing Company, Iowa, p. 301–316.

Mernagh, T. P., and Wilde, A. R., 1989, The use of the laser Raman microprobe for the determination of salinity in fluid inclusions: Geochim. et Cosmochim. Acta, v. 53, p. 765–771.

Mizuta, T., 1988, Interdiffusion rate of zinc and iron in natural sphalerite: Econ. Geol., v. 83, p. 1205–1220.

Mole, N. R., 1983, Sphalerite composition in relation to deposition and metamorphism of the Foss stratiform Ba–Zn–Pb deposit, Aberfeldy, Scotland: Mineral. Mag., v. 47, p. 487–500.

Naschwitz, W., 1985, Geochemistry of the Rosebery ore deposit: Unpub. Ph.D. thesis, Univ. of Tasmania, Hobart, 276p.

Neiva, A. M. R., 1974, Geochemistry of tourmaline (schorlite) from granites, aplites and pegmatites from Northern Portugal: Geochim. et Cosmochim. Acta, v. 38, p. 1307–1317.

Newberry, R. J., 1983, The formation of subcalcic garnet in scheelite-bearing skarns: Canadian Mineralogist, v. 21, p. 529–544.

Nysten, P., 1986, Gold in the volcanogenic mercury-rich sulphide deposits Langsele, Skellefte ore district, northern Sweden: Mineral. Deposita, v. 21, p. 116–120.

Oberthur, T., and Saager, R., 1986, Silver and mercury in gold particles from the Proterozoic Witwaterrand placer deposits of South Africa: Metallogenic and geochemical implications: Econ. Geol., v. 81, p. 20–31.

Ohmoto, H., 1972, Systematics of sulphur and carbon isotopes in hydrothermal ore deposits: Econ. Geol., v. 67, p. 551–579.

Ohmoto, H., 1986, Stable isotope geochemistry of ore deposits: *in* Stable isotopes in high temperature geological processes, eds., Valley, J. W., Taylor, Jr., H. P., and O'Neil, J. R., Mineral. Soc. Amer. Reviews in Mineralogy 16, p. 491–559.

Ohmoto, H., and Rye, R. O., 1979, Isotopes of suphur and carbon: *in* Geochemistry of Hydrothermal Ore Deposits, ed., Barnes, H. L., John Wiley and Sons, New York, p. 509–567.

Ohmoto, H., and Lasaga, A. C., 1982, Kinetics of reactions between aqueous sulphates and sulphides in hydrothermal systems: Geochim. et Cosmochim. Acta, v. 46, p. 1727–1745.

O'Neil, J. R., 1987, Preservation of H, C, and O isotopic ratios in the low temperature environment: *in* Stable Isotope Geochemistry of Low Temperature Fluids, ed., Kyser, T. K., Mineral. Assoc. Canada Short Course Vol. 13, pp. 85–128.

O'Neil, J. R., Clayton, R. N., and Mayeda, T. R., 1969, Oxygen isotope fractionation in divalent metal carbonates: Jour. Chem. Phys., v. 51, p. 5547–5558.

Osaki, S., 1973, Carbon and oxygen isotopic compositions of hydrothermal rhodocrhosite from Ae, Inakinaishi, Geochem. Jour., v. 6, p. 151–162.

Ozerova, N. A., Rusinov, V. L., and Ozerov, Y. K., 1975, The mercury in sulphide deposits emplaced in volcanic suites: Mineral. Deposita, v. 10, p. 228–233.

Parry, W. T., 1986, Estimation of $X_{CO_2}$, P, and fluid inclusion volume from fluid inclusion temperature measurements in the system NaCl–$CO_2$–$H_2O$: Econ. Geol., v. 81, p. 1009–1013.

Pasteris, J. D., Kuehn, C. A., and Bodnar, R. J., 1986, Application of the Laser Raman microprobe RAMANOR U-1000 to hydrothermal ore deposits: Carlin as an example: Econ. Geol., v. 81, p. 915–930.

Patterson, D. J., Ohmoto, H., and Solomon, M., 1981, Geologic setting and genesis of cassiterite–sulphide mineralisation at Renison Bell, western Tasmania: Econ. Geol., v. 76, p. 393–438.

Peter, J., McConachy, T. F., and Scott, S. D., 1987, A geological and geochemical comparison of hydrothermal vent deposits in the Southern Trough of Guaymas Basin, Gulf of California and 11°N, East Pacific Rise (Abstr.): *in* Program and Abstracts, Recent hydrothermal mineralisation at Seafloor Spreading Centres: Tectonic, Petrologic and Geochemical Constraints, Feb. 5–6, McGill Univ., Mineral Explor. Res. Inst.

Pisutha-Arnond, V., and Ohmoto, H., 1983, Thermal history, and chemical and isotopic compositions of the ore-forming fluids responsible for the Kuroko massive sulphide deposits in the Hokuroko district of Japan: *in* The Kuroko and related volcanogenic massive sulphide deposits, eds., Ohmoto, H., and Skinner, B. J., Econ. Geol., Mon. 5, p. 523–558.

Plimer, I. R., 1983, The association of tourmaline-bearing rocks with mineralisation at Broken Hill, N. S. W.: Proc. Australasian Inst. Mining Metallurgy Conf., Broken Hill, N.S.W., July, 1983, p. 157–176.

Plimer, I. R., 1986, Tourmalinites from the Golden Dyke Dome, northern Australia: Mineral. Deposita, v. 21, p. 263–270.

Plimer, I. R., 1987, Remobilisation in high-grade metamorphic environments: *in* Mechanisms and Chemical (Re)mobilisation of Metalliferous Mineralisation, eds, Marshall, B., and Gilligan, L. B., Ore Geology Reviews, v. 2, p. 231–246.

Plimer, I. R., 1988, Tourmalinites associated with Australian Proterozoic submarine exhalative ores: *in* Base Metal sulphide deposits, eds., Friedrich, G. H., and Herzig, P. M., Springer–Verlag, Berlin Heidelberg, p. 255–283.

Plimer, I. R., and Lees, 1988, Tourmaline-rich rocks associated with the submarine hydrothermal Rosebery Zn–Pb–Cu–Ag–Au deposit and granites in western Tasmania, Australia: Mineralogy and Petrology, v. 38, p. 81–103.

Polya, D. A., Solomon, M., Eastoe, C. J., and Walshe, J. L., 1986, The Murchison Gorge, Tasmania – a possible cross section through a Cambrian massive sulphide system: Econ. Geol., v. 81, p. 1341–1355.

Potter, II, R. W., Babcock, R. S., and Brown, D. L., 1977, A new method for determining the solubility of salts in aqueous solutions at elevated temperatures: Jour. Research U. S. Geol. Surv., 5, (3), p. 389–395.

Potter, II, R. W., Clynn, M. A., and Brown, D. L., 1978, Freezing point depression of aqueous sodium chloride solutions: Econ. Geol., v. 73, p. 284–285.

Prinz, W. C., 1964, Diagram for determining mineral composition in the system $MnCO_3$–$CaCO_3$–$MgCO_3$: Prof. Pap. U. S. Geol. Surv., No. 501–C, p. 84–85.

Purvis, J. G., 1985, Gold potential review report: Part I. Gold potential of the Rosebery Mine: Unpub. Report to Electrolytic Zinc Company of Australasia, 55 p.

Ramboz, C., and Charef, A., 1988, Temperature, pressure, burial history, and paleohydrology of the Les Malines Pb–Zn deposits: Reconstruction from aqueous inclusions in barite: Econ. Geol., v. 83, p. 784–800.

Ravenhurst, C. E., Reynolds, P. H., Zentilli, M., and Akande, S. O., 1987, Isotopic constraints on the genesis of Zn–Pb mineralisation at Gays River, Nova Scotia, Canada: Econ. Geol., v. 82, p. 1294–1308.

Reed, M. H., 1984, Geology, wall rock alteration, and massive sulphide mineralisation in a portion of the West Shasta district, California: Econ. Geol., v. 79, p. 1299–1318.

Reid, A. M., le Roex, A. P., and Minter, W. E. L., 1988, Composition of gold grains in the Vaal Placer, Klerksdorp, South Africa: Mineral. Deposita, v. 23, p. 211–217.

Reynolds, R. C., 1965, Geochemical behaviour of boron during the metamorphism of carbonate rocks: Geochim. et Cosmochim. Acta, v. 29, p. 1101–1114.

Ringler, R. W., 1979, Sphalerite geobarometry of the Calloway Mine, Ductown, Tennessee: Econ. Geol., v. 74, p. 937–942.

Ripley, E. M., and Ohmoto, H., 1977, Mineralogic, sulphur isotope, and fluid inclusion studies of the stratabound copper deposits at the Raul Mine, Peru: Econ. Geol., v. 72, p. 1017–1041.

Robinson, B. W., and Kusakabe, M., 1975, Quantitative preparation of sulphur dioxide, for $^{34}S/^{32}S$ analyses, from sulphides by combustion with cuprous oxide: Analytical Chemistry, v. 47, No. 7, p.1179–1181.

Roedder, E., 1984, Fluid Inclusions: Reviews in Mineralogy, v. 12, Mineral. Soc. America, Washington, D. C., 644 p.

Rosasco, G. J., and Roedder, E., 1979, Application of a new Raman microprobe spectrometer to nondestructive analysis of sulphate and other ions in individual phases in fluid inclusions in minerals: Geochim. et Cosmochim. Acta, v. 43, p. 1907–1915.

Rutherford, M. J., 1963, Geothermometry of liquid inclusions in quartz, Coronation Mine, Flin Flon area, Saskatchewan: Unpub. M.Sc. thesis, Univ. Saskatchewan, Saskatoon, Canada, 40 p.

Ryall, W. R., 1979a, Mercury in the Broken Hill (NSW, Australia) lead–zinc–silver lodes: Jour. Geochem. Expl., v. 11, p. 175–194.

Ryall, W. R., 1979b, Mercury distribution in the Woodlawn massive sulphide deposit, New South Wales: Econ. Geol., v. 74, p. 1471–1484.

Ryall, W. R., 1981, The forms of mercury in some Australian stratiform Pb–Zn–Ag deposits of different regional metamorphic grades: Mineral. Deposita, v. 16, v. 425–435.

Ryan, C. G., Cousens, D. R., Heinrich, C. A., Griffin, W. L., Sie, S. H., and Mernagh, T. P., 1991 in press, Quantitative PIXE microanalysis of fluid inclusions based on a layered yield model: Nuclear Instruments and Methods in Physics Research.

Rye, D. M., and Williams, N., 1981, Studies of the base metal suphide deposits at McArthur River, Northern Territory, Australia: III. The stable isotope geochemistry of the H.Y.C., Ridge, and Cooley deposits: Econ. Geol., v. 76, p. 1–26.

Rye, R. O., and Ohmoto, H., 1974, Sulphur and carbon isotopes and ore genesis: Econ. Geol., v. 69, p. 826–842.

Sangameshwar, S. R., and Marshall, B., 1980, Sphalerite geobarometry of deformed sulphides ores from CSA mine, Cobar, Australia: Mineral. Deposita, v. 15, p. 305–314.

Sato, T., 1972, Behaviours of ore-forming solutions in seawater: Mining Geology, v. 22, p. 31–42.

Scott, S. D., 1973, Experimental calibration of the sphaletite geobarometer: Econ. Geol., v.68, p.466–474.

Scott, S. D., 1976, Application of the sphalerite geobarometer to regionally metamorphosed terrains: Am. Mineralogist, v.61, p.661–670.

Scott, S. D., 1983, Chemical behaviour of sphalerite and arsenopyrite in hydrothermal and metamorphic environment: Mineral. Mag., v. 47, p. 427–435.

Scott, S. D., and Barnes, H. L., 1971, Sphalerite geothermometry and geobaromertry: Econ. Geol., v. 66, p. 653–669.

Scott, S. D., Both, R. A., and Kissin, S. A., 1977, Sulphide petrology of the Broken Hill region, New South Wales: Econ. Geol., v. 72, p. 1410–1425.

Sears, W. P., 1971, Mercury in base metal and gold ores of the province Quebec: *in* Proceeding of the 3rd International Geochemical Exploration Symposium, Toronto, April 1970, Trans. Can. Inst. Min. Met., v. 44, p. 384–390.

Seward, T. M., 1973, Thio complexes of gold in hydrothermal ore solutions: Geochim. et Cosmochim. Acta, v. 37, p. 379–399.

Seward, T. M., 1976, The stability of chloride complexes of silver in hydrothermal ore solutions up to 350°C: Geochim. et Cosmochim. Acta, v. 48, p. 1329–1341.

Shenberger, D. M., and Barnes, H. L., 1989, Solubility of gold in aqueous sulphide solution from 150° to 350°C, Geochim. et Cosmochim. Acta, v. 53, p. 269–278.

Shelton, K. L., 1983, Composition and origin of ore-forming fluids in a carbonate-hosted porphyry copper and skarn deposit: A fluid inclusion and stable isotope study of Mines Gaspe, Quebec: Econ. Geol., v. 78, p. 387–421.

Shepherd, T., Rankin, A. H., and Alderton, D. H. M., 1985, A practical guide to fluid inclusion studies: Blackie, Glasgow, 235p.

Shikazono, N., and Kawahata, H., 1987, Compositional differences in chlorite from hydrothermally altered rocks and hydrothermal ore deposits: Canadian Mineralogist, v. 25, p. 465–474.

Shikazono, N., and Shimizu, M., 1988, Mercurian gold from the Tsugu gold–antimony vein deposits in Japan: Canadian Mineralogist, v. 26, p. 423–428.

Shimazaki, Y., 1974, Ores of Kuroko-type deposits: *in* Geology of Kuroko deposits, ed., Ishihara, S., Min. Geol. Spec. Issue, No. 6, pp. 311–322.

Shimizu, M., and Shimazaki, H., 1981, Application of the sphalerite geobarometer to some skarn-type ore deposit: Mineral. Deposita, v. 16, p. 45–50.

Sillitoe, R. H., Halls, C., and Grant, N. J., 1975, Porphyry tin deposits in Bolivia: Econ. Geol., v. 70, p. 913–927.

Slack, J. F., 1982, Tourmaline in Appalachian–Caledonian massive sulphide deposits and its exploration significance: Trans. Inst. Mining. Met., Applied Earth Sci. 91B, p. B81–B89.

Slack J. F., and Coad, P. R., 1989, Multiple hydrothermal and metamorphic events in the Kidd Creek volcanogenic massive sulphide deposit, Timmins, Ontario: evidence from tourmalines and chlorites: Can. Jour. Earth Sci., v. 26, p. 694–715.

Slack, J. F., Herriman, N., Barnes, R. G., and Plimer, I. R., 1984, Stratiform tourmalinites in metamorphic terranes and their geologic significance: Geology, v. 14, p. 713–716.

Smith, R. N., 1975, Precious and volatile metal distributions in the ores and host rocks of the Rosebery sulphide deposit, Tasmania: Unpub. M.Sc. thesis, Univ. Melbourne, 130 p.

Skinner, B. J., and Johnson, C. A., 1987, Evidence for movement of ore materials during high-grade metamorphism: *in* Mechanisms and Chemical (Re)mobilisation of Metalliferous Mineralisation, eds, Marshall, B., and Gilligan, L. B., Ore Geology Reviews, v. 2, p. 191–204.

Solomon, M., 1962, The tectonic history of Tasmania: Geol. Soc. Australia Jour., v. 9, p. 311–339.

Solomon, M., 1964, The spillite–keratophyre association of west Tasmania and the ore deposits at Mt Lyell, Rosebery and Hercules: Unpub. Ph.D. thesis, Univ. Tasmania, Hobart, 419 p.

Solomon, M., 1965, Geology and mineralisation in Tasmania *in* Geology of Australian Ore Deposits, eds., J. McAndrew and Madigan, R. T., 8th Commonwealth Mining and Metallurgical Congress, Melbourne and the Australian Institute of Mining and Metallurgy, Melbourne, p. 464–467

Solomon, M., 1976, "Volcanic" massive sulphide deposits and their host rocks–a review and explanation: in Handbook of stratabound and stratiform ore deposits: Amsterdam, Elsevier, v.6, p. 21–54.

Solomon, M., 1981, Introduction to the geology and metallic ore deposits of Tasmania: Econ. Geol., v. 76, p. 194–208.

Solomon, M., Rafter, T. A., and Jensen, M. L.,1969, Isotope studies on the Rosebery, Mount Farrell and Mount Lyell Ores, Tasmania: Mineral. Deposita, v. 4, p. 172–199.

Solomon, M., Vokes, F. M., and Walshe, J. L., 1987, Chemical remobilization of volcanic-hosted sulphide deposits at Rosebery and Mt. Lyell, Tasmania: *in* Mechanisms and Chemical (Re)mobilisation of Metalliferous Mineralisation, eds, Marshall, B., and Gilligan, L. B., Ore Geology Reviews, v. 2, p. 173–190.

Solomon, M., Eastoe, C. J., Walshe, J. L., and Green, G. R., 1988, Mineral deposits and sulphur isotope abundances in the Mt Read Volcanics between Que River and Mt Darwin, Tasmania: Econ. Geol., v. 83, p. 1307–1328.

Spry, P. G., 1979, Manganese anomalies associated with volcanic exhalative sulphide deposits: the Broken Hill example [Abstr]: Geol. Assoc. Can. – Mineral. Assoc. Can., Program with Abstract, No. 4, p. 80.

Spry, P. G., and Wonder, J. D., 1989, Manganese-rich garnet rocks associated with the Broken Hill lead–zinc–silver deposit, New South Wales: Can. Mineralogist, v. 27, p. 275–292.

Stanton, R.L., 1972. Ore petrology: McGraw–Hill Book Company, New York, 713p.

Stillwell, F.L., 1934, Observations on the lead–zinc ore at Rosebery, Tasmania: Proc. Aust. Inst. Min. Metall., No. 94, p. 43–67.

Strauss, G. K., Madel, J., and Fdez Alonso, F., 1977, Exploration practice for stratabound volcanogenic sulphide deposits in the Spanish–Portuguese pyritic belt: Geology, Geophysics and Geochemistry: *in* Time and Stratabound Ore Deposits, eds., Klemm D. D., and Schneider, H-J., Springer–Verlag, Heidelberg, p. 55–93.

Stumpfl, E. F., 1979, Manganese haloes surrounding metamorphic stratabound base metal deposits: Mineral. Deposita., v. 14, p. 207–217.

Styrt, M. M., Brackmann, A. J., Holland, H. D., Clark, B. C., Pisutha-Arnold, V., Eldridge, C. S., and Ohmoto, H., 1981, The mineralogy and isotopic composition of sulphur in hydrothermal sulphide/ sulphate deposits on the East Pacific Rise, 21° latitude: Earth Planet. Sci. Lett., v. 53, p. 382–390.

Sundblad, K., Zachrisson, E., Smeds, S.-A.,Berglund, and Alinder, C., 1984, Sphalerite geobarometry and arsenopyrite geothermometry applied to metamorphosed sulphide ores in the Swedish Caledonides: Econ. Geol., v. 79, p. 1660–1668.

Sverjensky, D. A., 1981, Isotopic alteration of carbonate host rocks as a function of water to rock ratio – An example from the Upper Mississippi Valley zinc–lead district: Econ. Geol., v. 76, p. 154–172.

Taylor, B.E., 1987, Stable isotope geochemistry of ore-forming fluids: *in* Stable Isotope Geochemistry of Low Temperature Fluids, ed., Kyser, T. K., Mineral. Assoc. Canada Short Course Vol. 13, pp. 337–452.

Taylor, B.E., and Slack, J.F., 1984, Tourmalines from Appalachian–Caledonian massive sulphide deposits; textural, chemical, and isotopic relationships: Econ. Geol., v. 79, p. 1703–1726.

Taylor, H. P. Jr., 1979, Oxygen and hydrogen isotope relationships in hydrothermal mineral deposits: *in* Geochemistry of Hydrothermal Ore Deposits, ed., Barnes, H. L., 2nd edition, John Wiley and Sons, New York, p. 236–277.

Taylor, H. P. Jr., and Epstein, S., 1962, Relationship between $^{18}O/^{16}O$ ratios in coexisting minerals of igneous and metamorphic rocks, Part I: Geol. Soc. Amer. Bull., v. 73, p. 461–480.

Throop, A. H., 1974, Exploration of the South Hercules area: Unpub. Report to Electrolytic Zinc Company of Australasia, 25p.

Touray, J. C., Beny, C., Dubessy, J., and Guilhaumou, N., 1985, Microcharacterisation of fluid inclusions in minerals by Raman microprobe: *in* Scanning Electron Microscopy, Vol. I, p. 103–118.

Urabe, T., 1974. Iron content of sphalerite coexisting with pyrite from some Kuroko deposits: Soc. Mining Geologists Japan. Spec. Issue 6, p. 377–384.

Urabe, T., and Scott, S. D., 1983, Geology and footwall alteration of the South Bay massive sulphide deposit, northwestern Ontario, Canada: Can. Jour. Earth Sci., v. 20, No. 12, p. 1862–1879.

Valley, J. W., 1986, Stable isotope geochemistry of metamorphic rocks: *in* Stable isotopes in high temperature geological processes, eds., Valley, J. W., Taylor, Jr., H. P., and O'Neil, J. R., Mineral. Soc. Amer. Reviews in Mineralogy 16, p. 445–489.

Veizer, J., and Hoefs, J., 1976, The nature of $O^{18}/O^{16}$ and $C^{13}/C^{12}$ secular trends in sedimentary carbonate rocks: Geochim. et Cosmochim. Acta, v. 40, p. 1387–1395.

Veizer, J., Holser, W. T., and Wilgus, C. K., 1980, Correlation of $^{13}C/^{12}C$ and $^{34}S/^{32}S$ secular variations: Geochim. et Cosmochim. Acta, v. 44, p. 579–587.

Walshe, J. L., 1986, A six component chlorite solid solution model and the conditions of chlorite formation in hydrothermal and geothermal systems: Econ. Geol., v. 81, p. 681–703.

Walshe, J. L., and Solomon, M., 1981, An investigation into the environment of formation of the volcanic-hosted Mt. Lyell copper deposits, using geology, mineralogy, stable isotopes, and a six-component chlorite solid solution model: Econ. Geol., v. 76, p. 246–284.

Wenner, D. B., and Taylor, H. P., Jr., 1971, Temperatures of serpentinization of ultramafic rocks based upon $^{18}O/^{16}O$ fractionation between coexisting serpentine and magnetite: Contrib. Mineral. Petrol., v. 32, p. 165–185.

Wilde, A. R., Mernagh, T. P., Bloom, M. S., and Hoffmann, C. F., 1989, Fluid inclusion evidence on the origin of some Australian unconformity-related uranium deposits: Econ. Geol., v. 84, p. 1627–1642.

Wilkins, R. W. T., 1977, Fluid inclusion assemblages of the stratiform Broken Hill ore deposits, New South Wales, Australia: Science, v. 198, v. 185–187.

Wilkins, R. W. T., 1986, The mechanism of stretching and leaking of fluid inclusions in fluorite: Econ. Geol., v. 81, p. 1003–1008.

Willan, R. C. R., and Hall, A. J., 1980, Sphalerite geobarometry and trace-element studies on stratiform sulphide from McPhun's Cairn, Loch Fyne, Argyll, Scotland: Trans. Inst. Min. Metall., London, section B, v. 89, p. B31–B41.

Williams, K.L., 1960, Some less common minerals in the Rosebery and Hercules zinc–lead ores: Proc. Aust. Inst. Min. Metall., No. 196, p. 51–60.

Williams, K. L., 1974, Compositions of sphalerites from the zoned hydrothermal lead–zinc deposits at Zeehan, Tasmania: Econ. Geol., v. 69, p. 657–672.

White, J. L., Ore, R. L., and Hultgren, R., 1957, The thermodynamic properties of silver–gold alloys: Acta Metal, v. 5, p. 747–760.

Wolf, K. H., 1987, Ubiquity and inter-dependence of (re)mobilisation system–putting the matter into full context: A brief comments: Part I: *in* Mechanisms and Chemical (Re)mobilisation of Metalliferous Mineralisation, eds, Marshall, B., and Gilligan, L. B., Ore Geology Reviews, v. 2, p. 11–20.

Wonder, J. R., Spry, P. G., and Windom, K, E., 1988, Geochemistry and origin of manganese-rich rocks related to iron-formation and sulphide deposits, western Georgia: Econ. Geol., v. 83, p. 1070–1081.

Wu, I. J., and Mahaffey, E. J., 1978, Mercury in soils geochemistry on massive sulphide deposits in Arizona: *in* Geochemical Exploration, 1978, eds., Watterson, J. R., and Theobald, P. K., Proc. 7th International Geochemical Exploration Symposium, pp. 201–208.

Xuexin, S., 1984, Minor elements and ore genesis of the Fankou lead–zinc deposit, China: Mineral. Deposita., v. 19, p. 95–104.

Yamada, R., Suyama, T., and Ogushi, O., 1987, Gold-bearing siliceous ore of the Nurukawa Kuroko deposits, Akita Prefacture, Japan: Mining Geology (Japan), v. 37, p. 109–118.

# APPENDIX

**APPENDIX 6.1. Different silicate, sulphide and oxide minerals from the F(J) lens, Rosebery Mine, western Tasmania.**

| Minerals / Sample No. | garnet | helvite | biotite | tourm-aline | chlorite | sericite | K-feld-spar | carbo-nate | fluor-ite | py | po | mag | hem | sp | cp | ga | Au |
|---|---|---|---|---|---|---|---|---|---|---|---|---|---|---|---|---|---|
| R1920-12 (100mS) | +√ | | +√ | +√ | | | | + | | + | | | | | | | |
| 81R-10 (200mS) | | | + | +√ | +√ | + | | + | | + | | | | | + | | |
| 82R-7B (200mS) | | | + | + | | + | +√ | | + | + | | + | + | | | | |
| 88R-3A (200mS) | + | | √ | | | | | | + | + | + | + | | | | | |
| 88R-4A (200mS) | +√ | | +√ | +√ | | | +√ | | + | + | + | + | | | | | |
| 88R-6 (200mS) | +√ | +√ | +√ | +√ | | | | | | + | | + | | | | | |
| R3024-2 (200mS) | | | | | + | +√ | | + | | + | | | | +√ | + | + | |
| R3024-3A (220mS) | | | +√ | +√ | +√ | | | | | + | | + | | +√ | | | |
| R3024-3C (220mS) | | | +√ | | +√ | | | | | | | | | +√ | + | | @ |
| R3023-2 (270mS) | | | +√ | | +√ | + | | | | + | + | | | +√ | + | | |
| R3023-8 (270mS) | | | +√ | +√ | + | | | + | | + | + | + | | +√ | | | |
| R3034-4 (270mS) | | | + | | + | +√ | | | | + | | | | + | + | | |
| R3034-7 (270mS) | | | + | + | | | | | | + | + | + | | + | | | @ |
| R3492-3B (280mS) | | | | | + | +√ | | | | + | | | | +√ | + | + | |
| R3492-17 (280mS) | | | +√ | +√ | | | | | | + | + | | | | | | @ |
| R3492-28 (280mS) | | | +√ | | +√ | | | | | | + | | | | | | |
| R3033-27 (300mS) | | | +√ | | | | | | | + | + | | | | | | @ |
| R3033-29 (300mS) | | | + | +√ | | | | | | + | + | | | +√ | | | |
| R1477-11 (300mS) | | | +√ | | +√ | | | | + | + | | | | | | | |
| 17L-H (300mS) | | +√ | | | | | | | | | | | | | | | |

+ = identified by microscope in this study
√ = analysed by microprobe in this study
@ = gold grain found and probed in this study (Chapter 7)

py=pyrite, po=pyrrhotite, cp=chalcopyrite, sp=sphalerite (Chapter 8)
ga=galena, hem=hematite and mag=magnetite

APPENDIX 6.2. Compositional variation of garnet from the F(J) lens, Rosebery Mine, western Tasmania.

| Sample No. | 88R-4 | 88R-4 | 88R-4 | 88R-4 | 88R-4 | 88R-4 | 88R-4 | 88R-4 | 88R-4A | 88R-4A | 88R-4A | 88R-4A |
|---|---|---|---|---|---|---|---|---|---|---|---|---|
| Grain No. | 1 | 2 | 3 | 4 | 5 | 6 | 7 | 8 | 1 | 2 | 3 | 4 |
| SiO2 | 34.52 | 35.03 | 34.52 | 35.44 | 34.64 | 34.67 | 34.27 | 33.75 | 33.87 | 33.79 | 33.26 | 34.26 |
| TiO2 | - | - | - | - | - | - | - | - | - | 0.29 | 0.22 | 0.31 |
| Al2O3 | 20.54 | 19.64 | 19.72 | 19.98 | 20.17 | 20.00 | 20.26 | 20.62 | 19.98 | 19.53 | 19.27 | 19.90 |
| FeO | 5.61 | 6.44 | 6.47 | 5.87 | 4.85 | 5.54 | 5.44 | 6.14 | 4.88 | 6.56 | 8.62 | 5.36 |
| MnO | 37.60 | 34.71 | 35.35 | 35.22 | 35.47 | 34.72 | 37.66 | 38.35 | 35.44 | 36.66 | 34.38 | 36.15 |
| MgO | - | - | 0.03 | - | 0.02 | - | - | - | - | - | 0.19 | - |
| CaO | 1.74 | 3.36 | 2.77 | 3.59 | 4.68 | 4.35 | 1.64 | 1.17 | 5.82 | 3.17 | 4.11 | 4.12 |
| Total | 100.01 | 99.18 | 98.86 | 100.10 | 99.83 | 99.28 | 99.27 | 100.03 | 99.99 | 100.00 | 100.05 | 100.10 |
| number of ions on the basis of 12 oxygen | | | | | | | | | | | | |
| Si | 2.84 | 2.90 | 2.86 | 2.90 | 2.88 | 2.85 | 2.84 | 2.80 | 2.80 | 2.81 | 2.76 | 2.83 |
| Al(IV) | 0.16 | 0.10 | 0.14 | 0.10 | 0.12 | 0.15 | 0.16 | 0.20 | 0.20 | 0.19 | 0.24 | 0.17 |
| Al(VI) | 1.83 | 1.91 | 1.79 | 1.85 | 1.86 | 1.79 | 1.72 | 1.81 | 1.75 | 1.72 | 1.64 | 1.77 |
| Ti | - | - | - | - | - | - | - | - | - | 0.02 | 0.01 | 0.02 |
| Fe(+3) | 0.17 | 0.19 | 0.21 | 0.15 | 0.14 | 0.21 | 0.28 | 0.19 | 0.25 | 0.26 | 0.35 | 0.21 |
| Fe(+2) | 0.32 | 0.26 | 0.13 | 0.26 | 0.19 | 0.19 | 0.07 | 0.19 | 0.05 | 0.15 | 0.04 | 0.12 |
| Mn | 2.62 | 2.43 | 2.49 | 2.48 | 2.50 | 2.42 | 2.64 | 2.69 | 2.49 | 2.58 | 2.42 | 2.53 |
| Mg | - | - | 0.03 | - | 0.02 | - | - | - | - | - | 0.02 | - |
| Ca | 0.15 | 0.30 | 0.25 | 0.31 | 0.41 | 0.38 | 0.15 | 0.10 | 0.52 | 0.28 | 0.37 | 0.37 |
| Sum | 8.09 | 8.09 | 7.90 | 8.05 | 8.12 | 7.99 | 7.86 | 7.98 | 8.06 | 8.01 | 7.85 | 8.02 |
| Andradite | 5.21 | 5.97 | 6.82 | 4.69 | 4.32 | 6.56 | 8.92 | 5.99 | 7.55 | 7.95 | 11.01 | 6.50 |
| Spessertine | 80.37 | 76.42 | 80.84 | 77.50 | 77.16 | 75.63 | 84.08 | 84.86 | 75.23 | 78.90 | 76.10 | 78.33 |
| Almandine | 9.82 | 8.18 | 4.22 | 8.13 | 5.86 | 5.94 | 2.23 | 5.99 | 1.51 | 4.59 | 1.26 | 3.72 |
| Grossularite | 4.60 | 9.43 | 8.12 | 9.69 | 12.65 | 11.88 | 4.78 | 3.15 | 15.71 | 8.56 | 11.64 | 11.46 |
| Spess+Alm | 90.18 | 84.59 | 85.06 | 85.63 | 83.02 | 81.56 | 86.31 | 90.85 | 76.74 | 83.49 | 77.36 | |

| Sample No. | 88R-4A | 88R-4A | 88R-6 | 88R-6 | 88R-6 | 88R-6 | 88R-6 | 88R-6 | R1920-12 | R1920-12 | R1920-12 | R1920-12 |
|---|---|---|---|---|---|---|---|---|---|---|---|---|
| Grain No. | 5 | 6 | 1 | 2 | 3 | 4 | 5 | 6 | 1 | 2 | 3 | 4 |
| SiO2 | 33.83 | 34.39 | 35.31 | 34.38 | 34.79 | 34.52 | 34.83 | 34.74 | 34.56 | 34.44 | 35.09 | 34.85 |
| TiO2 | - | - | - | 0.19 | - | - | - | - | - | - | 0.25 | - |
| Al2O3 | 20.73 | 20.58 | 19.48 | 20.26 | 20.24 | 19.91 | 19.95 | 20.03 | 19.45 | 19.56 | 19.93 | 19.36 |
| FeO | 5.76 | 5.49 | 4.99 | 5.43 | 4.67 | 4.66 | 5.10 | 4.22 | 6.08 | 7.01 | 5.56 | 7.11 |
| MnO | 38.31 | 37.14 | 34.68 | 34.32 | 34.29 | 35.01 | 35.49 | 35.23 | 35.44 | 34.20 | 35.17 | 34.08 |
| MgO | - | - | - | 0.21 | - | - | - | - | 0.26 | 0.21 | - | 0.24 |
| CaO | 1.56 | 3.06 | 5.55 | 5.11 | 6.12 | 5.89 | 4.73 | 5.93 | 2.89 | 3.08 | 3.22 | 3.01 |
| Total | 100.19 | 100.66 | 100.01 | 99.90 | 100.11 | 99.99 | 100.10 | 100.15 | 98.68 | 98.50 | 99.22 | 98.65 |
| number of ions on the basis of 12 oxygen | | | | | | | | | | | | |
| Si | 2.83 | 2.85 | 2.89 | 2.83 | 2.85 | 2.85 | 2.86 | 2.88 | 2.92 | 2.91 | 2.93 | 2.90 |
| Al(IV) | 0.17 | 0.15 | 0.11 | 0.17 | 0.15 | 0.15 | 0.14 | 0.12 | 0.08 | 0.09 | 0.07 | 0.10 |
| Al(VI) | 1.88 | 1.86 | 1.77 | 1.79 | 1.81 | 1.79 | 1.80 | 1.84 | 1.85 | 1.86 | 1.89 | 1.85 |
| Ti | - | - | - | 0.01 | - | - | - | - | - | - | 0.02 | - |
| Fe(+3) | 0.12 | 0.14 | 0.23 | 0.20 | 0.19 | 0.21 | 0.20 | 0.16 | 0.15 | 0.14 | 0.09 | 0.15 |
| Fe(+2) | 0.28 | 0.24 | 0.11 | 0.14 | 0.10 | 0.08 | 0.11 | 0.13 | 0.28 | 0.36 | 0.30 | 0.35 |
| Mn | 2.72 | 2.64 | 2.40 | 2.39 | 2.39 | 2.45 | 2.48 | 2.48 | 2.54 | 2.45 | 2.49 | 2.47 |
| Mg | - | - | - | 0.26 | - | - | - | - | 0.03 | 0.03 | - | 0.03 |
| Ca | 0.14 | 0.27 | 0.19 | 0.45 | 0.54 | 0.52 | 0.42 | 0.53 | 0.26 | 0.28 | 0.29 | 0.28 |
| Sum | 8.14 | 8.15 | 7.70 | 8.24 | 8.03 | 8.05 | 8.01 | 8.14 | 8.11 | 8.12 | 8.08 | 8.13 |
| Andradite | 3.68 | 4.26 | 7.85 | 6.29 | 5.90 | 6.44 | 6.23 | 4.85 | 4.64 | 4.33 | 2.84 | 4.62 |
| Spessertine | 83.44 | 80.24 | 81.91 | 75.16 | 74.22 | 75.15 | 77.26 | 75.15 | 78.64 | 75.85 | 78.55 | 76.00 |
| Almandine | 8.59 | 7.29 | 3.75 | 4.40 | 3.11 | 2.45 | 3.43 | 3.94 | 8.67 | 11.15 | 9.46 | 10.77 |
| Grossularite | 4.29 | 8.21 | 6.48 | 14.15 | 16.77 | 15.95 | 13.08 | 16.06 | 8.05 | 8.67 | 9.15 | 8.62 |
| Spess+Alm | 92.02 | 87.54 | 85.67 | 79.56 | 77.33 | 77.61 | 80.69 | 79.09 | 87.31 | 87.00 | 88.01 | 86.77 |

Andradite=Ca3Fe2Si3O12 Grossularite=Ca3Al2Si3O12 Spessartine=(Mn, Fe)3Al2Si3O12

Almandine=(Fe, Mn)3Al2SiO3O12

**APPENDIX 6.3. Compositional variation of helvite group minerals from the F(J) lens, Rosebery Mine, western Tasmania.**

| Sample No. | 88R-6 | 88R-6 | 88R-6 | 17L-H | 17L-H | 17L-H | 17L-H | 17L-H | 17L-H | 17L-H | 17L-H | 17L-H |
|---|---|---|---|---|---|---|---|---|---|---|---|---|
| Grain No. | 1 | 2 | 3 | 1 | 2 | 3 | 4 | 5 | 6 | 7 | 8 | 9 | 10 |
| SiO2 | 35.52 | 35.12 | 35.61 | 35.23 | 34.83 | 34.96 | 35.19 | 34.69 | 34.22 | 34.76 | 34.93 | 35.09 | 35.19 |
| Al2O3 | 0.70 | 0.48 | 0.92 | 0.33 | 0.54 | 0.37 | 0.44 | 0.25 | 0.32 | 0.17 | 0.34 | 0.36 | 0.22 |
| FeO | 19.63 | 19.98 | 19.63 | 18.97 | 21.85 | 28.72 | 18.73 | 18.33 | 26.19 | 21.37 | 16.87 | 17.27 | 20.79 |
| MnO | 26.40 | 26.86 | 27.17 | 27.43 | 24.26 | 16.17 | 28.04 | 28.54 | 18.69 | 24.67 | 30.40 | 29.67 | 25.90 |
| ZnO | 6.65 | 6.43 | 6.67 | 5.48 | 5.41 | 6.70 | 4.79 | 4.75 | 6.14 | 4.52 | 4.27 | 4.57 | 4.62 |
| S | 5.50 | 5.64 | 5.59 | 5.48 | 5.48 | 5.47 | 5.45 | 5.40 | 5.51 | 5.57 | 5.63 | 5.56 | 5.53 |
| Total | 94.40 | 94.51 | 95.59 | 92.92 | 92.37 | 92.39 | 92.64 | 91.96 | 91.07 | 91.06 | 92.44 | 92.52 | 92.25 |
| number of ions on the basis of 12 oxygen | | | | | | | | | | | | | |
| Si | 3.68 | 3.66 | 3.64 | 3.72 | 3.69 | 3.71 | 3.70 | 3.69 | 3.69 | 3.13 | 3.69 | 3.70 | 3.72 |
| Al | 0.09 | 0.06 | 0.12 | 0.04 | 0.07 | 0.05 | 0.06 | 0.03 | 0.04 | 0.02 | 0.04 | 0.05 | 0.03 |
| Fe(+2) | 1.70 | 1.74 | 1.68 | 1.68 | 1.93 | 2.55 | 1.65 | 1.63 | 2.36 | 1.92 | 1.49 | 1.52 | 1.84 |
| Mn | 2.32 | 2.37 | 2.36 | 2.45 | 2.17 | 1.45 | 2.50 | 2.57 | 1.71 | 2.24 | 2.72 | 2.65 | 2.32 |
| Zn | 0.51 | 0.49 | 0.50 | 0.37 | 0.42 | 0.52 | 0.37 | 0.37 | 0.50 | 0.36 | 0.33 | 0.36 | 0.36 |
| S | 1.07 | 1.10 | 1.07 | 0.09 | 1.09 | 1.09 | 1.08 | 1.08 | 1.11 | 1.12 | 1.12 | 1.10 | 1.10 |
| Sum | 9.37 | 9.42 | 9.37 | 8.35 | 9.37 | 9.37 | 9.36 | 9.37 | 9.41 | 8.79 | 9.39 | 9.38 | 9.37 |
| Danalite | 37.26 | 37.51 | 36.71 | 36.57 | 42.41 | 55.67 | 36.33 | 35.51 | 51.33 | 42.27 | 32.73 | 33.53 | 40.52 |
| Helvite | 50.11 | 50.42 | 50.81 | 52.87 | 47.09 | 31.34 | 54.38 | 55.29 | 36.63 | 48.79 | 58.98 | 57.60 | 50.48 |
| Genthelvite | 12.62 | 12.07 | 12.47 | 10.56 | 10.50 | 12.99 | 9.29 | 9.20 | 12.03 | 8.94 | 8.28 | 8.87 | 9.00 |

| Sample No. | 17L-H | 17L-H | 17L-H | 17L-H | 17L-H | 17L-H | 17L-H | 17L-H | 17L-H | 17L-H | 17L-H | 17L-H | 17L-H |
|---|---|---|---|---|---|---|---|---|---|---|---|---|---|
| | Zone | Zone | Zone | Zone | Zone | Zone | Zone | Zone | Zone | Zone | Zone | Zone | Zone |
| | 1 | 2 | 3 | 4 | 5 | 6 | 7 | 8 | 9 | 10 | 11 | 12 | 13 |
| SiO2 | 35.36 | 36.08 | 36.83 | 36.07 | 36.63 | 37.36 | 34.03 | 36.42 | 36.92 | 36.99 | 35.27 | 36.41 | 37.36 |
| Al2O3 | 0.58 | 0.70 | 1.27 | 0.51 | 0.99 | 1.09 | 2.40 | 0.49 | 0.83 | 1.00 | 2.11 | 0.75 | 1.02 |
| FeO | 21.76 | 20.91 | 21.33 | 19.87 | 20.35 | 19.10 | 18.10 | 20.37 | 20.21 | 19.60 | 19.64 | 13.84 | 14.52 |
| MnO | 25.16 | 25.90 | 25.20 | 27.21 | 27.55 | 29.15 | 28.97 | 28.52 | 28.05 | 29.21 | 28.23 | 35.50 | 36.21 |
| ZnO | 6.39 | 7.05 | 6.75 | 6.48 | 6.17 | 6.00 | 5.81 | 6.58 | 6.82 | 6.17 | 6.18 | 4.43 | 4.59 |
| S | 5.74 | 5.73 | 5.63 | 5.75 | 5.69 | 5.80 | 5.55 | 5.83 | 5.95 | 6.01 | 5.09 | 5.73 | 6.06 |
| Total | 94.99 | 96.37 | 97.01 | 95.89 | 97.38 | 98.50 | 94.86 | 98.21 | 98.78 | 98.98 | 96.52 | 96.66 | 99.76 |
| number of ions on the basis of 12 oxygen | | | | | | | | | | | | | |
| Si | 3.66 | 3.67 | 3.68 | 3.68 | 3.67 | 3.68 | 3.51 | 3.65 | 3.66 | 3.66 | 3.42 | 3.64 | 3.65 |
| Al | 0.07 | 0.08 | 0.15 | 0.62 | 0.12 | 0.13 | 0.29 | 0.06 | 0.10 | 0.12 | 0.26 | 0.09 | 0.12 |
| Fe(+2) | 1.88 | 1.78 | 1.78 | 1.70 | 1.70 | 1.57 | 1.56 | 1.71 | 1.68 | 1.62 | 1.74 | 1.16 | 1.19 |
| Mn | 2.21 | 2.23 | 2.13 | 2.35 | 2.34 | 2.43 | 2.53 | 2.42 | 2.36 | 2.44 | 2.54 | 3.11 | 3.00 |
| Zn | 0.49 | 0.53 | 0.50 | 0.49 | 0.46 | 0.44 | 0.44 | 0.49 | 0.50 | 0.45 | 0.48 | 0.33 | 0.33 |
| S | 1.11 | 1.09 | 1.06 | 1.10 | 1.07 | 1.07 | 1.07 | 1.09 | 1.11 | 1.10 | 1.01 | 1.07 | 1.11 |
| Sum | 9.42 | 9.38 | 9.30 | 9.94 | 9.36 | 9.32 | 9.40 | 9.42 | 9.41 | 9.39 | 9.45 | 9.40 | 9.40 |
| Danalite | 40.82 | 38.82 | 40.03 | 37.10 | 37.64 | 35.21 | 34.23 | 36.72 | 36.69 | 35.65 | 36.34 | 25.74 | 26.25 |
| Helvite | 47.20 | 48.09 | 47.30 | 50.80 | 50.95 | 53.73 | 54.78 | 51.42 | 50.93 | 53.13 | 52.23 | 66.02 | 65.46 |
| Genthelvite | 11.99 | 13.09 | 12.67 | 12.10 | 11.41 | 11.06 | 10.99 | 11.86 | 12.38 | 11.22 | 11.43 | 8.24 | 8.30 |

Danalite=Fe(+2)4Be3(SiO4)3S  Helvite=Mn(+2)4Be3(SiO4)3S
Genthelvite=Zn(+2)4Be3(SiO4)3S

APPENDIX 6.4. Compositional variation of biotite from the F(J) lens, Rosebery Mine, western Tasmania

| Sample No. | R1920-12 | R1920-12 | R1920-12 | R1920-12 | 88R-6 | 88R-6 | 88R-6 | 88R-6 |
|---|---|---|---|---|---|---|---|---|
| Grain No. | 1 | 2 | 3 | 4 | 1 | 2 | 3 | 4 |
| Section | (100mS) | (100mS) | (100mS) | (100mS) | (200mS) | (200mS) | (200mS) | (200mS) |
| SiO2 | 37.59 | 37.80 | 33.20 | 37.85 | 36.33 | 35.84 | 33.19 | 35.23 |
| TiO2 | 0.73 | 0.98 | 0.79 | 0.65 | 0.25 | 0.26 | 0.55 | 0.27 |
| Al2O3 | 16.50 | 14.78 | 17.18 | 16.15 | 15.10 | 15.40 | 16.58 | 17.12 |
| FeO | 24.82 | 25.91 | 25.66 | 22.50 | 25.52 | 25.98 | 28.38 | 27.20 |
| MnO | 1.13 | 0.69 | 0.97 | 0.84 | 1.07 | 1.11 | 1.52 | 1.29 |
| MgO | 5.73 | 5.29 | 5.33 | 5.80 | 7.53 | 6.88 | 5.94 | 6.30 |
| CaO | - | - | - | - | - | - | 0.22 | 0.15 |
| K2O | 8.85 | 8.26 | 8.76 | 8.60 | 9.00 | 8.92 | 7.48 | 8.73 |
| Cl | 0.20 | 0.15 | 0.24 | 0.14 | 0.32 | 0.42 | 0.32 | 0.29 |
| Total | 95.55 | 93.86 | 92.13 | 92.53 | 95.12 | 94.81 | 94.18 | 96.58 |
| number of ions on the basis of 22 Oxygen | | | | | | | | |
| Al IV | 2.15 | 2.00 | 2.54 | 1.97 | 2.25 | 2.28 | 2.61 | 2.47 |
| Si | 5.85 | 6.00 | 5.46 | 6.03 | 5.75 | 5.72 | 5.39 | 5.53 |
| Ti | 0.09 | 0.12 | 0.10 | 0.07 | 0.03 | 0.03 | 0.07 | 0.03 |
| Al VI | 0.88 | 0.76 | 0.79 | 1.05 | 0.51 | 0.62 | 0.57 | 0.70 |
| Al | 3.03 | 2.76 | 3.33 | 3.02 | 2.82 | 2.90 | 3.18 | 3.17 |
| Fe(+2) | 3.23 | 3.44 | 3.53 | 3.10 | 3.38 | 3.47 | 3.86 | 3.57 |
| Mn | 0.15 | 0.09 | 0.14 | 0.11 | 0.14 | 0.15 | 0.21 | 0.17 |
| Mg | 1.33 | 1.25 | 1.31 | 1.37 | 1.78 | 1.64 | 1.44 | 1.48 |
| Ca | 0.00 | - | - | - | - | - | 0.04 | 0.03 |
| K | 1.76 | 1.67 | 1.84 | 1.74 | 1.82 | 1.82 | 1.55 | 1.75 |
| Cl | 0.05 | 0.04 | 0.07 | 0.04 | 0.09 | 0.11 | 0.09 | 0.08 |
| Σ Cations | 15.49 | 15.37 | 15.78 | 15.48 | 15.75 | 15.84 | 15.83 | 15.81 |
| Mg/Mg+Fe | 0.2917 | 0.2665 | 0.2707 | 0.3065 | 0.3450 | 0.3209 | 0.2717 | 0.2931 |

| Sample No. | 88R-6 | 88R-6 | 88R-3A | 88R-3A | R3024-3A | R3024-3A | R3024-3A | R3024-3A |
|---|---|---|---|---|---|---|---|---|
| Grain No. | 5 | 6 | 1 | 2 | 1 | 2 | 3 | 4 |
| Section | (200mS) | (200mS) | (200mS) | (200mS) | (220mS) | (220mS) | (220mS) | (220mS) |
| SiO2 | 32.92 | 36.10 | 36.06 | 36.44 | 39.45 | 38.89 | 40.30 | 40.12 |
| TiO2 | 0.33 | 0.30 | 1.01 | 1.02 | 0.62 | 0.33 | 0.19 | 0.82 |
| Al2O3 | 16.72 | 17.18 | 15.61 | 15.77 | 15.66 | 15.88 | 12.81 | 17.05 |
| FeO | 28.81 | 26.40 | 25.93 | 25.99 | 20.59 | 20.15 | 18.53 | 18.14 |
| MnO | 2.88 | 1.38 | 0.84 | 0.85 | 0.70 | 0.88 | 0.81 | 0.68 |
| MgO | 5.41 | 6.15 | 5.90 | 5.96 | 10.13 | 9.77 | 12.22 | 7.96 |
| CaO | 0.30 | - | - | - | - | - | - | - |
| K2O | 6.85 | 9.22 | 8.67 | 8.76 | 7.85 | 7.18 | 7.68 | 8.33 |
| Cl | 0.25 | 0.27 | 0.20 | 0.20 | - | - | 0.12 | - |
| Total | 94.47 | 97.00 | 94.22 | 94.99 | 95.00 | 93.08 | 92.66 | 93.10 |
| number of ions on the basis of 22 Oxygen | | | | | | | | |
| Al IV | 2.64 | 2.38 | 2.27 | 2.24 | 2.03 | 1.94 | 1.81 | 1.90 |
| Si | 5.36 | 5.62 | 5.73 | 5.76 | 5.97 | 6.06 | 6.19 | 6.10 |
| Ti | 0.04 | 0.04 | 0.12 | 0.12 | 0.07 | 0.04 | 0.02 | 0.12 |
| Al VI | 0.57 | 0.77 | 0.65 | 0.67 | 0.76 | 0.84 | 0.51 | 1.15 |
| Al | 3.21 | 3.15 | 2.92 | 2.94 | 2.79 | 2.74 | 2.32 | 3.05 |
| Fe(+2) | 3.92 | 3.44 | 3.16 | 3.43 | 2.61 | 2.87 | 2.26 | 2.31 |
| Mn | 0.40 | 0.18 | 0.11 | 0.11 | 0.09 | 0.11 | 0.10 | 0.03 |
| Mg | 1.31 | 1.43 | 1.40 | 1.40 | 2.28 | 2.16 | 2.09 | 1.22 |
| Ca | 0.05 | - | - | - | - | - | - | - |
| K | 1.42 | 1.83 | 1.76 | 1.77 | 1.51 | 0.98 | 1.42 | 1.62 |
| Cl | 0.07 | 0.07 | 0.06 | 0.06 | - | - | 0.03 | - |
| Σ Cations | 15.78 | 15.76 | 15.26 | 15.56 | 15.32 | 15.00 | 14.43 | 14.45 |
| Mg/Mg+Fe | 0.2505 | 0.2936 | 0.3070 | 0.2899 | 0.4663 | 0.4294 | 0.4805 | 0.3456 |

APPENDIX 6.4. Compositional variation of biotite from the F(J) lens, Rosebery Mine, western Tasmania (Continued).

| Sample No. | R3023-8 | R3023-8 | R3023-8 | R3023-8 | R3492-17 | R3492-17 | R3492-17 | 88R-4A |
|---|---|---|---|---|---|---|---|---|
| Grain No. | 1 | 2 | 3 | 4 | 1 | 2 | 3 | 1 |
| Section | (270mS) | (270mS) | (270mS) | (270mS) | (280mS) | (280mS) | (280mS) | (200mS) |
| SiO2 | 37.71 | 36.92 | 36.89 | 36.93 | 38.85 | 37.10 | 38.19 | 34.12 |
| TiO2 | 0.21 | 0.52 | 0.43 | 0.61 | - | 0.30 | 0.21 | 1.19 |
| Al2O3 | 12.97 | 13.47 | 13.23 | 13.27 | 11.85 | 12.10 | 11.77 | 15.37 |
| FeO | 25.54 | 26.27 | 25.74 | 25.59 | 23.28 | 23.75 | 23.53 | 27.50 |
| MnO | 0.61 | 0.66 | 0.56 | 0.26 | 0.24 | 0.24 | 0.32 | 1.10 |
| MgO | 9.59 | 9.18 | 9.19 | 9.35 | 12.34 | 11.11 | 12.44 | 5.89 |
| CaO | - | - | - | - | - | - | - | - |
| K2O | 9.15 | 9.02 | 8.73 | 8.66 | 8.86 | 8.77 | 8.51 | 8.49 |
| Cl | 0.21 | 0.2 | 0.26 | 0.18 | 0.24 | 0.33 | 0.15 | 0.20 |
| Total | 95.99 | 96.24 | 95.03 | 94.85 | 95.66 | 93.70 | 95.12 | 93.86 |
| number of ions on the basis of 22 Oxygen | | | | | | | | |
| Al IV | 2.10 | 2.24 | 2.19 | 2.17 | 2.04 | 2.13 | 2.11 | 2.45 |
| Si | 5.90 | 5.76 | 5.81 | 5.83 | 5.96 | 5.87 | 5.89 | 5.55 |
| Ti | 0.02 | 0.06 | 0.05 | 0.07 | - | 0.04 | 0.02 | 0.15 |
| Al VI | 0.29 | 0.25 | 0.17 | 0.30 | 0.11 | 0.13 | 0.02 | 0.50 |
| Al | 2.39 | 2.49 | 2.46 | 2.47 | 2.15 | 2.26 | 2.13 | 2.95 |
| Fe(+2) | 3.34 | 3.44 | 3.39 | 3.38 | 2.99 | 3.14 | 3.03 | 3.74 |
| Mn | 0.08 | 0.09 | 0.07 | 0.04 | 0.03 | 0.03 | 0.04 | 0.15 |
| Mg | 2.24 | 2.15 | 2.16 | 2.20 | 2.82 | 2.62 | 2.86 | 1.43 |
| Ca | - | - | - | - | - | - | - | - |
| K | 1.83 | 1.82 | 1.76 | 1.74 | 1.74 | 1.77 | 1.64 | 1.76 |
| Cl | 0.06 | 0.05 | 0.07 | 0.05 | 0.06 | 0.09 | 0.04 | - |
| Σ Cations | 15.86 | 15.86 | 15.67 | 15.78 | 15.75 | 15.82 | 15.65 | 15.73 |
| Mg/Mg+Fe | 0.4014 | 0.3846 | 0.3892 | 0.3943 | 0.4854 | 0.4549 | 0.4856 | 0.2766 |

| Sample No. | 88R-4A | 88R-4A | R3023-2 | R3023-2 | R3023-2 | R3033-27 | R3033-27 | R3033-27 |
|---|---|---|---|---|---|---|---|---|
| Grain No. | 2 | 3 | 1.00 | 2.00 | 3.00 | 1 | 2 | 3 |
| Section | (200mS) | (200mS) | (270mS) | (270mS) | (270mS) | (300mS) | (300mS) | (300mS) |
| SiO2 | 35.47 | 33.93 | 36.09 | 39.68 | 37.46 | 37.18 | 36.99 | 36.76 |
| TiO2 | 1.03 | 0.56 | 0.93 | 0.83 | 0.86 | - | 0.31 | 0.63 |
| Al2O3 | 15.33 | 18.29 | 15.11 | 21.67 | 16.21 | 12.27 | 13.83 | 12.29 |
| FeO | 27.03 | 24.99 | 26.78 | 19.72 | 25.47 | 31.37 | 27.48 | 26.23 |
| MnO | 1.13 | 0.76 | 0.48 | - | 0.23 | 0.67 | 0.37 | 0.28 |
| MgO | 6.35 | 6.80 | 7.45 | 5.03 | 7.45 | 5.98 | 8.44 | 9.03 |
| CaO | - | - | - | - | - | - | - | - |
| K2O | 9.04 | 8.82 | 8.69 | 8.71 | 7.94 | 8.21 | 8.76 | 8.85 |
| Cl | 0.21 | 0.26 | - | - | - | 0.19 | 0.21 | 0.19 |
| Total | 95.59 | 94.41 | 95.53 | 95.64 | 95.62 | 95.87 | 96.39 | 94.26 |
| number of ions on the basis of 22 Oxygen | | | | | | | | |
| Al IV | 2.43 | 2.70 | 2.33 | 2.13 | 2.23 | 2.03 | 2.23 | 2.12 |
| Si | 5.57 | 5.30 | 5.67 | 5.87 | 5.77 | 5.97 | 5.77 | 5.88 |
| Ti | 0.12 | 0.07 | 0.11 | 0.09 | 0.10 | - | 0.04 | 0.08 |
| Al VI | 0.41 | 0.67 | 0.47 | 1.65 | 0.71 | 0.09 | 0.11 | 0.20 |
| Al | 2.84 | 3.37 | 2.80 | 3.78 | 2.94 | 2.32 | 2.54 | 2.32 |
| Fe(+2) | 2.77 | 3.27 | 3.52 | 2.44 | 3.28 | 4.21 | 3.59 | 3.51 |
| Mn | 0.15 | 0.10 | 0.06 | - | 0.03 | 0.09 | 0.05 | 0.04 |
| Mg | 1.49 | 1.58 | 1.74 | 1.11 | 1.71 | 1.43 | 1.96 | 2.15 |
| Ca | - | - | - | - | - | - | - | - |
| K | 1.81 | 1.76 | 1.74 | 1.65 | 1.56 | 1.68 | 1.74 | 1.81 |
| Cl | 0.06 | 0.06 | - | - | - | 0.05 | 0.05 | 0.05 |
| Σ Cations | 14.81 | 15.51 | 15.64 | 14.94 | 15.39 | 15.55 | 15.54 | 15.84 |
| Mg/Mg+Fe | 0.3498 | 0.3258 | 0.3308 | 0.3127 | 0.3427 | 0.2535 | 0.3532 | 0.3799 |

APPENDIX 6.4. Compositional variation of biotite from the F(J) lens, Rosebery Mine, western Tasmania (Continued).

| Sample No. | R3492-28 | R3492-28 | R3492-28 | R3492-28 | R3492-28 | R3492-28 | R3492-28 | R3024-3C |
|---|---|---|---|---|---|---|---|---|
| Grain No. | 1 | 2 | 3 | 4 | 5 | 6 | 7 | 1.00 |
| Section | (280mS) | Brown | Green | Brown | Green | Brown | Green | (220mS) |
| SiO2 | 37.23 | 39.24 | 38.74 | 38.82 | 40.50 | 37.66 | 37.96 | 40.56 |
| TiO2 | 0.51 | 0.50 | 0.35 | - | 0.49 | 0.22 | 0.61 | 0.89 |
| Al2O3 | 12.83 | 11.20 | 12.78 | 12.17 | 10.67 | 13.49 | 13.18 | 21.32 |
| FeO | 24.78 | 22.97 | 25.58 | 24.38 | 23.67 | 25.11 | 25.87 | 19.44 |
| MnO | 0.65 | 1.00 | 0.76 | 0.78 | 0.96 | 0.87 | 0.90 | 0.23 |
| MgO | 9.97 | 11.48 | 9.99 | 10.84 | 11.44 | 9.64 | 9.58 | 4.34 |
| CaO | - | - | - | - | - | - | - | 0.14 |
| K2O | 8.94 | 8.87 | 9.15 | 9.13 | 8.90 | 9.06 | 9.26 | 5.93 |
| Cl | 0.17 | 0.22 | 0.18 | 0.12 | 0.17 | 0.00 | 0.21 | - |
| Total | 95.08 | 95.48 | 97.53 | 96.24 | 96.80 | 96.05 | 97.57 | 92.85 |
| number of ions on the basis of 22 Oxygen | | | | | | | | |
| Al IV | 2.14 | 1.91 | 2.09 | 2.02 | 1.81 | 2.14 | 2.15 | 1.93 |
| Si | 5.86 | 6.09 | 5.91 | 5.98 | 6.19 | 5.86 | 5.85 | 6.07 |
| Ti | 0.06 | 0.06 | 0.04 | 0.06 | 0.06 | 0.03 | 0.07 | 0.10 |
| Al VI | 0.24 | 0.14 | 0.24 | 0.19 | 0.11 | 0.33 | 0.25 | 1.83 |
| Al | 2.38 | 2.05 | 2.33 | 2.21 | 1.92 | 2.47 | 2.40 | 3.76 |
| Fe(+2) | 3.26 | 2.98 | 3.31 | 3.13 | 3.03 | 3.27 | 3.33 | 2.43 |
| Mn | 0.09 | 0.13 | 0.10 | 0.10 | 0.12 | 0.11 | 0.12 | 0.03 |
| Mg | 2.34 | 2.65 | 2.30 | 2.49 | 2.61 | 2.24 | 2.20 | 0.97 |
| Ca | - | - | - | - | - | - | - | 0.02 |
| K | 1.80 | 1.76 | 1.80 | 1.79 | 1.74 | 1.80 | 1.82 | 1.13 |
| Cl | 0.05 | 0.06 | 0.05 | 0.03 | 0.05 | 0.05 | 0.06 | - |
| Σ Cations | 15.84 | 15.78 | 15.84 | 15.79 | 15.72 | 15.83 | 15.85 | 14.51 |
| Mg/Mg+Fe | 0.4179 | 0.4707 | 0.4100 | 0.4431 | 0.4628 | 0.4065 | 0.3978 | 0.2853 |

| Sample No. | R3024-3C | R3024-3C | R3024-3C | R3024-3C | R3024-3C | R3024-3C | R1477-11 | R1477-11 |
|---|---|---|---|---|---|---|---|---|
| Grain No. | 1-Zone-1 | 1-Zone-2 | 1-Zone-3 | 1-Zone-4 | 1-Zone-5 | 1-Zone-6 | 1 | 2 |
| Section | (220mS) | (220mS) | (220mS) | (220mS) | (220mS) | (220mS) | (300mS) | (300mS) |
| SiO2 | 36.49 | 40.15 | 44.87 | 34.04 | 40.91 | 37.59 | 42.42 | 42.03 |
| TiO2 | 0.65 | 0.72 | 1.16 | 0.47 | 1.15 | 0.93 | 0.93 | 0.84 |
| Al2O3 | 19.99 | 20.49 | 26.70 | 21.92 | 21.80 | 19.63 | 29.86 | 29.77 |
| FeO | 28.54 | 24.02 | 12.46 | 29.24 | 20.16 | 27.84 | 7.71 | 9.15 |
| MnO | 0.49 | 0.29 | - | 0.98 | 0.32 | 0.43 | 0.68 | 0.84 |
| MgO | 5.03 | 4.46 | 3.39 | 4.67 | 4.65 | 5.10 | 5.10 | 6.11 |
| CaO | 0.15 | 0.00 | 0.14 | - | - | - | 0.15 | - |
| K2O | 4.86 | 4.82 | 7.23 | 3.75 | 6.71 | 5.23 | 7.88 | 7.34 |
| Cl | - | 0.09 | - | - | 0.09 | - | - | - |
| Total | 96.20 | 95.04 | 95.95 | 95.07 | 95.79 | 96.75 | 94.73 | 96.08 |
| number of ions on the basis of 22 Oxygen | | | | | | | | |
| Al IV | 2.47 | 2.02 | 1.80 | 2.73 | 2.02 | 2.33 | 2.12 | 2.22 |
| Si | 5.53 | 5.98 | 6.20 | 5.27 | 5.98 | 5.67 | 5.88 | 5.78 |
| Ti | 0.07 | 0.08 | 0.12 | 0.06 | 0.13 | 0.11 | 0.10 | 0.09 |
| Al VI | 1.10 | 1.58 | 2.55 | 1.26 | 1.74 | 1.16 | 2.75 | 2.60 |
| Al | 3.57 | 3.60 | 4.35 | 3.99 | 3.76 | 3.49 | 4.87 | 4.82 |
| Fe(+2) | 3.62 | 2.99 | 1.44 | 3.78 | 2.47 | 3.51 | 0.89 | 1.05 |
| Mn | 0.06 | 0.04 | 0.00 | 0.13 | 0.04 | 0.05 | 0.08 | 0.10 |
| Mg | 1.14 | 0.99 | 0.70 | 1.08 | 1.01 | 1.15 | 1.05 | 1.25 |
| Ca | 0.02 | - | 0.02 | - | - | - | 0.02 | - |
| K | 0.94 | 0.92 | 1.27 | 0.74 | 1.25 | 1.01 | 1.39 | 1.29 |
| Cl | - | 0.01 | - | - | 0.02 | - | - | - |
| Σ Cations | 14.95 | 14.61 | 14.10 | 15.05 | 14.66 | 14.99 | 14.28 | 14.38 |
| Mg/Mg+Fe | 0.2395 | 0.2487 | 0.3271 | 0.2222 | 0.2902 | 0.2468 | 0.5412 | 0.5435 |

**APPENDIX 6.5. Compositional variation of tourmaline from the F(J) lens, Rosebery Mine, western Tasmania.**

| Sample | R1920-12 | R1920-12 | R1920-12 | R1920-12 | R1920-12 | 88R-6 | 88R-6 | 88R-6 |
|---|---|---|---|---|---|---|---|---|
| Grain No. | 1 | 2 | 3 | 4 | 5 | 1 | 2 | 3 |
| SiO2 | 36.22 | 37.75 | 36.98 | 35.79 | 37.11 | 34.89 | 31.15 | 33.43 |
| TiO2 | 0.74 | 0.21 | 0.35 | 0.32 | - | - | - | - |
| Al2O3 | 29.85 | 31.11 | 32.07 | 31.16 | 32.46 | 30.12 | 28.18 | 29.38 |
| FeO | 15.19 | 13.38 | 14.07 | 14.65 | 14.50 | 17.69 | 15.60 | 16.92 |
| MnO | - | - | - | - | - | 0.24 | - | 0.26 |
| MgO | 4.03 | 4.29 | 3.93 | 3.39 | 3.29 | 2.64 | 1.84 | 2.84 |
| CaO | 0.24 | - | 0.17 | 0.20 | - | 0.18 | 0.22 | 0.43 |
| Na2O | 2.77 | 2.55 | 2.62 | 2.03 | 2.10 | 2.47 | 2.43 | 2.18 |
| K2O | - | - | - | - | - | 0.17 | 0.11 | 0.11 |
| Cl | - | - | - | - | - | - | - | - |
| Total | 89.04 | 89.29 | 90.19 | 87.54 | 89.46 | 88.40 | 79.53 | 85.55 |
| number of ions on the basis of 29 Oxygen | | | | | | | | |
| Si | 7.10 | 7.26 | 7.08 | 7.08 | 7.14 | 6.99 | 6.92 | 6.92 |
| Ti | 0.11 | 0.03 | 0.05 | 0.05 | - | - | - | - |
| Al | 6.89 | 7.05 | 7.23 | 7.26 | 7.36 | 7.12 | 7.38 | 7.17 |
| Fe | 2.49 | 2.15 | 2.25 | 2.42 | 2.33 | 2.97 | 2.90 | 2.93 |
| Mn | - | - | - | - | - | 0.04 | - | 0.05 |
| Mg | 1.18 | 1.23 | 1.12 | 1.00 | 0.94 | 0.79 | 0.61 | 0.88 |
| Ca | 0.05 | - | 0.03 | 0.04 | - | 0.04 | 0.05 | 0.10 |
| Na | 1.05 | 0.95 | 0.97 | 0.78 | 0.78 | 0.96 | 1.05 | 0.88 |
| K | - | - | - | - | - | 0.04 | 0.03 | 0.03 |
| Cl | - | - | - | - | - | - | - | - |
| Sum | 18.87 | 18.66 | 18.74 | 18.63 | 18.57 | 18.95 | 18.93 | 18.94 |
| Fe/Fe+Mg | 0.679 | 0.636 | 0.668 | 0.708 | 0.712 | 0.790 | 0.826 | 0.770 |

| Sample | 88R-6 | 88R-6 | 88R-6 | 88R-6 | 88R-6 | 88R-6 | 88R-4A | 88R-4A |
|---|---|---|---|---|---|---|---|---|
| Grain No. | 4 | 5 | 6 | 7 | 8 | 9 | 1 | 2 |
| SiO2 | 35.43 | 35.23 | 33.65 | 34.50 | 35.06 | 34.83 | 34.29 | 33.97 |
| TiO2 | - | - | - | 0.32 | - | 0.18 | 0.22 | 0.44 |
| Al2O3 | 30.03 | 30.00 | 31.12 | 28.31 | 30.72 | 28.56 | 27.26 | 26.03 |
| FeO | 16.58 | 16.85 | 15.65 | 16.46 | 14.73 | 16.39 | 15.49 | 14.99 |
| MnO | - | 0.24 | 0.41 | - | 0.22 | - | 0.76 | 0.47 |
| MgO | 3.16 | 3.03 | 3.24 | 3.31 | 3.28 | 3.81 | 3.41 | 4.97 |
| CaO | 0.25 | 0.30 | 0.27 | 0.33 | 0.22 | 0.21 | 0.35 | 1.33 |
| Na2O | 2.48 | 2.94 | 2.25 | 2.56 | 2.62 | 2.51 | 2.32 | 1.94 |
| K2O | - | - | 0.19 | 0.10 | 0.15 | - | - | - |
| Cl | - | - | - | - | - | - | - | - |
| Total | 87.93 | 88.59 | 86.78 | 85.89 | 87.00 | 86.49 | 84.10 | 84.14 |
| number of ions on the basis of 29 Oxygen | | | | | | | | |
| Si | 7.08 | 7.02 | 6.82 | 7.09 | 7.03 | 7.09 | 7.18 | 7.12 |
| Ti | - | - | - | 0.05 | - | 0.03 | 0.03 | 0.07 |
| Al | 7.07 | 7.05 | 7.43 | 6.86 | 7.26 | 6.85 | 6.73 | 6.43 |
| Fe | 2.77 | 2.81 | 2.65 | 2.83 | 2.47 | 2.79 | 2.71 | 2.63 |
| Mn | - | 0.04 | 0.07 | - | 0.04 | - | 0.13 | 0.08 |
| Mg | 0.94 | 0.90 | 0.98 | 1.01 | 0.98 | 1.16 | 1.06 | 1.55 |
| Ca | 0.05 | 0.06 | 0.06 | 0.07 | 0.05 | 0.05 | 0.08 | 0.30 |
| Na | 0.96 | 1.14 | 0.88 | 1.02 | 1.02 | 0.99 | 0.94 | 0.79 |
| K | - | - | 0.05 | 0.03 | 0.04 | - | - | - |
| Cl | - | - | - | - | - | - | - | - |
| Sum | 18.87 | 19.02 | 18.94 | 18.96 | 18.87 | 18.95 | 18.89 | 18.98 |
| Fe/Fe+Mg | 0.746 | 0.757 | 0.730 | 0.736 | 0.716 | 0.707 | 0.718 | 0.629 |

**APPENDIX 6.5. Compositional variation of tourmaline from the F(J) lens, Rosebery Mine, western Tasmania (Continued).**

| Sample | 88R-4A | 88R-4A | 88R-4A | 88R-10 | 88R-10 | 88R-10 | 88R-10 | R3023-8 |
|---|---|---|---|---|---|---|---|---|
| Grain No. | 3 | 4 | 5 | 1 | 2 | 3 | 4 | 1 |
| SiO2 | 33.68 | 34.18 | 34.12 | 35.97 | 36.33 | 35.93 | 35.78 | 36.07 |
| TiO2 | 0.32 | 0.35 | 0.29 | - | - | - | - | 0.18 |
| Al2O3 | 26.41 | 27.66 | 27.82 | 33.22 | 33.40 | 33.38 | 33.06 | 28.06 |
| FeO | 16.60 | 15.13 | 14.56 | 10.73 | 9.93 | 10.26 | 10.99 | 18.03 |
| MnO | 0.72 | 0.76 | - | - | - | - | - | - |
| MgO | 3.43 | 3.37 | 4.19 | 4.66 | 4.78 | 4.60 | 4.00 | 4.05 |
| CaO | 0.22 | 0.46 | 0.41 | 0.34 | 0.33 | 0.36 | - | 0.27 |
| Na2O | 2.55 | 2.21 | 2.34 | 1.87 | 2.11 | 1.94 | 1.68 | 2.68 |
| K2O | - | 0.15 | - | - | - | - | - | - |
| Cl | - | - | - | - | - | - | - | - |
| Total | 83.93 | 84.27 | 83.73 | 86.79 | 86.88 | 86.47 | 85.51 | 89.34 |
| number of ions on the basis of 29 Oxygen | | | | | | | | |
| Si | 7.14 | 7.14 | 7.12 | 7.01 | 7.05 | 7.01 | 7.07 | 7.16 |
| Ti | 0.05 | 0.05 | 0.05 | - | - | - | - | 0.03 |
| Al | 6.60 | 6.81 | 6.84 | 7.63 | 7.63 | 7.68 | 7.70 | 6.57 |
| Fe | 2.94 | 2.64 | 2.54 | 1.75 | 1.61 | 1.67 | 1.82 | 2.99 |
| Mn | 0.13 | 0.13 | - | - | - | - | - | - |
| Mg | 1.08 | 1.05 | 1.30 | 1.35 | 1.38 | 1.34 | 1.18 | 1.20 |
| Ca | 0.05 | 0.10 | 0.09 | 0.07 | 0.07 | 0.08 | - | 0.06 |
| Na | 1.05 | 0.90 | 0.95 | 0.71 | 0.79 | 0.73 | 0.64 | 1.03 |
| K | - | 0.04 | - | - | - | - | - | - |
| Cl | - | - | - | - | - | - | - | - |
| Sum | 19.04 | 18.87 | 18.89 | 18.53 | 18.53 | 18.51 | 18.40 | 19.04 |
| Fe/Fe+Mg | 0.731 | 0.716 | 0.661 | 0.564 | 0.538 | 0.556 | 0.607 | 0.714 |

| Sample | 17L-KZ | 17L-KZ | 17L-KZ | 17L-KZ | R3033-29 | R3033-29 | R3033-29 | R3033-29 |
|---|---|---|---|---|---|---|---|---|
| Grain No. | 1 | 2 | 3 | 4 | 1 | 2 | 3 | 4 |
| SiO2 | 34.51 | 34.24 | 34.05 | 33.98 | 34.77 | 36.15 | 36.63 | 35.43 |
| TiO2 | - | 0.18 | 0.20 | 0.29 | 1.08 | 0.66 | 0.34 | 1.29 |
| Al2O3 | 27.83 | 25.88 | 26.87 | 27.34 | 25.09 | 26.08 | 26.42 | 24.59 |
| FeO | 16.31 | 17.58 | 15.91 | 15.88 | 20.50 | 21.77 | 20.77 | 21.52 |
| MnO | - | - | - | 0.29 | 0.21 | - | - | - |
| MgO | 4.20 | 4.26 | 4.77 | 4.50 | 3.36 | 3.13 | 3.11 | 3.21 |
| CaO | 0.35 | 0.41 | 0.71 | 0.75 | 0.47 | 0.29 | 0.25 | 0.22 |
| Na2O | 2.52 | 2.57 | 2.27 | 2.13 | 2.59 | 2.85 | 2.97 | 2.66 |
| K2O | - | 0.15 | - | - | - | 0.12 | - | 0.14 |
| Cl | - | - | - | - | - | - | - | - |
| Total | 85.72 | 85.27 | 84.78 | 85.16 | 88.07 | 91.05 | 90.49 | 89.06 |
| number of ions on the basis of 29 Oxygen | | | | | | | | |
| Si | 7.10 | 7.17 | 7.09 | 7.05 | 7.16 | 7.21 | 7.29 | 7.24 |
| Ti | - | 0.03 | 0.03 | 0.05 | 0.17 | 0.10 | 0.05 | 0.20 |
| Al | 6.75 | 6.38 | 6.59 | 6.68 | 6.09 | 6.13 | 6.20 | 5.92 |
| Fe | 2.81 | 3.08 | 2.77 | 2.75 | 3.53 | 3.63 | 3.46 | 3.68 |
| Mn | - | - | - | 0.05 | 0.04 | - | - | - |
| Mg | 1.29 | 1.33 | 1.48 | 1.39 | 1.03 | 0.93 | 0.92 | 0.98 |
| Ca | 0.08 | 0.09 | 0.16 | 0.17 | 0.10 | 0.06 | 0.05 | 0.05 |
| Na | 1.01 | 1.04 | 0.92 | 0.86 | 1.03 | 1.10 | 1.15 | 1.05 |
| K | - | 0.04 | - | - | - | 0.03 | - | 0.04 |
| Cl | - | - | - | - | - | - | - | - |
| Sum | 19.03 | 19.16 | 19.04 | 18.99 | 19.15 | 19.19 | 19.13 | 19.15 |
| Fe/Fe+Mg | 0.685 | 0.698 | 0.652 | 0.664 | 0.774 | 0.796 | 0.789 | 0.790 |

**APPENDIX 6.5. Compositional variation of tourmaline from the F(J) lens, Rosebery Mine, western Tasmania (Continued).**

| Sample | 3492-17 | 3492-17 | 3492-17 | 3492-17 | 3492-17 | 3492-17 | R3492-17 | 3024-3A |
|---|---|---|---|---|---|---|---|---|
| Grain No. | 1 | 2 | 3 | 4 | 5 | 6 | 7 | 1 |
| SiO2 | 34.42 | 35.05 | 32.53 | 33.98 | 34.43 | 36.62 | 34.89 | 35.53 |
| TiO2 | 0.20 | 0.28 | 0.18 | - | 0.38 | 0.39 | - | - |
| Al2O3 | 22.80 | 24.99 | 22.47 | 24.55 | 22.05 | 23.22 | 26.63 | 30.39 |
| FeO | 24.50 | 20.44 | 24.50 | 21.77 | 23.58 | 21.49 | 19.14 | 13.57 |
| MnO | - | - | - | - | - | - | - | - |
| MgO | 2.96 | 3.97 | 3.59 | 3.82 | 4.25 | 3.74 | 3.81 | 4.02 |
| CaO | 0.39 | 0.32 | 0.32 | 0.23 | 0.34 | 0.30 | 0.15 | 0.15 |
| Na2O | 2.81 | 2.63 | 2.50 | 2.54 | 2.11 | 2.61 | 2.68 | 2.10 |
| K2O | - | 0.11 | - | - | 0.69 | 0.18 | - | 0.11 |
| Cl | - | - | - | - | - | - | - | - |
| Total | 88.08 | 87.79 | 86.09 | 86.89 | 87.83 | 88.55 | 87.30 | 85.87 |
| number of ions on the basis of 29 Oxygen | | | | | | | | |
| Si | 7.26 | 7.23 | 7.06 | 7.14 | 7.27 | 7.51 | 7.16 | 7.14 |
| Ti | 0.03 | 0.04 | 0.03 | - | 0.06 | 0.06 | - | - |
| Al | 5.67 | 6.07 | 5.75 | 6.08 | 5.49 | 5.61 | 6.44 | 7.19 |
| Fe | 4.32 | 3.52 | 4.45 | 3.83 | 4.16 | 3.69 | 3.29 | 2.28 |
| Mn | - | - | - | - | - | - | - | - |
| Mg | 0.93 | 1.22 | 1.16 | 1.20 | 1.34 | 1.14 | 1.17 | 1.20 |
| Ca | 0.09 | 0.07 | 0.07 | 0.05 | 0.08 | 0.07 | 0.03 | 0.03 |
| Na | 1.15 | 1.05 | 1.05 | 1.04 | 0.86 | 1.04 | 1.07 | 0.82 |
| K | - | 0.03 | - | - | 0.19 | 0.05 | - | 0.03 |
| Cl | - | - | - | - | - | - | - | - |
| Sum | 19.45 | 19.24 | 19.57 | 19.33 | 19.45 | 19.16 | 19.15 | 18.69 |
| Fe/Fe+Mg | 0.823 | 0.743 | 0.793 | 0.762 | 0.757 | 0.763 | 0.738 | 0.654 |

| Sample | 3024-3A | 82R-7B | 82R-7B | 82R-7B | 82R-7B | 82R-7B | 82R-7B | 82R-7B |
|---|---|---|---|---|---|---|---|---|
| Grain No. | 2 | 1 | 2 | 3 | 4 | 5 | 6 | 7 |
| SiO2 | 36.19 | 35.22 | 32.38 | 31.99 | 31.35 | 34.83 | 31.12 | 36.42 |
| TiO2 | - | 0.20 | - | - | - | - | - | 0.16 |
| Al2O3 | 31.69 | 25.99 | 27.24 | 27.32 | 26.09 | 27.64 | 25.31 | 26.20 |
| FeO | 12.91 | 12.79 | 12.83 | 16.85 | 17.11 | 22.86 | 18.11 | 12.28 |
| MnO | - | - | 0.22 | - | - | - | - | - |
| MgO | 3.79 | 2.86 | 3.44 | 1.87 | 2.03 | 1.54 | 1.85 | 3.11 |
| CaO | - | 0.53 | 0.60 | 0.00 | 0.00 | 0.19 | 0.00 | 0.38 |
| Na2O | 2.03 | 1.81 | 1.92 | 2.41 | 2.35 | 2.46 | 2.35 | 1.65 |
| K2O | - | 1.63 | 0.45 | - | - | 0.14 | - | 1.99 |
| Cl | - | - | - | - | - | - | - | - |
| Total | 86.61 | 81.03 | 79.08 | 80.44 | 78.93 | 89.66 | 78.74 | 82.19 |
| number of ions on the basis of 29 Oxygen | | | | | | | | |
| Si | 7.15 | 7.57 | 7.13 | 7.06 | 7.08 | 7.08 | 7.10 | 7.68 |
| Ti | - | 0.03 | - | - | - | - | - | 0.03 |
| Al | 7.38 | 6.58 | 7.07 | 7.10 | 6.94 | 6.62 | 6.80 | 6.51 |
| Fe | 2.13 | 2.30 | 2.36 | 3.11 | 3.23 | 3.89 | 3.45 | 2.16 |
| Mn | - | - | 0.04 | - | - | - | - | - |
| Mg | 1.12 | 0.92 | 1.13 | 0.61 | 0.68 | 0.47 | 0.63 | 0.98 |
| Ca | - | 0.12 | 0.14 | - | - | 0.04 | - | 0.09 |
| Na | 0.78 | 0.75 | 0.82 | 1.03 | 1.03 | 0.97 | 1.04 | 0.67 |
| K | - | 0.45 | 0.13 | - | - | 0.04 | - | 0.54 |
| Cl | - | - | - | - | - | - | - | - |
| Sum | 18.55 | 18.71 | 18.81 | 18.91 | 18.96 | 19.11 | 19.02 | 18.65 |
| Fe/Fe+Mg | 0.657 | 0.715 | 0.677 | 0.835 | 0.825 | 0.893 | 0.846 | 0.689 |

**APPENDIX 6.6. Compositional variation of chlorite from the F(J) lens, Rosebery Mine, western Tasmania.**

| Sample No. | R3024-3A | R3024-3A | R3024-3A | R3492-28 | R3492-28 | R3023-2 | R3023-2 | R3023-2 |
|---|---|---|---|---|---|---|---|---|
| Grain No. | 1 | 2 | 2 | 1 | 2 | 1 | 2 | 3 |
| Section | (220mS) | (Core) | (Rim) | (270mS) | (270mS) | (270mS) | (270mS) | (270mS) |
| SiO2 | 24.61 | 25.51 | 25.22 | 24.00 | 24.38 | 24.14 | 24.81 | 23.82 |
| TiO2 | - | - | - | - | - | - | - | - |
| Al2O3 | 18.22 | 19.46 | 18.45 | 19.28 | 18.61 | 19.11 | 18.80 | 19.83 |
| FeO | 33.04 | 34.02 | 32.95 | 38.06 | 38.03 | 38.60 | 37.41 | 37.96 |
| MnO | 2.24 | 2.23 | 2.56 | 2.41 | 1.98 | 1.15 | 1.06 | 1.13 |
| MgO | 9.12 | 8.24 | 9.18 | 5.46 | 5.32 | 5.20 | 5.46 | 4.86 |
| CaO | - | - | - | 0.27 | 0.60 | - | - | - |
| K2O | - | - | - | - | - | 0.24 | 0.74 | - |
| Cl | - | - | - | - | - | - | - | - |
| Total | 87.23 | 89.46 | 88.36 | 89.48 | 88.92 | 88.44 | 88.28 | 87.60 |
| number of ions on the basis of 28 Oxygen | | | | | | | | |
| Al (IV) | 2.47 | 2.42 | 2.42 | 2.60 | 2.48 | 2.51 | 2.38 | 2.56 |
| Si | 5.53 | 5.58 | 5.58 | 5.40 | 5.52 | 5.49 | 5.62 | 5.44 |
| Ti | - | - | - | - | - | - | - | - |
| Al (VI) | 2.36 | 2.60 | 2.39 | 2.52 | 2.48 | 2.61 | 2.64 | 2.78 |
| Al | 4.83 | 5.02 | 4.81 | 5.12 | 4.96 | 5.12 | 5.02 | 5.34 |
| Fe(+2) | 6.21 | 6.22 | 6.10 | 7.16 | 7.20 | 7.33 | 7.08 | 7.25 |
| Mn | 0.43 | 0.41 | 0.48 | 0.46 | 0.38 | 0.22 | 0.20 | 0.22 |
| Mg | 3.06 | 2.69 | 3.03 | 1.83 | 1.80 | 1.76 | 1.84 | 1.66 |
| Ca | - | - | - | 0.07 | 0.15 | - | - | - |
| K | - | - | - | - | - | 0.07 | 0.21 | |
| Cl | - | - | - | - | - | - | - | - |
| Σ Cations | 20.06 | 19.92 | 20.00 | 20.04 | 20.01 | 19.99 | 19.97 | 19.91 |
| Fe/Fe+Mg | 0.670 | 0.698 | 0.668 | 0.796 | 0.800 | 0.806 | 0.794 | 0.814 |
| Correction | 0.469 | 0.489 | 0.468 | 0.558 | 0.560 | 0.564 | 0.556 | 0.570 |
| Temperature (1) | 280.3 | 275.0 | 275.0 | 294.2 | 281.4 | 284.6 | 270.8 | 289.9 |
| Temperature (2) | 278.5 | - | 269.5 | - | - | - | - | - |
| fO2@ | -32.7 | - | -33.5 | - | - | - | - | - |
| fH2S# | -0.8 | - | -0.8 | - | - | - | - | - |

Temperature (1) was calculated using chlorite geothermometer developed by Cathelineau and Nieva (1985). Temperature (2), fO2 and fH2S were calculated using computer programme for six components chlorite solution model of Walshe (1986) provided by Dr. Geoff Green of Tasmanian Mines Department.

**APPENDIX 6.6. Compositional variation of chlorite from the F(J) lens, Rosebery Mine, western Tasmania (Continued).**

| Sample No. | R3023-2 | R3024-3C | R3024-3C | R3024-3C | R3024-3C | R3024-3C | R3024-3C | R3024-3C |
|---|---|---|---|---|---|---|---|---|
| Grain No. | 4 | 1 | 2 | 1-Zone-1 | 1-Zone-2 | 1-Zone-3 | 1-Zone-4 | 1-Zone-5 |
| Section | (270mS) | (220mS) | (220mS) | (220mS) | (220mS) | (220mS) | (220mS) | (220mS) |
| SiO2 | 23.21 | 24.77 | 24.21 | 23.61 | 24.11 | 24.97 | 25.24 | 24.39 |
| TiO2 | - | - | - | - | - | - | - | - |
| Al2O3 | 19.78 | 18.84 | 18.49 | 19.88 | 19.83 | 19.24 | 18.52 | 18.91 |
| FeO | 38.19 | 38.99 | 38.79 | 39.61 | 39.75 | 38.41 | 38.86 | 38.99 |
| MnO | 1.22 | 1.48 | 1.28 | 1.55 | 1.47 | 1.42 | 1.43 | 1.46 |
| MgO | 4.83 | 4.99 | 4.67 | 4.58 | 4.75 | 5.16 | 5.07 | 4.93 |
| CaO | - | - | - | - | - | - | - | - |
| K2O | 0.11 | 0.34 | 0.36 | - | - | 0.32 | 0.65 | 0.21 |
| Cl | - | - | - | - | - | - | - | - |
| Total | 87.34 | 89.41 | 87.8 | 89.23 | 89.91 | 89.52 | 89.77 | 88.88 |
| number of ions on the basis of 28 Oxygen | | | | | | | | |
| Al (IV) | 2.66 | 2.42 | 2.44 | 2.65 | 2.59 | 2.41 | 2.34 | 2.47 |
| Si | 5.34 | 5.58 | 5.56 | 5.35 | 5.41 | 5.59 | 5.66 | 5.53 |
| Ti | - | - | - | - | - | - | - | - |
| Al (VI) | 2.71 | 2.57 | 2.57 | 2.66 | 2.65 | 2.66 | 2.55 | 2.58 |
| Al | 5.37 | 4.99 | 5.01 | 5.31 | 5.24 | 5.07 | 4.89 | 5.05 |
| Fe(+2) | 7.35 | 7.34 | 7.46 | 7.50 | 7.46 | 7.19 | 7.28 | 7.39 |
| Mn | 0.24 | 0.28 | 0.25 | 0.30 | 0.28 | 0.27 | 0.27 | 0.28 |
| Mg | 1.66 | 1.68 | 1.60 | 1.54 | 1.59 | 1.72 | 1.70 | 1.67 |
| Ca | - | - | - | - | - | - | - | - |
| K | 0.03 | 0.10 | 0.11 | - | - | 0.09 | 0.19 | 0.06 |
| Cl | - | - | - | - | - | - | - | - |
| Σ Cations | 19.99 | 19.97 | 19.99 | 20.00 | 19.98 | 19.93 | 19.99 | 19.98 |
| Fe/Fe+Mg | 0.816 | 0.814 | 0.823 | 0.830 | 0.824 | 0.807 | 0.811 | 0.816 |
| Correction | 0.571 | 0.570 | 0.576 | 0.581 | 0.577 | 0.565 | 0.567 | 0.571 |
| Temperature (1) | 300.5 | 275.1 | 277.2 | 299.5 | 293.1 | 274.0 | 266.6 | 280.4 |
| Temperature (2) | - | - | - | - | - | - | - | - |
| fO2@ | - | - | - | - | - | - | - | - |
| fH2S# | - | - | - | - | - | - | - | - |

Temperature (1) was calculated using chlorite geothermometer developed by Cathelineau and Nieva (1985). Temperature (2), fO2 and fH2S were calculated using computer programme for six components chlorite solution model of Walshe (1986) provided by Dr. Geoff Green of Tasmanian Mines Department.

**APPENDIX 6.6. Compositional variation of chlorite from the F(J) lens, Rosebery Mine, western Tasmania (Continued).**

| Sample No. | R1477-11 | R1477-11 | R1477-11 | R1477-11 | R1477-11 | R1477-11 | R1477-11 | R1477-11 |
|---|---|---|---|---|---|---|---|---|
| Grain No. | 1 | 2 | 3 | 4 | 5 | 6 | 7 | 8 |
| Section | (300mS) | (300mS) | (300mS) | (300mS) | (300mS) | (300mS) | (300mS) | (300mS) |
| SiO2 | 24.96 | 25.16 | 25.87 | 25.16 | 25.54 | 25.26 | 25.36 | 25.85 |
| TiO2 | 0.17 | - | - | - | - | - | - | - |
| Al2O3 | 20.46 | 20.88 | 20.51 | 20.97 | 20.84 | 21.24 | 21.96 | 21.15 |
| FeO | 20.48 | 20.53 | 19.83 | 20.32 | 20.58 | 19.79 | 21.36 | 20.47 |
| MnO | 1.97 | 1.87 | 1.84 | 1.90 | 1.82 | 2.02 | 1.98 | 2.19 |
| MgO | 17.21 | 17.16 | 17.59 | 17.52 | 17.34 | 17.16 | 14.68 | 16.59 |
| CaO | - | - | - | - | - | - | 0.16 | - |
| K2O | 0.38 | 0.22 | 0.69 | 0.35 | 0.36 | - | 0.40 | - |
| Cl | - | - | - | - | - | - | - | - |
| Total | 85.63 | 85.82 | 86.33 | 86.22 | 86.48 | 85.47 | 85.90 | 86.25 |
| number of ions on the basis of 28 Oxygen | | | | | | | | |
| Al (IV) | 2.67 | 2.64 | 2.54 | 2.68 | 2.61 | 2.64 | 2.60 | 2.54 |
| Si | 5.33 | 5.35 | 5.46 | 5.32 | 5.39 | 5.36 | 5.40 | 5.45 |
| Ti | 0.03 | - | - | - | - | - | - | - |
| Al (VI) | 2.48 | 2.59 | 2.56 | 2.55 | 2.57 | 2.67 | 2.92 | 2.72 |
| Al | 5.15 | 5.23 | 5.10 | 5.23 | 5.18 | 5.31 | 5.52 | 5.26 |
| Fe(+2) | 3.66 | 3.65 | 3.49 | 3.60 | 3.63 | 3.51 | 3.81 | 3.61 |
| Mn | 0.36 | 0.34 | 0.33 | 0.34 | 0.33 | 0.36 | 0.36 | 0.39 |
| Mg | 5.48 | 5.44 | 5.53 | 5.53 | 5.45 | 5.43 | 4.66 | 5.21 |
| Ca | - | - | - | - | - | - | 0.04 | - |
| K | 0.10 | 0.06 | 0.19 | | 0.10 | - | 0.11 | - |
| Cl | - | - | - | - | - | - | | - |
| Σ Cations | 20.11 | 20.07 | 20.10 | 20.02 | 20.08 | 19.97 | 19.90 | 19.92 |
| Fe/Fe+Mg | 0.400 | 0.402 | 0.387 | 0.394 | 0.400 | 0.393 | 0.450 | 0.409 |
| Correction | 0.280 | 0.281 | 0.271 | 0.276 | 0.280 | 0.275 | 0.315 | 0.287 |
| Temperature (1) | 301.3 | 298.1 | 287.5 | 302.4 | 294.9 | 298.1 | 293.9 | 287.5 |
| Temperature (2) | - | - | 302.5 | - | 324.5 | - | 290.5 | 298.5 |
| fO2@ | - | - | -30.8 | - | -29.1 | - | -31.7 | -31.1 |
| fH2S# | - | - | -1.3 | - | -1.2 | - | -1.3 | -1.3 |

Temperature (1) was calculated using chlorite geothermometer developed by Cathelineau and Nieva (1985). Temperature (2), fO2 and fH2S were calculated using computer programme for six components chlorite solution model of Walshe (1986) provided by Dr. Geoff Green of Tasmanian Mines Department.

**APPENDIX 6.6. Compositional variation of chlorite from the F(J) lens, Rosebery Mine, western Tasmania (Continued).**

| Sample No. | 81R-10 | 81R-10 | 81R-10 | 81R-10 | 81R-10 | 81R-10 | 81R-10 | 81R-10 |
|---|---|---|---|---|---|---|---|---|
| Grain No. | 1 | 2 | 3 | 4 | 5 | 6 | 7 | 8 |
| Section | (200mS) | (200mS) | (200mS) | (200mS) | (200mS) | (200mS) | (200mS) | (200mS) |
| SiO2 | 24.18 | 25.01 | 23.48 | 23.71 | 23.11 | 24.21 | 23.45 | 24.58 |
| TiO2 | - | - | - | - | - | - | - | - |
| Al2O3 | 23.06 | 23.05 | 22.93 | 22.45 | 22.33 | 23.10 | 22.80 | 22.21 |
| FeO | 32.55 | 31.89 | 32.40 | 31.56 | 32.25 | 31.07 | 32.34 | 30.72 |
| MnO | 1.24 | 1.30 | 1.77 | 1.59 | 1.55 | 1.52 | 1.53 | 1.35 |
| MgO | 7.92 | 7.68 | 8.94 | 8.18 | 8.53 | 8.09 | 8.31 | 7.87 |
| CaO | - | - | - | - | - | - | - | - |
| K2O | 0.15 | 0.45 | - | 0.23 | - | 0.30 | 0.18 | 0.26 |
| Cl | - | - | - | - | - | - | - | - |
| Total | 89.10 | 89.38 | 89.52 | 87.72 | 87.77 | 88.29 | 88.61 | 86.99 |
| number of ions on the basis of 28 Oxygen | | | | | | | | |
| Al (IV) | 2.76 | 2.62 | 2.92 | 2.78 | 2.89 | 2.74 | 2.87 | 2.59 |
| Si | 5.24 | 5.38 | 5.08 | 5.22 | 5.11 | 5.26 | 5.13 | 5.41 |
| Ti | - | - | - | - | - | - | - | - |
| Al (VI) | 3.13 | 3.22 | 2.93 | 3.05 | 2.93 | 3.18 | 3.01 | 3.17 |
| Al | 5.89 | 5.84 | 5.85 | 5.83 | 5.82 | 5.92 | 5.88 | 5.76 |
| Fe(+2) | 5.90 | 5.73 | 5.86 | 5.81 | 5.95 | 5.65 | 5.91 | 5.66 |
| Mn | 0.23 | 0.24 | 0.32 | 0.29 | 0.29 | 0.30 | 0.28 | 0.26 |
| Mg | 2.56 | 2.46 | 2.88 | 2.68 | 2.81 | 2.62 | 2.71 | 2.58 |
| Ca | - | - | - | - | - | - | - | - |
| K | 0.04 | 0.12 | - | 0.07 | - | 0.08 | 0.05 | 0.07 |
| Cl | - | - | - | - | - | - | - | - |
| Σ Cations | 19.86 | 19.77 | 19.99 | 19.90 | 19.98 | 19.83 | 19.96 | 19.74 |
| Fe/Fe+Mg | 0.697 | 0.700 | 0.670 | 0.684 | 0.679 | 0.683 | 0.686 | 0.687 |
| Correction | 0.488 | 0.490 | 0.469 | 0.479 | 0.475 | 0.478 | 0.480 | 0.481 |
| Temperature (1) | 311.0 | 296.2 | 328.0 | 313.2 | 324.8 | 308.9 | 322.7 | 293.0 |
| Temperature (2) | 308.5 | - | - | 313.5 | 351.5 | 302.50 | - | - |
| fO2@ | -30.3 | - | - | -30.0 | -27.3 | -30.80 | - | - |
| fH2S# | -0.8 | - | - | -0.8 | -0.5 | -0.90 | - | - |

Temperature (1) was calculated using chlorite geothermometer developed by Cathelineau and Nieva (1985). Temperature (2), fO2 and fH2S were calculated using computer programme for six components chlorite solution model of Walshe (1986) provided by Dr. Geoff Green of Tasmanian Mines Department.

**APPENDIX 6.7. Compositional variation of sericite from the F(J) lens, Rosebery Mine, western Tasmania.**

| Sample No. | R3024-2 | R3024-2 | R3024-2 | R3023-2 | R3034-4 | R3034-4 | R3034-4 | R3492-3B | R3492-3B |
|---|---|---|---|---|---|---|---|---|---|
| Grain No. | 1 | 2 | 3 | 1 | 1 | 2 | 3 | 1 | 2 |
| Section | (220mS) | (220mS) | (220mS) | (270mS) | (270mS) | (270mS) | (270mS) | (280mS) | (280mS) |
| SiO2 | 47.19 | 47.89 | 50.06 | 45.78 | 46.97 | 47.74 | 47.28 | 47.74 | 49.51 |
| TiO2 | 1.38 | 1.40 | 1.25 | 0.59 | 0.56 | 0.31 | 0.27 | 0.65 | 0.34 |
| Al2O3 | 31.90 | 32.38 | 24.50 | 27.55 | 32.66 | 33.32 | 32.48 | 31.48 | 32.69 |
| FeO | 1.48 | 1.51 | 1.81 | 5.39 | 0.35 | 0.06 | - | 2.00 | 1.48 |
| MnO | - | - | - | - | - | - | - | 1.78 | 1.81 |
| MgO | 1.76 | 1.79 | 1.77 | 2.98 | 3.89 | 3.61 | 4.11 | - | - |
| CaO | - | - | - | - | - | - | - | - | - |
| K2O | 9.79 | 9.94 | 7.74 | 9.91 | 7.75 | 6.64 | 6.45 | 10.51 | 10.82 |
| Na2O | - | - | - | - | 1.22 | 1.41 | 1.50 | - | - |
| Cl | - | - | - | - | - | - | - | - | - |
| Total | 93.50 | 94.91 | 87.13 | 92.20 | 93.40 | 93.09 | 92.09 | 94.16 | 96.65 |
| number of ions on the basis of 22 Oxygen | | | | | | | | | |
| Al (IV) | 1.63 | 1.63 | 0.84 | 1.56 | 1.73 | 1.67 | 1.66 | 1.56 | 1.53 |
| Si | 6.37 | 6.37 | 7.16 | 6.44 | 6.27 | 6.33 | 6.34 | 6.44 | 6.47 |
| Ti | 0.14 | 0.14 | 0.13 | 0.06 | 0.06 | 0.03 | 0.03 | 0.07 | 0.03 |
| Al (VI) | 3.45 | 3.45 | 3.29 | 3.01 | 3.41 | 3.54 | 3.47 | 3.44 | 3.52 |
| Al | 5.08 | 5.08 | 4.13 | 4.57 | 5.14 | 5.21 | 5.13 | 5.00 | 5.04 |
| Fe(+2) | 0.17 | 0.17 | 0.14 | 0.63 | 0.04 | 0.01 | - | 0.22 | 0.16 |
| Mn | - | - | - | - | - | - | - | - | - |
| Mg | 0.35 | 0.36 | 0.38 | 0.63 | 0.77 | 0.74 | 0.82 | 0.37 | 0.35 |
| Ca | - | - | - | - | - | - | - | - | - |
| K | 1.69 | 1.69 | 1.41 | 1.78 | 1.32 | 1.12 | 1.10 | 1.81 | 1.81 |
| Na | - | - | - | - | 0.32 | 0.36 | 0.39 | - | - |
| Cl | - | - | - | - | - | - | - | - | - |
| Σ Cations | 13.80 | 13.81 | 13.35 | 14.11 | 13.92 | 13.80 | 13.81 | 13.91 | 13.87 |

**APPENDIX 6.8. Compositional variation of K-feldspar from the F(J) lens, Rosebery Mine, western Tasmania.**

| Sample No. | 88R-4A | 88R-4A | 82R-7A | 82R-7A | 82R-7A | 82R-7A | 82R-7A | 82R-7A |
|---|---|---|---|---|---|---|---|---|
| Grain No. | 1 | 2 | 3 | 1 | 2 | 3 | 4 | 5 |
| Section | (200mS) | (200mS) | (200mS) | (200mS) | (200mS) | (200mS) | (200mS) | (200mS) |
| SiO2 | 62.48 | 61.30 | 59.06 | 64.42 | 59.54 | 60.38 | 59.68 | 63.55 |
| TiO2 | 1.21 | 2.40 | 2.00 | 0.23 | 2.55 | 0.60 | 0.55 | 0.46 |
| Al2O3 | 18.33 | 19.07 | 18.33 | 18.93 | 18.49 | 17.58 | 17.31 | 18.43 |
| FeO | 0.45 | - | 2.67 | - | - | 0.53 | 0.45 | 2.90 |
| MnO | - | - | - | - | - | - | - | - |
| MgO | - | - | 0.50 | - | - | - | - | - |
| CaO | - | - | - | 0.57 | 0.25 | - | 0.18 | - |
| K2O | 14.66 | 14.15 | 13.96 | 16.16 | 13.89 | 14.98 | 14.66 | 14.91 |
| Na2O | 0.31 | 0.25 | - | - | - | - | - | - |
| Total | 97.44 | 97.17 | 96.52* | 100.31 | 94.72* | 94.07* | 92.83* | 100.25 |
| number of ions on the basis of 8 Oxygen | | | | | | | | |
| Si | 2.95 | 2.90 | 2.86 | 2.97 | 2.89 | 2.97 | 2.97 | 2.95 |
| Ti | 0.04 | 0.09 | 0.07 | 0.01 | 0.09 | 0.02 | 0.02 | 0.02 |
| Al | 1.02 | 1.06 | 1.04 | 1.03 | 1.05 | 1.02 | 1.02 | 1.01 |
| Fe(+2) | 0.02 | - | 0.11 | - | - | 0.02 | 0.02 | 0.11 |
| Mn | - | - | - | - | - | - | - | - |
| Mg | - | - | 0.04 | - | - | - | - | - |
| Ca | - | - | - | 0.03 | 0.01 | - | 0.01 | - |
| K | 0.88 | 0.85 | 0.86 | 0.95 | 0.86 | 0.94 | 0.93 | 0.88 |
| Na | 0.03 | 0.02 | - | - | - | - | - | - |
| $\Sigma$ Cations | 4.94 | 4.92 | 4.98 | 4.99 | 4.90 | 4.97 | 4.97 | 4.97 |
| Orthoclase | 0.97 | 0.98 | 1.00 | 0.97 | 0.99 | 1.00 | 0.99 | 1.00 |
| Albite | 0.03 | 0.02 | 0.00 | 0.00 | 0.00 | 0.00 | 0.00 | 0.00 |
| Anorthite | 0.00 | 0.00 | 0.00 | 0.03 | 0.01 | 0.00 | 0.01 | 0.00 |

*Total are low due to electron beam instability but as atomic ratios are correct, the data are reliable.

**Appendix 7.1. JEOL microprobe analysis of electrum from the F(J) lens, south-end of Rosebery Mine western Tasmania.**

| Sample No/Section | No. of grains | Au wt% | Ag wt% | Total | Fineness | Grain size | Associated sulphides |
|---|---|---|---|---|---|---|---|
| R3033-27/300mS | 1 | 44.44 | 52.40 | 96.84 | 459 | 3.0µm | in pyrite |
| | 2 | 43.40 | 51.97 | 95.37 | 455 | 0.8µm | in pyrite |
| | 3 | 45.40 | 54.57 | 99.97 | 454 | 1.6µm | in pyrite |
| | 4 | 45.66 | 53.83 | 99.49 | 459 | 2.4µm | in pyrite |
| | 5 | 43.82 | 49.92 | 93.74 | 467 | 2.1µm | in pyrite |
| | 6 | 45.70 | 52.07 | 97.77 | 467 | 8.0µm | in pyrite |
| R3492-17/280mS | 1 | 47.92 | 48.57 | 96.49 | 497 | 35.0µm | in pyrrhotite |
| | 2 | 49.51 | 45.94 | 95.45 | 519 | 40.0µm | in pyrrhotite |
| | 3 | 57.20 | 41.95 | 99.15 | 577 | 43.0µm | in pyrrhotite |
| R3024-3C/220mS | 1 | 72.10 | 27.04 | 99.14 | 727 | 20.0µm | with chalcopyrite |
| | 2 | 74.49 | 24.59 | 99.08 | 752 | 60.0µm | with chalcopyrite |
| | 3 | 74.42 | 24.51 | 98.93 | 752 | 63.0µm | with chalcopyrite |
| | 4 | 71.85 | 28.59 | 100.44 | 715 | 6.0µm | with chalcopyrite |
| | 5 | 73.60 | 26.30 | 99.90 | 737 | 13.5µm | with chalcopyrite |
| | 6 | 75.21 | 24.54 | 99.75 | 754 | 40.0µm | with chalcopyrite |
| | 7 | 75.74 | 23.25 | 98.99 | 765 | 82.5µm | with chalcopyrite |
| | 8 | 75.31 | 23.49 | 98.80 | 762 | 137.5µm | with chalcopyrite |
| R3034-7/270mS | 1 | 60.18 | 37.70 | 97.88 | 615 | 10.0µm | in pyrrhotite |
| | 2 | 58.69 | 38.02 | 96.71 | 607 | 140.0µm | in pyrrhotite |
| | 3 | 50.30 | 45.43 | 95.73 | 525 | 70.0µm | in pyrrhotite |
| | 4 | 51.14 | 44.03 | 95.17 | 537 | 23.0µm | in pyrrhotite |
| | 5 | 65.75 | 33.84 | 99.59 | 660 | 25.0µm | in pyrrhotite |
| | 6 | 63.72 | 35.90 | 99.62 | 640 | 12.0µm | in pyrrhotite |
| | 7 | 63.55 | 36.22 | 99.77 | 637 | 5.0µm | in pyrrhotite |
| | 8 | 57.81 | 37.78 | 95.59 | 605 | 6.0µm | in pyrrhotite |

**Appendix 7.2. JEOL microprobe analysis across individual electrum grains from the F(J) lens, south-end of Rosebery Mine, western Tasmania.**

| Sample No. | Au wt% | Ag wt% | Total | Au/Ag ratio | Fineness |
|---|---|---|---|---|---|
| **R3034-7** | | | | | |
| Spot 1 | 52.74 | 45.79 | 98.52 | 1.15 | 535 |
| Spot 2 | 58.81 | 40.44 | 99.25 | 1.45 | 593 |
| Spot 3 | 60.04 | 38.62 | 98.66 | 1.55 | 609 |
| Spot 4 | 59.88 | 38.46 | 98.34 | 1.56 | 609 |
| Spot 5 | 61.41 | 36.47 | 97.88 | 1.68 | 627 |
| Spot 6 | 60.52 | 37.45 | 97.98 | 1.62 | 618 |
| Spot 7 | 62.51 | 36.85 | 99.36 | 1.70 | 629 |
| Spot 8 | 62.14 | 36.31 | 98.45 | 1.71 | 631 |
| Spot 9 | 62.27 | 36.20 | 98.47 | 1.72 | 632 |
| Spot 10 | 62.27 | 36.29 | 98.56 | 1.72 | 632 |
| Spot 11 | 62.93 | 36.30 | 99.23 | 1.73 | 634 |
| Spot 12 | 62.97 | 36.39 | 99.36 | 1.73 | 634 |
| Spot 13 | 62.13 | 37.15 | 99.28 | 1.67 | 626 |
| Spot 14 | 62.37 | 36.99 | 99.35 | 1.69 | 628 |
| Spot 15 | 60.11 | 38.66 | 98.77 | 1.55 | 609 |
| **R3024-3C** | | | | | |
| Spot 1 | 72.48 | 27.13 | 99.61 | 2.67 | 728 |
| Spot 2 | 74.06 | 25.09 | 99.15 | 2.95 | 747 |
| Spot 3 | 74.10 | 24.13 | 98.22 | 3.07 | 754 |
| Spot 4 | 74.21 | 23.90 | 98.10 | 3.10 | 756 |
| Spot 5 | 74.98 | 23.47 | 98.45 | 3.20 | 762 |
| Spot 6 | 75.06 | 24.15 | 99.21 | 3.11 | 757 |
| Spot 7 | 73.81 | 25.17 | 98.99 | 2.93 | 746 |
| Spot 8 | 73.33 | 25.41 | 98.74 | 2.89 | 743 |
| Spot 9 | 72.67 | 25.46 | 98.12 | 2.85 | 741 |
| Spot 10 | 73.93 | 25.50 | 99.43 | 2.90 | 744 |
| Spot 11 | 73.59 | 25.29 | 98.88 | 2.91 | 744 |
| Spot 12 | 72.89 | 25.90 | 98.78 | 2.81 | 738 |
| Spot 13 | 54.12 | 44.23 | 98.36 | 1.22 | 550 |
| Spot 14 | 58.51 | 41.38 | 99.89 | 1.41 | 586 |
| spot 15 | 57.98 | 41.00 | 98.99 | 1.41 | 586 |
| **R3492-17** | | | | | |
| Spot 1 | 40.80 | 56.53 | 97.33 | 0.72 | 419 |
| Spot 2 | 43.51 | 54.07 | 97.56 | 0.80 | 446 |
| Spot 3 | 45.13 | 52.76 | 97.89 | 0.86 | 461 |
| Spot 4 | 45.24 | 52.88 | 98.12 | 0.86 | 461 |
| Spot 5 | 48.76 | 25.11 | 99.23 | 1.94 | 660 |
| Spot 6 | 49.94 | 49.02 | 98.96 | 1.02 | 505 |
| Spot 7 | 51.71 | 47.85 | 99.56 | 1.08 | 519 |
| Spot 8 | 56.46 | 43.53 | 99.99 | 1.30 | 565 |
| Spot 9 | 57.55 | 41.44 | 98.99 | 1.39 | 581 |
| Spot 10 | 56.12 | 43.46 | 99.58 | 1.29 | 564 |
| Spot 11 | 52.58 | 45.97 | 98.55 | 1.14 | 534 |
| Spot 12 | 55.45 | 43.33 | 98.78 | 1.28 | 561 |
| Spot 13 | 48.08 | 49.24 | 97.32 | 0.98 | 494 |
| Spot 14 | 46.34 | 51.78 | 98.12 | 0.89 | 472 |
| Spot 15 | 45.97 | 52.59 | 98.56 | 0.87 | 466 |

**APPENDIX 7.3. JEOL microprobe analysis of electrum from the South Hercules and Hercules deposits, western Tasmania.**

| Sample No/ Section | No. of grains | No. of spots | Au wt% | Ag wt% | Hg wt% | Total* | Fineness | Grain size | Remark |
|---|---|---|---|---|---|---|---|---|---|
| H1117-8/ | 1 | 1 | 55.29 | 34.03 | 10.96 | 100.28 | 619 | 12x20μ | Au in py |
| @ 48.1m | | 2 | 55.87 | 33.25 | 10.91 | 100.03 | 627 | 12x20μ | Au in py |
| 5600mN | | 3 | 26.26 | 23.27 | 0.00 | 49.53 | 530 | 12x20μ | Au in py |
| South Hercules | | 4 | 32.43 | 26.34 | 3.15 | 61.92 | 552 | 12x20μ | Au in py |
| | | 5 | 54.71 | 33.66 | 10.52 | 98.89 | 619 | 12x20μ | Au in py |
| | | 6 | 55.68 | 33.00 | 10.99 | 99.67 | 628 | 12x20μ | Au in py |
| | | 7 | 55.23 | 32.20 | 10.51 | 97.94 | 632 | 12x20μ | Au in py |
| | | 8 | 55.82 | 32.77 | 10.01 | 98.60 | 630 | 12x20μ | Au in py |
| | | 9 | 56.25 | 32.24 | 10.12 | 98.61 | 636 | 12x20μ | Au in py |
| | | 10 | 55.67 | 32.90 | 11.38 | 99.95 | 629 | 12x20μ | Au in py |
| | | 11 | 55.42 | 33.09 | 11.49 | 100.00 | 626 | 12x20μ | Au in py |
| | | 12 | 55.60 | 32.89 | 11.07 | 99.56 | 628 | 12x20μ | Au in py |
| | | 13 | 55.80 | 33.18 | 11.13 | 100.11 | 627 | 12x20μ | Au in py |
| | | 14 | 55.96 | 33.26 | 10.26 | 99.48 | 627 | 12x20μ | Au in py |
| | | 15 | 55.22 | 33.16 | 11.17 | 99.55 | 625 | 12x20μ | Au in py |
| | | 16 | 55.12 | 33.93 | 10.73 | 99.78 | 619 | 12x20μ | Au in py |
| | | 17 | 53.45 | 33.93 | 9.42 | 96.80 | 612 | 12x20μ | Au in py |
| | | average | 52.34 | 32.18 | 9.64 | 94.16 | 616 | 12x20μ | Au in py |
| H1142-2/ | 1 | 1 | 49.13 | 43.88 | 16.66 | 109.67 | 528 | 50μ | Au with ga |
| @ 43.0m | | 2 | 48.54 | 45.47 | 15.30 | 109.31 | 516 | 50μ | Au with ga |
| 5600mN | | 3 | 48.94 | 45.74 | 15.44 | 110.12 | 517 | 50μ | Au with ga |
| South Hercules | | 4 | 49.76 | 44.82 | 15.49 | 110.07 | 526 | 50μ | Au with ga |
| | | 5 | 49.20 | 44.98 | 15.12 | 109.30 | 522 | 50μ | Au with ga |
| | | 6 | 49.76 | 44.38 | 14.50 | 108.64 | 529 | 50μ | Au with ga |
| | | 7 | 49.41 | 45.09 | 14.89 | 109.39 | 523 | 50μ | Au with ga |
| | | 8 | 47.97 | 45.66 | 15.75 | 109.38 | 512 | 50μ | Au with ga |
| | | 9 | 47.82 | 46.36 | 15.18 | 109.36 | 508 | 50μ | Au with ga |
| | | 10 | 49.13 | 45.08 | 14.89 | 109.10 | 521 | 50μ | Au with ga |
| | | 11 | 49.68 | 45.53 | 14.58 | 109.79 | 522 | 50μ | Au with ga |
| | | 12 | 49.33 | 44.40 | 14.51 | 108.24 | 526 | 50μ | Au with ga |
| | | average | 49.06 | 45.12 | 15.19 | 109.36 | 521 | 50μ | Au with ga |
| H1148-2 | 1 | 1 | 50.85 | 43.00 | 6.79 | 100.64 | 542 | 60x75μ | Au-ga in py |
| @89.4m | | 2 | 50.57 | 43.11 | 6.30 | 99.98 | 540 | 60x75μ | Au-ga in py |
| 5600mN | | 3 | 50.73 | 42.62 | 6.90 | 100.25 | 543 | 60x75μ | Au-ga in py |
| South Hercules | | average | 50.72 | 42.91 | 6.66 | 100.29 | 542 | 60x75μ | Au-ga in py |
| | 2 | 1 | 47.87 | 44.20 | 7.93 | 100.00 | 520 | 25x25μ | Au-ga in py |
| | | 2 | 43.55 | 50.84 | 4.95 | 99.34 | 461 | 25x25μ | Au-ga in py |
| | | 3 | 46.26 | 46.60 | 7.35 | 100.21 | 498 | 25x25μ | Au-ga in py |
| | | 4 | 41.70 | 52.80 | 4.62 | 99.12 | 441 | 25x25μ | Au-ga in py |
| | | 5 | 46.19 | 47.17 | 7.26 | 100.62 | 495 | 25x25μ | Au-ga in py |
| | | 6 | 44.94 | 49.06 | 5.84 | 99.84 | 478 | 25x25μ | Au-ga in py |
| | | average | 45.09 | 48.45 | 6.33 | 99.86 | 482 | 25x25μ | Au-ga in py |
| | 3 | 1 | 48.05 | 44.53 | 8.26 | 100.84 | 519 | 5x5μ | Au-ga in py |
| | | 2 | 46.81 | 44.89 | 8.92 | 100.62 | 510 | 5x5μ | Au-ga in py |
| | | 3 | 46.47 | 43.86 | 8.55 | 98.88 | 514 | 5x5μ | Au-ga in py |
| | | 4 | 47.31 | 43.74 | 9.42 | 100.47 | 520 | 5x5μ | Au-ga in py |
| | | average | 47.16 | 44.26 | 8.79 | 100.20 | 516 | 5x5μ | Au-ga in py |

py = pyrite sp = sphalerite ga = galena tt = tetrahedrite

*Total may be low or high due to electron beam instability but as atomic ratios are correct, the data are reliable.

**APPENDIX 7.3. JEOL microprobe analysis of electrum from the South Hercules and Hercules deposits, western Tasmania (Continued).**

| Sample No/ Section | No. of grains | No. of spots | Au wt% | Ag wt% | Hg wt% | Total* | Fineness | Grain size | Remark |
|---|---|---|---|---|---|---|---|---|---|
| H1114-4/ | 1 | 1 | 53.60 | 22.90 | 14.19 | 90.69 | 701 | 5x40μ | Au in py |
| @ 36.3m | | 2 | 56.99 | 24.01 | 16.73 | 97.73 | 704 | 5x40μ | Au in py |
| 5630mN | | 3 | 54.75 | 23.56 | 14.13 | 92.44 | 699 | 5x40μ | Au in py |
| South Hercules | | 4 | 53.04 | 23.06 | 13.59 | 89.69 | 697 | 5x40μ | Au in py |
| | | average | 54.60 | 23.38 | 14.66 | 92.64 | 700 | 5x40μ | Au in py |
| | 2 | 1 | 79.69 | 19.73 | 9.03 | 108.45 | 802 | 14x25μ | Au in py |
| | | 2 | 79.42 | 19.06 | 8.76 | 107.24 | 806 | 14x25μ | Au in py |
| | | 3 | 74.22 | 17.81 | 8.19 | 100.22 | 806 | 14x25μ | Au in py |
| | | average | 77.78 | 18.87 | 8.66 | 105.30 | 805 | 14x25μ | Au in py |
| | 3 | 1 | 48.65 | 14.25 | 0.00 | 62.90 | 773 | 10x20μ | Au in py |
| | | 2 | 38.83 | 12.17 | 0.00 | 51.00 | 761 | 10x20μ | Au in py |
| | | 3 | 56.03 | 14.84 | 3.36 | 74.23 | 791 | 10x20μ | Au in py |
| | | 4 | 60.21 | 16.49 | 6.34 | 83.04 | 785 | 10x20μ | Au in py |
| | | average | 50.93 | 14.44 | 2.43 | 67.79 | 778 | 10x20μ | Au in py |
| | 4 | 1 | 47.51 | 7.39 | 0.00 | 54.90 | 865 | 8x23μ | Au in py |
| | | 2 | 39.52 | 7.40 | 0.00 | 46.92 | 842 | 8x23μ | Au in py |
| | | 3 | 77.88 | 10.75 | 0.00 | 88.63 | 879 | 8x23μ | Au in py |
| | | 4 | 73.79 | 10.54 | 1.88 | 86.21 | 875 | 8x23μ | Au in py |
| | | 5 | 51.26 | 7.47 | 0.00 | 58.73 | 873 | 8x23μ | Au in py |
| | | 6 | 76.94 | 10.92 | 0.00 | 87.86 | 876 | 8x23μ | Au in py |
| | | 7 | 81.96 | 10.68 | 0.00 | 92.64 | 885 | 8x23μ | Au in py |
| | | average | 64.12 | 9.31 | 0.27 | 73.70 | 871 | 8x23μ | Au in py |
| | 5 | 1 | 64.75 | 20.34 | 17.24 | 102.33 | 761 | 27x35μ | Au with cp |
| | | 2 | 66.09 | 20.17 | 19.20 | 105.46 | 766 | 27x35μ | Au with cp |
| | | 3 | 62.35 | 19.54 | 18.11 | 100.00 | 761 | 27x35μ | Au with cp |
| | | average | 64.40 | 20.02 | 18.18 | 102.60 | 763 | 27x35μ | Au with cp |
| H1114-5/ | 1 | 1 | 76.65 | 5.18 | 0.00 | 81.83 | 937 | 10x35μ | Au in py |
| @ 36.6m | | 2 | 87.03 | 5.55 | 2.19 | 94.77 | 940 | 10x35μ | Au in py |
| 5630mN | | 3 | 88.22 | 5.42 | 3.05 | 96.69 | 942 | 10x35μ | Au in py |
| South Hercules | | 4 | 86.31 | 5.19 | 2.63 | 94.13 | 943 | 10x35μ | Au in py |
| | | 5 | 71.27 | 4.74 | 0.00 | 76.01 | 938 | 10x35μ | Au in py |
| | | average | 81.90 | 5.22 | 1.57 | 88.69 | 940 | 10x35μ | Au in py |
| | 2 | 1 | 67.67 | 3.75 | 1.63 | 73.05 | 947 | 5x10μ | Au in py |
| | | 2 | 72.38 | 4.40 | 1.90 | 78.68 | 943 | 5x10μ | Au in py |
| | | 3 | 52.35 | 3.27 | 0.00 | 55.62 | 941 | 5x10μ | Au in py |
| | | 4 | 78.94 | 4.39 | 1.71 | 85.04 | 947 | 5x10μ | Au in py |
| | | 5 | 66.60 | 3.95 | 0.00 | 70.55 | 944 | 5x10μ | Au in py |
| | | average | 67.59 | 3.95 | 1.05 | 72.59 | 945 | 5x10μ | Au in py |
| | 3 | 1 | 65.36 | 26.48 | 4.40 | 96.24 | 712 | 10x45μ | Au in py |
| | | 2 | 63.11 | 24.51 | 5.28 | 92.90 | 720 | 10x45μ | Au in py |
| | | 3 | 71.61 | 27.12 | 6.80 | 105.53 | 725 | 10x45μ | Au in py |
| | | average | 66.69 | 26.04 | 5.49 | 98.22 | 719 | 10x45μ | Au in py |

py = pyrite sp = sphalerite ga = galena tt = tetrahedrite

*Total may be low or high due to electron beam instability but as atomic ratios are correct, the data are reliable.

**APPENDIX 7.3. JEOL microprobe analysis of electrum from the South Hercules and Hercules deposits, western Tasmania (Continued).**

| Sample No/ Section | No. of grains | No. of spots | Au wt% | Ag wt% | Hg wt% | Total* | Fineness | Grain size | Remark |
|---|---|---|---|---|---|---|---|---|---|
| H1114-5/ | 4 | 1 | 67.05 | 22.89 | 8.19 | 98.13 | 745 | 15x35µ | Au in py |
| @ 36.6m | | 2 | 72.41 | 24.44 | 8.50 | 105.35 | 748 | 15x35µ | Au in py |
| 5630mN | | 3 | 65.57 | 22.35 | 6.95 | 94.87 | 746 | 15x35µ | Au in py |
| South Hercules | | average | 68.34 | 23.23 | 7.88 | 99.45 | 746 | 15x35µ | Au in py |
| | 5 | 1 | 51.68 | 21.96 | 10.98 | 84.62 | 702 | 10x15µ | Au in py |
| | | 2 | 50.06 | 21.65 | 11.84 | 83.55 | 698 | 10x15µ | Au in py |
| | | average | 50.87 | 21.81 | 11.41 | 84.09 | 700 | 10x15µ | Au in py |
| | 6 | 1 | 41.47 | 25.86 | 15.01 | 82.34 | 616 | 5x5µ | Au in py |
| | 7 | 1 | 72.97 | 2.61 | 4.58 | 80.16 | 965 | 3x3µ | Au in py |
| | 8 | 1 | 55.80 | 31.53 | 0.00 | 87.33 | 639 | 3x8µ | Au in py |
| | 9 | 1 | 52.16 | 20.87 | 13.75 | 86.78 | 714 | 10x15µ | Au in py |
| H1118-13/ | 1 | 1 | 61.24 | 30.46 | 6.99 | 98.69 | 668 | 90x120µ | Au in sp |
| 29.9m | | 2 | 60.95 | 30.78 | 7.59 | 99.32 | 664 | 90x120µ | Au in sp |
| 5630mN | | 3 | 61.30 | 30.92 | 7.72 | 99.93 | 665 | 90x120µ | Au in sp |
| South Hercules | | 4 | 61.88 | 31.59 | 6.74 | 100.21 | 662 | 90x120µ | Au in sp, |
| | | average | 61.34 | 30.94 | 7.26 | 99.54 | 665 | 90x120µ | Au in sp. |
| | 2 | 1 | 63.45 | 30.46 | 6.89 | 100.80 | 676 | 15x15µ | Au in sp |
| | | 2 | 59.50 | 29.21 | 6.58 | 95.29 | 671 | 15x15µ | Au in sp |
| | | 3 | 62.54 | 29.92 | 62.54 | 6.36 | 676 | 15x15µ | Au in sp |
| | | average | 61.83 | 29.86 | 25.34 | 67.48 | 674 | 15x15µ | Au in sp |
| | 3 | 1 | 60.22 | 31.38 | 8.70 | 100.30 | 657 | 96x150µ | Au in sp |
| | | 2 | 60.44 | 31.55 | 7.77 | 99.76 | 657 | 96x150µ | Au in sp |
| | | 3 | 59.38 | 31.23 | 9.15 | 99.77 | 655 | 96x150µ | Au in sp |
| | | 4 | 59.98 | 31.65 | 7.98 | 99.61 | 655 | 96x150µ | Au in sp |
| | | average | 60.01 | 31.45 | 8.40 | 99.86 | 656 | 96x150µ | Au in sp |
| | 4-A | 1 | 42.57 | 38.06 | 19.77 | 100.40 | 528 | 10x25µ | Au in sp crack |
| | | 2 | 42.09 | 37.77 | 20.65 | 100.51 | 527 | 10x25µ | Au in sp crack |
| | | 3 | 42.10 | 37.81 | 18.80 | 98.71 | 527 | 10x25µ | Au in sp crack |
| | | average | 42.25 | 37.88 | 19.74 | 99.87 | 527 | 10x25µ | Au in sp crack |
| | 4B | 1 | 56.27 | 35.98 | 7.50 | 99.75 | 610 | 25x50µ | Au in sp crack |
| | | 2 | 56.35 | 35.93 | 7.85 | 100.13 | 611 | 25x50µ | Au in sp crack |
| | | 3 | 49.08 | 35.73 | 14.44 | 99.25 | 579 | 25x50µ | Au in sp crack |
| | | 4 | 55.99 | 34.80 | 8.47 | 99.26 | 617 | 25x50µ | Au in sp crack |
| | | average | 54.42 | 35.61 | 9.57 | 99.60 | 604 | 25x50µ | Au in sp crack |
| | 4C | 1 | 38.46 | 37.62 | 23.67 | 99.75 | 506 | 10x12µ | Au in sp crack |
| | | 2 | 39.36 | 38.18 | 23.31 | 100.85 | 508 | 10x12µ | Au in sp crack |
| | | average | 38.91 | 38.18 | 23.31 | 100.40 | 505 | 10x12µ | Au in sp crack |
| | 4D | 1 | 39.69 | 37.44 | 22.04 | 99.17 | 515 | 10x10µ | Au in sp crack |
| | | 2 | 39.46 | 37.82 | 21.60 | 98.88 | 511 | 10x10µ | Au in sp crack |
| | | average | 39.58 | 37.63 | 21.82 | 99.03 | 513 | 10x10µ | Au in sp crack |

py = pyrite sp = sphalerite ga = galena tt = tetrahedrite

*Total may be low or high due to electron beam instability but as atomic ratios are correct, the data are reliable.

**APPENDIX 7.3. JEOL microprobe analysis of electrum from the South Hercules and Hercules deposits, western Tasmania (Continued).**

| Sample No/ Section | No. of grains | No. of spots | Au wt% | Ag wt% | Hg wt% | Total* | Fineness | Grain size | Remark |
|---|---|---|---|---|---|---|---|---|---|
| H1118-13/ | 4E | 1 | 34.92 | 38.76 | 25.89 | 99.57 | 474 | 9.5x20μ | Au in sp crack |
| 29.9m | | 2 | 36.41 | 38.76 | 24.61 | 99.78 | 484 | 9.5x20μ | Au in sp crack |
| 5630mN | | 3 | 36.02 | 38.68 | 25.61 | 100.31 | 482 | 9.5x20μ | Au in sp crack |
| South Hercules | | average | 36.22 | 38.72 | 25.11 | 100.05 | 483 | 9.5x20μ | Au in sp crack |
| | 4F | 1 | 40.61 | 36.88 | 17.87 | 95.36 | 524 | 10x30μ | Au in sp crack |
| | | 2 | 41.59 | 36.38 | 18.97 | 96.94 | 533 | 10x30μ | Au in sp crack |
| | | average | 41.10 | 36.63 | 18.42 | 96.15 | 529 | 10x30μ | Au in sp crack |
| | 4G | 1 | 40.82 | 35.95 | 18.50 | 95.27 | 532 | 10.5x19.8μ | Au in sp crack |
| | | 2 | 40.35 | 36.02 | 19.10 | 95.47 | 528 | 10.5x19.8μ | Au in sp crack |
| | | average | 40.59 | 35.99 | 18.80 | 95.37 | 530 | 10.5x19.8μ | Au in sp crack |
| | 5 | 1 | 58.43 | 31.00 | 8.83 | 98.26 | 653 | 180x180μ | Au in sp |
| | | 2 | 56.47 | 35.35 | 4.86 | 96.68 | 615 | 180x180μ | Au in sp |
| | | 3 | 58.03 | 30.98 | 8.33 | 97.34 | 652 | 180x180μ | Au in sp |
| | | 4 | 57.38 | 30.44 | 8.44 | 96.26 | 653 | 180x180μ | Au in sp |
| | | 5 | 57.91 | 30.43 | 8.50 | 96.84 | 656 | 180x180μ | Au in sp |
| | | average | 57.64 | 31.64 | 7.79 | 97.08 | 646 | 180x180μ | Au in sp |
| | 6 | 1 | 60.48 | 30.89 | 8.28 | 99.65 | 662 | 93x150μ | Au in sp |
| | | 2 | 59.89 | 31.10 | 8.24 | 99.23 | 658 | 93x150μ | Au in sp |
| | | 3 | 60.58 | 31.34 | 7.91 | 99.83 | 659 | 93x150μ | Au in sp |
| | | average | 60.24 | 31.22 | 8.08 | 99.53 | 659 | 93x150μ | Au in sp |
| | 7 | 1 | 41.18 | 41.99 | 13.14 | 96.31 | 495 | 5x10μ | Au in sp |
| | | 2 | 40.26 | 41.47 | 13.94 | 95.67 | 493 | 5x10μ | Au in sp |
| | | average | 40.72 | 41.73 | 13.54 | 95.99 | 494 | 5x10μ | Au in sp |
| | 8 | 1 | 79.37 | 10.7 | 6.15 | 96.22 | 881 | 12x14μ | Au in sp |
| | | 2 | 81.88 | 11.55 | 1.82 | 95.25 | 876 | 12x14μ | Au in sp |
| | | 3 | 81.13 | 10.79 | 4.82 | 96.74 | 883 | 12x14μ | Au in sp |
| | | average | 81.51 | 11.17 | 3.32 | 95.99 | 879 | 12x14μ | Au in sp |
| | 9 | 1 | 63.52 | 29.85 | 4.95 | 98.32 | 680 | 20x20μ | Au in sp |
| | | 2 | 63.68 | 30.47 | 3.71 | 97.86 | 676 | 20x20μ | Au in sp |
| | | average | 63.60 | 30.16 | 4.33 | 98.09 | 678 | 20x20μ | Au in sp |
| | 10 | 1 | 63.02 | 30.46 | 2.21 | 95.69 | 674 | 25x30μ | Au in sp |
| | | 2 | 62.72 | 29.08 | 4.48 | 96.28 | 683 | 25x30μ | Au in sp |
| | | average | 62.87 | 29.77 | 3.35 | 95.99 | 679 | 25x30μ | Au in sp |
| | 11 | 1 | 32.93 | 44.19 | 18.64 | 95.76 | 427 | 45x45μ | Au-ga in sp |
| | | 2 | 32.78 | 43.77 | 19.71 | 96.26 | 428 | 45x45μ | Au-ga in sp |
| | | average | 32.86 | 43.98 | 19.18 | 96.01 | 428 | 45x45μ | Au-ga in sp |
| | 12 | 1 | 64.61 | 30.86 | 3.71 | 99.18 | 677 | 60x210μ | Au-ga in sp |
| | | 2 | 64.02 | 30.82 | 4.41 | 99.25 | 675 | 60x210μ | Au-ga in sp |
| | | average | 64.32 | 30.84 | 4.06 | 99.22 | 676 | 60x210μ | Au-ga in sp |

py = pyrite sp = sphalerite ga = galena tt = tetrahedrite

*Total may be low or high due to electron beam instability but as atomic ratios are correct, the data are reliable.

**APPENDIX 7.3. JEOL microprobe analysis of electrum from the South Hercules and Hercules deposits, western Tasmania (Continued).**

| Sample No/ Section | No. of grains | No. of spots | Au wt% | Ag wt% | Hg wt% | Total* | Fineness | Grain size | Remark |
|---|---|---|---|---|---|---|---|---|---|
| H1145-2A | 1 | 1 | 69.22 | 23.82 | 7.29 | 100.33 | 744 | 21x32μ | Au with ga |
| @ 61.3m | | 2 | 50.93 | 38.88 | 10.18 | 99.99 | 567 | 21x32μ | Au with ga |
| 5670mN | | 3 | 46.85 | 34.53 | 19.60 | 100.98 | 576 | 21x32μ | Au with ga |
| South Hercules | | 4 | 69.36 | 24.38 | 7.22 | 100.96 | 740 | 21x32μ | Au with ga |
| | | 5 | 50.76 | 33.52 | 16.39 | 100.67 | 602 | 21x32μ | Au with ga |
| | | 6 | 70.74 | 24.08 | 5.40 | 100.22 | 746 | 21x32μ | Au with ga |
| | | average | 357.86 | 179.21 | 66.08 | 100.56 | 666 | 21x32μ | Au with ga |
| H1145-2B | 1 | 1 | 49.22 | 39.88 | 27.48 | 116.58 | 552 | 14x25μ | Au with tt |
| @ 61.3m | | 2 | 31.94 | 31.11 | 14.75 | 77.80 | 507 | 14x25μ | Au with tt |
| 5670mN | | 3 | 49.86 | 37.53 | 23.78 | 111.17 | 571 | 14x25μ | Au with tt |
| South Hercules | | 4 | 45.68 | 36.64 | 25.64 | 107.96 | 555 | 14x25μ | Au with tt |
| | | 5 | 47.50 | 39.12 | 25.66 | 112.28 | 548 | 14x25μ | Au with tt |
| | | average | 44.84 | 36.86 | 23.46 | 105.16 | 547 | 14x25μ | Au with tt |
| | 2 | 1 | 46.30 | 38.42 | 27.16 | 111.88 | 547 | 14x30μ | Au with tt |
| | | 2 | 35.51 | 38.55 | 25.00 | 99.06 | 479 | 14x30μ | Au with tt |
| | | average | 40.91 | 38.49 | 26.08 | 105.47 | 513 | 14x30μ | Au with tt |
| | 3 | 1 | 49.86 | 32.70 | 14.39 | 96.95 | 604 | 5x5μ | Au with tt |
| | | 2 | 35.34 | 31.88 | 17.37 | 84.59 | 526 | 5x5μ | Au with tt |
| | | average | 42.60 | 32.29 | 15.88 | 90.77 | 565 | 5x5μ | Au with tt |
| H1129-2 | 1 | 1 | 51.14 | 34.62 | 3.00 | 88.76 | 596 | 10x10μ | Au in py |
| @ 79.8m | | 2 | 56.92 | 38.84 | 2.24 | 98.00 | 594 | 10x10μ | Au in py |
| 5720mN | | 3 | 56.79 | 38.07 | 2.86 | 97.72 | 599 | 10x10μ | Au in py |
| South Hercules | | average | 54.95 | 37.18 | 2.70 | 94.83 | 596 | 10x10μ | Au in py |
| | 2 | 1 | 67.63 | 31.44 | 2.39 | 101.46 | 683 | 10x20μ | Au in py |
| | | 2 | 63.02 | 28.87 | 3.14 | 95.03 | 686 | 10x20μ | Au in py |
| | | average | 65.33 | 30.16 | 2.77 | 98.25 | 684 | 10x20μ | Au in py |
| H145@227' | 1 | 1 | 60.03 | 39.84 | 2.81 | 102.68 | 601 | 20x20μ | Au in ga |
| R lens | | 2 | 44.47 | 35.96 | 0.00 | 80.43 | 553 | 20x20μ | Au in ga |
| Hercules | | 3 | 62.39 | 40.08 | 1.51 | 103.98 | 609 | 20x20μ | Au in ga |
| | | 4 | 57.35 | 35.35 | 1.03 | 93.73 | 619 | 20x20μ | Au in ga |
| | | 5 | 53.53 | 39.06 | 0.00 | 92.59 | 578 | 20x20μ | Au in ga |
| | | average | 55.55 | 38.06 | 1.07 | 94.68 | 592 | 20x20μ | Au in ga |
| | 2 | 1 | 63.58 | 37.56 | 0.00 | 101.14 | 629 | 10μx16μ | Au in ga |
| | | 2 | 64.06 | 37.70 | 0.00 | 101.76 | 630 | 10μx16μ | Au in ga |
| | | 3 | 50.57 | 37.48 | 0.00 | 88.05 | 574 | 10μx16μ | Au in ga |
| | | 4 | 64.01 | 37.47 | 0.26 | 101.74 | 631 | 10μx16μ | Au in ga |
| | | 5 | 64.27 | 37.81 | 0.10 | 102.18 | 630 | 10μx16μ | Au in ga |
| | | 6 | 64.61 | 37.78 | 0.21 | 102.60 | 631 | 10μx16μ | Au in ga |
| | | average | 61.85 | 37.63 | 0.10 | 99.58 | 621 | 10μx16μ | Au in ga |

py = pyrite sp = sphalerite ga = galena tt = tetrahedrite

*Total may be low or high due to electron beam instability but as atomic ratios are correct, the data are reliable.

**APPENDIX 7.3. JEOL microprobe analysis of electrum from the South Hercules and Hercules deposits, western Tasmania (Continued).**

| Sample No/ Section | No. of grains | No. of spots | Au wt% | Ag wt% | Hg wt% | Total* | Fineness | Grain size | Remark |
|---|---|---|---|---|---|---|---|---|---|
| H831-8 | 1 | 1 | 59.74 | 42.17 | 0.58 | 102.49 | 586 | 45µx25µ | Au in galena |
| R lens | | 2 | 59.72 | 42.00 | 0.88 | 102.60 | 587 | 45µx25µ | Au in galena |
| Hercules | | 3 | 59.92 | 41.94 | 1.00 | 102.86 | 588 | 45µx25µ | Au in galena |
| | | 4 | 53.41 | 40.97 | 0.78 | 95.16 | 566 | 45µx25µ | Au in galena |
| | | 5 | 60.49 | 41.42 | 0.69 | 102.60 | 594 | 45µx25µ | Au in galena |
| | | 6 | 59.27 | 42.79 | 0.77 | 102.83 | 581 | 45µx25µ | Au in galena |
| | | 7 | 57.99 | 42.42 | 0.79 | 101.20 | 578 | 45µx25µ | Au in galena |
| | | 8 | 57.37 | 42.52 | 0.61 | 100.50 | 574 | 45µx25µ | Au in galena |
| | | 9 | 57.15 | 43.87 | 0.90 | 101.92 | 566 | 45µx25µ | Au in galena |
| | | average | 58.34 | 42.23 | 0.78 | 101.35 | 580 | 45µx25µ | Au in galena |
| | 2A | 1 | 54.41 | 41.04 | 0.25 | 95.70 | 570 | 50µx75µ | Au in galena |
| | | 2 | 53.87 | 41.05 | 0.23 | 95.15 | 568 | 50µx75µ | Au in galena |
| | | 3 | 53.17 | 41.37 | 0.17 | 94.71 | 562 | 50µx75µ | Au in galena |
| | | 4 | 53.42 | 41.44 | 0.32 | 95.18 | 563 | 50µx75µ | Au in galena |
| | | 5 | 60.04 | 41.16 | 0.40 | 101.60 | 593 | 50µx75µ | Au in galena |
| | | 6 | 60.42 | 40.53 | 0.42 | 101.37 | 599 | 50µx75µ | Au in galena |
| | | 7 | 60.81 | 40.91 | 0.35 | 102.07 | 598 | 50µx75µ | Au in galena |
| | | 8 | 60.52 | 40.8 | 0.3 | 101.62 | 597 | 50µx75µ | Au in galena |
| | | 9 | 60.45 | 40.92 | 0.44 | 101.81 | 596 | 50µx75µ | Au in galena |
| | | 10 | 56.53 | 39.86 | 0.62 | 97.01 | 586 | 50µx75µ | Au in galena |
| | | average | 57.36 | 40.91 | 0.35 | 98.62 | 583 | 50µx75µ | Au in galena |
| | 2B | 1 | 54.89 | 40.76 | 0.24 | 95.89 | 574 | 25µx25µ | Au in galena |
| | | 2 | 53.06 | 41.42 | 0.45 | 94.93 | 562 | 25µx25µ | Au in galena |
| | | 3 | 53.43 | 40.85 | 0.37 | 94.65 | 567 | 25µx25µ | Au in galena |
| | | 4 | 51.60 | 41.17 | 0.38 | 93.15 | 556 | 25µx25µ | Au in galena |
| | | 5 | 54.34 | 40.89 | 0.45 | 95.68 | 571 | 25µx25µ | Au in galena |
| | | 6 | 52.55 | 41.26 | 0.53 | 94.34 | 560 | 25µx25µ | Au in galena |
| | | average | 53.31 | 41.06 | 0.40 | 94.77 | 565 | 25µx25µ | Au in galena |
| Sample-Illiff | 1 | 1 | 88.58 | 12.76 | 0.57 | 101.91 | 874 | 5mm | Au & fluorite |
| P lens | | 2 | 87.32 | 12.89 | 0.55 | 100.76 | 877 | 5mm | Au & fluorite |
| Hercules | | 3 | 88.36 | 12.39 | 1.75 | 102.50 | 877 | 5mm | Au & fluorite |
| | | 4 | 88.29 | 12.75 | 0.49 | 101.53 | 874 | 5mm | Au & fluorite |
| | | 5 | 89.50 | 12.58 | 0.67 | 102.75 | 877 | 5mm | Au & fluorite |
| | | average | 88.41 | 12.67 | 0.81 | 101.89 | 876 | 5mm | Au & fluorite |

py = pyrite sp = sphalerite ga = galena tt = tetrahedrite

*Total may be low or high due to electron beam instability but as atomic ratios are correct, the data are reliable.

**APPENDIX 7.4. CAMECA microprobe analysis of selected electrum grains from the South Hercules deposit, western Tasmania.**

| Sample No./ Section | No. of grain | No. of spot | Au wt % | Ag wt % | Hg wt % | Total* | Remark |
|---|---|---|---|---|---|---|---|
| H1118-13/ @ 29.9m 5630mN | 1 | 1 | 81.29 | 10.62 | 2.38 | 94.29 | single Au grain in sp |
| | 2 | 1 | 61.02 | 29.85 | 6.00 | 96.87 | large Au grain in sp |
| | | 2 | 60.36 | 30.18 | 6.57 | 97.11 | large Au grain in sp |
| average | 2 | 2 | 60.69 | 30.02 | 6.29 | 96.99 | large Au grain in sp |
| | 3 | 1 | 60.81 | 30.59 | 6.70 | 98.10 | single Au grain in sp |
| | | 2 | 59.71 | 30.59 | 6.80 | 97.10 | single Au grain in sp |
| | | 3 | 59.86 | 30.47 | 6.58 | 96.91 | single Au grain in sp |
| average | 3 | 3 | 60.13 | 30.55 | 6.69 | 97.37 | single Au grain in sp |
| | 4 | 1 | 45.40 | 38.71 | 8.69 | 92.80 | Au grain in sp crack |
| | | 2 | 39.66 | 34.44 | 7.52 | 81.62 | Au grain in sp crack |
| | 4 | 2 | 42.53 | 36.58 | 8.11 | 87.21 | Au grain in sp crack |
| | 5 | 1 | 54.17 | 24.87 | 4.14 | 83.18 | single Au grain in sp |
| | 6 | 1 | 49.00 | 34.34 | 12.42 | 95.76 | Au grain in sp crack |
| | | 2 | 40.60 | 37.80 | 16.12 | 94.52 | Au grain in sp crack |
| | | 3 | 38.94 | 37.69 | 17.31 | 93.94 | Au grain in sp crack |
| average | 6 | 3 | 42.85 | 36.61 | 15.28 | 94.74 | Au grain in sp crack |
| | 7 | 1 | 31.00 | 40.12 | 22.94 | 94.06 | Au grain in sp crack |
| | | 2 | 27.90 | 40.74 | 23.37 | 92.01 | Au grain in sp crack |
| | | 3 | 27.15 | 40.65 | 23.07 | 90.87 | Au grain in sp crack |
| average | 7 | 3 | 28.68 | 40.50 | 23.13 | 92.31 | Au grain in sp crack |
| | 8 | 1 | 32.96 | 38.91 | 20.79 | 92.66 | Au in sp crack |
| | 9 | 1 | 36.66 | 38.40 | 17.81 | 92.87 | 10μ Au in sp crack |
| | 10 | 1 | 83.66 | 10.77 | 2.13 | 96.56 | single Au in sp |
| | 11 | 1 | 38.76 | 37.32 | 19.00 | 95.08 | Au grain in sp crack |
| | | 2 | 39.79 | 37.60 | 17.49 | 94.88 | Au grain in sp crack |
| average | 11 | 2 | 39.28 | 37.46 | 18.25 | 94.98 | Au grain in sp crack |
| average of all grains | 11 | 20 | 51.17 | 30.48 | 11.36 | 93.01 | |
| H1145-2B | 1 | 1 | 43.19 | 35.05 | 19.04 | 97.28 | Au in tt |
| @ 61.3m | | 2 | 37.07 | 38.32 | 22.11 | 97.50 | Au in tt |
| 5670mN | | 3 | 47.20 | 33.62 | 17.97 | 98.79 | Au in tt |
| average | 1 | 3 | 42.49 | 35.66 | 19.71 | 97.86 | Au in tt |
| | 2 | 1 | 40.50 | 35.92 | 20.37 | 96.79 | Au in tt |
| | | 2 | 34.33 | 38.28 | 22.44 | 95.05 | Au in tt |
| | | 3 | 41.94 | 35.04 | 18.63 | 95.61 | Au in tt |
| average | 2 | 3 | 38.92 | 36.41 | 20.48 | 95.82 | Au in tt |
| | 3 | 1 | 29.89 | 40.97 | 24.32 | 95.18 | Au in tt |
| | | 2 | 31.01 | 38.23 | 25.18 | 94.42 | Au in tt |
| | | 3 | 30.62 | 41.17 | 24.32 | 96.11 | Au in tt |
| average | 3 | 3 | 30.51 | 40.12 | 24.61 | 95.24 | Au in tt |
| average of all grains | 3 | 9 | 37.31 | 37.40 | 21.60 | 96.30 | Au in tt |

tt = tetrahedrite, py = pyrite, ga = galena, cp = chalcopyrite, sp = sphalerite

*Total may be low or high due to electron beam instability but as atomic ratios are correct, the data are reliable.

**APPENDIX 7.4. CAMECA microprobe analysis of selected electrum grains from the South Hercules deposit, western Tasmania (Continued).**

| Sample No./ Section | No. of grain | No. of spot | Au wt % | Ag wt % | Hg wt % | Total* | Remark |
|---|---|---|---|---|---|---|---|
| H1142-2/ | 1 | 1 | 46.55 | 40.75 | 12.12 | 99.42 | Au in tt |
| @ 43.0m | | 2 | 45.08 | 41.34 | 11.98 | 98.40 | Au in tt |
| 5600mN | | 3 | 46.79 | 41.14 | 12.29 | 100.22 | Au in tt |
| | | 4 | 46.76 | 40.42 | 12.05 | 99.23 | Au in tt |
| | | 5 | 46.03 | 40.92 | 11.59 | 98.54 | Au in tt |
| average | 1 | 5 | 46.24 | 40.91 | 12.01 | 99.16 | Au in tt |
| H1148-2 | 1 | 1 | 58.91 | 45.13 | 6.00 | 110.04 | Au-ga in py |
| @ 89.4m | | 2 | 52.53 | 41.62 | 5.22 | 99.37 | Au-ga in py |
| 5600mN | | 3 | 49.17 | 42.88 | 5.12 | 97.17 | Au-ga in py |
| | | 4 | 46.63 | 45.74 | 6.28 | 98.65 | Au-ga in py |
| average | 1 | 4 | 51.81 | 43.84 | 5.66 | 101.31 | Au-ga in py |
| | 2 | 1 | 49.38 | 43.41 | 6.03 | 98.82 | Au-ga in py |
| | | 2 | 47.56 | 43.32 | 5.43 | 96.31 | Au-ga in py |
| | | 3 | 46.08 | 46.65 | 5.48 | 98.21 | Au-ga in py |
| average | 2 | 3 | 47.67 | 44.46 | 5.65 | 97.78 | Au-ga in py |
| | 3 | 1 | 46.80 | 42.71 | 5.64 | 95.15 | Au-ga in py |
| average of all grains | 3 | 8 | 48.76 | 43.67 | 5.65 | 98.08 | |
| H1114-4/ | 1 | 1 | 63.66 | 20.27 | 15.48 | 99.41 | Au-cp in py |
| @ 36.3m | | 2 | 65.13 | 20.11 | 14.41 | 99.65 | Au-cp in py |
| 5630mN | | 3 | 65.07 | 20.00 | 15.10 | 100.17 | Au-cp in py |
| average | 1 | 3 | 64.62 | 20.13 | 15.00 | 99.74 | Au-cp in py |
| | 2 | 1 | 40.21 | 17.04 | 9.92 | 67.17 | Au between two py grains |
| | | 2 | 55.76 | 23.87 | 14.43 | 94.06 | Au between two py grains |
| | | 3 | 57.72 | 24.72 | 14.48 | 96.92 | Au between two py grains |
| | | 4 | 57.60 | 24.94 | 14.48 | 97.02 | Au between two py grains |
| average | 2 | 4 | 52.82 | 22.64 | 13.33 | 88.79 | Au between two py grains |
| | 3 | 1 | 85.90 | 11.94 | 1.61 | 99.45 | Au locked in py |
| | | 2 | 85.60 | 11.60 | 1.78 | 98.98 | Au locked in py |
| | | 3 | 86.64 | 12.04 | 1.49 | 100.17 | Au locked in py |
| average | 3 | 3 | 86.05 | 11.86 | 1.63 | 99.53 | Au locked in py |
| average of all grains | 3 | 10 | 67.83 | 18.21 | 9.98 | 96.02 | |
| H1129-2 | 1 | 1 | 63.97 | 30.79 | 1.39 | 96.15 | Au in py |
| @ 79.8m | | 2 | 64.44 | 31.31 | 0.80 | 96.55 | Au in py |
| 5720mN | | 3 | 63.44 | 31.33 | 1.07 | 95.84 | Au in py |
| | | 4 | 63.52 | 30.98 | 0.94 | 95.44 | Au in py |
| | | 5 | 64.64 | 31.35 | 0.87 | 96.86 | Au in py |
| average | 1 | 5 | 64.00 | 31.15 | 1.01 | 96.17 | Au in py |

tt = tetrahedrite, py = pyrite, ga = galena, cp = chalcopyrite, sp = sphalerite

*Total may be low or high due to electron beam instability but as atomic ratios are correct, the data are reliable.

**Appendix 8.1. Compositional variation of sphalerite from A and B lens (Rosebery north-end), western Tasmania.**

| Sample No. | Grain No. | spot No. | Zn wt% | Fe wt% | Mn wt% | Cu wt% | Cd wt% | S wt% | Total wt% | FeS mole % | MnS mole % | CuS mole % | CdS mole % | Au g/t | Associated sulphides |
|---|---|---|---|---|---|---|---|---|---|---|---|---|---|---|---|
| R3391-100.5m | 1 | 1 | 60.02 | 6.14 | 0.00 | 0.00 | 0.41 | 33.21 | 99.79 | 10.66 | 0.00 | 0.00 | 0.32 | 3.90 | sp-py-ga-cp |
| | | 2 | 58.85 | 5.85 | 0.00 | 1.19 | 0.00 | 33.45 | 99.35 | 10.23 | 0.00 | 1.49 | 0.00 | 3.90 | sp-py-ga-cp |
| | | 3 | 59.08 | 4.66 | 0.20 | 0.87 | 0.00 | 33.15 | 97.96 | 8.31 | 0.93 | 1.10 | 0.00 | 3.90 | sp-py-ga-cp |
| | | 4 | 59.99 | 4.99 | 0.00 | 0.34 | 0.00 | 33.57 | 98.90 | 8.83 | 0.00 | 0.43 | 0.00 | 3.90 | sp-py-ga-cp |
| average | 1 | 4 | 59.49 | 5.41 | 0.05 | 0.60 | 0.10 | 33.35 | 99.00 | 9.51 | 0.23 | 0.76 | 0.08 | 3.90 | sp-py-ga-cp |
| R3391-122m | 1 | 1 | 61.29 | 4.51 | 0.00 | 0.00 | 0.51 | 33.68 | 99.99 | 7.89 | 0.00 | 0.00 | 0.40 | 1.40 | sp-py-ga |
| | | 2 | 60.29 | 5.05 | 0.20 | 0.44 | 0.22 | 33.77 | 99.97 | 8.82 | 0.91 | 0.55 | 0.17 | 1.40 | sp-py-ga |
| | | 3 | 61.56 | 4.85 | 0.16 | 0.00 | 0.00 | 34.21 | 100.78 | 8.42 | 0.75 | 0.00 | 0.00 | 1.40 | sp-py-ga |
| | 2 | 1 | 60.87 | 5.29 | 0.12 | 0.00 | 0.00 | 34.47 | 100.75 | 9.21 | 0.55 | 0.00 | 0.00 | 1.40 | sp-py-ga |
| | 3 | 1 | 61.27 | 4.84 | 0.11 | 0.00 | 0.00 | 33.65 | 99.87 | 8.45 | 0.52 | 0.00 | 0.00 | 1.40 | sp-py-ga |
| | | 2 | 61.21 | 4.95 | 0.12 | 0.00 | 0.00 | 33.60 | 99.88 | 8.63 | 0.57 | 0.00 | 0.00 | 1.40 | sp-py-ga |
| average | 3 | 6 | 61.08 | 4.92 | 0.12 | 0.07 | 0.12 | 33.90 | 100.21 | 8.57 | 0.55 | 0.09 | 0.10 | 1.40 | sp-py-ga |
| R3391-133.8m | 1 | 1 | 60.57 | 4.20 | 0.00 | 0.00 | 0.23 | 32.98 | 97.97 | 7.49 | 0.00 | 0.00 | 0.19 | 5.40 | sp-py-ga |
| | | 2 | 59.28 | 4.45 | 0.00 | 0.00 | 0.31 | 32.75 | 96.95 | 8.05 | 0.00 | 0.00 | 0.25 | 5.40 | sp-py-ga |
| | 2 | 1 | 61.37 | 4.36 | 0.14 | 0.00 | 0.00 | 33.00 | 98.87 | 7.66 | 0.69 | 0.00 | 0.00 | 5.40 | sp-py-ga |
| | 3 | 1 | 62.14 | 3.62 | 0.19 | 0.00 | 0.00 | 33.21 | 99.16 | 6.36 | 0.96 | 0.00 | 0.00 | 5.40 | small sp-py |
| | | 2 | 60.87 | 4.30 | 0.14 | 0.00 | 0.44 | 32.79 | 98.54 | 7.59 | 0.68 | 0.00 | 0.35 | 5.40 | small sp-py |
| | 4 | 1 | 61.32 | 4.36 | 0.25 | 0.00 | 0.00 | 33.35 | 99.27 | 7.65 | 1.22 | 0.00 | 0.00 | 5.40 | sp-py |
| average | 4 | 6 | 60.93 | 4.22 | 0.12 | 0.00 | 0.16 | 33.01 | 98.46 | 7.47 | 0.59 | 0.00 | 0.13 | 5.40 | sp-ga-py |
| R3391-138.5m | 1 | 1 | 61.67 | 4.42 | 0.00 | 0.32 | 0.00 | 33.26 | 99.67 | 7.70 | 0.00 | 0.40 | 0.00 | 23.20 | sp-py |
| | | 2 | 61.40 | 4.58 | 0.00 | 0.00 | 0.41 | 33.22 | 99.61 | 8.00 | 0.00 | 0.00 | 0.33 | 23.20 | sp-py |
| | | 3 | 61.54 | 4.67 | 0.00 | 0.00 | 0.23 | 33.37 | 99.81 | 8.14 | 0.00 | 0.00 | 0.18 | 23.20 | sp-py |
| | 2 | 1 | 60.32 | 5.08 | 0.00 | 0.95 | 0.00 | 33.18 | 99.52 | 8.84 | 0.00 | 1.19 | 0.00 | 23.20 | sp-ga-py |
| | | 2 | 58.67 | 5.42 | 0.00 | 1.64 | 0.00 | 32.97 | 98.69 | 9.51 | 0.00 | 2.06 | 0.00 | 23.20 | sp-ga-py |
| | 3 | 1 | 59.73 | 5.18 | 0.12 | 1.07 | 0.26 | 33.18 | 99.55 | 9.02 | 0.54 | 1.34 | 0.20 | 23.20 | sp-py |
| | 4 | 1 | 60.79 | 4.20 | 0.00 | 0.49 | 0.25 | 32.83 | 98.56 | 7.41 | 0.00 | 0.62 | 0.20 | 23.20 | sp-py |
| | | 2 | 60.28 | 4.21 | 0.00 | 0.53 | 0.00 | 33.05 | 98.07 | 7.49 | 0.00 | 0.68 | 0.00 | 23.20 | sp-py |
| average | 4 | 8 | 60.55 | 4.72 | 0.02 | 0.63 | 0.14 | 33.13 | 99.19 | 8.27 | 0.07 | 0.79 | 0.11 | 23.20 | sp-ga-py |
| R3391-140m | 1 | 1 | 61.94 | 4.10 | 0.00 | 0.00 | 0.22 | 33.86 | 100.12 | 7.18 | 0.00 | 0.00 | 0.17 | 23.20 | sp-ga-py |
| | | 2 | 61.69 | 3.86 | 0.00 | 0.00 | 0.00 | 33.87 | 99.42 | 6.82 | 0.00 | 0.00 | 0.00 | 23.20 | sp-ga-py |
| | | 3 | 61.62 | 3.97 | 0.14 | 0.00 | 0.21 | 34.05 | 99.99 | 6.98 | 0.68 | 0.00 | 0.17 | 23.20 | sp-ga-py |
| | 2 | 1 | 61.39 | 4.65 | 0.00 | 0.00 | 0.35 | 33.85 | 100.24 | 8.12 | 0.00 | 0.00 | 0.28 | 23.20 | sp-ga-py |
| average | 2 | 4 | 61.66 | 4.15 | 0.04 | 0.00 | 0.20 | 33.91 | 99.94 | 7.28 | 0.17 | 0.00 | 0.15 | 23.20 | sp-ga-py |
| R3391-142.5m | 1 | 1 | 66.20 | 1.40 | 0.00 | 0.00 | 0.00 | 33.13 | 100.73 | 2.42 | 0.00 | 0.00 | 0.00 | 10.40 | sp-cp-py |
| | 2 | 1 | 64.68 | 1.23 | 0.00 | 0.00 | 0.00 | 32.51 | 98.42 | 2.18 | 0.00 | 0.00 | 0.00 | 10.40 | sp-cp-py |
| | 3 | 1 | 63.56 | 1.24 | 0.00 | 0.00 | 0.00 | 32.52 | 97.32 | 2.23 | 0.00 | 0.00 | 0.00 | 10.40 | sp-cp-py |
| | 4 | 1 | 65.31 | 1.28 | 0.00 | 0.00 | 0.22 | 32.94 | 99.75 | 2.24 | 0.00 | 0.00 | 0.18 | 10.40 | sp-py-cp |
| | 5 | 1 | 65.44 | 1.21 | 0.21 | 0.00 | 0.35 | 33.14 | 100.35 | 2.10 | 1.17 | 0.00 | 0.28 | 10.40 | sp-py-cp |
| | | 2 | 65.20 | 1.01 | 0.00 | 0.00 | 0.31 | 32.98 | 99.50 | 1.78 | 0.00 | 0.00 | 0.25 | 10.40 | sp-py-cp |
| average | 5 | 6 | 65.07 | 1.23 | 0.04 | 0.00 | 0.15 | 32.87 | 99.35 | 2.16 | 0.20 | 0.00 | 0.12 | 10.40 | sp-py-cp |

sp = sphalerite, py = pyrite, ga = galena and cp = chalcopyrite

**Appendix 8.1. Compositional variation of sphalerite from A and B lens (Rosebery north-end), western Tasmania (Continued).**

| Sample No. | Grain No. | spot No. | Zn wt% | Fe wt% | Mn wt% | Cu wt% | Cd wt% | S wt% | Total wt% | FeS mole % | MnS mole % | CuS mole % | CdS mole % | Au g/t | Associated sulphides |
|---|---|---|---|---|---|---|---|---|---|---|---|---|---|---|---|
| R3382-270m | 1 | 1 | 65.16 | 1.65 | 0.00 | 0.00 | 0.00 | 32.69 | 99.49 | 2.88 | 0.00 | 0.00 | 0.00 | 2.80 | sp-barite |
| | 2 | 1 | 64.87 | 1.58 | 0.00 | 0.00 | 0.00 | 32.43 | 99.10 | 2.77 | 0.00 | 0.00 | 0.00 | 2.80 | sp-barite |
| | 3 | 1 | 64.70 | 1.41 | 0.00 | 0.00 | 0.00 | 32.50 | 98.89 | 2.49 | 0.00 | 0.00 | 0.00 | 2.80 | sp-barite |
| average | 3 | 3 | 64.91 | 1.55 | 0.00 | 0.00 | 0.00 | 32.54 | 99.16 | 2.71 | 0.00 | 0.00 | 0.00 | 2.80 | sp-barite |
| R3397-129m | 1 | 1 | 60.00 | 5.52 | 0.11 | 0.00 | 0.00 | 33.37 | 99.00 | 9.70 | 0.51 | 0.00 | 0.00 | 2.10 | sp-py-ga |
| | | 2 | 60.24 | 5.55 | 0.16 | 0.00 | 0.00 | 34.15 | 100.10 | 9.71 | 0.73 | 0.00 | 0.00 | 2.10 | sp-py-ga |
| | 2 | 1 | 58.54 | 5.38 | 0.20 | 0.00 | 0.00 | 32.98 | 97.10 | 9.68 | 0.94 | 0.00 | 0.00 | 2.10 | sp-py |
| | | 2 | 58.03 | 5.22 | 0.00 | 0.00 | 0.24 | 33.94 | 97.62 | 9.51 | 0.00 | 0.00 | 0.19 | 2.10 | sp-py |
| | 3 | 1 | 60.58 | 5.49 | 0.00 | 0.00 | 0.27 | 34.08 | 100.42 | 9.57 | 0.00 | 0.00 | 0.21 | 2.10 | big sp-py-ga |
| | | 2 | 60.47 | 5.48 | 0.00 | 0.00 | 0.00 | 34.36 | 100.31 | 9.59 | 0.00 | 0.00 | 0.00 | 2.10 | big sp-py-ga |
| average | 3 | 6 | 59.64 | 5.44 | 0.08 | 0.00 | 0.09 | 33.81 | 99.09 | 9.63 | 0.36 | 0.00 | 0.07 | 2.10 | big sp-py-ga |
| R3397-140.5m | 1 | 1 | 64.24 | 0.72 | 0.00 | 0.00 | 0.00 | 34.01 | 99.00 | 1.29 | 0.00 | 0.00 | 0.00 | 6.00 | sp-barite |
| | | 2 | 64.54 | 0.58 | 0.00 | 0.00 | 0.00 | 32.86 | 98.00 | 1.04 | 0.00 | 0.00 | 0.00 | 6.00 | sp-barite |
| | | 3 | 65.13 | 0.76 | 0.00 | 0.00 | 0.00 | 33.11 | 99.00 | 1.35 | 0.00 | 0.00 | 0.00 | 6.00 | sp-barite |
| | | 4 | 64.38 | 0.74 | 0.00 | 0.00 | 0.00 | 33.11 | 98.22 | 1.33 | 0.00 | 0.00 | 0.00 | 6.00 | sp-barite |
| | | 5 | 64.39 | 0.61 | 0.23 | 0.00 | 0.00 | 33.18 | 98.42 | 1.09 | 1.33 | 0.00 | 0.00 | 6.00 | sp-barite |
| | 2 | 1 | 66.08 | 0.83 | 0.00 | 0.00 | 0.00 | 33.95 | 100.85 | 1.45 | 0.00 | 0.00 | 0.00 | 6.00 | sp-barite |
| | | 2 | 65.97 | 0.79 | 0.00 | 0.00 | 0.00 | 33.34 | 100.10 | 1.38 | 0.00 | 0.00 | 0.00 | 6.00 | sp-barite |
| | | 3 | 65.64 | 0.79 | 0.00 | 0.00 | 0.26 | 33.09 | 99.78 | 1.39 | 0.00 | 0.00 | 0.21 | 6.00 | sp-barite |
| | | 4 | 65.52 | 0.69 | 0.00 | 0.00 | 0.38 | 32.93 | 99.51 | 1.21 | 0.00 | 0.00 | 0.31 | 6.00 | sp-barite |
| | | 5 | 64.49 | 0.77 | 0.00 | 0.00 | 0.00 | 33.11 | 98.37 | 1.38 | 0.00 | 0.00 | 0.00 | 6.00 | sp-barite |
| average | 2 | 10 | 65.04 | 0.73 | 0.02 | 0.00 | 0.06 | 33.27 | 99.13 | 1.29 | 0.13 | 0.00 | 0.05 | 6.00 | sp-barite |
| R3397-147m | 1 | 1 | 64.84 | 0.42 | 0.00 | 0.00 | 0.23 | 33.07 | 29.55 | 0.75 | 0.00 | 0.00 | 0.38 | 6.90 | sp-barite |
| | | 2 | 65.89 | 0.50 | 0.14 | 0.00 | 0.31 | 33.22 | 100.05 | 0.88 | 0.81 | 0.00 | 0.25 | 6.90 | sp-barite |
| | 2 | 1 | 65.38 | 0.65 | 0.00 | 0.00 | 0.40 | 32.91 | 99.33 | 1.15 | 0.00 | 0.00 | 0.33 | 6.90 | sp-barite |
| | | 2 | 65.62 | 0.63 | 0.11 | 0.00 | 0.00 | 33.00 | 99.50 | 1.11 | 0.65 | 0.00 | 0.00 | 6.90 | sp-barite |
| | 3 | 1 | 65.79 | 0.41 | 0.00 | 0.00 | 0.00 | 33.21 | 99.42 | 0.72 | 0.00 | 0.00 | 0.00 | 6.90 | sp-barite |
| Average | 3 | 5 | 65.50 | 0.52 | 0.05 | 0.00 | 0.19 | 33.08 | 85.57 | 0.92 | 0.29 | 0.00 | 0.19 | 6.90 | sp-barite |
| R3394-181m | 1 | 1 | 65.61 | 0.82 | 0.00 | 0.00 | 0.34 | 33.35 | 100.12 | 1.44 | 0.00 | 0.00 | 0.28 | 2.00 | sp-ga-py |
| | | 2 | 65.42 | 0.87 | 0.13 | 0.00 | 0.49 | 33.24 | 100.15 | 1.52 | 0.73 | 0.00 | 0.40 | 2.00 | sp-ga-py |
| | | 3 | 66.38 | 0.83 | 0.00 | 0.00 | 0.00 | 33.70 | 100.91 | 1.44 | 0.00 | 0.00 | 0.00 | 2.00 | sp-ga-py |
| | 2 | 1 | 65.72 | 0.82 | 0.11 | 0.00 | 0.00 | 33.71 | 100.36 | 1.44 | 0.63 | 0.00 | 0.00 | 2.00 | sp-ga-py |
| | | 2 | 66.12 | 0.77 | 0.13 | 0.00 | 0.00 | 33.46 | 100.48 | 1.34 | 0.75 | 0.00 | 0.00 | 2.00 | sp-ga-py |
| | | 3 | 65.66 | 0.83 | 0.00 | 0.00 | 0.00 | 33.64 | 100.13 | 1.46 | 0.00 | 0.00 | 0.00 | 2.00 | sp-ga-py |
| | 3 | 1 | 65.42 | 0.90 | 0.00 | 0.00 | 0.26 | 33.22 | 99.80 | 1.58 | 0.00 | 0.00 | 0.21 | 2.00 | sp-ga-py |
| | | 2 | 66.12 | 0.75 | 0.00 | 0.00 | 0.43 | 33.36 | 100.75 | 1.31 | 0.00 | 0.00 | 0.35 | 2.00 | sp-ga-py |
| | | 3 | 66.13 | 0.94 | 0.11 | 0.00 | 0.21 | 33.10 | 100.49 | 1.63 | 0.63 | 0.00 | 0.17 | 2.00 | sp-ga-py |
| | 4 | 1 | 65.07 | 0.75 | 0.12 | 0.00 | 0.31 | 33.66 | 99.91 | 1.32 | 0.68 | 0.00 | 0.25 | 2.00 | sp-ga-py |
| | | 2 | 65.67 | 0.90 | 0.00 | 0.00 | 0.22 | 33.64 | 100.43 | 1.58 | 0.00 | 0.00 | 0.18 | 2.00 | sp-ga-py |
| | | 3 | 64.97 | 0.80 | 0.20 | 0.00 | 0.00 | 33.91 | 99.87 | 1.42 | 1.13 | 0.00 | 0.00 | 2.00 | sp-ga-py |
| Average | 4 | 12 | 65.69 | 0.83 | 0.07 | 0.00 | 0.19 | 33.50 | 100.28 | 1.46 | 0.38 | 0.00 | 0.15 | 2.00 | sp-ga-py |
| R4340-15.6m | 1 | 1 | 63.35 | 1.83 | 0.29 | 0.00 | 0.34 | 34.07 | 99.88 | 3.24 | 1.52 | 0.00 | 0.27 | 13.8 | sp-py |
| | | 2 | 64.32 | 1.96 | 0.14 | 0.00 | 0.00 | 34.27 | 100.69 | 3.44 | 0.74 | 0.00 | 0.00 | 13.8 | sp-py |
| | 2 | 1 | 63.36 | 2.16 | 0.00 | 0.00 | 0.00 | 33.46 | 98.98 | 3.84 | 0.00 | 0.00 | 0.00 | 13.8 | massive sp |
| | | 2 | 64.87 | 1.48 | 0.00 | 0.00 | 0.26 | 34.23 | 100.84 | 2.60 | 0.00 | 0.00 | 0.21 | 13.8 | massive sp |
| average | 2 | 4 | 63.98 | 1.86 | 0.11 | 0.00 | 0.15 | 34.01 | 100.10 | 3.28 | 0.57 | 0.00 | 0.12 | 13.80 | |

sp = sphalerite, py = pyrite, ga = galena and cp = chalcopyrite

**Appendix 8.1. Compositional variation of sphalerite from A and B lens (Rosebery north-end), western Tasmania (Continued).**

| Sample No. | Grain No. | spot No. | Zn wt% | Fe wt% | Mn wt% | Cu wt% | Cd wt% | S wt% | Total wt% | FeS mole % | MnS mole % | CuS mole % | CdS mole % | Au g/t | Associated sulphides |
|---|---|---|---|---|---|---|---|---|---|---|---|---|---|---|---|
| R3382-265m | 1 | 1 | 62.93 | 3.58 | 0.14 | 0.00 | 0.00 | 33.57 | 100.22 | 6.23 | 0.70 | 0.00 | 0.00 | 1.70 | sp in py |
| | | 2 | 62.43 | 3.72 | 0.25 | 0.00 | 0.20 | 33.79 | 100.39 | 6.48 | 1.23 | 0.00 | 0.16 | 1.70 | sp in py |
| | | 3 | 62.62 | 3.70 | 0.22 | 0.00 | 0.00 | 34.14 | 100.69 | 6.44 | 1.08 | 0.00 | 0.00 | 1.70 | sp in py |
| | 2 | 1 | 63.09 | 3.51 | 0.18 | 0.00 | 0.00 | 33.86 | 100.65 | 6.09 | 0.90 | 0.00 | 0.00 | 1.70 | sp in py |
| | | 2 | 62.43 | 3.25 | 0.00 | 0.00 | 0.24 | 33.46 | 99.38 | 5.73 | 0.00 | 0.00 | 0.19 | 1.70 | sp in py |
| | | 3 | 62.79 | 3.54 | 0.18 | 0.00 | 0.00 | 33.61 | 100.12 | 6.17 | 0.90 | 0.00 | 0.00 | 1.70 | sp in py |
| | | 4 | 61.87 | 3.31 | 0.00 | 0.00 | 0.00 | 33.65 | 98.83 | 5.89 | 0.00 | 0.00 | 0.00 | 1.70 | sp in py |
| Average | 2 | 7 | 62.59 | 3.52 | 0.14 | 0.00 | 0.06 | 33.73 | 100.04 | 6.15 | 0.69 | 0.00 | 0.05 | 1.70 | sp in py |
| R4055-9.9m | 1 | 1 | 58.96 | 5.56 | 0.29 | 0.00 | 0.27 | 33.11 | 98.19 | 9.87 | 1.33 | 0.00 | 0.22 | 2.90 | sp-py |
| | | 2 | 59.94 | 5.74 | 0.26 | 0.00 | 0.31 | 33.78 | 100.02 | 10.01 | 1.17 | 0.00 | 0.24 | 2.90 | sp-py |
| | 2 | 1 | 60.62 | 5.35 | 0.24 | 0.00 | 0.00 | 33.86 | 100.92 | 9.32 | 1.11 | 0.00 | 0.00 | 2.90 | large sp |
| | | 2 | 60.07 | 5.74 | 0.36 | 0.00 | 0.33 | 33.60 | 100.10 | 9.97 | 1.62 | 0.00 | 0.26 | 2.90 | large sp |
| | 3 | 1 | 55.45 | 7.65 | 0.00 | 0.00 | 0.00 | 34.07 | 97.28 | 13.90 | 0.00 | 0.00 | 0.00 | 2.90 | sp in py |
| | | 2 | 57.24 | 5.85 | 0.00 | 0.00 | 0.32 | 31.68 | 95.10 | 10.65 | 0.00 | 0.00 | 0.26 | 2.90 | sp in py |
| average | 3 | 6 | 58.71 | 5.98 | 0.19 | 0.00 | 0.21 | 33.35 | 98.60 | 10.62 | 0.87 | 0.00 | 0.16 | 2.90 | sp in py |
| R4291-62.1m | 1 | 1 | 56.93 | 7.17 | 0.22 | 0.00 | 0.00 | 32.88 | 97.20 | 12.80 | 0.97 | 0.00 | 0.00 | 19.10 | massive sp |
| | | 2 | 57.23 | 7.58 | 0.00 | 0.00 | 0.00 | 32.86 | 97.67 | 13.42 | 0.00 | 0.00 | 0.00 | 19.10 | massive sp |
| | | 3 | 57.54 | 7.49 | 0.00 | 0.23 | 0.00 | 33.42 | 98.68 | 13.18 | 0.00 | 0.29 | 0.00 | 19.10 | massive sp |
| | 2 | 1 | 57.79 | 7.24 | 0.00 | 0.00 | 0.28 | 33.01 | 98.32 | 12.76 | 0.00 | 0.00 | 0.22 | 19.10 | massive sp |
| | | 2 | 57.30 | 7.22 | 0.21 | 0.00 | 0.00 | 32.64 | 97.37 | 12.80 | 0.93 | 0.00 | 0.00 | 19.10 | massive sp |
| | 3 | 1 | 57.02 | 5.77 | 0.00 | 0.00 | 0.27 | 34.16 | 97.22 | 10.56 | 0.00 | 0.00 | 0.21 | 19.10 | sp in py |
| | | 2 | 58.59 | 6.70 | 0.00 | 0.00 | 0.40 | 33.51 | 99.20 | 11.76 | 0.00 | 0.00 | 0.31 | 19.10 | sp in py |
| | | 3 | 56.56 | 6.99 | 0.00 | 0.00 | 0.78 | 32.65 | 96.98 | 12.55 | 0.00 | 0.00 | 0.62 | 19.10 | sp in py |
| | 4 | 1 | 60.18 | 6.34 | 0.00 | 0.00 | 0.00 | 34.16 | 100.68 | 10.98 | 0.00 | 0.00 | 0.00 | 19.10 | sp in py |
| | | 2 | 57.65 | 5.55 | 0.00 | 0.00 | 0.00 | 33.90 | 97.10 | 10.13 | 0.00 | 0.00 | 0.00 | 19.10 | sp in py |
| average | 4 | 10 | 57.68 | 6.81 | 0.04 | 0.02 | 0.17 | 33.32 | 98.04 | 12.09 | 0.19 | 0.03 | 0.14 | 19.10 | |
| R4289-73.0m | 1 | 1 | 65.96 | 0.36 | 0.22 | 0.00 | 0.00 | 33.42 | 99.96 | 0.63 | 1.28 | 0.00 | 0.00 | 17.0 | sp-py |
| | | 2 | 65.72 | 0.33 | 0.17 | 0.00 | 0.00 | 33.50 | 99.72 | 0.58 | 0.99 | 0.00 | 0.00 | 17.0 | sp-py |
| | 2 | 1 | 63.55 | 1.53 | 0.00 | 0.00 | 0.39 | 33.06 | 98.53 | 2.73 | 0.00 | 0.00 | 0.32 | 17.0 | sp-py |
| | | 2 | 65.44 | 0.84 | 0.17 | 0.00 | 0.00 | 32.65 | 99.10 | 1.48 | 0.99 | 0.00 | 0.00 | 17.0 | sp-py |
| | 3 | 1 | 65.58 | 1.07 | 0.16 | 0.00 | 0.00 | 33.08 | 99.89 | 1.87 | 0.91 | 0.00 | 0.00 | 17.0 | sp in py |
| | | 2 | 66.21 | 1.08 | 0.16 | 0.00 | 0.00 | 33.41 | 100.86 | 1.87 | 0.90 | 0.00 | 0.00 | 17.0 | sp in py |
| average | 3 | 6 | 65.41 | 0.87 | 0.15 | 0.00 | 0.07 | 33.19 | 99.68 | 1.53 | 0.85 | 0.00 | 0.05 | 17.0 | |
| R4296-51.4m | 1 | 1 | 62.43 | 1.70 | 0.14 | 0.00 | 0.00 | 32.27 | 96.54 | 3.08 | 0.79 | 0.00 | 0.00 | 28.5 | massive sp |
| | | 2 | 62.05 | 1.88 | 0.17 | 0.00 | 0.33 | 32.97 | 97.40 | 3.40 | 0.92 | 0.00 | 0.27 | 28.5 | massive sp |
| | 2 | 1 | 61.50 | 1.97 | 0.00 | 0.00 | 0.25 | 32.73 | 96.45 | 3.61 | 0.00 | 0.00 | 0.21 | 28.5 | sp in py |
| | | 2 | 61.67 | 1.88 | 0.30 | 0.00 | 0.00 | 32.44 | 96.29 | 3.43 | 1.66 | 0.00 | 0.00 | 28.5 | sp in py |
| average | 2 | 4 | 61.91 | 1.86 | 0.15 | 0.00 | 0.15 | 32.60 | 96.67 | 3.38 | 0.85 | 0.00 | 0.12 | 28.50 | |
| R4296-54.4m | 1 | 1 | 63.85 | 1.58 | 0.00 | 0.00 | 0.29 | 33.24 | 98.96 | 2.81 | 0.00 | 0.00 | 0.24 | 28.5 | sp in py |
| | | 2 | 63.09 | 1.79 | 0.00 | 0.00 | 0.39 | 32.73 | 98.00 | 3.20 | 0.00 | 0.00 | 0.32 | 28.5 | sp in py |
| | 2 | 1 | 62.69 | 1.81 | 0.20 | 0.00 | 0.00 | 32.53 | 97.23 | 3.26 | 1.12 | 0.00 | 0.00 | 28.5 | sp in py |
| | | 2 | 61.90 | 1.58 | 0.00 | 0.00 | 0.00 | 32.59 | 96.07 | 2.90 | 0.00 | 0.00 | 0.00 | 28.5 | sp in py |
| | | 3 | 62.35 | 1.36 | 0.00 | 0.00 | 0.29 | 32.73 | 96.73 | 2.48 | 0.00 | 0.00 | 0.24 | 28.5 | sp in py |
| average | 2 | 5 | 62.78 | 1.62 | 0.04 | 0.00 | 0.19 | 32.76 | 97.40 | 2.93 | 0.22 | 0.00 | 0.16 | 28.50 | sp in py |

sp = sphalerite, py = pyrite, ga = galena and cp = chalcopyrite

**Appendix 8.1. Compositional variation of sphalerite from A and B lens (Rosebery north-end), western Tasmania (Continued).**

| Sample No. | Grain No. | spot No. | Zn wt% | Fe wt% | Mn wt% | Cu wt% | Cd wt% | S wt% | Total wt% | FeS mole % | MnS mole % | CuS mole % | CdS mole % | Au g/t | Associated sulphides |
|---|---|---|---|---|---|---|---|---|---|---|---|---|---|---|---|
| R3391-145m | 1 | 1 | 63.53 | 1.71 | 0.00 | 0.00 | 0.34 | 33.61 | 99.20 | 3.05 | 0.00 | 0.00 | 0.28 | 0.70 | sp-ga |
| | | 2 | 63.61 | 1.75 | 0.00 | 0.00 | 0.00 | 33.57 | 99.13 | 3.12 | 0.00 | 0.00 | 0.00 | 0.70 | sp-ga |
| | | 3 | 64.52 | 1.60 | 0.00 | 0.00 | 0.00 | 34.11 | 100.23 | 2.82 | 0.00 | 0.00 | 0.00 | 0.70 | sp-ga |
| | 2 | 1 | 64.95 | 1.79 | 0.00 | 0.00 | 0.00 | 33.75 | 100.47 | 3.13 | 0.00 | 0.00 | 0.00 | 0.70 | large sp-ga |
| | | 2 | 64.29 | 1.67 | 0.00 | 0.00 | 0.00 | 34.43 | 100.39 | 2.95 | 0.00 | 0.00 | 0.00 | 0.70 | large sp-ga |
| | 3 | 1 | 64.19 | 1.41 | 0.19 | 0.00 | 0.33 | 33.92 | 100.05 | 2.49 | 1.02 | 0.00 | 0.27 | 0.70 | small sp-ga |
| | 4 | 1 | 63.47 | 1.67 | 0.00 | 0.00 | 0.48 | 33.11 | 98.74 | 2.98 | 0.00 | 0.00 | 0.39 | 0.70 | sp in ga |
| | | 2 | 63.31 | 1.58 | 0.17 | 0.00 | 0.28 | 33.14 | 98.49 | 2.82 | 0.93 | 0.00 | 0.23 | 0.70 | sp in ga |
| | 5 | 1 | 64.59 | 1.64 | 0.17 | 0.00 | 0.00 | 33.73 | 100.13 | 2.88 | 0.93 | 0.00 | 0.00 | 0.70 | sp-cp |
| average | 5 | 9 | 64.05 | 1.65 | 0.06 | 0.00 | 0.16 | 33.71 | 99.65 | 2.91 | 0.32 | 0.00 | 0.13 | 0.70 | sp-ga-cp-py |
| R3391-164m | 1 | 1 | 65.90 | 0.83 | 0.00 | 0.00 | 0.00 | 33.83 | 100.56 | 1.45 | 0.00 | 0.00 | 0.00 | 38.30 | sp-barite |
| | | 2 | 66.08 | 0.65 | 0.00 | 0.00 | 0.00 | 32.67 | 99.40 | 1.14 | 0.00 | 0.00 | 0.00 | 38.30 | sp-barite |
| | | 3 | 65.20 | 0.57 | 0.14 | 0.00 | 0.00 | 33.09 | 99.00 | 1.01 | 0.82 | 0.00 | 0.00 | 38.30 | sp-barite |
| | 2 | 1 | 66.17 | 0.65 | 0.00 | 0.00 | 0.00 | 33.09 | 99.90 | 1.14 | 0.00 | 0.00 | 0.00 | 38.30 | sp-barite |
| | | 2 | 65.71 | 0.57 | 0.21 | 0.00 | 0.00 | 33.48 | 99.97 | 1.00 | 1.21 | 0.00 | 0.00 | 38.30 | sp-barite |
| | 3 | 1 | 65.92 | 0.54 | 0.00 | 0.00 | 0.43 | 32.98 | 99.87 | 0.95 | 0.00 | 0.00 | 0.35 | 38.30 | sp-barite |
| | | 2 | 64.55 | 0.57 | 0.00 | 0.00 | 0.31 | 32.36 | 97.80 | 1.02 | 0.00 | 0.00 | 0.26 | 38.30 | sp-barite |
| average | 3 | 7 | 65.65 | 0.63 | 0.05 | 0.00 | 0.11 | 33.07 | 99.50 | 1.10 | 0.29 | 0.00 | 0.09 | 38.30 | sp-barite |
| R3391-166m | 1 | 1 | 64.35 | 0.65 | 0.00 | 0.00 | 0.00 | 32.72 | 97.71 | 1.17 | 0.00 | 0.00 | 0.00 | 38.30 | sp-barite |
| | 2 | 1 | 65.04 | 0.83 | 0.00 | 0.00 | 0.00 | 33.63 | 99.50 | 1.47 | 0.00 | 0.00 | 0.00 | 38.30 | sp-barite |
| | | 2 | 64.92 | 0.80 | 0.00 | 0.00 | 0.00 | 33.18 | 98.90 | 1.42 | 0.00 | 0.00 | 0.00 | 38.30 | sp-barite |
| | 3 | 1 | 64.08 | 0.75 | 0.00 | 0.00 | 0.45 | 32.67 | 97.96 | 1.35 | 0.00 | 0.00 | 0.37 | 38.30 | sp-barite |
| | | 2 | 64.13 | 0.69 | 0.00 | 0.00 | 0.00 | 32.50 | 97.31 | 1.24 | 0.00 | 0.00 | 0.00 | 38.30 | sp-barite |
| average | 3 | 5 | 64.50 | 0.74 | 0.00 | 0.00 | 0.09 | 32.94 | 98.28 | 1.33 | 0.00 | 0.00 | 0.07 | 38.30 | sp-barite |
| R3394-147.5m | 1 | 1 | 63.76 | 2.11 | 0.00 | 0.00 | 0.00 | 33.59 | 99.46 | 3.73 | 0.00 | 0.00 | 0.00 | 2.70 | sp-ga-py |
| | | 2 | 63.78 | 2.25 | 0.14 | 0.00 | 0.3 | 33.08 | 99.55 | 3.95 | 0.75 | 0.00 | 0.24 | 2.70 | sp-ga-py |
| | 2 | 1 | 64.24 | 1.91 | 0.15 | 0.00 | 0.00 | 33.37 | 99.67 | 3.35 | 0.82 | 0.00 | 0.00 | 2.70 | sp-ga-py |
| | | 2 | 63.90 | 2.19 | 0.00 | 0.00 | 0.31 | 33.81 | 100.21 | 3.85 | 0.00 | 0.00 | 0.25 | 2.70 | sp-ga-py |
| average | 2 | 4 | 63.92 | 2.12 | 0.07 | 0.00 | 0.15 | 33.46 | 99.72 | 3.72 | 0.39 | 0.00 | 0.12 | 2.70 | sp-ga-py |
| R3394-175m | 1 | 1 | 64.36 | 0.91 | 0.00 | 0.00 | 0.00 | 33.54 | 98.81 | 1.63 | 0.00 | 0.00 | 0.00 | 1.20 | sp-barite |
| | | 2 | 65.53 | 1.02 | 0.00 | 0.00 | 0.00 | 33.95 | 100.50 | 1.79 | 0.00 | 0.00 | 0.00 | 1.20 | sp-barite |
| | | 3 | 65.53 | 0.94 | 0.00 | 0.00 | 0.25 | 33.77 | 100.49 | 1.65 | 0.00 | 0.00 | 0.20 | 1.20 | sp-barite |
| | 2 | 1 | 65.67 | 0.63 | 0.00 | 0.00 | 0.00 | 33.85 | 100.14 | 1.11 | 0.00 | 0.00 | | | |
| | 3 | 1 | 64.54 | 1.28 | 0.00 | 0.19 | 0.00 | 33.97 | 99.88 | 2.26 | 0.00 | 0.24 | 0.00 | 1.20 | sp-barite |
| | | 2 | 65.73 | 0.88 | 0.00 | 0.00 | 0.43 | 33.60 | 100.65 | 1.54 | 0.00 | 0.00 | 0.35 | 1.20 | sp-barite |
| average | 3 | 6 | 65.23 | 0.94 | 0.00 | 0.03 | 0.11 | 33.78 | 100.08 | 1.66 | 0.00 | 0.04 | 0.11 | 1.20 | sp-barite |
| R3382-117m | 1 | 1 | 58.42 | 6.24 | 0.49 | 0.00 | 0.00 | 32.99 | 98.14 | 11.02 | 2.21 | 0.00 | 0.00 | - | sp-ga-py |
| | | 2 | 58.03 | 6.14 | 0.53 | 0.00 | 0.00 | 32.62 | 97.31 | 10.91 | 2.41 | 0.00 | 0.00 | - | sp-ga-py |
| | | 3 | 58.45 | 6.04 | 0.42 | 0.00 | 0.00 | 32.97 | 97.88 | 10.71 | 1.91 | 0.00 | 0.00 | - | sp-ga-py |
| | 2 | 1 | 59.54 | 5.61 | 0.45 | 0.00 | 0.43 | 33.11 | 99.14 | 9.82 | 2.04 | 0.00 | 0.34 | - | sp-ga-py |
| | | 2 | 59.52 | 5.25 | 0.19 | 0.00 | 0.38 | 33.28 | 98.63 | 9.30 | 0.88 | 0.00 | 0.30 | - | sp-ga-py |
| | | 3 | 59.00 | 6.20 | 0.52 | 0.00 | 0.26 | 33.36 | 99.35 | 10.83 | 2.30 | 0.00 | 0.20 | - | sp-ga-py |
| | 3 | 1 | 60.42 | 6.23 | 0.39 | 0.00 | 0.00 | 33.50 | 100.54 | 10.70 | 1.74 | 0.00 | 0.00 | - | sp-ga-py |
| | | 2 | 58.92 | 5.86 | 0.22 | 0.00 | 0.00 | 33.21 | 98.20 | 10.39 | 1.01 | 0.00 | 0.00 | - | sp-ga-py |
| | | 3 | 59.92 | 5.12 | 0.22 | 0.00 | 0.00 | 33.03 | 98.30 | 9.06 | 1.05 | 0.00 | 0.00 | - | sp-ga-py |
| average | 3 | 9 | 59.14 | 5.85 | 0.38 | 0.00 | 0.12 | 33.12 | 98.61 | 10.30 | 1.73 | 0.00 | 0.09 | - | sp-ga-py |

sp = sphalerite, py = pyrite, ga = galena and cp = chalcopyrite
Sample R3391-145m is a remoblised vein

**Appendix 8.2. Compositional variation of sphalerite from the F(J) lens, Rosebery south-end, western Tasmania.**

| Sample No. /Section | grain No. | spot No. | Zn wt% | Fe wt% | Mn wt% | Cu wt% | Cd wt% | S wt% | Total wt% | FeS mole% | MnS mole% | CuS mole% | CdS mole% | Au g/t | Associated sulphides/oxides |
|---|---|---|---|---|---|---|---|---|---|---|---|---|---|---|---|
| 3024-2/ | 1 | 1 | 64.30 | 1.41 | 0.00 | 0.00 | 0.26 | 33.20 | 99.16 | 2.50 | 0.00 | 0.00 | 0.21 | 13.8 | sp-cp-ga |
| 220mS | | 2 | 63.98 | 1.76 | 0.00 | 0.37 | 0.00 | 33.29 | 99.40 | 3.10 | 0.00 | 0.47 | 0.00 | 13.8 | sp-cp-ga |
| | | 3 | 63.49 | 1.95 | 0.00 | 0.50 | 0.00 | 33.23 | 99.12 | 3.44 | 0.00 | 0.63 | 0.00 | 13.8 | sp-cp-ga |
| | | 4 | 62.29 | 1.91 | 0.00 | 0.50 | 0.00 | 33.13 | 97.93 | 3.44 | 0.00 | 0.64 | 0.00 | 13.8 | sp-cp-ga |
| | | 5 | 64.01 | 1.69 | 0.00 | 0.40 | 0.00 | 33.54 | 99.65 | 2.98 | 0.00 | 0.50 | 0.00 | 13.8 | sp-cp-ga |
| average | 1 | 5 | 63.61 | 1.74 | 0.00 | 0.35 | 0.05 | 33.28 | 99.05 | 3.09 | 0.00 | 0.45 | 0.04 | 13.8 | sp-cp-ga |
| | 2 | 1 | 63.65 | 1.36 | 0.43 | 0.00 | 0.36 | 33.56 | 99.88 | 2.41 | 2.31 | 0.00 | 0.29 | 13.8 | isolated sp |
| | | 2 | 63.09 | 1.44 | 0.48 | 0.00 | 0.23 | 33.56 | 98.86 | 2.57 | 2.58 | 0.00 | 0.19 | 13.8 | isolated sp |
| | | 3 | 63.06 | 1.44 | 0.44 | 0.00 | 0.00 | 33.28 | 98.56 | 2.58 | 2.42 | 0.00 | 0.00 | 13.8 | isolated sp |
| average | | 3 | 63.27 | 1.41 | 0.45 | 0.00 | 0.20 | 33.47 | 99.10 | 2.52 | 2.44 | 0.00 | 0.16 | 13.8 | isolated sp |
| | 3 | 1 | 63.65 | 1.10 | 0.00 | 0.00 | 0.00 | 32.67 | 97.41 | 1.98 | 0.00 | 0.00 | 0.00 | 13.8 | sp-cp |
| | | 2 | 60.79 | 2.87 | 0.00 | 1.05 | 0.00 | 32.89 | 97.61 | 5.15 | 0.00 | 1.34 | 0.00 | 13.8 | sp-cp |
| | | 3 | 63.38 | 1.98 | 0.00 | 0.46 | 0.00 | 32.72 | 98.78 | 3.50 | 0.00 | 0.59 | 0.00 | 13.8 | sp-cp |
| | | 4 | 62.62 | 1.63 | 0.00 | 0.20 | 0.55 | 32.82 | 97.82 | 2.93 | 0.00 | 0.26 | 0.45 | 13.8 | sp-cp |
| | | 5 | 63.40 | 1.54 | 0.00 | 0.00 | 0.00 | 32.86 | 97.79 | 2.76 | 0.00 | 0.00 | 0.00 | 13.8 | sp-cp |
| average | | 5 | 62.77 | 1.82 | 0.00 | 0.34 | 0.11 | 32.79 | 97.88 | 3.27 | 0.00 | 0.44 | 0.09 | 13.8 | sp-cp |
| | 4 | 1 | 63.76 | 1.09 | 0.00 | 0.00 | 0.30 | 32.95 | 98.10 | 1.96 | 0.00 | 0.00 | 0.25 | 13.8 | sp-cp-ga |
| | | 2 | 64.45 | 1.08 | 0.20 | 0.00 | 0.00 | 32.96 | 98.67 | 1.92 | 1.14 | 0.00 | 0.00 | 13.8 | sp-cp-ga |
| | | 3 | 63.72 | 1.13 | 0.13 | 0.00 | 0.40 | 32.84 | 98.22 | 2.02 | 0.73 | 0.00 | 0.33 | 13.8 | sp-cp-ga |
| average | | 4 | 63.98 | 1.10 | 0.11 | 0.00 | 0.23 | 32.92 | 98.33 | 1.96 | 0.62 | 0.00 | 0.19 | 13.8 | sp-cp-ga |
| average | 4 | 16 | 63.41 | 1.52 | 0.14 | 0.17 | 0.15 | 33.11 | 98.59 | 2.71 | 0.77 | 0.22 | 0.12 | 13.8 | |
| R3024-3A/ | 1 | 1 | 59.39 | 6.61 | 0.24 | 0.00 | 0.21 | 33.99 | 100.44 | 11.46 | 1.05 | 0.00 | 0.16 | 8.2 | sp-mag |
| 220mS | | 2 | 57.55 | 6.38 | 0.18 | 0.00 | 0.20 | 33.60 | 97.71 | 11.43 | 0.80 | 0.00 | 0.16 | 8.2 | sp-mag |
| | | 3 | 59.96 | 6.71 | 0.14 | 0.00 | 0.40 | 33.13 | 100.34 | 11.51 | 0.62 | 0.00 | 0.31 | 8.2 | sp-mag |
| average | | 3 | 58.97 | 6.57 | 0.19 | 0.00 | 0.20 | 33.57 | 99.50 | 11.47 | 0.82 | 0.00 | 0.16 | 8.2 | sp-mag |
| | 2 | 1 | 60.58 | 6.34 | 0.30 | 0.00 | 0.27 | 33.37 | 100.86 | 10.83 | 1.33 | 0.00 | 0.21 | 8.2 | sp-mag |
| | | 2 | 60.59 | 6.14 | 0.26 | 0.00 | 0.36 | 33.32 | 100.67 | 10.52 | 1.16 | 0.00 | 0.28 | 8.2 | sp-mag |
| | | 3 | 61.15 | 5.35 | 0.12 | 0.31 | 0.00 | 33.09 | 100.02 | 9.23 | 0.56 | 0.39 | 0.00 | 8.2 | sp-mag |
| | | 4 | 60.17 | 6.25 | 0.29 | 0.00 | 0.00 | 34.27 | 100.98 | 10.79 | 1.28 | 0.00 | 0.00 | 8.2 | sp-mag |
| average | | 4 | 60.64 | 5.91 | 0.22 | 0.10 | 0.12 | 33.56 | 100.56 | 10.18 | 1.01 | 0.13 | 0.09 | 8.2 | sp-mag |
| average | 2 | 7 | 59.80 | 6.24 | 0.21 | 0.05 | 0.16 | 33.57 | 100.03 | 10.83 | 0.92 | 0.06 | 0.13 | 8.2 | |
| R3024-3C/ | 1 | 1 | 61.49 | 4.30 | 0.17 | 0.00 | 0.00 | 33.48 | 99.43 | 7.54 | 0.83 | 0.00 | 0.00 | 10.3 | isolated sp |
| 220mS | | 2 | 61.14 | 4.33 | 0.15 | 0.00 | 0.31 | 33.69 | 99.62 | 7.61 | 0.72 | 0.00 | 0.25 | 10.3 | isolated sp |
| average | | 2 | 61.32 | 4.32 | 0.16 | 0.00 | 0.16 | 33.59 | 99.53 | 7.58 | 0.77 | 0.00 | 0.13 | 10.3 | isolated sp |
| | 2 | 1 | 56.06 | 9.11 | 0.00 | 0.00 | 0.00 | 33.63 | 98.81 | 15.98 | 0.00 | 0.00 | 0.00 | 10.3 | sp-po-py* |
| | | 2 | 56.10 | 9.31 | 0.00 | 0.00 | 0.00 | 33.55 | 98.96 | 16.27 | 0.00 | 0.00 | 0.00 | 10.3 | sp-po-py* |
| average | | 2 | 56.08 | 9.21 | 0.00 | 0.00 | 0.00 | 33.59 | 98.89 | 16.12 | 0.00 | 0.00 | 0.00 | 10.3 | sp-po-py* |
| | 3 | 1 | 57.25 | 8.24 | 0.00 | 0.00 | 0.00 | 33.68 | 99.18 | 14.42 | 0.00 | 0.00 | 0.00 | 10.3 | sp-po-py# |
| | | 2 | 56.96 | 8.54 | 0.00 | 0.00 | 0.00 | 33.48 | 98.98 | 14.93 | 0.00 | 0.00 | 0.00 | 10.3 | sp-po-py# |
| | | 3 | 56.50 | 8.33 | 0.00 | 0.00 | 0.00 | 33.68 | 98.85 | 14.72 | 0.00 | 0.00 | 0.00 | 10.3 | sp-po-py# |
| | | 4 | 57.27 | 8.16 | 0.00 | 0.00 | 0.00 | 33.95 | 99.39 | 14.29 | 0.00 | 0.00 | 0.00 | 10.3 | sp-po-py# |
| average | | 4 | 57.00 | 8.32 | 0.00 | 0.00 | 0.00 | 33.70 | 99.10 | 14.59 | 0.00 | 0.00 | 0.00 | 10.3 | sp-po-py# |

py = pyrite, po = pyrrhotite, sp = sphalerite, ga=galena cp = chalcopyrite, and mag = magnetite

*sp-py-po in mutual contact
**sp locked in py with po
#sp-py-po not in mutual contact

**Appendix 8.2. Compositional variation of sphalerite from the F(J) lens, Rosebery south-end, western Tasmania (Continued).**

| Sample No./ Section | grain No. | spot No. | Zn wt% | Fe wt% | Mn wt% | Cu wt% | Cd wt% | S wt% | Total wt% | FeS mole % | MnS mole % | CuS mole % | CdS mole % | Au g/t | Associated sulphides/oxides |
|---|---|---|---|---|---|---|---|---|---|---|---|---|---|---|---|
| R3024-3C/ | 4 | 1 | 60.96 | 4.69 | 0.13 | 0.00 | 0.27 | 32.67 | 98.73 | 8.22 | 0.63 | 0.00 | 0.22 | 10.3 | isolated sp |
| 220mS | | 2 | 60.44 | 4.89 | 0.16 | 0.00 | 0.00 | 34.37 | 99.86 | 8.63 | 0.75 | 0.00 | 0.00 | 10.3 | isolated sp |
| average | | 2 | 60.70 | 4.79 | 0.15 | 0.00 | 0.14 | 33.52 | 99.30 | 8.42 | 0.69 | 0.00 | 0.11 | 10.3 | isolated sp |
| | 5 | 1 | 56.47 | 9.74 | 0.00 | 0.00 | 0.28 | 33.47 | 99.95 | 16.76 | 0.00 | 0.00 | 0.21 | 10.3 | sp-py-po** |
| | | 2 | 54.84 | 9.60 | 0.00 | 0.00 | 0.00 | 32.49 | 97.46 | 17.01 | 0.00 | 0.00 | 0.00 | 10.3 | sp-py-po** |
| | | 3 | 56.50 | 9.92 | 0.15 | 0.39 | 0.37 | 33.99 | 101.32 | 16.85 | 0.57 | 0.48 | 0.28 | 10.3 | sp-py-po** |
| average | | 3 | 55.94 | 9.75 | 0.05 | 0.13 | 0.22 | 33.32 | 99.58 | 16.87 | 0.20 | 0.16 | 0.17 | 10.3 | sp-py-po** |
| average | 5 | 13 | 58.21 | 7.28 | 0.07 | 0.03 | 0.10 | 33.54 | 99.28 | 12.72 | 0.33 | 0.03 | 0.08 | 10.3 | |
| R3023-2/ | 1 | 1 | 52.92 | 8.84 | 0.00 | 2.12 | 0.00 | 33.19 | 97.07 | 15.81 | 0.00 | 2.67 | 0.00 | 6.3 | sp-cp-py |
| 270mS | | 2 | 51.16 | 8.66 | 0.00 | 1.70 | 0.00 | 32.23 | 93.73 | 16.08 | 0.00 | 2.22 | 0.00 | 6.3 | sp-cp-py |
| | | 3 | 57.63 | 8.29 | 0.00 | 0.00 | 0.00 | 34.26 | 100.18 | 14.41 | 0.00 | 0.00 | 0.00 | 6.3 | sp-cp-py |
| | | 4 | 55.39 | 8.61 | 0.00 | 1.25 | 0.00 | 33.60 | 98.86 | 15.10 | 0.00 | 1.56 | 0.00 | 6.3 | sp-cp-py |
| average | | 4 | 54.28 | 8.60 | 0.00 | 1.27 | 0.00 | 33.32 | 97.46 | 15.33 | 0.00 | 1.61 | 0.00 | 6.3 | sp-cp-py |
| | 2 | 1 | 52.87 | 9.42 | 0.18 | 2.05 | 0.00 | 32.87 | 97.39 | 16.65 | 0.68 | 2.58 | 0.00 | 6.3 | sp-cp-py |
| | | 2 | 55.98 | 8.59 | 0.00 | 0.00 | 0.00 | 33.32 | 97.89 | 15.23 | 0.00 | 0.00 | 0.00 | 6.3 | sp-cp-py |
| | | 3 | 55.57 | 8.03 | 0.00 | 0.38 | 0.00 | 32.67 | 96.65 | 14.38 | 0.00 | 0.49 | 0.00 | 6.3 | sp-cp-py |
| | | 4 | 56.93 | 8.98 | 0.26 | 0.00 | 0.00 | 33.71 | 99.88 | 15.51 | 1.05 | 0.00 | 0.00 | 6.3 | sp-cp-py |
| | | 5 | 57.34 | 9.06 | 0.00 | 0.00 | 0.00 | 33.46 | 99.85 | 15.61 | 0.00 | 0.00 | 0.00 | 6.3 | sp-cp-py |
| | | 6 | 50.36 | 12.35 | 0.00 | 0.00 | 0.00 | 35.98 | 98.68 | 22.30 | 0.00 | 0.00 | 0.00 | 6.3 | sp-cp-py |
| | | 7 | 57.76 | 8.50 | 0.00 | 0.00 | 0.00 | 33.61 | 100.12 | 14.69 | 0.00 | 0.00 | 0.00 | 6.3 | sp-cp-py |
| | | 8 | 56.78 | 8.48 | 0.00 | 0.00 | 0.00 | 35.66 | 100.92 | 14.88 | 0.00 | 0.00 | 0.00 | 6.3 | sp-cp-py |
| | | 9 | 57.44 | 9.29 | 0.00 | 0.00 | 0.00 | 34.51 | 101.23 | 15.92 | 0.00 | 0.00 | 0.00 | 6.3 | sp-cp-py |
| | | 10 | 57.76 | 9.15 | 0.00 | 0.00 | 0.00 | 33.74 | 100.65 | 15.64 | 0.00 | 0.00 | 0.00 | 6.3 | sp-cp-py |
| | | 11 | 57.48 | 8.51 | 0.00 | 0.24 | 0.00 | 34.72 | 101.42 | 14.72 | 0.00 | 0.30 | 0.00 | 6.3 | sp-cp-py |
| | | 12 | 56.62 | 8.84 | 0.00 | 0.98 | 0.00 | 34.16 | 100.60 | 15.22 | 0.00 | 1.21 | 0.00 | 6.3 | sp-cp-py |
| average | | 12 | 56.07 | 9.10 | 0.04 | 0.30 | 0.00 | 34.03 | 99.61 | 15.88 | 0.16 | 0.38 | 0.00 | 6.3 | sp-cp-py |
| | 3 | 1 | 64.42 | 2.56 | 0.00 | 0.00 | 0.00 | 33.92 | 100.90 | 4.44 | 0.00 | 0.00 | 0.00 | 6.3 | sp locked in py |
| | | 2 | 65.70 | 2.63 | 0.00 | 0.00 | 0.00 | 34.86 | 100.10 | 4.48 | 0.00 | 0.00 | 0.00 | 6.3 | sp locked in py |
| | | 3 | 64.49 | 2.94 | 0.28 | 0.00 | 0.00 | 35.08 | 102.79 | 5.04 | 1.38 | 0.00 | 0.00 | 6.3 | sp locked in py |
| | | 4 | 64.10 | 3.08 | 0.00 | 0.00 | 0.00 | 34.29 | 101.48 | 5.32 | 0.00 | 0.00 | 0.00 | 6.3 | sp locked in py |
| average | | 4 | 64.68 | 2.80 | 0.07 | 0.00 | 0.00 | 34.54 | 101.32 | 4.82 | 0.36 | 0.00 | 0.00 | 6.3 | sp locked in py |
| | 4 | 1 | 59.10 | 8.29 | 0.00 | 0.00 | 0.26 | 33.85 | 101.51 | 14.07 | 0.00 | 0.00 | 0.20 | 6.3 | sp-py |
| | | 2 | 58.95 | 7.62 | 0.00 | 0.00 | 0.00 | 34.37 | 100.94 | 13.14 | 0.00 | 0.00 | 0.00 | 6.3 | sp-py |
| | | 3 | 57.61 | 8.55 | 0.00 | 0.05 | 0.00 | 34.11 | 100.51 | 14.79 | 0.00 | 0.06 | 0.00 | 6.3 | sp-py |
| average | | 3 | 58.55 | 8.15 | 0.00 | 0.02 | 0.09 | 34.11 | 100.99 | 14.00 | 0.00 | 0.02 | 0.07 | 6.3 | sp-py |
| | 5 | 1 | 56.69 | 9.02 | 0.00 | 0.00 | 0.00 | 34.38 | 100.08 | 15.70 | 0.00 | 0.00 | 0.00 | 6.3 | sp-po-py* |
| | | 2 | 58.02 | 8.25 | 0.00 | 0.00 | 0.00 | 33.80 | 100.07 | 14.27 | 0.00 | 0.00 | 0.00 | 6.3 | sp-po-py* |
| | | 3 | 51.81 | 10.39 | 0.00 | 0.00 | 0.00 | 36.46 | 98.66 | 19.01 | 0.00 | 0.00 | 0.00 | 6.3 | sp-po-py* |
| average | | 3 | 55.51 | 9.22 | 0.00 | 0.00 | 0.00 | 34.88 | 99.60 | 16.28 | 0.00 | 0.00 | 0.00 | 6.3 | sp-po-py* |
| | 6 | 1 | 55.67 | 9.61 | 0.00 | 0.00 | 0.25 | 34.07 | 99.61 | 16.77 | 0.00 | 0.00 | 0.19 | 6.3 | sp-po-py** |
| | | 2 | 56.76 | 9.56 | 0.15 | 0.00 | 0.00 | 33.78 | 100.48 | 16.43 | 0.60 | 0.00 | 0.00 | 6.3 | sp-po-py** |
| | | 3 | 56.50 | 9.54 | 0.00 | 0.00 | 0.00 | 33.87 | 99.91 | 16.50 | 0.00 | 0.00 | 0.00 | 6.3 | sp-po-py** |
| average | | 3 | 56.31 | 9.57 | 0.05 | 0.00 | 0.08 | 33.91 | 100.00 | 16.57 | 0.20 | 0.00 | 0.06 | 6.3 | sp-po-py** |

py = pyrite, po = pyrrhotite, sp = sphalerite, ga=galena cp = chalcopyrite, and mag = magnetite

*sp-py-po in mutual contact
**sp locked in py with po
#sp-py-po not in mutual contact

**Appendix 8.2. Compositional variation of sphalerite from the F(J) lens, Rosebery south-end, western Tasmania (Continued).**

| Sample No./ Section | grain No. | spot No. | Zn wt% | Fe wt% | Mn wt% | Cu wt% | Cd wt% | S wt% | Total wt% | FeS mole % | MnS mole % | CuS mole % | CdS mole % | Au g/t | Associated sulphides/oxides |
|---|---|---|---|---|---|---|---|---|---|---|---|---|---|---|---|
| R3023-2/ | 7 | 1 | 56.33 | 9.42 | 0.00 | 0.00 | 0.00 | 34.07 | 99.82 | 16.37 | 0.00 | 0.00 | 0.00 | 6.3 | sp-po-py** |
| 270mS | | 2 | 56.32 | 9.28 | 0.00 | 0.00 | 0.00 | 33.78 | 99.38 | 16.17 | 0.00 | 0.00 | 0.00 | 6.3 | sp-po-py** |
| | | 3 | 56.53 | 9.35 | 0.00 | 0.00 | 0.00 | 33.76 | 99.64 | 16.22 | 0.00 | 0.00 | 0.00 | 6.3 | sp-po-py** |
| | | 4 | 56.27 | 8.92 | 0.00 | 0.39 | 0.00 | 34.54 | 99.83 | 15.56 | 0.00 | 0.49 | 0.00 | 6.3 | sp-po-py** |
| | | 5 | 56.52 | 9.27 | 0.00 | 0.00 | 0.00 | 33.63 | 99.22 | 16.11 | 0.00 | 0.00 | 0.00 | 6.3 | sp-po-py** |
| average | | 5 | 56.39 | 9.25 | 0.00 | 0.08 | 0.00 | 33.96 | 99.58 | 16.08 | 0.00 | 0.10 | 0.00 | 6.3 | sp-po-py** |
| | 8 | 1 | 58.70 | 7.99 | 0.00 | 0.00 | 0.00 | 34.25 | 100.94 | 13.74 | 0.00 | 0.00 | 0.00 | 6.3 | sp-py |
| | | 2 | 57.40 | 8.64 | 0.00 | 0.00 | 0.00 | 34.43 | 100.47 | 14.98 | 0.00 | 0.00 | 0.00 | 6.3 | sp-py |
| | | 3 | 57.73 | 8.95 | 0.00 | 0.00 | 0.00 | 35.15 | 101.83 | 15.36 | 0.00 | 0.00 | 0.00 | 6.3 | sp-py |
| average | | 3 | 57.94 | 8.53 | 0.00 | 0.00 | 0.00 | 34.61 | 101.08 | 14.69 | 0.00 | 0.00 | 0.00 | 6.3 | sp-py |
| | 9 | 1 | 55.08 | 10.15 | 0.00 | 0.00 | 0.00 | 33.80 | 99.02 | 17.74 | 0.00 | 0.00 | 0.00 | 6.3 | sp-po-py** |
| | | 2 | 55.30 | 9.26 | 0.00 | 0.81 | 0.00 | 33.54 | 98.91 | 16.18 | 0.00 | 1.02 | 0.00 | 6.3 | sp-po-py** |
| | | 3 | 54.96 | 9.09 | 0.00 | 0.59 | 0.00 | 33.31 | 97.95 | 16.07 | 0.00 | 0.75 | 0.00 | 6.3 | sp-po-py** |
| average | | 3 | 55.11 | 9.50 | 0.00 | 0.47 | 0.00 | 33.55 | 98.63 | 16.67 | 0.00 | 0.60 | 0.00 | 6.3 | sp-po-py** |
| | 10 | 1 | 57.12 | 9.39 | 0.22 | 0.00 | 0.00 | 33.81 | 100.53 | 16.08 | 0.88 | 0.00 | 0.00 | 6.3 | sp-py |
| | | 2 | 56.02 | 8.37 | 0.15 | 0.00 | 0.00 | 33.86 | 99.27 | 14.85 | 0.62 | 0.00 | 0.00 | 6.3 | sp-py |
| | | 3 | 56.81 | 8.22 | 0.19 | 0.00 | 0.00 | 33.24 | 98.46 | 14.43 | 0.80 | 0.00 | 0.00 | 6.3 | sp-py |
| average | | 3 | 56.65 | 8.66 | 0.19 | 0.00 | 0.00 | 33.64 | 99.42 | 15.13 | 0.77 | 0.00 | 0.00 | 6.3 | sp-py |
| | 11 | 1 | 57.02 | 8.34 | 0.00 | 0.00 | 0.00 | 34.72 | 100.11 | 14.62 | 0.00 | 0.00 | 0.00 | 6.3 | sp-cp-po-py |
| | | 2 | 57.13 | 8.82 | 0.00 | 0.00 | 0.00 | 34.24 | 100.28 | 15.31 | 0.00 | 0.00 | 0.00 | 6.3 | sp-cp-po-py |
| average | | 2 | 57.08 | 8.58 | 0.00 | 0.00 | 0.00 | 34.48 | 100.20 | 14.96 | 0.00 | 0.00 | 0.00 | 6.3 | sp-cp-po-py |
| | 12 | 1 | 56.60 | 8.13 | 0.00 | 0.23 | 0.00 | 32.73 | 97.69 | 14.34 | 0.00 | 0.30 | 0.00 | 6.3 | sp-py |
| | | 2 | 52.01 | 11.16 | 0.00 | 0.00 | 0.00 | 33.83 | 97.01 | 20.07 | 0.00 | 0.00 | 0.00 | 6.3 | sp-py |
| | | 3 | 56.22 | 8.24 | 0.00 | 0.38 | 0.00 | 32.40 | 97.24 | 14.56 | 0.00 | 0.49 | 0.00 | 6.3 | sp-py |
| | | 4 | 55.74 | 8.46 | 0.00 | 0.00 | 0.00 | 32.72 | 96.91 | 15.09 | 0.00 | 0.00 | 0.00 | 6.3 | sp-py |
| | | 5 | 56.61 | 8.34 | 0.00 | 0.00 | 0.00 | 33.50 | 98.46 | 14.71 | 0.00 | 0.00 | 0.00 | 6.3 | sp-py |
| average | | 5 | 55.44 | 8.87 | 0.00 | 0.12 | 0.00 | 33.04 | 97.46 | 15.74 | 0.00 | 0.15 | 0.00 | 6.3 | sp-py |
| | 13 | 1 | 56.61 | 8.34 | 0.00 | 0.00 | 0.00 | 33.91 | 98.86 | 14.71 | 0.00 | 0.00 | 0.00 | 6.3 | sp-cp-po-py |
| | | 2 | 56.80 | 8.73 | 0.00 | 0.00 | 0.00 | 33.89 | 99.67 | 15.25 | 0.00 | 0.00 | 0.00 | 6.3 | sp-cp-po-py |
| | | 3 | 47.61 | 11.96 | 0.00 | 5.83 | 0.00 | 33.94 | 99.35 | 20.71 | 0.00 | 6.86 | 0.00 | 6.3 | sp-cp-po-py |
| | | 4 | 55.22 | 8.89 | 0.00 | 1.01 | 0.25 | 34.07 | 99.44 | 15.58 | 0.00 | 1.25 | 0.19 | 6.3 | sp-cp-po-py |
| average | | 4 | 54.06 | 9.48 | 0.00 | 1.71 | 0.06 | 33.95 | 99.33 | 16.57 | 0.00 | 2.11 | 0.05 | 6.3 | sp-cp-po-py |
| | 14 | 1 | 55.08 | 10.15 | 0.00 | 0.00 | 0.00 | 33.80 | 99.02 | 17.74 | 0.00 | 0.00 | 0.00 | 6.3 | sp-po-py** |
| | | 2 | 55.30 | 9.26 | 0.00 | 0.81 | 0.00 | 33.54 | 98.91 | 16.18 | 0.00 | 1.02 | 0.00 | 6.3 | sp-po-py** |
| | | 3 | 54.96 | 9.09 | 0.00 | 0.59 | 0.00 | 33.31 | 97.95 | 16.07 | 0.00 | 0.75 | 0.00 | 6.3 | sp-po-py** |
| | | 4 | 55.98 | 9.87 | 0.00 | 1.08 | 0.00 | 33.56 | 100.49 | 16.83 | 0.00 | 1.34 | 0.00 | 6.3 | sp-po-py** |
| | | 5 | 56.81 | 9.40 | 0.00 | 0.33 | 0.00 | 33.96 | 100.40 | 16.14 | 0.00 | 0.41 | 0.00 | 6.3 | sp-po-py** |
| average | | 5 | 55.63 | 9.55 | 0.00 | 0.56 | 0.00 | 33.63 | 99.35 | 16.60 | 0.00 | 0.71 | 0.00 | 6.3 | sp-po-py** |
| average | 14 | 59 | 56.69 | 8.56 | 0.02 | 0.32 | 0.02 | 33.97 | 99.57 | 14.95 | 0.11 | 0.41 | 0.01 | 6.3 | |

py = pyrite, po = pyrrhotite, sp = sphalerite, ga=galena cp = chalcopyrite, and mag = magnetite

*sp-py-po in mutual contact
**sp locked in py with po
#sp-py-po not in mutual contact

**Appendix 8.2. Compositional variation of sphalerite from the F(J) lens, Rosebery south-end, western Tasmania (Continued).**

| Sample No./ Section | grain No. | spot No. | Zn wt% | Fe wt% | Mn wt% | Cu wt% | Cd wt% | S wt% | Total wt% | FeS mole % | MnS mole % | CuS mole % | CdS mole % | Au g/t | Associated sulphides/oxides |
|---|---|---|---|---|---|---|---|---|---|---|---|---|---|---|---|
| R3023-8/ | 1 | 1 | 60.23 | 4.95 | 0.00 | 0.00 | 0.00 | 33.01 | 98.18 | 8.78 | 0.00 | 0.00 | 0.00 | 26.2 | texture unknown |
| 270mS | | 2 | 60.68 | 5.23 | 0.11 | 0.00 | 0.22 | 33.23 | 99.48 | 9.13 | 0.52 | 0.00 | 0.17 | 26.2 | texture unknown |
| | | 3 | 61.35 | 5.23 | 0.00 | 0.00 | 0.00 | 33.51 | 100.09 | 9.07 | 0.00 | 0.00 | 0.00 | 26.2 | texture unknown |
| | | 4 | 60.33 | 5.07 | 0.14 | 0.00 | 0.35 | 32.92 | 98.80 | 8.91 | 0.66 | 0.00 | 0.28 | 26.2 | texture unknown |
| | | 5 | 61.01 | 5.31 | 0.00 | 0.00 | 0.31 | 33.07 | 99.84 | 9.22 | 0.00 | 0.00 | 0.25 | 26.2 | texture unknown |
| average | | 5 | 60.72 | 5.16 | 0.08 | 0.00 | 0.18 | 33.15 | 99.28 | 9.02 | 0.38 | 0.00 | 0.14 | 26.2 | texture unknown |
| | 2 | 1 | 53.89 | 8.26 | 0.20 | 0.00 | 0.30 | 33.22 | 95.86 | 15.11 | 0.83 | 0.00 | 0.24 | 26.2 | sp-po-py-mag |
| | | 2 | 56.10 | 8.80 | 0.00 | 0.00 | 0.00 | 33.91 | 98.81 | 15.51 | 0.00 | 0.00 | 0.00 | 26.2 | sp-po-py-mag |
| average | | 2 | 57.93 | 8.53 | 0.10 | 0.00 | 0.15 | 33.57 | 97.34 | 14.66 | 0.41 | 0.00 | 0.12 | 26.2 | sp-po-py-mag |
| | 3 | 1 | 62.43 | 4.21 | 0.16 | 0.00 | 0.19 | 33.37 | 100.36 | 7.28 | 0.78 | 0.00 | 0.15 | 26.2 | texture unknown |
| | | 2 | 60.66 | 3.99 | 0.00 | 0.00 | 0.00 | 33.01 | 97.95 | 7.15 | 0.00 | 0.00 | 0.00 | 26.2 | texture unknown |
| average | | 2 | 61.55 | 4.10 | 0.08 | 0.00 | 0.10 | 33.19 | 99.16 | 7.22 | 0.40 | 0.00 | 0.08 | 26.2 | texture unknown |
| | 4 | 1 | 60.39 | 4.16 | 0.00 | 0.00 | 0.22 | 32.66 | 97.43 | 7.45 | 0.00 | 0.00 | 0.18 | 26.2 | texture unknown |
| | | 2 | 59.13 | 4.30 | 0.11 | 0.00 | 0.19 | 32.16 | 95.60 | 7.82 | 0.55 | 0.00 | 0.16 | 26.2 | texture unknown |
| average | | 2 | 59.76 | 4.23 | 0.06 | 0.00 | 0.21 | 32.41 | 96.52 | 7.63 | 0.30 | 0.00 | 0.17 | 26.2 | texture unknown |
| | 5 | 1 | 52.16 | 8.22 | 0.00 | 0.47 | 0.43 | 33.72 | 94.99 | 15.39 | 0.00 | 0.60 | 0.34 | 26.2 | sp-po-py-mag |
| | | 2 | 57.56 | 8.22 | 0.00 | 0.00 | 0.00 | 33.88 | 99.79 | 14.32 | 0.00 | 0.00 | 0.00 | 26.2 | sp-po-py-mag |
| average | | 2 | 54.86 | 8.22 | 0.00 | 0.24 | 0.22 | 33.80 | 97.39 | 14.84 | 0.00 | 0.31 | 0.17 | 26.2 | sp-po-py-mag |
| | 6 | 1 | 60.53 | 6.62 | 0.00 | 0.00 | 0.00 | 32.91 | 100.05 | 11.35 | 0.00 | 0.00 | 0.00 | 26.2 | texture unknown |
| | | 2 | 60.25 | 6.56 | 0.00 | 0.00 | 0.00 | 33.17 | 99.98 | 11.30 | 0.00 | 0.00 | 0.00 | 26.2 | texture unknown |
| | | 3 | 60.95 | 6.91 | 0.00 | 0.00 | 0.00 | 32.84 | 100.69 | 11.72 | 0.00 | 0.00 | 0.00 | 26.2 | texture unknown |
| average | | 3 | 60.60 | 6.74 | 0.00 | 0.00 | 0.00 | 33.01 | 100.34 | 11.51 | 0.00 | 0.00 | 0.00 | 26.2 | texture unknown |
| average | 6 | 16 | 59.24 | 6.16 | 0.05 | 0.04 | 0.14 | 33.19 | 98.33 | 10.81 | 0.25 | 0.05 | 0.11 | 26.2 | |
| R3492-3B/ | 1 | 1 | 63.73 | 2.94 | 0.26 | 0.00 | 0.00 | 33.10 | 100.03 | 5.10 | 1.35 | 0.00 | 0.00 | 22.0 | sp-cp-py-ga |
| 280mS | | 2 | 63.48 | 3.15 | 0.14 | 0.00 | 0.00 | 33.00 | 99.77 | 5.48 | 0.73 | 0.00 | 0.00 | 22.0 | sp-cp-py-ga |
| | | 3 | 63.06 | 2.98 | 0.29 | 0.00 | 0.00 | 33.76 | 100.09 | 5.21 | 1.48 | 0.00 | 0.00 | 22.0 | sp-cp-py-ga |
| average | | 3 | 63.42 | 3.02 | 0.23 | 0.00 | 0.00 | 33.29 | 99.96 | 5.26 | 1.19 | 0.00 | 0.00 | 22.0 | sp-cp-py-ga |
| | 2 | 1 | 63.96 | 2.95 | 0.32 | 0.00 | 0.29 | 33.52 | 99.93 | 5.08 | 1.62 | 0.00 | 0.23 | 22.0 | sp-cp-py-ga |
| | | 2 | 64.02 | 2.91 | 0.00 | 0.00 | 0.28 | 33.56 | 100.78 | 5.04 | 0.00 | 0.00 | 0.22 | 22.0 | sp-cp-py-ga |
| average | | 2 | 63.99 | 2.93 | 0.16 | 0.00 | 0.29 | 33.54 | 100.36 | 5.06 | 0.82 | 0.00 | 0.23 | 22.0 | sp-cp-py-ga |
| average | 2 | 5 | 63.71 | 2.98 | 0.20 | 0.00 | 0.14 | 33.41 | 100.16 | 5.16 | 1.00 | 0.00 | 0.11 | 22.0 | |
| R3033-29/ | 1 | 1 | 61.36 | 3.59 | 0.18 | 0.00 | 0.38 | 33.48 | 98.98 | 6.37 | 0.89 | 0.00 | 0.31 | 9.3 | isolated sp |
| 300mS | | 2 | 61.71 | 3.44 | 0.15 | 0.00 | 0.00 | 33.76 | 99.06 | 6.11 | 0.76 | 0.00 | 0.00 | 9.3 | isolated sp |
| | | 3 | 61.75 | 3.69 | 0.20 | 0.00 | 0.00 | 33.85 | 99.49 | 6.51 | 0.99 | 0.00 | 0.00 | 9.3 | isolated sp |
| average | | 3 | 61.61 | 3.57 | 0.18 | 0.00 | 0.13 | 33.70 | 99.18 | 6.33 | 0.88 | 0.00 | 0.10 | 9.3 | isolated sp |
| | 2 | 1 | 60.97 | 4.03 | 0.14 | 0.00 | 0.24 | 33.48 | 98.86 | 7.15 | 0.69 | 0.00 | 0.19 | 9.3 | isolated sp |
| | | 2 | 60.34 | 4.44 | 0.00 | 0.00 | 0.39 | 34.03 | 99.20 | 7.90 | 0.00 | 0.00 | 0.31 | 9.3 | isolated sp |
| | | 3 | 60.48 | 4.26 | 0.18 | 0.00 | 0.00 | 33.75 | 98.67 | 7.59 | 0.87 | 0.00 | 0.00 | 9.3 | isolated sp |
| average | | 3 | 60.60 | 4.24 | 0.11 | 0.00 | 0.21 | 33.75 | 98.91 | 7.55 | 0.53 | 0.00 | 0.17 | 9.3 | isolated sp |
| | 3 | 1 | 56.86 | 8.18 | 0.00 | 0.18 | 0.00 | 33.67 | 98.90 | 14.37 | 0.00 | 0.23 | 0.00 | 9.3 | sp-po-py# |
| | | 2 | 57.92 | 8.41 | 0.00 | 0.00 | 0.00 | 33.65 | 99.98 | 14.53 | 0.00 | 0.00 | 0.00 | 9.3 | sp-po-py# |
| | | 3 | 57.64 | 7.96 | 0.00 | 0.00 | 0.26 | 33.96 | 99.81 | 13.88 | 0.00 | 0.00 | 0.20 | 9.3 | sp-po-py# |
| average | | 3 | 57.47 | 8.18 | 0.00 | 0.06 | 0.09 | 33.76 | 99.56 | 14.26 | 0.00 | 0.08 | 0.07 | 9.3 | sp-po-py# |
| average | 3 | 9 | 59.89 | 5.33 | 0.10 | 0.02 | 0.14 | 33.74 | 99.22 | 9.38 | 0.47 | 0.03 | 0.11 | 9.3 | |

py = pyrite, po = pyrrhotite, sp = sphalerite, ga=galena cp = chalcopyrite, and mag = magnetite

*sp-py-po in mutual contact
**sp locked in py with po
#sp-py-po not in mutual contact

**APPENDIX 8.3. Compositional variation of sphalerites from J-K(P) and R lens, Hercules deposit, western Tasmania.**

| Sample No. | Grain No. | spot No. | Zn wt% | Fe wt% | Mn wt% | Cu wt% | Cd wt% | S wt% | Total wt% | FeS mole% | MnS mole% | CuS mole% | CdS mole% | Au g/t | Associated sulphides |
|---|---|---|---|---|---|---|---|---|---|---|---|---|---|---|---|
| H145-1 | 1 | 1 | 64.07 | 1.09 | 0.00 | 0.34 | 0.22 | 33.70 | 99.42 | 1.94 | 0.00 | 0.53 | 0.19 | 9.0 | sp-ga-Au-py |
| @135' | | 2 | 64.14 | 1.15 | 0.00 | 0.32 | 0.28 | 33.52 | 99.41 | 2.04 | 0.00 | 0.50 | 0.25 | 9.0 | |
| average | | 2 | 64.11 | 1.12 | 0.00 | 0.33 | 0.25 | 33.61 | 99.42 | 1.99 | 0.00 | 0.52 | 0.22 | 9.0 | |
| | 2 | 1 | 64.05 | 1.59 | 0.00 | 0.54 | 0.00 | 33.48 | 99.66 | 2.80 | 0.00 | 0.84 | 0.00 | 9.0 | sp-ga-Au-py |
| | | 2 | 64.52 | 1.20 | 0.00 | 0.00 | 0.40 | 34.83 | 100.95 | 2.12 | 0.00 | 0.00 | 0.35 | 9.0 | |
| average | | 2 | 64.29 | 1.40 | 0.00 | 0.27 | 0.20 | 34.16 | 100.31 | 2.46 | 0.00 | 0.42 | 0.18 | 9.0 | |
| average | 2 | 4 | 64.24 | 1.33 | 0.00 | 0.29 | 0.21 | 34.02 | 100.08 | 2.34 | 0.00 | 0.44 | 0.19 | 9.0 | |
| H1033-6 | 1 | 1 | 60.97 | 4.42 | 0.21 | 0.02 | 0.13 | 30.94 | 96.69 | 7.78 | 0.38 | 0.03 | 0.11 | 1.4 | massive sp |
| @ 131' | | 2 | 60.69 | 4.36 | 0.23 | 0.03 | 0.18 | 31.51 | 97.00 | 7.71 | 0.41 | 0.05 | 0.16 | 1.4 | |
| | | 3 | 61.29 | 4.49 | 0.26 | 0.03 | 0.15 | 32.99 | 99.21 | 7.85 | 0.46 | 0.05 | 0.13 | 1.4 | |
| | | 4 | 61.43 | 4.47 | 0.22 | 0.02 | 0.15 | 32.92 | 99.21 | 7.81 | 0.39 | 0.03 | 0.13 | 1.4 | |
| average | | 4 | 61.10 | 4.44 | 0.23 | 0.03 | 0.15 | 32.09 | 98.03 | 7.79 | 0.41 | 0.04 | 0.13 | 1.4 | |
| | 2 | 1 | 61.38 | 4.40 | 0.25 | 0.02 | 0.15 | 33.09 | 99.29 | 7.69 | 0.44 | 0.03 | 0.13 | 1.4 | massive sp |
| | | 2 | 61.01 | 4.61 | 0.24 | 0.00 | 0.16 | 33.09 | 99.11 | 8.08 | 0.43 | 0.00 | 0.14 | 1.4 | |
| average | | 2 | 61.20 | 4.51 | 0.25 | 0.01 | 0.16 | 33.09 | 99.20 | 7.89 | 0.44 | 0.02 | 0.13 | 1.4 | |
| average | 2 | 6 | 61.17 | 4.49 | 0.24 | 0.01 | 0.15 | 32.84 | 98.91 | 7.86 | 0.43 | 0.02 | 0.13 | 1.4 | |
| H802-1 | 1 | 1 | 65.38 | 1.79 | 0.08 | 0.37 | 0.13 | 32.72 | 100.47 | 3.08 | 0.14 | 0.56 | 0.11 | 4.4 | sp-py |
| @ 30.6' | | 2 | 65.12 | 2.06 | 0.09 | 0.09 | 0.11 | 32.85 | 100.32 | 3.56 | 0.16 | 0.14 | 0.09 | 4.4 | |
| | | 3 | 64.91 | 1.94 | 0.15 | 0.01 | 0.08 | 33.01 | 100.10 | 3.37 | 0.26 | 0.02 | 0.07 | 4.4 | |
| average | | 3 | 65.14 | 1.93 | 0.11 | 0.16 | 0.11 | 32.86 | 100.30 | 3.33 | 0.19 | 0.24 | 0.09 | 4.4 | |
| | 2 | 1 | 64.87 | 1.87 | 0.11 | 0.16 | 0.15 | 32.92 | 100.08 | 3.25 | 0.19 | 0.24 | 0.13 | 4.4 | sp-py |
| | | 2 | 64.63 | 1.99 | 0.11 | 0.06 | 0.17 | 32.89 | 99.85 | 3.46 | 0.19 | 0.09 | 0.15 | 4.4 | |
| average | | 2 | 64.75 | 1.93 | 0.11 | 0.11 | 0.16 | 32.91 | 99.97 | 3.35 | 0.19 | 0.17 | 0.14 | 4.4 | |
| average | 2 | 5 | 64.85 | 1.93 | 0.11 | 0.12 | 0.15 | 32.89 | 100.05 | 3.35 | 0.19 | 0.19 | 0.13 | 4.4 | |
| H831-9 | 1 | 1 | 64.06 | 2.06 | 0.12 | 0.22 | 0.18 | 32.65 | 99.29 | 3.60 | 0.21 | 0.34 | 0.16 | 12.9 | sp-py |
| @ 95.0' | | 2 | 63.73 | 1.83 | 0.07 | 0.17 | 0.14 | 32.66 | 98.60 | 3.24 | 0.13 | 0.26 | 0.12 | 12.9 | |
| | | 3 | 64.04 | 2.13 | 0.13 | 0.02 | 0.21 | 32.55 | 99.08 | 3.73 | 0.23 | 0.03 | 0.18 | 12.9 | |
| average | | 3 | 63.94 | 2.01 | 0.11 | 0.14 | 0.18 | 32.62 | 98.99 | 3.52 | 0.19 | 0.21 | 0.15 | 12.9 | |
| | 2 | 1 | 62.76 | 2.51 | 0.07 | 0.92 | 0.13 | 32.78 | 99.17 | 4.40 | 0.12 | 1.42 | 0.11 | 12.9 | sp in py |
| | | 2 | 64.24 | 1.66 | 0.04 | 0.15 | 0.16 | 32.50 | 98.75 | 2.92 | 0.07 | 0.23 | 0.14 | 12.9 | |
| | | 3 | 64.61 | 1.67 | 0.07 | 0.12 | 0.19 | 32.86 | 99.52 | 2.92 | 0.12 | 0.18 | 0.17 | 12.9 | |
| average | | 3 | 63.87 | 1.95 | 0.06 | 0.40 | 0.16 | 32.71 | 99.15 | 3.42 | 0.11 | 0.61 | 0.14 | 12.9 | |
| average | 2 | 6 | 63.88 | 1.96 | 0.07 | 0.34 | 0.16 | 32.69 | 99.12 | 3.44 | 0.12 | 0.53 | 0.14 | 12.9 | |
| H1034-4 | 1 | 1 | 61.32 | 3.18 | 0.17 | 1.95 | 0.10 | 32.79 | 99.51 | 5.53 | 0.30 | 2.98 | 0.09 | 7.9 | sp locked in py |
| @ 119' | | 2 | 60.26 | 3.86 | 0.05 | 2.80 | 0.12 | 32.97 | 100.06 | 6.67 | 0.09 | 4.25 | 0.10 | 7.9 | |
| | | 3 | 60.78 | 3.76 | 0.05 | 2.10 | 0.17 | 32.86 | 99.72 | 6.52 | 0.09 | 3.20 | 0.15 | 7.9 | |
| | | 4 | 58.99 | 7.25 | 0.29 | 0.22 | 0.14 | 32.86 | 99.75 | 12.46 | 0.51 | 0.33 | 0.12 | 7.9 | |
| average | | 4 | 60.34 | 4.51 | 0.14 | 1.77 | 0.13 | 32.87 | 99.76 | 7.80 | 0.25 | 2.69 | 0.11 | 7.9 | |
| H794-2 | 1 | 1 | 61.82 | 3.90 | 0.55 | 0.04 | 0.15 | 32.52 | 98.98 | 6.80 | 0.97 | 0.06 | 0.13 | 0.5 | massive sp |
| @ 37' | | 2 | 62.34 | 3.77 | 0.49 | 0.04 | 0.16 | 33.25 | 100.05 | 6.54 | 0.86 | 0.06 | 0.14 | 0.5 | |
| average | | 2 | 62.08 | 3.84 | 0.52 | 0.04 | 0.16 | 32.89 | 99.52 | 6.67 | 0.92 | 0.06 | 0.13 | 0.5 | |
| | 2 | 1 | 62.74 | 3.22 | 0.28 | 0.45 | 0.08 | 33.25 | 100.02 | 5.60 | 0.49 | 0.69 | 0.07 | 0.5 | sp-py |
| | | 2 | 62.32 | 3.89 | 0.40 | 0.25 | 0.17 | 33.37 | 100.40 | 6.73 | 0.70 | 0.38 | 0.15 | 0.5 | |
| average | | 2 | 62.53 | 3.56 | 0.34 | 0.35 | 0.13 | 33.31 | 100.21 | 6.16 | 0.60 | 0.53 | 0.11 | 0.5 | |
| | 3 | 1 | 60.79 | 5.33 | 0.51 | 0.04 | 0.15 | 33.11 | 99.93 | 9.21 | 0.90 | 0.06 | 0.13 | 0.5 | sp locked in py |
| | | 2 | 61.04 | 5.23 | 0.50 | 0.00 | 0.22 | 33.32 | 100.31 | 9.02 | 0.88 | 0.00 | 0.19 | 0.5 | |
| average | 3 | 2 | 60.92 | 5.28 | 0.51 | 0.02 | 0.19 | 33.22 | 100.12 | 9.11 | 0.89 | 0.03 | 0.16 | 0.5 | |
| average | 3 | 6.00 | 61.77 | 4.33 | 0.44 | 0.16 | 0.16 | 33.21 | 100.07 | 7.50 | 0.77 | 0.25 | 0.13 | 0.5 | |

sp = sphalerite, py = pyrite, ga = galena, tt = tetrahedrite and Au = electrum

**APPENDIX 8.4. Compositional variation of sphalerite from the South Hercules deposit, western Tasmania.**

| Sample No. /Section | Grain No. | spot No. | Zn wt% | Fe wt% | Mn wt% | Cu wt% | Cd wt% | S wt% | Total wt% | FeS mole% | MnS mole% | CuS mole% | CdS mole% | Au g/t | Associated sulphides |
|---|---|---|---|---|---|---|---|---|---|---|---|---|---|---|---|
| H1106 | 1 | 1 | 60.54 | 1.23 | 0.26 | 0.00 | 0.00 | 36.17 | 98.20 | 2.31 | 0.50 | 0.00 | 0.00 | 0.8 | sp locked in py |
| @ 28.5m | | 2 | 62.45 | 1.33 | 0.40 | 0.00 | 0.00 | 34.72 | 98.90 | 2.41 | 0.74 | 0.00 | 0.00 | 0.8 | |
| 5600mN | | 2 | 61.50 | 1.28 | 0.33 | 0.00 | 0.00 | 35.45 | 98.55 | 2.36 | 0.62 | 0.00 | 0.00 | 0.8 | |
| | 2 | 1 | 62.18 | 1.35 | 0.43 | 0.00 | 0.00 | 33.68 | 97.64 | 2.46 | 0.80 | 0.00 | 0.00 | 0.8 | sp attached to py |
| | | 2 | 62.50 | 1.69 | 0.66 | 0.00 | 0.00 | 33.85 | 98.70 | 3.03 | 1.20 | 0.00 | 0.00 | 0.8 | |
| average | | 2 | 62.34 | 1.52 | 0.55 | 0.00 | 0.00 | 33.77 | 98.17 | 2.75 | 1.00 | 0.00 | 0.00 | 0.8 | |
| | 3 | 1 | 62.31 | 2.13 | 1.03 | 0.00 | 0.00 | 33.33 | 98.80 | 3.78 | 1.86 | 0.00 | 0.00 | 0.8 | isolated sp bleb |
| | | 2 | 63.32 | 1.24 | 0.35 | 0.00 | 0.00 | 33.32 | 98.23 | 2.23 | 0.64 | 0.00 | 0.00 | 0.8 | |
| | | 3 | 63.34 | 1.69 | 0.53 | 0.00 | 0.00 | 33.86 | 99.42 | 3.00 | 0.96 | 0.00 | 0.00 | 0.8 | |
| average | | 3 | 62.99 | 1.69 | 0.64 | 0.00 | 0.00 | 33.50 | 98.82 | 3.00 | 1.15 | 0.00 | 0.00 | 0.8 | |
| | 4 | 1 | 63.00 | 1.84 | 0.61 | 0.00 | 0.00 | 33.75 | 99.20 | 3.27 | 1.10 | 0.00 | 0.00 | 0.8 | isolated sp grain |
| | | 2 | 64.18 | 1.82 | 0.51 | 0.00 | 0.00 | 33.27 | 99.78 | 3.18 | 0.91 | 0.00 | 0.00 | 0.8 | |
| average | | 2 | 63.59 | 1.83 | 0.56 | 0.00 | 0.00 | 33.51 | 99.49 | 3.23 | 1.00 | 0.00 | 0.00 | 0.8 | |
| | 5 | 1 | 59.85 | 5.93 | 0.37 | 0.00 | 0.00 | 33.44 | 99.59 | 10.32 | 0.65 | 0.00 | 0.00 | 0.8 | sp near py |
| | | 2 | 58.40 | 5.95 | 0.59 | 0.00 | 0.33 | 32.85 | 98.12 | 10.51 | 1.06 | 0.00 | 0.29 | 0.8 | |
| | | 3 | 59.99 | 5.85 | 0.50 | 0.00 | 0.00 | 33.27 | 99.61 | 10.15 | 0.88 | 0.00 | 0.00 | 0.8 | |
| average | | 3 | 59.41 | 5.91 | 0.49 | 0.00 | 0.11 | 33.19 | 99.11 | 10.33 | 0.86 | 0.00 | 0.10 | 0.8 | |
| | 6 | 1 | 60.23 | 5.69 | 0.48 | 0.00 | 0.00 | 33.61 | 100.01 | 9.87 | 0.85 | 0.00 | 0.00 | 0.8 | sp-py |
| | | 2 | 59.80 | 4.89 | 0.43 | 0.00 | 0.23 | 33.20 | 98.55 | 8.65 | 0.77 | 0.00 | 0.20 | 0.8 | |
| | | 3 | 58.94 | 5.67 | 0.55 | 0.00 | 0.32 | 33.25 | 98.73 | 9.99 | 0.99 | 0.00 | 0.28 | 0.8 | |
| average | | 3 | 59.66 | 5.42 | 0.49 | 0.00 | 0.18 | 33.35 | 99.10 | 9.51 | 0.87 | 0.00 | 0.16 | 0.8 | |
| average | 6 | 17 | 61.45 | 3.34 | 0.53 | 0.00 | 0.06 | 33.55 | 98.93 | 5.88 | 0.96 | 0.00 | 0.05 | 0.8 | |
| H1117-8/ | 1 | 1 | 59.79 | 5.60 | 0.29 | 0.00 | 0.00 | 33.90 | 99.58 | 9.83 | 0.52 | 0.00 | 0.00 | 4.0 | sp locked in py |
| @ 48.1m | | 2 | 60.86 | 5.08 | 0.30 | 0.00 | 0.00 | 34.17 | 100.41 | 8.85 | 0.53 | 0.00 | 0.00 | 4.0 | |
| 5600mN | | 3 | 59.89 | 5.62 | 0.21 | 0.00 | 0.00 | 33.31 | 99.03 | 9.86 | 0.37 | 0.00 | 0.00 | 4.0 | |
| average | | 3 | 60.18 | 5.43 | 0.27 | 0.00 | 0.00 | 33.79 | 99.67 | 9.51 | 0.47 | 0.00 | 0.00 | 4.0 | |
| | 2 | 1 | 59.53 | 5.85 | 0.49 | 0.00 | 0.21 | 33.51 | 99.59 | 10.21 | 0.87 | 0.00 | 0.18 | 4.0 | recrystallised sp |
| | | 2 | 60.50 | 5.80 | 0.30 | 0.00 | 0.00 | 33.49 | 100.09 | 10.04 | 0.53 | 0.00 | 0.00 | 4.0 | |
| | | 3 | 58.14 | 5.06 | 0.13 | 2.33 | 0.35 | 34.07 | 100.08 | 8.86 | 0.23 | 3.59 | 0.30 | 4.0 | |
| average | | 3 | 59.39 | 5.57 | 0.31 | 0.78 | 0.19 | 33.69 | 99.92 | 9.70 | 0.54 | 1.19 | 0.16 | 4.0 | |
| average | 2 | 6 | 59.55 | 5.54 | 0.30 | 0.62 | 0.15 | 33.71 | 99.87 | 9.67 | 0.53 | 0.96 | 0.13 | 4.0 | |
| H1142-2/ | 1 | 1 | 63.42 | 3.06 | 0.63 | 0.00 | 0.22 | 33.17 | 100.50 | 5.28 | 1.10 | 0.00 | 0.19 | 22.3 | sp-ga-Au in |
| @ 43.0m | | 2 | 61.78 | 3.04 | 0.70 | 0.00 | 0.23 | 33.99 | 99.74 | 5.37 | 1.26 | 0.00 | 0.20 | 22.3 | py crack |
| 5600mN | | 3 | 61.86 | 3.24 | 0.55 | 0.00 | 0.00 | 33.91 | 99.56 | 5.72 | 0.99 | 0.00 | 0.00 | 22.3 | |
| average | | 3 | 62.35 | 3.11 | 0.63 | 0.00 | 0.15 | 33.69 | 99.93 | 5.45 | 1.12 | 0.00 | 0.13 | 22.3 | |
| | 2 | 1 | 61.71 | 3.22 | 0.62 | 0.00 | 0.24 | 33.70 | 99.49 | 5.68 | 1.11 | 0.00 | 0.21 | 22.3 | sp-ga-Au in |
| | | 2 | 61.89 | 3.06 | 0.70 | 0.00 | 0.27 | 33.77 | 99.69 | 5.39 | 1.25 | 0.00 | 0.24 | 22.3 | py crack |
| | | 3 | 62.40 | 3.07 | 0.61 | 0.00 | 0.00 | 33.81 | 99.89 | 5.39 | 1.09 | 0.00 | 0.00 | 22.3 | |
| average | | 3 | 62.00 | 3.12 | 0.64 | 0.00 | 0.17 | 33.76 | 99.69 | 5.49 | 1.15 | 0.00 | 0.15 | 22.3 | |
| average | 2 | 6 | 62.07 | 3.12 | 0.64 | 0.00 | 0.17 | 33.75 | 99.74 | 5.48 | 1.14 | 0.00 | 0.15 | 22.3 | |

sp = sphalerite, py = pyrite, ga = galena, tt = tetrahedrite and Au = electrum

**APPENDIX 8.4. Compositional variation of sphalerite from the South Hercules deposit, western Tasmania (Continued).**

| Sample No./ Section | gr No. | spot No. | Zn wt% | Fe wt% | Mn wt% | Cu wt% | Cd wt% | S wt% | Total wt% | FeS mole % | MnS mole% | CuS mole % | CdS mole % | Au g/t | Associated sulphides |
|---|---|---|---|---|---|---|---|---|---|---|---|---|---|---|---|
| H1142-4/ | 1 | 1 | 61.20 | 3.68 | 1.32 | 0.00 | 0.00 | 33.38 | 99.58 | 6.42 | 2.34 | 0.00 | 0.00 | 2.2 | large brown sp |
| @ 45.5m | | 2 | 64.16 | 4.35 | 1.33 | 0.00 | 0.00 | 29.60 | 99.44 | 7.19 | 2.23 | 0.00 | 0.00 | 2.2 | in contact with tt |
| 5600mN | | 3 | 58.11 | 4.58 | 1.55 | 0.00 | 0.00 | 30.73 | 94.97 | 8.21 | 2.82 | 0.00 | 0.00 | 2.2 | which hosts Au |
| | | 4 | 59.57 | 4.21 | 1.59 | 0.00 | 0.00 | 34.11 | 99.48 | 7.42 | 2.85 | 0.00 | 0.00 | 2.2 | grains |
| average | | 4 | 60.76 | 4.21 | 1.45 | 0.00 | 0.00 | 31.96 | 98.37 | 7.30 | 2.56 | 0.00 | 0.00 | 2.2 | |
| | 2 | 1 | 60.06 | 4.40 | 1.45 | 0.00 | 0.00 | 33.65 | 99.56 | 7.69 | 2.58 | 0.00 | 0.00 | 2.2 | sp near Au grain |
| | | 2 | 60.96 | 3.99 | 1.28 | 0.00 | 0.26 | 33.55 | 100.04 | 6.94 | 2.26 | 0.00 | 0.22 | 2.2 | |
| | | 3 | 59.88 | 5.00 | 1.62 | 0.00 | 0.00 | 33.70 | 100.20 | 8.65 | 2.85 | 0.00 | 0.00 | 2.2 | |
| average | | 3 | 60.30 | 4.46 | 1.45 | 0.00 | 0.09 | 33.63 | 99.93 | 7.76 | 2.56 | 0.00 | 0.07 | 2.2 | |
| | 3 | 1 | 62.01 | 3.13 | 1.32 | 0.00 | 0.00 | 34.08 | 100.54 | 5.45 | 2.34 | 0.00 | 0.00 | 2.2 | small sp grain |
| | | 2 | 62.02 | 2.95 | 1.14 | 0.00 | 0.00 | 34.01 | 100.12 | 5.17 | 2.03 | 0.00 | 0.00 | 2.2 | locked in tt |
| average | | 2 | 62.02 | 3.04 | 1.23 | 0.00 | 0.00 | 34.05 | 100.33 | 5.31 | 2.18 | 0.00 | 0.00 | 2.2 | |
| average | 3 | 9 | 61.00 | 3.90 | 1.37 | 0.00 | 0.04 | 33.58 | 99.89 | 6.78 | 2.42 | 0.00 | 0.04 | 2.2 | |
| H1148-2/ | 1 | 1 | 60.10 | 3.62 | 0.60 | 1.11 | 0.00 | 33.73 | 99.16 | 6.40 | 1.08 | 1.73 | 0.00 | 1.5 | sp locked in py |
| @ 89.4m | | 2 | 62.05 | 3.10 | 0.46 | 0.33 | 0.00 | 33.26 | 99.20 | 5.45 | 0.82 | 0.51 | 0.00 | 1.5 | near Au grains |
| 5600nN | | 3 | 60.45 | 3.65 | 0.42 | 1.22 | 0.36 | 33.52 | 99.62 | 6.41 | 0.75 | 1.88 | 0.31 | 1.5 | |
| average | | 3 | 60.87 | 3.46 | 0.49 | 0.89 | 0.12 | 33.50 | 99.33 | 6.09 | 0.88 | 1.37 | 0.10 | 1.5 | |
| | 2 | 1 | 61.45 | 3.18 | 0.70 | 0.69 | 0.39 | 33.42 | 99.83 | 5.56 | 1.24 | 1.06 | 0.34 | 1.5 | sp with Au-ga-cp |
| | | 2 | 62.79 | 2.80 | 0.73 | 0.00 | 0.00 | 33.34 | 99.66 | 4.90 | 1.30 | 0.00 | 0.00 | 1.5 | locked in py |
| average | | 2 | 62.12 | 2.99 | 0.72 | 0.35 | 0.20 | 33.38 | 99.75 | 5.23 | 1.27 | 0.53 | 0.17 | 1.5 | |
| average | 2 | 5 | 61.81 | 3.11 | 0.66 | 0.48 | 0.18 | 33.41 | 99.64 | 5.44 | 1.17 | 0.74 | 0.15 | 1.5 | |
| H1114-4/ | 1 | 1 | 59.93 | 3.83 | 0.62 | 1.48 | 0.00 | 34.07 | 99.93 | 6.72 | 1.11 | 2.28 | 0.00 | 13.2 | sp attached to py |
| @ 36.3m | | 2 | 52.65 | 4.80 | 0.22 | 0.86 | 0.00 | 32.00 | 90.53 | 9.46 | 0.44 | 1.49 | 0.00 | 13.2 | grain which |
| 5630mN | | 3 | 60.00 | 4.20 | 0.17 | 1.08 | 0.00 | 34.43 | 99.88 | 7.42 | 0.31 | 1.68 | 0.00 | 13.2 | hosts Au grain |
| average | | 3 | 57.53 | 4.28 | 0.34 | 1.14 | 0.00 | 33.50 | 96.78 | 7.81 | 0.62 | 1.83 | 0.00 | 13.2 | |
| | 2 | 1 | 60.43 | 3.52 | 0.00 | 1.32 | 0.00 | 33.78 | 99.05 | 6.25 | 0.00 | 2.06 | 0.00 | 13.2 | sp near py and |
| | | 2 | 60.69 | 3.39 | 0.13 | 1.04 | 0.28 | 34.08 | 99.61 | 6.01 | 0.61 | 1.29 | 0.22 | 13.2 | Au grain |
| average | | 2 | 60.56 | 3.46 | 0.07 | 1.18 | 0.14 | 33.93 | 99.33 | 6.13 | 0.31 | 1.46 | 0.11 | 13.2 | |
| | 3 | 1 | 60.68 | 3.32 | 0.00 | 1.61 | 0.00 | 34.02 | 99.63 | 5.87 | 0.00 | 2.50 | 0.00 | 13.2 | isolated sp near |
| | | 2 | 60.45 | 3.73 | 0.19 | 1.60 | 0.00 | 33.84 | 99.81 | 6.55 | 0.34 | 2.47 | 0.00 | 13.2 | sp and Au grain |
| | | 3 | 59.60 | 3.56 | 0.25 | 1.45 | 0.00 | 32.88 | 97.74 | 6.36 | 0.45 | 2.28 | 0.00 | 13.2 | |
| average | | 3 | 60.24 | 3.54 | 0.15 | 1.55 | 0.00 | 33.58 | 99.06 | 6.26 | 0.26 | 2.42 | 0.00 | 13.2 | |
| | 4 | 1 | 60.05 | 4.88 | 1.05 | 0.00 | 0.00 | 33.58 | 99.56 | 8.52 | 1.86 | 0.00 | 0.00 | 13.2 | sp enclosed in py |
| | | 2 | 60.55 | 4.92 | 1.00 | 0.00 | 0.00 | 33.90 | 100.37 | 8.53 | 1.76 | 0.00 | 0.00 | 13.2 | grains and near |
| | | 3 | 60.24 | 5.00 | 0.95 | 0.00 | 0.30 | 33.76 | 100.25 | 8.68 | 1.68 | 0.00 | 0.26 | 13.2 | Au grain |
| average | | 3 | 60.28 | 4.93 | 1.00 | 0.00 | 0.10 | 33.75 | 100.06 | 8.58 | 1.77 | 0.00 | 0.09 | 13.2 | |
| average | 4 | 11 | 60.11 | 4.04 | 0.43 | 0.91 | 0.07 | 33.72 | 99.27 | 7.13 | 0.81 | 1.36 | 0.06 | 13.2 | |

sp = sphalerite, py = pyrite, ga = galena, tt = tetrahedrite and Au = electrum

**APPENDIX 8.4. Compositional variation of sphalerite from the South Hercules deposit, western Tasmania (Continued).**

| Sample No./ Section | gr No. | spot No. | Zn wt% | Fe wt% | Mn wt% | Cu wt% | Cd wt% | S wt% | Total wt% | FeS mole% | MnS mole% | CuS mole% | CdS mole% | Au g/t | Associated sulphides |
|---|---|---|---|---|---|---|---|---|---|---|---|---|---|---|---|
| H1114-5/ | 1 | 1 | 60.22 | 5.60 | 0.81 | 0.00 | 0.00 | 32.48 | 99.11 | 9.68 | 1.42 | 0.00 | 0.00 | 13.2 | sp locked in py |
| @ 36.6m | | 2 | 60.13 | 5.78 | 0.68 | 0.00 | 0.00 | 33.39 | 99.98 | 9.99 | 1.20 | 0.00 | 0.00 | 13.2 | and near Au grains |
| 5630mN | | 2 | 60.18 | 5.69 | 0.75 | 0.00 | 0.00 | 32.94 | 99.55 | 9.83 | 1.31 | 0.00 | 0.00 | 13.2 | |
| | 2 | 1 | 59.73 | 4.70 | 1.00 | 0.00 | 0.00 | 33.45 | 98.88 | 8.28 | 1.79 | 0.00 | 0.00 | 13.2 | recrystallised sp |
| | | 2 | 59.79 | 4.46 | 1.00 | 0.00 | 0.00 | 32.73 | 97.98 | 7.89 | 1.80 | 0.00 | 0.00 | 13.2 | bleb |
| average | | 2 | 59.76 | 4.58 | 1.00 | 0.00 | 0.00 | 33.09 | 98.43 | 8.08 | 1.79 | 0.00 | 0.00 | 13.2 | |
| | 3 | 1 | 59.93 | 4.16 | 0.97 | 0.00 | 0.22 | 33.14 | 98.42 | 7.37 | 1.75 | 0.00 | 0.19 | 13.2 | recrystallised sp |
| | | 2 | 60.75 | 4.18 | 0.89 | 0.31 | 0.23 | 33.82 | 100.18 | 7.29 | 1.58 | 0.47 | 0.20 | 13.2 | bleb near Au grain |
| average | | 2 | 60.34 | 4.17 | 0.93 | 0.16 | 0.23 | 33.48 | 99.30 | 7.33 | 1.66 | 0.24 | 0.20 | 13.2 | |
| | 4 | 1 | 60.33 | 3.76 | 0.68 | 0.00 | 0.36 | 33.57 | 98.70 | 6.69 | 1.23 | 0.00 | 0.32 | 13.2 | small isolated |
| | | 2 | 59.77 | 4.13 | 0.72 | 0.00 | 0.00 | 33.58 | 98.20 | 7.38 | 1.31 | 0.00 | 0.00 | 13.2 | sp grain |
| average | | 2 | 60.05 | 3.95 | 0.70 | 0.00 | 0.18 | 33.58 | 98.45 | 7.04 | 1.27 | 0.00 | 0.16 | 13.2 | |
| average | 4 | 8 | 60.06 | 4.38 | 0.86 | 0.05 | 0.12 | 33.34 | 98.81 | 7.72 | 1.55 | 0.07 | 0.11 | 13.2 | |
| H1118-13/ | 1 | 1 | 60.56 | 4.66 | 0.73 | 0.00 | 0.38 | 33.64 | 99.97 | 8.13 | 1.29 | 0.00 | 0.33 | 11.3 | large sp bleb |
| @ 29.9m | | 2 | 61.36 | 4.60 | 0.85 | 0.00 | 0.00 | 33.70 | 100.51 | 7.95 | 1.49 | 0.00 | 0.00 | 11.3 | which hosts |
| 5630mN | | 3 | 62.55 | 4.00 | 0.78 | 0.00 | 0.00 | 33.41 | 100.74 | 6.87 | 1.36 | 0.00 | 0.00 | 11.3 | many Au grains |
| | | 4 | 61.10 | 4.29 | 0.88 | 0.00 | 0.00 | 33.70 | 99.97 | 7.48 | 1.56 | 0.00 | 0.00 | 11.3 | |
| | | 5 | 60.23 | 4.62 | 0.87 | 0.00 | 0.00 | 33.64 | 99.36 | 8.11 | 1.55 | 0.00 | 0.00 | 11.3 | |
| average | | 5 | 61.16 | 4.43 | 0.82 | 0.00 | 0.08 | 33.62 | 100.11 | 7.70 | 1.45 | 0.00 | 0.07 | 11.3 | |
| H1145-2A/ | 1 | 1 | 59.29 | 3.98 | 1.38 | 0.00 | 0.00 | 32.98 | 97.63 | 7.10 | 2.50 | 0.00 | 0.00 | 0.7 | recrystallised ? sp |
| @ 61.3m | | 2 | 59.57 | 3.97 | 1.23 | 0.00 | 0.27 | 33.67 | 98.71 | 7.06 | 2.22 | 0.00 | 0.24 | 0.7 | with Au and tt |
| 5670mN | | 3 | 58.52 | 4.46 | 1.58 | 0.00 | 0.00 | 33.18 | 97.74 | 7.96 | 2.86 | 0.00 | 0.00 | 0.7 | |
| average | | 3 | 59.13 | 4.14 | 1.40 | 0.00 | 0.09 | 33.28 | 98.03 | 7.37 | 2.53 | 0.00 | 0.08 | 0.7 | |
| H1129-2/ | 1 | 1 | 59.77 | 5.78 | 0.71 | 0.00 | 0.48 | 32.97 | 99.71 | 10.00 | 1.25 | 0.00 | 0.41 | 7.3 | sp-Au locked |
| 79.8m | | 2 | 58.10 | 5.79 | 0.81 | 0.00 | 0.33 | 32.74 | 97.77 | 10.26 | 1.46 | 0.00 | 0.29 | 7.3 | in py |
| 5720mN | | 3 | 59.34 | 5.55 | 0.80 | 0.00 | 0.46 | 33.18 | 99.33 | 9.69 | 1.42 | 0.00 | 0.40 | 7.3 | |
| | | 4 | 59.48 | 5.63 | 0.79 | 0.00 | 0.29 | 33.91 | 100.10 | 9.81 | 1.40 | 0.00 | 0.25 | 7.3 | |
| | | 5 | 60.20 | 5.35 | 0.70 | 0.00 | 0.21 | 33.71 | 100.17 | 9.29 | 1.24 | 0.00 | 0.18 | 7.3 | |
| average | | 5 | 59.38 | 5.62 | 0.76 | 0.00 | 0.35 | 33.30 | 99.42 | 9.81 | 1.35 | 0.00 | 0.31 | 7.3 | |
| | 2 | 1 | 59.98 | 5.50 | 0.70 | 0.00 | 0.00 | 33.50 | 99.68 | 9.57 | 1.24 | 0.00 | 0.00 | 7.3 | sp-Au locked |
| | | 2 | 60.54 | 5.63 | 0.77 | 0.00 | 0.00 | 32.97 | 99.91 | 9.68 | 1.35 | 0.00 | 0.00 | 7.3 | in py |
| | | 3 | 59.83 | 5.86 | 0.56 | 0.00 | 0.00 | 33.37 | 99.62 | 10.18 | 0.99 | 0.00 | 0.00 | 7.3 | |
| average | | 3 | 60.12 | 5.66 | 0.68 | 0.00 | 0.00 | 33.28 | 99.74 | 9.81 | 1.19 | 0.00 | 0.00 | 7.3 | |
| average | 2 | 8 | 59.75 | 5.64 | 0.72 | 0.00 | 0.18 | 33.29 | 99.58 | 9.81 | 1.27 | 0.00 | 0.15 | 7.3 | |

sp = sphalerite, py = pyrite, ga = galena, tt = tetrahedrite and Au = electrum

**APPENDIX 9.1. Oxygen and carbon isotopic composition of the carbonates from the Rosebery, Hercules and South Hercules deposits together with the isotopic data of carbonates from the Cleveland and Renison Bell tin deposits, western Tasmania.**

| Deposit | Sample No. | textural relation | textural types* | ∂O18 SMOW | ∂C13 PDB |
|---|---|---|---|---|---|
| | | | | ‰ | ‰ |
| N.end, Rosebery/A&Blens | 1120mN-1. 15L | massive carbonate | massive | 11.4 | -5.0 |
| N.end, Rosebery/A&Blens | 1120mN-3, 15L | spotty carbonate | spots | 11.2 | -1.8 |
| N.end, Rosebery/A&Blens | 1120mN-4,15L | spotty carbonate | spots | 11.8 | -1.2 |
| N.end, Rosebery/A&Blens | 1250mN, 15L | vein carbonate+chlorite | vein | 10.7 | -2.4 |
| N.end, Rosebery/A&Blens | R3374@114.5m | massive pink carbonate | massive | 11.7 | -5.0 |
| N.end, Rosebery/A&Blens | R3394@175.3m | vein carbonate | vein @@ | 11.5 | -8.8 |
| N.end, Rosebery/A&Blens | R3421@116.5m | spotty carbonate | spots | 10.8 | -1.4 |
| N.end, Rosebery/A&Blens | R3456@288.5m | vein carbonate | vein | 11.3 | -3.7 |
| N.end, Rosebery/A&Blens | R4297B@35.5m | vein carbonate+chlorite+quartz | vein | 12.4 | -3.3 |
| N.end, Rosebery/A&Blens | R4482@72.5m | spherulitic carbonate | spheroids | 11.9 | -0.6 |
| N.end, Rosebery/A&Blens | R4482A@72.8m | vein carbonate+chlorite+quartz | vein | 10.6 | -3.2 |
| N.end, Rosebery/A&Blens** | 60482-950mN | spherulitic, colloform carbonate | spheroids | 9.9 | -4.3 |
| S.end, Rosebery/D,E,G,Hlens** | 60372-196mN | recrystallised massive carbonate | massive | 10.8 | -3.4 |
| S.end, Rosebery/D,E,G,Hlens** | 60390-238mS | packed carbonate spherulite | spheroids | 11.8 | -1.8 |
| S.end, Rosebery/D,E,G,Hlens** | 60417-219mN | carbonate concretion | spheroids | 11.6 | -3.9 |
| S.end, Rosebery/D,E,G,Hlens** | 60419-227mN | brecciated carbonate | blebs | 10.9 | -3.4 |
| S.end, Rosebery/D,E,G,Hlens** | 60469-260mN | nodular carbonate pod | spheroids | 10.7 | -1.5 |
| S.end, Rosebery/D,E,G,Hlens** | 60477-255mN | zoned dolomite rhomb | dolomite | 11.7 | -2.7 |
| S.end, Rosebery/D,E,G,Hlens** | 60486-455mN | colloform, layered carbonate | spheroids | 12.2 | -2.7 |
| S.end, Rosebery/D,E,G,Hlens** | 60488-245mN | carbonate-quartz vein | vein | 11.2 | -4.4 |
| S.end, Rosebery/D,E,G,Hlens** | 60489-139mN | massive carbonate | massive | 11.3 | -0.7 |
| S.end, Rosebery/F(J)lens | 17L-1 | spherulitic carbonate | spheroids | 12.6 | -1.5 |
| S.end, Rosebery/F(J)lens | R1477-5@992' | spotty carbonate | spots | 12.4 | -1.9 |
| S.end, Rosebery/F(J)lens | R1477-9@1047' | massive pink carbonate | massive | 10.7 | -2.4 |
| S.end, Rosebery/F(J)lens | R1625@1016' | bleby pink carbonate | blebs | 10.7 | -2.8 |
| S.end, Rosebery/F(J)lens | R1770-14 @ 2712' | bleby or patchy carbonate | blebs | 10.6 | -4.1 |
| S.end, Rosebery/F(J)lens | R3011-25@182' | bleby brown carbonate | blebs @@ | 13.5 | -6.8 |
| S.end, Rosebery/F(J)lens | R3024-4@142' | brecciated, bleby carbonate | blebs | 11.9 | -3.6 |
| S.end, Rosebery/F(J)lens | R3034-10@112' | vein carbonate | vein | 10.9 | -1.7 |
| S.end, Rosebery/F(J)lens | R3491-1 @17' | massive pink carbonate | massive | 11.2 | -2.2 |
| S.end, Rosebery/F(J)lens** | 60351-273mS | massive carbonate | massive | 10.2 | -2.0 |
| S.end, Rosebery/F(J)lens** | 60366-583mS | bleby to poddy carbonate | blebs | 11.2 | -3.3 |
| S.end, Rosebery/F(J)lens** | 60396-238mS | brecciated, bleby carbonate | blebs | 10.9 | -2.2 |
| S.end, Rosebery/F(J)lens** | 60397-226mS | massive carbonate | massive | 12.4 | -1.4 |
| Hercules | H802 @ 114' | massive pink carbonate | massive | 14.3 | -0.9 |
| Hercules | H802 @ 71' | vein pink carbonate | vein | 13.9 | -2.3 |
| Hercules | H802A @ 71' | massive carbonate | massive | 13.2 | -1.6 |
| Hercules | H1032-4B @ 200' | bleby or patchy carbonate | blebs | 13.2 | -0.5 |
| Hercules | H831-4B @ 80' | massive pink carbonate | massive | 10.8 | -3.3 |
| Hercules | H1033-2 @ 120' | spotty carbonate | spots | 12.2 | -0.9 |
| Hercules | H1062-4A @ 199' | spotty carbonate | spots | 8.7 | -2.4 |
| Hercules | M lens | massive carbonate | massive | 13.0 | -2.1 |

* textural type of carbonates used for ∂18O vs. ∂13C plots
**data from Dixon (1980)
***data from Collins (1981)
****data from Patterson et al., (1981)
@@ average of two analyses

**APPENDIX 9.1. Oxygen and carbon isotopic composition of the carbonates from the Rosebery, Hercules and South Hercules deposits together with the isotopic data of carbonates from the Cleveland and Renison Bell tin deposits, western Tasmania (Continued).**

| Deposit | Sample No. | textural relation | textural types* | ∂O18 SMOW | ∂C13 PDB |
|---|---|---|---|---|---|
| | | | | ‰ | ‰ |
| South Hercules | H1108-1 @ 29.5m | massive carbonate | massive | 15.0 | -1.3 |
| South Hercules | H1108-1A@29.5m | pink carbonate vein | vein | 13.4 | -2.2 |
| South Hercules | H1132-5 @ 74.0m | cannon ball pink carbonate | coalesced spheroids | 9.8 | -3.5 |
| South Hercules | H1132-3 @ 64.0m | massive carbonate | massive | 11.1 | -3.2 |
| South Hercules | H1142-5 @ 45.7m | vein pink carbonate | vein | 13.2 | -1.9 |
| South Hercules | H1117-B @ 21.0m | bleby or bloby pink carbonate | blebs | 15.4 | -1.0 |
| South Hercules | H1108-4 @ 38.2m | coalesced spherulitic carbonate | coalesced spheroids | 13.7 | -1.8 |
| South Hercules | H1108-3 @34.5m | vein pink carbonate | vein | 12.6 | -2.8 |
| South Hercules | H1108-3A@34.5m | massive carbonate | massive | 16.7 | 0.6 |
| South Hercules | H1108-10@50.2m | spherulitic carbonate | spheroids | 9.9 | -3.5 |
| South Hercules | H1108-10a@50.2m | vein pink carbonate | vein | 12.7 | -3.4 |
| South Hercules | H1108-3B@35.2m | massive carbonate | massive | 12.8 | -1.7 |
| Cleveland*** | 4369 | ore carbonate, stage II | Devonian carbonate | 16.7 | -7.0 |
| Cleveland*** | 4442 | ore carbonate, stage II | Devonian carbonate | 16.6 | -5.1 |
| Cleveland*** | 4365 | vein carbonate, stage IV | Devonian carbonate | 14.9 | -2.5 |
| Cleveland*** | 4368 | vein carbonate, stage IV | Devonian carbonate | 15.7 | -2.8 |
| Cleveland*** | 4361 | vein carbonate, stage IV | Devonian carbonate | 15.4 | -2.4 |
| Cleveland*** | 4364 | vein carbonate, stage IV | Devonian carbonate | 15.7 | -3.0 |
| Cleveland*** | 4347 | vein carbonate, stage IV | Devonian carbonate | 16.2 | -2.7 |
| Cleveland*** | 4301 | vuggy carbonate, stage IV | Devonian carbonate | 11.2 | -1.8 |
| Renison**** | 104128 | ore carbonate, stage II | Devonian carbonate | 12.7 | -6.0 |
| Renison**** | 104272 | vein calcite, stage V | Devonian carbonate | 14.9 | -4.2 |
| Renison**** | 104273 | vein calcite, stage V | Devonian carbonate | 15.3 | -4.4 |
| Renison**** | 104276 | vug calcite, stage VI? | Devonian carbonate | 24.0 | 4.3 |
| Cleveland*** | 8335 | Cambrian limestone | Cambrian limestone | 13.7 | -1.5 |
| Cleveland*** | 8291 | Cambrian limestone | Cambrian limestone | 13.0 | -2.3 |
| Cleveland*** | 8293 | Cambrian limestone | Cambrian limestone | 13.2 | -1.7 |
| Cleveland*** | 8298 | Cambrian limestone | Cambrian limestone | 12.1 | -2.1 |
| Renison**** | 103765 | Cambrian sedimentary dolomite | Cambrian dolomite | 20.9 | -2.8 |
| Renison**** | 103768 | Cambrian sedimentary dolomite | Cambrian dolomite | 19.8 | -1.9 |
| Renison**** | 103772 | Cambrian sedimentary dolomite | Cambrian dolomite | 11.4 | -1.1 |
| Renison**** | 104129 | Cambrian sedimentary dolomite | Cambrian dolomite | 21.3 | 1.3 |

* textural type of carbonates used for ∂18O vs. ∂13C plots
**data from Dixon (1980)
***data from Collins (1981)
****data from Patterson et al., (1981)
@@ average of two analyses

**Appendix 9.2. Atomic absorption spectrophotometric analysis of carbonate minerals from Rosebery, Hercules and South Hercules deposits, western Tasmania (textural types and isotopic data are also shown in Appendix 9.1).**

| Deposit | Sample No. | Mg (%) | Mn (%) | Ca (%) | Fe (%) | Sr ppm | Na ppm | ∂O10 per mil | ∂C13 per mil | textural types |
|---|---|---|---|---|---|---|---|---|---|---|
| N.end, Rosebery/A&Blens | 1120mN-1. 15L | 0.3 | 1.9 | 33.3 | 0.0 | 1215 | 144 | 11.4 | -5.0 | massive |
| N.end, Rosebery/A&Blens | 1120mN-3, 15L | 6.6 | 3.8 | 15.8 | 0.0 | 274 | 398 | 11.2 | -1.8 | spots |
| N.end, Rosebery/A&Blens | 1120mN-4,15L | 5.4 | 3.6 | 18.1 | 0.7 | 453 | 204 | 11.8 | -1.2 | spots |
| N.end, Rosebery/A&Blens | 1250mN, 15L | 0.7 | 4.8 | 32.4 | 0.0 | 1276 | 158 | 10.7 | -2.4 | vein |
| N.end, Rosebery/A&Blens | R3374@114.5m | 2.5 | 25.3 | 6.1 | 0.0 | 194 | 212 | 11.7 | -5.0 | massive |
| N.end, Rosebery/A&Blens | R3394@175.3m | 0.3 | 1.0 | 39.6 | 0.0 | 498 | 135 | 11.5 | -8.8 | vein |
| N.end, Rosebery/A&Blens | R3421@116.5m | 4.7 | 10.0 | 15.6 | 0.0 | 234 | 332 | 10.8 | -1.4 | spots |
| N.end, Rosebery/A&Blens | R3456@288.5m | 1.1 | 16.6 | 15.6 | 0.0 | 250 | 195 | 11.3 | -3.7 | vein |
| N.end, Rosebery/A&Blens | R4297B@35.5m | 3.2 | 12.8 | 16.3 | 5.6 | 223 | 178 | 12.4 | -3.3 | vein |
| N.end, Rosebery/A&Blens | R4482@72.5m | 7.0 | 4.3 | 21.0 | 2.5 | 319 | 203 | 11.9 | -0.6 | spheroids |
| N.end, Rosebery/A&Blens | R4482A@72.8m | 0.6 | 2.6 | 33.9 | 1.3 | 368 | 144 | 10.6 | -3.2 | vein |
| S.end, Rosebery/F(J)lens | 17L-1 | 7.0 | 6.2 | 19.2 | 2.1 | 134 | 189 | 12.6 | -1.5 | spheroids |
| S.end, Rosebery/F(J)lens | R1477-5@992' | 2.5 | 7.0 | 10.2 | 0.0 | 142 | 206 | 12.4 | -1.9 | spots |
| S.end, Rosebery/F(J)lens | R1477-9@1047' | 3.7 | 15.1 | 16.9 | 3.6 | 762 | 91 | 10.7 | -2.4 | massive |
| S.end, Rosebery/F(J)lens | R1625@1016' | 3.5 | 14.5 | 16.3 | 0.0 | 475 | 209 | 10.7 | -2.8 | blebs |
| S.end, Rosebery/F(J)lens | R1770-14 @ 2712' | 0.5 | 34.9 | 1.3 | 0.0 | 5 | 121 | 10.6 | -4.1 | blebs |
| S.end, Rosebery/F(J)lens | R3011-25@182' | 1.0 | 23.5 | 0.4 | 0.0 | <5 | 143 | 13.5 | -6.8 | blebs |
| S.end, Rosebery/F(J)lens | R3024-4@142' | 2.8 | 4.5 | 8.3 | 0.9 | 162 | 5430 | 11.9 | -3.6 | blebs |
| S.end, Rosebery/F(J)lens | R3034-10@112' | 1.2 | 3.3 | 3.4 | 0.0 | 10 | 4700 | 10.9 | -1.7 | vein |
| S.end, Rosebery/F(J)lens | R3491-1 @17' | 3.0 | 21.5 | 14.3 | 1.0 | 319 | 143 | 11.2 | -2.2 | massive |
| Hercules | H802 @ 114' | 1.1 | 30.1 | 5.1 | 0.0 | 45 | 172 | 14.3 | -0.9 | massive |
| Hercules | H802 @ 71' | 1.9 | 24.8 | 5.2 | 0.0 | 56 | 79 | 13.9 | -2.3 | vein |
| Hercules | H802A @ 71' | 0.9 | 24.4 | 1.6 | 0.0 | 25 | 249 | 13.2 | -1.6 | massive |
| Hercules | H1032-4B @ 200' | 1.6 | 11.9 | 18.9 | 0.0 | 168 | 136 | 13.2 | -0.5 | blebs |
| Hercules | H831-4B @ 80' | 1.1 | 2.1 | 18.9 | 0.0 | 324 | 87 | 10.8 | -3.3 | massive |
| Hercules | H1033-2 @ 120' | 8.4 | 23.2 | 14.7 | 0.0 | 137 | 86 | 12.2 | -0.9 | spots |
| Hercules | H1062-4A @ 199' | 0.9 | 18.8 | 0.1 | 0.0 | 20 | 401 | 8.7 | -2.4 | spots |
| Hercules | M lens | 0.8 | 33.0 | 1.6 | 0.0 | 10 | 159 | 13.0 | -2.1 | massive |
| South Hercules | H1108-1 @ 29.5m | 2.5 | 17.5 | 13.5 | 0.0 | 142 | 222 | 15.0 | -1.3 | massive |
| South Hercules | H1108-1a@ 29.5m | 3.3 | 19.0 | 16.6 | 1.4 | 101 | 161 | 13.4 | -2.2 | vein |
| South Hercules | H1132-5 @ 74.0m | 0.3 | 35.5 | 3.0 | 2.3 | 56 | 174 | 9.8 | -3.5 | spheroids |
| South Hercules | H1132-3 @ 64.0m | 0.9 | 18.0 | 4.2 | 0.7 | 71 | 79 | 11.1 | -3.2 | massive |
| South Hercules | H1142-5 @ 45.7m | 0.9 | 38.2 | 5.2 | 1.3 | 46 | 46 | 13.2 | -1.9 | vein |
| South Hercules | H1117-B @ 21.0m | 0.3 | 30.5 | 3.9 | 0.0 | 67 | 115 | 15.4 | -1.0 | blebs |
| South Hercules | H1108-4 @ 36.2m | 0.4 | 32.3 | 1.9 | 0.0 | 40 | 147 | 13.7 | -1.8 | spheroids |
| South Hercules | H1108-3 @34.5m | 0.9 | 22.1 | 19.3 | 0.9 | 261 | 86 | 12.6 | -2.8 | vein |
| South Hercules | H1108-3A@34.5m | 0.8 | 29.9 | 9.5 | 0.0 | 86 | 232 | 16.7 | 0.6 | massive |
| South Hercules | H1108-10@50.2m | 0.4 | 35.9 | 1.3 | 0.0 | 10 | 117 | 9.9 | -3.5 | spheroids |
| South Hercules | H1108-10a@50.2m | 0.2 | 34.8 | 5.1 | 1.4 | 20 | 346 | 12.7 | -3.4 | vein |
| South Hercules | H1108-3B@35.2m | 0.5 | 20.4 | 15.7 | 0.0 | 230 | 158 | 12.8 | -1.7 | massive |

**Appendix 9.3. Oxygen isotopic ratio of quartz, carbonate, chlorite, biotite, magnetite and tourmaline and oxygen isotope geothermometric data of mineral pairs from the Rosebery, Hercules and South Hercules deposits, western Tasmania.**

| Sample No./ Section | Mineral | ∂18O(SMOW) ‰ | Δqtz-cal (T°C) | Δtz-chl (T°C) | Δcal-chl (T°C) | Δqtz-bic (T°C) | Δqtz-mag (T°C) |
|---|---|---|---|---|---|---|---|
| Rosebery N-end | | | | | | | |
| R3391 @ 145.75' | quartz | 13.46 | | | | | |
| R3456 @ 288.50' | quartz | 11.90 | 727 | | | | |
| | carbonate | 11.30 | | | | | |
| R4031 @ 61.70m | chlorite | 7.40 | | | | | |
| R4297 @ 35.5m | quartz | 14.75 | 232 | 383 | 259 | | |
| | chlorite | 8.09 | | | | | |
| | carbonate | 12.40 | | | | | |
| R4298 @ 46.70m | chlorite | 9.29 | | | | | |
| R4482 @ 72.80m | quartz | 12.09 | 361 | 1712 | 826 | | |
| | chlorite | 9.59 | | | | | |
| | carbonate | 10.60 | | | | | |
| R4540 @ 46.30m | chlorite | 8.78 | | | | | |
| 15L-880mN* | quartz | 15.14 | | 694 | | | |
| | chlorite | 11.00 | | | | | |
| Rosebery S-end | | | | | | | |
| R3024-7 @ 156.0' | quartz | 12.64 | | | | | |
| R3024-8 @ 156.6' | biotite | 7.19 | | | | | |
| R3023-11 @ 163' | quartz | 13.50 | | | | 424 | |
| | biotite | 7.42 | | | | | |
| R3023-13 @ 165' | quartz | 11.61 | | | | | |
| R3034-5B @ 18' | biotite | 6.71 | | | | | |
| R3334-6B @ 21' | quartz | 11.82 | | | | 375 | |
| | biotite | 4.92 | | | | | |
| R3334-9 @ 51.2' | biotite | 5.90 | | | | | |
| R3334-11 @ 56.3' | quartz | 10.73 | | | | | |
| R3011-10 @ 76.6' | biotite | 5.40 | | | | | |
| R3164-8 @ 108' | quartz | 12.50 | | | | 518 | |
| | biotite | 7.59 | | | | | |

*Underground samples

Experimental or empirical fractionation data reported by O'Neil et al. (1969), Bottinga and Javoy (1973, 1975), Masuhisa et al. (1979), Wenner and Taylor (1971), Lafferty and Golding (1985) and Faure (1986) were used to calculate the fractionation for the mineral pair geothermometers: Δq-cal=Δquartz-calcite, Δq-chl=quartz-chlorite, Δcal-chl=calcite-chlorite, Δq-bio=quartz-biotite and Δq-mag=quartz-magnetite

**Appendix 9.3. Oxygen isotopic ratio of quartz, carbonate, chlorite, biotite, magnetite and tourmaline and oxygen isotope geothermometric data of mineral pairs from the Rosebery, Hercules and South Hercules deposits, western Tasmania (Continued).**

| Sample No./ Section | Mineral | ∂18O(SMOW) ‰ | Δq-cal (T°C) | Δq-chl (T°C) | Δcal-chl (T°C) | Δq-bio (T°C) | Δq-mag (T°C) |
|---|---|---|---|---|---|---|---|
| Rosebery s-end (continued) | | | | | | | |
| R3492-4 @ 52' | biotite | 5.12 | | | | | |
| R3492-10 @ 82' | biotite | 7.30 | | | | | |
| R3492-19B/140' | biotite | 7.37 | | | | | |
| R3492-21 @ 143' | quartz | 11.39 | | | | 540 | |
| | biotite | 6.70 | | | | | |
| R3016-6 @ 64' | quartz | 12.56 | | | | 1428 | |
| | biotite | 10.10 | | | | | |
| R3016-23C @ 207' | quartz | 13.71 | | | | | |
| | tourmaline | 10.57 | | | | | |
| R3016-27 @ 251' | quartz | 11.54 | | | | 949 | |
| | biotite(chlorite) | 8.99 | | | | | |
| R3033-22A @ 150' | quartz | 12.91 | | | | | 402 |
| | magnetite | 1.50 | | | | | |
| R3033-31A @ 170' | quartz | 13.10 | | | | 602 | |
| | biotite | 8.93 | | | | | |
| R3033-33 @ 181' | quartz | 12.33 | | | | 664 | |
| | biotite | 8.59 | | | | | |
| | tourmaline | 11.85 | | | | | |
| 15L-tm* | quartz | 14.20 | | | | | |
| | tourmaline | 10.76 | | | | | |
| 16L-1* | quartz | 12.50 | | | | | |
| | tourmaline | 10.62 | | | | | |
| 106780* | tourmaline | 10.35 | | | | | |
| R4272 @ 41.7m | biotite(chlorite) | 6.18 | | | | | |
| | magnetite | 1.83 | | | | | |
| R4372 @ 12.4m | magnetite | 1.78 | | | | | |
| 18L* | magnetite | 2.13 | | | | | |
| R1920-1 @ 1800' | tourmaline | 10.67 | | | | | |

*Underground samples

Experimental or empirical fractionation data reported by O'Neil et al. (1969), Bottinga and Javoy (1973, 1975), Masuhisa et al. (1979), Wenner and Taylor (1971), Lafferty and Golding (1985) and Faure (1986) were used to calculate the fractionation for the mineral pair geothermometers: Δq-cal=Δquartz-calcite, Δq-chl=quartz-chlorite, Δcal-chl=calcite-chlorite, Δq-bio=quartz-biotite and Δq-mag=quartz-magnetite

**Appendix 9.3. Oxygen isotopic ratio of quartz, carbonate, chlorite, biotite, magnetite and tourmaline and oxygen isotope geothermometric data of mineral pairs from the Rosebery, Hercules and South Hercules deposits, western Tasmania (Continued).**

| Sample No./ Section | Mineral | ∂18O(SMOW) ‰ | Δq-cal (T°C) | Δq-chl (T°C) | Δcal-chl (T°C) | Δq-bio (T°C) | Δq-mag (T°C) |
|---|---|---|---|---|---|---|---|
| Hercules | | | | | | | |
| H831-14A @ 112' | quartz | 15.26 | | 381 | | | |
| | chlorite | 8.57 | | | | | |
| H1008-22 @ 122.5' | quartz | 12.95 | | 431 | | | |
| | chlorite | 6.91 | | | | | |
| H1032-4B @ 200' | quartz | 15.61 | 146 | 722 | 1141 | | |
| | chlorite | 11.59 | | | | | |
| | carbonate | 12.20 | | | | | |
| H1033-2 @ 120' | quartz | 13.03 | | 480 | | | |
| | chlorite | 7.50 | | | | | |
| H1034-5 @ 119.2' | quartz | 13.45 | | | | | |
| South Hercules | | | | | | | |
| H1106-2 @ 36.5m | vein quartz | 14.95 | | | | | |
| H1108-1 @ 29.5m | vein quartz | 14.33 | 530 | | | | |
| | carbonate | 13.40 | | | | | |
| H1108-10A @ 50.2m | chlorite | 6.65 | | | 176 | | |
| | carbonate | 12.70 | | | | | |
| H1114-13A @ 50.0m | vein quartz | 14.86 | | | | | |
| H1117-A @ 21.0m | cherty quartz | 15.23 | | | | | |
| H1117-1 @ 28.2m | cherty quartz | 15.86 | | | | | |
| H1118-15 @ 32.7m | quartz | 13.99 | | | | | |
| H1129-8 @ 84.3m | quartz | 14.21 | | | | | |
| H1132-5 @ 74.0m | chlorite | 9.60 | | | 2197 | | |
| | carbonate | 9.80 | | | | | |
| H1142-4B @ 45.5m | cherty quartz | 15.10 | | | | | |

Experimental or empirical fractionation data reported by O'Neil et al. (1969), Bottinga and Javoy (1973, 1975), Masuhisa et al. (1979), Wenner and Taylor (1971), Lafferty and Golding (1985) and Faure (1986) were used to calculate the fractionation for the mineral pair geothermometers: Δq-cal=Δquartz-calcite, Δq-chl=quartz-chlorite, Δcal-chl=calcite-chlorite, Δq-bio=quartz-biotite and Δq-mag=quartz-magnetite

**Appendix 9.4. Sulphur isotopic composition of different sulphide minerals from Rosebery south-end and the South Hercules deposit, western Tasmania.**

| Sample No. | ∂34S ‰ | Mineral | Texture | Au g/t |
|---|---|---|---|---|
| **South Hercules** | | | | |
| H1108-3B @ 35.0m | 9.86 | pyrite | massive | 0.3 |
| H1114-4 @ 36.3m | 13.41 | sphalerite | bleb | 13.2 |
| H1114-16B @ 59.0m | 11.37 | sphalerite | massive | 4.9 |
| H1117-C @ 24.3m | 9.43 | pyrite | massive | 1.4 |
| H1117-2 @ 29.5m | 10.06 | pyrite | colloform | 1.9 |
| H1118-13 @ 29.9m | 11.92 | galena | patches | 11.3 |
| H1118-16 @ 33.0m | 11.68 | sphalerite | bleb | 3.7 |
| H1163-2 @ 67.5m | 14.07 | pyrite | colloform | 9.0 |
| H1142-2 @ 43.0m | 9.67 | pyrite | massive | 22.3 |
| H1142-3 @ 44.3m | 11.34 | pyrite | massive | 12.2 |
| H1142-4A @ 45.5m | 8.22 | sphalerite | in vein | 2.2 |
| H1142-4A @ 45.5m | 7.77 | tetrahedrite | in vein | 2.2 |
| H1145-2A @ 61.3m | 8.22 | pyrite | massive | 5.0 |
| H1148-2 @ 89.5m | 11.43 | sphalerite | bleb | 1.5 |
| **Rosebery south-end** | | | | |
| R3023-13 @ 165' | 16.75 | pyrite | | - |
| R3023-13 @ 165' | 16.94 | pyrrhotite | | - |
| R3023-12B | 12.98 | chalcopyrite | | - |
| R4259-1 @ 71.6m | 15.29 | pyrite | | - |
| **Rosebery south-end (across Pb-Zn zone to pyrrhotite-pyrite zone)** | | | | |
| Rep-KZ1 | | | | |
| Spot-1 | 15.96 | sphalerite-galena+pyrite | - | - |
| Spot-2 | 17.45 | sphalerite-galena+pyrite | - | - |
| Spot-3 | 15.36 | sphalerite-galena+pyrite | - | - |
| Spot-4 | 18.61 | sphalerite-galena+pyrite | - | - |
| Spot-5 | 16.67 | pyrite-pyrrhotite+chalcopyrite | - | - |
| Spot-6 | 16.59 | pyrite-pyrrhotite+chalcopyrite | - | - |
| Spot-7 | 16.08 | pyrite-pyrrhotite+chalcopyrite | - | - |
| Spot-8 | 16.39 | pyrite-pyrrhotite+chalcopyrite | - | - |
| Spot-9 | 16.97 | pyrite-pyrrhotite+chalcopyrite | - | - |
| Spot-10 | 17.16 | pyrite-pyrrhotite+chalcopyrite | - | - |

**APPENDIX 10.1. Description of fluid inclusion samples from the Rosebery deposit, western Tasmania.**

| Sample No./section | Mineral studied | Description and occurrence | Associated minerals |
|---|---|---|---|
| Hangingwall | | | |
| 17L-2, 12mN, Glens | carbonate/ barite | as carbonate spheroids in siliceous host rock | quartz |
| 19L-1, 125N, E lens | quartz | as irregular quartz-carbonate vein | carbonate |
| 88R-3A@1145.3m, F lens | fluorite | as vein in hangingwall | tourmaline, magnetite |
| Ore zone | | | |
| R3808 @ 153m, H lens | barite | barite zone | pyrite, galena |
| 16L-2, 35N, E lens | barite/ sphalerite | massive sphalerite | quartz, galena |
| R4174 @ 33m, F lens | barite/ sphalerite | in massive sulphide with minor banding | quartz, galena |
| R1526 @ 1046', F lens | sphalerite | dark brown massive sphalerite | quartz |
| R4495@52.2m, H lens | sphalerite | in remobilised quartz-sphalerite vein | quartz |
| Footwall | | | |
| R4407 @ 0.9m, B lens | quartz | intercalated with sulphides in chloritic footwall | pyrite, chalcopyrite. |
| R4406 @ 105.5m, B lens | quartz | intercalated with sulphides in chloritic footwall | chalcopyrite, sphalerite |
| 17L-3, 12mN, G lens | quartz | intercalated with sulphides in footwall | chalcopyrite, pyrite, galena |
| 15L-1, 600mN, D lens | quartz | as thin quartz-chalcopyrite vein in massive pyrite | chalcopyrite |
| R1477-11 @ 1093.6', Flens | fluorite | fluorite in gash vein in chloritic footwall | pyrite |
| Remobilised veins | | | |
| 15L-2, 300mN, G lens | quartz/ carbonate | remobilised quartz-carbonate vein | galena, pyrite |
| 16L-4, 100mS, H lens | quartz | remobilised, irregular vein | galena cube, sphalerite |
| Magnetite-biotite zone | | | |
| 88R-6 @ 1200.8m, F lens | helvite | from magnetite-biotite zone | garnet, biotite, magnetite |
| R3033-31A @ 170', F lens | quartz | from magnetite-biotite zone | chalcopyrite, magnetite |
| R3033-22A @ 150', F lens | quartz | from magnetite-biotite zone | pyrite, tourmaline |
| Pyrrhotite-pyrite zone | | | |
| R3492-20 @ 142', F lens | quartz | in pyrrhotite-pyrite zone | minor magnetite |
| R3492-28 @ 177', F lens | quartz | in pyrrhotite-pyrite zone | minor magnetite |
| R3034-7 @ 100.5', F lens | quartz | in pyrrhotite-pyrite zone | minor magnetite |
| Quartz-tourmaline zone | | | |
| 16L-3 between G lens and H lens | quartz | in quartz-tourmaline-hematite zone | hematite, magnetite chlorite |
| 106780, F lens | quartz | in tourmaline-quartz zone | pyrite |
| KZFR-1, F lens | fluorite | vein cutting massive biotite | carbonate, quartz |

**APPENDIX 10.2. Description of fluid inclusion samples from the Hercules and South Hercules deposits, western Tasmania.**

| Sample No./section | Mineral studied | Description and occurrence | Associated minerals |
|---|---|---|---|
| **J(K)-P lens of Hercules deposit** | | | |
| H1032-5 @ 202' 4" | quartz | in strongly chloritic host rock | chlorite+sphalerite galena+carbonate |
| H1032-6C @ 202' | quartz/ sphalerite | in strongly chloritic host rock | chalcopyrite+sphalerite |
| H1034-2 @ 109' | quartz | quartz-pyrite-chalcopyrite ore | sphalerite+chalcopyrite |
| H1034-5 @ 119' 2" | quartz | | pyrite-chalcopyrite |
| H1062-1 @ 185' | fluorite gashes | in sericitic, chloritic host rock | qtz+pyrite-sericite chlorite |
| H1062-4A @ 199' | carbonate | spherulitic carbonate-quartz-chlorite-fluorite vein | chlorite+quartz+fluorite |
| H-1450N/200W | barite | in massive barite zone | pyrite |
| **South Hercules deposit** | | | |
| H1132-2 @ 62.2m 5585mN | vein fluorite | in siliceous, stringery sulphide ore zone | pyrite, sphalerite |
| H1142-5 @ 45.7m 5600mN | quartz/ sphalerite | as quartz-carbonate-sphalerite vein in siliceous, stringery sulphide ore zone | tetrahedrite |
| H1148-3 @ 90.8m 5600mN | fluorite | in sphalerite-galena ore zone | sphalerite, pyrite, galena, chlorite and carbonate |
| H1114-5 @ 36.6m 5630mN | vein fluorite | in siliceous, stringery sulphide ore zone | sphalerite, pyrite, quartz, gold |
| H1114-13 @ 50.0m 5630mN | fluorite/ sphalerite | in siliceous, stringery sulphide ore zone | galena, sulpho-salt |
| H1163-3 @ 68.0m 5630mN | fluorite | as discrete fluorite grains in massive pyrite zone with many rhomb-shape arsenopyrite grains | arsenopyrite, pyrite and sericite |
| H1108-2 @ 30.3m 5670mN | vein quartz | as late quartz-carbonate vein in massive carbonate zone | carbonate |
| H1108-8 @ 42.8m 5670mN | fluorite | in sphalerite-galena ore zone | pyrite, sphalerite, galena, sericite, and quartz |
| H1108-9A @ 46.0m 5670mN | carbonate | in strongly sheared, pyritic zone with abundant colloform pyrite | seicite, quartz |
| H1145-2A @ 61.3m 5670mN | barite | as massive barite in pyrite-barite zone at the upper part of orebody | pyrite, carbonate, sulphosalt and gold |
| H1100-1 @ 29.5m 5720mN | barite | with pyrite in siliceous, tuffaceous host rock | pyrite |
| H1100-2 @ 63.5m 5720mN | barite | in massive pyrite-barite zone | pyrite, sphalerite |
| H1129-5 @ 81.5m 5720mN | fluorite | in siliceous, stringery sulphide ore zone | pyrite,sphalerite, barite, sericite |

**APPENDIX 10.3. Fluid inclusion heating/freezing data for the different minerals from the Rosebery deposit, western Tasmania.**

| Sample No. | Mineral studied | Inclusion type | Th(L-V)-L | ThCO2 (L-V)-V | Tm-ice | Tm-NaCl | Te-Ch | NaCl eq. wt% | 1st-ice Tm |
|---|---|---|---|---|---|---|---|---|---|
| R3033-31A @ 170' | quartz | I | 208.3 | | | | | | |
| Biotite-magnetite | | I | 206.8 | | -4.6 | | | 7.3 | |
| zone | | I | 295.5 | | | | | | |
| F(J) lens | | II | 259.4(d) | | | | | | |
| | | II | 315.2(d) | | | | | | |
| | | II | 325.5(d) | | | | | | |
| | | III | | 25.2 | | | | | |
| | | III | | 24.8 | | | | | |
| | | III | | 13.8 | | | | | |
| | | III | | 16.6 | | | | | |
| R3033-22A @ 150' | quartz | I | 234.3 | | | | | | -35.8 |
| Biotite-magnetite | | I | 235.0 | | | | | | |
| zone | | I | 250.5 | | | | | | -31.2 |
| F(J) lens | | I | 225.8 | | | | | | |
| | | II | 279.0(d) | | | | | | |
| | | II | 310.5(d) | | | | | | |
| | | II | 345.6(d) | | | | | | |
| | | II | 330.4(d) | | | | | | |
| | | II | | | | 140.0 | | 29.4 | |
| | | II | | | | 251.3 | | 34.8 | |
| | | II | | | | 290.0 | | 37.3 | |
| | | II | | | | | 0.5 | 15.0 | |
| | | II | | | | | 1.2 | 14.2 | |
| | | II | | | | | 0.7 | 14.8 | |
| | | II | | | | | 0.4 | 15.1 | |
| | | III | | 27.0 | | | | | |
| | | III | | 21.4 | | | | | |
| | | III | | 19.8 | | | | | |
| | | III | | 20.9 | | | | | |
| 88R-6 @ 1200.8m | Helvite | II | 300.0 | | | | | | |
| Biotite-magnetite | | II | 326.4 | | | | | | |
| zone | | II | 328.8 | | | | | | |
| F(J) lens | | II | 330.0 | | | | | | |
| | | II | 318.7 | | | | | | |
| | | II | 328.5 | | | | | | |
| | | II | | | -10.8 | | | 14.8 | |
| | | II | | | -8.6 | | | 12.4 | |
| 17L-3, G lens, | quartz | I | 238.4 | | -5.6 | | | 8.7 | |
| Footwall | | I | 222.9 | | -3.9 | | | 6.3 | |

Th (L-V)-L = temperature of homogenisation into liquid phase
ThCO2(L-V)-V = temperature of homogenisation of CO2 into liquid phase
Tm-NaCl=decomposition temperature of NaCl
Tm-ice = temperature of last ice melting
Te-Ch = temperature of clathrate melting
(d) = temperature of decrepitation
1st-ice Tm = temperature of first ice melting

Salinity were calculated using equations of Potter et al. (1977), Potter et al. (1978) and Bozzo et al. (1973).

**APPENDIX 10.3. Fluid inclusion heating/freezing data for the different minerals from the Rosebery deposit, western Tasmania (Continued).**

| Sample No. | Mineral studied | Inclusion type | Th(L-V)-L | ThCO2 (L-V)-V | Tm-ice | Tm-NaCl | Te-Ch | NaCl eq. wt% | 1st-ice Tm |
|---|---|---|---|---|---|---|---|---|---|
| R4407 @ 0.9m, | quartz | II | 295.5 | | | | | | |
| B lens | | II | 296.0 | | | | | | -41.3 |
| Footwall | | II | 320.0 | | -13.5 | | | 17.5 | |
| | | II | 259.0 | | -0.3 | | | 0.5 | |
| | | II | 220.2 | | -3.1 | | | 5.1 | |
| | | II | 335.2 | | -13.6 | | | 17.6 | |
| | | II | 289.0 | | | | | | -39.0 |
| | | II | 278.0 | | | | | | |
| 15L-1, 600mN | quartz | I | 194.1 | | -3.2 | | | 5.2 | |
| D lens | | I | 198.1 | | -2.8 | | | 4.6 | |
| Footwall | | II | 201.9 | | -20.1 | | | 22.7 | |
| | | II | 258.4 | | -11.6 | | | 15.6 | |
| | | II | 273.5 | | -13.1 | | | 17.1 | |
| | | II | 260.8 | | | | 2.2 | 13.0 | |
| R3492-20 @ 142' | quartz | II | 323.9 | | -5.9 | | | 9.1 | -36.1 |
| Pyrrhotite-pyrite | | II | 320.8 | | -5.0 | | | 7.9 | |
| zone, F(J) lens | | II | 330.8 | | -1.9 | | | 3.2 | |
| | | II | 224.7 | | -12.0 | | | 16.0 | |
| | | II | 219.8 | | | | | | |
| R3034-7 @ 100.5' | quartz | II | 273.1 | | -3.6 | | | 5.8 | |
| Pyrrhotite-pyrite | | II | 295.8 | | -11.6 | | | 15.6 | |
| zone, F(J) lens | | II | 330.0(d) | | | | | | |
| Sample No. | quartz | I | 188.8 | | -1.4 | | | 2.4 | |
| 16780-16L | | II | 221.5 | | | | | | |
| Tourmaline-quartz | | II | 185.1 | | | | | | |
| zone, F(J) lens | | II | 185.0 | | | | | | |
| | | II | 336.0 | | | | | | |
| | | II | 324.2 | | | | | | |
| | | II | 222.8 | | -4.2 | | | 6.7 | |
| | | II | 281.6 | | | | | | |
| | | II | 246.8 | | | | | | |
| | | II | 295.7 | | | | | | |
| 16L-3 between | quartz | II | 277.5 | | | | 4.2 | 10.3 | |
| G & H lens | | II | 332.2 | | | | 3.8 | 10.9 | |
| Tourmaline-quartz | | II | 333.4 | | | | 6.2 | 7.1 | |
| zone, F(J) lens | | II | 189.0 | | -2.0 | | | 3.4 | |
| KZFR-1, F lens | fluorite | II | 237.2 | | -1.1 | | | 1.9 | |
| fluorite vein | | | 245.5 | | | | | | |
| | | | 265.1 | | -3.7 | | | 6.0 | |
| | | | 244.5 | | | | | | |
| | | | 250.3 | | | | | | |
| | | | | | -2.3 | | | 3.9 | |

Th (L-V)-L = temperature of homogenisation into liquid phase
ThCO2(L-V)-V = temperature of homogenisation of CO2 into liquid phase
Tm-NaCl=decomposition temperature of NaCl
Tm-ice = temperature of last ice melting
Te-Ch = temperature of clathrate melting
(d) = temperature of decrepitation
1st-ice Tm = temperature of first ice melting

Salinity were calculated using equations of Potter et al. (1977), Potter et al. (1978) and Bozzo et al. (1973).

**APPENDIX 10.4. Fluid inclusion heating/freezing data for the different minerals from the South Hercules deposit, western Tasmania.**

| Sample No. | Mineral studied | Inclusion types | Th (L-V)-V | Tm-ice | Te-Ch | NaCl eq wt % | 1st-ice Tm |
|---|---|---|---|---|---|---|---|
| H1108-8 | fluorite | I | 145.3 | -0.5 | | 0.9 | |
| @ 42.8m | | I | 167.4 | -0.4 | | 0.7 | |
| 5670mN | | I | 172.3 | -0.9 | | 1.6 | |
| | | I | 170.3 | | | | |
| | | I | 170.8 | | | | |
| | | II | 148.7 | -16.2 | | 19.8 | |
| | | II | 149.6 | -15.5 | | 19.2 | -35.3 |
| | | II | 171.4 | | | | |
| | | II | 200.0 | -15.8 | | 19.5 | -45.0 |
| H1148-3 | fluorite | II | 175.0 | -4.2 | | 6.7 | -42.6 |
| @ 90.8m | | II | 169.5 | -4.5 | | 7.1 | -45.0 |
| 5600mN | | II | 170.9 | -5.8 | | 8.9 | |
| | | II | 172.0 | -0.8 | | 1.4 | |
| | | II | 177.9 | | | | |
| | | II | 181.5 | -4.2 | | 6.7 | -42.9 |
| | | II | 180.0 | -4.9 | | 7.7 | -39.9 |
| | | II | 172.6 | -3.4 | | 5.5 | |
| | | II | 165.4 | -3.9 | | 6.3 | |
| | | II | 142.2 | -2.7 | | 4.5 | |
| | | II | 192.7 | -10.4 | | 14.4 | -49.7 |
| | | II | 197.8 | -11.1 | | 15.1 | -40.0 |
| | | II | 181.0 | -5.5 | | 8.5 | -23.2 |
| | | II | 201.8 | -8.3 | | 12.1 | -29.5 |
| | | II | 172.5 | -8.1 | | 11.8 | -37.6 |
| | | II | 156.8 | -9.2 | | 13.1 | -41.2 |
| | | II | 182.3 | -5.0 | | 7.9 | |
| | | II | 188.5 | -9.7 | | 13.7 | |
| | | II | 154.2 | -8.1 | | 11.8 | -25.0 |
| | | II | 153.8 | -8.0 | | 11.7 | -31.0 |
| H1145-2B | Barite | I | 157.6 | -1.8 | | 3.1 | |
| @ 61.3m | | I | 167.2(d) | | | | |
| 5670mN | | I | 150.0 | | | | |
| | | I | 186.6 | -2.5 | | 4.2 | |
| | | I | 209.7 | -0.4 | | 0.6 | |
| | | I | 209.8 | -0.6 | | 1.0 | |
| | | I | 156.6 | -1.5 | | 2.6 | -44.0 |
| | | I | 161.0 | -0.3 | | 0.5 | |
| | | I | 209.9 | -0.4 | | 0.7 | |
| | | I | 173.9 | -0.4 | | 0.7 | |
| | | II | 210.6 | -4.0 | | 6.4 | |

Th (L-V)-V = temperature of homogenisation into liquid phase
Tm-ice = temperature of last ice melting
Te-Ch = temperature of clathrate melting
(d) = temperature of decrepitation
1st-ice Tm = temperature of first ice melting

Salinity were calculated using equations of Potter et al. (1977), Potter et al. (1978) and Bozzo et al. (1973).

**APPENDIX 10.4. Fluid inclusion heating/freezing data for the different minerals from the South Hercules deposit, western Tasmania (Continued).**

| Sample No. | mineral studied | Inclusion types | Th (L-V)-V | Tm-ice | Te-Ch | NaCl eq wt % | 1st-ice Tm |
|---|---|---|---|---|---|---|---|
| H1142-5 | sphalerite | I | 180.4 | | | | |
| @ 45.7m | | I | 182.5 | -0.2 | | 0.4 | |
| 5600mN | | I | 184.5 | | | | |
| | | I | 129.2 | -0.4 | | 0.7 | -38.0 |
| | | I | 150.0 | | | | |
| | | I | 148.8 | | | | |
| | | I | 131.2 | | | | |
| | | II | 124.0 | -4.4 | | 7.0 | |
| | | II | 173.5 | -2.5 | | 4.2 | -23.0 |
| | | II | 173.8 | | | | |
| | | II | 170.0 | | | | |
| | quartz | II | 147.9 | | | | |
| | | II | 169.7 | | | | |
| | | II | 174.7 | | | | |
| | | II | 139.3 | | | | |
| | | II | 166.0 | | | | |
| | | II | 142.0 | | | | |
| | | II | 185.0 | | | | |
| | | II | 149.5 | | | | |
| | | II | 209.0 | | | | |
| | | II | 138.4 | -8.9 | | 12.8 | -46.4 |
| | | II | 140.1 | -9.7 | | 13.6 | -27.5 |
| | | II | 150.1 | -0.4 | 2.0 | 13.3 | -27.3 |
| | | II | 144.5 | -2.8 | | 4.6 | -34.4 |
| | | II | 132.1 | -7.2 | | 10.7 | -34.8 |
| | | II | 151.3 | -7.3 | | 10.9 | -41.4 |
| | | II | 149.5 | -3.3 | | 5.3 | -43.3 |
| | | II | 153.6 | -6.8 | | 10.2 | -24.8 |
| | | II | 225.5 | | | | |
| | | II | 287.3 | | | | |
| | | II | 298.6 | -2.2 | | 3.7 | -24.5 |
| | | II | 268.8 | -0.3 | | 0.5 | |
| | | II | 267.4 | -2.2 | | 3.7 | |
| | | II | 296.6 | | | | |
| | | II | 250.1 | -3.4 | | 5.5 | |
| | | II | 299.5 | | | | |
| | | II | 298.0 | | | | |

Th (l-V)-V = temperature of homogenisation into liquid phase
Tm-ice = temperature of last ice melting
Te-Ch = temperature of clathrate melting
(d) = temperature of decrepitation
1st-ice Tm = temperature of first ice melting

Salinity were calculated using equations of Potter et al. (1977), Potter et al. (1978) and Bozzo et al. (1973).

**Table 1. Samples from Rosebery deposit, western Tasmania.**

| Catalogue No. | Field No. | Location | Sample type | Description | Sample prepared |
|---|---|---|---|---|---|
| 107541 | R1920-12 @ 1967' | 100mS, F(J) lens | R(DC), PT | Fine- to medium-grained garnet-biotite-tourmaline-pyrite assemblage | electron µprobe analysis>silicates |
| 107542 | 81R-10 @ 1221.0m | 200mS, F(J) lens | R(DC), PT | Medium-grained biotite-tourmaline-chlorite-sercite-pyrite assemblage | electron µprobe analysis>silicates |
| 107543 | 82R-7B @ 1195.4m | 200mS, F(J) lens | R(DC), PT | Dark green biotite-tourmaline-fluorite-magnetite-pyrite-quartz assemblage | electron µprobe analysis>silicates |
| 107544 | 88R-3A @ 1145.3m | 200mS, F(J) lens | R(DC), PT | Pink garnet-biotite flakes-magnetite-pyrite-pyrrhotite-fluorite assemblage> | electron µprobe analysis>silicates |
| | | | R(DC), F | Fluorite-tourmaline-magnetite vein in hangingwall volcanics> | FIPetrography>fluorite |
| 107545 | 88R-4A @ 1197.0m | 200mS, F(J) lens | R(DC), PT | Garnet-biotite-tourmaline-magnetite-pyrite-pyrrhotite-fluorite assemblage | electron µprobe analysis>silicates |
| 107546 | 88R-6 @ 1200.8m | 200mS, F(J) lens | R(DC), PT | Creamy garnet-pink helvite rhombs-biotite-tourmaline-magnetite-assemblage | electron µprobe analysis>silicates |
| | | | and F | Pink helvite rhombs and garnet from biotite-magnetite zone> | FIPetrography&LRS>helvite |
| 107547 | R3024-2 @ 104.0' | 220mS, F(J) lens | R(DC), PT | Medium grey, fine-grained chlorite-sericite-sulphide-carbonate assemblage> | electron µprobe analysis>silicates |
| | | | | Sphalerite-galena-chalcopyrite> | electron µprobe analysis>sphalerite |
| 107548 | R3024-3A @ 136.2' | 220mS, F(J) lens | R(DC), PT | Medium-grained biotite-tourmaline-chlorite-magnetite-pyrite assemblage> | electron µprobe analysis>silicates |
| | | | | Sphalerite-magnetite> | electron µprobe analysis>sphalerite |
| 107549 | R3024-3C @ 137.0' | 220mS, F(J) lens | R(DC), PT | Dark grey, fine-grained biotite-chlorite-sulphide assemblage> | electron µprobe analysis>silicates&gold |
| | | | | Sphalerite-pyrrhotite-pyrite> | electron µprobe analysis>sphalerite |
| 107550 | R3023-2 @ 125.0' | 270mS, F(J) lens | R(DC), PT | Dark grey, fine-grained biotite-chlorite-sericite-sulphide assemblage> | electron µprobe analysis>silicates |
| | | | | Sphalerite-pyrrhotite-pyrite-chalcopyrite> | electron µprobe analysis>sphalerite |
| 107551 | R3023-8 @ 146.0' | 270mS, F(J) lens | R(DC), PT | Green biotite-tourmaline-chlorite-magnetite-pyrite-carbonate assemblage> | electron µprobe analysis>silicates |
| | | | | Sphalerite-pyrrhotite-pyrite-magnetite> | electron µprobe analysis>sphalerite |
| 107552 | R3034-4 @ 78.0' | 270mS, F(J) lens | R(DC), PT | Dark grey, fine-grained biotite-chlorite-sericite-sulphide assemblage | electron µprobe analysis>silicates |
| 107553 | R3034-7 @ 100.5' | 270mS, F(J) lens | R(DC), PT | Medium-grained biotite-tourmaline-magnetite-pyrrhotite-pyrite assemblage | electron µprobe analysis>silicates&gold |
| | | | and F | Quartz-pyrrhotite-pyrite> | FIPetrography>quartz |
| 107554 | R3492-3B @ 50.8' | 280mS, F(J) lens | R(DC), PT | Dark grey, fine-grained chlorite-sericite-sulphide assemblage> | electron µprobe analysis>silicates |
| | | | | Sphalerite-chalcopyrite-pyrite-galena> | electron µprobe analysis>sphalerite |
| 107555 | R3492-17 @ 118.0' | 280mS, F(J) lens | R(DC), PT | Dark green biotite-tourmaline-pyrrhotite-pyrite assemblage | electron µprobe analysis>silicates&gold |
| 107556 | R3492-28 @ 177.0' | 280mS, F(J) lens | R(DC), PT | Dark green, fine-grained biotite-pyrite-pyrrhotite assemblage | electron µprobe analysis>silicates |
| | | | and F | Quartz-pyrrhotite-biotite-pyrite> | FIPetrography>quartz |
| 107557 | R3033-27 @ 161.0' | 300mS, F(J) lens | R(DC), PT | Fine-grained biotite-chlorite-pyrite assemblage | electron µprobe analysis>silicates&gold |
| 107558 | R3033-29 @ 165.0' | 300mS, F(J) lens | R(DC), PT | Dark green biotite-tourmaline-pyrrhotite-pyrite-sphalerite assemblage> | electron µprobe analysis>silicates |
| | | | | Sphalerite-pyrrhotite-pyrite> | electron µprobe analysis>sphalerite |
| 107559 | R1477-11 @ 1093.6' | 300mS, F(J) lens | R(DC), PT | Fine-grained biotite-chlorite-pyrite-fluorite assemblage> | electron µprobe analysis>silicates |
| | | | and F | Fluorite gash vein in chloritic footwall> | FIPetrography>fluorite |
| 107560 | 17L-H | 17 Level, F(J) lens | R(UG), PT | Pink rhomb-shaped helvite in dark green biotite-magnetite assemblage | electron µprobe analysis>silicates |

R=Hand specimen, DC=Drill core sample, UG=Underground sample, PT=Polished thin section, T=Thin section and F=Fluid inclusion plates
*Samples provided by D. L. Huston
FIPetrography=Fluid inclusion petrography and LRS=Laser Raman spectroscopic studies

**Table 1. Samples from Rosebery deposit, western Tasmania (Continued).**

| Catalogue No. | Field No. | Location | Sample type | Description | Sample prepared |
|---|---|---|---|---|---|
| 107561 | 1120mN-1, 15L | 15 Level, A&Blens | R(UG) | Blebby carbonate in strongly chloritic volcanic host rock | ∂C/∂O & trace element analysis>carbonate |
| 107562 | 1120mN-3, 15L | 15 Level, A&Blens | R(UG) | Blebby carbonate in sericitic and chloritic host rock with pyrite specks | ∂C/∂O & trace element analysis>carbonate |
| 107563 | 1120mN-4,15L | 15 Level, A&Blens | R(UG) | Spotty carbonate in cherty, sliceous volcanic host rock | ∂C/∂O & trace element analysis>carbonate |
| 107564 | 1250mN, 15L | 15 Level, A&Blens | R(UG) | Vein carbonate+chlorite+chalcopyrite in tuffaceous volcanic host rock | ∂C/∂O & trace element analysis>carbonate |
| 107565 | R3374@114.5m* | A&Blens | R(DC) | Massive pink carbonate associated with galena specks | ∂C/∂O & trace element analysis>carbonate |
| 107566 | R3394@175.3m* | A&Blens | R(DC) | Vein carbonate in pyritic, tuffaceous rock | ∂C/∂O & trace element analysis>carbonate |
| 107567 | R3421@116.5m* | A&Blens | R(DC) | Spotty carbonate in sericitic, tuffaceous volcanic host rock | ∂C/∂O & trace element analysis>carbonate |
| 107568 | R3456@288.5m* | A&Blens | R(DC) | Vein carbonate in sphalerite-galena-pyrite ore | ∂C/∂O & trace element analysis>carbonate, and ∂O>quartz |
| 107569 | R4297B@35.5m | A&Blens | R(DC) | Vein carbonate+chlorite+quartz in strongly chloritic volcanic host rock | ∂C/∂O & trace element analysis>carbonate, and ∂O>quartz and chlorite |
| 107570 | R4482@72.5m | A&Blens | R(DC) | Spherulitic carbonate in sericitic, chloritic volcanic rock | ∂C/∂O & trace element analysis>carbonate |
| 107571 | R4482A@72.8m | A&Blens | R(DC) | Vein carbonate+chlorite+quartz in sericitic, chloritic volcanic rock | ∂C/∂O & trace element analysis>carbonate, and ∂O>quartz and chlorite |
| 107572 | R3391 @ 145.8'* | A&Blens | R(DC) | Quartz with patches of sphalerite and galena and minor carbonate | ∂O analysis>quartz |
| 107573 | R4031 @ 61.7m | A&Blens | R(DC) | Green chlorite intercalated with dark brown sphalerite and pyrite spots | ∂O analysis>chlorite |
| 107574 | R4298 @ 46.7m | A&Blens | R(DC) | Dark green chlorite with pyritic sphalerite-galena ore | ∂O analysis>chlorite |
| 107575 | R4540 @ 46.3m | A&Blens | R(DC) | Chlorite altered tuffaceous volcaniclastic host rock | ∂O analysis>chlorite |
| 107576 | 15L-880mN | 15 Level, A&Blens | R(UG) | Quartz-chlorite vein in tuffaceous volcanic host rock | ∂O analysis>quartz&chlorite |
| 107577 | 17L-1 | 17 Level, F(J) lens | R(UG) | Spherulitic carbonate in sericitic, chloritic, tuffaceous host rock | ∂C/∂O & trace element analysis>carbonate |
| 107578 | R1477-5 @ 992' | 300mS, F(J) lens | R(DC) | Blebby carbonate in siliceous volcaniclastics | ∂C/∂O & trace element analysis>carbonate |
| 107579 | R1477-9 @ 1047' | 300mS, F(J) lens | R(DC) | Massive pink carbonate with minor quartz, sphalerite and galena | ∂C/∂O & trace element analysis>carbonate |
| 107580 | R1625 @ 1016' | 200mS, F(J) lens | R(DC) | Blebby pink carbonate in sericitic, tuffaceous volcanics | ∂C/∂O & trace element analysis>carbonate |
| 107581 | R1770-14 @ 1712' | 200mS, F(J) lens | R(DC) | Blebby or patchy carbonate in pyritic high-grade massive sulphide ore | ∂C/∂O & trace element analysis>carbonate |
| 107582 | R3011-25 @ 182' | 280mS, F(J) lens | R(DC) | Blebby brown carbonate in strongly chloritic volcanic host rock | ∂C/∂O & trace element analysis>carbonate |
| 107583 | R3024-4 @ 142' | 220mS, F(J) lens | R(DC) | Brecciated, blebby carbonate in pyritic, galena-sphalerite ore | ∂C/∂O & trace element analysis>carbonate |
| 107584 | R3034-10 @ 112' | 270mS, F(J) lens | R(DC) | Vein carbonate in siliceous volcanic host rock with galena specks | ∂C/∂O & trace element analysis>carbonate |
| 107585 | R3491-1 @ 17' | 300mS, F(J) lens | R(DC) | Massive pink carbonate associated with and pyrite cubes | ∂C/∂O & trace element analysis>carbonate |
| 107586 | R3024-7 @ 156.0' | 220mS, F(J) lens | R(DC) | Vein quartz with biotite and pyrite | ∂O analysis>quartz |
| 107587 | R3024-8 @ 156.6' | 220mS, F(J) lens | R(DC) | Vein quartz with green biotite and minor magnetite | ∂O analysis>biotite |
| 107588 | R3023-11 @ 163.0' | 270mS, F(J) lens | R(DC), T | Fine-grained biotite and quartz with pyrrhotite and chalcopyrite | ∂O analysis>quartz&biotite |
| 107589 | R3023-13 @ 165.0' | 270mS, F(J) lens | R(DC), T | Massive pyrite-pyrrhotite with quartz patches><br>Massive pyrite-pyrrhotite with quartz patches> | ∂O analysis>quartz<br>∂S analysis>pyrite&pyrrhotite |
| 107590 | R3034-5B @ 18.0' | 270mS, F(J) lens | R(DC) | Massive dark green biotite and magnetite | ∂O analysis>biotite |

R=Hand specimen, DC=Drill core sample, UG=Underground sample, PT=Polished thin section, T=Thin section and F=Fluid inclusion plates
*Samples provided by D. L. Huston
FIPetrography=Fluid inclusion petrography and LRS=Laser Raman spectroscopic studies

Table 1. Samples from Rosebery deposit, western Tasmania (Continued).

| Catalogue No. | Field No. | Location | Sample type | Description | Sample prepared |
|---|---|---|---|---|---|
| 107591 | R3334-6B @ 21.0' | 280mS, F(J) lens | R(DC), T | Fine-grained massive biotite intermixed with quartz | ∂O analysis>quartz&biotite |
| 107592 | R3334-9 @ 51.2' | 280mS, F(J) lens | R(DC) | Massive biotite | ∂O analysis>biotite |
| 107593 | R3334-11 @ 56.3' | 280mS, F(J) lens | R(DC), T | Quartz associated with pyrrhotite, pyrite and minor biotite | ∂O analysis>quartz |
| 107594 | R3011-10 @ 76.6' | 280mS, F(J) lens | R(DC), T | Fine-grained massive biotite | ∂O analysis>biotite |
| 107595 | R3164-8 @ 108.0' | 280mS, F(J) lens | R(DC), T | Massive dark green biotite with quartz patches | ∂O analysis>quartz&biotite |
| 107596 | R3492-4 @ 52.0' | 280mS, F(J) lens | R(DC) | Fine-grained massive biotite | ∂O analysis>biotite |
| 107597 | R3492-10 @ 82.0' | 280mS, F(J) lens | R(DC), T | Fine-grained massive biotite | ∂O analysis>biotite |
| 107598 | R3492-19B @ 140.0' | 280mS, F(J) lens | R(DC) | Massive biotite | ∂O analysis>biotite |
| 107599 | R3492-21 @ 143.0' | 280mS, F(J) lens | R(DC), T | Fine-grained massive biotite with quartz and pyrrhotite | ∂O analysis>quartz&biotite |
| 107600 | R3016-6 @ 64.0' | 300mS, F(J) lens | R(DC), T | Dark green massive biotite intermixed with quartz | ∂O analysis>quartz&biotite |
| 107601 | R3016-23C @ 207.0' | 300mS, F(J) lens | R(DC), T | Dark grey prismatic tourmaline associated with quartz | ∂O analysis>quartz&tourmaline |
| 107602 | R3016-27 @ 251.0' | 300mS, F(J) lens | R(DC), T | Dark green biotite with quartz and minor pyrite cubes | ∂O analysis>quartz&biotite |
| 107603 | R3033-22A @ 150.0' | 300mS, F(J) lens | R(DC), F | Coarse-grained magnetite and quartz with minor biotite and pyrite><br>Quartz-pyrite with minor tourmaline in biotite-magnetite zone> | ∂O analysis>quartz&magnetite<br>FIPetrography>quartz |
| 107604 | R3033-31A @ 170.0' | 300mS, F(J) lens | R(DC), F | Medium-grained green biotite with quartz and pyrite cubes><br>Medium-grained green biotite with quartz and pyrite cubes> | ∂O analysis>quartz&biotite<br>FIPetrography&LRS>quartz |
| 107605 | R3033-33 @ 181.0' | 300mS, F(J) lens | R(DC) | | ∂O analysis>quartz, biotite & tourmaline |
| 107606 | 15L-tm | 15 Level, F(J) lens | R(DC) | Banded thin tourmaline layers associated with quartz | ∂O analysis>quartz&tourmaline |
| 107607 | 16L-1 | 16 Level, H lens | R(DC) | Massive pyrite with quartz and tourmaline | ∂O analysis>quartz&tourmaline |
| 107608 | 106780 | 15 Level, F(J) lens | R(DC), F | Massive pyrite with quartz and tourmaline | ∂O analysis>tourmaline |
| 107609 | R4272 @ 41.7m | F(J) lens | R(DC) | Massive magnetite and biotite (chlorite) with minor pyrite and fluorite | ∂O analysis>biotite(chlorite)&magnetite |
| 107610 | R4372 @ 12.4m | F(J) lens | R(DC), T | Massive magnetite and biotite with minor pyrite and pyrrhotite | ∂O analysis>magnetite |
| 107611 | KZ-1, 100mS | 18 Level, F(J) lens | R(DC) | Banded magnetite and pyrite | ∂O analysis>magnetite |
| 107612 | R1920-1 @ 1800' | 100mS, F(J) lens | R(DC), T | Banded tourmaline and quartz | ∂O analysis>tourmaline |
| 107613 | R3023-12B @ 164.6' | 270mS, F(J) lens | R(DC) | Massive pyrite with minor pyrrhotite, quartz, biotite and magnetite | ∂S analysis>chalcopyrite |
| 107614 | R4259-1 @ 71.6m | F(J) lens | R(DC) | Massive pyrite, hematite and barite assemblages | ∂S analysis>pyrite |
| 107615 | KZ-3, 300mS | 16/2 Level, F lens | R(UG) | Massive sphalerite-galena ore transgressed by pyrrhotite-pyrite assemblage | ∂S analysis>bulk sulphides |
| 107616 | 17L-2 | 12mN, Glens | R(UG), F | Carbonate spheroids and barite with minor quartz in hangingwall volcanics | FIPetrography&LRS>carbonate&barite |
| 107617 | 19L-1 | 125mN, E lens | R(UG), F | Irregular quartz-carbonate vein in hangingwall volcanics | FIPetrography>quartz |
| 107618 | 16L-2 | 35mN, E lens | R(UG), F | Massive sphalerite and galena with barite and minor quartz in ore zone | FIPetrography&LRS>barite&sphalerite |
| 107619 | 16L-3 | between G&H lens | R(UG), F | Irregular quartz-hematite vein with minor pyrite in ore zone | FIPetrography>quartz&carbonate |
| 107620 | R3808 @ 153m | H lens | R(DC), F | Barite with minor pyrite and galena in barite ore zone | FIPetrography&LRS>barite |

R=Hand specimen, DC=Drill core sample, UG=Underground sample, PT=Polished thin section, T=Thin section and F=Fluid inclusion plates
*Samples provided by D. L. Huston
FIPetrography=Fluid inclusion petrography and LRS=Laser Raman spectroscopic studies

**Table 1. Samples from Rosebery deposit, western Tasmania (Continued).**

| Catalogue No. | Field No. | Location | Sample type | Description | Sample prepared |
|---|---|---|---|---|---|
| 107621 | R4174 @ 33m | F(J) lens | R(DC), F | Barite and sphalerite patches in crudely banded massive sulphide ore | FIPetrography>barite&sphalerite |
| 107622 | R1526 @ 1046' | F(J) lens | R(DC), F | Dark brown sphalerite with minor quartz in ore zone | FIPetrography>sphalerite |
| 107623 | R4407 @ 0.9m | B lens | R(DC), F | Quartz-pyrite-chalcopyrite vein in chloritic footwall volcanics | FIPetrography&LRS>quartz |
| 107624 | R4406 @ 105.5m | B lens | R(DC), F | Quartz-pyrite-chalcopyrite-sphalerite vein in chloritic footwall volcanics | FIPetrography>quartz |
| 107625 | 15L-1 | 600mN, D lens | R(UG), F | Thin quartz-chalcopyrite vein in footwall massive pyrite zone | FIPetrography&LRS>quartz |
| 107626 | 17L-3 | G lens | R(UG), F | Quartz interclated with chalcopyrite, sphalerite, galena in footwall volcanics | FIPetrography>quartz |
| 107627 | 15L-2 | 300mN, G lens | R(UG), F | Remobilised quartz-carbonate vein with minor galena and pyrite | FIPetrography>quartz&carbonate |
| 107628 | 16L-4 | 400mN, H lens | R(UG), F | Irregular remobilised quartz vein with minor sphalerite and galena cubes | FIPetrography&LRS>quartz |
| 107629 | R4495 @ 52.2m | H lens | R(DC), F | Sphalerite in remobilised quartz-sphalerite vein with pink carbonate | FIPetrography&LRS>sphalerite |
| 107630 | KZFR-1 | F(J) lens | R(UG), F | Late fluorite-carbonate vein cutting biotite-magnetite assemblages | FIPetrography>fluorite |
| 107631 | R3492-20 @ 142' | F(J) lens | R(UG), F | Quartz-pyrite-pyrrhotite-minor biotite assemblages | FIPetrography>quartz |
| 107632 | R3391-100.5m* | A & B Lens | R(DC), PT | Sphalerite-pyrite-galena-chalcopyrite | electron μprobe analysis>sphalerite |
| 107633 | R3391-122m* | A & B Lens | R(DC), PT | Sphalerite-pyrite-galena | electron μprobe analysis>sphalerite |
| 107634 | R3391-133.8m* | A & B Lens | R(DC), PT | Sphalerite-pyrite-galena | electron μprobe analysis>sphalerite |
| 107635 | R3391-138.5m* | A & B Lens | R(DC), PT | Sphalerite-galena-pyrite | electron μprobe analysis>sphalerite |
| 107636 | R3391-140m* | A & B Lens | R(DC), PT | Sphalerite-galena-pyrite | electron μprobe analysis>sphalerite |
| 107637 | R3391-142.5m* | A & B Lens | R(DC), PT | Sphalerite-chalcopyrite-pyrite | electron μprobe analysis>sphalerite |
| 107638 | R3391-145m* | A & B Lens | R(DC), PT | Sphalerite-pyrite-galena-chalcopyrite | electron μprobe analysis>sphalerite |
| 107639 | R3391-164m* | A & B Lens | R(DC), PT | Sphalerite-barite | electron μprobe analysis>sphalerite |
| 107640 | R3391-166m* | A & B Lens | R(DC), PT | Sphalerite-barite | electron μprobe analysis>sphalerite |
| 107641 | R3394-147.5m* | A & B Lens | R(DC), PT | Sphalerite-galena-pyrite | electron μprobe analysis>sphalerite |
| 107642 | R3394-175m* | A & B Lens | R(DC), PT | Sphalerite-barite | electron μprobe analysis>sphalerite |
| 107643 | R3382-117m* | A & B Lens | R(DC), PT | Sphalerite-galena-pyrite | electron μprobe analysis>sphalerite |
| 107644 | R3382-270m* | A & B Lens | R(DC), PT | Sphalerite-barite | electron μprobe analysis>sphalerite |
| 107645 | R3397-129m* | A & B Lens | R(DC), PT | Sphalerite-pyrite-galena | electron μprobe analysis>sphalerite |
| 107646 | R3397-140.5m* | A & B Lens | R(DC), PT | Sphalerite-barite | electron μprobe analysis>sphalerite |
| 107647 | R3397-147m* | A & B Lens | R(DC), PT | Sphalerite-barite | electron μprobe analysis>sphalerite |
| 107648 | R3394-181m* | A & B Lens | R(DC), PT | Sphalerite-galena-pyrite | electron μprobe analysis>sphalerite |
| 107649 | R4340-15.6m* | A & B Lens | R(DC), PT | Sphalerite-pyrite | electron μprobe analysis>sphalerite |
| 107650 | R3382-265m* | A & B Lens | R(DC), PT | Sphalerite-pyrite | electron μprobe analysis>sphalerite |
| 107651 | R4055-9.9m | A & B Lens | R(DC), PT | Sphalerite-pyrite | electron μprobe analysis>sphalerite |
| 107652 | R4291-62.1m | A & B Lens | R(DC), PT | Sphalerite-pyrite | electron μprobe analysis>sphalerite |
| 107653 | R4289-73.0m | A & B Lens | R(DC), PT | Sphalerite-pyrite | electron μprobe analysis>sphalerite |
| 107654 | R4296-51.4m | A & B Lens | R(DC), PT | Sphalerite-pyrite | electron μprobe analysis>sphalerite |
| 107655 | R4296-54.4m | A & B Lens | R(DC), PT | Sphalerite-pyrite | electron μprobe analysis>sphalerite |
| 107656 | KZ-2 | 18L, H lens | R(DC) | Biotite-magnetite with recrystallised pyrite cubes | |
| 107657 | KZ-4 | 16/1 level, Flens | R(DC) | Pyrrhotite-pyrite assemblages cut by tourmaline-quartz vein | |

R=Hand specimen, DC=Drill core sample, UG=Underground sample, PT=Polished thin section, T=Thin section and F=Fluid inclusion plates
*Samples provided by D. L. Huston
FIPetrography=Fluid inclusion petrography and LRS=Laser Raman spectroscopic studies

**Table 2. Samples from Hercules and South Hercules deposits, western Tasmania.**

| Catalogue No. | Field No. | Location | Sample type | Description | Sample preparation |
|---|---|---|---|---|---|
| 107660 | H802 @ 114' | 243.8mN, R lens, Hercules | R(DC) | Massive pink carbonate associated with quartz and chlorite | ∂C/∂O & trace element analysis>carbonate |
| 107661 | H802 @ 71' | 243.8mN, R lens, Hercules | R(DC) | Vein pink carbonate associated with minor green chloritic flakes | ∂C/∂O & trace element analysis>carbonate |
| 107662 | H802A @ 71' | 243.8mN, R lens, Hercules | R(DC) | Massive carbonate associated with minor green chloritic flakes | ∂C/∂O & trace element analysis>carbonate |
| 107663 | H1032-4B @ 200' | 91.4mN, R lens, Hercules | R(DC) | Blebby or patchy carbonate with chlorite and quartz | ∂C/∂O & trace element analysis>carbonate |
| 107664 | H831-4B @ 80' | 188.9mN, R lens, Hercules | R(DC) | Massive pink carbonate with quartz and chlorite | ∂C/∂O & trace element analysis>carbonate |
| 107665 | H1033-2 @ 120' | 30.5mS, J(K) lens, Hercules | R(DC) | Spotty carbonate with dark green chlorite and cut by quartz vein | ∂C/∂O & trace element analysis>carbonate and ∂O analysis>quartz&chlorite |
| 107666 | H1062-4A @ 199' | 30.5mS, P lens, Hercules | R(DC) | Spotty carbonate with dark green chlorite flakes | ∂C/∂O & trace element analysis>carbonate and ∂O analysis>quartz&chlorite |
| 107667 | M lens | from Glory Hole, Hercules | R(Sur) | Massive carbonate with chlorite and fluorite | ∂C/∂O & trace element analysis>carbonate |
| 107668 | H1108-1 @ 29.5m | 5670mN, South Hercules | R(DC) | Massive carbonate associated with semi-massive pyrite | ∂C/∂O & trace element analysis>carbonate |
| 107669 | H1108-1A @ 29.5m | 5670mN, South Hercules | R(DC) | Pink carbonate in quartz-carbonate vein cutting volcanic host rock | ∂C/∂O & trace element analysis>carbonate and ∂O analysis>quartz |
| 107670 | H1132-5 @ 74.0m | 5585mN, South Hercules | R(DC) | Cannon ball pink carbonate in silicelous ore with fluorite specks | ∂C/∂O & trace element analysis>carbonate and ∂O analysis>chlorite |
| 107671 | H1132-3 @ 64.0m | 5585mN, South Hercules | R(DC) | Massive carbonate in siliceous, tuffaceous host rock | ∂C/∂O & trace element analysis>carbonate |
| 107672 | H1142-5 @ 45.7m | 5600mN, South Hercules | R(DC) | Vein pink carbonate with quartz, tetrahedrite, and sphalerite blebs | ∂C/∂O & trace element analysis>carbonate |
| 107673 | H1117-B @ 21.0m | 5600mN, South Hercules | R(DC) | Blebby pink carbonate in pyritic, tuffaceous host rock | ∂C/∂O & trace element analysis>carbonate |
| 107674 | H1108-4 @ 38.2m | 5670mN, South Hercules | R(DC) | Coalesced spherulitic carbonate in chloritic host rock | ∂C/∂O & trace element analysis>carbonate |
| 107675 | H1108-3 @ 34.5m | 5670mN, South Hercules | R(DC) | Vein pink carbonate in pyritic, tuffaceous host rock | ∂C/∂O & trace element analysis>carbonate |
| 107676 | H1108-3A @ 34.5m | 5670mN, South Hercules | R(DC) | Massive carbonate cut by quartz-carbonate vein | ∂C/∂O & trace element analysis>carbonate |
| 107677 | H1108-10 @ 50.2m | 5670mN, South Hercules | R(DC) | Spherulitic carbonate in siliceous volcanics with minor pyrites | ∂C/∂O & trace element analysis>carbonate |
| 107678 | H1108-10A @ 50.2m | 5670mN, South Hercules | R(DC) | Vein pink carbonate with pyrite and fluorite specks | ∂C/∂O & trace element analysis>carbonate and ∂O analysis>chlorite |
| 107679 | H1108-3B @ 35.2m | 5670mN, South Hercules | R(DC) | Massive carbonate associated with siliceous, pyritic volcanics | ∂C/∂O & trace element analysis>carbonate |
| 107680 | H831-14A @ 112.0' | 188.9mN, R lens, Hercules | R(DC) | Dark green, cleaved chlorite and quartz with pyrite specks | ∂O analysis>quartz&chlorite |
| 107681 | H1008-22 @ 122.5' | 30.5mS, J(K) lens, Hercules | R(DC) | Chlorite flakes with quartz and minor carbonate | ∂O analysis>quartz&chlorite |
| 107682 | H1034-5 @ 119.2' | 45.7mS, J(K) lens, Hercules | R(DC) | Quartz patches with chalcopyrite in volcanic host rock | ∂O analysis>quartz |
| 107683 | H1106-2 @ 36.5m | 5600mN, South Hercules | R(DC) | Quartz-pink carbonate vein in siliceous host rock | ∂O analysis>quartz |
| 107684 | H1117-A @ 21.0m | 5600mN, South Hercules | R(DC) | Cherty quartz intermixed with colloform pyrite | ∂O analysis>cherty quartz |
| 107685 | H1117-1 @ 28.2m | 5600mN, South Hercules | R(DC) | Cherty quartz intermixed with colloform pyrite | ∂O analysis>cherty quartz |
| 107686 | H1118-15 @ 32.7m | 5630mN, South Hercules | R(DC) | Stringery quartz-sulphide vein in silicified host rock | ∂O analysis>quartz |
| 107687 | H1129-8 @ 84.3m | 5720mN, South Hercules | R(DC) | Quartz associated with chlorite flakes in host hock | ∂O analysis>quartz |
| 107688 | H1142-4B @ 45.5m | 5600mN, South Hercules | R(DC) | Quartz-carbonate vein in sericitic, carbonate altered host rock | ∂O analysis>quartz |

R=Hand specimen, and DC=Drill core sample

Table 2. Samples from Hercules and South Hercules deposits, western Tasmania (Continued).

| Catalogue No. | Field No. | Location | Sample type | Description | Sample preparation |
|---|---|---|---|---|---|
| 107689 | H1114-4 @ 36.3m | 5630mN, South Hercules | R(DC) | Spotty sphalerite blebs with fluorite gash vein | ∂S analysis>sphalerite |
| 107690 | H1114-16B @ 59.0m | 5630mN, South Hercules | R(DC) | Massive sphalerite-galena ore | ∂S analysis>sphalerite |
| 107691 | H1117-C @ 24.3m | 5600mN, South Hercules | R(DC) | Massive pyrite | ∂S analysis>pyrite |
| 107692 | H1117-2 @ 29.5m | 5600mN, South Hercules | R(DC) | Semi-massive, colloform pyrite with minor sphalerite and galena | ∂S analysis>pyrite |
| 107693 | H1118-13 @ 29.9m | 5630mN, South Hercules | R(DC) | Massive pyrite with minor sphalerite and galena | ∂S analysis>galena |
| 107694 | H1118-16 @ 33.0m | 5630mN, South Hercules | R(DC) | Sphalerite blebs in siliceous stringery ore | ∂S analysis>sphalerite |
| 107695 | H1163-2 @ 67.5m | 5630mN, South Hercules | R(DC) | Colloform pyrite with minor fluorite | ∂S analysis>pyrite |
| 107696 | H1142-2 @ 43.0m | 5600mN, South Hercules | R(DC) | Massive pyrite with minor sphalerite and galena | ∂S analysis>pyrite |
| 107697 | H1142-3 @ 44.3m | 5600mN, South Hercules | R(DC) | Massive pyrite with minor sphalerite and galena | ∂S analysis>pyrite |
| 107698 | H1142-4A @ 45.5m | 5600mN, South Hercules | R(DC) | Sphalerite and tetrahedrite with minor sulphide | ∂S analysis>sphalerite&terahedrite |
| 107699 | H1145-2A @ 61.3m | 5670mN, South Hercules | R(DC) | Massive pyrite with barite patches | ∂S analysis>pyrite |
| 107700 | H1148-2 @ 89.5m | 5600mN, South Hercules | R(DC) | Spotty sphalerite blebs rimmed by sericite in stringery ore | ∂S analysis>sphalerite |
| 107701 | H1032-5 @ 202' 4" | 91.4mN, R lens, Hercules | R(DC), F | Quartz vein with chlorite-chalcopyrite-carbonate in host rock | FIPetrography>quartz |
| 107702 | H1032-6C @ 203' | 91.4mN, R lens, Hercules | R(DC), F | Quartz-sphalerite-chalcopyrite in ore zone | FIPetrography>quartz&sphalerite |
| 107703 | H1034-2 @ 109' | 45.7mS, J(K) lens, Hercules | R(DC), F | Quartz-pyrite-dark sphalerite-chalcopyrite in ore zone | FIPetrography>quartz |
| 107704 | H1034-5 @ 119' 2" | 45.7mS, J(K) lens, Hercules | R(DC), F | Quartz-pyrite-chalcopyrite in ore zone | FIPetrography>quartz |
| 107705 | H1062-1 @ 185' | 30.5mS, P lens, Hercules | R(DC), F | Fluorite gashes with quartz and pyrite in sericitic, chloritic host rock | FIPetrography>fluorite |
| 107706 | H1062-4A @ 199' | 30.5mS, P lens, Hercules | R(DC), F | Spherulitic carbonate-quartz-chlorite-fluorite vein | FIPetrography>carbonate |
| 107707 | H-1450N/200W | G lens, Hercules | R(Sur), F | Barite with pyrite from G lens | FIPetrography>barite |
| 107708 | H1132-2 @ 62.2m | 5585mN, South Hercules | R(DC), F | Vein fluorite in siliceous, stringery sulphide ore zone | FIPetrography&LRS>fluorite |
| 107709 | H1142-5 @ 45.7m | 5600mN, South Hercules | R(DC), F | Quartz-carbonate-sphalerite-tetrahedrite vein in siliceous, stringer ore | FIPetrography&LRS>quartz&sphalerite |
| 107710 | H1148-3 @ 90.8m | 5600mN, South Hercules | R(DC), F | Fluorite with pyrite, chlorite, galena and carbonate in ore zone | FIPetrography>fluorite |
| 107711 | H1114-5 @ 36.6m | 5630mN, South Hercules | R(DC), F | Vein fluorite in siliceous, stringery sulphide ore zone | FIPetrography&LRS>fluorite |
| 107712 | H1114-13 @ 50.0m | 5630mN, South Hercules | R(DC), F | Fluorite and sphalerite with galena and sulphosalt in siliceous ore | FIPetrography&LRS>fluorite&sphalerite |
| 107713 | H1163-3 @ 68.0m | 5630mN, South Hercules | R(DC), F | Fluorite spots in massive pyrite zone with minor arsenopyrite | FIPetrography>fluorite |
| 107714 | H1108-2 @ 30.3m | 5670mN, South Hercules | R(DC), F | Quartz-carbonate vein in massive carbonate zone | FIPetrography>quartz |
| 107715 | H1108-8 @ 42.8m | 5670mN, South Hercules | R(DC), F | Fluorite-pyrite-sphalerite-galena-sericite-quartz in sulphide ore zone | FIPetrography>fluorite |
| 107716 | H1108-9A @ 46.0m | 5670mN, South Hercules | R(DC), F | Carbonate-quartz-sericite in sheared colloform pyrite zone | FIPetrography>carbonate |
| 107717 | H1145-2A @ 61.3m | 5670mN, South Hercules | R(DC), F | Massive barite with pyrite-gold-carbonate-sulphosalt at top of ore lens | FIPetrography>barite |
| 107718 | H1100-1 @ 29.5m | 5720mN, South Hercules | R(DC), F | Barite-pyrite in siliceous tuffaceous host rock | FIPetrography>barite |
| 107719 | H1100-2 @ 63.5m | 5720mN, South Hercules | R(DC), F | Barite in massive pyrite-barite zone | FIPetrography>barite |
| 107720 | H1129-5 @ 81.5m | 5720mN, South Hercules | R(DC), F | Fluorite-pyrite-sphalerite-sericite in siliceous ore zone | FIPetrography>fluorite |

R=Hand specimen, DC=Drill core sample, and Sur=Surface sample
F=Fluid inclusion plates, FIP=Fluid inclusion petrography
and LRS=Laser Raman spectroscopic studies

Table 2. Samples from Hercules and South Hercules deposits, western Tasmania (Continued).

| Catalogue No. | Field No. | Location | Sample type | Description | Sample preparation |
|---|---|---|---|---|---|
| 107721 | H145 @ 227.0' | R lens, Hercules | R(DC), PT | Sphalerite-galena-gold-pyrite assemblage in ore zone | electron μprobe analysis>sphalerite&gold |
| 107722 | H1033-6 @ 131.0' | Hercules | R(DC), PT | Massive sphalerite ore | electron μprobe analysis>sphalerite |
| 107723 | H802-1 @ 30.6' | Hercules | R(DC), PT | Sphalerite-pyrite in ore zone | electron μprobe analysis>sphalerite |
| 107724 | H831-9 @ 95.5' | Hercules | R(DC), PT | Sphalerite-pyrite in ore zone | electron μprobe analysis>sphalerite |
| 107725 | H1034-4 @ 119.0' | Hercules | R(DC), PT | Sphalerite-pyrite in ore zone | electron μprobe analysis>sphalerite |
| 107726 | H794-2 @ 37.0' | Hercules | R(DC), PT | Massive sphalerite and pyrite | electron μprobe analysis>sphalerite |
| 107727 | H1106 @ 28.5m | 5600mN, South Hercules | R(DC), PT | Blebby sphalerite and pyrite in ore zone | electron μprobe analysis>sphalerite |
| 107728 | H1117-8 @ 48.1m | 5600mN, South Hercules | R(DC), PT | Recrystallised? dark brown sphalerite with pyrite | electron μprobe analysis>sphalerite&gold |
| 107729 | H1142-2 @ 43.0m | 5600mN, South Hercules | R(DC), PT | Sphalerite-galena-gold-pyrite assemblage in ore zone | electron μprobe analysis>sphalerite&gold |
| 107730 | H1142-4 @ 45.5m | 5600mN, South Hercules | R(DC), PT | Coarse-grained, light brown sphalerite-tetrahedrite-gold assemblage | electron μprobe analysis>sphalerite |
| 107731 | H1148-2 @ 89.4m | 5600mN, South Hercules | R(DC), PT | Sphalerite-galena-gold-chalcopyrite assemblage in ore zone | electron μprobe analysis>sphalerite&gold |
| 107732 | H1114-4 @ 36.3m | 5630mN, South Hercules | R(DC), PT | Sphalerite-gold-pyrite assemblage in ore zone | electron μprobe analysis>sphalerite&gold |
| 107733 | H1114-5 @ 36.6m | 5630mN, South Hercules | R(DC), PT | Sphalerite-gold assemblage in ore zone | electron μprobe analysis>sphalerite&gold |
| 107734 | H1118-13 @ 29.9m | 5630mN, South Hercules | R(DC), PT | Sphalerite-gold assemblage in ore zone | electron μprobe analysis>sphalerite&gold |
| 107735 | H1145-2A @ 61.3m | 5670mN, South Hercules | R(DC), PT | Sphalerite-tetrahedrite-quartz-gold assemblage in ore zone | electron μprobe analysis>sphalerite |
| 107736 | H1129-2 @ 79.8m | 5720mN, South Hercules | R(DC), PT | Sphalerite-gold-pyrite assemblage in ore zone | electron μprobe analysis>sphalerite |
| 107737 | H1145-2B @ 61.3m | 5670mN, South Hercules | R(DC), PT | Sphalerite-tetrahedrite-quartz-gold assemblage in ore zone | electron μprobe analysis>gold |
| 107738 | H1117-3 @ 30.1m | 5600mN, South Hercules | R(DC) | Colloform massive pyrite | |
| 107739 | H1142-3 @ 62.3m | 5600mN, South Hercules | R(DC) | Prismatic barite crystal in semi-massive pyrite | |
| 107740 | H1142-4 @ 62.5m | 5600mN, South Hercules | R(DC) | Prismatic barite crystal in semi-massive pyrite | |
| 107741 | H1142-5 @ 70.3m | 5600mN, South Hercules | R(DC) | Colloform pyrite in massive barite | |
| 107742 | H1142-6 @ 49.6m | 5600mN, South Hercules | R(DC) | Carbonate spheroids in chloritic, sericitic host rock | |
| 107743 | H1164-1 @ 94.2m | 5630mN, South Hercules | R(DC) | Sheared massive pyrite | |

R=Hand specimen, and DC=Drill core sample
PT=Polished thin section